

SOILS and ROCKS

An International Journal of Geotechnical and Geoenvironmental Engineering

Editor

Renato Pinto da Cunha
University of Brasília, Brazil

Co-editor

Ana Vieira
National Laboratory for Civil Engineering, Portugal

Associate Editors

António Alberto S. Correia
University of Coimbra, Portugal

Cristiana Ferreira
University of Porto, Portugal

Fernando Feitosa Monteiro
Unichristus, Brazil

Gilson de F. N. Gitirana Jr.
Federal University of Goiás, Brazil

José A. Schiavon
Aeronautics Institute of Technology, Brazil

Juliane Marques
Federal University of Alagoas / AGM, Brazil

Karina C. Arruda Dourado
Federal Institute of Pernambuco, Brazil

Leandro Neves Duarte
Federal University of São João del-Rei, Brazil

Luciano Soares da Cunha
University of Brasília, Brazil

Luis Araújo Santos
Polytechnic Institute of Coimbra, Portugal

Marcio Leão
Federal University of Viçosa / IBMEC-BH, Brazil

Margarida Pinho Lopes
University of Aveiro, Portugal

Neusa M. B. Mota
University Center of Brasília, Brazil

Nuno Cristelo
University of Trás-os-Montes and Alto Douro, Portugal

Paulo J. R. Albuquerque
Campinas State University, Brazil

Rui Carrilho Gomes
Technical University of Lisbon, Portugal

Sara Rios
University of Porto, Portugal

Silvrano Adonias Dantas Neto
Federal University of Ceará, Brazil

Teresa M. Bodas Freitas
Technical University of Lisbon, Portugal

Advisory Panel

Alejo O. Sfriso
University of Buenos Aires, Argentina

Harry Poulos
University of Sidney, Australia

Luis A. Vallejo
Complutense University of Madrid, Spain

Emanuel Maranhã das Neves
Technical University of Lisbon, Portugal

Michele Jamiolkowski
Studio Geotecnico Italiano, Italy

Roger Frank
École des Ponts ParisTech, France

Willy Lacerda
Federal University of Rio de Janeiro, Brazil

Editorial Board

Abdelmalek Bouazza
Monash University, Australia

Alessandro Mandolini
University of Naples Federico II, Italy

Alessio Ferrari
École Polytechnique Fédérale de Lausanne, Switzerland

Antônio Roque
National Laboratory for Civil Engineering, Portugal

Antônio Viana da Fonseca
University of Porto, Portugal

Armando Antão
NOVA University Lisbon, Portugal

Beatrice Baudet
University College of London, UK

Catherine O'Sullivan
Imperial College London, UK

Cristhian Mendoza
National University of Colombia, Colombia

Cristina Tsuha
University of São Paulo at São Carlos, Brazil

Daniel Dias
Antea Group / Grenoble-Alpes University, France

Debasis Roy
Indian Institute of Technology Kharagpur, India

Denis Kalumba
Cape Town University, South Africa

Fangwei Yu
Inst. Mt. Haz. Env. Chinese Acad. of Sci. China

Ian Schumann M. Martins
Federal University of Rio de Janeiro, Brazil

Jean Rodrigo Garcia
Federal University of Uberlândia, Brazil

José Muralha
National Laboratory for Civil Engineering, Portugal

Kátia Vanessa Bicalho
Federal University of Espírito Santo, Brazil

Krishna R. Reddy
University of Illinois at Chicago, USA

Limin Zhang
The Hong Kong Univ. of Science Technology, China

Márcio de Souza Soares de Almeida
Federal University of Rio de Janeiro, Brazil

Marcelo Javier Sanchez Castilla
Texas A&M University College Station, USA

Marco Barla
Politecnico di Torino, Italy

Marcos Arroyo
Polytechnic University of Catalonia, Spain

Marcos Massao Futai
University of São Paulo, Brazil

Maria de Lurdes Lopes
University of Porto, Portugal

Maurício Martines Sales
Federal University of Goiás, Brazil

Nilo Cesar Consoli
Federal University of Rio Grande do Sul, Brazil

Olavo Francisco dos Santos Júnior
Federal University of Rio Grande do Norte, Brazil

Orianne Jenck
Grenoble-Alpes University, France

Paulo Venda Oliveira
University of Coimbra, Portugal

Pijush Samui
National Institute of Technology Patna, India

Rafaela Cardoso
Technical University of Lisbon, Portugal

Roberto Quental Coutinho
Federal University of Pernambuco, Brazil

Sai K. Vanapalli
University of Ottawa, Canada

Samir Maghous
Federal University of Rio Grande do Sul, Brazil

Satoshi Nishimura
Hokkaido University, Japan

Siang Huat Goh
National University of Singapore, Singapore

Tácio Mauro Campos
Pontifical Catholic University of Rio de Janeiro, Brazil

Tiago Miranda
University of Minho, Portugal

Zhen-Yu Yin
Hong Kong Polytechnic University, China

Zhongxuan Yang
Zhejiang University, China

Honorary Members

André Pacheco de Assis
Clovis Ribeiro de M. Leme (in memoriam)

Delfino L. G. Gambetti
Eduardo Soares de Macedo

Ennio Marques Palmeira
Eraldo Luporini Pastore

Francisco de Rezende Lopes
Francisco Nogueira de Jorge

Jaime de Oliveira Campos
João Augusto M. Pimenta

José Carlos A. Cintra
José Carlos Virgili

José Couto Marques
José Jorge Nader

José Maria de Camargo Barros
Manuel Matos Fernandes

Maurício Abramento
Maurício Erlich

Newton Moreira de Souza
Orencio Monje Villar

Osni José Pejon
Paulo Eduardo Lima de Santa Maria

Paulo Scarano Hemi
Ricardo Oliveira

Ronaldo Rocha
Rui Taiji Mori (in memoriam)

Susumu Niyama
Vera Cristina Rocha da Silva

Waldemar Coelho Hachich
Willy Lacerda

Soils and Rocks publishes papers in English in the broad fields of Geotechnical Engineering, Engineering Geology, and Geoenvironmental Engineering. The Journal is published quarterly in March, June, September and December. The first issue was released in 1978, under the name *Solos e Rochas*, being originally published by the Graduate School of Engineering of the Federal University of Rio de Janeiro. In 1980, the Brazilian Association for Soil Mechanics and Geotechnical Engineering took over the editorial and publishing responsibilities of *Solos e Rochas*, increasing its reach. In 2007, the journal was renamed Soils and Rocks and acquired the status of an international journal, being published jointly by the Brazilian Association for Soil Mechanics and Geotechnical Engineering, by the Portuguese Geotechnical Society, and until 2010 by the Brazilian Association for Engineering Geology and the Environment.

Soils and Rocks

1978,	1 (1, 2)
1979,	1 (3), 2 (1,2)
1980-1983,	3-6 (1, 2, 3)
1984,	7 (single number)
1985-1987,	8-10 (1, 2, 3)
1988-1990,	11-13 (single number)
1991-1992,	14-15 (1, 2)
1993,	16 (1, 2, 3, 4)
1994-2010,	17-33 (1, 2, 3)
2011,	34 (1, 2, 3, 4)
2012-2019,	35-42 (1, 2, 3)
2020,	43 (1, 2, 3, 4)
2021,	44 (1, 2, 3, 4)
2022,	45 (1,2,

ISSN 1980-9743
ISSN-e 2675-5475

CDU 624.131.1

Soils and Rocks

An International Journal of Geotechnical and Geoenvironmental Engineering
ISSN 1980-9743 ISSN-e 2675-5475

Publication of

ABMS - Brazilian Association for Soil Mechanics and Geotechnical Engineering
SPG - Portuguese Geotechnical Society
Volume 45, N. 2, April-June 2022

Table of Contents

ARTICLES

Comparative analysis of non-recursive three-dimensional (3D) modifications of Hoek-Brown failure criterion
Nnamdi Emmanuel Ezendiokwere, Ogbonna Friday Joel, Victor Joseph Aimikhe, Adewale Dosunmu

Evaluation of stress history and undrained shear strength of three marine clays using semi-empirical methods based on Piezocone Test
Danielle Caroline Ferreira, Faïçal Massad

A numerical approach to evaluating the asymmetric ground settlement response to twin-tunnel asynchronous excavation
Alireza Seghateh Mojtahedi, Ali Nabizadeh

Mechanical behavior analysis of polymer stabilized gold ore tailings
Giovanna Monique Alelvan, Michéle Dal Toé Casagrande, Nilo Cesar Consoli

The structure of tropical lateritic soils as an impacting factor in the shape of soil-water characteristic curves
Alana Dias de Oliveira, Flávia Gonçalves Pissinati Pelaquim, Renan Felipe Braga Zanin,
Thadeu Rodrigues de Melo, João Tavares Filho, Avacir Casanova Andreello, Raquel Souza Teixeira

Sample dimension effect on cement-stabilized sandy soil mechanical behavior
José Wilson dos Santos Ferreira, Michéle Dal Toé Casagrande, Raquel Souza Teixeira

Study on guardrail post behavior located on organic soil using simplified experimental and numerical methods
Hamid Reza Manaviparast, Nuno Araújo, Nuno Cristelo, Tiago Miranda

The mechanics of iron tailings from laboratory tests on reconstituted samples collected in post-mortem Dam I in Brumadinho
António Viana da Fonseca, Diana Cordeiro, Fausto Molina-Gómez, Davide Besenon, António Fonseca, Cristiana Ferreira

Automated true triaxial apparatus development for soil mechanics investigation
Dionatas Hoffmann Andreghetto, Lucas Festugato, Gustavo Dias Miguel, Andressa da Silva

Behavioural analysis of iron ore tailings through critical state soil mechanics
João Paulo de Sousa Silva, Pedro Pazzoto Cacciari, Vidal Felix Navarro Torres, Luís Fernando Martins Ribeiro, André Pacheco de Assis

Contaminant transport model in transient and unsaturated conditions applied to laboratory column test with tailings
Eliu James Carbaja, Mariana dos Santos Diniz, Roberto Lorenzo Rodriguez-Pacheco, André Luís Brasil Cavalcante

Execution energy of continuous flight auger piles as an assessment tool to evaluate the mechanical response of the soil mass
Darym Júnior Ferrari de Campos, Luan Carlos de Sena Monteiro Ozelim, André Luís Brasil Cavalcante, Carlos Medeiros Silva, José Camapum de Carvalho

TECHNICAL NOTES

Undrained shear strength correlation analysis based on vane tests in the Jacarepaguá Lowlands, Brazil
Magnos Baroni, Marcio de Souza Soares de Almeida

Influence of addition of butadiene copolymer and modified styrene on the mechanical behavior of a sand
Thiago Manes Barreto, Lucas Mendes Repsold, Nathália Araújo Boaventura de Souza e Silva, Michéle Dal Toé Casagrande

CASE STUDY

Effect of engineering geological properties on dam type selection of the Qadis Khordak Dam, Afghanistan
Sayed Mohammad Alipoori, Gholam Reza Lashkaripour, Mohammad Ghafoori, Naser Hafezi Moghadas

ARTICLES

Soils and Rocks
v. 45, n. 2

Comparative analysis of non-recursive three-dimensional (3D) modifications of Hoek-Brown failure criterion

Nnamdi Emmanuel Ezendiokwere^{1#} , Ogbonna Friday Joel¹ ,

Victor Joseph Aimikhe² , Adewale Dosunmu² 

Article

Keywords

Hoek & Brown failure criterion
Non-recursive failure criteria
Geomaterials
Intermediate principal stress
Rock strength

Abstract

A comparative analysis of three-dimensional (3D) modifications of Hoek & Brown (1988) rock failure criterion was carried out. The correlations between failure stress and the other principal stresses were first determined using polyaxial test data for five geomaterials including KTB amphibolites, Westerly granite, Dunham dolomite, Shirahama sandstone and Yuubari shale. The prediction accuracies of five non-recursive, three-dimensional modifications to Hoek-Brown failure criteria and the original two-dimensional Hoek-Brown criterion were later investigated using root mean square error and coefficient of determination as measures of misfit. The results reveal that the intermediate principal stress significantly affects strength in geomaterials like the Dunham dolomite. It also moderately affects the strength of geomaterials like the KTB amphibolites, the Westerly granite and the Yuubari shale. Moreover, the intermediate principal stress has mixed effects on strength in the Shirahama sandstone. In addition, the original Hoek-Brown failure criterion could still be used with reasonable accuracy for geomaterials whose strength shows low dependence on the intermediate principal stress. While a three-dimensional Hoek-Brown criterion must be used for geomaterials like the Dunham dolomite, whose strength shows a high dependence on the intermediate principal stress. The original Hoek-Brown failure criteria should be used with caution for geomaterials like the Shirahama sandstone, the KTB amphibolites, the Westerly granite, and the Yuubari shale, whose strength shows either mixed or intermediate dependence on the intermediate principal stress. Average prediction accuracies followed the order: simplified Priest (2012), Ma et al. (2020), and Jiang & Zhao (2015). Both original Hoek & Brown (1988) and Li et al. (2021) criteria were tied, while Liu et al. (2019) was the least.

1. Introduction

Geomaterials can be found either buried underground (occasionally with outcrops) or on the surface as remnants of weathering processes (Ranjith et al., 2017). Underground geomaterials are usually subjected to complex states of stress that are non-hydrostatic (Zhou et al., 2014). Hence, the principal stresses all have different magnitudes (Elyasi & Goshtasbi, 2015). This state of underground stress is also referred to as polyaxial or true triaxial, suggesting different values for each principal stress. The non-hydrostatic state of stress is usually quite common in regions of high tectonic and geologic activities (Jaeger et al., 2010). How geomaterials behave under various states of stress is considered highly important (Lorenzo et al., 2013), especially for underground

and engineering constructions (Zuo et al., 2015). This is because geomaterials have failure stress thresholds beyond which they do tend to yield or fail (Yua et al., 2002).

The strength of materials, including geomaterials, is usually predicted using strength or failure criteria (Jiang, 2017). A failure criterion is a simple expression describing failure stress in terms of confining principal stresses and material properties (Singh & Singh, 2012). Its main use is for predicting the level of stress that a given material can withstand without failing. Numerous failure criteria have been proposed over the years by different researchers (Li et al., 2021). These failure criteria were mostly developed empirically by using best-fitting curves to describe experimental strength data of principal stresses (Ma et al., 2020). Among the numerous failure criteria developed so far, one of the most popular is

[#]Corresponding author. E-mail address: nnamdi_ezendiokwere@uniport.edu.ng

¹University of Port Harcourt, World Bank Africa Centre of Excellence in Oilfield Chemicals Research, Department of Petroleum and Gas Engineering, Port Harcourt, Rivers State, Nigeria.

²University of Port Harcourt, Department of Petroleum and Gas Engineering, Port Harcourt, Rivers State, Nigeria.

Submitted on May 7, 2021; Final Acceptance on December 2, 2021; Discussion open until August 31, 2022.

<https://doi.org/10.28927/SR.2022.070821>



This is an Open Access article distributed under the terms of the Creative Commons Attribution License, which permits unrestricted use, distribution, and reproduction in any medium, provided the original work is properly cited.

the Hoek-Brown failure criterion (Liu et al., 2019). It was empirically developed for jointed or intact geomaterials using a large number of triaxial test data.

For over thirty years, the Hoek & Brown failure criterion has been widely applied in rock mechanics and rock engineering design (Ma et al., 2020). A possible explanation for its wide adoption is that its parameters can easily be gotten from simple uniaxial compression tests, discontinuity characterizations and mineralogical investigations (Jiang & Zhao, 2015). Although the original Hoek & Brown criterion has satisfactorily predicted failure stress in numerous applications, it has also given unsatisfactory results in other cases (Zhang et al., 2013). The reason is that the Hoek & Brown failure criterion in its original form is two-dimensional (2-D). Consequently, the original Hoek & Brown failure criterion has two major shortcomings. First, the original Hoek & Brown criterion neglects the non-linearity of strength behavior in geomaterials. Also, the conventional Hoek & Brown failure criterion does not incorporate the influence of the intermediate stress on strength in geomaterials (Mogi, 2007).

The influence of the intermediate stress on strength and failure in intact rocks can be gauged by the difference in failure stress recorded in conventional triaxial extension and compression tests (Liu et al., 2019). Hence, Murrell (1965), by analyzing results of two leading rock mechanics experts of that time, deduced that the difference in strength under compressive and extensive stress conditions can be traced to the influence of the intermediate stress. Similarly, other researchers like Handin et al. (1967) and Mogi (1967) in separate experiments later confirmed Murrell's findings. The above findings later inspired numerous researchers to consider independently applying the principal stresses during experiments. More recent experiments have equally demonstrated that the influence of the intermediate stress cannot be ignored (Zuo et al., 2015).

In addition, available three-dimensional (3D) modifications of Hoek-Brown are either recursive or non-recursive. The recursive three-dimensional (3D) modifications of Hoek-Brown require recursive numerical strategy in computing the predicted failure stress (Li et al., 2021). As such, they are computationally complex, since they require advanced algorithms for determining strength of geomaterials. The non-recursive criteria on the other hand, do not pose any serious computational inconvenience. They are quite easy to use, as no iterative procedure is required for estimating strength when using them (Li et al., 2021). Following extensive literature search, most of the earlier three-dimensional modifications to Hoek-Brown failure criterion are recursive in nature and have benefitted from considerable research effort in the past. While most non-recursive three-dimensional modifications of Hoek-Brown were more recently proposed.

Hence, there appears a dearth of research publications that have conducted comparative performance study exclusively for non-recursive three-dimensional (3D) modifications of Hoek-Brown rock failure criterion. It is this research void that this study intends to fill using experimental polyaxial data of some geomaterials usually encountered in the engineering practice. So, a comparative analysis of non-recursive three-dimensional (3D) modifications of Hoek-Brown failure criterion was carried out. It is believed that anyone planning to use Hoek-Brown criterion in three dimensions would find this study useful. Especially, those who do not have available the necessary equipment and software able to handle the recursive 3D modifications. Results obtained from studies like this could also be useful in selecting failure criteria for inclusion in geomechanical software. Choosing the non-recursive criteria would reduce the computational power requirements and complexity of the software.

2. Hoek & Brown failure criterion

Using a set of wide-ranged experimental data, Hoek & Brown (1980) proposed the original Hoek & Brown failure criterion as follows.

$$\sigma_1 = \sigma_3 + \sigma_c \left(m \frac{\sigma_3}{\sigma_c} + s \right)^{0.5} \quad (1)$$

where σ_1 and σ_3 are maximum and minimum effective principal stresses at failure, σ_c is uniaxial compressive strength of intact rock, m and s are dimensionless parameters depending on rock properties. Parameter s equals 1 for intact rocks, while the values of m depend upon rock texture and mineralogy and are found in Hoek & Brown (1997). It was subsequently updated (Hoek & Brown, 1988) and modified (Hoek et al., 1992) to current generalized form:

$$\sigma_1 = \sigma_3 + \sigma_c \left(m_b \frac{\sigma_3}{\sigma_c} + s \right)^a \quad (2)$$

where m_b is the value of m for the rock-mass; s and a are constants which depend on the rock-mass properties. Parameters m_b , s and a are derivable from the Geological Strength Index (GSI) as follows (Hoek et al., 2002):

$$m_b = \exp \left(\frac{GSI - 100}{28 - 14D} \right) m_i \quad (3)$$

$$s = \exp \left(\frac{GSI - 100}{9 - 3D} \right) \quad (4)$$

$$a = 0.5 + \frac{1}{6} \left[\exp(-GSI/15) - \exp(-20/3) \right] \quad (5)$$

where the disturbance factor D , is a factor depending on the degree of disturbance from blast damage and stress relaxation, with values ranging from 0 for undisturbed in situ rock-masses to 1 for very disturbed rock-masses. Criteria for selecting D are found in literature.

2.1. Some existing three-dimensional modifications of Hoek & Brown failure criterion

2.1.1. Pan-Hudson criterion

Pan & Hudson (1988) developed a three-dimensional version of Hoek & Brown strength criterion expressed as

$$\frac{3}{\sigma_c} J_2 + \frac{\sqrt{3}}{2} m \sqrt{J_2} - m \frac{I_1}{3} = s \sigma_c \quad (6)$$

where I_1 and J_2 are first stress invariant and second deviatoric stress invariant given by

$$I_1 = \sigma_1 + \sigma_2 + \sigma_3 \quad (7)$$

$$J_2 = \frac{(\sigma_1 - \sigma_2)^2 + (\sigma_2 - \sigma_3)^2 + (\sigma_3 - \sigma_1)^2}{6} \quad (8)$$

Where σ_1 , σ_2 , and σ_3 are major, intermediate and minor effective principal stresses.

2.1.2. Priest criterion

Priest (2005) proposed a three-dimensional version of generalized Hoek & Brown failure criterion by incorporating Drucker & Prager (1952) criterion. This criterion is expressed as follows.

$$J_2^{1/2} = A J_1 + B \quad (9)$$

where A and B are empirical parameters; and J_1 is the mean effective stress ($I_1/3$). The idea is to calculate values of A and B parameters for Drucker & Prager failure surface intersecting Hoek & Brown failure point (σ_1 , σ_2 , σ_3). The process is similar to identifying Drucker & Prager parameters giving circumscribed fit for the Mohr-Coulomb strength criterion. Priest criterion was later simplified in 2012 to (Li et al., 2021):

$$\sigma_1 = 3 \left[\omega \sigma_2 + (1 - \omega) \sigma_3 \right] + \sigma_c \left[m_b \frac{\omega \sigma_2 + (1 - \omega) \sigma_3}{\sigma_c} + s \right]^a - (\sigma_2 + \sigma_3) \quad (10)$$

Where ω is the intermediate stress parameter.

2.1.3. Zhang & Zhu criterion

Zhang & Zhu (2007) equally developed a three-dimensional version of the original Hoek & Brown failure criterion. They presented their extension of Hoek & Brown criterion by combining the general Mogi (1971) criterion with the original Hoek & Brown criterion. The Zhang & Zhu criterion is published in Zhang (2008) as:

$$\frac{9}{2\sigma_c} \tau_{oct}^2 + \frac{3}{2\sqrt{2}} m \tau_{oct} - m \sigma_{m,2} = s \sigma_c \quad (11)$$

where τ_{oct} and $\sigma_{m,2}$ are respectively the octahedral shear stress and the effective mean stress given by

$$\tau_{oct} = \frac{1}{3} \sqrt{(\sigma_1 - \sigma_2)^2 + (\sigma_2 - \sigma_3)^2 + (\sigma_3 - \sigma_1)^2} \quad (12)$$

$$\sigma_{m,2} = \frac{\sigma_1 + \sigma_3}{3} \quad (13)$$

2.1.4. Jiang & Zhao criterion

Jiang & Zhao (2015) also developed a three-dimensional extension to the original Hoek & Brown criterion. They arrived to the new criterion substituting a group of parameters in the original Hoek & Brown criterion by the second deviatoric stress invariant function. The proposed criterion can be expressed as:

$$\frac{\sqrt{3J_2}}{\sigma_c} = \left(m \frac{\sigma_3}{\sigma_c} + s \right)^a \quad (14)$$

2.1.5. Liu et al. criterion

Liu et al. (2019) equally proposed a three-dimensional modification of the Hoek & Brown criterion. They generated the new failure criterion replacing the deviatoric stress component with the same second deviatoric stress invariant function used by Jiang & Zhao (2015). In addition, they also replaced the least principal stress component in the original Hoek & Brown criterion by a function of the new parameter ω . According to them, the parameter ω , is an additional rock property which quantifies the influence of the intermediate principal stress on the compressive stress failure of geomaterials. They also suggested that both the intermediate and least principal stresses have strengthening effects on the rock strength. The proposed failure criterion is expressed as follows.

$$\sqrt{3J_2} = \sigma_c \left(\frac{m_b}{\sigma_c} \omega \sigma_2 + (1 - \omega) \sigma_3 + s \right)^a \quad (15)$$

2.1.6. Ma et al. criterion

Ma et al. (2020) developed a three-dimensional criterion modifying the generalized Hoek & Brown criterion and considering the strength enhancement due to high values of the intermediate principal stress. Mogi (1967) stated that the strength at failure increases with σ_2 by an amount proportional to σ_2 . Therefore, Mogi suggested a general empirical function to correlate the maximum shear stress and the effective normal stress. The empirical function has the following expression, where n is a constant no bigger than 1. The monotonically increasing function f gives a failure envelope depending on the rock type.

$$\frac{\sigma_1 - \sigma_3}{\sigma_c} = \left(m \frac{\sigma_3 + n\sigma_2}{\sigma_c} + s \right)^a \quad (16)$$

where the term $n\sigma_2$ represents contribution of σ_2 to normal stress on the failure plane, with the parameter n ranging between 0 and 0.5. Considering the general form of Mogi (1967) criterion, the above modified Hoek & Brown criterion was developed by supplanting σ_3 in the generalized Hoek & Brown criterion. Clearly, the difference between the new criterion and the generalized Hoek & Brown criterion is the introduced term $n\sigma_2$. So, when n equals 0, the failure criterion reduces to the generalized Hoek & Brown criterion.

2.1.7. Li et al. criterion

Li et al. (2021) proposed another three-dimensional modification to the original Hoek & Brown criterion incorporating the influence of the intermediate principal stress. They did this through direct substitution of the maximum principal stress in the high intermediate stress dependence range and substituting the least principal stress in the low intermediate stress dependence range. According to them, the ultimate influence of the intermediate stress is to transform the straight line failure curves of the two-dimensional original Hoek & Brown criterion in the $\sigma_1 - \sigma_2$ space into parabolic curves. These curves can then be conveniently divided into two sections: a region of high σ_2 dependence and a region of low σ_2 dependence separated by a point of peak stress at σ_2^* . With this demarcation, they were able to arrive at two separate criteria characterizing the two regions of intermediate stress dependences.

$$\sigma_1 = \frac{b\sigma_2 + \sigma_3}{b+1} + \sigma_c \left(\frac{m}{\sigma_c} \frac{b\sigma_2 + \sigma_3}{b+1} + s \right)^a \quad (\sigma_2 \leq \sigma_2^*) \quad (17)$$

$$\frac{b\sigma_2 + \sigma_1}{b+1} = \sigma_3 + \sigma_c \left(m \frac{\sigma_3}{\sigma_c} + s \right)^a \quad (\sigma_2^* \geq \sigma_2) \quad (18)$$

Where b is the intermediate stress parameter

2.2. Classification of the three-dimensional (3D) modifications for the Hoek & Brown failure criterion

From the literature, it can be deduced that the methods generally employed by researchers in generating three-dimensional modifications of Hoek & Brown failure criterion can be categorized into three groups (Li et al., 2021). The first group corresponding to three dimensional modifications is derived by the incorporation of a deviatoric shape function into the Hoek & Brown criterion e.g. Zhang et al. (2013), Jiang & Zhao (2015), Jiang (2017), among others. A popular method of doing this is by introducing Lode dependence into the deviatoric plane, based on tensile and compressive meridian radii ratio. However, the failure criteria generated using the Lode dependency are generally complicated (Jiang & Zhao, 2015). The second group corresponds to the use of a three-dimensional versions of the Hoek & Brown failure criterion by combining the Hoek & Brown criterion with other three-dimensional criteria e.g. Priest (2005) (the comprehensive Priest criterion), and Zhang & Zhu (2007). The third group generate their own three-dimensional Hoek & Brown criterion by incorporating a weighted combination of the intermediate and least principal stresses; e.g. Priest (2012) (the simplified Priest criterion), Liu et al. (2019), Ma et al. (2020), Li et al. (2021) and so on.

In addition, these three groups can further be divided into recursive and non-recursive criteria, based on the computational method and requirements. The recursive criteria require some level of recursive numerical strategy in computing the predicted failure stress (Li et al., 2021). Apart from the simplified versions, most recursive criteria are found among the first and second categories described above. Examples of the recursive three-dimensional Hoek & Brown criteria include Jiang et al. (2011), Lee et al. (2012), Jiang & Xie (2012) etc. But the non-recursive criteria, on the other hand, do not pose serious computational inconvenience. Examples of the non-recursive three-dimensional Hoek & Brown criteria include the simplified Priest (2012) criterion, Jiang & Zhao (2015), Liu et al. (2019), Li et al. (2020) etc.

3. Materials and methods

The aim of this study was to conduct a comparative analysis of failure predictability of three-dimensional (3D) modifications of Hoek & Brown rock failure criterion. An extensive literature search was conducted to identify various three-dimensional (3D) modifications to Hoek & Brown failure criterion. The classification schemes discussed above

also show a method of classification based on computational procedure, which divides modified three-dimensional Hoek & Brown criteria into two. However, from review of related literature, extensive studies seem to have been conducted on the recursive criteria. And this group have equally benefited by far from more research activities, as can be found in studies like Zhang (2008), Li et al. (2021), Ma et al. (2020) among others. But no study has been carried out exclusively on the non-recursive group of criteria.

Here, polyaxial test data from different geomaterials were obtained from literature, including polyaxial test data of KTB amphibolite, Westerly granite, Dunham dolomite, Shirahama sandstone and Yuubari shale. The sources of the polyaxial test data used are given in Table 1 and the Hoek & Brown criterion parameters for studied geomaterials are given in Table 2. Then, using the obtained data, the failure predictabilities of the selected non-recursive three-dimensional (3D) Hoek & Brown rock failure criteria were compared. The comparison was limited to the non-recursive group of

modified three-dimensional criteria based on the calculations suited the obtained data. Based on the generated results, the failure stress prediction accuracies of the selected rock failure criteria were also determined, while identifying which criterion performed best for each type of the geomaterial studied.

Also, the measure of the intermediate principal stress dependency of the geomaterials was determined using both correlation coefficient and partial correlation coefficient. Partial correlation coefficient was introduced because partial correlation coefficient is known to measure the relationship between a pair of variables, under the influence of a third variable (Ma et al., 2020). So, measuring the relationship between the failure stress and the least principal stress without neglecting the effect of the least principal stress on the failure stress gives a more intuitive intermediate stress dependency. Consequently, the intermediate stress dependency parameter values for the studied geomaterials were also obtained for the selected three-dimensional failure criteria as captured in Table 3.

Table 1. Sources of polyaxial test data.

Geomaterial	Number of data points	Source
KTB Amphibolite	40	Chang & Haimson (2000) Colmenares & Zoback (2002) Al-Ajmi & Zimmerman (2005) Zhang (2008)
Westerly granite	45	Haimson & Chang (2000) Al-Ajmi & Zimmerman (2005) Zhang (2008)
Dunham dolomite	53	Mogi (1971) Al-Ajmi & Zimmerman (2005) Zhang (2008)
Shirahama sandstone	38	Takahashi & Koide (1989), Colmenares & Zoback (2002)
Yuubari shale	26	Takahashi & Koide (1989) Colmenares & Zoback (2002)

Table 2. Hoek & Brown criterion parameters for studied geomaterials (Li et al., 2021).

Geomaterial	σ_c	m_i
KTB Amphibolite	165	35.17
Westerly granite	201	38.62
Dunham dolomite	261.5	9.6
Shirahama sandstone	80	8.1
Yuubari shale	61.7	10.2

Table 3. Intermediate stress dependency parameter values for studied geomaterials.

Geomaterial	σ_1 -dependence parameter value			
	Liu et al. (2019)	Li et al. (2021)	Ma et al. (2020)	Simplified Priest (2012)
KTB Amphibolite	0.05	0.410	0.10	0.24
Westerly granite	0.06	0.269	0.11	0.24
Dunham dolomite	0.10	0.606	0.30	0.29
Shirahama sandstone	0.05	0.421	0.04	0.29
Yuubari shale	0.05	0.325	0.15	0.28

The correlation coefficient between the failure stress and the intermediate principal stress is given by (Colmenares & Zoback, 2002):

$$r[\sigma_1, \sigma_2] = \frac{Cov[\sigma_1, \sigma_2]}{\sqrt{Var[\sigma_1]Var[\sigma_2]}} \quad (19)$$

Where $r[\sigma_1, \sigma_2]$ is the correlation coefficient between σ_1 and σ_2 , $r[\sigma_i, \sigma_j]$ is the covariance of σ_i and σ_j , $Var[\sigma_1]$ and $Var[\sigma_2]$ are the deviations of σ_1 and σ_2 respectively. And the partial correlation coefficient between failure stress and intermediate principal stress, given the least principal stress given is mathematically expressed as (Ma et al., 2020):

$$r[\sigma_1, \sigma_2 : \sigma_3] = \frac{r[\sigma_1, \sigma_2] - r[\sigma_1, \sigma_3]r[\sigma_2, \sigma_3]}{\sqrt{(1 - r^2[\sigma_1, \sigma_3])(1 - r^2[\sigma_2, \sigma_3])}} \quad (20)$$

Where $r[\sigma_1, \sigma_2 : \sigma_3]$ is the partial correlation coefficient between σ_1 and σ_2 given σ_3 , $r[\sigma_i, \sigma_j]$ is the correlation coefficient between σ_i and σ_j , $r^2[\sigma_i, \sigma_j]$ is the square of the correlation coefficient between σ_i and σ_j . The comparative results between the correlation and the partial correlation coefficients for the various geomaterials considered are shown in Figure 1. One of the measure of the misfit between the calculated and test used is the root mean squared error (RMSE) given by (Li et al., 2021):

$$RMSE = \sqrt{\frac{1}{N} \sum_{i=1}^N (\sigma_{li}^{cal} - \sigma_{li}^{test})^2} \quad (21)$$

where N is the number of test data pairs; and σ_{li}^{cal} and σ_{li}^{test} are the i th calculated and measured values of σ_1 respectively. Another measure of misfit that was equally used is the coefficient of determination (DC). Given the fact that some of the three modifications directly predicted failure stress, while the others predicted other combinations of rock properties (like the second deviatoric stress invariant, J_2) that still incorporated the failure stress, σ_1 , the DC was introduced to remove any mathematical bias thereof. Mathematically, the coefficient of determination is given by (Jiang & Zhao, 2015):

$$DC = 1 - \frac{\sum_{i=1}^N (\sigma_{li}^{cal} - \sigma_{li}^{test})^2}{\sum_{i=1}^N (\sigma_{li}^{cal} - \bar{\sigma}^{test})^2} \quad (22)$$

Where,

$$\bar{\sigma}^{test} = \frac{\sum_{i=1}^N \sigma_{li}^{test}}{N} \quad (23)$$

The root mean square error and the coefficient of determination were later used in ascertaining the failure stress prediction accuracies of the selected criteria for the geomaterials studied as depicted in Figures 2-6. Meanwhile, according to Ma et al. (2020), the statistical values of the correlation coefficients for the different geomaterials can also be utilized in classifying their principal stress interdependencies. For this purpose, we utilized the following range of r values to classify the principal stress interdependencies into low, intermediate and high dependences as follows:

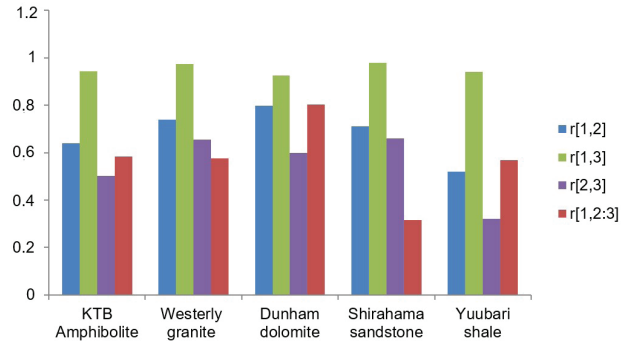


Figure 1. Correlation and partial correlation coefficients between the principal stress components.

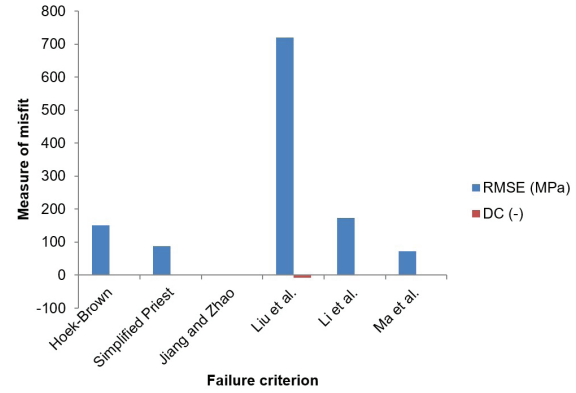


Figure 2. Measures of misfit for KTB Amphibolite.

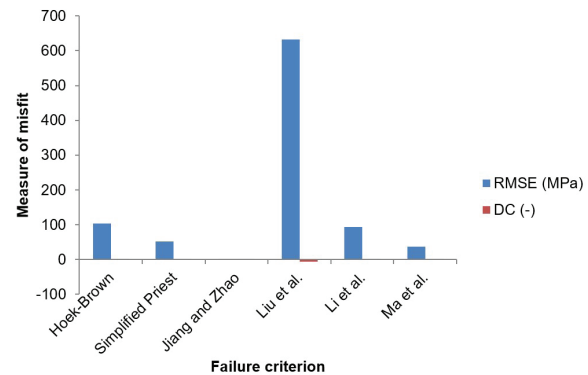


Figure 3. Measures of misfit for Westerly granite.

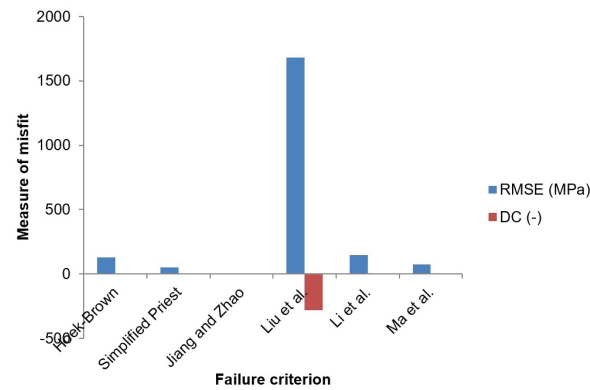


Figure 4. Measures of misfit for Dunham dolomite.

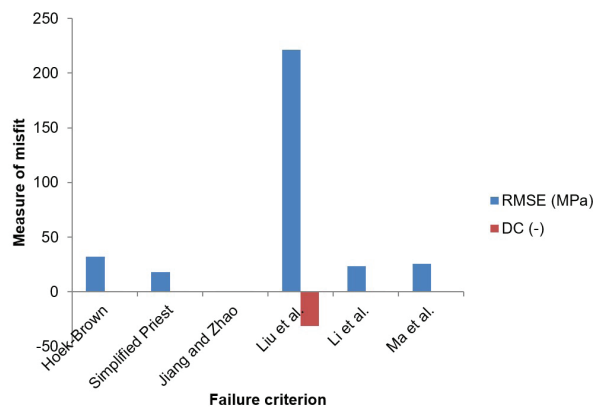


Figure 5. Measures of misfit for Shirahama sandstone.

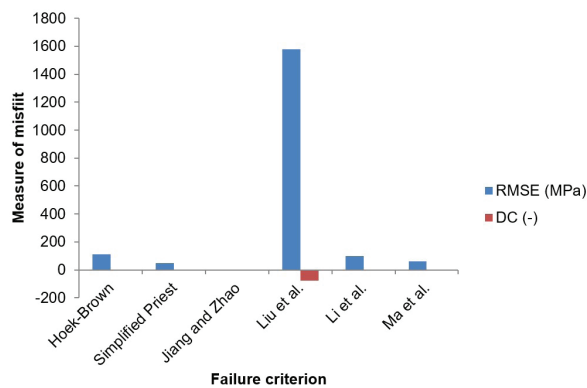


Figure 6. Measures of misfit for Yuubari shale.

- $0 < r < 0.4$ represents geomaterials with low dependence
- $0.4 \leq r < 0.7$ represents geomaterials with intermediate dependence
- $0.7 \leq r < 1$ represents geomaterials with high dependence.

4. Analysis and results

Table 4 shows the values of the correlation and partial correlation coefficients between the principal stress components. Following the classification scheme developed above, the correlation between the rock strength or failure stress and other principal stresses can be described as high, intermediate or low. The second column in Table 4 shows the correlation between the failure stress and the intermediate principal stress for the geomaterials studied. The result reveals that both KTB amphibolites and Yuubari shale had correlation coefficients which suggests an intermediate dependency of failure stress on the intermediate stress. While the Westerly granite, the Dunham dolomite and the Shirahama sandstone all showed correlation coefficients suggesting a high dependence of failure stress on the intermediate stress.

Table 4 also shows the correlation between the rock strength and the least principal stress in the third column. From the table, a very high correlation can be seen between the failure stress and the least principal stress for all the studied geomaterials. This high level of correlation is actually expected since classical rock mechanics demonstrates that the failure stress for any given geomaterial is largely influenced by the least principal stress (Jaeger et al., 2010). In addition, Table 4 equally shows the correlation between the intermediate stress and the least principal stress in the fourth column. The results obtained reveals that the KTB amphibolites, the Westerly granite, the Dunham dolomite, and the Shirahama sandstone all had correlation coefficients suggesting an intermediate correlation between the intermediate stress and the least principal stress. While the Yuubari shale results showed a low correlation between the intermediate stress and the least principal stress.

In order to give a better representation of the relationship between the failure stress and the intermediate stress, a partial correlation was also carried out. The partial correlation captures the dependence of strength on the intermediate stress in the presence of the least principal stress. Results from Table 4 and Table 5 show that the KTB amphibolite, the Westerly granite and the Yuubari shale all showed intermediate dependence on the intermediate stress. While the Dunham dolomite and the Shirahama sandstone displayed high and low dependence respectively.

Furthermore, the above results agree with the results of Colmenares & Zoback (2002), who also outlined these geomaterials (except Westerly granite, which they did not consider) as having intermediate to high strength dependence on the intermediate stress. However, Colmenares & Zoback (2002) reported mixed (high and low, depending on σ_3 values) σ_2 dependency results for the Shirahama sandstone. Which means that the Shirahama sandstone gave high correlation coefficient, but low partial correlation values between failure stress and intermediate stress in this study. Colmenares & Zoback (2002) also reported a strong strength dependency on σ_2 for confining stresses less than 100 MPa. But low

Table 4. Correlation and partial correlation coefficients between the principal stress components.

Geomaterial	$r[1,2]$	$r[1,3]$	$r[2,3]$	$r[1,2,3]$
KTB Amphibolite	0.640532	0.943167	0.500845	0.584602
Westerly granite	0.738096	0.972383	0.654320	0.577058
Dunham dolomite	0.797761	0.925552	0.599201	0.802214
Shirahama sandstone	0.710847	0.979049	0.660457	0.315420
Yuubari shale	0.518859	0.939148	0.321015	0.567598

Table 5. Categories of principal stress interdependencies for the studied geomaterials.

Geomaterial	$r[1,2]$	$r[1,3]$	$r[2,3]$	$r[1,2,3]$
KTB Amphibolite	intermediate	high	intermediate	Intermediate
Westerly granite	High	high	intermediate	Intermediate
Dunham dolomite	High	high	intermediate	High
Shirahama sandstone	High	high	intermediate	Low
Yuubari shale	intermediate	high	Low	Intermediate

Table 6. Measures of misfit for KTB Amphibolite.

Failure Criterion	RMSE (MPa)	DC (-)
Hoek & Brown (1980)	151.5995	0.7730
Simplified Priest (2012)	87.65936	0.9241
Jiang & Zhao (2015)	0.556811	0.8640
Liu et al. (2019)	719.3018	-7.3383
Li et al. (2021)	173.2040	0.7037
Ma et al. (2020)	73.11651	0.9472

Table 7. Measures of misfit for the Westerly granite.

Failure Criterion	RMSE (MPa)	DC (-)
Hoek & Brown (1980)	103.0620	0.8636
Simplified Priest (2012)	51.61271	0.9658
Jiang & Zhao (2015)	0.345612	0.9135
Liu et al. (2019)	632.5512	-6.1747
Li et al. (2021)	93.62682	0.8874
Ma et al. (2020)	38.04349	0.9814

strength dependency on σ_2 for confining stresses higher than 100 MPa, which agrees with the results of this study. Results showed in Table 5 completely agrees with the results by Ma et al. (2020), who reported exact categories of strength dependency on σ_2 for the geomaterials in this study. Figure 1 shows a pictorial presentation of the above results.

Figure 2 and Table 6 show the measures of misfit of failure stress predictions for KTB Amphibolite using root mean square error and coefficient of determination. From Figure 2, the highest RMSE was recorded by Liu et al. (2019) criterion, followed by Li et al. (2021), original Hoek & Brown (1980), simplified Priest (2012) and Ma et al. (2020) criteria, while the lowest was given by Jiang & Zhao (2015) criterion. But based on the coefficient of determination, the failure criterion with the highest coefficient of determination is Ma et al. (2020), followed by simplified Priest (2012), Jiang & Zhao (2015), Hoek & Brown (1980), and Li et al. (2021) criteria. While Liu et al. (2019) criterion showed a negative coefficient of determination. This result shows that the best three-dimensional modified Hoek & Brown criterion for

KTB Amphibolite is the Ma et al. (2020) three-dimensional criterion as exemplified by the criterion having the highest coefficient of determination.

While the worst three-dimensional modified Hoek & Brown criterion for KTB Amphibolite is the Liu et al. (2019) criterion since the criterion had an unusually high root mean square error (RMSE) and negative coefficient of determination (DC). The negative DC also shows that the criterion does not describe the obtained polyaxial data for KTB Amphibolite. In addition, Table 6 shows a coefficient of determination of 0.7730 for the original Hoek & Brown (1980) criterion, which suggests that it could still be used for KTB Amphibolite with reasonable accuracy. But caution needs to be exercised due to the intermediate σ_2 -dependence of strength for KTB Amphibolite (Ma et al., 2020). So, a two-dimensional criterion like the original Hoek & Brown (1980) criterion may not sufficiently predict failure stress for KTB Amphibolite.

Figure 3 and Table 7 show the measures of misfit of failure stress predictions for the Westerly granite using root

mean square error and coefficient of determination. From Figure 3, the highest RMSE was recorded by Liu et al. (2019) criterion, followed by original Hoek & Brown (1980), Li et al. (2021), simplified Priest (2012), and Ma et al. (2020) criteria, while the lowest was given by Jiang & Zhao (2015) criterion. But based on the coefficient of determination, the failure criterion with the highest coefficient of determination is the one by Ma et al. (2020), followed by the simplified Priest (2012), Jiang & Zhao (2015), Li et al. (2021) and Hoek & Brown (1980) criteria. While Liu et al. (2019) had the least and also showed a negative coefficient of determination. This result shows that the best three-dimensional modified Hoek & Brown criterion for Westerly granite is the Ma et al. (2020) three-dimensional criterion as exemplified by the criterion having the highest coefficient of determination.

While the worst three-dimensional modified Hoek & Brown criterion for Westerly granite is the Liu et al. (2019) criterion since the criterion had an unusually high RMSE and negative DC. The negative DC also shows that the criterion does not describe the obtained polyaxial data for Westerly granite. In addition, Table 7 shows a coefficient of determination of 0.8636 for the original Hoek & Brown (1980) criterion, which suggests it could also be used for Westerly granite with reasonable accuracy. But caution needs to be exercised due to the intermediate σ_2 -dependence of strength for Westerly granite (Ma et al., 2020). So, a two-dimensional criterion like the original Hoek & Brown (1980) criterion may not sufficiently predict failure stress for Westerly granite.

Figure 4 and Table 8 show the measures of misfit of failure stress predictions for Dunham dolomite using root mean square error and coefficient of determination. From Figure 4, the highest RMSE was recorded by Liu et al. (2019) criterion, followed by Li et al. (2021), original Hoek & Brown (1980), Ma et al. (2020), and simplified Priest (2012) criteria, while the lowest was given by Jiang & Zhao (2015)

criterion. But based on the coefficient of determination, the failure criterion with the highest coefficient of determination was simplified Priest criterion, followed by Ma et al. (2020), Jiang & Zhao (2015), Hoek & Brown (1980) and Li et al. (2021) criteria. While Liu et al. (2019) criterion had the least and also showed a negative coefficient of determination. This result shows that the best three-dimensional modified Hoek & Brown criterion for Dunham dolomite is the simplified Priest (2012) three-dimensional criterion as exemplified by the criterion having the highest coefficient of determination.

While the worst three-dimensional modified Hoek & Brown criterion for Dunham dolomite is the Liu et al. (2019) criterion since the criterion had an unusually high RMSE and the least DC. The negative DC also shows that the criterion does not describe the obtained polyaxial data for Dunham dolomite. However, with a very low coefficient of determination of 0.264412 as depicted in Table 8, it means that the original Hoek & Brown criterion should not be used for Dunham dolomite. The reason for this can be explained by the high σ_2 -dependence of strength for Dunham dolomite (Colmenares & Zoback, 2002; Ma et al., 2020). So, a two-dimensional criterion like the original Hoek & Brown criterion cannot predict failure stress for Dunham dolomite.

Figure 5 and Table 9 show the measures of misfit of failure stress predictions for Shirahama sandstone using root mean square error and coefficient of determination. From Figure 5, the highest RMSE was recorded by Liu et al. (2019) criterion, followed by original Hoek & Brown (1980), Ma et al. (2020), Li et al. (2021), and simplified Priest (2012) criteria, while the lowest was given by Jiang & Zhao (2015) criterion. But based on the coefficient of determination, the failure criterion with the highest coefficient of determination was simplified Priest (2012) criterion, followed by Jiang & Zhao (2015), Li et al. (2021), Ma et al. (2020), and Hoek & Brown (1980) criteria. While Liu et al. (2019) criterion had the least and

Table 8. Measures of misfit for Dunham dolomite.

Failure Criterion	RMSE (MPa)	DC (-)
Hoek & Brown (1980)	126.8728	0.2644
Simplified Priest (2012)	53.00868	0.8736
Jiang & Zhao (2015)	0.259971	0.4307
Liu et al. (2019)	1682.973	-279.878
Li et al. (2021)	145.0804	0.1025
Ma et al. (2020)	74.29655	0.7372

Table 9. Measures of misfit for Shirahama sandstone.

Failure Criterion	RMSE (MPa)	DC (-)
Hoek & Brown (1980)	31.98625	0.6791
Simplified Priest (2012)	17.98074	0.8981
Jiang & Zhao (2015)	0.196489	0.8707
Liu et al. (2019)	221.4067	-31.0186
Li et al. (2021)	23.43394	0.8269
Ma et al. (2020)	25.74247	0.7911

also showed a negative coefficient of determination. This result shows that the best three-dimensional modified Hoek & Brown criterion for Shirahama sandstone is the simplified Priest (2012) three-dimensional criterion as exemplified by the criterion having the highest coefficient of determination.

While the worst three-dimensional modified Hoek & Brown criterion for Shirahama sandstone is the Liu et al. (2019) criterion since the criterion had an unusually high RMSE and the least DC. The negative DC also shows that the criterion does not describe the obtained polyaxial data for Shirahama sandstone. From Table 9, given a coefficient of determination of 0.6791, it means that the original Hoek & Brown criterion should be used with caution for Shirahama sandstone. The reason for this can be explained by the intermediate or mixed σ_2 -dependence of strength for Shirahama sandstone (Colmenares & Zoback, 2002; Ma et al., 2020). So, a two-dimensional criterion like the original Hoek & Brown criterion may not sufficiently predict failure stress for Shirahama sandstone.

Figure 6 and Table 10 show the measures of misfit of failure stress predictions for the Yuubari shale using the root mean square error and the coefficient of determination. From Figure 6, the highest RMSE was recorded by Liu et al. (2019) criterion, followed by original Hoek & Brown (1980), Li et al. (2021), Ma et al. (2020), and simplified Priest (2012) criteria, while the lowest was given by Jiang & Zhao (2015) criterion. But based on the coefficient of determination, the failure criterion with the highest coefficient of determination was Ma et al. (2020), followed by simplified Priest (2012) criterion, Jiang & Zhao (2015), Hoek & Brown (1980) and Li et al. (2021) criteria. While Liu et al. (2019) criterion had the least and also showed a negative coefficient of determination. This result shows that the best three-dimensional modified Hoek & Brown

criterion for Yuubari shale is the Ma et al. (2020) three-dimensional criterion as exemplified by the criterion having the highest coefficient of determination.

The worst three-dimensional modified Hoek & Brown criterion for the Yuubari shale is again the Liu criterion since the criterion had an unusually high RMSE and the least DC. The negative DC also shows that the criterion does not describe the obtained polyaxial data for Yuubari shale. Again, From Table 10, given a low coefficient of determination of 0.5939, it means that the original Hoek & Brown criterion should also be used with caution for the Yuubari shale. The reason for this can be explained by the σ_2 -dependence of strength for Yuubari shale, which can be categorized as intermediate (Colmenares & Zoback, 2002; Ma et al., 2020). So, a two-dimensional criterion like the original Hoek & Brown criterion might not sufficiently predict failure stress for Yuubari shale.

Table 11 shows the ranking of failure criteria based on failure stress prediction accuracy. Ranking was done in such a way that 1 went to the criterion with the highest coefficient of determination for a given geomaterial and 5 went to the criterion with the least coefficient of determination for same geomaterial. The average rank was then generated by taking the arithmetic average of the ranks of the criteria for each of the studied geomaterials. This was done to ascertain the failure criterion which best predicted the failure stress for the studied geomaterials. And from the result obtained in this study, the failure criterion with best average prediction accuracy is the simplified Priest (2012) failure criterion, followed by Ma et al. (2020), and Jiang & Zhao (2015) criteria. Both the original Hoek & Brown and Li et al. (2021) criteria were tied, while the least failure criterion for all the studied geomaterials was Liu et al. (2019) failure criterion.

Table 10. Measures of misfit for Yuubari shale.

Failure Criterion	RMSE (MPa)	DC (-)
Hoek & Brown (1980)	110.4301	0.5939
Simplified Priest (2012)	48.53427	0.9183
Jiang & Zhao (2015)	0.291664	0.8458
Liu et al. (2019)	1576.939	-76.0232
Li et al. (2021)	96.84813	0.3895
Ma et al. (2020)	61.49562	0.9269

Table 11. Ranking of failure criteria based on the failure stress prediction accuracy.

Failure Criterion	KTB amphibolite	Westerly granite	Dunham dolomite	Shirahama sandstone	Yuubari shale	Average rank
Hoek & Brown (1980)	4	5	4	5	4	4
Simplified Priest (2012)	2	2	1	1	2	1
Jiang & Zhao (2015)	3	3	3	2	3	3
Liu et al. (2019)	6	6	6	6	6	6
Li et al. (2021)	5	4	5	3	5	4
Ma et al. (2020)	1	1	2	4	1	2

5. Conclusion

From this study, the following conclusions can be drawn.

- (a) The intermediate principal stress significantly affects strength in geomaterials like the Dunham dolomite. It also moderately affects the strength of geomaterials like KTB amphibolites, Westerly granite and Yuubari shale. While the intermediate principal stress has mixed effects on strength in Shirahama sandstone.
- (b) Based on results obtained here, it can be said that the original Hoek & Brown failure criteria could still be used with reasonable accuracy in predicting the failure stress for geomaterials whose strength shows low dependence on the intermediate principal stress.
- (c) While a three-dimensional form of the Hoek & Brown criterion must be used in predicting failure stress for geomaterials like Dunham dolomite, whose strength shows a high dependence on the intermediate principal stress.
- (d) But the original Hoek & Brown failure criteria should be used with caution in predicting failure stress for geomaterials like Shirahama sandstone, KTB amphibolites, Westerly granite, and Yuubari shale, whose strength shows either mixed or intermediate dependence on the intermediate principal stress.
- (e) Based on the results of this study, the three-dimensional failure criterion with best average prediction accuracy was the simplified Priest (2012) failure criterion, followed by the Ma et al. (2020), and Jiang & Zhao (2015) criteria. Both the original Hoek & Brown and Li et al. (2021) criteria were tied, while the least failure criterion for all the studied geomaterials was Liu et al. (2019) failure criterion.

Acknowledgements

The authors wish to thank the Petroleum Technology Development Fund (PTDF), Nigeria, for sponsorship of this research with grant number PTDF-SPandD-AOGRG-V. III-117-011B.

Declaration of interest

The authors hereby declare no inherent conflict of interest in this study.

Authors' contributions

Nnamdi Emmanuel Ezendiokwere: Conceptualization, Data acquisition, Project administration, Visualization, Writing – original draft. Ogbonna Friday Joel: Funding acquisition, Project administration, Supervision. Victor Joseph Aimikhe: Formal Analysis, Investigation, Supervision. Adewale Dosunmu: Supervision, Validation, Project administration.

List of symbols

σ_1	maximum effective principal stresses at failure, MPa
σ_2	intermediate effective principal stresses at failure, MPa
σ_3	minimum effective principal stresses at failure, MPa
σ_c	uniaxial compressive strength of the intact rock, MPa
m	and s Hoek & Brown dimensionless parameters related to the characteristic of rock masses
m_b	value of Hoek & Brown constant, m for the rock mass in jointed rocks
a	Hoek & Brown constant that depend on the characteristics of the rock mass
GSI	Geological Strength Index
D	disturbance factor measuring disturbance due to blast damage and stress relaxation.
I_1	first stress invariant stress invariant, MPa
J_2	second deviatoric stress invariant, (MPa) ²
A and B	Drucker-Prager empirical parameters
τ_{oct}	octahedral shear stress, MPa
$\sigma_{m,2}$	effective mean stress, MPa
n	Ma et al. σ_2 -dependency parameter, dimensionless
β	Mogi σ_2 -dependency parameter, dimensionless
b	Li et al. σ_2 -dependency parameter, dimensionless
ω	Priest, Liu et al. σ_2 -dependency parameter, dimensionless
$r[\sigma_1, \sigma_2]$	coefficient of correlation between σ_1 and σ_2 , dimensionless
$Cov[\sigma_1, \sigma_2]$	covariance between σ_1 and σ_2
$Var[\sigma_1]$	variance of σ_1
$r[\sigma_1, \sigma_2 : \sigma_3]$	partial coefficient of correlation between σ_1 and σ_2 , given σ_3 , dimensionless
RMSE	root mean square error, MPa
DC	coefficient of determination, dimensionless



References

- Al-Ajmi, A.M., & Zimmerman, R.W. (2005). Relation between the Mogi and the Coulomb failure criteria. *International Journal of Rock Mechanics and Mining Sciences*, 42(3), 431-439. <http://dx.doi.org/10.1016/j.ijrmms.2004.11.004>.
- Chang, C., & Haimson, B.C. (2000). True Triaxial strength and deformability of the German continental deep drilling program (KTB) deep hole amphibolite. *Journal of Geophysical Research*, 105(B8), 8999-9013. <http://dx.doi.org/10.1029/2000JB900184>.
- Colmenares, L.B., & Zoback, M.D. (2002). A statistical evaluation of intact rock failure criteria constrained by polyaxial test data for five different rocks. *International Journal of Rock Mechanics and Mining Sciences*, 39(6), 695-729. [http://dx.doi.org/10.1016/S1365-1609\(02\)00048-5](http://dx.doi.org/10.1016/S1365-1609(02)00048-5).

- Drucker, D.C., & Prager, W. (1952). Soil mechanics and plastic analysis for limit design. *Quarterly of Applied Mathematics*, 10(2), 157-165.
- Elyasi, A., & Goshtasbi, K. (2015). Using different rock failure criteria in wellbore stability analysis. *Geomechanics for Energy and the Environment*, 2, 15-21. <http://dx.doi.org/10.1016/j.gete.2015.04.001>.
- Haimson, B.C., & Chang, C. (2000). A new true triaxial cell for testing mechanical properties of rock, and its use to determine rock strength and deformability of Westerly Granite. *International Journal of Rock Mechanics and Mining Sciences*, 37(1-2), 285-296. [http://dx.doi.org/10.1016/S1365-1609\(99\)00106-9](http://dx.doi.org/10.1016/S1365-1609(99)00106-9).
- Handin, J., Heard, H.C., & Magouirk, J.N. (1967). Effects of the intermediate principal stress on the failure of limestone, dolomite, and glass at different temperatures and strain rates. *Journal of Geophysical Research*, 72(2), 611-640. <http://dx.doi.org/10.1029/JZ072i002p00611>.
- Hoek, E., & Brown, E.T. (1980). Empirical strength criterion for rock masses. *Journal of Geotechnical Engineering*, 106(9), 1013-1035. <http://dx.doi.org/10.1061/AJGEB6.0001029>.
- Hoek, E., & Brown, E.T. (1988). The Hoek-Brown failure criterion: a 1988 update. In J.H. Curran (Ed.), *15th Canadian Rock Mechanics Symposium: rock engineering for underground excavations* (pp. 31-38). Toronto, Canada: University of Toronto Press.
- Hoek, E., & Brown, E.T. (1997). Practical estimates of rock mass strength. *International Journal of Rock Mechanics and Mining Sciences & Geomechanics Abstracts*, 34(8), 1165-1186. [http://dx.doi.org/10.1016/S1365-1609\(97\)80069-X](http://dx.doi.org/10.1016/S1365-1609(97)80069-X).
- Hoek, E., Carranza-Torres, C., & Corkum, B. (2002). Hoek-Brown failure criterion: 2002 edition. In R. Hammah (Ed.), *Proceedings of the 5th North American Rock Mechanics Symposium* (Vol. 1, pp. 267-273), Toronto, Canada: University of Toronto Press.
- Hoek, E., Wood, D., & Hudson, S.S.J.A. (14-17 September, 1992). A modified Hoek-Brown criterion for jointed rock masses. In J. Hudson (Ed.), *Rock Characterization: ISRM Symposium* (pp. 209-214). Chester, UK: British Geotechnical Society.
- Jaeger, J.C., Cook, N.G.W., & Zimmerman, R.W. (2010). *Fundamentals of rock mechanics* (5th ed.). Malden: Blackwell Publishing.
- Jiang, H. (2017). A failure criterion for rocks and concrete based on the Hoek-Brown criterion. *International Journal of Rock Mechanics and Mining Sciences*, 95, 62-72. <http://dx.doi.org/10.1016/j.ijrmms.2017.04.003>.
- Jiang, H., & Xie, Y. (2012). A new three-dimensional Hoek-Brown strength criterion. *Lixue Xuebao*, 28(2), 393-406. <http://dx.doi.org/10.1007/s10409-012-0054-2>.
- Jiang, H., & Zhao, J. (2015). A simple three-dimensional failure criterion for rocks based on the Hoek-Brown criterion. *Rock Mechanics and Rock Engineering*, 48, 1807-1819. <http://dx.doi.org/10.1007/s00603-014-0691-9>.
- Jiang, H., Wang, X.W., & Xie, Y.L. (2011). New strength criteria for rocks under polyaxial compression. *Canadian Geotechnical Journal*, 48(8), 1233-1245. <http://dx.doi.org/10.1139/t11-034>.
- Lee, Y.K., Pietruszczak, S., & Choi, B.H. (2012). Failure criteria for rocks based on smooth approximations to Mohr-Coulomb and Hoek-Brown failure functions. *International Journal of Rock Mechanics and Mining Sciences*, 56, 146-160. <http://dx.doi.org/10.1016/j.ijrmms.2012.07.032>.
- Li, H., Guo, T., Nan, Y., & Han, B. (2021). A simplified three-dimensional extension of Hoek-Brown strength criterion. *Journal of Rock Mechanics and Geotechnical Engineering*, 13(2), 568-578. <http://dx.doi.org/10.1016/j.jrmge.2020.10.004>.
- Liu, C., Han, Y., Liu, H.-H., & Abousleiman, Y. (2019). Wellbore stability analysis by integrating a modified Hoek-Brown failure criterion with dual porochemoelectroelastic theory. *SPE Journal*, 24(5), 1957-1981. <http://dx.doi.org/10.2118/195685-PA>.
- Lorenzo, R., Cunha, R.P., & Cordão-Neto, M.P. (18-20 September, 2013). Material point method for geotechnical problems involving large deformation. In M. Bischoff, E. Ramm, E. Oñate, R. Owen & P. Wriggers (Eds.), *III International Conference on Particle-Based Methods: Fundamentals and Applications* (pp. 510-521). Stuttgart: CINME.
- Ma, L., Li, Z., Wang, M., Wu, J., & Li, G. (2020). Applicability of a new modified explicit three-dimensional Hoek-Brown failure criterion to eight rocks. *International Journal of Rock Mechanics and Mining Sciences*, 133, 104311. <http://dx.doi.org/10.1016/j.ijrmms.2020.104311>.
- Mogi, K. (1967). Effect of the intermediate principal stress on rock failure. *Journal of Geophysical Research*, 72(20), 5117-5131. <http://dx.doi.org/10.1029/JZ072i020p05117>.
- Mogi, K. (1971). Fracture and flow of rocks under high triaxial compression. *Journal of Geophysical Research*, 76, 1255-1269. <http://dx.doi.org/10.1029/JB076i005p01255>.
- Mogi, K. (2007). *Experimental rock mechanics*. London: Taylor and Francis.
- Murrell, S.A.F. (1965). The effect of triaxial stress systems on the strength of rocks at atmospheric temperatures. *Geophysical Journal International*, 10(3), 231-281. <http://dx.doi.org/10.1111/j.1365-246X.1965.tb03155.x>.
- Pan, X.D., & Hudson, J.A. (1988). A simplified three-dimensional Hoek-Brown yield criterion. In M. Romana (Ed.), *Rock mechanics and power plants* (pp. 95-104). Madrid: Balkema.
- Priest, S. (2005). Determination of shear strength and three-dimensional yield strength for the Hoek-Brown criterion. *Rock Mechanics and Rock Engineering*, 38(6), 299-327. <http://dx.doi.org/10.1007/s00603-005-0056-5>.
- Priest, S. (2012). Three-dimensional failure criteria based on the Hoek-Brown criterion. *Rock Mechanics and Rock*

- Engineering*, 45(6), 989-993. <http://dx.doi.org/10.1007/s00603-012-0277-3>.
- Ranjith, P.G., Zhao, J., Ju, M., Silva, R.V.S., Rathnaweera, T.D., & Bandara, A.K.M.S. (2017). Opportunities and challenges in deep mining: a brief review. *Engineering*, 3(4), 546-551. <http://dx.doi.org/10.1016/J.ENG.2017.04.024>.
- Singh, M., & Singh, B. (2012). Modified Mohr–Coulomb criterion for non-linear triaxial and polyaxial strength of jointed rocks. *International Journal of Rock Mechanics and Mining Sciences*, 51, 43-52. <http://dx.doi.org/10.1016/j.ijrmms.2011.12.007>.
- Takahashi, M., & Koide, H. (1989). Effect of the intermediate principal stress on strength and deformation behavior of sedimentary rocks at the depth shallower than 2000 m. In V. Maury (Ed.), *Rock at great depth: rock mechanics and rock physics at great depth (pp. 19-26)*. Rotterdam: Balkema.
- Yua, M., Zana, Y., Zhaob, J., & Yoshimine, M. (2002). A unified strength criterion for rock material. *International Journal of Rock Mechanics and Mining Sciences*, 39, 975-989. [http://dx.doi.org/10.1016/S1365-1609\(02\)00097-7](http://dx.doi.org/10.1016/S1365-1609(02)00097-7).
- Zhang, L., & Zhu, H. (2007). Three-dimensional Hoek–Brown strength criterion for rocks. *Journal of Geotechnical and Geoenvironmental Engineering*, 133(9), 1128-1135. [http://dx.doi.org/10.1061/\(ASCE\)1090-0241\(2007\)133:9\(1128\)](http://dx.doi.org/10.1061/(ASCE)1090-0241(2007)133:9(1128)).
- Zhang, L.Y. (2008). A generalized three-dimensional Hock–Brown strength criterion. *Rock Mechanics and Rock Engineering*, 41(6), 893-915. <http://dx.doi.org/10.1007/s00603-008-0169-8>.
- Zhang, Q., Zhu, H., & Zhang, L. (2013). Modification of a generalized three-dimensional Hoek–Brown strength criterion. *International Journal of Rock Mechanics and Mining Sciences*, 59, 80-96. <http://dx.doi.org/10.1016/j.ijrmms.2012.12.009>.
- Zhou, X., Shou, Y., Qian, Q., & Yu, M. (2014). Three-dimensional non-linear strength criterion for rock-like materials based on the micromechanical method. *International Journal of Rock Mechanics and Mining Sciences*, 72, 54-60. <http://dx.doi.org/10.1016/j.ijrmms.2014.08.013>.
- Zuo, J., Liu, H., & Li, H. (2015). A theoretical derivation of the Hoek–Brown failure criterion for rock materials. *Journal of Rock Mechanics and Geotechnical Engineering*, 7(4), 361-366. <http://dx.doi.org/10.1016/j.jrmge.2015.03.008>.

Evaluation of stress history and undrained shear strength of three marine clays using semi-empirical methods based on Piezocone Test

Danielle Caroline Ferreira^{1#} , Faïçal Massad¹ 

Article

Keywords

Piezocone test
Geological history
Marine clays
Consolidation mechanisms
Pre-consolidation pressure
Undrained shear strength

Abstract

The paper presents a comparative study between semi-empirical methods for the estimation of pre-consolidation pressure and undrained shear strength from Piezocone (*CPTu*) data. The first method, proposed by Massad, was developed from observing the variation of these parameters with depth; the second method, proposed by Mayne, was developed from simplifications and relationships between the Spherical Cavity Expansion Theory (*SCET*) and the Critical State Theory; the third method was proposed by Mayne, which considers the variations due to soil type from the *CPT* Index to estimate the pre-consolidation pressure. The methods were validated based on their applications to the marine clay from Santos Coastal Plain, Brazil, Bothkennar clay from Scotland, and Torp Clay from Sweden. It is intended to verify if the results are consistent with each other, with the stress history of these soils and with the available test results. The application of the Massad's method led to results close to the available reference values. The results of the Mayne's method based on *SCET* showed great variability in behavior comparing to the test data depending on the case study. By the Mayne's method based on *CPT* Index values, the calculated pre-consolidation pressures were slightly higher than the values of the available test data. The variations in the results highlighted the importance of validating estimates based on semi-empirical methods through specific tests and the knowledge of geological history contributes to predicting the behavior of clays, since they showed good agreement with the available data from oedometer tests.

1. Introduction

Due to the recurrence of *CPTu* test in field investigations, it is common to use its results to estimate geotechnical parameters, such as pre-consolidation pressure (σ'_a) and undrained shear strength (S_u), instead of performing a large number of specific tests, such as Vane Test (*VT*) and oedometer test, which makes the geotechnical investigation more expensive.

The correlation proposed by Kulhawy & Mayne (1990, apud Coutinho & Oliveira, 1993) is often used to determine the σ'_a , given by:

$$\sigma'_a = \frac{q_t - \sigma_{v0}}{N_{\sigma t}} \quad (1)$$

In general, $N_{\sigma t}$ is in the order of 3.3 (Mayne et al., 1998) to 3.4 (Demers & Leroueil, 2002), among other values.

For the estimation of S_u , Lunne et al. (1985) proposed the second term of Equation 2, based on the Spherical Cavity Expansion Theory (*SCET*), while Tavenas et al. (1982) proposed its determination in terms of excess pore pressure induced by cone penetration (Δu), as the third term of Equation 2.

$$S_u = \frac{q_t - \sigma_{v0}}{N_{kt}} = \frac{\Delta u}{N_{\Delta u}} \quad (2)$$

The most common empirical factor is N_{kt} which varies from 10 to 15 to normally consolidated clays and from 15 to 19 to overconsolidated clays according to Senneset et al. (1989). In practice, its value is usually determined with *VT*.

This paper aims to evaluate three recent studies of semi-empirical methodologies for estimating σ'_a and S_u from *CPTu* data. The Massad's method (2009, 2010, 2016) is based on observations of the variations of σ'_a , S_u and *CPTu* data with depth. Mayne (2016) proposed the method

[#]Corresponding author. E-mail address: danielleferreiraengcivil@gmail.com

¹Universidade de São Paulo, Escola Politécnica, Departamento de Engenharia de Estruturas e Geotécnica, São Paulo, SP, Brasil.

Submitted on September 14, 2021; Final Acceptance on December 16, 2021; Discussion open until August 31, 2022.

<https://doi.org/10.28927/SR.2022.075221>



This is an Open Access article distributed under the terms of the Creative Commons Attribution License, which permits unrestricted use, distribution, and reproduction in any medium, provided the original work is properly cited.

from the relationship between *SCET* and the Critical State Theory and from simplifications in the determination of some parameters difficult to be obtained directly. Mayne (2017) considered the influence of the particle size to estimate σ'_a from *CPT* Index.

These methods were applied to marine clays from Santos Coastal Plain (Brazil), Bothkennar (Scotland), and Torp area (Sweden). It is intended to verify if the estimates are consistent with each other, with the geological history of the clay deposits and with the available test data.

2. Massad's method (2009, 2010, 2016)

Massad (2009, 2010, 2016) presented solutions for estimating both σ'_a and S_u for *SFL* clays (from Sediments-Fluvial Lagoon-Bay) in Santos Coastal Plain, based on their variations with depth and the geological history of these sediments.

2.1 Pre-consolidation pressure obtained by Massad's method (2009, 2010, 2016)

From 20 underground profiles of Santos Coastal Plain with oedometer test data, Massad (2009) noted strong linearity and parallelism in the relationship between σ'_a and σ'_{v0} with depth for the *SFL* clay layer, which suggests overconsolidation due to preloading ($\Delta p = cte$) and allowing to assume the following expression:

$$\sigma'_a = \Delta p + \sigma'_{v0} \quad (3)$$

For other deposits that have the influence of ageing on overconsolidation, the relationship between σ'_a and σ'_{v0} deviates from parallelism. Therefore, the r factor was inserted in Equation 3 as presented in the relationship between the first and second terms of Equation 4.

$$r = \frac{\sigma'_a}{\sigma'_{v0} + \Delta p} = \left(\frac{t}{t_p} \right)^{\frac{C_{ae}/C_c}{1 - C_r/C_c}} \quad (4)$$

The determination of the r factor in terms of C_c , C_r and C_{ae} , as presented in Equation 4, was proposed by Massad (2009) as an adaptation to the formula of Mesri & Choi (1979) with the introduction of Δp to combine the effects of ageing and preloading.

It is observed from Equation 4 that, when admitting that $r = 1$, the effect of ageing is disregarded (Equation 3); on the other hand, by assuming that there is no preloading ($\Delta p = 0$), then $r = OCR > 1$ and σ'_a would vary linearly with depth (Massad, 2009).

From *CPTus* data performed in Santos Coastal Plain, Massad (2009) observed that the *SFL* clays presented a practically linear relationship between the cone tip resistance (q_t) and the depth (z) at a rate “ b ”, so that:

$$q_t = a + b \cdot z \quad (5)$$

By introducing both the relationship between the first and second terms of Equation 4 and the Equation 5 in Equation 1 and matching the dependent terms of the depth, Massad (2009, 2010, 2016) obtained the following formula to determine $N_{\sigma t}$:

$$N_{\sigma t} = \frac{b - \gamma_n}{r \cdot \gamma'} \quad (6)$$

2.2 Undrained shear strength obtained by Massad's method (2009, 2010, 2016)

Hundreds of *VTs* performed on *SFL* clays in Santos city, compiled by Massad (2009, 2010), showed that S_u varies linearly with depth, so that:

$$S_u = c_0 + c_1 \cdot z \quad (7)$$

By relating the Equations 2, 5 and 7 and matching the dependent terms of the depth, Massad (2016) proposed to determine N_{kt} as follows:

$$N_{kt} = \frac{b - \gamma_n}{c_1} \quad (8)$$

3. Mayne's method (2016 and 2017)

The penetration of the *CPTu* generates a very complex stress state and deformation in the surrounding soil mass. Therefore, simplifying hypotheses are used to interpret the boundary conditions, such as the *SCET*.

The equations formulated by Vesić (1972, 1977), from the *SCET* study, are functions of the empirical factors, N_{kt} and $N_{\Delta u}$, and the rigidity index (I_R) as follows:

$$N_{kt} = \frac{4}{3} [\ln(I_R) + 1] + \frac{\pi}{2} + 1 \quad (9)$$

$$N_{\Delta u} = \frac{4}{3} \ln(I_R) \quad (10)$$

According to Mayne (2016), I_R can be determined as an exponential function of pore pressure parameter (B_q) from its relationship with the empirical factors ($N_{\Delta u} = B_q \cdot N_{kt}$) and using the Equations 9 and 10, which was validated through the analysis of $CPTu$ data from 34 soft to firm clays where B_q ranged from 0.45 to 0.75.

3.1 Pre-consolidation pressure obtained by Mayne's method (2016 and 2017)

Mayne (2016) searched a relationship between σ'_a and S_u to apply the *SCET* equations, function of N_{kt} or $N_{\Delta u}$, previously presented. This relationship was made through the Critical State Theory, which provided the following equation:

$$S_u = \left(\frac{M_c}{2} \right) \left(\frac{OCR}{2} \right)^\Lambda \sigma'_{v0} \quad (11)$$

where $M_c = 6 \cdot \sin \phi' / (3 - \sin \phi')$ and $\Lambda = 1 - C_r / C_c$ that ranges from 0.8 to 0.9 (Jamiolkowski et al., 1985; Larsson & Åhnberg, 2005), but Mayne (2016) assumed $\Lambda = 1$ in a simplified way.

Mayne (2016) used the second term of Equation 2 plus Equations 9 and 11 to get the following expression for estimating the σ'_a in terms of cone tip resistance:

$$\sigma'_a = \frac{q_t - \sigma'_{v0}}{M_c \cdot \left(1 + \frac{1}{3} \ln I_R \right)} \quad (12)$$

To estimate in terms of pore pressure, Mayne (2016) used the third expression of Equation 2 and considered the determination of the empirical factor $N_{\Delta u}$ by Equation 10, so that:

$$\sigma'_a = \frac{\Delta u}{\frac{1}{3} M_c \cdot \ln I_R} \quad (13)$$

It can be noted that the denominator of Equation 12 is equivalent to the empirical factor N_{kt} of Equation 1.

In a more recent publication, Mayne (2017) proposed an adaptation of Equation 1 to consider variations due to soil type. The author made a compilation of a data set from a variety of natural soil formations and observed a tendency to divide them into ranges of variation based on their particle size. Therefore, Mayne (2017) introduced the exponent m' that increases with fine contents and decreases with mean grain size, so that:

$$\sigma'_a = 0.33 (q_t - \sigma'_{v0})^{m'} [\text{kPa}] \quad (14)$$

Because m' varies with the soil type, Mayne (2017) noted a strong relationship between this exponent and the *CPT* index (I_c), which allowed him to establish the empirical formula presented below:

$$m' = 1 - \frac{0.28}{1 + \left(\frac{I_c}{2.65} \right)^{25}} \quad (15)$$

In general, the values of I_c and the exponent m' vary according to the soil type, as indicated in Table 1.

3.2 Undrained shear strength obtained by Mayne's Method (2016)

Mayne (2016) reformulated the Equations 9 and 10 putting them as an exponential function of B_q (as previously mentioned) and then replaced it with its definition $B_q = \Delta u / (q_t - \sigma'_{v0})$, getting a simple equation to determine the S_u :

$$S_u = \frac{q_t - u_2 - \sigma'_{v0}}{3.90} \quad (16)$$

By rearranging Equation 16 to define it in terms of the empirical factor N_{kt} , Mayne (2016) got:

$$N_{kt} = \frac{3.90}{(1 - B_q)} \quad (17)$$

4. Applications to soils with known geological history

Three case studies will be presented in which both information about the geological history of the soils and tests of the most varied types are available. The first refers to a

Table 1. Relationship between m' and soil type (Robertson, 1990; Mayne, 2017).

Soil Type	SBT zones	I_c	m'
Sands to silty sands	6	1.31-2.05	0.72
Silty sands to sandy silts	5	2.05-2.60	0.8
Clayey silts to silty clays	4	2.60-2.95	0.85
Silty clays to clays	3	2.95-3.60	0.9 ± 0.1
Organic clays	2	> 3.6	0.9 ± 0.1

marine clay from Santos Coastal Plain, Brazil, the second is about a silty clay from Bothkennar, Scotland, and the third refers to the Torp Clay, Sweden.

4.1 SFL clay in Santos (close to Barnabé Island)

In the area close to Barnabé Island, in Santos Coastal Plain, several tests were performed due to the need to build an embankment for a container yard in the Santos Harbor Channel, where the final level of the earth fills should emerge up to an elevation of +3.5 m in relation to sea level.

4.1.1 Geological history and overconsolidation for the SFL Clay in Santos

The genesis of quaternary sediments in Santos Coastal Plain was explained by Suguio & Martin (1978), who indicated that the relative fluctuations in sea level, both in the Pleistocene and in the Holocene, were the main causes of the formation of sedimentary deposits.

At the peak of the last glaciation, near 15,000 years ago, with the great retreat of the sea level at an elevation of -110 m in relation to the current one, there was an intense erosive process, forming deep valleys. The Santos Transgression, about 7,000 years ago, rose the sea level roughly 6 m above the current level. The sea entered the lower areas, originating an extensive system of lagoons, forming the SFL clays, and eroded partially the Pleistocene sediments, originating the SFL sandy deposits (Massad, 2009).

Close to Barnabé Island, the local SFL clays are highly overconsolidated due to dunes that were active in the area until about 50 to 100 years ago, with $OCR > 2$. These facts imply that $r \approx 1.0$, as shown in Table 2.

There are reports of the existence of dunes about 4 m high on Santo Amaro Island, close to Barnabé Island. By

Table 2. Determination of the r factor of the SFL clay close to Barnabé Island.

Geotechnical Parameters	Values	References
C_{ac}	0.1%	Lambe & Whitman (1979) and Massad (2009)
$C_c/(1+e_0)$	0.43	Massad (2009)
C_{ac}/C_c	0.0023	$C_{ac}/C_c = C_{ac} (1+e_0)$
C_r/C_c	10%	Massad (2009)
C_v	3.00×10^{-6} cm ² /s	Massad et al. (2013)
H_d	10 m	CPTu 101
t_p	1.192 years	Terzaghi's Theory*
t	100 years	Adopted**
r	1.011	Equation 4
r adopted	1	-

*Calculated by Terzaghi's Theory of Consolidation (Terzaghi, 1943): $T = 1.128$ was adopted to represent 95% of degree of consolidation (the end of primary consolidation);

** $t = 100$ years based on geological history, as the dunes were active until recently.

assuming $r = 1$ and $\gamma_n = 19$ kN/m³, the preload due to the dunes is equivalent to $\Delta p \approx 76$ kPa, then it can be said that the equation that represents the geological history of the SFL clay in the area is given by:

$$\sigma'_a = \sigma'_{v0} + 76 [\text{kPa}] \quad (18)$$

as shown by the dotted lines in Figure 1a and Figure 1b.

4.1.2 Soil profile, CPTu and VT for the SFL Clay in Santos

The Figure 2a and Figure 2b presents the CPTu 101 data performed in the area close to Barnabé Island. It is noticed the presence of an upper layer with about 2 to 3 m of a very soft clay (mangrove) followed by sand to the depth of 6 m, where the thick layer of SFL clay begins. The first 6 meters and the isolated points that indicate the occurrence of sand lenses were neglected in the analyses.

From Figure 3, for depths greater than 6 m, $c_f = 1.85$ kPa/m for the VT points performed close to CPTu 101 hole. However, in general, the VTs performed in the area, compiled by Massad (2009), revealed a trend of $c_f = 1.47$ kPa/m, value adopted in the analyses.

4.1.3 Geotechnical parameters and considerations for the SFL Clay in Santos

With the underground profile information, CPTu data and the knowledge of the geological history of the SFL clay in the area close to Barnabé Island, it was possible to fill the Table 3 below.

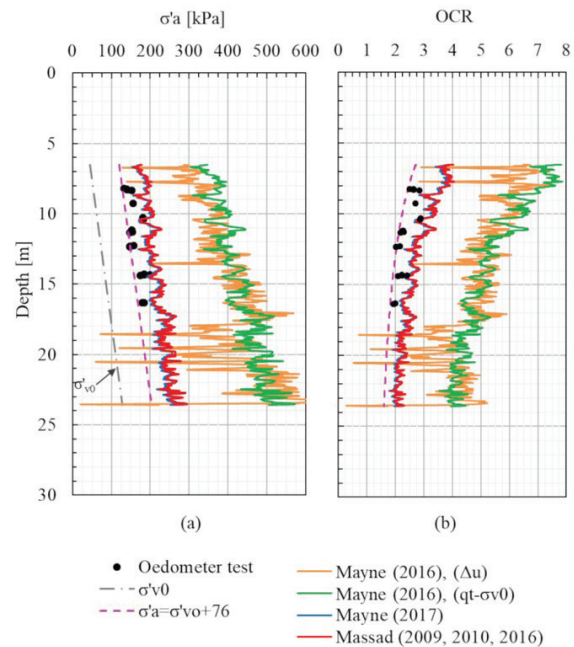


Figure 1. (a) Pre-consolidation pressure (σ'_a) and (b) OCR for the SFL Clay in Santos in the context of its geological history and the application of the semi-empirical methods.

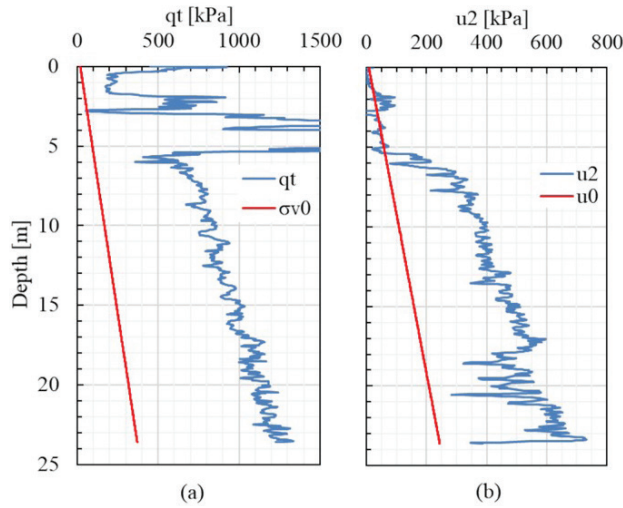


Figure 2. CPTu 101 performed in the area close to Barnabé Island: (a) qt vs. depth and (b) u2 vs. depth.

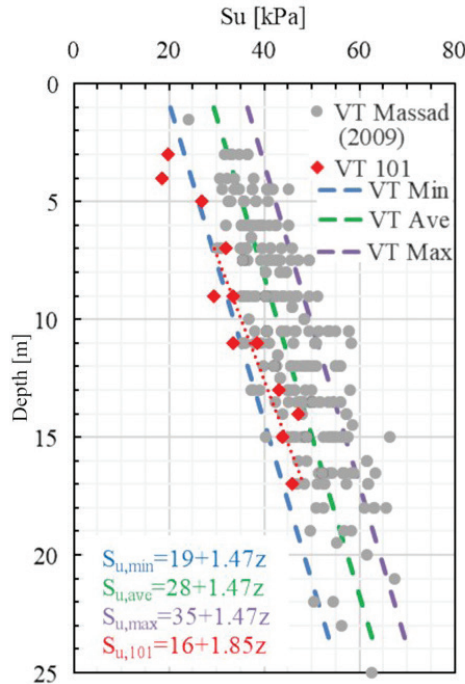


Figure 3. VTs performed in the area close to Barnabé Island.

Figure 4a and Figure 4b show the *SBT* Charts with the *CPTu* 101 data, performed close to Barnabé Island, and with the *CPTu* data from the other case studies presented in this paper.

4.1.4 Analyses of results for the *SFL* Clay in Santos

The analyses of results for *SFL* clay from Barnabé Island area are presented below.

4.1.4.1 Pre-consolidation pressure

By analyzing the results of Figure 1a, the estimates by Massad's (2009, 2010, 2016) and Mayne's (2017) methods

Table 3. Geotechnical parameters of *SFL* clay from the Barnabé Island area to estimate the pre-consolidation pressure and undrained shear strength.

Geotechnical Parameters	Values	References
γ_n	14.9 kN/m ³	<i>CPTu</i> 101 data
b	30.98 kPa/m	<i>CPTu</i> 101 data
r	1.00	Table 2
c_l	1.47 kPa/m	Massad (2009) (Figure 3)
$N_{\sigma t}$ (Massad)	3.28	Equation 6
N_{kt} (Massad)	10.94	Equation 8
B_q	0.03 to 0.70	$B_q = \Delta u / (q_t - \sigma_{v0})$
B_q average	0.42	$B_q = \Delta u / (q_t - \sigma_{v0})$
B_q adopted	0.45	Minimum value studied by Mayne (2016)
I_R	10.99	$I_R = \exp[2.93.B_q / (1 - B_q)]$
ϕ'	24°	Massad (2009)
M_c	0.94	$M_c = 6.\sin\phi' / (3 - \sin\phi')$
$N_{\sigma t}$ (Mayne, 2016)	1.69	Denominator of Equation 12
N_{kt} (Mayne, 2016)	7.10	Equation 17
Q_t	6 to 13	Figure 4ab
F_R	0.4 to 3.0%	Figure 4b
I_c	2.95	Figure 4ab and Table 1
m'	0.982	Equation 15
$N_{\sigma t}$ (Mayne, 2017)	-	Indeterminable

practically coincided and came close to oedometer test data performed by Andrade (2009) using Shelby samples extracted at a certain distance from the *CPTu* 101 borehole, with regular to good qualities. Taking as reference the *OCR* values indicated by Massad et al. (2013) for the Barnabé Island area, $OCR > 2$, and for Santo Amaro Island (close to Barnabé Island), $OCR = 2.5$, it is noticed (Figure 1b) that the oedometer test data and the applications of Massad's (2009, 2010, 2016) and Mayne's (2017) methods led to results closer to those expected from the geological history of the local soil. The application of Mayne's method (2016), however, led to mean *OCR* of 5, with great dispersion, which does not represent the studied clay.

The empirical factor $N_{\sigma t}$ obtained by Mayne's (2016) method, both in terms of cone tip resistance and pore pressure, was $N_{\sigma t} = 1.69$, thus half of the value obtained by Massad's (2009, 2010, 2016) method, $N_{\sigma t} = 3.28$, which resembled the available reference values (3.3 to 3.4). It should be mentioned that this figure corresponds to the *CPTu* 101. Working with results of 15 *CPTus*, in this same area, including the former one, Massad (2016) arrived to $N_{\sigma t} = 3.9$ as an average value.

Figure 5a was built to analyze the sensitivity of the available parameters entered in the calculation to estimate σ'_a by the Mayne's method (2016) and it was noted that

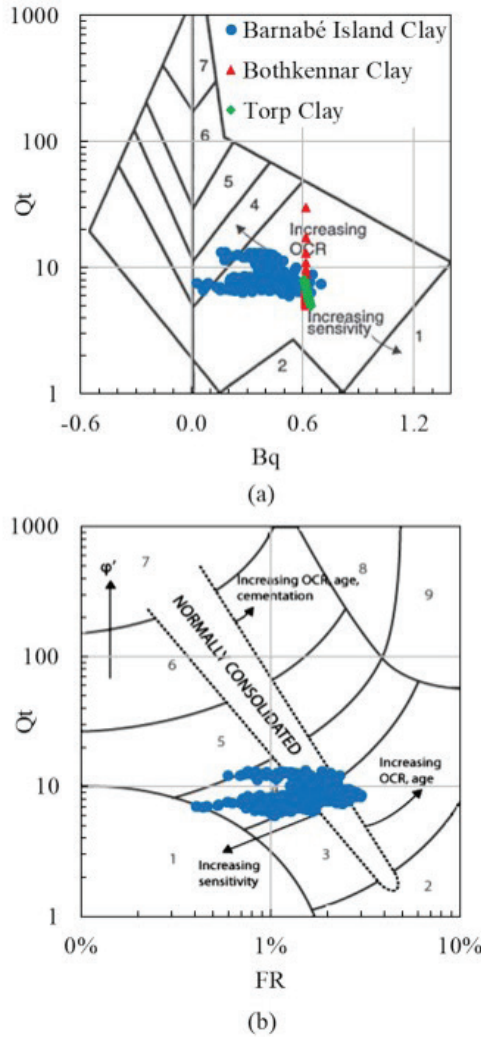


Figure 4. Robertson's SBT Charts (Robertson, 1990): (a) data from all case studies in Q_t vs. B_q Chart and (b) data from the area close to Barnabé Island in Q_t vs. FR Chart.

variations in B_q (used in the calculation of I_R as proposed by Mayne (2016)) greatly affect the results (N_{σ} values). The range of B_q between 0.45 and 0.75 was the same used by Mayne (2016).

Although the effects of the variations of B_q have been minimized by using an average value for the entire profile, as proposed by Mayne (2016), and restricting it to 0.45, the magnitude of N_{σ} was much lower than the reference values. The relatively low ϕ' (used in the calculation of M_c as indicated by Mayne (2016)) of the *SFL* clay also contributed to reduce N_{σ} , as shown in Figure 5a.

4.1.4.2 Undrained Shear Strength

The Figure 6 shows the results of applying the methods of Massad (2009, 2010, 2016) and Mayne (2016), the *VT* data, the correlations S_u vs. z presented by Massad (2009) to the Barnabé Island area and the curve related to $N_{kt} = 15$.

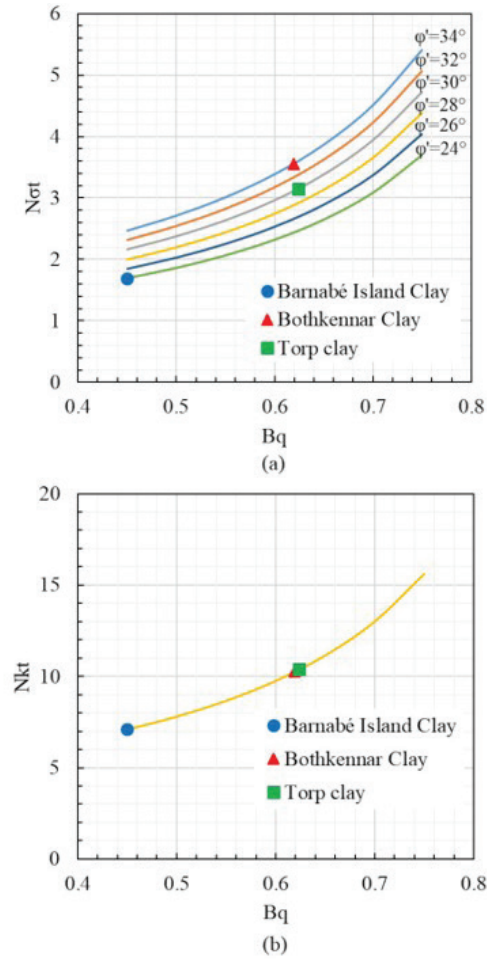


Figure 5. Parametric sensitivity analysis for estimating (a) Net factor and (b) N_{kt} factor by Mayne's method (Mayne, 2016) for all case studies.

The application of Massad's method (2009, 2010 and 2016) resulted in S_u around 20 kPa higher than the "*VT Ave*" as shown in Figure 6. The Mayne's method (2016) revealed an even greater difference, with resistance values of about 50 kPa higher than the available data.

For the range of B_q values used by Mayne (2016) ($0.45 < B_q < 0.75$), it can be seen from Figure 5b that N_{kt} varies between 7.1 and 15.6. Senneset et al. (1989) indicated N_{kt} ranging from 10 to 15 for normally consolidated clays and from 15 to 19 for overconsolidated clays. Therefore, the range of the Mayne (2016) dataset is restricted to typical values of normally consolidated clays.

However, as seen above, the *SFL* clay from Barnabé Island area is overconsolidated, which according to Senneset et al. (1989) would lead to N_{kt} greater than 15, well above the values estimated by Mayne's (2016) and Massad's (2009, 2010, 2016) methods, 7.1 and 10.9, respectively. As shown in Figure 6, the curve for S_u calculated with $N_{kt} = 15$ overlapped the "*VT Ave*" curve, getting very close to the *VT* data, confirming that N_{kt} estimated by the studied methods were lower than expected values.

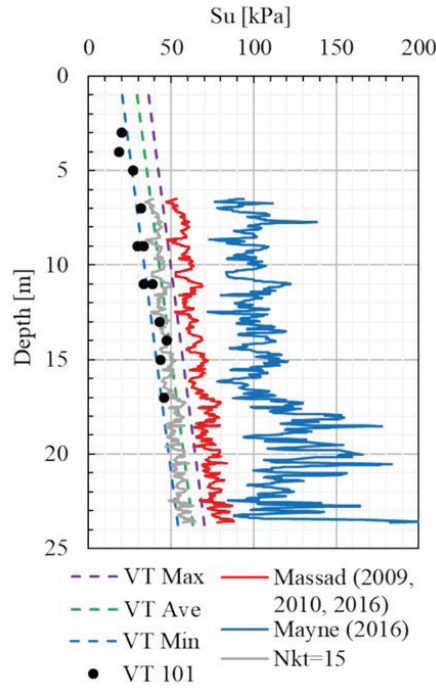


Figure 6. Comparison of different methods for estimating undrained shear strength for SFL clay from Barnabé Island area.

Finally, an evaluation of the S_u/σ'_a relationship was made for the studied methods: by Massad's method (2009, 2010, 2016), $S_u/\sigma'_a = 0.30$ was obtained; for Mayne's method (2016), this value was 0.25 in terms of cone tip resistance and 0.30 in terms of pore pressure. Thus, although the S_u and σ'_a values have been quite different between the methods, their ratios were close.

As a reference, there is the following empirical correlation:

$$\frac{S_u}{\sigma'_a} = \frac{\sqrt{I_p}}{22} \quad (19)$$

proposed by Mayne & Mitchell (1988), where I_p is the plasticity index of the soil. From the tests performed by Andrade (2009), $I_p = 75\%$ for the SFL clay in the Barnabé Island area, leading to $S_u/\sigma'_a = 0.39$, significantly higher than the figures presented above.

4.2 Bothkennar Clay

The study site is in the Bothkennar region, on the edge of the River Forth, situated between Edinburgh and Glasgow, Scotland, UK.

The soft silty clay at Bothkennar attracted the interest of many researchers due to its homogeneity, described by Nash et al. (1992a) as being "remarkably uniform" when compared to other locations in the UK.

4.2.1 Geological history and overconsolidation for Bothkennar Clay

Around 7,000 years ago, the Bothkennar region was going through a process of sediment deposition, which reached a level about +4.5 m in relation to the current sea level (Nash et al., 1992a). Later, with the marine regression and the consequent erosive processes, part of this material was removed, thus the Bothkennar clay suffered an overconsolidation by preloading, which according to Nash et al. (1992a), was equivalent to a load of $\Delta p = 15$ kPa. This observation allowed the authors to assume that the σ'_a of this clay could be obtained by the following equation, also represented in a curve in Figure 7a and Figure 7b:

$$\sigma'_a = \sigma'_{v0} + 15 \text{ [kPa]} \quad (20)$$

The curve suggested by Nash et al. (1992a) resulted in lower pressures in relation to the oedometer tests data for which Nash et al. (1992a) proposed a second curve (see Figure 7a and Figure 7b), with $OCR = 1.55$, mean value of the oedometer tests, given by:

$$\sigma'_a = 1.55 \cdot \sigma'_{v0} \quad (21)$$

There is a gap between the curves of the two expressions proposed by Nash et al. (1992a). The authors attributed this difference to the possibility that ageing had a greater influence on clay overconsolidation. However, it is evident that there is a contradiction between the premises that gave rise to the two curves: the curve given by Equation 20 only considers the influence of preload while the curve related to Equation 21 assumes that only ageing is responsible for the clay overconsolidation, by considering that OCR is constant.

To combine both overconsolidation mechanisms, ageing + preloading, a third curve is being proposed based on the adjustment of the expression of Equation 20 proposed by Nash et al. (1992a) with the insertion of the r factor given by Equation 4, so that:

$$\sigma'_a = 1.33 \cdot (\sigma'_{v0} + 15) \text{ [kPa]} \quad (22)$$

As shown in Table 4, $r = 1.33$ to the Bothkennar Clay.

4.2.2 Soil Profile, $CPTu$ and VT for Bothkennar Clay

Figure 8a and Figure 8b show the $CPTu$ data performed at the Bothkennar test site by Powell & Lunne (2005). The water level was found at -0.8 m of depth in relation to the ground level and it is important to highlight the existence of a dry crust, up to a depth of 2 to 3 m, which was probably

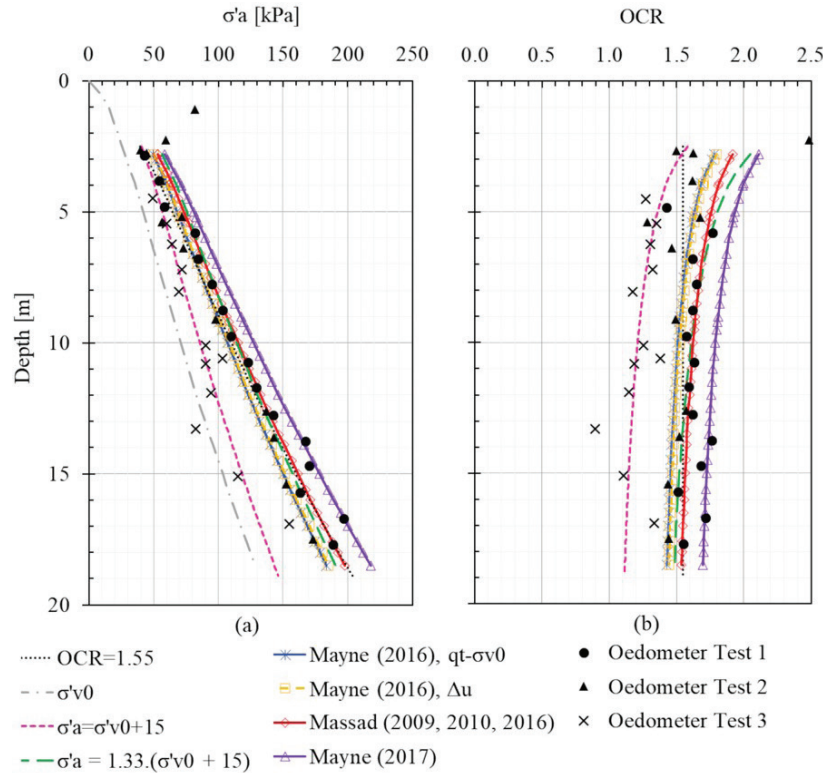


Figure 7. (a) Pre-consolidation pressure (σ'_a) and (b) OCR for the Bothkennar Clay in the context of its geological history and the application of the semi-empirical methods.

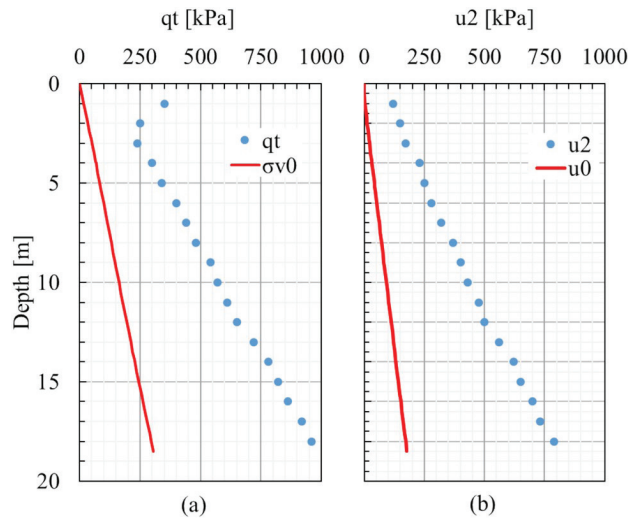


Figure 8. CPTu performed in Bothkennar test site: (a) qt vs. depth and (b) u_2 vs. depth (Powell & Lunne (2005) data).

formed due to variations in sea level according to Nash et al. (1992a). The existence of this crust affected the resistance of the soil; therefore, the first 2.5 m were neglected in the analyses.

Nash et al. (1992a) performed laboratory (triaxial UU) and field (VT and pressuremeter) tests to measure S_u . The authors also performed an indirect evaluation of this parameter using dilatometer test (DMT) data. Figure 9 presents the results.

Table 4. Determination of the r factor of the Bothkennar Clay.

Geotechnical Parameters	Values	References
$C_{\alpha e}/C_c$	0.04	Nash et al. (1992b)
C_r/C_c	0.10	Nash et al. (1992b)
C_v	$3.17 \times 10^{-7} \text{ m}^2/\text{s}$	Nash et al. (1992a)
H_d	10 m	Nash et al. (1992a)
t_p	10 years	Terzaghi's Theory*
t	6,000 years	Nash et al. (1992a)
r	1.33	Equation 4

*Calculated by Terzaghi's Theory of Consolidation (Terzaghi, 1943): $T = 1.128$ was adopted to represent 95% of degree of consolidation (the end of primary consolidation).

It is possible that the line of the “Average VT ” was obtained considering the dry crust. Therefore, to avoid taking parameters distorted by the crust, it was decided to consider the pressuremeter data to estimate the coefficient c_f , disregarding the points above 3 m depth; thereby, $c_f = 2.94 \text{ kPa/m}$ was obtained.

4.2.3 Geotechnical parameters and considerations for Bothkennar Clay

With the underground profile information, $CPTu$ data and the knowledge of the geological history of Bothkennar clay, it was possible to fill the Table 5 below.

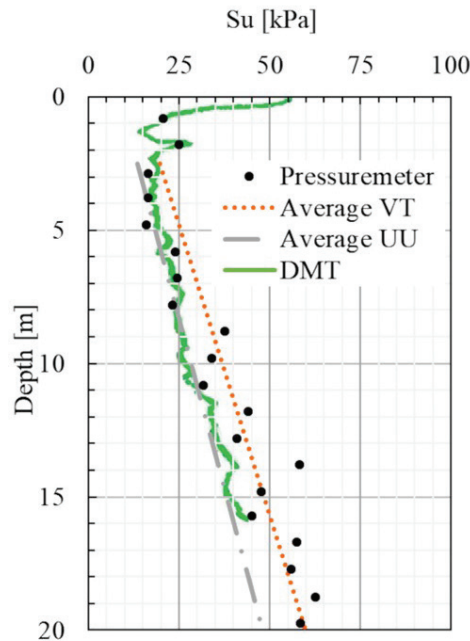


Figure 9. VT, Pressuremeter, triaxial UU and DMT performed in Bothkennar test site (Nash et al. (1992a) data).

Table 5. Geotechnical parameters of Bothkennar clay to estimate the pre-consolidation pressure and undrained shear strength.

Geotechnical Parameters	Values	References
γ_n	16.7 kN/m ³	Mayne (2016)
b	46.12 kPa/m	<i>CPTu</i> data
r	1.33	Table 4
c_l	2.94 kPa/m	Pressuremeter data
N_{ot}	3.30	Equation 6
(Massad)		
N_{kt}	9.99	Equation 8
(Massad)		
B_q	0.619	Mayne (2016)
I_R	116.78	$I_R = \exp[2.93.B_q/(1-B_q)]$
ϕ'	34°	Mayne (2016)
M_c	1.37	$M_c = 6.\sin\phi'/(3-\sin\phi')$
N_{ot}	3.56	Denominator of
(Mayne, 2016)		Equation 12
N_{kt}	10.24	Equation 17
(Mayne, 2016)		
Q_i	5 to 30	Figure 4a
I_c	3.275	Figure 4a and Table 1
m'	0.9986	Equation 15
m' adopted	1	-
N_{ot}	3.0	As $m' = 1$, $N_{ot} = 1/0.33$
(Mayne, 2017)		

4.2.4 Analyses of results for Bothkennar Clay

The analyses of results for Bothkennar Clay are presented below.

4.2.4.1 Pre-consolidation pressure

By the results presented in Figure 7a and Figure 7b, it is evident the great approximation between the values estimated for the σ'_a and the *OCR* by the Mayne's (2016) and Massad's (2009, 2010, 2016) methods. When applying the Mayne's method (2017), the resulting curve indicated a slightly higher overconsolidation, drifting away from the curve of Nash et al. (1992a) adapted with the *r* factor and the curves proposed by Nash et al. (1992a).

As for this case of Bothkennar clay $m' = 1$, the value of 3.0 referring to the inverse of the factor of Equation 14 (1/0.33) can be compared with the values of N_{ot} obtained by the Mayne's (2016) and Massad's (2009, 2010, 2016) methods: 3.56 and 3.30, respectively, highlighting the proximity between them. The Mayne's (2016) and Massad's (2009, 2010, 2016) methods were the closest to the values referenced by Mayne et al. (1998) and Demers & Leroueil (2002): 3.3 and 3.4.

4.2.4.2 Undrained shear strength

Figure 10 shows the results of applying the methods of Massad (2009, 2010, 2016) and Mayne (2016), the pressuremeter, triaxial *UU* and *VT* data and the indirect evaluation of S_u by *DMT* data.

The curves of the Massad's (2009, 2010, 2016) and Mayne's (2016) methods were very close to each other and had a good agreement with S_u values obtained from the pressuremeter and the "Average *VT*" data, showing a small deviation for greater depths ($z > 12$ m), possibly because Nash et al. (1992a) did not disregard the points of the *VT*s obtained at depths below 3 m (dry crust occurrence) when tracing the "Average *VT*" line. If the value of $c_l = 2.30$ kPa/m from the *VT* data was taken as a reference, the curve proposed with the Mayne's method (2016) would not be affected, only the Massad's curve (2009, 2010, 2016) would suffer a displacement towards *DMT* and "Average *UU*" data.

The N_{kt} values obtained by the Mayne's (2016) and Massad's (2009, 2010, 2016) methods, 10.2 and 10, respectively, are almost the same. Senne set al. (1989) indicated a range of N_{kt} from 15 to 19 for overconsolidated clays, as Bothkennar clay, which suffered overconsolidation due to ageing and preloading. However, it would lead to lower S_u values, moving away from pressuremeter data and "Average *VT*", getting closer to other test data (*DMT* and "Average *UU*").

The S_u/σ'_a relationship obtained was 0.33 by the Massad's (2009, 2010, 2016) method and 0.35 by the Mayne's (2016) method, in terms of cone tip resistance, and 0.34, in terms of

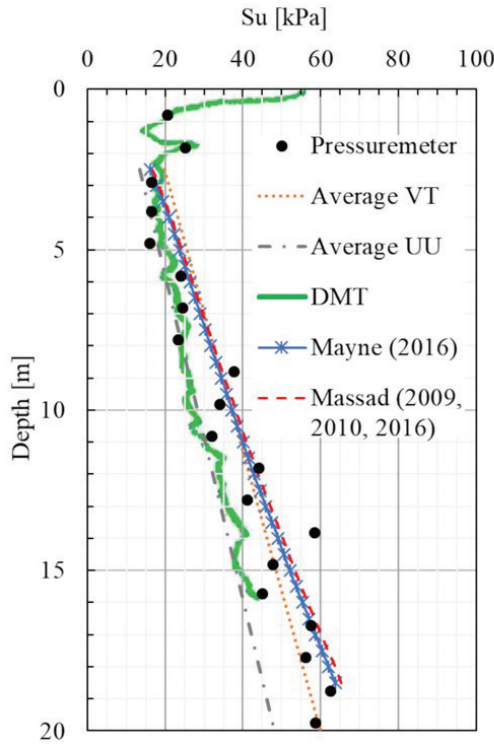


Figure 10. Comparison of different methods for estimating undrained shear strength for Bothkennar Clay.

pore pressure. Knowing that for Bothkennar clay $I_p = 40\%$, the correlation of Mayne & Mitchell (1988), Equation 19, gives $S_u/\sigma'_a = 0.29$, quite close to the above figures.

4.3 Torp Clay

Torp Clay is found in the southern part of the municipality of Munkedal, Sweden, in the Torp area, which is located on the west bank of the river Örekilsälven.

In the so-called Section C of the Torp area, *CPTu*, *VT* and oedometer tests were performed in points of interest such as: at the bottom of the river channel, in excavated areas and at the top of the slope crest. In this study, it was decided to apply the semi-empirical methods only at a point in an excavated area, denominated point *S9*, because it is the location with the greatest depth and because it was also the object of analysis by Mayne (2017).

4.3.1 Geological history and overconsolidation for Torp Clay

According to Larsson & Åhnberg (2003), during the last glaciation, the Torp area was covered by ice. About 12,400 years ago, with the retreat of the ice front and the progress of the isostatic uplift of the land, the sea level gradually became shallower, and the deposition of sediments began: postglacial sediments started to overlay the glacial deposits. With the further decline in sea level, the river was formed in

the higher areas and the eroded particles were transported by the river and started to deposit far from the river mouth.

Erosive processes, slides in the slopes of the riverbanks and excavations in the area were the main factors responsible for overconsolidating the Torp Clay, involving, above all, preloading and ageing mechanisms.

The Torp Clay consolidated until reaching the maximum preload of $\Delta p \approx 100$ kPa, so that:

$$\sigma'_a = \sigma'_{v0} + 100 \text{ [kPa]} \quad (23)$$

and then suffered a slight overconsolidation due to ageing equivalent to $r = 1.15$, so that:

$$\sigma'_a = 1.15 \cdot (\sigma'_{v0} + 100) \text{ [kPa]} \quad (24)$$

as shown by the dotted lines in Figure 11a and Figure 11b. It is possible to assume that *OCR* varies from 1.3 to 3.2, thereby it is an overconsolidated clay, confirming the geological history of the area.

4.3.2 Soil Profile, *CPTu* and *VT* for Torp Clay

As described by Larsson & Åhnberg (2003), the underground profile of the area is heterogeneous, composed of a sandy layer at the top, followed by clay with silt/sand lenses and, at greater depths, it returns to granular material. An analysis of the *CPTus* at Point *S9* (Figure 12a and Figure 12b) and at neighboring points (not shown) allowed to identify that the clay layer, with silt/sand lenses, occurs between elevations +3 and -23 m, which, for Point *S9*, correspond to depths 11 to 37 m.

Figure 13 presents the results of the *VTs* performed in Point *S9* of the Torp area by Larsson & Åhnberg (2003). It is possible to assume $c_f = 1.15$ kPa/m for the Torp Clay layer.

4.3.3 Geotechnical parameters and considerations for Torp Clay

With the underground profile information, *CPTu* data and the knowledge of the geological history of Torp Clay, it was possible to fill the Table 6 below.

4.3.4 Analyses of results for Torp Clay

The analyses of results for Torp Clay are presented below.

4.3.4.1 Pre-consolidation pressure

The Figure 11a and Figure 11b show the results of Massad's (2009, 2010, 2016) and Mayne's (2016 and 2017) methods in the context of geological history of the Torp area, as mentioned above. There is a good approximation between them. Moreover, comparing the results of these methods with the available data by Larsson & Åhnberg (2003), the estimated

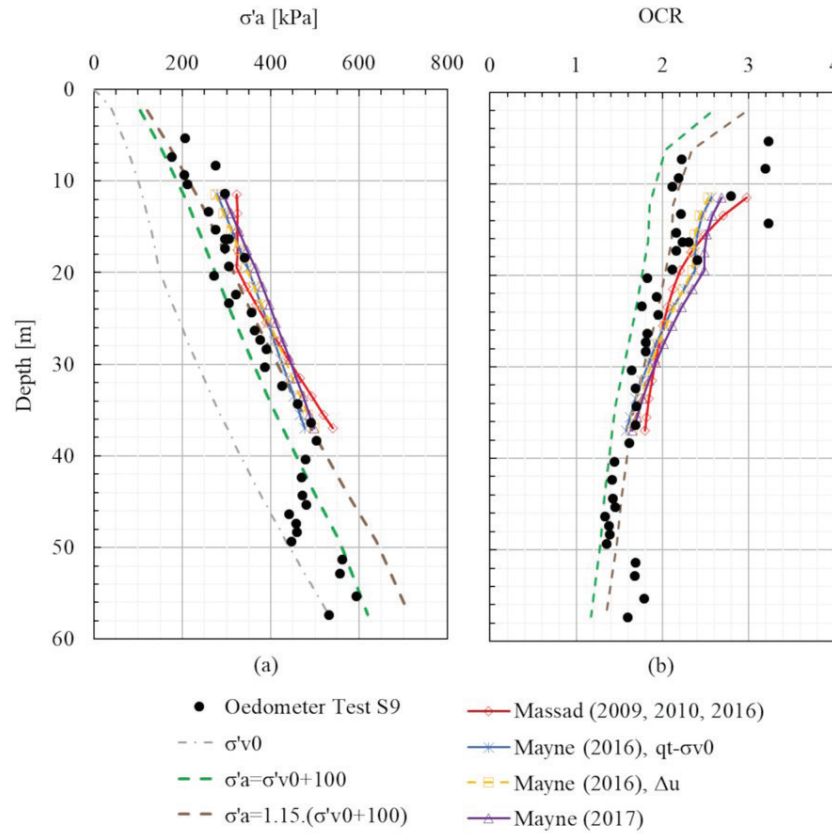


Figure 11. (a) Pre-consolidation pressure (σ'_a) and (b) OCR for Torp Clay in the context of its geological history and the application of the semi-empirical methods.

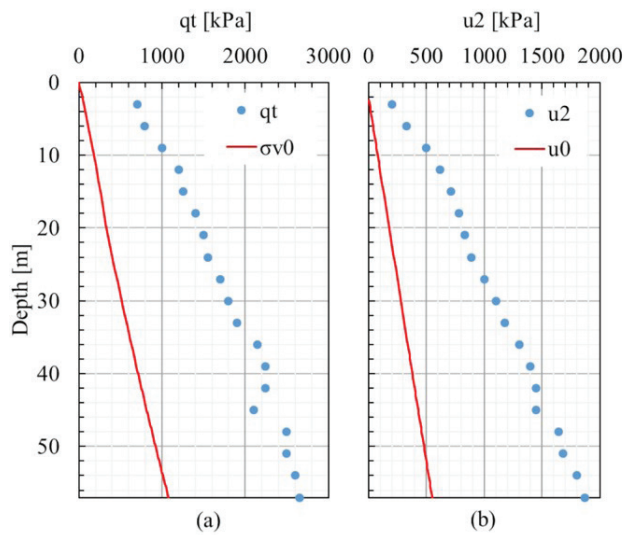


Figure 12. CPTu data from Point S9 of the Torp area (a) qt vs. depth and (b) u2 vs. depth (Larsson & Åhnberg (2003) data).

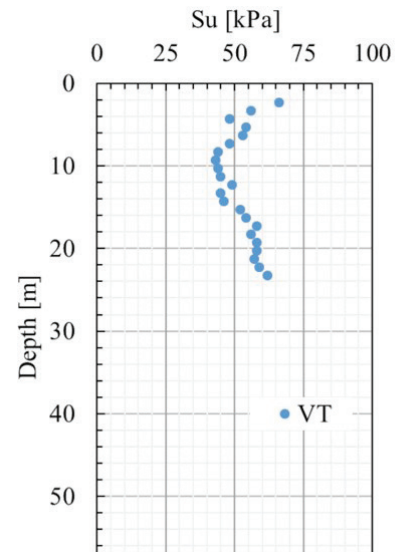


Figure 13. VT data from Point S9 of the Torp area (Larsson & Åhnberg (2003) data).

pre-consolidation pressures were slightly higher than the curve given by Equation 24, situation in which both preloading and ageing acted. For Point S9, as expected, the occurrence of excavations led the clay to a highly overconsolidated condition, with OCR between 1.5 and 3.0.

As shown in Table 6, the N_{ot} values obtained by Mayne's (2016 and 2017) and Massad's (2009, 2010, 2016) methods were very similar, being slightly lower than the values referenced by Mayne et al. (1998) and Demers & Leroueil (2002): 3.3 and 3.4.

Table 6. Geotechnical parameters of Torp Clay to estimate the pre-consolidation pressure and undrained shear strength.

Geotechnical Parameters	Values	References
γ_n	16.4 to 17.7 kN/m ³	Larsson & Åhnberg (2003)*
b	41.8 kPa/m	CPTu data
r	1.15	Larsson & Åhnberg (2003)
c_l	1.15 kPa/m	VT data (Figure 12)
N_{ot}	2.75 to 3.50	Equation 6
(Massad)		
N_{kt}	21 to 22	Equation 8
(Massad)		
B_q average	0.624	$B_q = \Delta u / (q_t - \sigma_{v0})$
I_R	129.35	$I_R = \exp[2.93 \cdot B_q / (1 - B_q)]$
ϕ'	30°	Larsson & Åhnberg (2003)
M_c	1.20	$M_c = 6 \cdot \sin \phi' / (3 - \sin \phi')$
N_{ot}	3.14	Denominator of
(Mayne, 2016)		Equation 12
N_{kt}	10.37	Equation 17
(Mayne, 2016)		
Q_t	5 to 8	Figure 4a
I_c	3.275	Figure 4a and Table 1
m'	0.9986	Equation 15
m' adopted	1	-
N_{ot}	3.0	As $m' = 1$, $N_{ot} = 1/0.33$
(Mayne, 2017)		

*From γ_n vs. z graph between elevations +3 and -23 m for Point S9.

4.3.4.2 Undrained shear strength

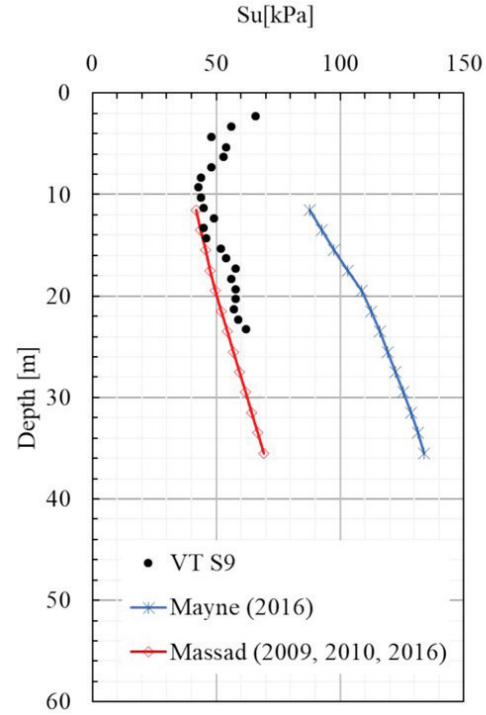
Figure 14 shows the results of applying the methods of Massad (2009, 2010, 2016) and Mayne (2016) and the VT data performed at the test site.

The curve for the application of the Massad's method (2009, 2010, 2016) was closer to the VT data when compared to the curve of the Mayne's method (2016).

There is a large difference between the N_{kt} values obtained by the Mayne's (2016) and Massad's (2009, 2010, 2016) methods, 10.4 and 21.5, respectively. The last number is close to the upper limit indicated by Senneset et al. (1989) for overconsolidated clays, as mentioned above.

The S_u/σ'_a relationship obtained by the methods was quite different: $0.13 < S_u/\sigma'_a < 0.15$ by the Massad's method (2009, 2010, 2016) and $0.27 < S_u/\sigma'_a < 0.32$ by the Mayne's method (2016), both in terms of pore pressure and in terms of cone tip resistance. To determine S_u/σ'_a by the correlation of Mayne & Mitchell (1988), Equation 19, the value of I_p was estimated between 40 and 56%, based on I_p data presented by Larsson & Åhnberg (2003) for the elevations of interest (between +3 and -23 m), resulting $0.29 < S_u/\sigma'_a < 0.34$.

It is interesting to present the studies by Larsson & Åhnberg (2003) regarding the S_u/σ'_a relationship. The authors

**Figure 14.** Comparison of different methods for estimating undrained shear strength for Torp Clay.

proposed an empirical correlation based on direct shear tests data performed on Torp Clay samples that indicated the trend given, mathematically, by:

$$\frac{S_u}{\sigma'_a} = a^* \cdot OCR^{b^* - 1} \quad (25)$$

where $a^* = 0.22$ and $b^* = 0.8$.

For the studied clay layer, OCR varies between 1.3 and 3.2, so that, from Equation 25, it follows $0.17 < S_u/\sigma'_a < 0.21$, therefore, greater than the mean value of 0.14 obtained by Massad's method (2009, 2010, 2016), but far below the mean values of 0.29 and 0.32 of Mayne's (2016) method and Mayne & Mitchell's (1988) correlation (Equation 19), respectively. This inconsistency was widely discussed by Larsson & Åhnberg (2005).

5. Conclusions

For all case studies, the curves obtained from $\sigma'_a = r \cdot (\sigma'_{v0} + \Delta p)$, calculated with knowledge of geological history, considering preloading and ageing mechanisms, had a close approximation with the available oedometer test data.

It was observed that, in general, the application of the Massad's method (2009, 2010, 2016), both to estimate σ'_a and S_u , led to results consistent with those obtained through specific tests and with the geological history of the deposits. For all studied marine clays, the application of the Mayne's

method (2017) led to overconsolidation slightly higher than expected by the same verifications mentioned above. For the Mayne's method (2016), it was noticed that extreme values of B_q greatly affected the results, impairing the analyses and it presented better agreement for two clays, in terms of σ'_a , and for one clay, in terms of S_u .

The variability of results by different methods on different clays evidences that the use of semi-empirical methods to estimate geotechnical parameters provides a reduction in the number of specific tests required, but do not replace them, because they are essential for validation purposes, considering the knowledge of geological history of the test site.

Acknowledgements

The authors acknowledge the EPUSP (Escola Politécnica da Universidade de São Paulo) and CNPq (Conselho Nacional de Desenvolvimento Científico e Tecnológico) for the support given to the research.

Declaration of interest

The authors have no conflicts of interest to declare. All co-authors have observed and affirmed the contents of the paper and there is no financial interest to report.

Authors' contributions

Danielle Caroline Ferreira: Conceptualization, Data curation, Methodology, Validation, Writing – original draft, review and editing, Visualization. Faíçal Massad: Conceptualization, Data acquisition, Methodology, Supervision. Validation, Writing – review and editing.

List of symbols

a	Cone tip resistance at the surface
ave	Average
a*	Soil constant proposed by Larsson & Åhnberg (2003)
b	Cone tip resistance rate of increase with depth
b*	Soil constant proposed by Larsson & Åhnberg (2003)
B_q	Pore pressure parameter
c_0	Undrained shear strength at the surface
c_1	Undrained shear strength rate of increase with depth
C_c	Virgin compression index
CPT	Cone Penetration Test
CPTu	Piezcone Test
C_r	Recompression index
C_v	Vertical coefficient of primary compression
C_{ac}	Vertical coefficient of secondary compression in function of void ratio variation

C_{ac}	Vertical coefficient of secondary compression
DMT	Dilatometer Test
e_0	Initial void raio
F_R	Normalized friction ratio
H_d	Drainage height
I_c	CPT index
I_p	Plasticity index
I_R	Rigidity index
min	Minimum
max	Maximum
m'	Exponent relative to soil type
M_c	Frictional parameter for triaxial compression
N_{kt}	Empirical factor to determine S_u in terms of $(q_t - \sigma_{v0})$
$N_{\Delta u}$	Empirical factor to determine S_u in terms of Δu
$N_{\sigma a}$	Empirical factor to determine σ'_a
OCR	Over consolidation ratio
q_t	Cone tip resistance
Q_t	Normalized cone resistance
r	Ageing effect consideration factor
S9	Point of study in Torp test site
SBT	Soil Behavioural Type
SCET	Spherical Cavity Expansion Theory
SFL	Sediments-Fluvial Lagoon-Bay
S_u	Undrained Shear strength
t	Time of secondary compression
T	Terzaghi's Time factor
t_p	Time of primary compression
u_0	Hydrostatic pressure
u_2	Pore pressure measured behind the cone
UU	Unconsolidated undrained triaxial test
VT	Vane Test
z	Depth in relation to the ground level
Δp	Preloading
Δu	Excess pore pressure
φ'	Effective friction angle
γ'	Submerged unit weight
γ_n	Unit weight
Λ	Plastic volumetric strain ratio
σ'_a	Pre-consolidation pressure
σ'_{v0}	Vertical effective pressure
σ_{v0}	Total overburden pressure

References

- Andrade, M.E.S. (2009). *Contribution to the study of soft clays from the city of Santos* [Master's dissertation]. Universidade Federal do Rio de Janeiro, Rio de Janeiro (in Portuguese).
- Coutinho, R.Q., & Oliveira, J.T.R. (November, 1993). Caracterização geotécnica de uma argila mole do Recife. In *Anais do Simpósio Geotécnico COPPEGEO*. Rio de Janeiro, Brazil. (in Portuguese).
- Demers, D., & Leroueil, S. (2002). Evaluation of preconsolidation pressure and the overconsolidation ratio from piezcone

- tests of clay deposits in Quebec. *Canadian Geotechnical Journal*, 39(1), 174-192. <http://dx.doi.org/10.1139/t01-071>.
- Jamiolkowski, M., Ladd, C.C., Germaine, J.T., & Lancellotta, R. (1985). New developments in field and lab testing of soils proceedings. In *11th International Conference on Soil Mechanics and Foundation Engineering* (pp. 57-153). San Francisco.
- Kulhawy, F.H., & Mayne, P.W. (1990). *Manual on estimating soil properties for foundation design (Electric Power Research Institute)*. Palo Alto, CA: Geotechnical Engineering Group.
- Lambe, T.W., & Whitman, R.V. (1979). *Soil mechanics, SI version*. New York: Wiley.
- Larsson, R., & Åhnberg, H. (2003). *Long-term effects of excavations at crests of slopes*. Linköping: Statens geotekniska institut.
- Larsson, R., & Åhnberg, H. (2005). On the evaluation of undrained shear strength and preconsolidation pressure from common field tests in clay. *Canadian Geotechnical Journal*, 42(4), 1221-1231. <http://dx.doi.org/10.1139/t05-031>.
- Lunne, T., Christoffersen, H.P., & Tjelta, T.I. (1985). Engineering use of Piezocone data in North Sea clays. In *11th International Conference on Soil Mechanics and Foundation Engineering* (pp. 907-912). San Francisco.
- Massad, F. (2009). *Solos marinhas da baixada santista: características e propriedades geotécnicas*. São Paulo: Oficina de Textos (in Portuguese).
- Massad, F. (2010). Nova proposta para a estimativa das pressões de pre-adensamento de argilas marinhas com base no CPTU. In *XV COBRAMSEG: Engenharia Geotécnica para o Desenvolvimento, Inovação e Sustentabilidade*. Gramado, Brasil: ABMS (in Portuguese).
- Massad, F. (2016). Estimation of geotechnical parameters of Santos marine clays using piezocone and vane tests in statistical basis. In *XVIII COBRAMSEG: Engenharia Geotécnica para o Desenvolvimento, Inovação e Sustentabilidade*, Belo Horizonte, Brasil: ABMS.
- Massad, F., Teixeira, A.H., Carvalho, C.T., & Grangé, L.F.A. (2013). Settlements of earth fills on thick layers of overconsolidated soft clays without geodrains. In P. Delage, J. Desrues, R. Frank, A. Puech & F. Schlosser (Eds.), *Proceedings of the 18th International Conference on Soils Mechanics and Geotechnical Engineering*. Paris: Presses des Ponts.
- Mayne, P.W. (2016). Evaluating effective stress parameters and undrained shear strengths of soft-firm clays from CPT and DMT. *Australian Geomechanics Journal*, 51(4), 27-55. Retrieved in September 14, 2021, from <https://geosystems.ce.gatech.edu/Faculty/Mayne/papers>
- Mayne, P.W. (2017). Stress history of soils from cone penetration tests (Manual rocha lecture). *Soils and Rocks*, 40(3), 203-218. <http://dx.doi.org/10.28927/SR.403203>.
- Mayne, P.W., & Mitchell, J.K. (1988). Profiling of overconsolidation ratio in clays by field vane. *Canadian Geotechnical Journal*, 25(1), 150-157. <http://dx.doi.org/10.1139/t88-015>.
- Mayne, P.W., Robertson, P.K., & Lunne, T. (1998). Clay stress history evaluated from seismic piezocone tests. In: P.K. Robertson & P.W. Mayne (Eds.), *Geotechnical site characterization* (pp. 1113-1118). Rotterdam: Balkema.
- Mesri, G., & Choi, Y.K. (1979). Strain rate behavior of Saint-Jean Vianney clay: discussion. *Canadian Geotechnical Journal*, 16(4), 831-834. <http://dx.doi.org/10.1139/t79-092>.
- Nash, D.F.T., Powell, J.J.M., & Lloyd, I.M. (1992a). Initial investigations of the soft clay test bed site at Bothkennar clay site. *Geotechnique*, 42(2), 163-181. <http://dx.doi.org/10.1680/geot.1992.42.2.163>.
- Nash, D.F.T., Sills, G.C., & Davison, L.R. (1992b). One-dimensional consolidation testing of soft clay from Bothkennar. *Geotechnique*, 42(2), 241-256. <http://dx.doi.org/10.1680/geot.1992.42.2.241>.
- Powell, J.J.M., & Lunne, T. (2005). A comparison of different sized piezocones in UK clays. In *Proceedings of the 16th International Conference on Soil Mechanics and Geotechnical Engineering* (Vol. 1, pp. 729-734). Burke: IOS press.
- Robertson, P.K. (1990). Soil classification using the cone penetration test. *Canadian Geotechnical Journal*, 27(1), 151-158. <http://dx.doi.org/10.1139/t90-014>.
- Senneset, K., Sandven, R., & Janbu, N. (1989). Evaluation of soil parameters from piezocone tests. *Transportation Research Record: Journal of the Transportation Research Board*, (1235), 24-37.
- Suguio, K., & Martin, L. (September 11-18, 1978). Formações quaternárias marinhas do litoral paulista e sul fluminense. In *International Symposium on Coastal Evolution in the Quaternary*. São Paulo: USP/SBG (in Portuguese).
- Tavenas, F., Leroueil, S., & Roy, M. (May 24-27, 1982). The piezocone test in clay: use and limitations. In A. Verruijt (Ed.), *European Symposium on Penetration Testing II* (pp. 889-894). Boca Raton: CRC Press.
- Terzaghi, K. (1943). *Theoretical soil mechanics*. New York: Wiley.
- Vesić, A.S. (1972). Expansion of cavities in infinite soil mass. *Journal of the Soil Mechanics and Foundations Division*, 98(3), <http://dx.doi.org/10.1061/JSFEAQ.0001740>.
- Vesić, A.S. (1977). Design of pile foundations. *NCHRP synthesis of highway practice*, (42), 1-68.

A numerical approach to evaluating the asymmetric ground settlement response to twin-tunnel asynchronous excavation

Alireza Seghateh Mojtahedi¹ , Ali Nabizadeh^{2#} 

Article

Keywords

Twin-tunnel
Ground surface settlement
Centrifuge test
Numerical modeling

Abstract

Due to the importance of surface and subsurface settlements to prevent damages to building foundations and sensitive structures in the urban cities, in this study, the ABAQUS finite element software has used to conduct a series of numerical modeling analysis on ground surface settlement caused from the asynchronous excavation of twin-tunnel. The effects of tunnel diameter, center-to-center tunnel spacing, and tunnel depth are discussed in detail and the shape of the surface settlement curves is also plotted. The numerical modeling has been verified by the results of three sequential twin-tunneling centrifuge tests conducted by the City University of London with 94.22%, 98.71% and 99.56% accuracy, respectively. Based on the results of this study, reducing the tunnel diameter decreases the amount of the maximum ground surface settlements and reducing the depth of tunnels and the distance between twin-tunnel to less than 2D (D is the diameter of the tunnels) increase the maximum surface settlements. Installation of 30 cm of tunnel lining can decrease the maximum ground surface settlement up to almost 79%.

1. Introduction

Due to the scarcity of available land within cities, underground structures such as transportation tunnels and water supply are continuously developing in populous cities. The tunnel boring machine (TBM) is an efficient excavation equipment and tunneling method, which makes highly advanced excavation machines by a high level of circular cutting control. Underground excavation causes ground surface displacements and may in effect damage the foundation of buildings and sensitive structures. Therefore, foreseeing ground surface settlements caused by the excavation of single or twin-tunnel is of great concern and should be considered before the start of excavation operations. These ground surface movements can be reduced by the use of modern tunneling technology. The difference between the shapes of an excavated tunnel and a final designed tunnel in the cutting process, which the shape of excavated tunnel is always larger than the final shape and causes volume differences due to 'volume loss' and is normally presented as a percentage. The soil mass deformation phenomenon, observed especially at the surface, leads to the possibility of structural failure caused by ground deformation (Mair & Taylor, 1997). Many researchers have studied the effect of single tunnel excavation on ground

surface displacements (e.g. Attewell & Yeates, 1984). Mair & Taylor (1997) conducted research on the ground deformation caused by tunneling. Almost all transportation tunneling systems are excavated in twin-tunnel (e.g. Jubilee Line Extension described by Burland et al., 2001). To estimate the surface settlement of twin-tunnel using superposition of each single tunnel is a common theory, which assumes that excavating the second tunnel is not affected by the first close tunnel. Initial numerical investigations have shown that the superposition technique may not be enough. Hunt (2005) investigated the consequence of low spacing in construction tunnels employed by the finite element method and proffered several differences from the superposition method. Ground deformation and tunnel excavation were widely controlled in certain critical projects, such as the St James Park located in UK (Nyren, 1998), Lafayette Park located in USA (Cording & Hansmire, 1975), and The Heathrow Express located in UK, (Cooper & Chapman, 1998). Twin-tunnel excavations were observed in each of the surface settlements, which were asymmetric to the ground displacements. Divall & Goodey (2012) explored ground behaviour following the excavation of close tunnels in over consolidated clay.

Moreover, several plane strain centrifuge tests were performed on over consolidated clay to investigate ground

[#]Corresponding author. E-mail address: ali.nabizadeh@sru.ac.ir

¹Amirkabir University of Technology (Tehran Polytechnic), Department of Civil and Environmental Engineering, Tehran, Iran.

²Shahid Rajaei Teacher Training University, Department of Civil Engineering, Tehran, Iran.

Submitted on May 11, 2021; Final Acceptance on January 27, 2022; Discussion open until August 31, 2022.

<https://doi.org/10.28927/SR.2022.071021>



This is an Open Access article distributed under the terms of the Creative Commons Attribution License, which permits unrestricted use, distribution, and reproduction in any medium, provided the original work is properly cited.

surface settlements caused by twin-tunnel excavations in different horizontal, vertical, or oblique arrangements. In these experiments, ground displacements are calculated in a vertical direction perpendicular to the tunnel, and the important contents presented by the investigators are summarized as follows (Divall, 2013; Zlatanovic & Lukic, 2014).

- a) Single tunneling surface and subsurface settlement can also be calculated by Gaussian distributions; although, the modification of ground surface settlements can improve twin-tunneling estimations because of second tunnel excavations;
- b) Volume loss (given as a percentage) can be best described as the comparison of relative increases in settlements caused by the second tunneling. Wider spacing between the twin-tunnel can reduce the influence of second tunneling;
- c) Researchers (Peck, 1969; O'Reilly & New, 1982; Mair et al., 1981) investigated modifications of equations to better estimate ground surface settlements caused by second tunnel excavation. They found the maximum displacement and curve shape of surface deformations to be wider than the first tunnel displacement.

Results of the numerical analysis of this research are in good agreement with the above explorations. Ranken & Ghaboussi (1976) conducted one of the first numerical researches in the ground surface settlement of parallel tunnels. Herzog (1985) presented a prediction for the maximum amount of ground surface displacement. Addenbrooke & Potts (2001) investigated the two-dimensional finite element analysis using a nonlinear elastic-perfectly plastic soil model for multiple tunnels. A numerical analysis which employed isotropic models with a linear elastic-perfectly plastic soil behaviour calculated the surface movement to be slightly wider than that perceived by the Gaussian scatter (Mair et al., 1981). Nonlinear elastic-perfectly plastic models have improved the estimations that change the curve shape of the results, making them more similar to those of field observations. Chahade & Shahrouh (2008) investigated the effect of tunnel spacing on the curved shape and value of a settlement. They found that the maximum amount of settlement occurs at a distance of twice the diameter of the tunnels ($SP/D=2$, SP is the spacing of the tunnels and D is the diameter of the tunnels). They also observed that a spacing of three times the tunnel diameter did not significantly influence the excavation ($SP/D=3$). Chakeri et al. (2011) investigated the interactions between tunnels and concluded that two close tunnels in transportation tunnel line can be excavated with the maximum spacing of three times the tunnel diameter ($SP/D=3$; Divall & Goodey, 2012; Zlatanovic & Lukic, 2014). Chakeri et al. (2015) investigated the effect of fault zone on twin-tunnel driven with EPBM in urban areas. Zhu & Li (2017) investigated surface displacement caused by shield tunneling at Xi'an metro. Yang & Zhang (2018) investigated the failure mechanism of circular twin-tunnel by

considering surface displacements as a theoretical basis for designing twin-tunnel roofs. Wu et al. (2020) investigated the impact of tunnel construction on an adjacent existing tunnel using the 3D discrete element and propose a new method to protect the existing tunnel.

According to the normalized results of this study, the ground surface displacements caused by the excavation of twin-tunnel in urban regions can be estimated for the same soil properties and geometric conditions of different geometric arrangements of twin-tunnel or ground characteristics; and the same numerical simulation analysis of twin-tunnel excavation procedures can give the maximum displacement value and shape of the ground surface deformations. Numerical modeling can also be considered in arbitrary configurations and with different values of tunnel diameters, tunnel spacing, or tunnel depths, either by excavating underground twin-tunnel simultaneously or excavating new tunnels adjacent to old ones. Therefore, to prevent maximum ground surface movements caused by the excavation of twin-tunnel and damage to structure foundations, accurate prediction and control of ground surface displacements caused by excavation are the most important issues to consider prior to excavation.

A series of numerical modeling was conducted for the present study using the finite element method (FEM), ABAQUS software, to study ground surface displacement caused by the asynchronous excavation of twin-tunnel. The effect of four parameters, specifically tunnel diameters, center-to-center tunnel spacing, tunnel depth, and tunnel lining are described in details. Results of the numerical modeling were verified by the results of three sequential twin-tunneling centrifuge tests conducted by Divall & Goodey (2012) and Divall et al. (2012) in the City University London with 94.22%, 98.71% and 99.56% accuracy for center-to-center tunnels spacing of $1.5D$, $3D$ and $4.5D$ (D is the tunnel diameter), respectively.

2. Verification of numerical modeling via centrifuge test of twin-tunnel

The finite element method (FEM), ABAQUS/CAE, was used to conduct numerical analyses on surface settlements resulting from the excavation of twin-tunnel and the effects of the parameters. Modeling analyses were verified by the following procedure of three centrifuge tests of twin-tunneling with center-to-center spacing of $1.5D$, $3D$ and $4.5D$ (D is the diameter of the tunnel).

2.1 Summary description of the centrifuge modeling and its geometry

In order to predict ground surface displacement caused by twin-tunnel excavation, several centrifuge tests performed in the City University London were conducted in 2012 to simulate prototype conditions. The results of these tests are used as basis for verifying the numerical modeling

analysis in this study. These tests were carried out in the plane strain condition and in a special box called ‘strongbox’ at an acceleration of 100g with two circular tunnels over consolidated clay. The tunnel holes in the strongbox were maintained by pouring fluid into the latex membranes to simulate the excavation of each tunnel. The fluid control system that was used to control fluid extraction is referred to as the ‘volume loss’ (Divall & Goodey, 2012). The twin-tunnel and soil model dimensions are presented in Figure 1. Clay samples were prepared at a cover depth equal to twice the diameter of the tunnel ($H_c/D=2$). The tunnel diameters of the twin-tunnel were 40 mm, the center of the tunnels was about 82 mm higher than the bottom of the strongbox and the center-to-center tunnel spacing was about 120 mm in the middle of the strongbox, which was drilled according to the test conditions (Divall & Goodey, 2012).

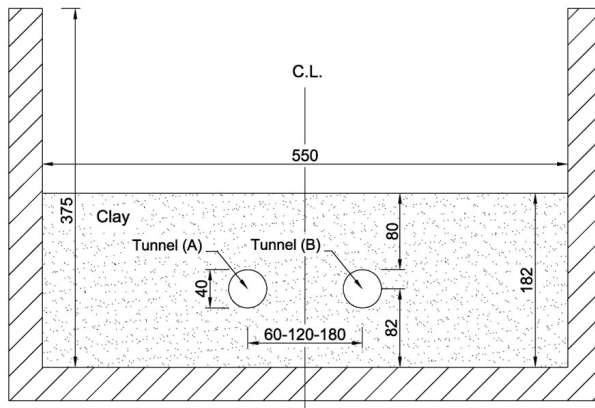


Figure 1. Twin-tunnel arrangements in the centrifuge test strongbox (dimensions in mm and C.L. is the center line of the strongbox) (Divall & Goodey, 2012; Divall et al., 2012).

2.2 Two-dimensional finite element mesh and boundary conditions of twin-tunnel modeling

Figure 2 shows the two-dimensional finite element mesh and boundary conditions used to analyze the aforementioned centrifuge test of twin-tunnel. The mesh dimensions used in the numerical analysis were 550 mm × 182 mm and were adapted to the centrifuge test exactly. A 4-nodes bilinear plane strain quadrilateral reduced integration with hourglass control continuum element type (CPE4R) was used to model the twin-tunnel (Mirhabibi & Soroush, 2012). The mesh dimension of the numerical models was selected almost 4 mm × 4 mm around the tunnel cavities at the model scale (dense meshing) which was increase to 10 mm × 10 mm near the model boundaries, based on several sensitivity analyses the results were not influenced. The Nlgeom (geometric nonlinearity) condition was active during all steps of the analysis, controlling the inclusion of the nonlinear effects of large displacements and affecting the subsequent steps. The movements were restricted in a perpendicular direction of the outer boundaries (at both left and right sides of the model) of the mesh. Pinned supports were utilized to constrain the displacements in two directions of the base boundary of the model.

2.3 Constitutive models and soil parameters

The linear elastic perfectly-plastic Mohr-Coulomb (MC) yield criterion model was selected for the Speswhite kaolin clay in the ABAQUS/CAE with a critical state of friction angle (ϕ) and saturated unit weight (γ) of 23° and 17.44 kN/m³, respectively. A Poisson's ratio (ν) and dilation angle (ψ) of 0.3 and 0.1° were selected, respectively. The Young's modulus (E) and undrained shear strength (S_u) used for the model were 11500 kN/m² and 49.8 kN/m²,

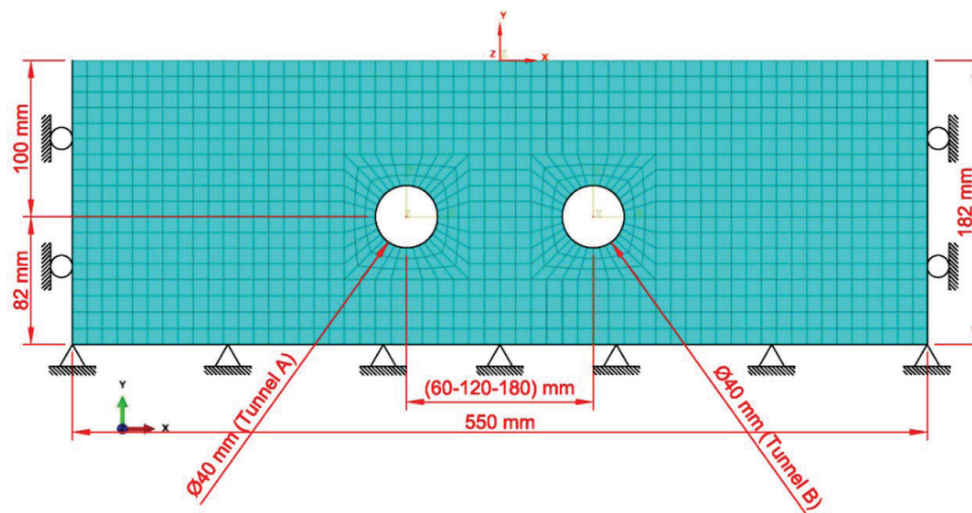


Figure 2. Two-dimensional finite element mesh and boundary conditions of twin-tunnel centrifuge excavation tests in this study.

respectively (Divall, 2013). The coefficient of lateral earth pressure ($K_0 = 1 - \sin \phi$) was assumed to be 0.61.

2.4 Numerical modeling procedure

Once the pore water pressure was balanced in the test model, the following procedure was conducted: a) Tunnel valve B was closed so that tunnel A was controlled individually by the control system. b) Water from tunnel A was extracted to simulate tunnel excavation. c) A time period was considered to simulate the construction time. d) During this time, the valve of tunnel A was closed and the valve of tunnel B was opened. e) Water from tunnel B was extracted to simulate tunnel asynchronous excavation (Divall & Goodey, 2012; Divall, 2013).

The numerical modeling of the twin-tunnel asynchronous excavation basically followed the centrifuge test procedure. Detailed of the simulation procedure is summarized as follows:

- The initial boundary and geostatic stress conditions at an acceleration of 100g were assigned as the initial steps (i.e., geostatic stress condition with the coefficient of lateral earth pressure, $K_0 = 0.61$);
- Body forces and horizontal and vertical equilibrium forces on all circumference nodes of both tunnel A and tunnel B cavities at an acceleration of 100g were assigned as step-1. These equilibrium forces of circumference nodes are calculated in a separate model by defining the displacement constraints in two directions for all circumference nodes of tunnel A and tunnel B cavities;
- In this step, only tunnel A excavation is simulated by reducing uniformly and then eliminating the horizontal and vertical equilibrium forces of all tunnel A circumference nodes, while the horizontal and vertical equilibrium forces of tunnel B nodes from step-2 are still active in this step;
- In this step, all nodes of tunnel A are restrained once the excavation simulation of tunnel A is completed, and regarding to asynchronous excavation of twin-tunnel, the excavation simulation of tunnel B is activated as mentioned in step-3 by reducing and eliminating the horizontal and vertical equilibrium forces of all nodes of tunnel B cavity.

2.5 Verification of the modeling of center-to-center spacing of 1.5D, 3D and 4.5D

The two-dimensional numerical analysis of center-to-center spacing of 1.5D, 3D and 4.5D of the twin-tunnel, shown in Figure 3, was verified by comparing the results to those of the centrifuge tests conducted by Divall & Goodey (2012) and Divall et al. (2012) at the City University of London, respectively. Table 1 and Figure 3 show comparison of these results. According to Figure 3 shows the maximum results of the surface settlements obtained by the twin-tunnel

excavations of center-to-center spacing of 1.5D, in which a centrifuge device of -517.68 μm is used in the model scale ($S_{\max}/D = -0.01294$), (Divall et al., 2012). According to Figure 3, the maximum results obtained from the surface settlement caused by the twin-tunnel were -487.77 μm in the model scale ($S_{\max}/D = -0.01219$). These values are in agreement with the centrifuge test results and the curve shape of surface displacements created by the numerical analysis of the twin-tunnel with 94.22% accuracy.

According to Figure 3, the maximum results of surface settlements obtained by excavating the twin-tunnel at 3D center-to-center spacing through the centrifuge device was found to be -316.18 μm in the model scale ($S_{\max}/D = -0.00790$; Divall & Goodey, 2012). As shown in the figure, the maximum result of the surface settlement resulting from the twin-tunnel generated by a numerical analysis is -312.11 μm in the model scaling ($S_{\max}/D = -0.00780$). Comparing these values shows a good agreement between the centrifuge test results and the curve shape of surface displacements created by the numerical analysis of the twin-tunnel with 98.71% accuracy.

According to the safety factors used in geotechnical designs, 1.29% of the verification error between the results is acceptable. The errors and slight differences between the results may be caused by:

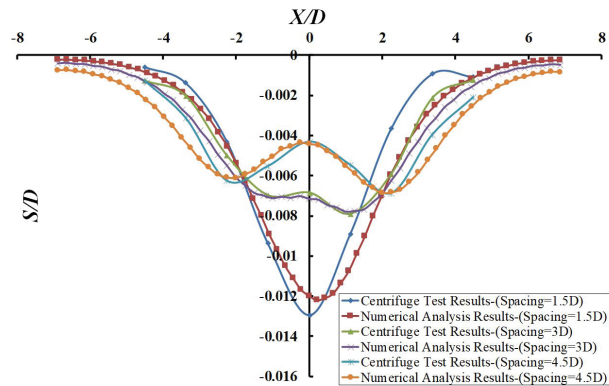


Figure 3. Verification of the numerical analysis results through the centrifuge test results of center-to-center spacing of 1.5D, 3D and 4.5D (X/D : Horizontal distance from center of twin-tunnel (or center of strongbox)/Diameter of the tunnel, S/D : Vertical settlement of the ground surface/Diameter of the tunnel).

Table 1. Comparison of the normalized results of the maximum surface settlements.

Tunnel Spacing	Max. vertical settlement / tunnel diameter (S_{\max}/D)		Accuracy (%)
	Centrifuge test	Numerical analysis	
1.5D	-0.01294	-0.01219	94.22
3D	-0.00790	-0.00780	98.71
4.5D	-0.00688	-0.00685	99.56

- a) Errors in the results of both the centrifuge test and numerical modeling analysis;
- b) The Mohr-Coulomb yield criterion model selected for the material behaviour in the ABAQUS/CAE software;
- c) Assumption of the plane strain condition in the numerical modeling;
- d) The difference between the boundary conditions defined in the numerical modeling and the conditions in the strongbox of the centrifuge test;
- e) The difference in the accuracy of the results at the top and bottom of the strongbox of the centrifuge test;
- f) The difference between assumptions of continuous media conditions in numerical modeling and conditions in the centrifuge test soil;

- g) The length of the device arm (rotational radius of the centrifuge test).

Figure 3 shows the results of the twin-tunnel numerical analysis of surface settlements created by the excavation of tunnels A and then B, respectively, according to the centrifuge test conditions. Figure 3 also shows a good agreement between the curves and surface settlement results of the numerical analysis of 3D center-to-center spacing and the aforementioned centrifuge test. Those centrifuge test results generally agree with the numerical predictions of researchers such as Hunt (2005) and works conducted on field measurements at St James Park, where large surface settlements were placed upon the construction of the second tunnel (Standing et al., 1996).

Figures 4 and 5 show numerical analysis results of twin-tunnel vertical displacement contours (U2) of 3D center-

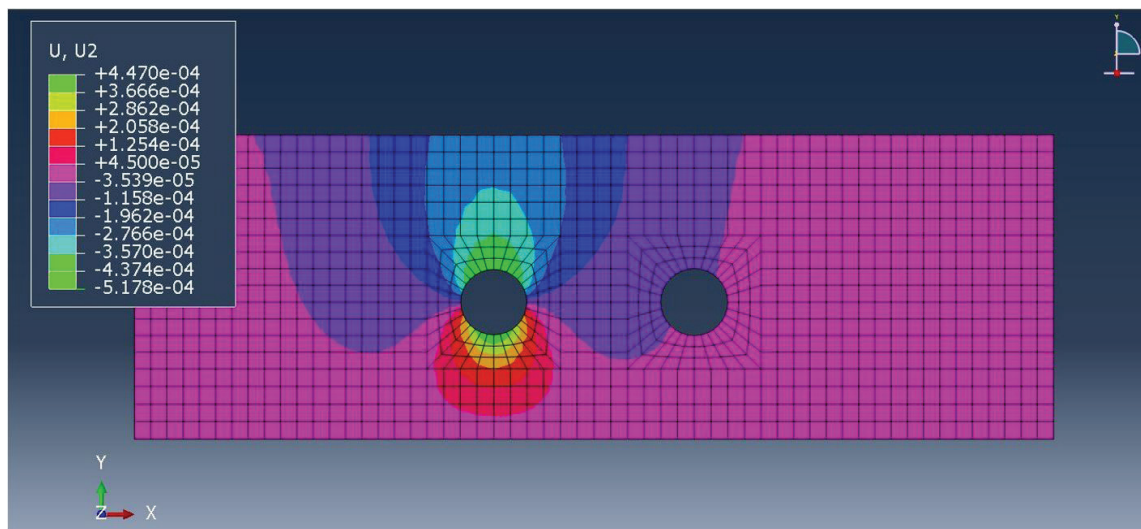


Figure 4. Vertical displacement contours (U2) of center-to-center spacing of 3D generated by the excavated tunnel A, (dimensions in m).

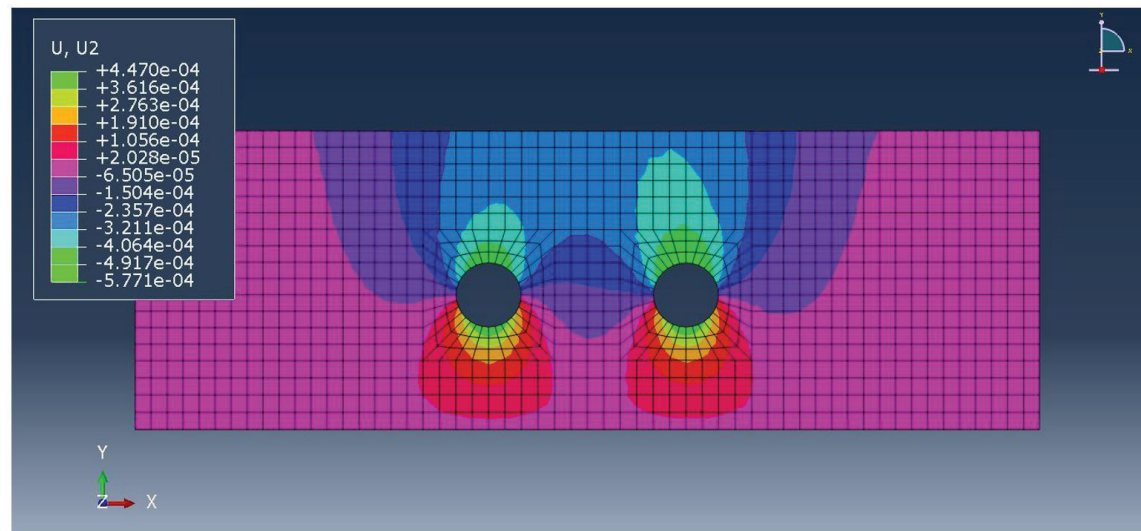


Figure 5. Vertical displacement contours (U2) of center-to-center spacing of 3D generated by the excavation of tunnel A and tunnel B, respectively (dimensions in m).

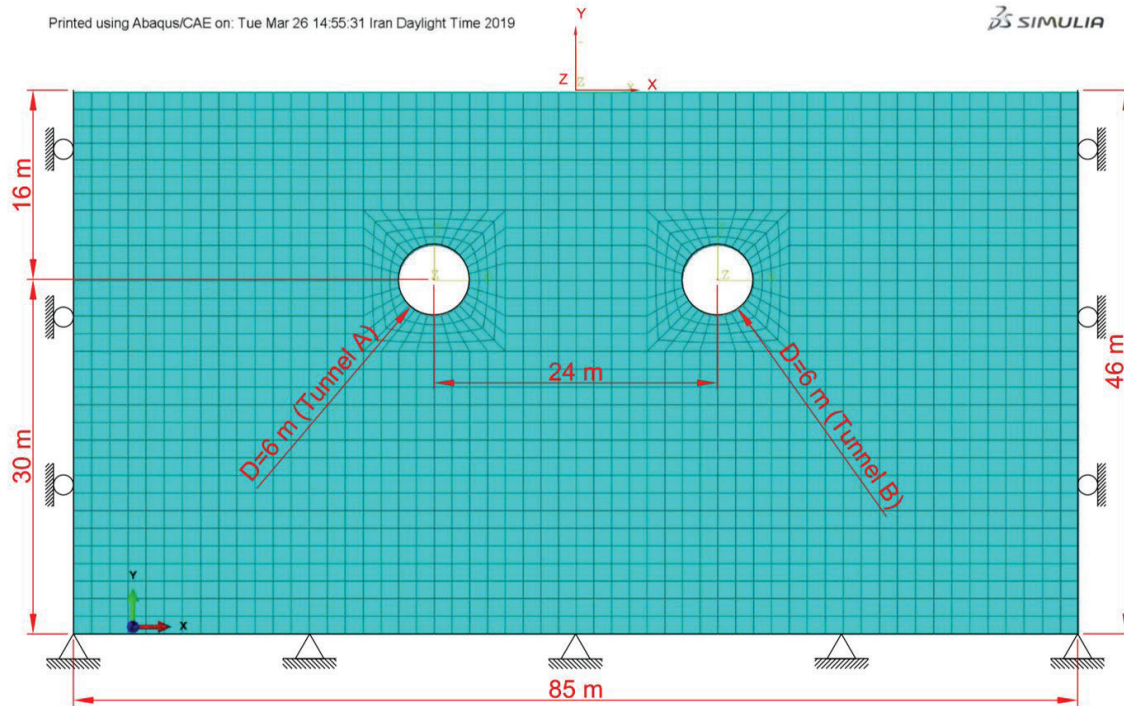


Figure 6. Maximum dimension of two-dimensional finite element mesh and boundary conditions of twin-tunnel excavations in this study.

to-center spacing generated by the excavations of tunnel (A) and tunnel (B), respectively. As shown in Figure 5, the contours of vertical displacements have not reached to the bottom boundary constraints. The maximum vertical reaction force (RF2) before starting the excavation in step-1 is equal to 3174 N, whereas this amount is decreased in the model scaling to 3128 N after the excavation of the twin-tunnel in step-3. A 1.45% difference is acceptable. But since the vertical displacements of the surface are strongly dependent on the model depth, the model used in the numerical modeling of this study was expanded to $5D$ center-to-center spacing for each configuration of the twin-tunnel, see Figure 6.

Figure 3 shows the maximum results of surface settlements obtained by the excavation of the twin-tunnel with $4.5D$ center-to-center spacing using the centrifuge device to be $-275.18 \mu\text{m}$ in the model scaling ($S_{\text{max}}/D = -0.00688$), (Divall et al., 2012). According to Figure 7, the maximum result of surface settlement obtained from the twin-tunnel and generated by the numerical analysis is $-273.97 \mu\text{m}$ in the model scaling ($S_{\text{max}}/D = -0.00685$). These values show a good agreement between the centrifuge test results and the curve shape of surface displacements created by the numerical analysis of the twin-tunnel with 99.56% accuracy.

In addition to the abovementioned reasons for the differences in the results, the 5.78% verification error between the results of center-to-center spacing of $1.5D$ may be due to the proximity of the tunnels, which cause inaccuracy either in the centrifuge test results or in the modeling results.

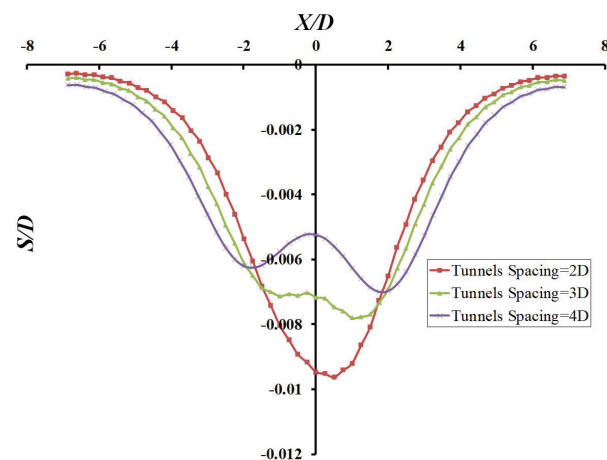


Figure 7. Numerical results of the asymmetric ground surface settlement curves generated by asynchronous excavation of the twin-tunnel ($H=10 \text{ m}$ and $D=4 \text{ m}$).

3. Expansion of two dimensional numerical modeling for different dimensions and geometric arrangements of twin-tunnel

To investigate the effects of three parameters: tunnels diameter, center-to-center tunnel spacing, and tunnel depth on surface settlement caused by the excavation of twin-tunnel, 24 numerical analysis modeling were conducted using the

ABAQUS software and according to the condition and procedures of the verified modeling; the results are presented in Table 2. The geometric dimensions of the models were changed (Figure 6 shows the maximum dimensions of the numerical modeling which is changed to $85 \text{ m} \times 46 \text{ m}$ for maximum tunnel spacing of $4D$) to allow for the development of any possible collapse mechanism. According to the Chakeri et al. (2015) approach and as well as several constructed models, showed that by choosing the model lateral distance and model depth equivalent to $5D$ from center of each tunnel, any influence of the boundaries on the results can be ignored. The discussions pertaining the effects of those parameters on the ground surface settlements are as follow.

3.1 The effects of center-to-center tunnels spacing

Until only recently, only a limited part of the interaction of twin-tunnel and its effect on the asymmetric ground surface settlements has been investigated, and more research is needed to illustrate these effects. Three values of center-to-center tunnel spacing ($2D$, $3D$, and $4D$; D is the diameter of the tunnel) were selected to explore their effects. Figures 7 and 8 show the numerical results of the ground surface settlement value resulting from asynchronous excavation of the twin-tunnel at similar tunnel depth of $H=10 \text{ m}$ and $D=4 \text{ m}$ and 6 m , respectively.

It is clear that the distance between the twin-tunnel influences both the maximum value of ground surface vertical displacements and the curve shape. According to the numerical ABAQUS results, in low distances between tunnels, the shape of the ground settlement curve resulting from twin-tunnel excavation is similar to the curve shape of a single tunnel, except that the ground surface settlements have a greater value due to the interactions between the twin-tunnel. The maximum ground surface displacement value of a single tunnel is -26.01 mm shown in Table 2, while this value is 38.48 mm of the twin-tunnel excavations at a $2D$ distance between the tunnels ($SP/D=2$), 10 m depth and 4 m tunnel diameter. Increases in the amount of ground deformation at the ground surface caused by the excavation of twin-tunnel is a major and challenging issue that should be considered before beginning any excavating operation. The effect of interaction between tunnels is decreased in larger distances between twin-tunnel (tunnel spacing of more than $3D$), and the curve shape and magnitude of maximum ground surface

displacements over each tunnel are changed to single tunnel conditions. For example, the maximum surface settlement value at a distance of $4D$ between twin-tunnel ($SP/D=4$) is equal to -28.02 mm in the model scaling, in which $H=10 \text{ m}$ and $D=4 \text{ m}$.

According to the results of this research, it is understood that in order to reduce the effect of the twin-tunnel excavation on the ground movements, it is necessary to increase the distance between the tunnels as much as possible to control the amount of the ground settlements and minimizing damage to the building foundations. It is important to note that the effect of center-to-center spacing between the tunnels depends on the tunnel diameter. This means that for a specific SP/D , the effect of center-to-center tunnel spacing between twin-tunnel is greater for a tunnel with a smaller diameter, and the curve shape of the surface deformation is more similar to that of a single tunnel.

3.2 Effects of twin-tunnel diameter

In order to explore the effects of the diameter of twin-tunnel, two values of tunnel diameters ($D=4 \text{ m}$ and 6 m) were considered. Figure 9 shows the numerical results of the asymmetric ground surface displacement value obtained from asynchronous excavation of the twin-tunnel for three

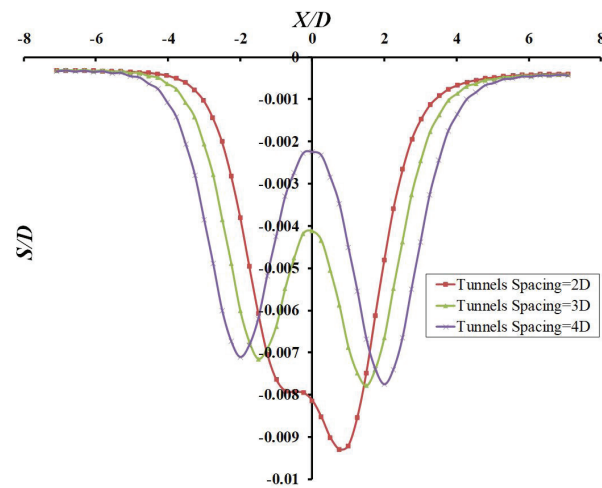


Figure 8. Numerical results of the asymmetric ground surface settlement curves generated by asynchronous excavation of the twin-tunnel ($H=10 \text{ m}$ and $D=6 \text{ m}$).

Table 2. Modeling results of the maximum vertical settlement/ tunnel diameter (S_{\max}/D) $\times 10^3$ after excavation of single tunnel and twin-tunnel in prototype scale (all results should be multiplied by 10^{-3}).

Tunnel Height		$H=10 \text{ m}$			$H=12 \text{ m}$			$H=14 \text{ m}$			$H=16 \text{ m}$		
Tunnel Spacing (SP)		$2D$	$3D$	$4D$	$2D$	$3D$	$4D$	$2D$	$3D$	$4D$	$2D$	$3D$	$4D$
$D=4 \text{ m}$	Tunnel (A)	-6.503	-6.155	-6.579	-4.465	-4.537	-4.367	-4.616	-4.746	-4.692	-7.294	-6.966	-6.996
	Tunnel (B)	-9.621	-7.803	-7.006	-9.479	-6.679	-5.923	-12.228	-8.493	-7.928	-15.188	-12.245	-10.771
$D=6 \text{ m}$	Tunnel (A)	-6.899	-6.903	-6.883	-5.913	-6.016	-6.439	-6.594	-6.686	-9.848	-7.192	-10.363	-6.941
	Tunnel (B)	-9.890	-7.886	-7.755	-10.221	-7.574	-7.407	-13.576	-10.403	-8.697	-17.059	-13.989	-12.373

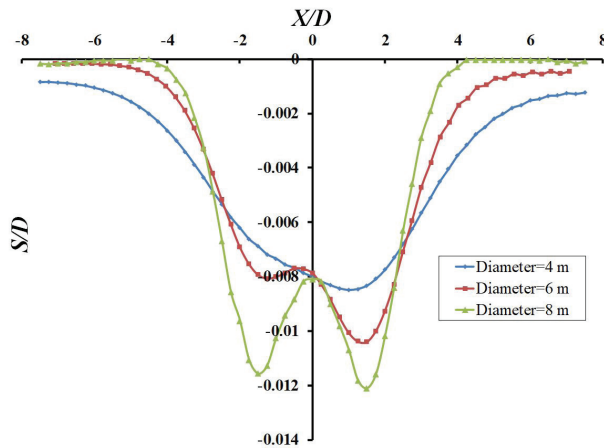


Figure 9. Numerical results of the asymmetric ground surface settlement curves generated by asynchronous excavation of the twin-tunnel ($H=14$ m and $SP=3D$).

values of tunnel diameter ($D=4$ m, 6 m and 8 m), center-to-center distance between the tunnels equal to $3D$ and at the same depth of the tunnels, $H=14$ m.

The numerical results of this study show that increasing the tunnel diameter increases the ground surface settlement, and its value depends on twin-tunnel spacing. This spacing should be increased as far as possible in order to decrease the ground surface settlement value and reduce any damage to the existing foundations of buildings. This paper shows that the largest vertical displacement caused by the excavation of twin-tunnel occurs at a 6 m diameter in the model scaling. The maximum vertical displacement value of the ground surface for a 6 m diameter, shown in Table 2, has a tunnel depth of $H=10$ m and a $4D$ center-to-center tunnel spacing of -46.53 mm; whereas, this value is -55.74 mm for a tunnel spacing of $2D$ for same depth and diameter size of the prototype scaling. The maximum vertical displacement value of the ground surface (Table 2) for a 4 m diameter, 16 m tunnel depth and $2D$ tunnel spacing is -60.75 mm in the model scaling ($S_{\max}/D = -0.015188$); whereas, this value reaches -102.356 mm after twin-tunnel excavations in the prototype scaling ($S_{\max}/D = -0.017059$) for a 6 m tunnel diameter, $2D$ tunnel spacing and 16 m tunnel depth.

3.3 Effects of twin-tunnel depths

In order to explore the effects of the twin-tunnel depths, two depths ($H=10$ m and 12 mm) were selected in the model scaling. Figure 10 shows the numerical results of the asymmetric ground surface settlement values obtained from the asynchronous excavation of the twin-tunnel for each center-to-center tunnel spacing ($3D$ and $4D$) with the same tunnel diameters of $D=4$ m, in the prototype scaling. The numerical results of this paper show a decrease in the ground surface settlement when the tunnel depth is increased and

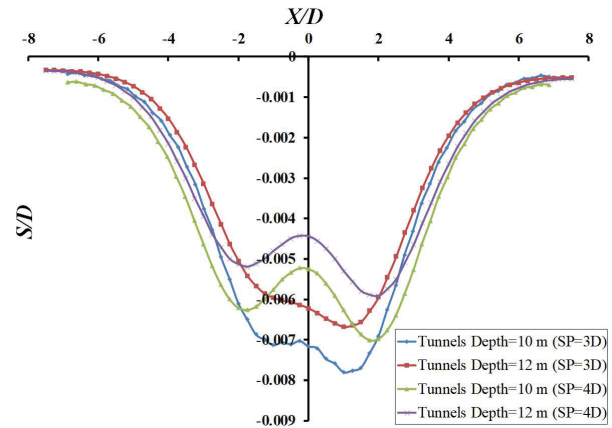


Figure 10. Numerical results of the asymmetric ground surface settlement curves generated by asynchronous excavation of the twin-tunnel ($D=4$ m and $SP=3D$ and $4D$).

its value depends on the tunnel diameter and tunnel spacing between twin-tunnel. As seen in Figure 10 and Table 2, the values of the maximum ground surface settlement of a $3D$ tunnel spacing and tunnels depths of 10 m and 12 m for a tunnel diameter of 4 m are equal to -31.21 mm, -26.715 mm, respectively. While, the maximum ground surface settlements of a $4D$ tunnel spacing and 10 m and 12 m tunnel depth for the same tunnel diameter are equal to -28.00 mm and -23.69 mm, respectively. So if in a project with similar condition it was necessary to reduce the excavation depth of the twin-tunnel from 12 m to 10 m, increasing the distance of spacing between tunnels from $3D$ to $4D$, due to the close values of the maximum settlement can be an appropriate solution for controlling of the ground surface settlements, instead of keeping $3D$ distance spacing between the tunnels.

It should be notice that in this study because of selecting the linear elastic-perfectly plastic Mohr-Coulomb (MC) yield criterion in numerical modelling, decreasing the vertical displacements of the ground surface was depended on the H/D ratio (D is the diameter of the tunnels, H is tunnels depth), in which the results for H/D ratio of less than 2.5 to 3 had an acceptable accuracy.

3.4 Effects of tunnel lining

In order to explore the effects of the tunnel lining, for three tunnel spacing of $2D$, $3D$ and $4D$, and with the depth of 10 m were selected in the prototype scaling. Figure 11 shows the amount and the shape of surface settlements in the presence of tunnel lining comparing with the asymmetric excavation condition. In the numerical modelling the thickness of lining tunnel was assumed as an isotropic linear elastic behavior with a thickness of 300 mm in prototype scale, and also the tunnel lining was connected to soil rigidly and the mesh considered as B21 a 2-node linear Timoshenko beam

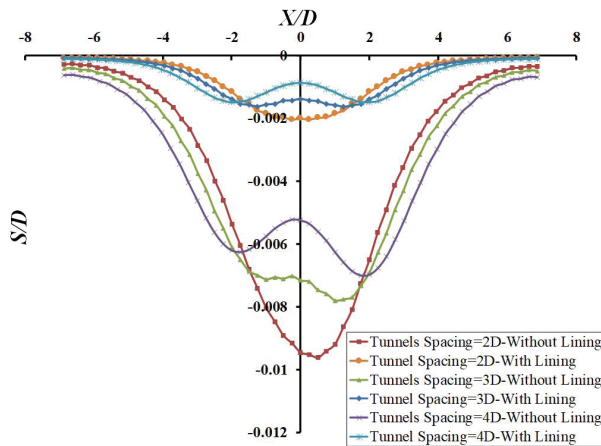


Figure 11. Numerical results of the amount and the shape of the surface settlements in the presence of tunnel lining comparing with the asymmetric excavation condition of twin-tunnel (for $H=10$ m and $D=4$ m).

element in a plane (Mirhabibi & Soroush, 2012). Tunnel lining concrete was assumed with material properties of unit weight $\gamma=24$ kN/m³, Young's modulus $E=33,700$ MPa, and Poisson's ratio $\nu=0.2$ (Mirhabibi & Soroush, 2012). According to the results of numerical modelling in Figure 11, the maximum surface settlements for the tunnel spacing of $2D$, $3D$, and $4D$ is equal to -8.146 mm, -6.540 mm, and -5.940 mm, respectively which indicates almost a 79% reduction in the amount of the maximum ground surface settlement in the presence of tunnel lining conditions.

4. Conclusion

Numerical approaches can consider more various factors and characteristics in twin-tunnel modeling, such as soil mass geo-mechanic specifications and various tunnel configurations (tunnel diameter, tunnel spacing, and tunnel depth). On the other hand, subsurface deformations and the interaction between twin-tunnel can be investigated together with different dimensions and geometric arrangements of twin-tunnel for either the concurrent excavation of twin-tunnel or the excavation of a new tunnel adjacent to an existing tunnel. For this purpose, a two-dimensional numerical analysis method by ABAQUS is employed in this study. Verification of the numerical modeling results is conducted using the actual values measured from the centrifuge test. The results of the numerical model were observed to be in good agreement with the results of the centrifuge test. A strong interaction between the twin-tunnel and curve shape of the asymmetric surface settlements was observed for the center-to-center tunnel spacing of less than $3D$. In other words, tunnel spacing larger than $3D$ affects the shape of the asymmetric ground surface displacement curve, similar to changing it to the curve shape of the excavation of two

separated tunnels and decreasing the maximum value of the asymmetric ground surface displacement. The diameters of twin-tunnel and tunnel depth have less effect than the tunnel spacing on the maximum asymmetric surface settlement. In this study was observed when the diameter of a tunnel with 12 m depth and $3D$ spacing is varied from 4 m to 6 m, the maximum surface displacement value increases by about 1.13 times, and changing the tunnel depth from 12 m to 10 m for tunnels with a 4 m diameter and a $3D$ center-to-center spacing, increases the maximum surface settlement value by about 1.17 times. while for a tunnel with 4 m diameter and 12 m depth, decreasing center-to-center distance between tunnels from $3D$ to $2D$ increases the maximum asymmetric surface settlement value by about 1.42 times. Also the ground surface settlement in the presence of tunnel lining was studied in this research which shows almost a 79% decreasing in the maximum amount of the surface settlement.

Declaration of interest

The authors have no conflicts of interest to declare. All co-authors have observed and affirmed the contents of the paper and there is no financial interest to report.

Author's contributions

Alireza Seghateh Mojtahedi: conceptualization, methodology, validation, investigation, writing – original draft, writing – review & editing, data curation. Ali Nabizadeh: supervision, writing – review & editing.

List of symbols

D	Diameter of the tunnel
E	Young's modulus
H	Depth of the tunnel (the height from center of the tunnel to the ground surface)
H_c	Burial depth of tunnel (overburden pressure)
S	Vertical settlement of the ground surface
S_{max}	Maximum vertical settlement of the ground surface
SP	Tunnel spacing (horizontal distance between the tunnels)
S_u	Undrained shear strength
X	Horizontal distance from center of twin-tunnel (or center of strongbox)
ϕ	Friction angle
γ	Unit weight
ν	Poisson's ratio
ψ	Dilation angle

References

Addenbrooke, T.I., & Potts, D.M. (2001). Twin tunnel interaction: surface and subsurface effects. *International*

- Journal of Geomechanics*, 1(2), 249-271. [http://dx.doi.org/10.1061/\(ASCE\)1532-3641\(2001\)1:2\(249\)](http://dx.doi.org/10.1061/(ASCE)1532-3641(2001)1:2(249)).
- Attewell, P.B., & Yeates, J.B. (1984). Tunnelling in soil. In P.B. Attewell & R.K. Taylor (Eds.), *Ground movements and their effects on structures* (pp. 132-215). London: Surrey University Press.
- Burland, J.B., Standing, J.R., & Jardine, F.M. (2001). *Building response to tunnelling: case studies from construction of the jubilee line extension, London, Volume 2, Case studies*. London: Thomas Telford.
- Chakeri, H., Hasanpour, R., Hindistan, M.A., & Ünver, B. (2011). Analysis of interaction between tunnels in soft ground by 3D numerical modelling. *Bulletin of Engineering Geology and the Environment*, 70(3), 439-448. <http://dx.doi.org/10.1007/s10064-010-0333-8>.
- Chakeri, H., Ozelik, Y., & Ünver, B. (2015). Investigation of ground surface settlement in twin tunnels driven with EPBM in urban area. *Arabian Journal of Geosciences*, 8(9), 7655-7666. <http://dx.doi.org/10.1007/s12517-014-1722-2>.
- Chahade, F.H., & Shahrour, I. (2008). Numerical analysis of the interaction between twin-tunnels: influence of the relative position and construction procedure. *Tunnelling and Underground Space Technology*, 23(2), 210-214. <http://dx.doi.org/10.1016/j.tust.2007.03.004>.
- Cooper, M.L., & Chapman, D.N. (1998). Movements of the Piccadilly Line tunnels caused by the new Heathrow Express tunnels. In *Tunnels and Metropolises. Proceedings of the World Tunnel Congress '98 on Tunnels and Metropolises*, Sao Paulo, Brazil, Balkema, pp. 254-294.
- Cording, E.J., & Hansmire, W.H. (1975). Displacement around soft tunnels. In *Proceedings of the 5th Pam-Am Conf. on Soil Mechanics and Foundation Engineering* (Vol. 4, pp. 571-633), Buenos Aires, Argentina.
- Divall, S. (2013). *Ground movements associated with twin-tunnel construction in clay* [Unpublished doctoral thesis]. City University London, London, UK. Retrieved in May 11, 2021, from <https://ethos.bl.uk/OrderDetails.do?uin=uk.bl.ethos.573637>
- Divall, S., & Goodey, R.J. (2012). Apparatus for centrifuge modeling of twin-tunnel construction. *International Journal of Physical Modelling in Geotechnics*, 12(3), 102-111. <http://dx.doi.org/10.1680/ijpmg.11.00014>.
- Divall, S., Goodey, R.J., & Taylor, R.N. (2012). Ground movements generated by sequential Twin-tunnelling in over-consolidated clay. In *Proceedings of the 2nd European Conference on Physical Modeling in Geotechnics*, Delft. <https://doi.org/10.4233/uuid:f71fabea-424b-42e5-93aa-701715eed17d>.
- Herzog, M. (1985). Die Setzungsmulde Über Seicht Liegenden Tunneln, Berlin. *Bautechnik*, 11, 375-377.
- Hunt, D.V.L. (2005). *Predicting the ground movements above twin tunnels constructed in London clay* [PhD thesis]. University of Birmingham, Birmingham, UK. Retrieved in May 11, 2021, from <https://ethos.bl.uk/OrderDetails.do?uin=uk.bl.ethos.496150>
- Mair, R.J., & Taylor, R.N. (1997). Bored tunnelling in the urban environment. In *Proceedings of the 14th International Conference on Soil Mechanics and Foundation Engineering* (Vol. 4, pp. 2353-2385), Hamburg, Germany.
- Mair, R.J., Gunn, M.J., & O'Reilly, M.P. (1981). Centrifugal testing of model tunnels in soft clay. In *Proceedings of the 10th International Conference on Soil Mechanics and Foundation Engineering* (Vol. 1, pp. 323-328), Stockholm, Sweden.
- Mirhabibi, A., & Soroush, A. (2012). Effects of surface buildings on twin tunnelling-induced ground settlements. *Tunnelling and Underground Space Technology*, 29, 40-51. <http://dx.doi.org/10.1016/j.tust.2011.12.009>.
- Nyren, R. (1998). *Field measurements above twin tunnels in London Clay* [PhD thesis]. Imperial College, London, UK.
- O'Reilly, M.P., & New, B.M. (1982). Settlements above tunnels in the United Kingdom: their magnitude and prediction. In *Proceedings in Tunneling '82* (pp. 173-181). London: Institution of Mining & Metallurgy. Retrieved in May 11, 2021, from <http://worldcat.org/isbn/090048862X>
- Peck, R.B. (1969). Deep excavation and tunneling in soft ground. In *Proceedings of the 7th International Conference on Soil Mechanics and Foundation Engineering, State of the Art Volume* (pp. 225-290), Mexico City.
- Ranken, R.E., & Ghaboussi, J. (1976). *Analysis of interaction between two parallel tunnels*. Washington: Department of Transportation.
- Standing, J.R., Nyren, R.J., Burland, J.B., & Longworth, T.I. (1996). The measurement of ground movements due to tunneling at two control sites along the Jubilee Line Extension. In R.J. Mair & R.N. Taylor (Eds.), *Geotechnical Aspects of Underground Construction in Soft Ground, Proceedings of the International Symposium* (pp. 751-756), London, UK.
- Wu, L., Zhang, X., Zhang, Z., & Sun, W. (2020). 3D discrete element method modelling of tunnel construction impact on an adjacent tunnel. *KSCE Journal of Civil Engineering*, 24(2), 657-669. <http://dx.doi.org/10.1007/s12205-020-2054-2>.
- Yang, X.L., & Zhang, R. (2018). Limit analysis of stability of twin shallow tunnels considering surface settlement. *KSCE Journal of Civil Engineering*, 22(5), 1967-1977. <http://dx.doi.org/10.1007/s12205-017-1398-8>.
- Zhu, C., & Li, N. (2017). Prediction and analysis of surface settlement due to shield tunneling for Xi'an Metro. *Canadian Geotechnical Journal*, 54(4), 529-546. <http://dx.doi.org/10.1139/cgj-2016-0166>.
- Zlatanovic, E., & Lukic, D. (2014). Ground surface settlement induced by twin tunneling. In *Proceedings of the 40th International Conference Contemporary Achievements in Civil Engineering* (pp. 921-927), Subotica, Serbia. <http://dx.doi.org/10.14415/konferencijaGFS2014.123>.

Mechanical behavior analysis of polymer stabilized gold ore tailings

Giovanna Monique Alelvan^{1#} , Michéle Dal Toé Casagrande¹ ,

Nilo Cesar Consoli² 

Article

Keywords

Gold ore tailings
Direct shear test
Unconfined compressive strength
Polymer
Tailings stabilization

Abstract

Chemical stabilization for mining tailings is a promising alternative to enable their use as construction materials. For this, it is necessary to evaluate the behavior of these composites to ensure minimum design requirements. This research aims to demonstrate that an addition of 15% of polymeric solution content, corresponding to 6% of polymer by tailings mass unit, can improve considerably the mechanical strength of gold ore mining tailings. To this end, unconfined compression and direct shear tests were conducted, indicating an increase in compressive and shear strength, especially with 28 days of curing time and at maximum dry unit weight. Microstructural and chemical tests were also performed, demonstrating that the tailings have silt-sized particles, mostly composed of quartz, muscovite, and kaolinite. Despite its granulometry, the tailings do not exhibit cohesive behavior and require to be considered perhaps as rock sediments. Scanning Electron Microscope analysis showed that the particles are lamellar, and a more stable arrangement contributes to the polymer's performance as a binder. It was observed that the strength gain occurs due to polymer bond effect and to the matric suction.

1. Introduction

Wijewickreme et al. (2005) define mining tailings as being essentially crushed rock particles derived from ore processing. The mineralogy, grain size, and morphology of the ore tailings particles vary significantly as a function of the composition of the parent rock and the beneficiation process to which they were subjected (Kiventera et al., 2019). This evidence demonstrates the need to expand studies in this area, to understand the behavior of these materials through the classical theories of Geotechnics.

The investigation of the mechanical behavior of tailings is important not only for safe design inside the mine but also as validation to be used in other structures, such as compacted embankments, sub-base of pavements, and mining backfill (Consoli et al., 2017). The proposed use of tailings as construction materials is directly related to stabilization and reinforcement techniques, due to the need to improve the mechanical properties of these materials.

The investigation of tailings behavior through mechanical testing has been an approach used by many authors (Bhanbhro, 2014; Islam, 2021; Carneiro & Casagrande,

2020; Sotomayor et al., 2021). Several others have also been exploring reinforcement and stabilization alternatives to improve the properties of the tailings (Festugato et al., 2015; Consoli et al., 2017; Zheng et al., 2019; Xue et al., 2021).

Chemical stabilization has been an interesting proposal, especially using traditional additives such as lime, fly ash, and cement. On the other hand, non-traditional additives, such as polymers and enzymes, have been under-explored as solutions to enable the use of tailings as construction materials (Huang et al., 2021).

The objective of this work is to investigate gold ore tailings in a pure state and stabilized with a polymeric solution. The mechanical analyses were conducted through geotechnical characterization, compaction, unconfined compression and direct shear tests. Chemical, microstructural, mineralogical, and matric suction analyses were also performed to help understand the mechanical behavior.

2. Experimental program

The gold ore tailings used was extracted from the Morro do Ouro deposit in Minas Gerais State, Brazil.

[#]Corresponding author. E-mail address: giovannaalelvan@gmail.com

¹Universidade de Brasília, Departamento de Engenharia Civil e Ambiental, Brasília, DF, Brasil.

²Universidade Federal do Rio Grande do Sul, Departamento de Engenharia Civil, Porto Alegre, RS, Brasil.

Submitted on September 29, 2021; Final Acceptance on January 7, 2022; Discussion open until August 31, 2022.

<https://doi.org/10.28927/SR.2022.075421>



This is an Open Access article distributed under the terms of the Creative Commons Attribution License, which permits unrestricted use, distribution, and reproduction in any medium, provided the original work is properly cited.

The deposit is hosted in the carbonaceous phyllites of the Paracatu Formation belonging to the Canastra Group, which is composed of an association of detrital metasedimentary rocks characterized by layers of grey phyllites with quartz intercalations (Amorim, 2007).

The sample received was friable and with a large amount of gravel. Only the fine fraction of the tailings was used in this research. All the material was sieved on the 2.0 mm mesh to separate the coarse portion. A visual-tactile analysis indicated little roughness and plasticity only at higher moistures. The dry sample presented resistant clods and particles with low sedimentation speed, compared to sandy soils.

The stabilizer used in this research consists of an organic acrylic-styrene copolymer obtained randomly and presented in the form of an aqueous emulsion of anionic character. The polymer has a pH of 8.0-9.0, a density of 0.98-1.04 g/cm³, a viscosity of 3,000-10,000 centiPoise (cP) and is completely soluble in water. The product is frequently used as pavement sealing and soil stabilizer. Silva (2020) and Carneiro & Casagrande (2020) performed studies on the chemical and biological characterization of the polymer to better understand its composition. The X-ray Fluorescence Spectrometry (XRF/EDX) and Elemental Analysis of CHN tests indicated that the polymer has a large amount of carbon (69%), followed by hydrogen (7%), nitrogen (0.5%), and other chemical elements arising from the polymerization process. In addition, the same authors analyzed leachate from composites formed by sandy and ore tailings with this polymer. They concluded that the use of this stabilizer is not hazardous to the environment, since the chemical concentrations obtained were lower than the standard limits established by the National Council of Environment (CONAMA) in Brazil.

For physical characterization of pure tailings, the grain size was determined by laser granulometer. Besides that, specific gravity of soil was measured by the pycnometer equipment model PENTAPYC 5200e, as ASTM D5550-14 "Standard Test Method for Specific Gravity of Soil Solids by Gas Pycnometer" (ASTM, 2016).

Proctor Compaction Tests with normal compaction energy were performed for the pure tailings and the composite, where the polymeric solution was added (ABNT, 2016a; ASTM, 2011). The polymeric solution is composed of water and polymer, in the percentages of 60% and 40%, respectively. The amount of polymer solution inserted (15%, corresponding to the water content choose) is calculated according to the mass of tailings. Therefore, the composite tailings-polymer formed has 6% of polymer in mass of tailings.

Unconfined compression and direct shear tests were performed to evaluate the mechanical strength of the pure tailings and the composite, for two dry unit weight (1.7 g/cm³ and 1.8 g/cm³) and two curing periods (7 and 28 days). The dry unit weight values were chosen according to the compaction curve in order to evaluate the influence of the structure on mechanical strength.

The curing of the specimens was done through exposure to air, since the polymer flocculation occurs through exposure to atmospheric oxygen. The following criteria to accept the samples were considered: (i) height variation of ± 1 cm; (ii) degree of compaction $\pm 1\%$. All the samples were submitted to the ultrasonic test to verify their uniformity.

For the unconfined compression test, specimens of 5 cm in diameter and 10 cm height were molded (ABNT, 2016b). The specimens were statically compacted in three layers inside a steel cylinder. For each layer, the dry unit weight was verified, and the top of the layers was scarified for better adherence to the others. At the end of the process, they were immediately removed from the mold and weighed, and the dimensions were obtained. The unconfined compression test speed was 1.27 mm/min, and it was conducted until total loss of strength of the specimen. The tests were performed in triplicates and the arithmetic average of unconfined compressive strength was used.

The direct shear test was conducted to determine the soil strength parameters (cohesion and friction angle) from the establishment of the Mohr-Coulomb strength envelope (ASTM, 2012). The specimens were built using a mold, which has dimensions of the small shear box (60 mm \times 60 mm \times 25 mm), at the optimum moisture content, according to the compaction test. The following criteria to accept the samples were considered: (i) height variation of ± 0.5 cm; (ii) degree of compaction $\pm 1\%$. Normal stresses of 50 kPa, 100 kPa, 200 kPa were applied to obtain the strength envelope.

Suction measurement tests were performed on the pure tailings and the composite to evaluate the influence of suction on strength gain as curing progress. For this, the psychrometer equipment (WP4C) was used. Cylindrical samples were molded for the test at the two dry unit weight analyzed, and the curing times were defined as 7 days, 14 days, and 28 days.

Mineralogical characterization tests were conducted to identify the minerals present in the crystalline structure. Samples of the pure tailings and the composite were analyzed using the tests X-Ray Diffraction (XRD) and X-Ray Fluorescence Spectrometry (XRF/EDX). The microstructural characterization was done by analyzing the images from Optical Microscopy (OM) and Scanning Electron Microscopy (SEM). In the same way, the tests were performed for the pure samples and in the composites on the tested specimens.

3. Results and analysis

The specific gravity of soil particle obtained was 2.81 g/cm³. The size distribution curve is shown in Figure 1. According to the ABNT NBR 6502 particle size classification (ABNT, 2016b), the tailings have silt size. Despite the granulometry, the tailings studied do not perform as a cohesive material since they have not undergone the geological process of soil formation. For this reason, the tailings are an intermediate material to the rocks and soils, which could be understood

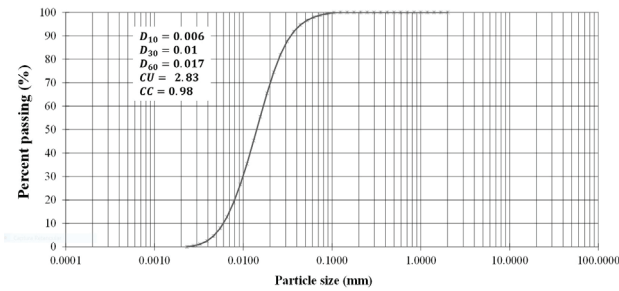


Figure 1. Soil particle size distribution.

as rock sediments. Hence, the considerations made to the mechanical behavior from the classification of soils should not be considered for tailings.

Previously, to define which content of polymer solution (P) would be investigated, a battery of unconfined compression tests was performed on specimens. For this, polymeric solutions with different polymer and water contents were elaborated: 10% polymer and 90% water (P_1.5); 20% polymer and 80% water (P_3); 30% polymer and 70% water (P_4.5); 40% polymer and 60% water (P_6); and 50% polymer and 50% water (P_7.5). The results are shown in Figure 2. The legend is composed of the acronym GT, which stands for Gold Tailings, followed by the letter P and the polymer content in the sample. These specimens were molded at the optimum moisture content (15%) of the pure tailing and with a dry unit weight of 1.8 g/cm³.

For all composites, the curves have a similar shape, where it is noted a well-defined peak with a rapid loss of strength in the post-peak region. It is observed that an increase in polymer content leads to a gain in unconfined compressive strength, except for the 50% (GT_7.5). From these results, it was decided to investigate the composites with 6% of polymer in mass of tailings (GT_P6).

The compaction curve for the gold ore pure tailings (GT) and the gold ore tailings polymer solution stabilized composite (GT_P6), with 6% of polymer by tailings mass unit, is shown in Figure 3. Analyzing the presented curve and comparing the behavior of GT and GT_P6, it is observed that the composite curve has a slightly closer shape. In addition, there is a decrease of approximately 5% of the optimum moisture content. Carneiro & Casagrande (2020) and Silva (2020) observed the same decrease in composites of iron ore and sand matrix.

The flocculation and dispersion theory proposed by Lambe & Whitman (1979) can also assist in the comprehension of the compaction curve. As discussed by the author, during compaction there is a physical-chemical interaction between the particles that leads to the well-known parabolic behavior of the compaction curves of soils.

On the dry side the amount of added water is insufficient for chemical interaction. This causes a high electrolyte concentration and the repulsion forces are not fully developed. With this, the forces of attraction predominate and then a

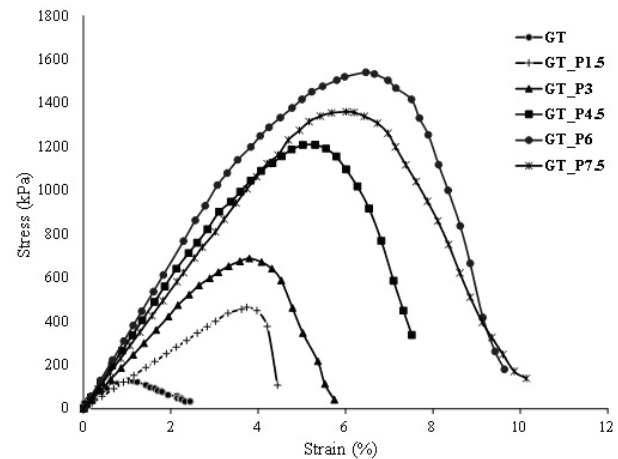


Figure 2. Unconfined compression test curves for distinct polymer content.

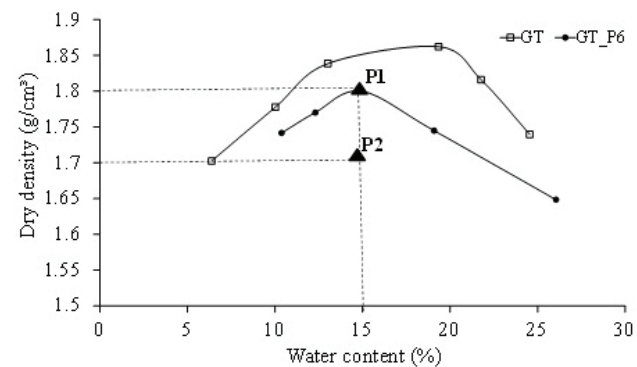


Figure 3. Compaction curves for gold ore pure tailings (GT) and composite (GT_P6).

flocculated structure with a disordered arrangement of the particles and a lower specific dry weight.

From this observation, comparing the dry unit weight of the GT and GT_P6, it is observed a decrease in the composite, since the inclusion of the polymer leads to a more flocculated structure. This flocculation is exactly the expected behavior of this synthetic organic polymer.

However, as the moisture content increases reaching the optimum point, the amount of water inserted is sufficient to reduce the electrolyte concentration and generate an increase in the repulsion forces. Thus, there is a more oriented structure for the composites, but still more flocculated than in the pure tailings and therefore lower specific weight.

From the composite compaction curve were defined the molding points of the specimens for the unconfined compression test and direct shear test. They are indicated in Figure 3 as P1 and P2. The analysis of two dry unit weights was done to verify the effectiveness of the polymer in different structures.

The results for the GT_P6 compared to GT are presented in Figure 4. While pure tailings have maximum stress of 50 kPa, the composite reached close to 1000 kPa. It is also possible to see the stiffness gain with increasing density, by the initial slope of the curves. These results indicate that curing time and the dry specific weight are significant in increasing the strength of the composite.

The direct shear tests were performed under the same curing time and dry unit weight conditions. The results are shown in Figure 5. Peaks have been observed with a slight drop-off before reaching the residual resistance, especially for a dry unit weight of 1.8 g/cm³.

Figure 6 shows the results of the strength envelopes. The results for cohesion and friction angle found are presented in Table 1. The cohesive intercept and the friction angle increased for the composite. The best mechanical arrangement was defined by the dry unit weight of 1.8 g/cm³ at 28 days.

In the case of GT, the cohesive intercept increases with curing time. This increment is probably due to the increase in suction. There was no significant modification in the friction

angle. However, analyzing the composites, the curing time caused an increase in the cohesive intercept only for the dry unit weight of 1.8 g/cm³. In the case of 1.7 g/cm³, the enhancement probably did not occur since the structural arrangement was not efficient in creating the bridges between the particles with adsorbed polymers.

As shown in the microstructural results, the tailings particles are lamellar. Therefore, a higher dry unit weight provides a more stable arrangement, since the particles are closer, and a larger surface area is available to create bridges between them.

Regarding friction angle, an increase is observed with the dry unit weight. This demonstrates that with a more solid arrangement, the polymer acted on the frictional characteristics of the particles. This supports the previous finding regarding cohesive intercept.

The XRF/EDX analysis indicated the following components in pure tailings: Si (53%); Al (21%); K (13%); Fe (9%); others. The analysis conducted on the composite showed no differences since the polymer is mostly composed of carbon that is not detected in this test.

The XRD analysis indicated minerals for the pure tailings namely: quartz, muscovite, and kaolinite, as shown

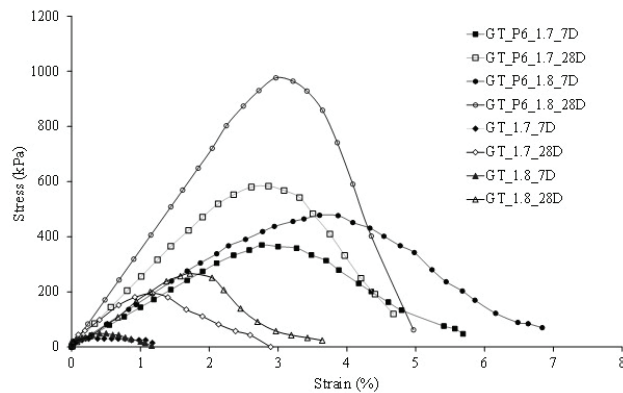


Figure 4. Uniaxial compression curves of GT and GT_P6 for distinct dry specific weight and curing time.

Table 1. Cohesive intercept and friction angle for GT and GT_P6.

	Sample	Cohesive intercept (kPa)	Friction angle (°)
GT	GT_1.7_7D	29	22.78
	GT_1.7_28D	31.5	27.55
	GT_1.8_7D	18.5	22.87
	GT_1.8_28D	27.5	24.91
GT_P6	GT_P6_1.7_7D	72.5	32.68
	GT_P6_1.7_28D	29.5	37.29
	GT_P6_1.8_7D	64	44.17
	GT_P6_1.8_28D	83.5	44.46

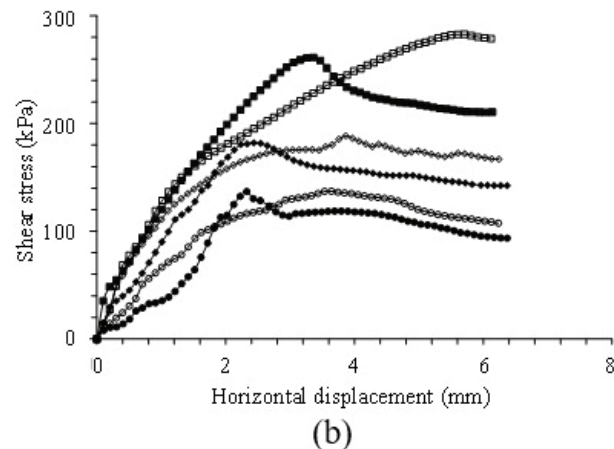
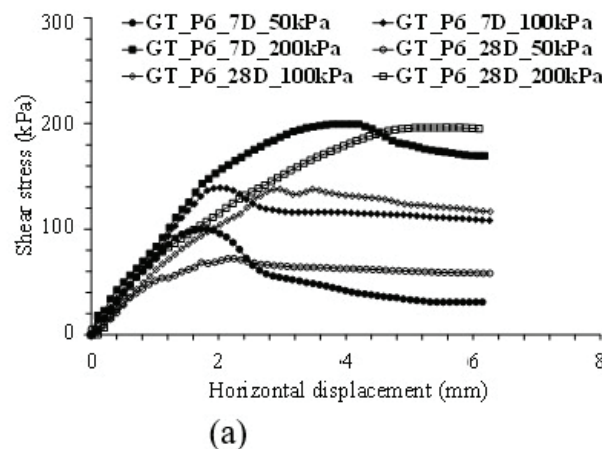


Figure 5. Shear-horizontal displacement curve. (a) composite with dry specific weight of 1.7 g/cm³; (b) composite with dry specific weight of 1.8 g/cm³.

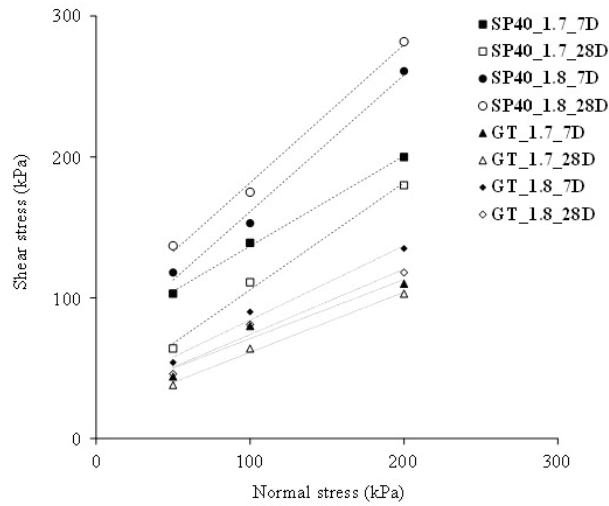


Figure 6. Shear strength envelopes.

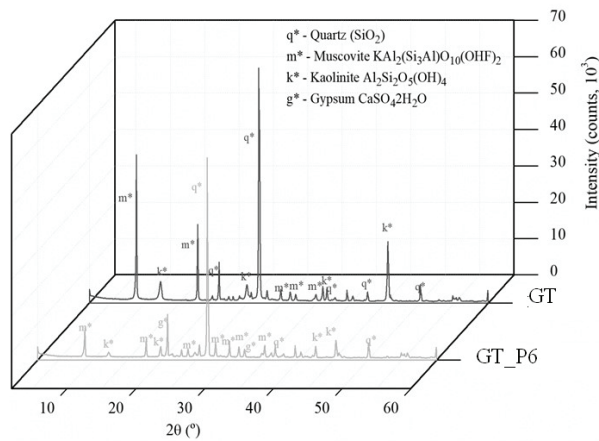


Figure 7. XRD results for GT and GT_P6.

in Figure 7. These minerals are the most present in the carbonaceous phyllites of the ore extraction region. This statement corroborates the fact that tailings are a material that should be treated as a rock sediment. The ore beneficiation process (fragmentation) that originated this material acted only as a physical weathering.

Gypsum was also identified in the composite in addition to the three minerals mentioned. Gypsum belongs to the class of hydrated sulfates, and is the most abundant mineral in this class. However, in fact, the composite did not generate a new mineral. This XRD identification is due to the classification technique used, which consults the mineral database through the JADE 9.0 software.

Each crystalline structure produces a characteristic diffraction pattern. Therefore, for interpretation of the results, a database is used, and comparison is made with the patterns produced by known, previously analyzed structures. In this case, the polymer was classified as isostructural to the gypsum.

Figure 8 shows an optical microscopy image at 10x magnification for the pure tailings and the composite. It is possible to observe the fine grain size of the material and the conglomerates formed by the flocculation process of the polymer. However, due to the grain size of the material, SEM analysis is more appropriate for analyzing the interface grain-polymer.

Figure 9 shows the morphological analysis obtained by SEM. It is observed that the pure tailings are composed of a lamellar isotextural structure, randomly oriented and with tightly interlocking packets. Keller et al. (1986) say that micromorphology and texture can be used to support mineral identification. In comparison with other authors, it is observed that kaolinite and muscovite are detected, in agreement with the XRD analyses (Relosi et al., 2018).

The tendency to form aggregates (polymer flocculation effect) in the composite, shown in Figure 9b, is directly related to particle size and surface area availability (Relosi et al.,

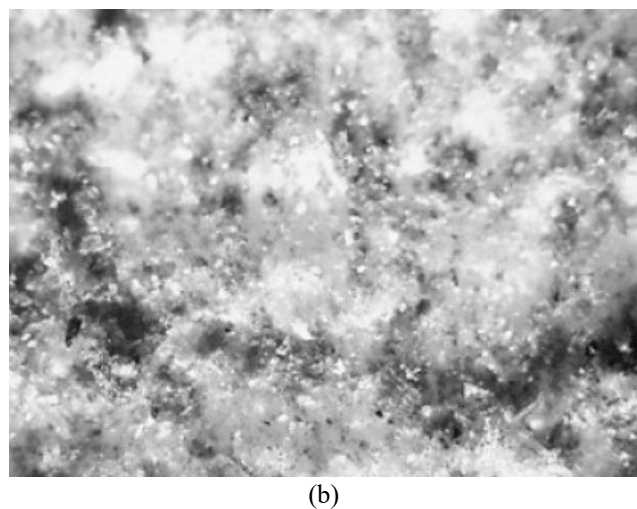
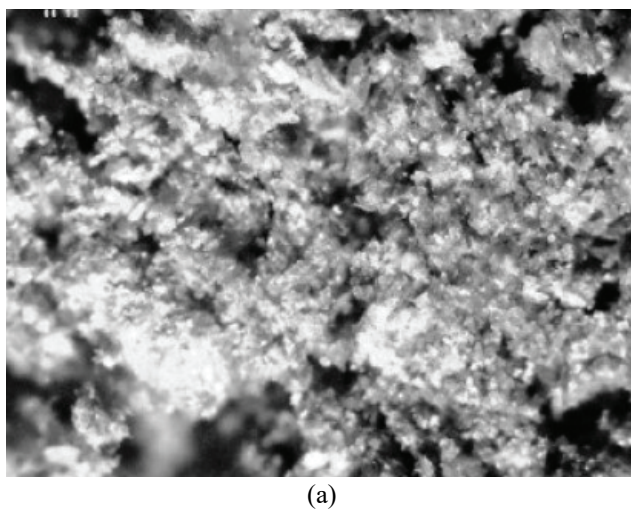


Figure 8. Optical Microscopy. (a) pure tailings; (b) composite.

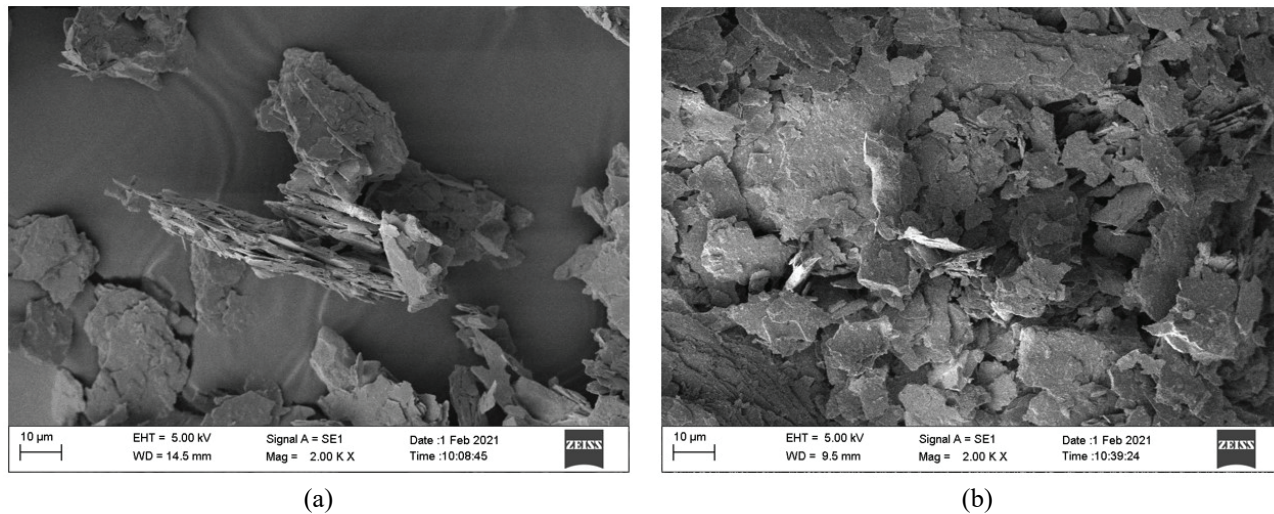


Figure 9. SEM analysis. (a) pure tailings; (b) composite.

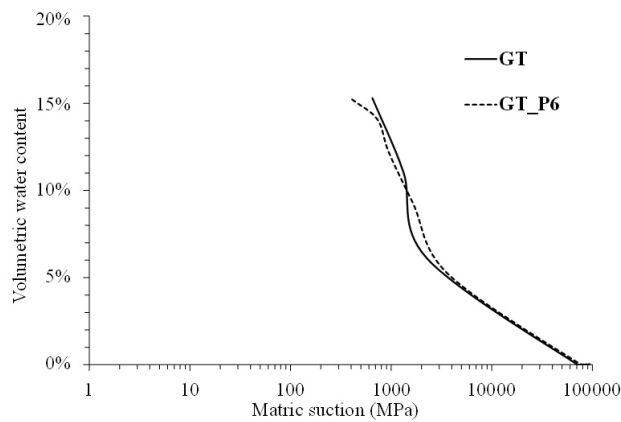


Figure 10. Matric suction results in pure tailings and composite.

2018). The lamellar packages present in the pure tailings decrease the surface area for polymer contact. This may generate the brittle behavior observed in the mechanical tests.

The analysis of the matric suction showed similar behavior for the pure tailings and the composite, as shown in Figure 10. From this analysis, it may be concluded that there are two parcels contributing to the strength gain: (i) polymer cure effect; (ii) matric suction increase.

The contribution of each parcel could not be evaluated by this work. For this, it is recommended to conduct mechanical tests with saturated specimens and monitoring the pore water pressures. In the case of this material, due to the significant loss of fine material, saturation was not possible.

4. Conclusions

This work investigated the mechanical, chemical, and microstructural behavior of a gold ore tailings stabilized with

a polymer solution. From the tests conducted, it was possible to conclude that the stabilization was efficient in improving the mechanical properties of the material.

The polymeric solution used was composed of water and polymer, which react with atmospheric oxygen to initiate the curing process and gain strength. Thus, two curing periods for two dry unit weight were evaluated.

A 40% polymer solution was chosen to be investigated since in the initial tests it proved to be more efficient. The solution was then added by mass to the polymer at the optimum moisture content, representing approximately 6% by mass.

The tailings matrix, which has silt size, showed neither plastic nor cohesive behavior. Therefore, the polymer proved to be an interesting alternative to increase cohesion between the particles, as shown in the direct shear tests, compaction curve and microstructural analysis. The matric suction analysis also showed that the strength gain happens due to two factors: (i) polymer flocculation effect; (ii) suction increase.

The results of the mechanical tests showed increased stiffness and unconfined compressive strength, especially in cases of higher dry unit weight. This stabler arrangement contributes to the cohesive effect of the polymer and to the frictional characteristics of the particles, as observed in direct shear test. This finding is interesting since it is directly related to the lamellar shape seen in the SEM analysis.

The mineralogical characterization also showed the relationship of the tailings to the parent material. This corroborates the fact that the tailings need to be evaluated through a different optic than soils and rocks, and perhaps as a rock sediment.

Therefore, the chemical stabilization using the polymeric solution that was investigated in this work is feasible. The recommendation for the compacted composite is to perform at the optimum moisture content and dry unit weight. This enables the use of tailings as construction materials in various engineering structures.

Acknowledgements

The authors thank the Brazilian research funding agencies *Conselho Nacional de Desenvolvimento Científico e Tecnológico* (CNPq) and *Coordenação de Aperfeiçoamento de Pessoal de Nível Superior* (CAPES).

Declaration of interest

The authors have no conflicts of interest to declare. All co-authors have observed and affirmed the contents of the paper and there is no financial interest to report.

Authors' contributions

Giovanna Alelvan: conceptualization, data curation, investigation, visualization, writing – original draft. Michéle Casagrande: conceptualization, data curation, methodology, supervision, validation, ting – review and editing. Nilo Consoli: conceptualization, data curation, methodology, supervision, validation, writing – review and editing.

List of symbols



CONAMA	National Council of Environment
GT	Gold Tailings
GT_P6	Composite tailings-polymer
OM	Optical Microscopy
SEM	Scanning Electron Microscopy
WP4C	Water Potential Meter
XRD	X-ray Diffraction
XRF/EDX	X-ray Fluorescence Spectrometry

References

- ABNT NBR 12770. (2016b). *Solo coesivo – Determinação da resistência à compressão não confinada – Método de ensaio*. ABNT - Associação Brasileira de Normas Técnicas, Rio de Janeiro, RJ (in Portuguese).
- ABNT NBR 7182. (2016a). *Solo – Ensaio de compactação*. ABNT - Associação Brasileira de Normas Técnicas, Rio de Janeiro, RJ (in Portuguese).
- Amorim, E.F. (2007). *Efeitos do processo de deposição hidráulica no comportamento de um rejeito de mineração de ouro*. [Master's dissertation, University of Brasília]. University of Brasília's repository (in Portuguese). <http://repositorio.unb.br/handle/10482/2673>
- ASTM D1557-12e1. (2011). *Standard test methods for laboratory compaction characteristics of soil using modified effort*. ASTM International, West Conshohocken, PA. <https://doi.org/10.1520/D1557-12>.
- ASTM D3080-11. (2012). *Standard test method for direct shear test of soils under consolidated drained conditions*. ASTM International, West Conshohocken, PA. <https://doi.org/10.1520/D3080-11>.
- ASTM D5550-14. (2016). *Standard test method for specific gravity of soil solids by gas pycnometer*. ASTM International, West Conshohocken, PA. <https://doi.org/10.1520/D5550-14>.
- Bhanbhro, R. (2014). *Mechanical properties of tailings: basic description of a tailings material from Sweden*. [Doctoral thesis, Luleå University of Technology]. Luleå University of Technology's repository. <http://urn.kb.se/resolve?urn=urn:nbn:se:ltu:diva-16952>
- Carneiro, A.A., & Casagrande, M.D.T. (2020). Mechanical and environmental performance of polymer stabilized iron ore tailings. *Soils & Rocks*, 43(4), 679-689. <http://dx.doi.org/10.28927/SR.434679>.
- Consoli, N.C., Silva, A.P., Nierwinski, H.P., & Sosnoski, J. (2017). Durability, strength and stiffness of compacted gold tailings-cement mixes. *Canadian Geotechnical Journal*, 55(4), 486-494. <http://dx.doi.org/10.1139/cgj-2016-0391>.
- Festugato, L., Consoli, N.C., & Fourie, A. (2015). Cyclic shear behaviour of fibre-reinforced mine tailings. *Geosynthetics International*, 22(2), 196-206. <http://dx.doi.org/10.1680/gein.15.00005>.
- Huang, J., Kogbara, R.B., Hariharan, N., Masad, E.A., & Little, D.N. (2021). A state-of-the-art review of polymers used in soil stabilization. *Construction and Building Materials*, 305, 124685. <https://doi.org/10.1016/j.conbuildmat.2021.124685>
- Islam, S. (2021). A study on the mechanical behaviour of three different fine-grained mine tailings. *Journal of King Saud University*. In Press. <http://dx.doi.org/10.1016/j.jksues.2021.04.001>.
- Keller, W.D., Reynolds, R.C., & Inoue, A. (1986). Morphology of clay minerals in the smectite-to-illite conversion series by scanning electron microscopy. *Clays and Clay Minerals*, 34(2), 187-197.
- Kiventera, J., Piekkari, K., Isteri, V., Ohenoja, K., Tanskanen, P., & Illikainen, K. (2019). Solidification/stabilization of gold mine tailings using calcium sulfoaluminate-belite cement. *Journal of Cleaner Production*, 239, <http://dx.doi.org/10.1016/j.jclepro.2019.118008>.
- Lambe, T.W., & Whitman, R.V. (1979). *Soil Mechanics*, SI version. New York: John Wiley & Sons.
- Relosi, N., Neuwald, O.S., Zattera, A.J., Piazza, D., Kunst, S.R., & Birriel, E.J. (2018). Effect of addition of clay materials on the properties of epoxy/polyester powder coatings. *Polímeros*, 28(4), 355-367. <http://dx.doi.org/10.1590/0104-1428.01616>.
- Silva, N.A.B.S. (2020). *Desempenho de um compósito solo-polímero para aplicabilidade em obras geotécnicas e de pavimentação*. [Master's dissertation, University of Brasília]. University of Brasília's repository (in Portuguese). <https://repositorio.unb.br/handle/10482/38789>.
- Sotomayor, J.M.G., Alelvan, G.M., & Casagrande, M.D.T. (2021). Influence of polypropylene fiber-reinforcement on

- the mechanical behavior of gold ore tailings through direct shear tests. *Journal of Materials in Civil Engineering*, 33(10), 04021256. [https://doi.org/10.1061/\(ASCE\)MT.1943-5533.0003878](https://doi.org/10.1061/(ASCE)MT.1943-5533.0003878)
- Wijewickreme, D., Sanin, M.V., & Greenaway, R.G. (2005). Cyclic shear response of fine-grained mine tailings. *Canadian Geotechnical Journal*, 42, 1408-1421. <http://dx.doi.org/10.1139/t05-058>.
- Xue, G., Yilmaz, E., Feng, G., & Cao, S. (2021). Bending behavior and failure mode of cemented tailings backfill composites incorporating different fibers for sustainable construction. *Construction and Building Materials*, 289, 123163. <https://doi.org/10.1016/j.conbuildmat.2021.123163>.
- Zheng, B., Zhang, D., Liu, W., Yang, Y., & Yang, H. (2019). Use of basalt fiber-reinforced tailings for improving the stability of tailings dam. *Materials*, 12(8), 1306. <https://doi.org/10.3390/ma12081306>.

The structure of tropical lateritic soils as an impacting factor in the shape of soil-water characteristic curves

Alana Dias de Oliveira^{1#} , Flávia Gonçalves Pissinati Pelaquim¹ ,

Renan Felipe Braga Zanin¹ , Thadeu Rodrigues de Melo² ,

João Tavares Filho² , Avacir Casanova Andrello³ , Raquel Souza Teixeira¹ 

Article

Keywords

Lateritic soils
Filter paper method
Pressure plate method
Soil-water characteristic curve
Porosimetry

Abstract

The presence of unsaturated flow in tropical lateritic soils of unknown hydromechanical behavior may lead to severe geotechnical problems. It is known that soil-water characteristic curves (SWCC) are a valuable tool to define this behavior and facilitate the suction estimation, acting on tests performed with no control of such parameter. This article aimed to determine and model the SWCC for 3 unprecedented tropical soils, in the undisturbed and the compacted conditions, from the Paraná state, located in the south of Brazil. The soils studied are one clay and two sands, all lateritic. The pressure plate and the filter paper methods were used to determine the SWCC. The samples were carved and submitted to the drying paths. Furthermore, Mercury Intrusion Porosimetry (MIP) tests were performed in samples of the studied soils in order to obtain the pore size distribution (PSD), contributing to the bimodal definition of curves and the prediction of SWCC main parameters. Both techniques (pressure plate and filter paper) were combined and the SWCC was adjusted by Gitirana & Fredlund model, which efficiently represents the shape of the traditional curves for tropical soils. Furthermore, the SWCCs were predicted by PSD and obtained satisfactory numerical fits. All SWCC presented air entry values in the macropores that are characteristic of soils as the lateritic, given that its structure was considered a key factor in the shape of the curves.

1. Introduction

Lateritic soils are widely used in civil construction, since they generally present high shear resistance (Sun et al., 2016). However, there are limited research regarding their hydromechanical behavior, soil-water characteristic curves (SWCC) and structure.

The analysis of water retention behavior in the soil is important for various geotechnical engineering applications, being fundamental to comprehend water flow, deformation process and shear resistance in unsaturated soils. The SWCC represents the soil capacity of storing and/or releasing water in the presence of different suctions. The SWCC performs a significant role on estimating hydraulic conductivity, shear parameters and volume variation of unsaturated soils (Vanapalli et al., 1996; Ajdari et al., 2012), becoming, then, an essential component in certain recent constitutive models for unsaturated soils.

According to Fredlund & Rahardjo (1993), the SWCC can be defined as the relation between suction and moisture content or saturation degree. It is usually sigmoid-shaped, though, several authors affirm that the SWCC shape is dependent on few factors, such as the granulometry (Marinho, 2005; Chiu et al., 2012; Carvalho & Gitirana, 2021), the soil structure (Vanapalli et al., 1999; Zhou et al., 2014), the temperature (Chahal, 1965; Romero et al., 2001) and the tension state (Vanapalli et al., 1999; Tavakoli Dastjerdi et al., 2014). According to Gitirana & Fredlund (2004), the pore size distribution might influence the soil-water characteristic curve shape, which may present an “S” shape – unimodal, containing only one dominating pore size – or “Double S” shape – bimodal, containing macro and micropores.

Moreover, the type of soil and structure may directly affect the SWCC shape of undisturbed and compacted soils. This structure can also be represented by the pore

[#]Corresponding author. E-mail address: oliveira.alana@uel.br

¹Universidade Estadual de Londrina, Departamento de Construção Civil, Londrina, PR, Brasil.

²Universidade Estadual de Londrina, Departamento de Agronomia, Londrina, PR, Brasil.

³Universidade Estadual de Londrina, Departamento de Física, Londrina, PR, Brasil.

Submitted on May 6, 2021; Final Acceptance on March 18, 2022; Discussion open until August 31, 2022.

<https://doi.org/10.28927/SR.2022.070521>



This is an Open Access article distributed under the terms of the Creative Commons Attribution License, which permits unrestricted use, distribution, and reproduction in any medium, provided the original work is properly cited.

size distribution (PSD) obtained through mercury intrusion porosimetry (MIP) (Romero et al., 1999).

Although some researchers report this determination, most of them concern only compacted soil (Vanapalli et al., 1999; Kim & Kim, 2010) or undisturbed soil (Aung et al., 2001; Miguel & Vilar, 2009; Miguel & Bonder, 2012), individually. Therefore, there is a lack of knowledge on gathering both conditions.

This paper aims to verify the influence of soil pore distribution on SWCC of three unprecedented tropical soils from the south of Brazil, determining and modeling it along the drying branch of undisturbed and compacted samples.

2. Materials and methods

2.1 Materials

The lateritic soils used in this study were collected in a range of 2 meters depth from three municipalities of the Paraná state, south region of Brazil: Londrina, Tuneiras do Oeste and Mandaguaçu, as illustrated in Figure 1. The three soils do not have the same geological origin: Londrina's is a residual basalt, Tuneiras do Oeste's is from a geological transition area, between sandstones and basaltic flows, and Mandaguaçu's is a sedimentary soil from a sandstone origin (Gonçalves et al., 2018).

Disturbed and undisturbed samples were collected in the field for laboratory tests, the first being used for compaction according to NBR 7182 (ABNT, 2016), using the Normal Proctor Energy (6 kgf.cm/cm^3). A cylinder 12.7 cm high and 10 cm in diameter was used, where 3 layers of soil of equal masses were sequentially arranged, each one being compacted with 26 blows given by a 2.5 kg and 30 cm high of fall socket. It should be noted that there was scarification of the first and second layers before receiving the next one. The main

characteristics of the soils, as well as the undisturbed and compacted samples used in the tests are presented in Table 1.

2.2 Methods

2.2.1 Mercury intrusion porosimetry (MIP)

Mercury Intrusion Porosimetry (MIP) tests were performed in samples of the studied soils in order to obtain the pore size distribution (PSD), contributing to the bimodal definition of curves and the prediction of SWCC main parameters.

During preparation of soil samples for MIP test, the method of greenhouse drying was used. The greenhouse was chosen because it results in less changes in the intra-aggregate pore shape once the changes of these pores are related to the processes of wetting and drying. Furthermore, due the shorter period of drying, the capacity of the particles to reorganize is limited (Li & Zhang, 2009; Sasanian & Newson, 2013; Otalvaro et al., 2016).

The pore distribution curves were obtained by means of mercury intrusion porosimetry tests (MIP tests) with specimens of about 1 cm of nominal dimensions (ASTM, 2018). The applied mercury pressures ranged from approximately 0.7 to 414000 kPa, with the application of pressure steps until the mercury could no longer be intruded in the soil void volume.

2.2.2 Soil-water characteristic curves (SWCC)

Two different methods were applied to measure the hydromechanical behavior of unsaturated soils for a wide range of suction. For suctions ranging between 10 and 1000 kPa, the pressure plate device was used based on the principle of axis translation, or pressure plate method (PPM). The filter paper method (FPM) was applied to obtain suctions along the entire range of suction values varying between 1 and 10^6 kPa, according to ASTM (2016).

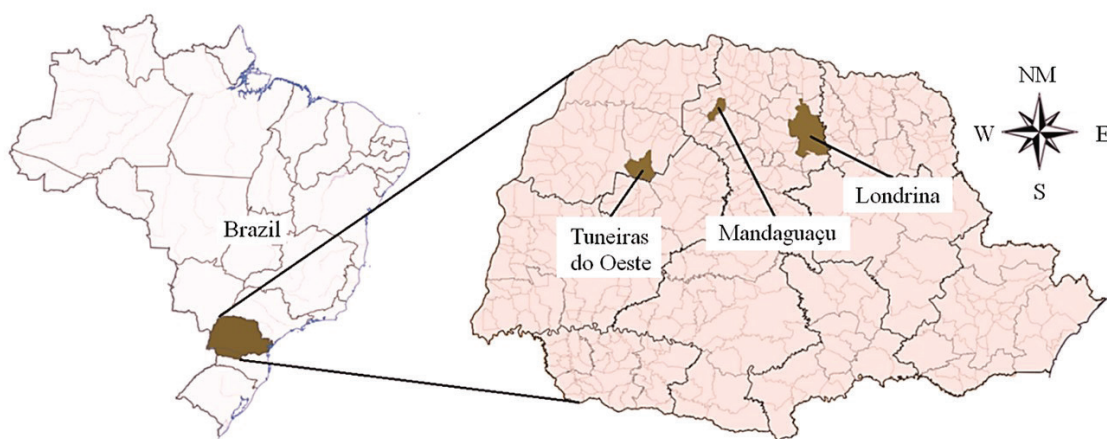


Figure 1. Location of soil collection.

Table 1. Characteristics of three lateritic soils (Cancian et al., 2017; Gonçalves et al., 2017; Gonçalves et al., 2019).

Soil	Londrina	Tuneiras do Oeste	Mandaguaçu
Physical indexes			
Specific gravity, G_s	3.03	2.89	2.69
Limit of liquidity (%)	51.0	20.0	31.0
Plasticity index (%)	13.0	7.0	16.0
Particle size distribution with deflocculant – ABNT (1995) and ASTM (2017)			
Sand – $0.06 < \phi < 2.0$ mm (%)	21.0	74.3	71.0
Silt – $0.002 < \phi < 0.06$ mm (%)	23.5	4.7	15.5
Clay – $\phi < 0.002$ mm (%)	55.5	21.0	13.5
Coefficient of uniformity - C_U	3.3	156.8	148.2
Coefficient of curvature - C_C	0.3	30.2	37.1
Particle size distribution without deflocculant – ABNT (1995) and ASTM (2017)			
Sand – $0.06 < \phi < 2.0$ mm (%)	20.0	74.3	84.0
Silt – $0.002 < \phi < 0.06$ mm (%)	77.5	23.7	16.0
Clay – $\phi < 0.002$ mm (%)	2.5	2.0	0.0
Coefficient of uniformity- C_U	1.9	50.0	9.5
Coefficient of curvature - C_C	0.3	9.2	2.4
Classifications ⁽¹⁾			
USCS – ASTM (2017)	CM	SC	SM
MCT - Nogami e Villibor (1981)	LG'	LA'	LA'
Mineralogical composition			
Kaolinite (%)	41.9	16.4	13.0
Gibbsite (%)	7.5	-	-
Undisturbed samples characteristics			
Mean molding moisture content (%)	32.0	8.0	3.0
Mean dry density (g/cm^3)	1.14	1.45	1.61
Saturated moisture content (%)	47.0	26.0	19.0
Initial void ratio - e_0	1.7	1.0	0.7
Compacted samples characteristics			
Optimal moisture content (%)	32.4	10.8	14.0
Maximum dry density (g/cm^3)	1.43	1.96	1.86
Saturated moisture content (%)	40.0	17.0	20.0
Initial void ratio - e_0	1.1	0.5	0.4

⁽¹⁾Notes - Classifications: USCS – Unified Soil Classification System; MCT - Miniature, Compacted, Tropical. LG' – Lateritic clay soils; LA' – Lateritic sandy soils.

In PPM and FPM, undisturbed and compacted samples of varied sizes were used, molded with the aid of plastic rings. The size of the specimens for the filter paper method was 21 mm in height and 47 mm in diameter. For the pressure plate method, the specimens were 25 mm in height and 35 mm in diameter.

2.2.2.1 Pressure plate method (PPM)

Part of the pressure plate system is a high air entry (HAE) ceramic plate, covered on one side by a thin neoprene diaphragm, secured to the edges of the plate. The diameter of the ceramic plate was 280 mm and can support up to 15 bars (1500 kPa). This system operates based on the principle of shaft translation, which involves increasing the air pressure (u_a), keeping the water pressure (u_w) (Marinho et al., 2008).

Four specimens of each condition (undisturbed and compacted) from each soil were previously saturated by

capillary action and placed on the HAE plate inside the pressure cell. The tests were carried out increasing the matric suction from 10 to 300 kPa in several steps. When the amount of water in the sample reached equilibrium then the next level of suction could be applied. Equilibrium was considered reached after the constant mass of the specimens, meaning that for that pressure there was no longer a pore size prone to losing water.

2.2.2.2 Filter paper method (FPM)

The principle about FPM is that after balancing, the soil and paper suction are the same. Filter paper is a porous material and as such can retain water like soil (Chandler et al., 1992). Basically, filter paper achieves equilibrium with the soil through vapor (total suction) or liquid flow (matric suction).

For the experimental points of the SWCCs to be representative of the drying branch, it was decided to control

the masses of the specimens over time while drying in the open air, using a 0.0001g precision scale. That is, estimates were made about the weight of the specimens for several different moisture contents. As soon as the weighing indicated the calculated mass, it would be verified that it had reached the desired moisture content.

Ten specimens of each condition (undisturbed and compacted) of each soil were previously saturated and the partial air-drying process began. For the measurement of matric suction, each specimen received two Whatman n° 42 filter papers, one under and one over the specimen. Total suction was not measured in this study. Each filter paper was cut so that when placed in contact with the specimen, its entire surface would remain in contact with it without interference from the plastic ring.

After assembly, the set was wrapped in plastic film and then in aluminum foil. The packaging process was necessary to guarantee the balance of the specimens with the filter paper without external interference (unforeseen loss or gain of moisture). In addition, the specimens were placed in a polystyrene box to keep the temperature controlled for 21 days, based on Marinho (1997).

With the balance of the water potential between the filter paper and the specimen, it was possible to measure their

volumetric moisture contents. The filter paper technique obtains the matric suction indirectly, using for this determination the correlations proposed by Chandler et al. (1992), as shown in Equations 1 and 2.

$$w_{paper} \leq 47\% \rightarrow \Psi_{paper} = 10^{(4,84 - 0,0622 \cdot w_{paper})} \quad (1)$$

$$w_{paper} > 47\% \rightarrow \Psi_{paper} = 10^{(6,05 - 2,48 \cdot \log w_{paper})} \quad (2)$$

Where Ψ_{paper} is the suction of the filter paper in (kPa), and w_{paper} is the volumetric moisture content of the filter paper in (%).

3. Results

3.1 MIP test results and SWCCs in the full suction range

Figure 2 presents the PSD and the cumulative distribution of undisturbed and compacted samples for CM, SC and SM soils. In Figure 2a, all three undisturbed soils exhibit distinct bimodal PSD, given its first peak next to 0.01 μm for CM

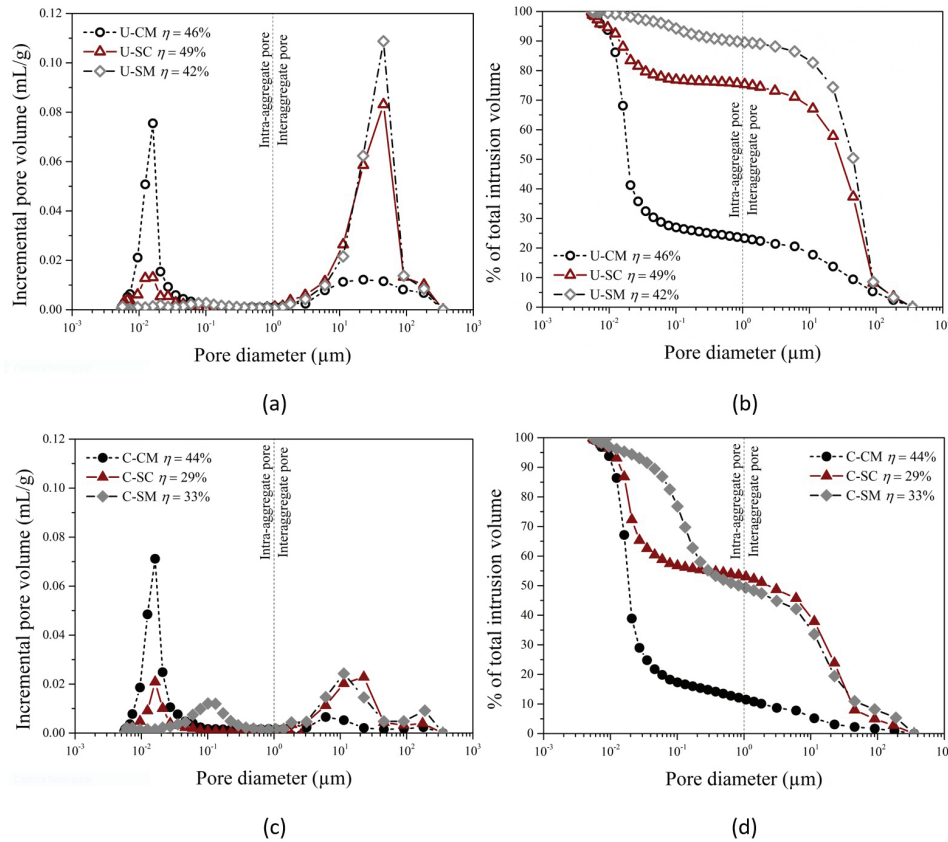


Figure 2. PSD of undisturbed samples (a) incremental pore volume and (b) cumulative % of total intrusion volume; and compacted samples (c) incremental pore volume and (d) % of total intrusion volume.

and SC samples, and near to 0.1 μm for SM sample. The second peak for all samples of soils is located between 10 and 100 μm .

For all three unsaturated compacted soils, illustrated in Figure 2c, it was also verified bimodal PSD with first peak next to 0.01 μm for CM and SC samples, and close to 0.1 μm for SM sample. The second peak is observed for all three soil samples between 1 and 10 μm . It should be noted that the trimodal behavior observed in SM compacted soils is probably due some failure during MIP, as clarified by Sasanian & Newson (2013).

The tendency in the PSD observed in Figure 2 defines the existence of two main pore families: intra-aggregate (diameter until 1 μm) and interaggregate (diameter greater than 1 μm), as cited by Gutierrez et al. (2008) and Li & Zhang (2009). The authors explain that the intra-aggregate pores are formed from the composition of mineral agglomerates and the interaction between them in the clayey matrix of the soil, while the interaggregate pores are characterized by conditioning the structural porosity, that is, they are related to the arrangement of the grains in themselves. The existence of a separation interval between the dominant pores observed, is a particular characteristic of lateritic soils very weathered in Brazil, noted also by Miguel & Bonder (2012) and Otalvaro et al. (2016).

The amount of PSD with a diameter of up to 1 μm , intra-aggregate, was more expressive for the CM soil sample than for the others (SC and SM), which was expected due to the more clayey character and the recognized microaggregation of this soil (Gonçalves et al., 2019).

Comparing the compacted and undisturbed samples, the CM curves showed a similar trend (especially for the intra-aggregate pores), even under different initial void indices (1.7 and 1.1, respectively). The finding that compaction has practical implications only in pores with larger soil diameters had already been reported by several authors (Delage et al., 1995; Simms & Yanful, 2001; Sun et al., 2016; Gao & Sun, 2017). This result implies that the porosity (the relationship between the void volume and the sample volume) of the CM soil remains practically unchanged with the use of compaction. On the other hand, the expressive variation of interaggregate pores for SC and SM is a direct result of the restructuring process, with a consequent decrease in porosity, for the same reason.

It is noteworthy that for CM soil the compaction process increased the discrepancy between intra and interaggregate pores (with the evident maintenance of the first family and reduction only in the second) and for SC and SM soils there is an equivalence between the proportion of the volume of pores, with differences of less than 15% between them. Furthermore, the percentage difference between the intra-aggregate pores, when going from undisturbed to compacted condition, for all three soils (CM, SC and SM) was 13, 25 and 44%, respectively. This allows us to conclude that the transition of pore volume from inter to intra-aggregate due to

compaction is more expressive, as the soil is more granular and/or has a lower clay fraction.

Finally, the total intrusion volume for CM for the undisturbed and compacted conditions is clearly lower than the values for SC and SM, as can be seen in Figure 2b and 2d. According to Nimmo (2005), this occurs because the formation of intra-aggregate pores occurs in the clay soil matrix, which is considerably larger in CM soil than in the others. Thus, a higher intra-aggregate pores amount caused a lower amount of mercury intruded into the CM soil.

From the determination of the pore distribution as bimodal for all three soils studied, both in the undisturbed and compacted condition, it is possible to predict that the variation in the volumetric moisture content and/or the saturation degree with the soil suction will have the existence of transition zones, with intermediate and well-defined levels characterized by low variation in moisture content for a wide range of suction. This shape corresponds to the typical shapes of a bimodal soil, like the shapes obtained by Burger & Shackelford (2001) and Carvalho et al. (2002).

Figure 3 shows the results obtained by the drying process using the PPM and FPM methods for undisturbed and compacted soils. Some of the points resulting from the different methods for the same suction values do not coincide perfectly, however, the discrepancy is low, enabling the assertive inference of the curve. It is noteworthy that the samples tested had similar void ratios (with coefficients of variation lower than 10% for undisturbed soils and 5% for compacted soils). This implies considering that the observed discrepancies are restricted to factors such as intrinsic structural differences and the uncontrollable heterogeneity of the material itself.

It is recognized that the shape of the SWCC depends on both the pore size distribution and the particle size distribution. Gerscovich (2001) indicates that sandy soils tend to show a sudden loss of moisture when suction exceeds AEV_1 , while clayey soils tend to have smoother curves. Thus, considering the percentages of particle size fractions, the behavior mentioned was evidenced for the soils in this study.

Furthermore, the same author emphasizes that, with a less considerable influence, the same behavior can be expected when comparing characteristic curves of uniform soils and well-graded soils, respectively.

For an adequate adjustment to the behavior of soils that present micro and macro structures composed of clay aggregates, typical of tropical and subtropical environments, the bimodal model proposed by Gitirana & Fredlund (2004) is recommended. Its application is shown in Figure 3 together with the sampling points. Table 2 shows the parameters of the model by Gitirana & Fredlund (2004), obtained from these curves. The results suggest good fits of the experimental data to the model of Gitirana & Fredlund (2004) with the presented parameters (coefficients of determination R^2 all above 0.9).

As already mentioned in the presentation of the porosimetry results, soil compaction decreased the amount

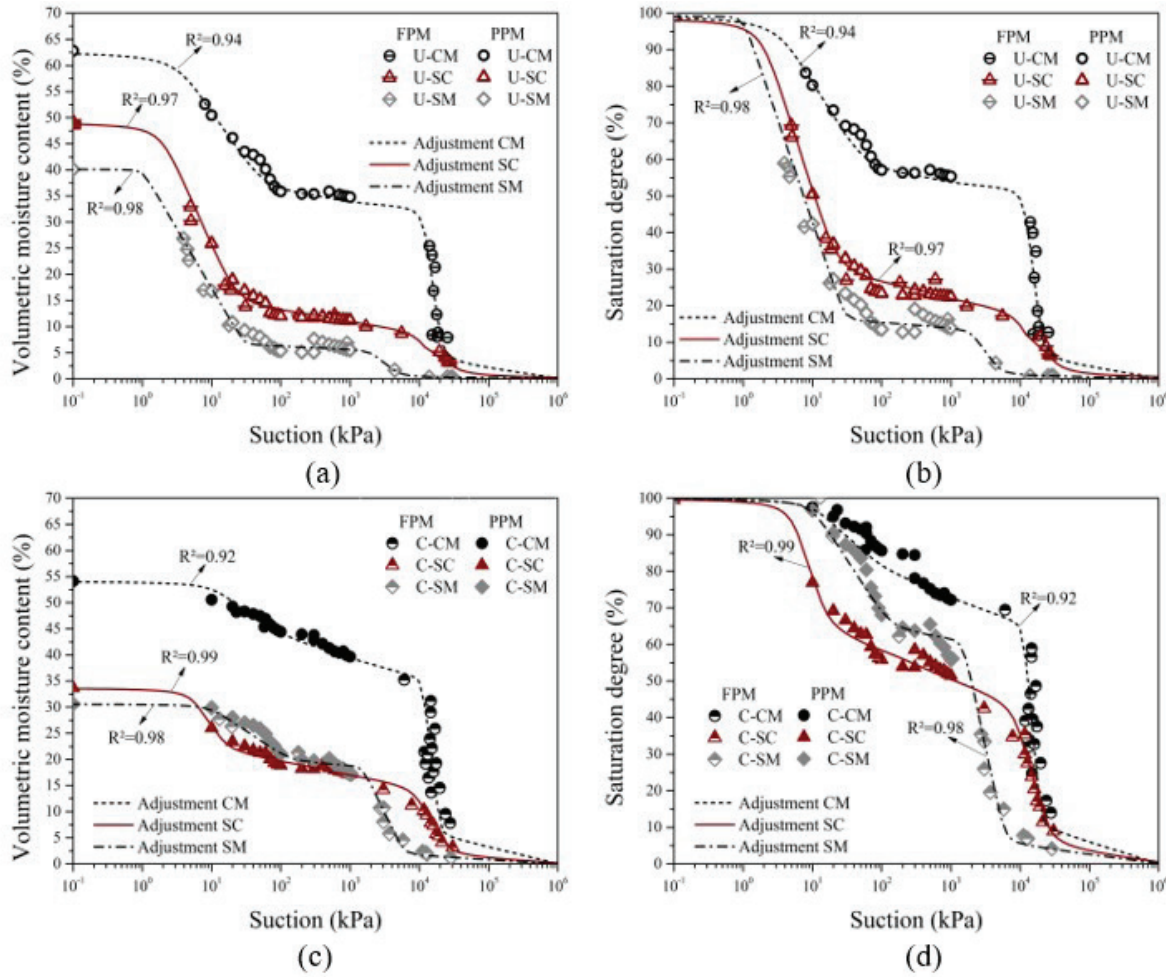


Figure 3. SWCC in the drying branch for a wide suction range: (a) and (c) volumetric moisture content and (b) and (d) saturation degree, respectively.

Table 2. SWCC parameters for three compacted and undisturbed lateritic soils.

Soil sample	1 st Portion				2 nd Portion				a
	θ_{sat} (%)	AEV_1 (kPa)	Ψ_{res1} (kPa)	Sr_{res1} (%)	AEV_2 (kPa)	Sr_{b2} (%)	Ψ_{res2} (kPa)	Sr_{res2} (%)	
U-CM	63	4	45	55	12000	53	20000	5	0.08
U-SC	49	2	21	27	13000	20	22000	0.1	0.09
U-SM	40	1	30	16	2000	14	5000	1	0.02
C-CM	54	12	70	80	11000	66	20000	10	0.04
C-SC	34	6	13	63	10000	45	21000	4	0.10
C-SM	31	10	170	63	1500	62	6000	6	0.04

of interaggregated pores, implying a decrease in the amount of water needed to saturate the soil. Can this be noticed in the θ_{sat} presented in Table 2, where the saturation moisture values for compacted soils are lower than for undisturbed soils, for all soils.

The two AEV found corroborate the ranges of values as a function of particle size presented by Aubertin et al. (1998). It is noteworthy that this statement is true only when particle size analysis is used regardless of the deflocculant.

Undisturbed soils with a higher percentage of fines had typically higher AEV_1 than for those with a lower percentage, in agreement with Vanapalli et al. (1999). For compacted soils, this trend was not evidenced, since for SM soil the AEV_1 obtained was superior to that of SC and practically equal to that of CM.

This C-SM sample's behavior may be related to the intra-aggregate pore size density and, consequently, to the mercury total intrusion volume. After the compaction process,

the pore size density of all soil samples has changed. A higher variation of total intrusion volume is observed for SM (from 10% to 50%) than for SC (from 25% to 45%) and CM (from 75% to 90%). This way, as shown in Figure 2, SM soil assumes a higher quantity of intra-aggregates compared to SC soil. Therefore, for compacted soils the pore size density seems to impact AEV_1 more than the presence of fines.

Regarding AEV_2 , it was noted that they were higher for soils with a higher clay fraction, however, not proportionally for undisturbed soils. When observing the two structures, for each type of soil, a certain similarity is observed, indicating again that the proportion of initial voids does not affect the water-soil characteristic curve at high suction, as discussed in this article (Gao & Sun, 2017). Furthermore, similar AEV_2 values, especially for CM and SC, indicate that there was an influence of the similar mineralogical composition of the studied soils (Gonçalves et al., 2017), since this is the suction range where the adsorption effects occur (Romero et al., 1999).

For undisturbed soils, the trend is evident that the more granular the soil, the lower the values of Sr_{resl} , which is in accordance with the theory of water adsorption by specific surface area of the particles (the larger the effective particle diameter, smaller specific surface area, less possibility of water adsorption). As for the compacted soils, a higher value of Sr_{resl} was also found for the CM soil, as expected, however, the values for the two sandy soils (SC and SM) were coincident. Possibly the explanation for this is correlated to the fact that the pore distribution for these two soils, after the use of compaction, has remained practically the same (percentage difference between the interaggregate pores after compaction equal to 3%).

As explained by Carvalho & Leroueil (2004), regardless of the initial void ratio that a soil sample may have, there is the possibility of presenting a characteristic suction curve that

is unique, removing the interference of this parameter from the assessment. This means that even if two specimens of the same soil initially have different void ratios, the parameter “ $e \times Sr$ ” appears as a constant, unless other factors intervene, such as structural differences (for example, undisturbed and compacted samples), cementation breakage with pore distribution variation or the hysteresis phenomenon itself. To obtain the transformed SWCC, Figure 4 shows the relationships between $e \times pF$ (which is the logarithm of suction in $\text{cm.H}_2\text{O}$) and the saturation degree (S_r). It is noteworthy that such curves were obtained from those previously defined by Gitirana & Fredlund model (2004), which presented satisfactory adjustments to the experimental data.

Silva et al. (2020) and Carvalho & Gitirana (2021) explain that for deeply weathered soils, the quantity and distribution of pores define the slope of the plateau present in the transformed SWCC ($e \times pF$ versus saturation degree). The smoother this slope, the greater the amount of interaggregate pores. For the studied soils, it is possible to notice that the curves of undisturbed soils presented levels with lower slopes than the curves of compacted soils. This once again confirms the decrease in interaggregated pores because of compaction.

In addition, it is highlighted that the curves presented can be taken as generic for any analyzes that require the estimation of the suction of unsaturated specimens for the studied soils and conditions, even if the samples have a slight variation in the initial void ratio, safeguarding only the possible interferences of the drying and moistening cycles.

3.2 SWCC predicted by PSD

In MIP test, it is assumed the soils contain pores with diameter (d) in the shape of cylindrical flow channels, which are filled with mercury under a determined pressure

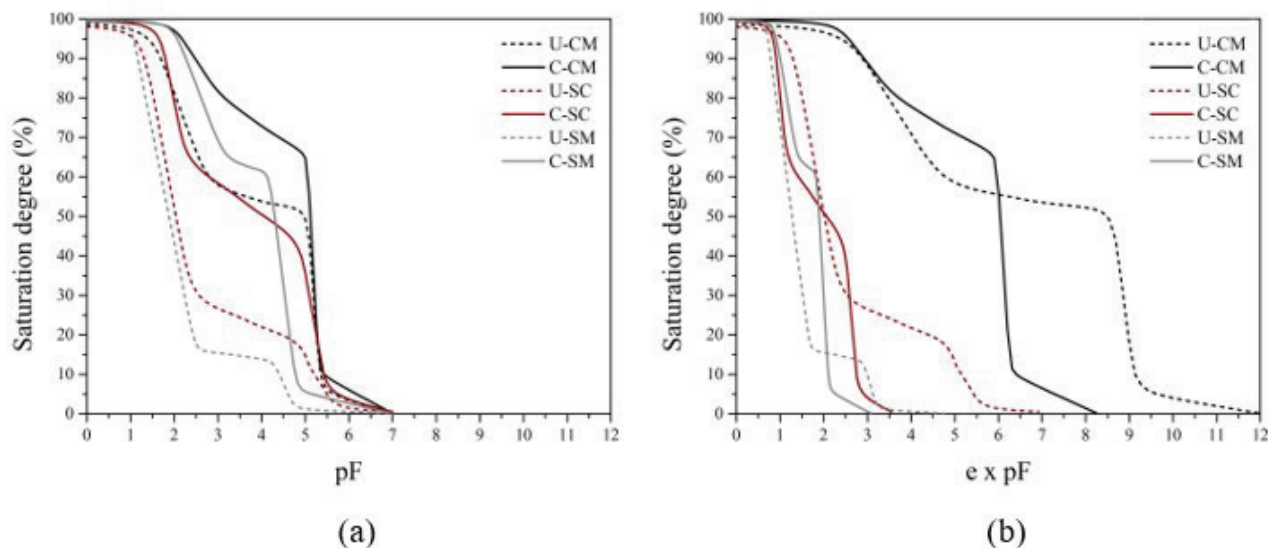


Figure 4. SWCC transformed in the drying arm for a wide range of suction versus saturation degree.

application. The necessary pressure to completely fill the pores with mercury is inversely proportional to the pore size. This relation was firstly pointed by Washburn (1921), and it is shown in Equation 3:

$$P = \frac{4\sigma_{Hg} \cos \alpha_{Hg}}{D} \quad (3)$$

Where D is the pore diameter in (μm), σ_{Hg} is the air/mercury surface tension of 0.484 N/m, α_{Hg} is the contact angle, assumed as 140° (Otalvaro et al., 2016), and P is the pressure in (kPa). As σ_{Hg} and α_{Hg} are constants, the application of a known pressure produces the dimension of corresponding pores.

Some researchers as Delage et al. (1995), Aung et al. (2001), Simms & Yanful (2001), Zhang & Li (2010) and Mascarenha et al. (2010), affirm that the mercury intrusion in a porous medium occurs similarly to the application of pressure in a saturated soil, in other words, like the drying curve of the SWCC. Therefore, according to Otalvaro et al. (2016), the suction may be obtained by replacing the pressure in Equation 4:

$$(u_a - u_w) = \frac{4\sigma_w \cos \alpha_w}{D} \quad (4)$$

Where $(u_a - u_w)$ is the matric suction in (kPa), σ_w is the surface tension of the interface air/water of 0.073 N/m at 20°C , according to Fredlund & Rahardjo (1993), α_w is the contact angle assumed as zero, according to Philip & De Vries (1957). Considering the diameters of the Equations 3 and 4 as similar, the relation $P \approx 5.10 (u_a - u_w)$ is attainable. Thus, it is possible to convert mercury intrusion pressure into matric suction.

With this premise, works such as those by Sun et al. (2016) sought a simplified approach for predicting the soil characteristic curve using only the results of MIP tests. According to the authors, good fits were found for compacted soils by predicting AEV_1 or AEV_2 from the estimated suction for the pore diameter at the region peak of inter or intra-aggregate, respectively. Despite the same authors emphasizing that the predictions for undisturbed soils may be less accurate, especially for those with a high content of

finer, given the possibility of contraction and the appearance of cracks in the specimen during drying, the same technique was applied here, since two of all three soils studied were characterized as sandy.

Table 3 presents the AEV_1 and AEV_2 estimated by the method of Sun et al. (2016). It is observed that the AEV_1 for the soil with higher fines content remained higher than the others, regardless of the condition. However, considering the adjustment shown in Figure 5, all estimated values were higher than those obtained. For the AEV_2 values, a numerical trend was noted like the adjustment of the curve by Gitirana & Fredlund (2004), but in this case with estimated values lower than those obtained. For practical purposes, discrepancies suggest that the simplification, although imprecise, may be acceptable.

Regarding the slope of different parts of the curves, Sun et al. (2016) points out that the peak in the interaggregated pore zone can determine the slope of the first segment of the SWCC, the intra-aggregate pore peak is related to the slope of the third segment, and the flat segment between the two peaks influences the slope of the middle segment in the SWCC.

Thus, according to the authors, a cumulative distribution function (called $F_{(d)}$) represents the volume of pores with diameters greater than d in a gram of dry soil. $F_{(d)}$ can be determined based on the results of MIP tests showed in Figures 2b and 2d and the saturation degree in one gram of dry soil (S_e) is given by Equation 5:

$$S_e = 100 \times \frac{S_r - S_{re}}{100 - S_{re}} \quad (5)$$

Where $S_{re} = 100(e_a - e_e)/e_a$ with e_a being the void ratio before MIP tests, $e_e = \rho_w \cdot F_{(d_{min})} \cdot G_s$ and $F_{(d_{min})}$ is the accumulated volume of mercury for the smallest diameter measured by MIP test, and G_s is the specific gravity. From the parameters obtained (Table 3), the curves predicted by the PSD results of this study are shown in Figure 5.

The coefficients of determination indicate good fits between the data predicted by the PSD and those adjusted by Gitirana & Fredlund (2004) model, both in the undisturbed and compacted conditions. For SC and SM soils, both with a sandier character, the forecast for undisturbed samples was

Table 3. Estimated parameters for prediction of SWCC by PSD - Sun et al. (2016).

Soil sample	AEV_1 (kPa)	AEV_2 (kPa)	G_s	e_a	$F(d_{min})$
U-CM	10	15000	3.08	0.9	0.28
U-SC	5	15000	3.46	1.0	0.29
U-SM	5	2400	2.81	0.7	0.26
C-CM	40	15000	3.14	0.8	0.25
C-SC	10	15000	2.85	0.4	0.14
C-SM	20	2000	2.96	0.5	0.17

Note: Data G_s , e_a and $F(d_{min})$ obtained in MIP tests reports.

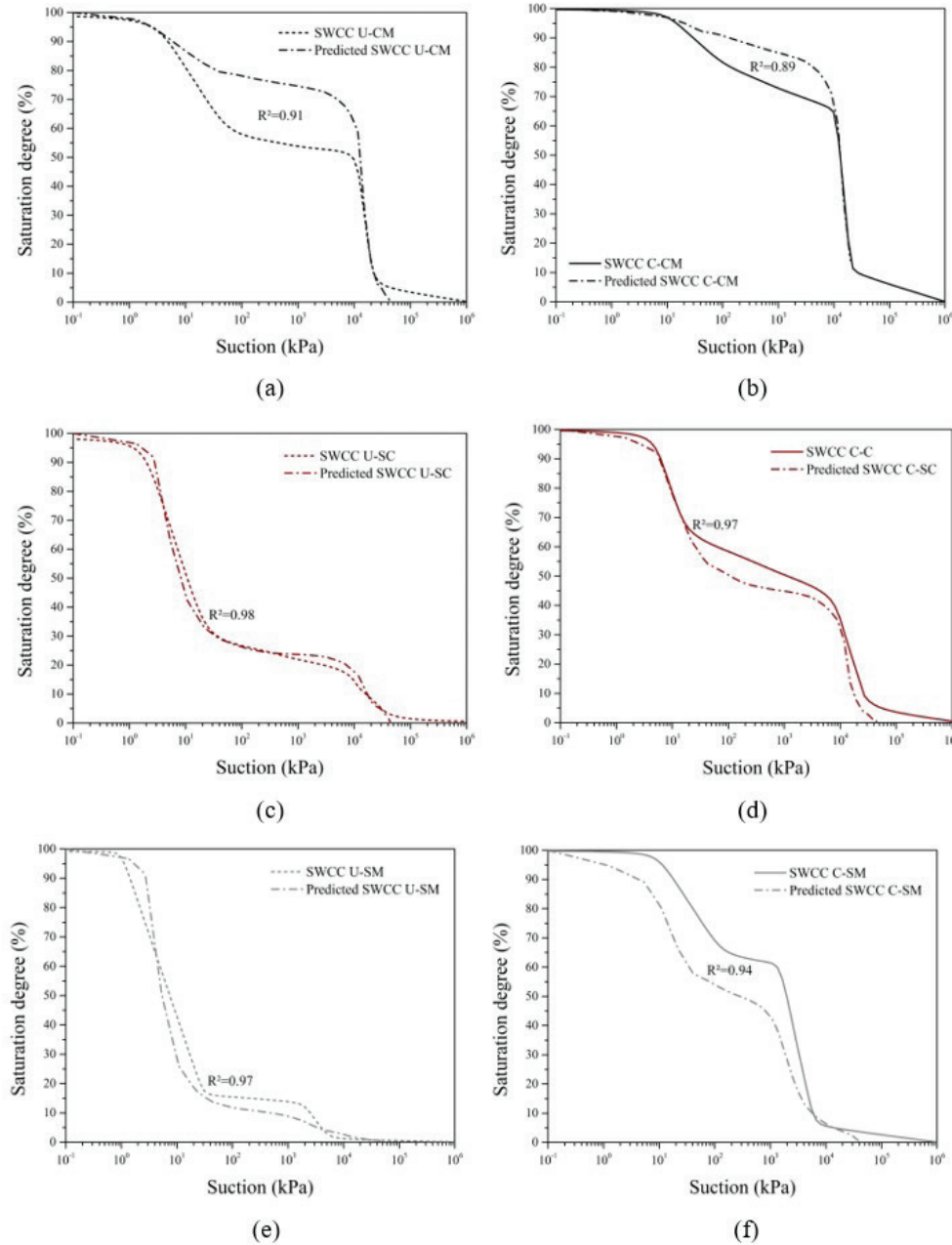


Figure 5. SWCC adjusted and predicted results in drying arm for a wide range of suction *versus* saturation degree.

better than compacted samples, contrary to what was presented by Sun et al. (2016), who described better adjustments for the compacted condition.

On the other hand, the CM soil, despite the satisfactory numerical fit, did not show agreement between the shape of the adjusted and predicted curves for the interaggregated pore region and transition zone. The explanation for this may also be related due to the significant difference between the values of e_{θ} and e_a that was evidenced. Yan et al. (2021) emphasizes that the SWCC of clayey soils can present inaccuracy when transformed directly from the PSD. This

is because the pore structure changes with suction during the SWCC test, while in the test to obtain the PSD, this characteristic remains constant.

Furthermore, still explaining the prediction behavior for the CM soil, according to Campos et al. (2017), MIP test presents high precision in the quantification of open pores, but does not allow the detection of closed pores, in addition to compressing the material, which may change the actual pore sizes. Therefore, it is reasonable to say that for a soil with a considerable number of fines and micro-aggregation, characteristics of the CM soil (Teixeira et al., 2010;

Gonçalves et al., 2017), the test itself may have influenced the underestimated determination of voids characteristic of intra-aggregates pores, smoothing the curve.

4. Conclusions

There were obtained SWCC for compacted and undisturbed samples of three tropical lateritic soils of the south of Brazil, in addition to MIP tests aiming to study the soil structure. The following conclusions were achieved:

1. The SWCC of compacted and undisturbed samples for CM, SC and SM soils present similar shape to the usual bimodal SWCC (noting the presence of macro and micropores in the soil mass), when using both suction measuring methods. The AEV values of undisturbed samples were reasonably low during the desaturation of macropores, due to the aggregation of fine particles that result in greater pore sizes. The granulometric distribution curves obtained without using deflocculant during the sedimentation phase indicated this microaggregation.
2. The undisturbed samples for all three soil types exhibit distinct bimodal PSD. The compacted samples present similar bimodal PSD for sandy soils, given that clayey soil is different due to its considerable content of fines. The void ratio variation for CM soil, which occurs by the compaction process, alters only the interaggregate pore volume, while the intra-aggregate pore volume remains nearly unaltered.
3. The SWCCs predicted by PSD obtained satisfactory numerical fits when comparing with those adjusted by Gitirana & Fredlund model. The SC and SM soils forecast for undisturbed samples was better than for compacted samples. The CM soil did not show agreement between the shape of the adjusted and predicted curves for the interaggregated pore region and transition zone.

Acknowledgements

The authors thank the Coordination of Improvement of Higher Education Personnel (CAPES) for funding the research.

Declaration of interest

The authors have no conflicts of interest to declare. All co-authors have observed and affirmed the contents of the paper and there is no financial interest to report.

Authors' contributions

Alana Dias de Oliveira: conceptualization, data curation, formal analysis, investigation, writing – original draft. Flávia

Gonçalves Pissinati Pelaquim: investigation, data curation, writing – review & editing. Renan Felipe Braga Zanin: investigation, data curation, writing – review & editing. Thadeu Rodrigues de Melo: resources, supervision. João Tavares Filho: resources, supervision. Avacir Casanova Andreello: data curation, formal analysis, investigation, resources. Raquel Souza Teixeira: funding acquisition, methodology, resources, supervision, validation, writing – review & editing.

List of symbols

a	Parameter of Gitirana & Fredlund model (2004)
AEV_1	Air entry value of the 1 st portion (kPa)
AEV_2	Air entry value of the 2 nd portion (kPa)
C	Compacted
C_c	Curvature coefficient
C_{NU}	Non-uniformity coefficient
CM	Clayey silt
D	Pores diameter (μm)
e_0	Initial void ratio
e_a	Void ratio before MIP
e_e	Accumulated volume of mercury for the smallest diameter measured by MIP
$F(d)$	Cumulative distribution function
$F(d_{min})$	Accumulated volume of mercury for the smallest diameter measured by MIP
FPM	Filter paper method
G_s	Specific gravity
HAE	High Air Entry
LA'	Lateritic sandy soils
LG'	Lateritic clay soils
MCT	Miniature, Compacted, Tropical.
MIP	Mercury intrusion porosimetry
P	Pressure (kPa)
pF	Logarithm of suction ($\text{cm.H}_2\text{O}$)
PPM	Pressure plate method
PSD	Pore size distribution
R^2	Coefficient of determination (adjustment)
SC	Sandy clay
SM	Sandy silt
S_r	Saturation degree (%)
S_e	Saturation degree in one gram of dry soil (%)
$S_{r.b2}$	Saturation of the beginning of the 2 nd portion (%)
$S_{r.res1}$	Residual saturation of the 1 st portion (%)
$S_{r.res2}$	Residual saturation of the 2 nd portion (%)
SWCC	Soil-water characteristic curve
U	Undisturbed
USCS	Unified Soil Classification System
u_a	Air pressure (kPa)
u_w	Water pressure (kPa)
w_{paper}	Content of water of the filter paper (%)
α_{Hg}	Contact angle of the air/mercury ($^\circ$)
α_w	Contact angle of the air/water ($^\circ$)
θ_{sat}	Saturation volumetric moisture content (%)
ρ_w	Water specific gravity (g/cm^3)

σ_{Hg}	Surface tension of the air/mercury (N/m)
σ_w	Surface tension of the air/water (N/m)
Ψ_{paper}	Suction of the filter paper (kPa)
Ψ_{res1}	Residual suction of the 1 st portion (kPa)
Ψ_{res2}	Residual suction of the 2 nd portion (kPa)

References

- ABNT NBR 6502. (1995). *Rocks and soils - Terminology*. ABNT – Associação Brasileira de Normas Técnicas, Rio de Janeiro, RJ (in Portuguese).
- ABNT NBR 7182. (2016). *Soil - Compaction test*. ABNT – Associação Brasileira de Normas Técnicas, Rio de Janeiro, RJ (in Portuguese).
- Ajdari, M., Habibagahi, G., & Ghahramani, A. (2012). Predicting effective stress parameter of unsaturated soils using neural networks. *Computers and Geotechnics*, 40, 89-96. <http://dx.doi.org/10.1016/j.compgeo.2011.09.004>.
- ASTM D2487-17. (2017). *Standard practice for classification of soils for engineering purposes (unified soil classification system)*. ASTM International, West Conshohocken, PA. <https://doi.org/10.1520/D2487-17>
- ASTM D4404-18. (2018). *Standard Test Method for Determination of Pore Volume and Pore Volume Distribution of Soil and Rock by Mercury Intrusion Porosimetry*. ASTM International, West Conshohocken, PA. <https://doi.org/10.1520/D4404-18>
- ASTM D5298-16. (2016). *Standard test method for measurement of soil potential (suction) using filter paper*. ASTM International, West Conshohocken, PA. <https://doi.org/10.1520/D5298-16>
- Aubertin, M., Ricard, J., & Chapuis, R.P. (1998). A predictive model for the water retention curve: application to tailings from hard-rock mines. *Canadian Geotechnical Journal*, 35(1), 55-69. <http://dx.doi.org/10.1139/t97-080>.
- Aung, K.K., Rahardjo, H., Leong, E.C., & Toll, D.G. (2001). Relationship between porosimetry measurement and soil-water characteristic curve for an unsaturated residual soil. *Geotechnical and Geological Engineering*, 19, 401-416. <http://dx.doi.org/10.1023/A:1013125600962>.
- Burger, C.A., & Shackelford, C.D. (2001). Evaluating dual porosity of pelletized diatomaceous earth using bimodal soil-water characteristic curve functions. *Canadian Geotechnical Journal*, 38(1), 53-66. <http://dx.doi.org/10.1139/t00-084>.
- Campos, J.V., Lavagnini, I.R., Ferreira, J.A., Montrazi, E.T., Bonagamba, T.J., & Pallone, E.M.J.A. (2017). Comparative analysis between different porosimetric tests on macroporous alumina. *Revista Matéria*, 22(1): e11929 (in Portuguese). <https://doi.org/10.1590/S1517-707620170005.0265>
- Cancian M.A., Cancian V.A., Teixeira R.S., Fontenele H.B., & Costa Branco C.J.M. (2017). Influence of moisture content, porosity and time interval until application of the soil-cement mixture on road pavement. *Transportes*, 25(1), 41-50 (in Portuguese). <https://doi.org/10.14295/transportes.v25i1.1126>
- Carvalho J.C., & Gitirana G.F.N. (2021). Unsaturated soils in the context of tropical soils. *Soils and Rocks*, 44(3), e2021068121. <https://doi.org/10.28927/SR.2021.068121>
- Carvalho, J.C., & Leroueil, S. (2004). Transformed soil-water characteristic curve. *Soils and Rocks*, 27(3), 231-242 (in Portuguese).
- Carvalho, J.C., Guimarães, R.C., & Pereira, J.H.F. (2002). Courbes de rétention d'eau d'un profil d'altération. In J.F.T. Jucá, T.M.P. Campos & F.A.M. Marinho (Eds.), *Proc. 3rd International Conference on Unsaturated Soils* (pp. 289-294), Recife, Brazil. Swets & Zeitlinger (in French).
- Chahal, R.S. (1965). Effect to temperature and trapped air on matric suction. *Soil Science*, 100(4), 262-266.
- Chandler, R.J., Crilly, M.S., & Montgomery-Smith, G. (1992). A low-cost method of assessing clay desiccation for low-rise buildings. *Proceedings of the Institution of Civil Engineers: Civil Engineering*, 92(2), 82-89. <http://dx.doi.org/10.1680/icien.1992.18771>.
- Chiu, C.F., Yan, W.M., & Yuen, K.V. (2012). Estimation of water retention curve of granular soils from particle-size distribution - A Bayesian probabilistic approach. *Canadian Geotechnical Journal*, 49(9), 1024-1035. <http://dx.doi.org/10.1139/t2012-062>.
- Delage, P., Audiguier, M., Cui, Y.J., & Deveugèle, M. (1995). Propriétés de rétention d'eau et Microstructure de différents géomatériaux. In Hanrahan (Ed.), *Proc. 9th European Conference on Soil Mechanics and Foundation Engineering* (pp. 43-48). Dublin, Ireland. CRC Press (in French).
- Fredlund, D.G., & Rahardjo, H. (1993). *Soil mechanics for unsaturated soils*. John Wiley & Sons. <https://doi.org/10.1002/9780470172759>
- Gao, Y., & Sun, D. (2017). Soil-water retention behavior of compacted soil with different densities over a wide suction range and its prediction. *Computers and Geotechnics*, 91, 17-26. <http://dx.doi.org/10.1016/j.compgeo.2017.06.016>.
- Gerscovich, D.M.S. (2001). Equations for modeling the soil-water characteristic curve applied to Brazilian soils. In W.Y.Y. Gehling, & F. Schnaid (Eds.), *Proc. 4th Brazilian Symposium on Unsaturated Soils*. (pp. 76-92), Porto Alegre. Palloti (in Portuguese).
- Gitirana, G.F.N., & Fredlund, D.G. (2004). Soil-water characteristic curve equation with independent properties. *Journal of Geotechnical and Geoenvironmental Engineering*, 130(2), 209-212. [http://dx.doi.org/10.1061/\(asce\)1090-0241\(2004\)130:2\(209\)](http://dx.doi.org/10.1061/(asce)1090-0241(2004)130:2(209)).
- Gonçalves F., Souza C.H.U., Tahira F.S., Fernandes F., & Teixeira R.S. (2017). Increment of sludge from water treatment plant in waterproofing barriers of sanitary landfill. *Revista DAE*, 65, 5-14 (in Portuguese). <https://doi.org/10.4322/dae.2016.018>

- Gonçalves, F., Correa, C.Z., Lopes, D.D., Vendrame, P.R.S., & Teixeira, R.S. (2019). Monitoring of the process of waste landfill leachate diffusion in clay and sandy soil. *Environmental Monitoring and Assessment*, 191, 577. <http://dx.doi.org/10.1007/s10661-019-7720-9>.
- Gonçalves, F., Zanin, R.F.B., Somera, L.F., Oliveira, A.D., Ferreira, J.W.S., Costa Branco, C.J.M., & Teixeira, R.S. (2018). Physical-chemical and mineralogical characterization of three soils in the state of Paraná. In *Proc. 19th Brazilian Congress of Soil Mechanics and Geotechnical Engineering*, Salvador, BA, Brazil. ABMS.
- Gutierrez, N.H.M., Nobrega, M.T., & Vilar, O.M. (2008). Influence of the microstructure in the collapse of a residual clayey tropical soil. *Bulletin of Engineering Geology and the Environment*, 68(1), 107-116. <http://dx.doi.org/10.1007/s10064-008-0180-z>.
- Kim, C.K., & Kim, T.H. (2010). Behavior of unsaturated weathered residual granite soil with initial water contents. *Engineering Geology*, 113(4), 1-10. <http://dx.doi.org/10.1016/j.enggeo.2009.09.004>.
- Li, X., & Zhang, L.M. (2009). Characterization of dual-structure pore-size distribution of soil. *Can Geotech*, 46(2), 129-141. <http://dx.doi.org/10.1139/t08-110>.
- Marinho, F.A.M. (1997). Soil suction measurement. In T.M.P. Campos, & E.A. Vargas Junior (Eds.), *Proc. 3rd Brazilian Symposium on Unsaturated Soils*. (pp. 373-397). Rio de Janeiro, RJ, Brazil. Freitas Bastos Editora (in Portuguese).
- Marinho, F.A.M. (2005). Nature of soil-water characteristic curve for plastic soils. *Journal of Geotechnical and Geoenvironmental Engineering*, 131(5), 654-661. [http://dx.doi.org/10.1061/\(ASCE\)1090-0241\(2005\)131:5\(654\)](http://dx.doi.org/10.1061/(ASCE)1090-0241(2005)131:5(654)).
- Marinho, F.A.M., Take, W.A., & Tarantino, A. (2008). Measurement of matric suction using tensiometric and axis translation techniques. *Geotechnical and Geological Engineering*, 26, 615. <http://dx.doi.org/10.1007/s10706-008-9201-8>.
- Mascarenha, M.M.A., Cordão-Neto, M.P., & Romero, E. (2010). Influence of the microstructure on the hydro-mechanical behaviour of a natural silty clay. In E. Alonso, & A. Gens (Eds.), *Unsaturated soils*, London, UK. CRC Press. <https://doi.org/10.1201/9781003026365>
- Miguel, M.G., & Bonder, B.H. (2012). Soil-water characteristic curves obtained for a colluvial and lateritic soil profile considering the macro and micro porosity. *Geotechnical and Geological Engineering*, 30(6), 1405-1420. <http://dx.doi.org/10.1007/s10706-012-9545-y>.
- Miguel, M.G., & Vilar, O.M. (2009). Study of the water retention properties of a tropical soil. *Canadian Geotechnical Journal*, 46(9), 1084-1092. <http://dx.doi.org/10.1139/t09-039>.
- Nimmo, J.R. (2005). Porosity and pore size distribution. In D. Hillel (Ed.), *Encyclopedia of Soils in the Environment*, (pp. 295-303). Academic Press. <https://doi.org/10.1016/B0-12-348530-4/00404-5>
- Nogami, J.S., & Villibor, D.F. (1981). A new soil classification for road purposes. In *Brazilian Symposium on Tropical Soils in Engineering*, (pp. 289-294). Rio de Janeiro, Brazil. COPPE/UFRJ, CNPq, ABMS (in Portuguese).
- Otalvaro, I.F., Cordão Neto, M.P., Delage, P., & Caicedo, B. (2016). Relationship between soil structure and water retention properties in a residual compacted soil. *Engineering Geology*, 205, 73-80. <http://dx.doi.org/10.1016/j.enggeo.2016.02.016>.
- Philip, J.R., & De Vries, D.A. (1957). Moisture movement in porous materials under temperature gradient. *Transactions: American Geophysical Union*, 38(2), 222-232. <http://dx.doi.org/10.1029/TR038i002p00222>.
- Rocha G.C., Barros O.N.F., & Guimarães M.F. (1991). Spatial distribution and soil characteristics of the campus of the State University of Londrina, PR. *Semina: Ciências Agrárias*, 12(1), 21-25 (in Portuguese). <https://doi.org/10.5433/1679-0359.1991v12n1p25>
- Romero, E., Gens, A., & Lloret, A. (1999). Water permeability, water retention and microstructure of unsaturated compacted Boom clay. *Engineering Geology*, 54(1-2), 117-127. [http://dx.doi.org/10.1016/S0013-7952\(99\)00067-8](http://dx.doi.org/10.1016/S0013-7952(99)00067-8).
- Romero, E., Gens, A., & Lloret, A. (2001). Temperature effects on the hydraulic behavior of an unsaturated clay. *Geotechnical and Geological Engineering*, 19(3), 311-332. <http://dx.doi.org/10.1023/A:1013133809333>.
- Sasanian, S., & Newson, T.A. (2013). Use of mercury intrusion porosimetry for microstructural investigation of reconstituted clays at high water contents. *Engineering Geology*, 158, 15-22. <http://dx.doi.org/10.1016/j.enggeo.2013.03.002>.
- Silva F.C., Cabral, S.M., Cabral, R.M., Carvalho, J.C., Cordão Neto, M.P., Oliveira, R.B., & Côrtes, H.A. (2020). Determination of the characteristic curve and influence of macro and micropores on a residual soil profile. *Geotecnica*, 149, 101-128 (in Portuguese). <http://doi.org/10.24849/j.geot.2020.149.06>
- Simms, P.H., & Yanful, E.K. (2001). Measurement and estimation of pore shrinkage and pore distribution in a clayey till during soil-water characteristic curve tests. *Canadian Geotechnical Journal*, 38(4), 741-754. <http://dx.doi.org/10.1139/t01-014>.
- Sun, D., You, G., Annan, Z., & Daichao, S. (2016). Soil-water retention curves and microstructures of undisturbed and compacted Guilin lateritic clay. *Bulletin of Engineering Geology and the Environment*, 75(2), 781-791. <http://dx.doi.org/10.1007/s10064-015-0765-2>.
- Tavakoli Dastjerdi, M.H., Habibagahi, G., & Nikooee, E. (2014). Effect of confining stress on soil water retention curve and its impact on the shear strength of unsaturated soils. *Vadose Zone Journal*, 13(5), 1-11. <http://dx.doi.org/10.2136/vzj2013.05.0094>.
- Teixeira, R.S., Cambier, P., Dias, R.D., Pinese, J.P.P., & Jaulin-Soubelet, A. (2010). Mobility of potentially harmful metals in latosols impacted by the municipal solid waste

- deposit of Londrina, Brazil. *Applied Geochemistry*, 25(1), 1-15. <http://dx.doi.org/10.1016/j.apgeochem.2009.09.022>.
- Vanapalli, S.K., Fredlund, D.G., Pufahl, D.E., & Clifton, A.W. (1996). Model for the prediction of shear strength with respect to soil suction. *Canadian Geotechnical Journal*, 33(3), 379-392. <http://dx.doi.org/10.1139/t96-060>.
- Vanapalli, S.K., Pufahl, D.E., & Fredlund, D.G. (1999). The effect of soil structure and stress history on the soil-water characteristics of a compacted till. *Geotechnique*, 49(2), 143-159. <http://dx.doi.org/10.1680/geot.1999.49.2.143>.
- Washburn, E.W. (1921). Note on a method of determining the distribution of pore sizes in a porous material. *Proceedings of the National Academy of Sciences of the United States of America*, 7(4), 115-116. <http://dx.doi.org/10.1073/pnas.7.4.115>.
- Yan, W., Birle, E., & Cudmani, R. (2021). A simple approach for predicting soil water characteristic curve of clayey soils using pore size distribution data. *MATEC Web of Conferences*, 337: 02012. <https://doi.org/10.1051/mateconf/202133702012>
- Zhang, L., & Li, X. (2010). Microporosity structure of coarse granular soils. *Journal of Geotechnical and Geoenvironmental Engineering*, 136(10), 1425-1436. [http://dx.doi.org/10.1061/\(ASCE\)GT.1943-5606.0000348](http://dx.doi.org/10.1061/(ASCE)GT.1943-5606.0000348).
- Zhou, W.H., Yuen, K.V., & Tan, F. (2014). Estimation of soil-water characteristic curve and relative permeability for granular soils with different initial dry densities. *Engineering Geology*, 179, 1-9. <http://dx.doi.org/10.1016/j.enggeo.2014.06.013>.

Sample dimension effect on cement-stabilized sandy soil mechanical behavior

José Wilson dos Santos Ferreira^{1#} , Michéle Dal Toé Casagrande¹ ,

Raquel Souza Teixeira² 

Article

Keywords

Dimension effect
Indirect tensile strength
Nondestructive tests
Soil-cement
Unconfined compression strength
Ultrasonic testing

Abstract

Stabilized soil with cement has been a widely used solution in geotechnical projects and requires the molding of numerous specimens to investigate their properties in destructive tests, restraining the reuse for other analysis. Also, distinct sample dimension has been utilized in the research without taking this effect into account. Recognizing these needs, the height and diameter (H/D) ratio effect on cement-stabilized soil mechanical behavior was assessed in the present work. Using sandy soil, Unconfined Compression Strength (UCS), Indirect Tensile Strength (ITS) and Ultrasonic Pulse Velocity tests were performed varying the curing period (7 and 28 days), cement type (I and III) and content (6, 7, 8, 9 and 10%), based on conventional (127 x 100 mm) and reduced dimension (105 x 50 mm) specimens. All variables, individually and combined, affected the compression and tensile strengths of the mixtures, resulting in greater gains for the ones molded with type III cement in reduced dimension, at 28 days of curing. The dimension as an influential variable was statistically established using the variance analysis (ANOVA) at a significance level (α) of 0.05, in which reduced dimension showed an average superior resistance of 21.3%. Mixtures molded with $H/D \geq 2$ demonstrated strong correlation ($R^2 = 0.93$), pointing to the possibility of ITS prevision through the P-wave velocity nondestructive tests.

1. Introduction

The improvement of properties and behavior of local soils through the incorporation of stabilizing agents has great applicability in geotechnical projects. Satisfying technical, economic and environmental requirements, the stabilization technique can be used for canal lining, support layers for shallow foundations, stabilization and protection of slopes, preventing liquefaction of loose granular soils and pavement base layers.

The most common agents applied in the stabilization technique are cement, lime, fly ashes, asphalt emulsion, and construction and demolition residue (Abdullah & Al-Abdul Wahhab, 2018; Baldovino et al., 2018; Consoli et al., 2010, 2011, 2013; Ingunza et al., 2015; Mohammadinia et al., 2014; Su et al., 2017; Sukprasert et al., 2019). Herein, the use of cement has been extensively investigated in the literature from the perspective of the chemical reactions involved and the cementation influence on the mechanical behavior (Clough et al., 1981; Croft, 1967; Horpibulsuk et al., 2006; Ismail et al., 2002; Lorenzo & Bergado, 2004), the

determination of variables and relations that rule the behavior and its prevision (Baldovino et al., 2020; Cardoso et al., 2017; Consoli et al., 2007; Diambra et al., 2017; Ferreira et al., 2021; Stracke et al., 2012).

Increases in strength, stiffness, durability, volumetric stability, as well as reduction in permeability and compressibility occur through hydration and hardening reactions of the cement and its interactions with clay minerals. In this sense, the properties of soil-cement mixtures depend on factors such as the soil grain size and mineralogy, cement type and content, moisture content, mixture porosity, compaction effort and curing conditions (Gajewska et al., 2017; Joel & Agbede, 2011; Le Kouby et al., 2017; Mandal et al., 2017).

Notwithstanding the gains from the technique, the molding of numerous samples used in destructive tests, besides the requirement of high volume of soil, restrain the reuse for other analysis. Nondestructive tests using acoustic emission have been investigated for geotechnical applications in non-stabilized and stabilized soil. Khan et al. (2006) applied the pulse-velocity method to characterize a cemented sand, identifying changes in wave velocity according to the

[#]Corresponding author. E-mail address: ferreira.jose@aluno.unb.br

¹Universidade de Brasília, Departamento de Engenharia Civil e Ambiental, Brasília, DF, Brasil.

²Universidade Estadual de Londrina, Departamento de Construção Civil, Londrina, PR, Brasil.

Submitted on September 25, 2021; Final Acceptance on March 15, 2022; Discussion open until August 31, 2022.

<https://doi.org/10.28927/SR.2022.075321>



This is an Open Access article distributed under the terms of the Creative Commons Attribution License, which permits unrestricted use, distribution, and reproduction in any medium, provided the original work is properly cited.

initial water and cement content; Toohey & Mooney (2012) provided satisfactory estimation of the elastic modulus growth by seismic tests of a lime-stabilized soil during curing; correlating flexural strength and P-wave velocity for clay, silt, sand and gravel materials stabilized with fly ash and lime, strong relationships were reported by Mandal et al. (2016); even though velocity is a low-strain property and strength is a large-strain property of the material, Kutanaei & Choobbasti (2016) obtained satisfactory correlations between unconfined compression strength and ultrasonic velocity, evaluating the nanosilica particle and polyvinyl alcohol (PVA) fibers' effect on the ultrasonic pulse velocity and mechanical properties of cemented sand.

Additionally, there is the sample dimension variability in improvement and stabilization studies. Consoli et al. (2007) applied samples of 100 mm high and 50 mm in diameter on the analysis of the parameters that control the resistance to compression of artificially cemented sands. The same cylindrical size was applied by Ho et al. (2017) under drying curing condition of cemented-treated soils; specimens of 140 x 70 mm and 76 x 38 mm (high and diameter, respectively) were used by Rios et al. (2013; 2012), based on the pressure level of triaxial compression tests; Reis et al. (2015) utilized molds of 127 x 100 mm (height and diameter, respectively) when studying the use of soil, cement and residues of construction and demolition for pavement; Cardoso et al. (2017) used samples of 140 cm high and 7 cm in diameter, when verifying the influence of the curing period, cement content and water-cement relation on the bonding effect in soil-cement mixtures.

All the studies were performed according to normalizations, although the variation of the factor H/D may affect the mechanical behavior for the same dosing conditions. Thus, the present paper focuses on evaluating the effect of varying

the relation H/D in laboratorial soil-cement mixtures for different curing period, contents and types of cement, seeking to establish relations between the investigated variables and the mechanical behavior, in destructive (UCS and ITS) and nondestructive tests of Ultrasonic Pulse Velocity.

2. Materials and methods

2.1 Materials

The soil used in this study, granulometrically characterized as a medium silty fine sand, was obtained near the Federal Highway BR-376 in the city of Mandaguaçu, in the northwest of the Paraná State, Brazil (Figure 1). The soil belongs to the Caiuá formation, made up mainly of fine and very fine sandstones (França Junior et al., 2010). From the chemical soil characterization by X-ray fluorescence analyzer was seen the presence of Si (55.1%), Al (27.9%), Fe (13.4%), and Ti (2.7%), in agreement with the mineral composition identified in X-ray diffraction, consisted mainly by quartz (SiO₂), iron oxide (Fe₂O₃) and kaolinite (Al₂Si₂O₅(OH)₄).

The Atterberg limits are liquid limit of 27% and plastic limit of 17%. The specific gravity of solids is 2.69. According to the Unified Soil Classification System (USCS) and American Association of State Highway and Transportation Officials (AASHTO), the soil can be classified as clay sand (SC) and belongs to group A-2-4, respectively.

Portland cement (PC) with addition of pozzolan (Type I) and Portland cement of high initial strength (Type III) were used as the cementing agents, presenting specific gravity of 3.13 and 3.24 for type I and III, respectively. Distilled water was used for characterization of materials and homogenization of the mixture during the compaction.

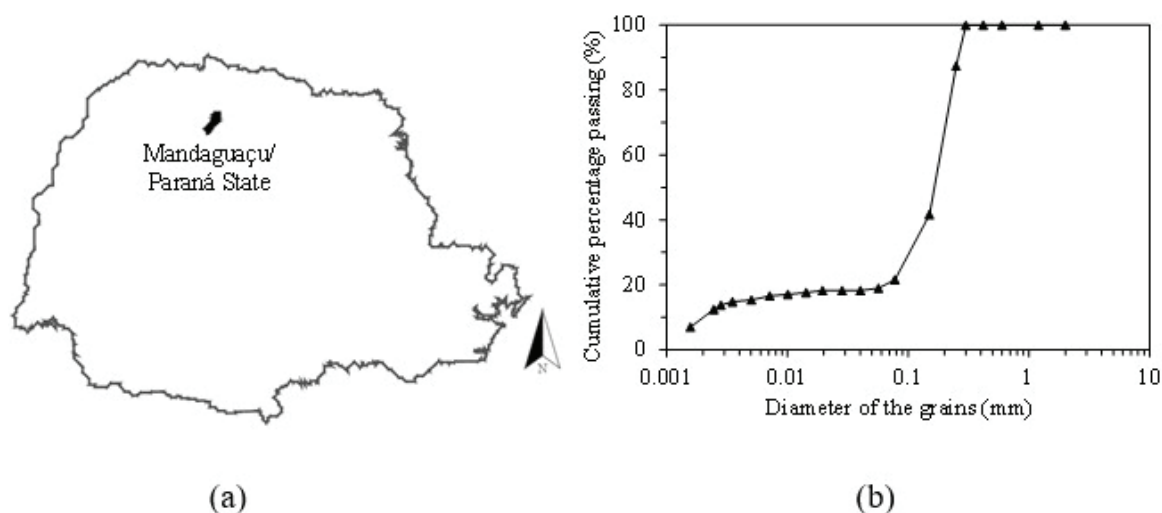


Figure 1. Sandy soil used: (a) Collection site; (b) Particle-size distribution curve.

2.2 Specimen preparation

Cement contents of 6, 7, 8, 9 and 10%, in relation to the dry mass of soil, were used in the study, based on literature and Brazilian experience, in which these cement percentages are commonly used for base and subbase layers of road pavement (Antunes et al., 2017; Baldovino et al., 2018; 2020; Consoli et al., 2007, 2017; Ferreira et al., 2021; Mola-Abasi et al., 2018).

For the purpose of investigating the effect of the sample dimension on the mechanical behavior, dimensions of Proctor cylinder (127 mm high and 100 mm in diameter), denominated Conventional Dimension (CD), and Reduced Dimension (RD), with height and diameter of 105 x 50 mm were adopted, based on the Brazilian standard for studies of soil-cement dosing (ABNT, 2012a), and the recommendation of height and diameter relation between 2 and 2.5 (ASTM, 2017). It is important to highlight that the dimensions used in the study are in agreement with soil stabilization works present in the literature (Baldovino et al., 2020; Consoli et al., 2007; Ferreira et al., 2021; Ho et al., 2017; Lukiantchuki et al., 2020; Portelinha et al., 2012; Reis et al., 2015).

The specimens molding proceeded similar to the compaction using normal energy in Proctor cylinder (600 kJ/m³). Considering the mixtures molded in reduced dimension, the energy imposed was varied, controlling the height of each of the three layers. Although the conventional and reduced dimension demand distinct compaction processes, the compaction control was strictly followed to ensure that for the same experimental condition the samples in the conventional and reduced dimensions were statistically identical regarding the defined compaction parameters.

Samples with compacting degree tolerances of $100 \pm 2\%$ and optimum moisture content variation ($\Delta\omega$) of $\pm 0.5\%$ were stored in plastic bags and taken to the humidity chamber, at the temperature of 23 ± 2 °C and air relative humidity not inferior to 95%. The curing periods were 7 and 28 days.

2.3 Testing methods

Unconfined Compression Strength (UCS) tests for the soil and mixtures were carried out following the ABNT (2012b), in triplicate, which is similar to standard ASTM (2017). Subsequent to the curing stage, the mixtures were immersed for 4 hours. This stage was not performed for the soil, due the occurrence of disaggregation. The test was performed with controlled deformation in 1.27 mm/min average rate, and the maximum load recorded. The Indirect Tensile Strength (ITS) tests was assessed per Brazilian test method (ASTM, 2016b), in duplicate, adopting a similar procedure to UCS.

In order to statistically verify the investigated variables (dimension, curing period and cement content) and interactions on the mixtures mechanical behavior, variance analysis (ANOVA) at the level of significance (α) of 0.05 for each

type of cement was carried out, through the hypothesis test if the mean values are equal (null hypothesis), or if they differ in at least one treatment (alternative hypothesis).

The test conclusion may be expressed by the comparison of the F-value with the critical value obtained from the theoretical distribution or from the significance probability (p-value), calculated assuming that the null hypothesis is true. Thus, values equal or lower than 0.05 indicate the existence of significant differences between the treatments. All mixtures presented normal distribution of probability, verified by Shapiro-Wilk normality test.

The ultrasonic tests were performed in specimens referred to the ITS, since the tests are nondestructive, using Pundit Lab equipment. The test consists in measuring the ultrasonic pulse velocity (P-wave) emitted and received through two transducers (emitter/receptor) located in opposing faces of the material – direct transmission. Before testing, the equipment was calibrated and settings as transducer frequency of 54 kHz, pulse width (automatically adjusted), and correction factor (1 – standard recommended by the manufacturer) were established, according to ASTM (2016a).

To minimize the effects of refraction and reflection of the ultrasonic pulse occasioned by the presence of air between the surfaces of the sample and transducer, a fine layer of industrial gel was applied on both surfaces prior to testing. Two readings were performed on each face of the specimens, inverting both transducers with the view to eliminate bias during the data acquisition, which occurred before (Pulse I) and after the immersion phase (Pulse II). The execution scheme is illustrated in Figure 2.

3. Results and discussion

3.1 Compaction parameters

The average results for the maximum dry unit mass (ρ_d max) and optimum moisture content (ω_{opt}) are presented in Figure 3.

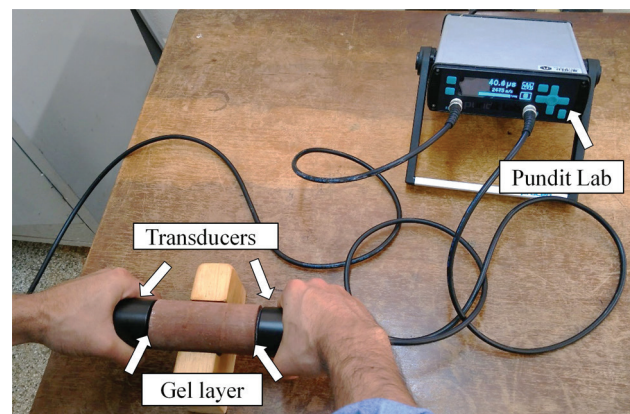


Figure 2. Ultrasonic test execution.

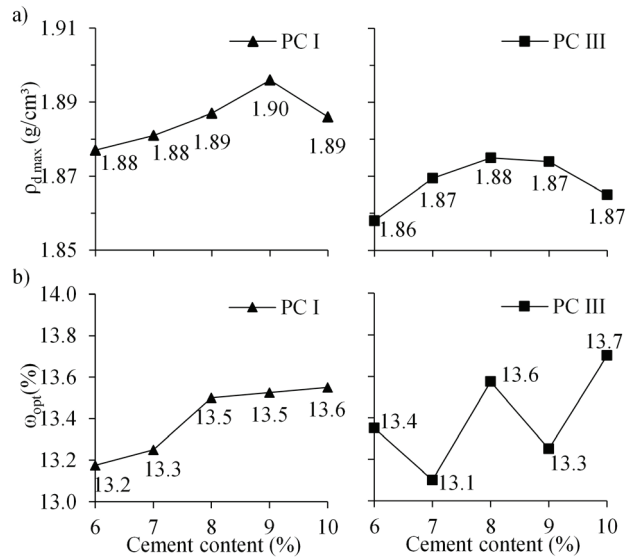


Figure 3. Maximum dry unit mass (a) and optimum moisture content (b) of the mixtures.

Considering both cementing agents, it was observed a tendency of increasing the maximum dry unit mass until a given content, from which occurs decrease. The increase is attributed to filling the soil voids through the addition of cement particles, which presented superior specific gravity in comparison to the soil grains, while the reduction is possibly caused by the formation of transitional components that presented higher densities for a specific range of addition, as seen by Osinubi (1998), Osinubi & Nwaiwu (2006), and Portelinha et al. (2012).

Since this event was observed for both stabilizing agents, it is assumed the mixture density becomes less sensitive to cement addition. This behavior is related to the granulometric characteristics of the soil, a very graduated sand (uniformity coefficient C_u of 9.7 and gradation coefficient C_c of 2.9), with approximately 23% of the material smaller than 0.075 mm, indicating the compacted non-stabilized soil already presents satisfactory grain and particle interlocking.

The additions of cement result in the increase of surface to be hydrated and, consequently, demand more water, as verified by the type I cement. Nevertheless, the decrease on the optimum moisture content may be related to the increase of ions exchange reactions, resulting in a significant flocculation and, therefore, an increase on the grain size, so the mixture demands less water for compaction, as presented by type III cement (Osula, 1989).

3.2 Sample dimension effect

The mechanical behavior depending on the type and cement content, sample dimension and curing period, for unconfined compression strength and indirect tensile strength are shown in Figure 4 and Figure 5, respectively. Satisfactory

coefficients of determination were obtained for the addition range investigated in this research ($R^2 > 0.88$), under second order lines of exponential tendency.

Comparing unconfined compression responses of the mixtures and pure soil, corresponding to 0.43 MPa in conventional and 0.62 MPa in reduced dimension, the minimum and maximum gain for the type I was about 3.5 (6% cement, 7 days, RD) and 10.8 times (10% cement, 28 days, CD), while for the type III, these increases were about 5.2 (6% cement, 7 days, RD) and 14.1 times (10% cement, 28 days, CD).

For the type I cement, the minimum and maximum gains considering indirect tensile strength, in relation to the non-stabilized soil (0.07 MPa for CD and 0.06 MPa for RD), were of 3.3 (6% of cement, 7 days, CD) and 11.3 times (10% of cement, 28 days, RD); as for the cement Type III, the increments were about 5.0 (6% cement, 7 days, CD) and 12.8 times (10% of cement, 28 days, RD).

Independently of the experimental condition, the increase of the curing period improved the strength of the natural soil (Aiban et al., 1998; Baldovino et al., 2020; Cardoso et al., 2017; Joel & Agbede, 2011). The mixtures performed with the Portland cement of high initial strength presented superior resistance for both curing periods. In contrast, the average increases of strength with the increment of curing period were superior for the type I. The unconfined compressive strength increments were between 63% and 59% for the CD and RD, when compared to the Type III – 43% and 37% for the CD and RD. Considering the indirect tensile strength, the same trend was seen; gains of 65% (CD) and 50% (RD) were obtained for type I, while increments of 37% (CD) and 39% (RD) were reached under type III cement. This behavior is derived from the limestone and clay dosing process and the cement finer milling of type III cement, leading to high initial strength.

The effect of the H/D relation, for the same experimental condition (cement content, type of cement and curing period), varying only the specimen dimension, indicated a higher resistance in reduced dimension mixtures, which is emphasized in Figure 6.

It is assumed that the increase of the relation improved the stress distribution, owing to the effects of the geometry. Yilmaz et al. (2015) supplemented that the samples in low volume reduce the number of microfissures and matrix pores, resulting in superior strength.

Furthermore, at a lower level of effect, the variation of the microstructural arrange resultant from the compaction process possibly contributes for the different mechanical behavior. In conventional dimension the energy was applied over the area of subsequent blows, due to its diameter ($\varnothing = 100$ mm) being larger than the diameter of the rammer used for the hits ($\varnothing = 50$ mm); considering the specimens of reduce dimension ($\varnothing = 50$ mm), there is compatibility between these two dimensions, so the energy of each blow is distributed over the entire area. Thus, the variation of

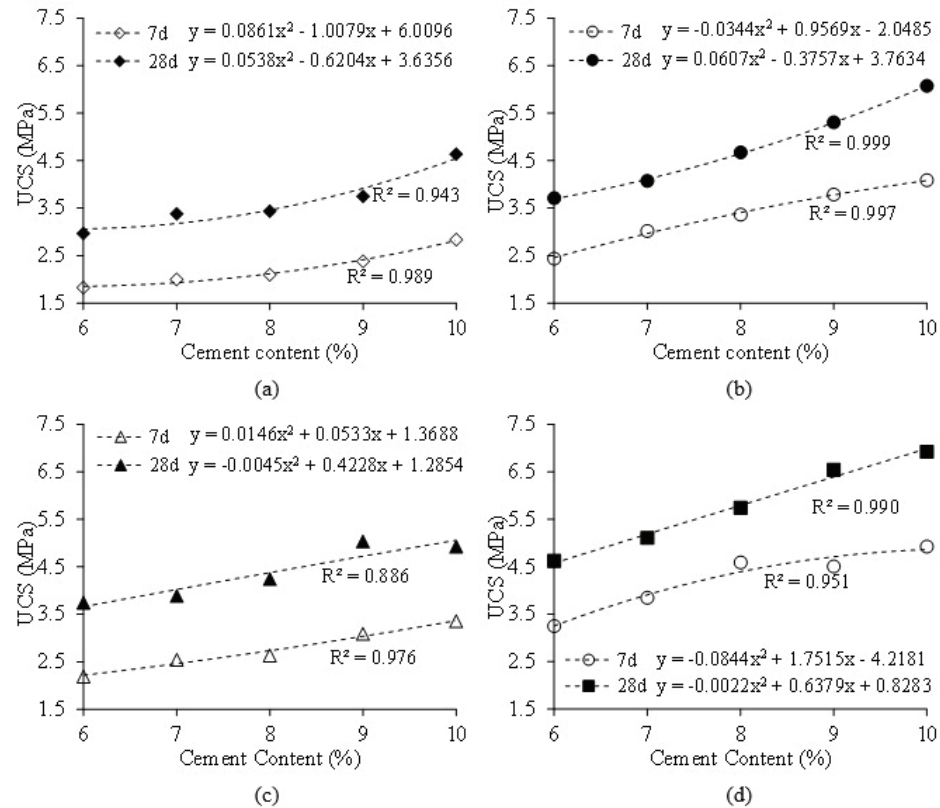


Figure 4. UCS for cement type and dimension: (a) PC I, CD; (b) PC III, CD; (c) PC I, RD; (d) PC III, RD.

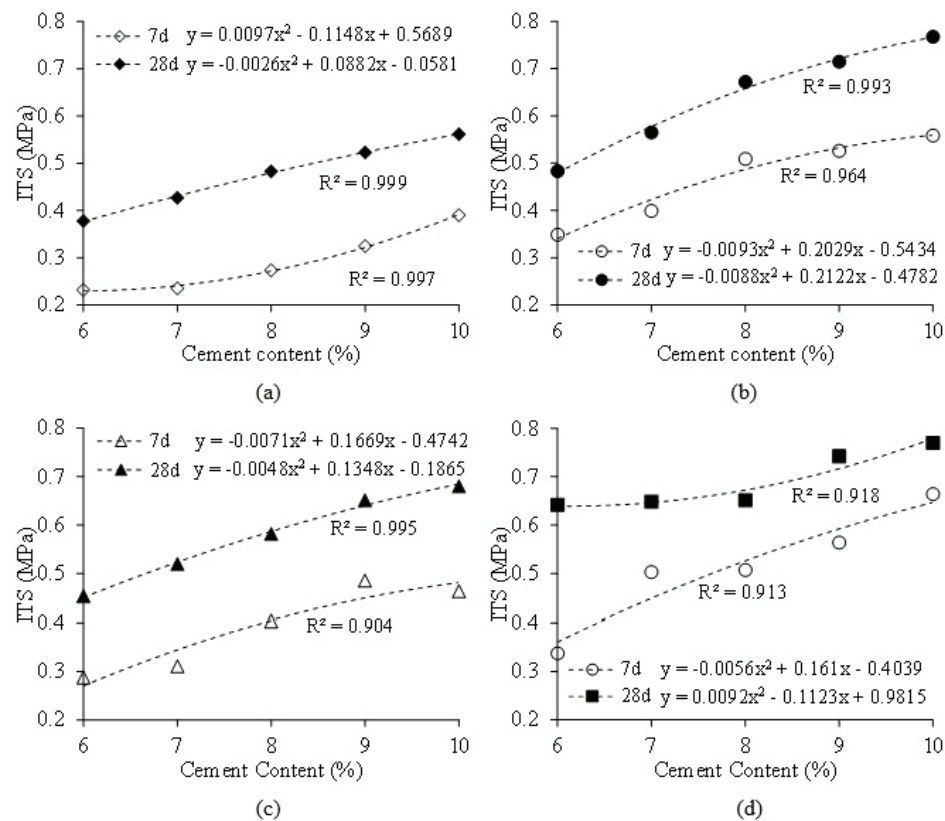


Figure 5. ITS for cement type and dimension: (a) PC I, CD; (b) PC III, CD; (c) PC I, RD; (d) PC III, RD.

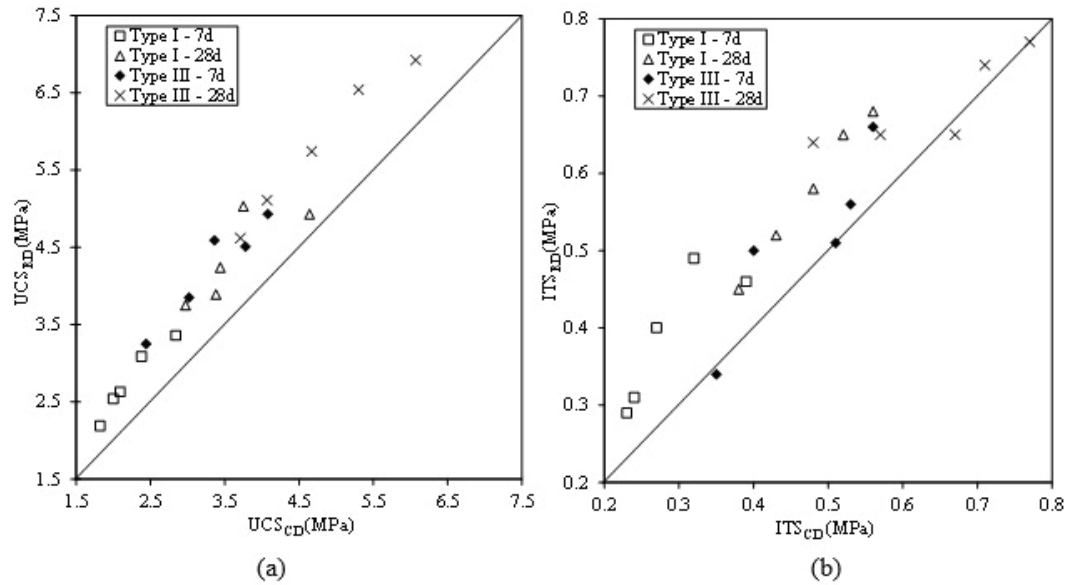


Figure 6. Dimension effect on mechanical behavior: (a) UCS; (b) ITS.

Table 1. P-value results obtained from the variance analysis (ANOVA).

Factor	P-value			
	UCS Type I	UCS Type III	ITS Type I	ITS Type III
Dimension	< 0.0001	< 0.0001	< 0.0001	0.0002
Curing age	< 0.0001	< 0.0001	< 0.0001	< 0.0001
Cement content	< 0.0001	< 0.0001	< 0.0001	< 0.0001
Dimension:Curing age	0.0896	0.436	0.849	0.8772
Dimension:Cement content	0.7486	0.989	0.114	0.2198
Curing age:Cement content	0.0222	0.001	0.447	0.2357
Dimension:Curing age:Cement content	0.4131	0.921	0.994	0.0021

the microstructural arrangement resultant from the compaction process contributes for the different mechanical behavior under identical molding parameters (Leandro et al., 2017).

As demonstrated by the variance analysis performed for all obtained results (Table 1), the effect of dimension as an influential variable in the compression mechanical behavior was confirmed, besides the variables of curing period and cement content, individually and combined.

The ratio between reduced and conventional dimension [RD/CD] for UCS situated in range from 1.06 to 1.37, while for ITS the established relation was between 0.97 and 1.49, presenting after 28 days a tendency of approximately constant, which was not observed after 7 days of curing. On average, mixtures molded in reduced dimension showed 21.3% higher UCS and ITS results, not being considered the multiplication factor of 1.10 suggested by ASTM (2017). The difficulty to establish a unique relationship is associated with the interaction between the variables dimension, curing period and content, which is shown by the statistical study as significative.

3.3 Ultrasonic pulse velocity

The use of ultrasonic tests is commonly adopted in the area of concrete materials, although it is an incipient technique in the study of the soil and cement-stabilized soil behavior. As a result of the large quantity of tests required for the verification of the mechanical properties, the use of nondestructive tests has shown to be an important instrument to increase the agility and to facilitate the mechanical investigation.

Figure 7 depicts the P-wave velocity trend obtained on the mixtures, presenting the results for type III cement in CD and RD, at 7 and 28 days, before (pulse 1) and after immersion (pulse 2).

Superior pulse magnitudes were obtained in the after-immersion condition for all scenarios. Since the wave is not propagated through the mixture voids, when the open pores are partially filled with water, the time of transmission is decreased.

The P-wave velocity were of 758 and 1039 m/s for the soil and in the range from 2350 to 3050 m/s for cement-stabilized

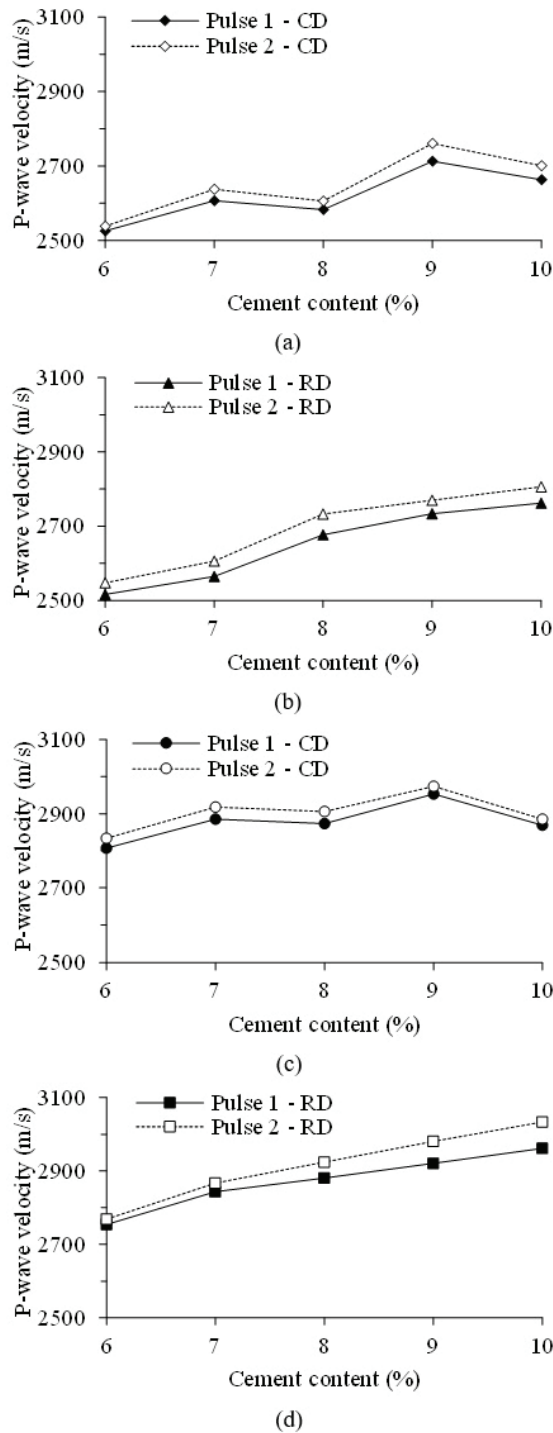


Figure 7. P-wave velocity for PC III cement-stabilized soil at 7 (a, b) and 28 days of curing (c, d).

soil. Increasing the curing period from 7 to 28 days caused the growth on the wave velocity for both stabilizing agents, and it is associated with the cement hardening mechanisms and secondary reaction among the stabilizing agent and the soil matrix. In general, the mixtures demonstrated that the pulse velocity rises as the cement content increases, presenting a

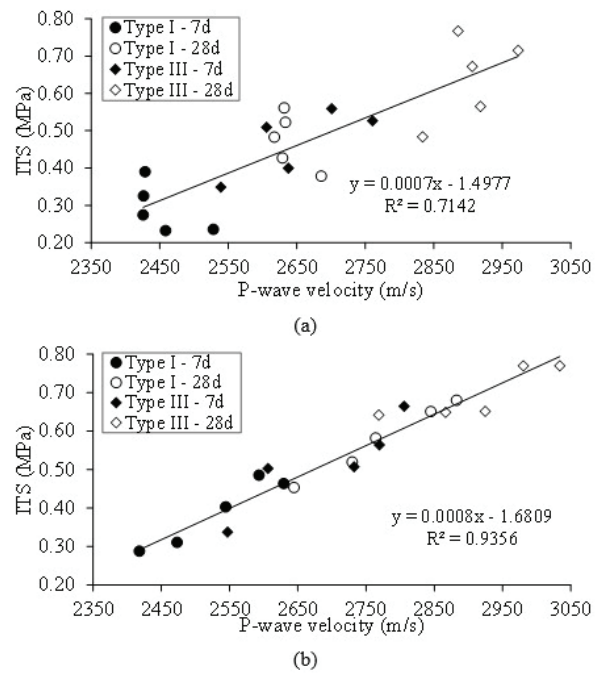


Figure 8. Relation between P-wave velocity and ITS for: (a) CD and (b) RD.

more satisfactory trend to the specimens molded with H/D of 2.1 (Khan et al., 2006; Toohey & Mooney, 2012).

The correlation between P-wave velocity and indirect tensile strength is presented in Figure 8. It is important to note that the non-stabilized soil tests resulted in low values of receiving signal based on the dimension, 2% to 7% and 50% to 55% for CD and RD, in comparison with 100% level obtained from the soil-cement mixtures, even when keeping the compaction parameters equal.

An elevated variability is observed for the mixtures with height and diameter smaller than 2, independently of cement type and curing period, resulting in poor relationship ($R^2 = 0.71$). On the other hand, stabilized sandy soil in reduced dimension proved to be consistent, leading to satisfactory linear agreement ($R^2 = 0.93$) and, further, pointing to the possibility of tensile strength prevision by the ultrasonic pulse velocity.

4. Conclusions

Based on the purpose of verifying the effect of the ratio H/D on the mechanical behavior of soil-cement mixtures, it was observed that:

- Considering the range of cement addition investigated, gains of 3.5 to 14.1 times for compressive strength and 3.3 to 12.8 times for tensile strength in relation to pure soil were obtained, with coefficients of determination $R^2 > 0.88$.
- The variable dimension is statistically significant for UCS and ITS (p-value < 0.05), in which the

mixtures with ratio H/D equal to 2.1 presented higher strengths, regardless of the type of cement.

- Portland cement type III presented superior resistance for both curing periods. Nevertheless, the strength gains between 7 and 28 days were superior for type I, considering both dimensions on UCS and ITS.
- On average, the relation between the reduced and conventional dimension for compression and tensile strength demonstrated 21.3% higher. Factors as curing period, content and type of cement affect the relationship.
- The contribution of increased content and curing time to the response of cemented mixtures was proven in destructive and non-destructive tests, based on the results of UCS, ITS and ultrasonic pulse velocity.
- The addition of cement increased the ultrasonic wave velocity from the range of 758-1039 m/s to 2350-3050 m/s, due to cement hardening mechanisms and secondary reactions. Regardless of the experimental conditions, the ultrasonic pulse velocity tests pointed to the possibility of predicting the indirect tensile strength by the p-wave velocity using the reduced dimension ($R^2 = 0.93$).

Acknowledgements

The authors wish to express their gratitude to the financial supports, from Araucaria Foundation for the Support of Scientific and Technological Development of the State of Paraná (FA), for providing the Master scholarship to develop this study, and from the National Council for Scientific and Technological Development (CNPq), for the Productivity Research scholarship.

Declaration of interest

The authors have no conflicts of interest to declare. All co-authors have observed and affirmed the contents of the paper and there is no financial interest to report.

Authors' contribution

José Wilson dos Santos Ferreira: conceptualization, data curation, analysis, writing – original draft. Michéle Dal Toé Casagrande: conceptualization, supervision. Raquel Souza Teixeira: conceptualization, supervision.




References

- Abdullah, G.M.S., & Al-Abdul Wahhab, H.I. (2018). Stabilisation of soils with emulsified sulphur asphalt for road applications. *Road Materials and Pavement Design*, 20(5), 1228-1242. <http://dx.doi.org/10.1080/14680629.2018.1436465>.
- ABNT NBR 12024. (2012a). *Soil-cement — Molding and curing of cylindric specimens — Procedure*. ABNT - Associação Brasileira de Normas Técnicas, Rio de Janeiro, RJ (in Portuguese).
- ABNT NBR 12025. (2012b). *Soil-cement — Simple compression test of cylindrical specimens — Method of test*. ABNT - Associação Brasileira de Normas Técnicas, Rio de Janeiro, RJ (in Portuguese).
- Aiban, S.A., Al-Abdul Wahhab, H.I., Al-Amoudi, O.S.B., & Ahmed, H.R. (1998). Performance of a stabilized marl base: A case study. *Construction & Building Materials*, 12(6–7), 329-340. [http://dx.doi.org/10.1016/S0950-0618\(98\)00023-3](http://dx.doi.org/10.1016/S0950-0618(98)00023-3).
- Antunes, V., Simão, N., & Freire, A.C. (2017). A soil-cement formulation for road pavement base and sub base layers: a case study. *Transportation Infrastructure Geotechnology*, 4(4), 126-141. <http://dx.doi.org/10.1007/s40515-017-0043-9>.
- ASTM C597. (2016a). *Standard Test Method for Pulse Velocity Through Concrete*. ASTM International, West Conshohocken, PA. <http://dx.doi.org/10.1520/C0597-16.2>
- ASTM D1633. (2017). *Standard Test Methods for Compressive Strength of Molded Soil-Cement Cylinders*. ASTM International, West Conshohocken, PA. <http://dx.doi.org/10.1520/D1633-17>
- ASTM D3967. (2016b). *Standard Test Method for Splitting Tensile Strength of Intact Rock Core Specimens*. ASTM International, West Conshohocken, PA.
- Baldovino, J.A., Moreira, E.B., Izzo, R.L. dos S., & Rose, J.L. (2018). Empirical relationships with unconfined compressive strength and split tensile strength for the long term of a lime-treated silty soil. *Journal of Materials in Civil Engineering*, 30(8), 06018008. [http://dx.doi.org/10.1061/\(asce\)mt.1943-5533.0002378](http://dx.doi.org/10.1061/(asce)mt.1943-5533.0002378).
- Baldovino, J.J.A., Izzo, R.L.S., Pereira, M.D., Rocha, E.V.G., Rose, J.L., & Bordignon, V.R. (2020). Equations Controlling tensile and compressive strength ratio of sedimentary soil–cement mixtures under optimal compaction conditions. *Journal of Materials in Civil Engineering*, 32(1), 04019320. [http://dx.doi.org/10.1061/\(ASCE\)MT.1943-5533.0002973](http://dx.doi.org/10.1061/(ASCE)MT.1943-5533.0002973).
- Cardoso, R., Ribeiro, D., & Néri, R. (2017). Bonding effect on the evolution with curing time of compressive and tensile strength of sand-cement mixtures. *Soil and Foundation*, 57(4), 655-668. <http://dx.doi.org/10.1016/j.sandf.2017.04.006>.
- Clough, G.W., Sitar, N., Bachus, R.C., & Rad, N.S. (1981). Cemented sands under static loading. *Journal of the Geotechnical Engineering Division*, 107(6), 799-817. <http://dx.doi.org/10.1061/AJGEB6.0001152>.
- Consoli, N.C., Cruz, R.C., Floss, M.F., & Festugato, L. (2010). Parameters controlling tensile and compressive strength of artificially cemented sand. *Journal of Geotechnical and Geoenvironmental Engineering*, 136(5), 759-763. [http://dx.doi.org/10.1061/\(asce\)gt.1943-5606.0000278](http://dx.doi.org/10.1061/(asce)gt.1943-5606.0000278).

- Consoli, N.C., Festugato, L., Rocha, C.G., & Cruz, R.C. (2013). Key parameters for strength control of rammed sand-cement mixtures: influence of types of portland cement. *Construction & Building Materials*, 49, 591-597. <http://dx.doi.org/10.1016/j.conbuildmat.2013.08.062>.
- Consoli, N.C., Foppa, D., Festugato, L., & Heineck, K.S. (2007). Key parameters for strength control of artificially cemented soils. *Journal of Geotechnical and Geoenvironmental Engineering*, 133(2), 197-205. [http://dx.doi.org/10.1061/\(asce\)1090-0241\(2007\)133:2\(197\)](http://dx.doi.org/10.1061/(asce)1090-0241(2007)133:2(197)).
- Consoli, N.C., Quiñónez, R.A., González, L.E., & López, R.A. (2017). Influence of molding moisture content and porosity/cement index on stiffness, strength, and failure envelopes of artificially cemented fine-grained soils. *Journal of Materials in Civil Engineering*, 29(5), 04016277. [http://dx.doi.org/10.1061/\(asce\)mt.1943-5533.0001819](http://dx.doi.org/10.1061/(asce)mt.1943-5533.0001819).
- Consoli, N.C., Rosa, A.D., & Saldanha, R.B. (2011). Variables governing strength of compacted soil-fly ash-lime mixtures. *Journal of Materials in Civil Engineering*, 23(4), 432-440. [http://dx.doi.org/10.1061/\(asce\)mt.1943-5533.0000186](http://dx.doi.org/10.1061/(asce)mt.1943-5533.0000186).
- Croft, J.B. (1967). The influence of soil mineralogical composition on cement stabilization. *Geotechnique*, 17(2), 119-135. <http://dx.doi.org/10.1680/geot.1967.17.2.119>.
- Diambra, A., Ibraim, E., Peccin, A., Consoli, N.C., & Festugato, L. (2017). Theoretical derivation of artificially cemented granular soil strength. *Journal of Geotechnical and Geoenvironmental Engineering*, 143(5), 04017003. [http://dx.doi.org/10.1061/\(asce\)gt.1943-5606.0001646](http://dx.doi.org/10.1061/(asce)gt.1943-5606.0001646).
- Ferreira, J.W.S., Casagrande, M.D.T., & Teixeira, R.S. (2021). Sample dimension effect on equations controlling tensile and compressive strength of cement-stabilized sandy soil under optimal compaction conditions. *Case Studies in Construction Materials*, 15, e00763. <http://dx.doi.org/10.1016/j.cscm.2021.e00763>.
- França Junior, P., Petsch, C., Villa, M.E.C.D., & Manieri, D.D. (2010). Relato de campo sobre os aspectos físicos do terceiro planalto paranaense (Maringá aos terraços do Rio Paraná). *Boletim Geográfico*, 28(2), 185-195. <http://dx.doi.org/10.4025/bolgeogr.v28i2.10599>.
- Gajewska, B., Kraszewski, C., & Rafalski, L. (2017). Significance of cement-stabilised soil grain size distribution in determining the relationship between strength and resilient modulus. *Road Materials and Pavement Design*, 19(7), 1692-1701. <http://dx.doi.org/10.1080/14680629.2017.1324808>.
- Ho, L.S., Nakarai, K., Ogawa, Y., Sasaki, T., & Morioka, M. (2017). Strength development of cement-treated soils: effects of water content, carbonation, and pozzolanic reaction under drying curing condition. *Construction & Building Materials*, 134, 703-712. <http://dx.doi.org/10.1016/j.conbuildmat.2016.12.065>.
- Horpibulsuk, S., Katkan, W., Sirilerdwattana, W., & Rachan, R. (2006). Strength development in cement stabilized low plasticity and coarse grained soils: laboratory and field study. *Soil and Foundation*, 46(3), 351-366. <http://dx.doi.org/10.3208/sandf.46.351>.
- Ingunza, M.P.D., Pereira, K.L.A., & Santos Junior, O.F. (2015). Use of sludge ash as a stabilizing additive in soil-cement mixtures for use in road pavements. *Journal of Materials in Civil Engineering*, 27(7), 06014027. [http://dx.doi.org/10.1061/\(asce\)mt.1943-5533.0001168](http://dx.doi.org/10.1061/(asce)mt.1943-5533.0001168).
- Ismail, M.A., Joer, H.A., Sim, W.H., & Randolph, M.F. (2002). Effect of cement type on shear behavior of cemented calcareous soil. *Journal of Geotechnical and Geoenvironmental Engineering*, 128(6), 520-529. [http://dx.doi.org/10.1061/\(asce\)1090-0241\(2002\)128:6\(520\)](http://dx.doi.org/10.1061/(asce)1090-0241(2002)128:6(520)).
- Joel, M., & Agbede, I.O. (2011). Mechanical-cement stabilization of laterite for use as flexible pavement material. *Journal of Materials in Civil Engineering*, 23(2), 146-152. [http://dx.doi.org/10.1061/\(asce\)mt.1943-5533.0000148](http://dx.doi.org/10.1061/(asce)mt.1943-5533.0000148).
- Khan, Z., Majid, A., Cascante, G., Hutchinson, D.J., & Pezeshkpour, P. (2006). Characterization of a cemented sand with the pulse-velocity method. *Canadian Geotechnical Journal*, 43(3), 294-309. <http://dx.doi.org/10.1139/t06-008>.
- Kutanaei, S.S., & Choobbasti, A.J. (2016). Effects of nanosilica particles and randomly distributed fibers on the ultrasonic pulse velocity and mechanical properties of cemented sand. *Journal of Materials in Civil Engineering*, 29(3), 04016230. [http://dx.doi.org/10.1061/\(asce\)mt.1943-5533.0001761](http://dx.doi.org/10.1061/(asce)mt.1943-5533.0001761).
- Le Kouby, A., Guimond-Barrett, A., Reiffsteck, P., & Pantet, A. (2017). Influence of drying on the stiffness and strength of cement-stabilized soils. *Geotechnical and Geological Engineering*, 36(3), 1463-1474. <http://dx.doi.org/10.1007/s10706-017-0401-y>.
- Leandro, R.P., Vasconcelos, K.L., & Bernucci, L.L.B. (2017). Evaluation of the laboratory compaction method on the air voids and the mechanical behavior of hot mix asphalt. *Construction & Building Materials*, 156, 424-434. <http://dx.doi.org/10.1016/j.conbuildmat.2017.08.178>.
- Lorenzo, G.A., & Bergado, D.T. (2004). Fundamental parameters of cement-admixed clay: new approach. *Journal of Geotechnical and Geoenvironmental Engineering*, 130(10), 1042-1050. [http://dx.doi.org/10.1061/\(ASCE\)1090-0241\(2004\)130:10\(1042\)](http://dx.doi.org/10.1061/(ASCE)1090-0241(2004)130:10(1042)).
- Lukiantchuki, J.A., Oliveira, J.R.M.S., Almeida, M.S.S., Reis, J.H.C., Silva, T.B., & Guideli, L.C. (2020). Geotechnical behavior of Construction Waste (CW) as a partial replacement of a lateritic soil in fiber-reinforced cement mixtures. *Geotechnical and Geological Engineering*, 39(2), 919-942. <http://dx.doi.org/10.1007/s10706-020-01533-w>.
- Mandal, T., Edil, T.B., & Tinjum, J.M. (2017). Study on flexural strength, modulus, and fatigue cracking of cementitiously stabilised materials. *Road Materials and Pavement Design*, 19(7), 1546-1562. <http://dx.doi.org/10.1080/14680629.2017.1325772>.
- Mandal, T., Tinjum, J.M., & Edil, T.B. (2016). Non-destructive testing of cementitiously stabilized materials using ultrasonic pulse velocity test. *Transportation Geotechnics*, 6, 97-107. <http://dx.doi.org/10.1016/j.trgeo.2015.09.003>.

- Mohammadinia, A., Arulrajah, A., Sanjayan, J., Disfani, M.M., Bo, M.W., & Darmawan, S. (2014). Laboratory evaluation of the use of cement-treated construction and demolition materials in pavement base and subbase applications. *Journal of Materials in Civil Engineering*, 27(6), 04014186. [http://dx.doi.org/10.1061/\(asce\)mt.1943-5533.0001148](http://dx.doi.org/10.1061/(asce)mt.1943-5533.0001148).
- Mola-Abasi, H., Khajeh, A., & Naderi Semsani, S. (2018). Effect of the ratio between porosity and SiO₂ and Al₂O₃ on tensile strength of zeolite-cemented sands. *Journal of Materials in Civil Engineering*, 30(4), 04018028. [http://dx.doi.org/10.1061/\(asce\)mt.1943-5533.0002197](http://dx.doi.org/10.1061/(asce)mt.1943-5533.0002197).
- Osinubi, K.J. (1998). Influence of compactive efforts and compaction delays on lime-treated soil. *Journal of Transportation Engineering*, 124(2), 149-155. [http://dx.doi.org/10.1061/\(ASCE\)0733-947X\(1998\)124:2\(149\)](http://dx.doi.org/10.1061/(ASCE)0733-947X(1998)124:2(149)).
- Osinubi, K.J., & Nwaiwu, C.M. (2006). Compaction delay effects on properties of lime-treated soil. *Journal of Materials in Civil Engineering*, 18(2), 250-258. [http://dx.doi.org/10.1061/\(asce\)0899-1561\(2006\)18:2\(250\)](http://dx.doi.org/10.1061/(asce)0899-1561(2006)18:2(250)).
- Osula, D.O.A. (1989). Evaluation of admixture stabilization for problem laterite. *Journal of Transportation Engineering*, 115(6), 674-687. [http://dx.doi.org/10.1061/\(ASCE\)0733-947X\(1989\)115:6\(674\)](http://dx.doi.org/10.1061/(ASCE)0733-947X(1989)115:6(674)).
- Portelinha, F.H.M., Lima, D.C., Fontes, M.P.F., & Carvalho, C.A.B. (2012). Modification of a lateritic soil with lime and cement: an economical alternative for flexible pavement layers. *Soils and Rocks*, 35(1), 51-63.
- Reis, J.H.C., Soares Silva, S., Ildefonso, J.S., & Yshiba, J.K. (2015). Evaluation of soil, cement and construction and demolition waste (CDW) mixtures for use in road pavement base and sub-base applications. *Key Engineering Materials*, 634, 247-255. <http://dx.doi.org/10.4028/www.scientific.net/KEM.634.247>.
- Rios, S., Fonseca, A.V., & Baudet, B.A. (2012). Effect of the porosity/cement ratio on the compression of cemented soil. *Journal of Geotechnical and Geoenvironmental Engineering*, 138(11), 1422-1426. [http://dx.doi.org/10.1061/\(asce\)gt.1943-5606.0000698](http://dx.doi.org/10.1061/(asce)gt.1943-5606.0000698).
- Rios, S., Fonseca, A.V., Consoli, N.C., Floss, M., & Cristelo, N. (2013). Influence of grain size and mineralogy on the porosity/cement ratio. *Géotechnique Letters*, 3(3), 130-136. <http://dx.doi.org/10.1680/geolett.13.00003>.
- Stracke, F., Jung, J.G., Korf, E.P., & Consoli, N.C. (2012). The influence of moisture content on tensile and compressive strength of artificially cemented sand. *Soils and Rocks*, 35(3), 303-308.
- Su, N., Xiao, F., Wang, J., & Amirkhanian, S. (2017). Characterizations of base and subbase layers for mechanistic-empirical pavement design. *Construction & Building Materials*, 152, 731-745. <http://dx.doi.org/10.1016/j.conbuildmat.2017.07.060>.
- Sukprasert, S., Hoy, M., Horpibulsuk, S., Arulrajah, A., Rashid, A.S.A., & Nazir, R. (2019). Fly ash based geopolymer stabilisation of silty clay/blasted furnace slag for subgrade applications. *Road Materials and Pavement Design*, 22(2), 357-371. <http://dx.doi.org/10.1080/14680629.2019.1621190>.
- Toohy, N.M., & Mooney, M.A. (2012). Seismic modulus growth of lime-stabilised soil during curing. *Geotechnique*, 62(2), 161-170. <http://dx.doi.org/10.1680/geot.9.P.122>.
- Yilmaz, E., Belem, T., & Benzaazoua, M. (2015). Specimen size effect on strength behavior of cemented paste backfills subjected to different placement conditions. *Engineering Geology*, 185, 52-62. <http://dx.doi.org/10.1016/j.enggeo.2014.11.015>.

Study on guardrail post behavior located on organic soil using simplified experimental and numerical methods

Hamid Reza Manaviparast^{1#} , Nuno Araújo¹ , Nuno Cristelo² ,

Tiago Miranda¹ 

Article

Keywords

Guardrail post
Road safety
Organic soil
Static loading
Dynamic loading

Abstract

For the purpose of road safety, it is vital to reduce the severity of road accidents and increase safety around the roadway area by deploying guardrails. In case of a car crash, a guardrail post must be deformable so that such restraint is not too abrupt due to the occupant's sensitivity. Soil type influences on the guardrail post behavior have been a somewhat unfounded variable due to the high soil heterogeneity and challenging interpretation of its real implications on the safety of guardrail systems. Since little attention is concentrated on evaluating the guardrail post behavior through simplified procedures, this article aims to provide a simplified experimental and numerical approach to study the behavior of guardrail posts located on organic soil. Results of laboratory and in-situ tests indicated that guardrail posts behavior located on organic soil depends on section orientation, driving depth, and loading speed. To confirm and compare the in-situ tests, simplified numerical simulations through Plaxis 3D software were carried out, and data from numerical modeling approved the accuracy of in-situ results.

1. Introduction

Infrastructures are always considered vital physical systems of a region or even a nation. These systems are primarily high-cost investments and are crucial to the prosperity and economy of a country. As an example of infrastructures, road infrastructure plays an essential role in the economy by helping to transport goods and services. It also plays a vital role in every community by keeping people connected to other regions and making it simple to commute to different regions.

Since road infrastructures have always played an essential role in developing civilizations, there was a need to create safe infrastructures. Road transport is a crucial aspect of today's society, in which the mobility of people and goods and traffic accidents resulting from this mobility has to be considered (Cui, 2020; Neves et al., 2018). The utilization of engineering treatments to enhance traffic safety is relevant to road safety design, and guardrails are one of the most widely used passive safety devices for roads (Mikusova, 2017). Guardrails, including W-beam, are labeled as weak or strong posts that adequately absorb a vehicle's impact to reduce the severity of vehicle crashes (Li et al., 2018; Gutowski et al., 2017). Worldwide, most guardrails are made of steel or concrete. Concrete barriers usually do not

include a foundation directly placed on the road surface. Hence, soil-barrier interaction for concrete barriers is not an issue. However, steel guardrail posts are usually bolted to a concrete deck or driven into the soil (Örnek et al., 2019). For the sake of soil influences on steel guardrails, the soil properties such as soil density, friction angle, and also post embedment depth become essential parameters affecting the guardrail behavior and performance (Örnek et al., 2019; Atahan et al., 2019; Sassi, 2011). With a lack of interaction between soil and adjacent structures, the steel guardrail cannot play a role as intended and cannot provide adequate safety for the impacting vehicles. Few studies have been done to evaluate the behavior of guardrail posts based on experimental analyses, but assessing the behavior of guardrail post located on organic soil through a simplified approach is scarce and needs more consideration to shed light on. Since the crash-test standards do not contain details of the soil properties, meaning that the guardrail post is embedded regardless of considering the in-situ soil condition (Ozcanan & Atahan, 2020; Yun et al., 2018), simplified in-situ tests were carried out to fully consider the effects of organic soil located beneath the guardrail post.

Pajouh et al. (2018) and Rohde et al. (1996) stressed that the guardrail post performance primarily depends on the interaction between the post and the surrounding soil.

[#]Corresponding author. E-mail address: id8028@alunos.uminho.pt

¹University of Minho, Department of Civil Engineering, Guimarães, Portugal.

²University of Trás-os-Montes e Alto Douro, School of Science and Technology, Vila Real, Portugal.

Submitted on November 27, 2021; Final Acceptance on March 23, 2022; Discussion open until August 31, 2022.

<https://doi.org/10.28927/SR.2022.077921>



This is an Open Access article distributed under the terms of the Creative Commons Attribution License, which permits unrestricted use, distribution, and reproduction in any medium, provided the original work is properly cited.

Tomlinson & Woodward (2007) revealed that in a guardrail post under a horizontal loading, driven into poor quality soil, a considerable part of the applied load was transferred to the post base and some of it to the surrounding soil. Gutowski et al. (2017) and Sassi (2011) revealed that the guardrail post tends to rotate alongside the imposed loading, soil blisters in the surrounding area, and the guardrail post compresses the soil in the front, causing it to fail. They also stated that the post might break at the pavement level in the dense soil, where the bending moment is maximum. Patzner et al. (1999) found that the guardrail post deflection tends to increase in soils with lower specific weight and decrease when the soil specific gravity increases. Based on Lim (2009) and Jeyapalan et al. (1984), steel guardrail post without the presence of concrete foundation indicates proper structural behavior during static and dynamic tests. Consequently, based on their investigations, it was decided not to consider the foundation effects on guardrail post performance as a simplified approach during this study.

To evaluate the performance of a guardrail post as a roadside safety device, as a common method, destructive full-scale crash testing is employed by engineers to assess the effects of impact on a guardrail post through a bogie vehicle. The extracted results serve to understand the dynamic and static behavior of the guardrail post. However, these tests are costly and need an extensive setup, instrumentation, and test vehicle wrecking. Consequently, this study decided to use a simplified approach instead of a costly setup as an advantageous option. Several simplified in-situ tests were conducted as experimental studies to provide results helping to evaluate the behavior of guardrail posts located on organic soil. For the purpose of more accuracy in the evaluation process of the guardrail post, several numerical models were analyzed using Plaxis 3D software as a numerical study to compare them with in-situ results.

2. Materials and methods

Finding and determining proper material properties are helpful to predict the material behavior better by engineers.

For this purpose, this study decided to study organic soil beneath the guardrail post, representing the adjacent soils found on the carriageways of ancient municipal roads in Portugal, the city of Guimarães. The selected test site belonged to the municipality of Guimarães. As a first step, there was a need to estimate the geotechnical parameters accurately. Hence, a set of tests was performed to determine the water content, organic matter content, particle size, consistency limits, and solid particle density. Triaxial and suction tests were also performed in the Civil Engineering Laboratory of the University of Minho.

For the post (Figure 1), the elastic and plastic deformability limits and the yield stress were analyzed in Civil and Mechanical Engineering laboratories at the University of Minho. The geometry of the guardrail post is the most typical type used in Portuguese municipal roads.

2.1 Soil characterization

Soil characterization is a necessary part of determining various geotechnical parameters of the soil. This process is vital to evaluate the fundamental parameters and determine other required geotechnical factors utilized during the execution of every geotechnical project. Regarding the fundamental geotechnical tests, the grain distribution curve (Figure 2) was obtained according to LNEC (1966). About other geotechnical parameters, it comprises 7% clay, 26% silt, and 67% of sand and gravel. The liquid (51%) and plastic (NP) Atterberg limits were obtained according to IGPAI (1969). The density of the solid particles was 2.5 (IGPAI, 1965), with an organic matter content of 6.1% (LNEC, 1967). Several undisturbed specimens (Figure 3) were collected in-situ, for the laboratory tests, with average volumetric weights of 15.3 kN/m³ (natural) and 12.3 kN/m³ (dry) and water contents between 17% and 29%.

A suction test, using the filter paper method (ASTM, 1994), was performed to obtain the retention curve by adjusting the van Genuchten model. Nine undisturbed specimens were collected, oven-dried at 110°C for 24 hours,

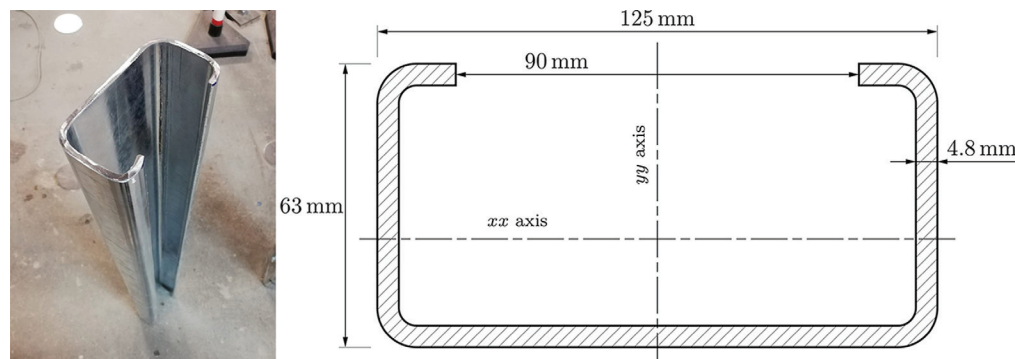


Figure 1. Geometry of the post used in the study.

Note: The axis *xx* and *yy* are defined.

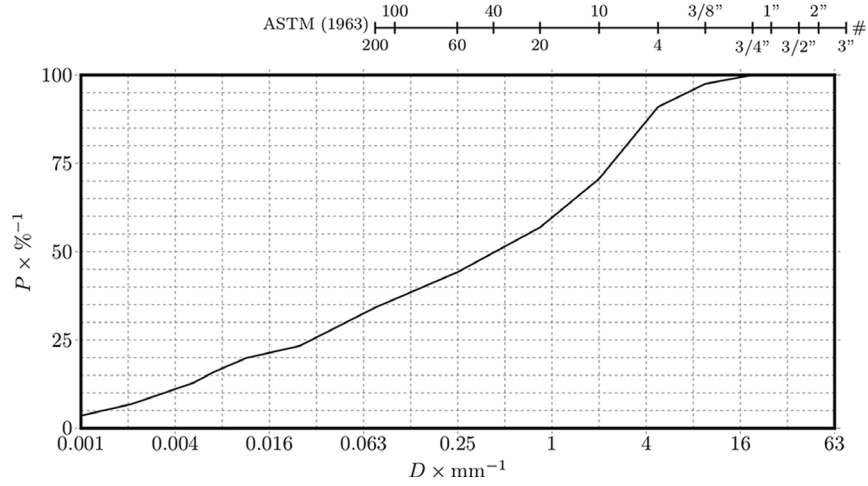


Figure 2. Particle size distribution of the soil (ASTM, 1963).



Figure 3. Extraction of undisturbed in-situ specimens.

and 3 filter papers (and water) were added and applied to each specimen so that the water content ranged from near zero to near saturated. One of the specimens was not used because it lost its integrity during assembly. The van Genuchten model (Equation 1) was used due to its high capacity for adjustment and convergence, in which ω_s is the saturated water content (in the study soil around 40%). The model has four parameters: ω_r (residual water content), α , n , and m . After adjustment to the experimental curve (Figure 4), $\omega_r = 3\%$, $\alpha = 0.15 \text{ kPa}^{-1}$, $n = 0.62$, and $m = 0.71$. The R -squared (R^2) of the fitting curve is equal to 0.985.

$$\omega = \omega_r \frac{\omega_s + \omega_r}{[1 + (\alpha \psi)^n]^m} \quad (1)$$

The results presented in Figure 5 to Figure 7 were obtained from triaxial tests on specimens extracted at a depth of 50 cm, according to BSI (1990). Figure 5 refers to a consolidation test

in which the pore pressure was maintained constant, and the confining pressure increased at a rate of 7 kPa/h from 1010 kPa to 1500 kPa, then reduced to 1010 kPa and finally raised to 1700 kPa while the backpressure was always 1000 kPa. During the test procedure in Figure 6 and Figure 7, the test speed was equal to $84 \cdot 10^{-6} \text{ mm/s}$. Figure 5 represents the specific volume v , the normal compression line (Equation 2) – obtained from the adjustment of the experimental results in the range $p' = [200 \text{ to } 700] \text{ kPa}$ – and the critical state line (Equation 3). The resulting strength parameters were $c' = 0 \text{ kPa}$, $\phi' = 34^\circ$, $c_u = 45 \text{ kPa}$, $\phi_u = 12^\circ$ (under saturated conditions), and $E = 3.8 \text{ MPa}$.

$$v(\text{NCL}) = \Gamma_{\text{ICL}} - \lambda_{\text{NCL}} \log_{10} \frac{p'}{1 \text{ kPa}} = 2.263 - 0.241 \log_{10} \frac{p'}{1 \text{ kPa}} \quad (2)$$

$$v(\text{CSL}) = \Gamma_{\text{CSL}} - \lambda_{\text{CSL}} \log_{10} \frac{p'}{1 \text{ kPa}} = 2.186 - 0.241 \log_{10} \frac{p'}{1 \text{ kPa}} \quad (3)$$

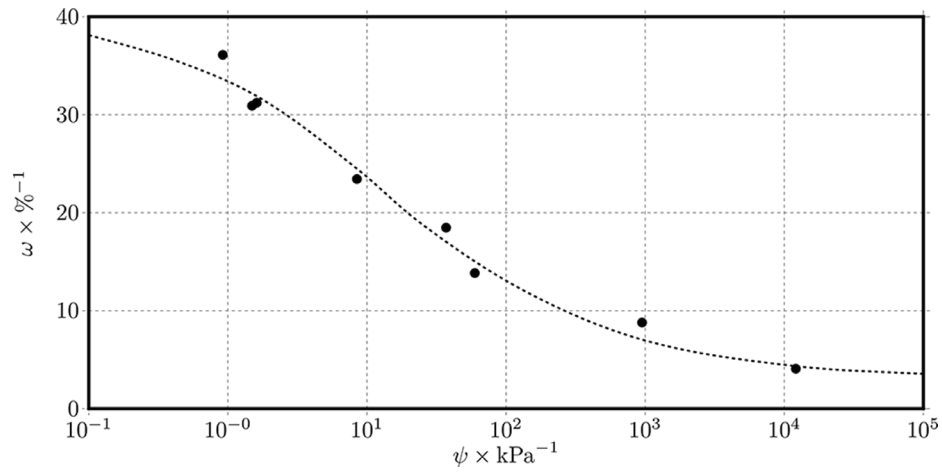


Figure 4. Wet soil retention curve (results and van Genuchten (1980) model adjustment).

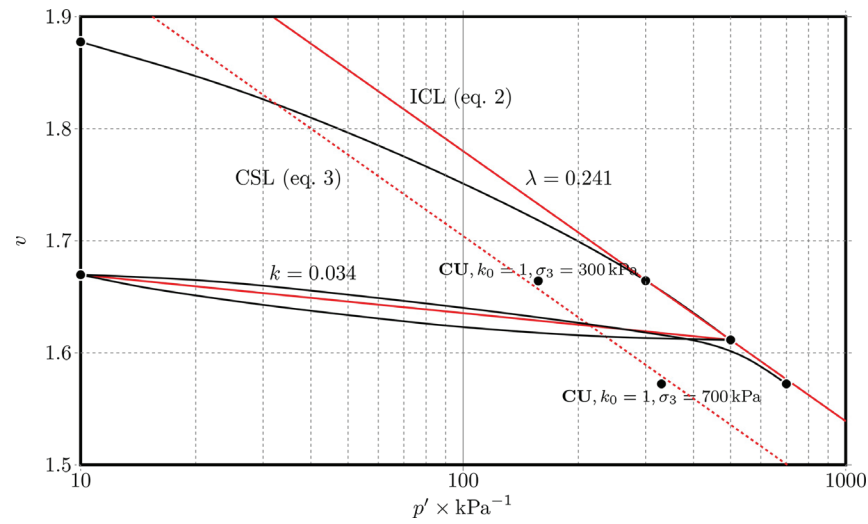


Figure 5. Triaxial tests results in the space $v = f(p')$.

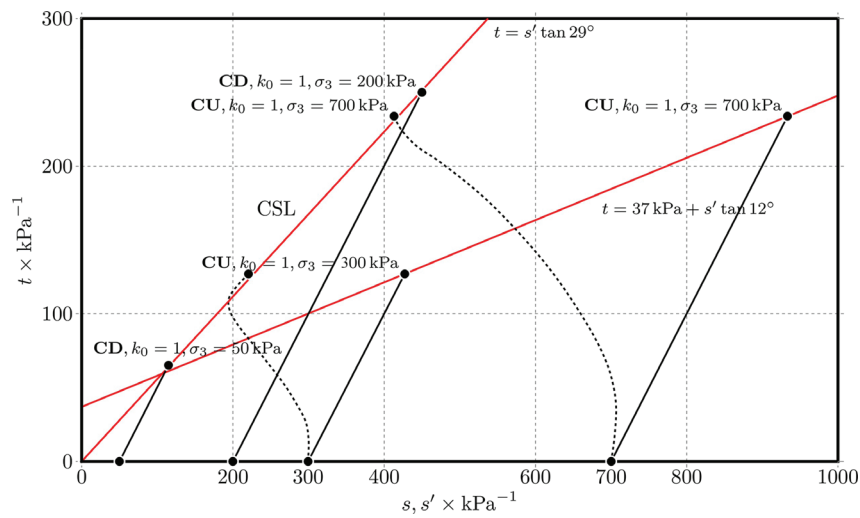


Figure 6. Triaxial tests results in the space $t = f(s \text{ or } s')$.

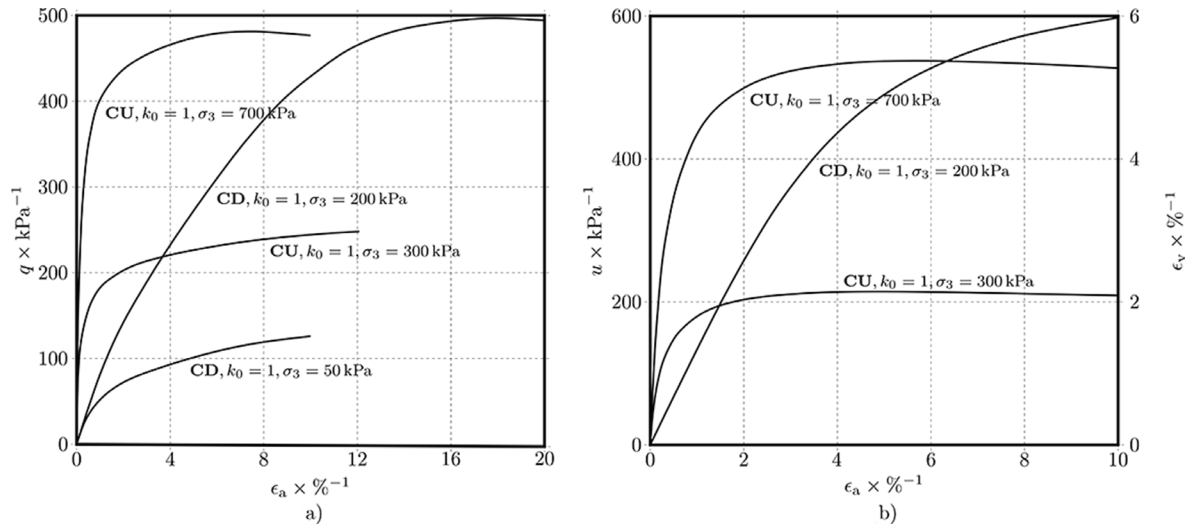


Figure 7. Triaxial tests results in the space a) $q = f(\epsilon_a)$; b) $(u \text{ or } \epsilon_v) = f(\epsilon_a)$.

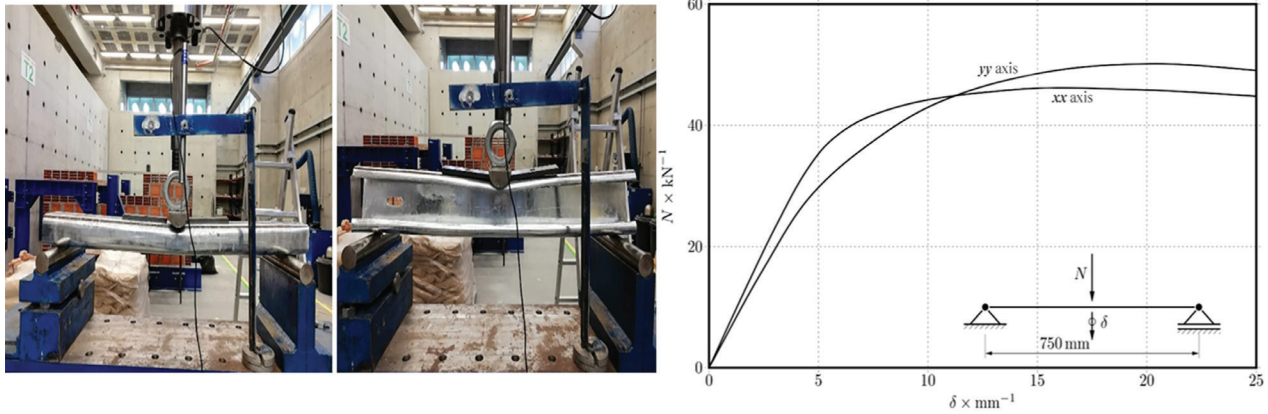


Figure 8. 3-point loading flexural test.

2.2 Post characterization

After performing the process of determining different geotechnical parameters of the soil, the guardrail post material was determined to start the evaluation of the guardrail post behavior under loading. The cold-formed metallic element (made from S235JR steel) forming the guardrail post has a C-shaped cross-section, with density $\rho = 7.86 \text{ Mg/m}^3$, Young modulus $E = 210 \text{ GPa}$, Poisson ratio $\nu = 0.3$ and yield stress $F_y = 235 \text{ MPa}$. It was acquired with two distinct lengths – 1.2 m or 1.7 m. It was loaded according to both moments of inertia using a hydraulic actuator (Figure 8). From the interpreted results, it was clear that it is not relevant which axis is loaded, as both responses are very similar.

3. Experimental results

An experimental test as the main component of each scientific study involves manipulating various factors in a

system to observe how that affects the final results. It is also helpful to offer a realistic prediction for real-world systems to be utilized by scientists and engineers. In order to assess road safety and evaluate the behavior of the guardrail post against static and dynamic loading, this study aimed to perform a proper characterization of the system through an experimental campaign comprising 8 posts. The main target of the campaign was changing (a) loading directions, (b) post depths, and (c) load speed (i.e., in static and dynamic conditions). All tests were carried out according to the conditions and water content found in situ, meaning that after the driving phase, no further compaction procedure was carried out on the surrounding soil. The guardrail posts were fully instrumented to indicate their real behavior during static and dynamic loading. In addition, in-situ geotechnical characterization of the soil profile was developed to define its geotechnical parameters better. It is noteworthy that all tests were performed with in-situ water content between 17% and 29%.

3.1 Geotechnical investigation

Geotechnical investigation is an operation in which engineers evaluate the geotechnical parameters of every project site to determine if the site is appropriate for the proposed purpose. The primary goal of each geotechnical investigation during every project is to investigate the soil conditions through performing various tests to provide accurate data for geotechnical engineers. Three different tests were performed in-situ: (a) dynamic penetrometer, (b) Marchetti dilatometer, and (c) plate load test (adapted for horizontal loading). The dynamic penetrometer test (Figure 9) was performed according to ISO (2005) through four drill holes to assure foundation homogeneity and confirm that the organic soil was present in the vicinity and along the entire length of the post. The Marchetti dilatometer test was carried out according to ISO (2017), mainly to obtain the coefficient of thrust at rest K_0 of the soil base. Nevertheless, it also allowed the estimation of the friction angle (ϕ) and the over-consolidation ratio (OCR). Surface results (i.e., up to about half a meter) were disregarded due to the influence of vegetation, desiccation, and low applied vertical stress σ_v . Since vertical stress is near zero up to about half a meter, it induces discrepancy when estimating the parameters. The obtained data interpretation made it possible to define $K_0 = 1.1$, OCR = 7, and $\phi = 39^\circ$ (in unsaturated conditions).

During the plate load test, it was decided to adopt the conventional test, which defines a vertical loading to a horizontal compression of the soil, thus mobilizing its passive earth pressure limit. The guardrail post movement depicts the evolution from the resting state to the passive limit state. It was performed by keeping the effective vertical stress constant while increasing the effective horizontal stress.

To perform the test, a hole was initially dug in the ground (Figure 10) with a length of 55 cm, a width of 37 cm, and a depth of 60 cm. By using a hydraulic jack, two plates with 30 cm in diameter were spread away at an average rate of 3 cm/min—two loading cycles were applied (Figure 11). For the 1st cycle, the plates were displaced until they were spread by 15 cm. Since the movement is symmetrical, an average individual displacement of 7.5 cm of each plate was reached. A 2nd cycle was then applied, after unloading, until failure was detected. Figure 10 shows that such point was reached when the soil horizontal compression was 330 kPa, as concluded from the cracks on the soil surface.

3.2 Post testing

Eight posts were deployed to assess and evaluate the behavior of the guardrail post through using test variables: (a) the two axes of inertia, (b) two post lengths, and (c) several imposed horizontal displacements (designed as *static test*) or forces (designed as *dynamic test*). To do so, it was required to define two testing procedures and instrumentation setup.

Regarding instrumentation, the guardrail post was instrumented with two load cells (Figure 12a) with the range of 0.50 kN to acquire the horizontal stress σ_h evolution during loading, which was calculated from the applied force, divided by the section of the dish (3 cm diameter) placed on each load cell. Two dishes were set at 15 cm and 30 cm below the surface to obtain the most significant stress associated with the passive thrust applied by the soil. Two accelerometers with the maximum admissible acceleration of 55g were also added to be used only on the dynamic tests, one at the surface (Figure 12b) and the other leveled with the horizontal loading force. Furthermore, five potentiometers with variable

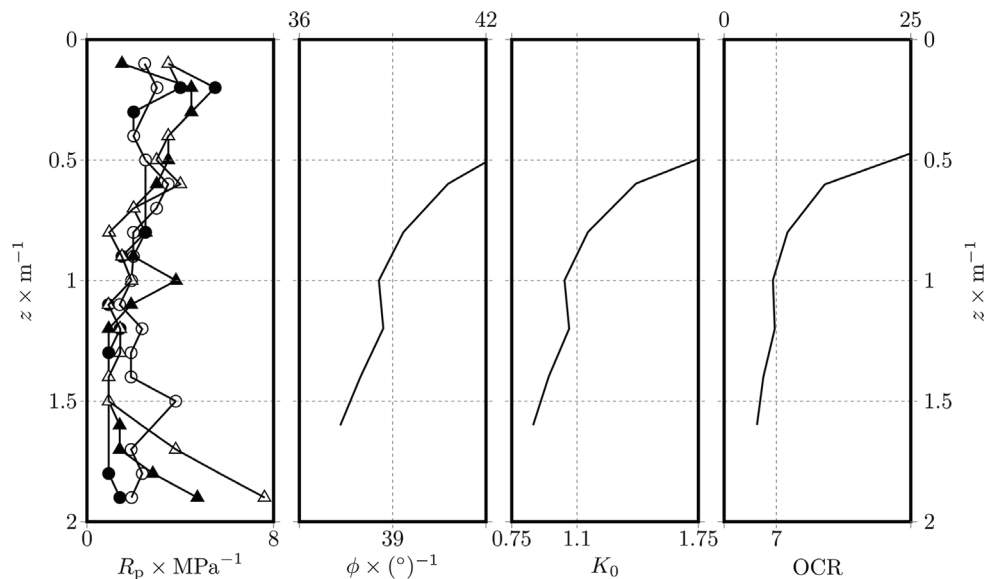


Figure 9. Geotechnical survey results (penetrometer and dilatometer).

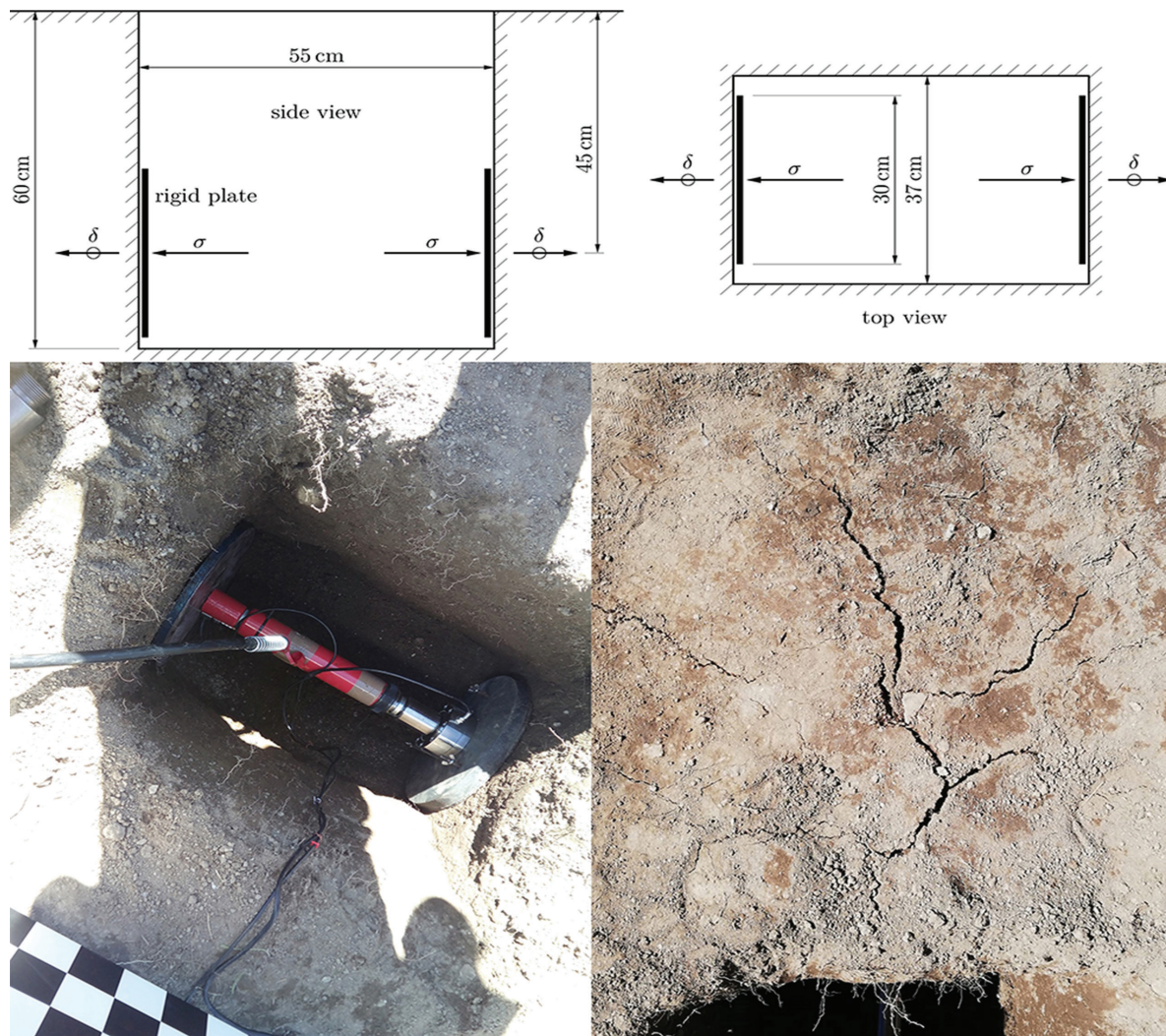


Figure 10. Horizontal load plate test geometry, assembly, and induced cracks.

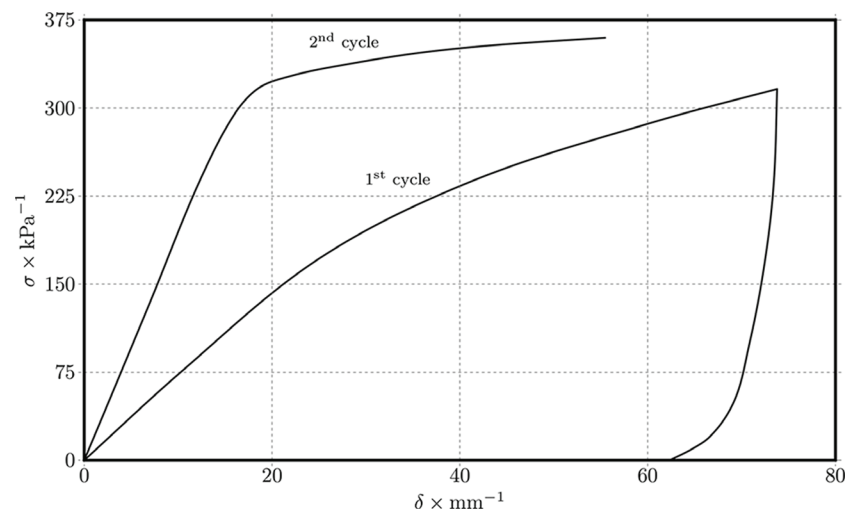


Figure 11. Horizontal load plate test results.

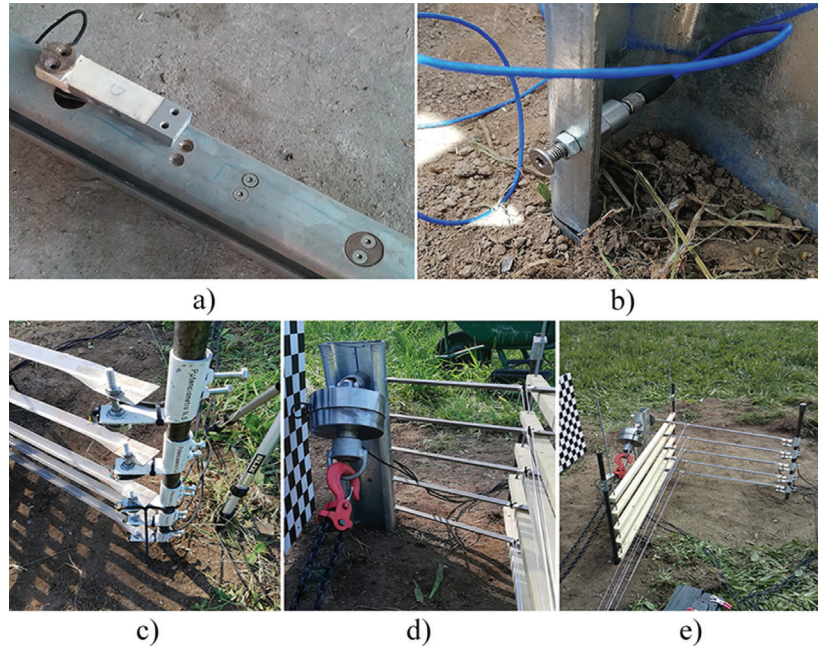


Figure 12. Field instrumentation setup: (a) load cells, (b) accelerometers, (c) potentiometers, (d) third load cell, (e) view final.

electrical resistance from zero to 1 k Ω were utilized to acquire the horizontal displacements of the guardrail post during loading, installed at 10 cm from each other, with the first at surface level (Figure 12c). Finally, a third load cell with the range of 130 kN was installed 50 cm above the surface to measure the applied horizontal loading force (Figure 12d). The final setup is shown in Figure 12e.

Regarding the test procedures, two configurations were deployed. The first one was designed as the static test configuration and consisted of loading the guardrail post at a monotonic displacement rate of 3 cm/min. To do so, two posts were driven into the ground and used for the reaction. In the dynamic test configuration (Figure 13), it was intended to apply a dynamic horizontal loading in the guardrail post, 0.5 m above the surface. To do so, a vehicle with a mass of around 1950 kg was used, moving with the speed of 15 km/h (speed component perpendicular to the guardrail post) at the time of impact. A vehicle impact with the guardrail post was supposed to happen at a narrow angle; to do that, only the component of the speed perpendicular to the guardrail post was considered.

Eight tests were defined by combining the axis of inertia, post length, and test procedure (Table 1). Figure 14 provides all the relevant geometric parameters used in the field tests.

3.2.1 Static test results

The number of potentiometers used in this study (5 in total) was later found redundant when the data was analyzed. Therefore, only the data from three potentiometers (1, 4, and 5) was considered. Potentiometer 4 was mainly used because



Figure 13. Test set-up used for the in-situ testing of the posts.

Table 1. Parameters considered for the in-situ testing of the posts.

Test ID	Mobilized axis	Length	Loading
x120s	xx	1.2 m	static
y120s	yy	1.2 m	static
x170s	xx	1.7 m	static
y170s	yy	1.7 m	static
x120d	xx	1.2 m	dynamic
y120d	yy	1.2 m	dynamic
x170d	xx	1.7 m	dynamic
y170d	yy	1.7 m	dynamic

ID: Identification.

its data was 'cleaner' than that collected by potentiometer 5, which was affected by some interference from the load cells.

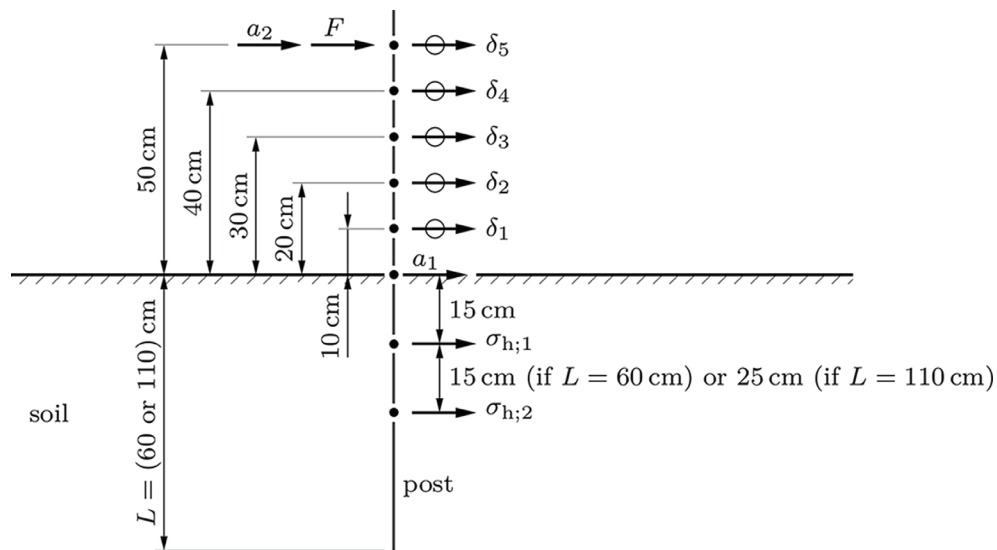


Figure 14. Geometric parameters used in all field tests (elevation view).

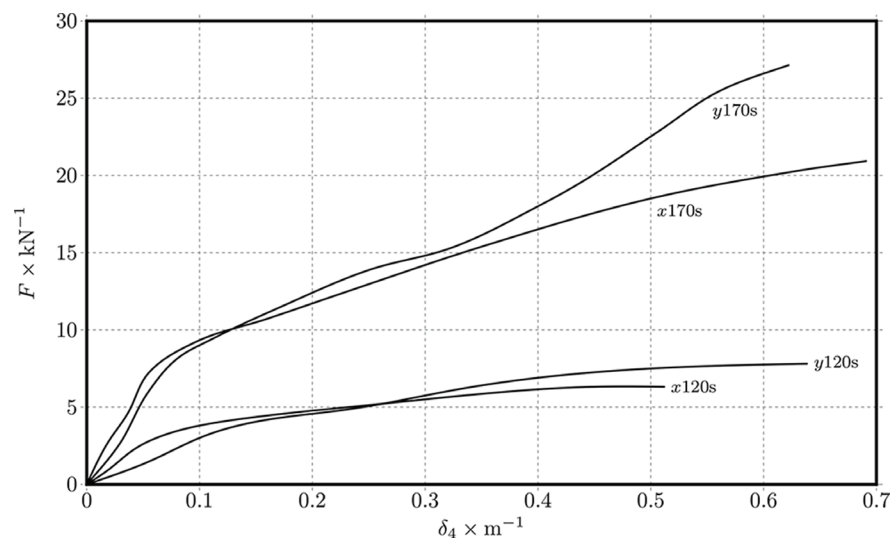


Figure 15. Static post testing - horizontal force (F) development along the imposed displacement δ_5 (represented as a function of δ_4).

The load-displacement curve presented in Figure 15 showed no peak, and the maximum static load was approximately 27 kN, at a late loading stage. The short post reached its maximum loading (7 kN) in the yy axis of inertia and the minimum loading (6 kN) in the xx axis of inertia. Similarly, the long post experienced its maximum and minimum loading in the yy axis of inertia (27 kN) and xx axis of inertia (21 kN), respectively. Regarding the imposed displacement, the short post reached its maximum displacement (0.64 m) in the yy axis and its minimum displacement (0.51 m) in the xx axis. In contrast, the long post reached its maximum displacement, of 0.69 m, around the xx axis, while the yy axis registered a lower displacement of 0.61 m. The long post absorbed a maximum loading, in the yy axis, approximately 4 times the

maximum measured loading for the short post. The long post also showed a maximum displacement, in the xx axis of inertia, higher than the maximum displacement presented by the short post in the yy axis. However, the axis of inertia was less crucial for the long post, despite experiencing an overall maximum displacement than the short post.

In terms of minimum and maximum displacements (Figure 16), at 50 cm above the ground (δ_5), the short post reached its maximum limit displacement along the yy axis of inertia, which is higher than the maximum displacement experienced by the short post around the xx axis of inertia. The long post experienced higher maximum displacements than the short post, regardless of the axis of inertia. The combined maximum limit displacement was, thus, reached by the long post.

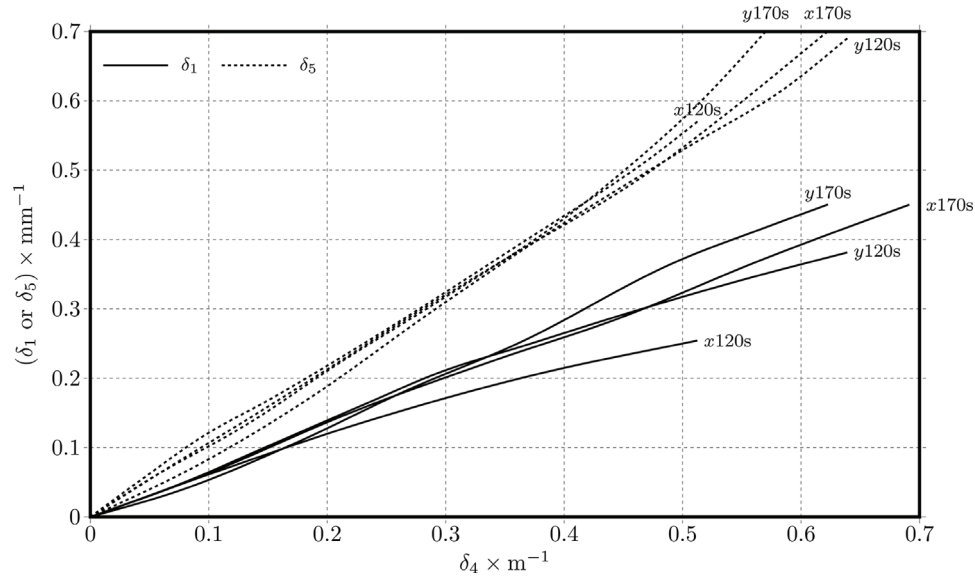


Figure 16. Static post testing - development of the minimum and maximum measured displacements (δ_1 and δ_5) as a function of the displacement δ_4 .

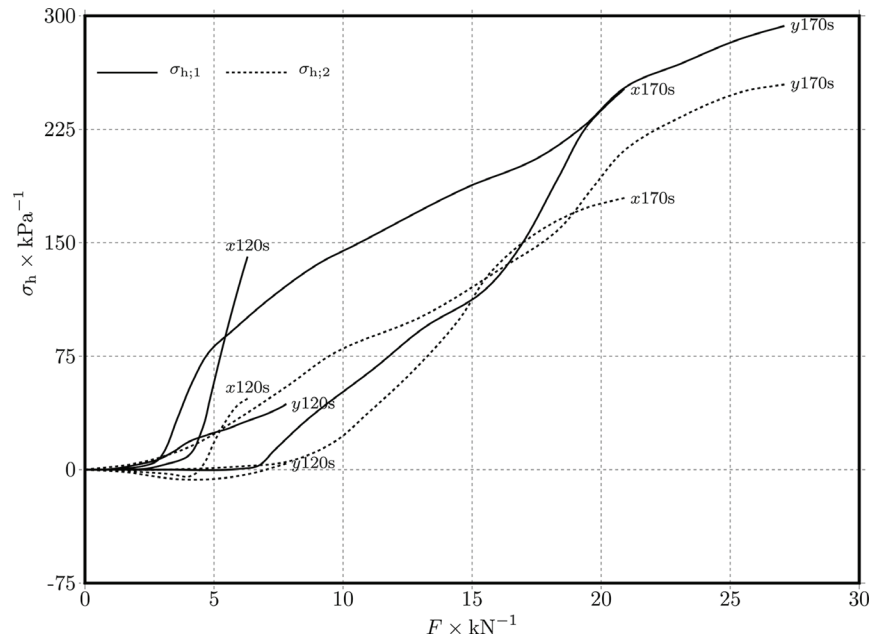


Figure 17. Static post testing - horizontal stress (σ_h) development as a function of the horizontal force (F).

At a depth of 10 cm above the ground (δ_1), the short post experienced its maximum displacement in the yy axis of inertia, while the long post showed similar displacement values for both axes of inertia. The maximum limit displacement was reached by the long post.

Regarding the horizontal stress (Figure 17), the short post in the xx axis experienced higher horizontal stress at a depth of 15 cm ($\sigma_{h,1}$) than at a depth of 30 cm ($\sigma_{h,2}$). Regarding the yy axis of inertia, the horizontal stress at 15 cm was also

higher than that at 30 cm. For the short post, the xx axis, at a depth of 15 cm, registered the maximum horizontal stress.

For the long post, the xx axis of inertia, at a depth of 25 cm, experienced higher horizontal stress than the yy axis, at a depth of 50 cm. The same situation was found regarding the 25 cm in the yy axis, which experienced higher horizontal stress than the xx axis, at 50 cm. The maximum horizontal stress registered for the long post was in the yy axis, at a depth of 25 cm.

3.2.2 Dynamic test results

During dynamic tests, accelerometers did not provide quality data due to the noise induced by the vehicle movement and belt oscillations – accelerometer a_1 provided unreadable data, and accelerometer a_2 only provided valuable data in two of the four tests performed (even if the sensor could not capture the initial response because it had a maximum range of 55 g).

Regarding the dynamic loading, the maximum dynamic peak loading was approximately 19 kN (Figure 18), reached at the middle stage of the test, in the xx axis of inertia. On the contrary, the short post experienced a higher dynamic loading (11 kN) in the yy axis of inertia. The long post absorbed a maximum loading of approximately 2 times the measured loading on the short post.

In terms of displacement (Figure 19), the short post registered a maximum value (50 cm above the surface) in the xx axis of inertia than in the yy axis. On the contrary, the long post suffered a maximum displacement in the yy axis of inertia than in the xx axis. At 50 cm above the surface, the maximum displacement was obtained by the short post in the xx axis of inertia. Regarding the minimum displacement (10 cm above the surface), the short post also showed a displacement higher in the xx axis of inertia than in the yy axis. The long post, contrary to what was observed for the maximum displacement, showed a higher minimum value in the xx axis of inertia. The displacement showed by the short post, in the xx axis of inertia, was the higher registered for 10 cm above the surface.

Regarding the acceleration spectrum (Figure 20), as expected, the long post experienced higher terminal accelerations, with higher values at both the beginning and end of the movement, as compared with the short post.

4. Numerical results

Numerical modeling in the world of geotechnical engineering is a process in which it tries to represent a real-world system through mathematical formulations that can be analyzed and computed by computational methods. In geotechnical engineering, numerical modeling is a widespread engineering technique to solve or tackle complex geotechnical subjects by computational simulation or deploying advanced equations under different geotechnical scenarios. A numerical model was created based on the results obtained from in-situ and laboratory tests. Models with optimal dimensions were created by the Plaxis 3D software to assess the behavior of guardrail posts around the two axes of inertia and different driving depths. Hardening soil constitutive model was chosen to create guardrail post models. To define the constitutive model, parameters including $E = 3.8$ MPa, $E_{ur} = 11.4$ MPa, $e_{init} = 0.779$, $v_{unsat} = 15.12$ kN/m³, $v_{sat} = 18.54$ kN/m³, $R_{inter} = 0.7$, and $\Psi = 4$ were utilized. The effect of soil suction was not considered because suction in the unsaturated zone above the phreatic level is ignored in Plaxis 3D software. Damping was not ignored (i.e., damping equal to 0) because high plastic failure is presented on the model. Due to the shallow buried depth of guardrail posts and for the sake of simplicity, it was decided to utilize constant values for the parameters of soil shown in Figure 9 during modeling.

4.1 Static model results

Guardrail posts, according to Table 1 and Figure 14, with different lengths and axis of inertia were modeled in the Plaxis 3D software. For all models created for guardrail

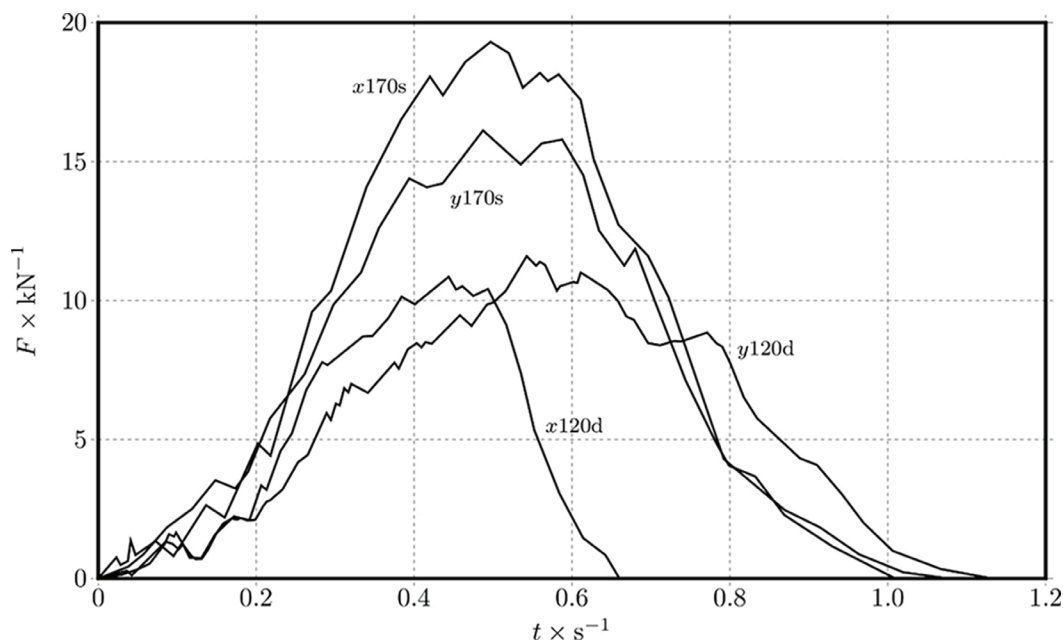


Figure 18. Dynamic post testing: horizontal force F imposed by the vehicle moving at 15 km/h.

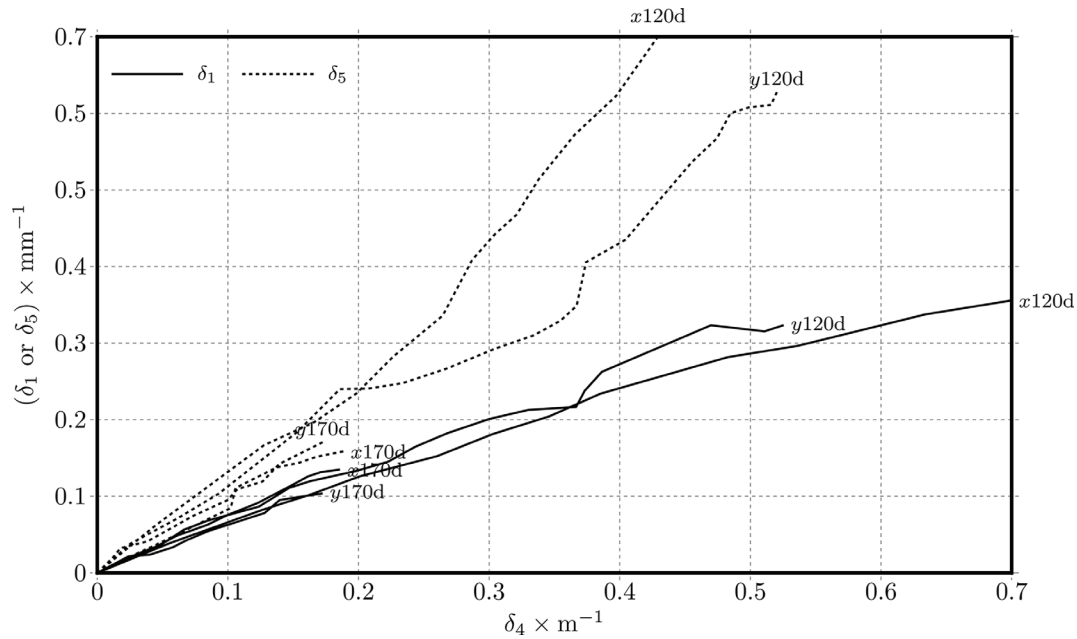


Figure 19. Dynamic post testing - development of the minimum and maximum measured displacements (δ_1 and δ_5) as a function of the displacement δ_4 .

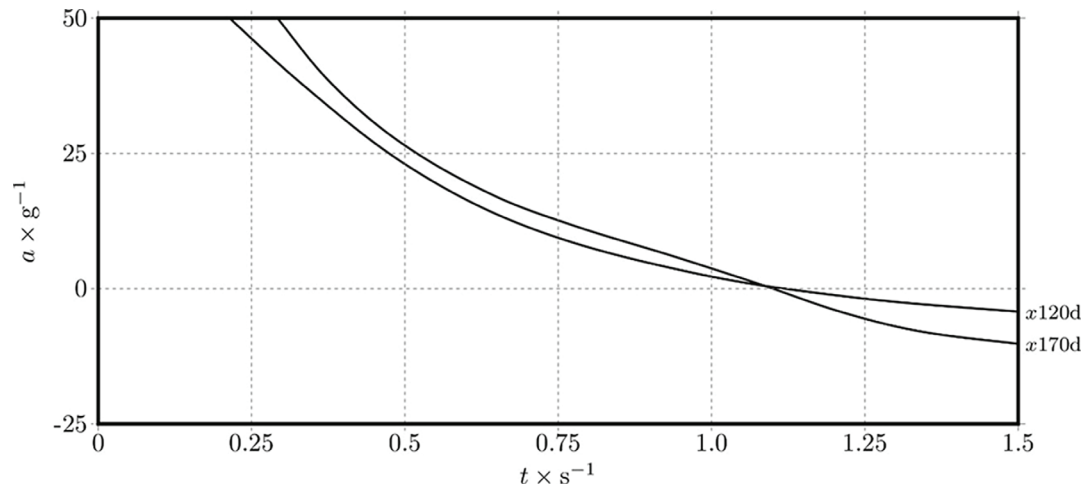


Figure 20. Dynamic post testing - acceleration spectra (time domain).

posts, loading was applied at a distance of 0.50 cm from the ground. Finally, a point displacement load proportional to the value achieved from the in-situ test was applied to models. An overview of the created model is shown in Figure 21.

After modeling guardrail posts and interpreting posts behavior, the Plaxis 3D software results indicated that numerical and experimental data are approximately equal. The final comparison to evaluate guardrail posts behavior during static loading between in-situ tests and Plaxis 3D software modeling is shown in Figure 22. Results of the comparison are based on different post lengths and axis of inertia.

4.2 Dynamic model results

Based on the in-situ results of guardrail posts behavior located on organic soil, it was decided to perform a dynamic simulation by Plaxis 3D software to validate the results between in-situ tests and Plaxis 3D models. Long posts approximately indicated equal in-situ displacement around both axis of inertia, so it was decided to just model one axis. After dynamic simulation, the results obtained in Plaxis 3D software indicated that numerical and in-situ results are almost the same, approving the accuracy of the results.

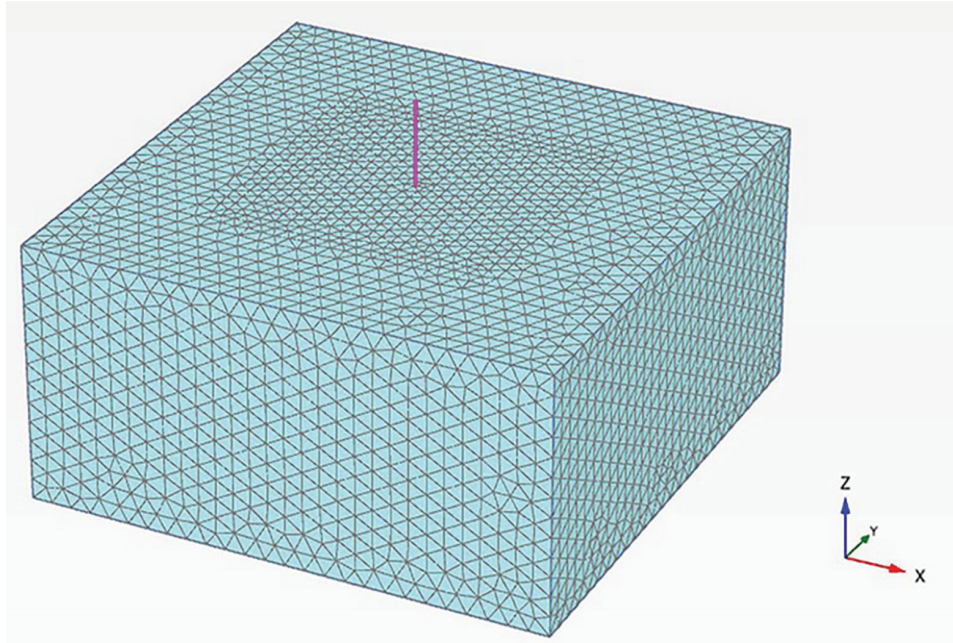


Figure 21. Guardrail post model overview.

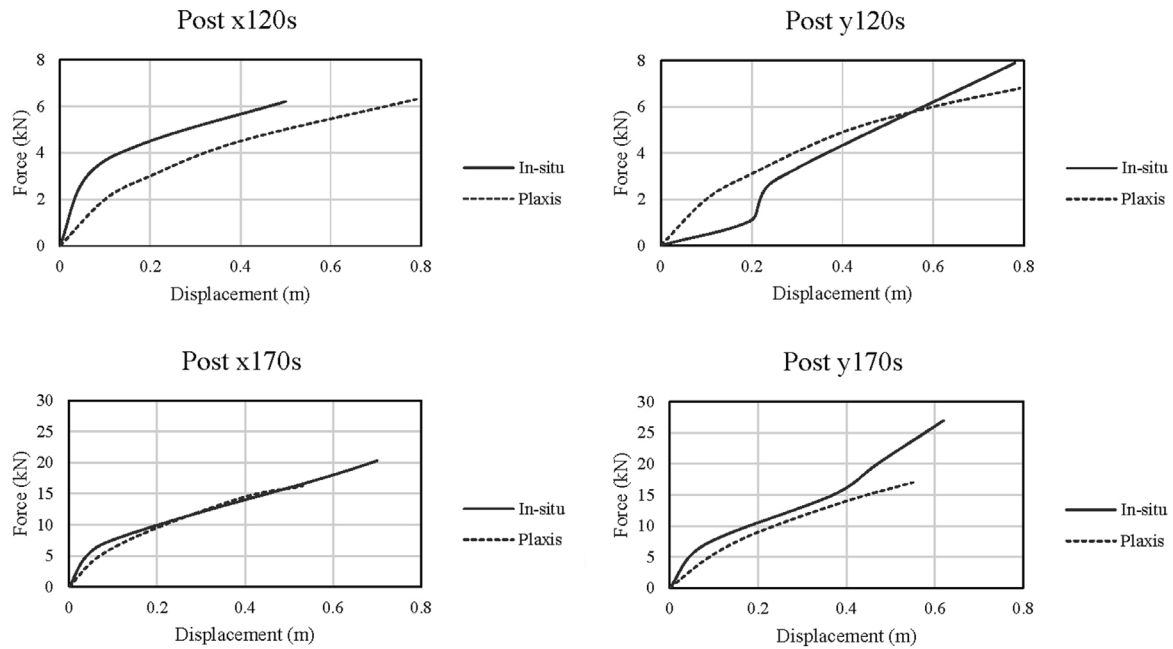


Figure 22. In-situ and Plaxis 3D results comparison in static loading.

Results of comparison based on different lengths and axis of inertia are shown in Figure 23.

5. Discussion

The dynamic and static results indicated that long guardrail posts reached maximum loading in comparison with

short posts. Besides, the short guardrail posts experienced higher minimum and maximum displacements in dynamic loading, while the long guardrail posts experienced higher minimum and maximum displacements in static loading.

From the experimental tests and results obtained, it was possible to state some critical opinions. When loading, short guardrail posts present greater deformations in the

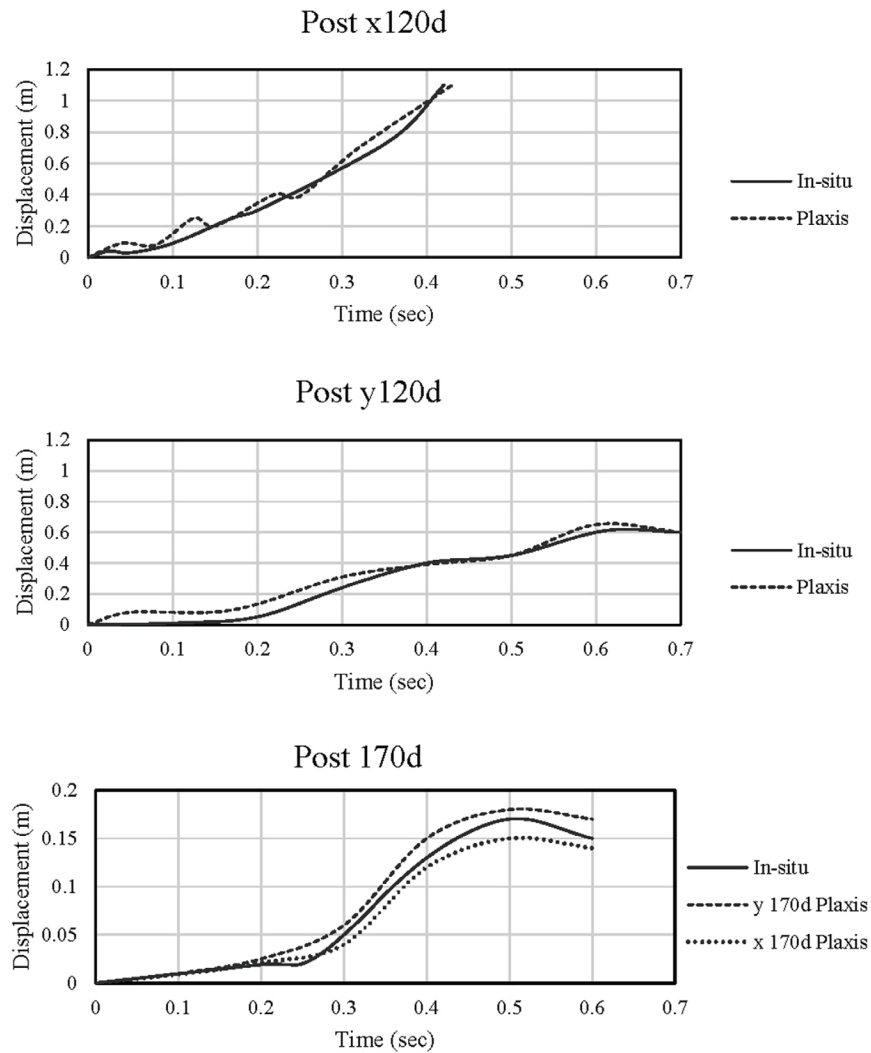


Figure 23. In-situ and Plaxis 3D results comparison in dynamic loading.

surrounding soil, while the soil under study remains stable during the loading in long guardrail posts. The guardrail posts assumed an elastic behavior due to their dimension, depth of driving, and soil strength. In addition, no relevant permanent post deformation was achieved on all tests. The guardrail post behavior turns out to be quite similar in both directions against loading.

Regarding the short guardrail posts, where the driving length was 0.6 m, it was concluded that the driving position influences the surrounding soil, both in static and dynamic tests. About long guardrail posts, where the driving length was 1.10 m, presented a much more coherent behavior due to increased driving depth. In terms of damage to the surrounding soil, the short guardrail post had a greater tendency to rotate and caused greater blistering in the surrounding soil due to the proximity of the post base on the surface. In contrast, long guardrail posts tendency to cause blistering, and tears are not evident destructively, with only occasional cracks in the soil.

6. Conclusion

This study aimed to achieve specific goals initially defined to increase knowledge of guardrail post behavior against static and dynamic loading. Despite being robust, guardrail posts start to show high ductility to protect the occupants against the impact of vehicles. After performing simplified experimental programs, it was concluded that the axis of inertia, embedment depth, and loading speed vary guardrail post behavior. Simplified numerical modeling was done to confirm the experimental results, and received data fully approved the in-situ tests. The results obtained are believed to be practical and relevant for in-situ operations and design procedures. Overall, long posts in both static and dynamic tests reached maximum loading in comparison with short posts. Short posts experienced maximum displacement in dynamic loading, while long posts experienced maximum displacement in static loading. However, it is still necessary

to provide a complete definition of the model and investigate other soil types.

Acknowledgments

The authors acknowledge the financial support by FCT / MCTES through national funds (PIDDAC) under the R&D Unit Institute for Sustainability and Innovation in Structural Engineering (ISISE), under reference UIDB/04029/2020; and ANI through national funds (Portugal 2020), under project “BARROD - Barreiras de Segurança Rodoviária”, reference 33497.

Declaration of interest

The authors have no conflicts of interest to declare. All co-authors have observed and affirmed the contents of the paper and there is no financial interest to report.

Authors' contributions

Hamid Reza Manaviparast: Conceptualization, Data curation, Visualization, Writing – original draft. Nuno Araújo: Conceptualization, Data curation, Methodology, Supervision, Validation, Funding acquisition, Project administration, Resources, Software, Writing – original draft. Nuno Cristelo: Formal Analysis, Investigation, Methodology, Tiago Miranda: Supervision, Validation, Writing – review & editing. The authors above kindly granted the permission of using parts of their publications in this template.

List of symbols

a	Acceleration
c'	Effective cohesion
c_u	Undrained cohesion
e_{init}	Initial void ratio
m	van Genuchten model parameter
n	van Genuchten model parameter
p'	Average effective stress
q	Deviatoric stress
t	Time
u	Pore water pressure
z	Depth
CD	Isotropically consolidated drained compression triaxial tests
CU	Isotropically consolidated undrained compression triaxial tests
CSL	Critical state line
D	Particle size
E	Young modulus
E_{ur}	Young modulus of unloading/reloading
F	Horizontal Force
F_y	Yield stress

K_0	Coefficient of thrust at rest
N	Vertical load
NCL	Normal compression line
OCR	Over-consolidation ratio
P	Cumulative particle size (percentage)
R^2	R-squared
R_{inter}	Reduction factor for interfaces
R_p	Soil penetration resistance
α	van Genuchten model parameter
δ	Displacement
ε_a	Axial strain
ε_v	Volumetric strain
γ_{unsat}	Unsaturated unit weight
γ_{sat}	Saturated unit weight
φ	Friction angle
φ'	Effective friction angle
φ_u	Undrained friction angle
ν	Poisson ratio
ρ	Volumetric weight
σ	Normal stress
σ_v	Vertical total stress
σ_h	Horizontal total stress
σ_3	Triaxial test chamber pressure
v	Specific volume
ω_s	Saturated water content
ω_r	Residual water content
ω	Water content
ψ	Soil suction
Ψ	Dilatancy angle

References

- ASTM D422-1963. (1963). *Standard Test Method for Particle-Size Analysis of Soils*. ASTM International, West Conshohocken, PA.
- ASTM D5298-94. (1994). *Standard Test Method for Measurement of Soil Potential (Suction) Using Filter Paper*. ASTM International, West Conshohocken, PA.
- Atahan, A. O., Büyük, M., Örnek, M., Erdem, M., & Turedi, Y. (2019). Determination of optimum post embedment depth for C120 steel posts using field and full scale crash test. *International Journal of Crashworthiness*, 24(5), 533-542. <https://doi.org/10.1080/13588265.2018.1479499>.
- BSI BS 1377-8. (1990). *Soil for civil engineering purposes. Shear strength test (effective stress)*. British Standards Institution, London.
- Cui, T. (2020). Research on design technology of safety facilities in highway traffic engineering. *IOP Conference Series: Earth and Environmental Science*, 587, 012006. <https://doi.org/10.1088/1755-1315/587/1/012006>.
- Gutowski, M., Palta, E., & Fang, H. (2017). Crash analysis and evaluation of vehicular impacts on W-beam guardrails placed on sloped medians using finite element simulations. *Advances in Engineering Software*, 112, 88-100. <http://dx.doi.org/10.1016/j.advengsoft.2017.04.004>.

- IGPAI NP-83. (1965). *Determinação da densidade das partículas*. IGPAI, Lisbon.
- IGPAI NP-143. (1969). *Determinação dos limites de consistência*. IGPAI, Lisbon.
- ISO ISO 22476-2:2005(E). (2005). *Geotechnical investigation and testing - Field testing - Part 2: Dynamic probing*. International Organization for Standardization, Switzerland.
- ISO ISO 22476-11:2017(E). (2017). *Geotechnical investigation and testing - Field testing - Part 11: Flat dilatometer test*. International Organization for Standardization, Switzerland.
- Jeyapalan, J.K., Dewey Junior, J.F., Hirsch, T.J., Ross Junior, H.E., & Cooner, H. (1984). Soil-foundation interaction behavior of highway guardrail posts. *Transportation Research Record: Journal of the Transportation Research Board*, (970), 37-47.
- Li, N., Park, B.B., & Lambert, J.H. (2018). Effect of guardrail on reducing fatal and severe injuries on freeways: real-world crash data analysis and performance assessment. *Journal of Transportation Safety & Security*, 10(5), 455-470. <http://dx.doi.org/10.1080/19439962.2017.1297970>.
- Lim, Y.J. (2009). Static and dynamic stability evaluation of model guardrail posts based on geotechnical properties. *International Journal of Highway Engineering*, 11(1), 233-245.
- LNEC E196. (1966). *Análise granulométrica*. LNEC, Lisbon.
- LNEC E201. (1967). *Solos. Determinação do teor em matéria orgânica*. LNEC, Lisbon.
- Mikusova, M. (2017). Crash avoidance systems and collision safety devices for vehicle occupants. In *MATEC Web of Conferences* (Vol. 107, pp. 00024). EDP Sciences. <https://doi.org/10.1051/mateconf/201710700024>.
- Neves, R.R., Fransplass, H., Langseth, M., Driemeier, L., & Alves, M. (2018). Performance of some basic types of road barriers subjected to the collision of a light vehicle. *Journal of the Brazilian Society of Mechanical Sciences and Engineering*, 40(6), 1-14. <http://dx.doi.org/10.1007/s40430-018-1201-x>.
- Örnek, M., Atahan, A.O., Turedi, Y., Erdem, M.M., & Buyuk, M. (2019). Soil based design of highway guardrail post depths using pendulum impact tests. *Acta Geotechnica Slovenica*, 16(2), 77-89. <http://dx.doi.org/10.18690/actageotechslov.16.2.77-89.2019>.
- Ozcanan, S., & Atahan, A.O. (2020). Radial basis function surrogate model-based optimization of guardrail post embedment depth in different soil conditions. *Proceedings of the Institution of Mechanical Engineers. Part D, Journal of Automobile Engineering*, 234(2-3), 739-761. <http://dx.doi.org/10.1177/0954407019848548>.
- Pajouh, M.A., Schmidt, J., Bielenberg, R.W., Reid, J.D., & Faller, R.K. (2018). Simplified Soil-Pile Interaction Modeling under Impact Loading. In S.J. Brandenburg & M.T. Manzari (Eds.), *Geotechnical Earthquake Engineering and Soil Dynamics V: Numerical Modeling and Soil Structure Interaction* (pp. 269-280). American Society of Civil Engineers.
- Patzner, G.S., Plaxico, C.A., & Ray, M.H. (1999). Effects of post and soil strength on performance of modified eccentric loader breakaway cable terminal. *Transportation Research Record: Journal of the Transportation Research Board*, 1690(1), 78-83. <http://dx.doi.org/10.3141/1690-08>.
- Rohde, J.R., Rosson, B.T., & Smith, R. (1996). Instrumentation for determination of guardrail-soil interaction. *Transportation Research Record: Journal of the Transportation Research Board*, 1528(1), 109-115. <http://dx.doi.org/10.1177/0361198196152800111>.
- Sassi, A. (2011). *Analysis of W-beam guardrail systems subjected to lateral impact*. University of Windsor.
- Tomlinson, M., & Woodward, J. (2007). *Pile design and construction practice*. CRC press. <https://doi.org/10.4324/9780203964293>.
- van Genuchten, M.T. (1980). A Closed Form Equation for Predicting the Hydraulic Conductivity of Unsaturated Soils. *Soil Science Society of America Journal*, 44(5), 892-898. <http://dx.doi.org/10.2136/sssaj1980.03615995004400050002x>.
- Yun, J.S., Han, K.J., Ahn, H., Falcon, S.S., Kim, K.D., & Choo, Y.W. (2018, June). Numerical Study on Static Behavior of Guardrail Supporting Piles Subjected to Horizontal Load. In *The 28th International Ocean and Polar Engineering Conference*. OnePetro.

The mechanics of iron tailings from laboratory tests on reconstituted samples collected in post-mortem Dam I in Brumadinho

António Viana da Fonseca¹ , Diana Cordeiro¹ , Fausto Molina-Gómez¹ ,
Davide Besenon^{1,2} , António Fonseca¹ , Cristiana Ferreira^{1#} 

Article

Keywords

Geotechnical laboratory tests
Iron ore tailings
Critical state soil mechanics
Tailings dam failure
Instability
Liquefaction

Abstract

Dam B1 was approximately 85 m high and 700 m long along the crown when it suddenly failed in 25th of January, after 41 years of operations and deposition of tailings at the Paraopeba mining complex (Córrego de Feijão), in Minas Gerais, Brazil. More than 250 people died and vast economic, social and environmental damages resulted from the collapse. Given the need to geotechnically characterise the tailings within the dam for a credible computational model of the failure, an extensive sampling and laboratory testing campaign took place. The geotechnical laboratory of the Civil Engineering Department at the Faculty of Engineering of the University of Porto (Portugal) was invited by CIMNE, under a contract with VALE, with MPF agreement, to conduct this program. This paper will present a description of the sampling campaigns in the remaining post-mortem dam/reservoir tailings where the failure instability mechanics developed and the experimental program undertaken to test the tailings in advanced laboratory tests. The results that embrace evaluations of the physical, hydraulic and mechanical properties, deduced from integral samples selectively collected and prepared as described, which allowed to define the geotechnical parameters necessary for the referred analyses are here resumed.

1. Introduction

Dam I in the municipality of Brumadinho suddenly failed at 12:28 p.m. local time on January 25th of 2019, after more than 40 years of operation and deposition of tailings processed from the natural rocks extracted from the Córrego de Feijão mine of the Paraopeba Complex, in Minas Gerais (MG), Brazil. The recorded images showed that the dam failure was sudden and abrupt, with no apparent signs of distress prior to the failure, developing across approximately 80% of the face of the dam in about 5 seconds. The failed slope material quickly turned into a mudflow. LiDAR post-failure topography indicates that 9.7 Mm³ of material were lost from the dam, which approximately corresponds to 75% of the pre-failure volume, causing a catastrophic damage downstream and is considered one of the most dramatic tragedies in recent years, in Brazil (Figure 1). As a direct consequence of the failure, many people died and vast economic, social and environmental damages were caused. The failure was the result of flow (static) liquefaction within the materials of the dam (Robertson et al., 2019).

Dam B1 was approximately 85 m high and 700 m long along the crest when it failed. The tailings disposal had stopped about 2.5 years before the failure and no large-scale operations were being performed at the time. The dam's construction history provides insight as to the possible reasons for the failure. The deficient upstream construction and the poor drainage conditions created a dam that was composed of mostly loose, saturated, heavy, and brittle tailings that had high shear stresses within the downstream slope, resulting in a marginally stable dam (i.e., close to failure in undrained conditions). What remained unclear was how the liquefaction process was initiated i.e., what was the event that started shearing in some region of the dam and triggered the liquefaction response. Special attention was given to the operations going on during the last year before the failure, namely the sub horizontal drilling operations to install drains and the perforation of vertical boreholes to install piezometers.

Extensive forensic activities and post-liquefaction studies, including advanced numerical simulations, were carried out to understand the tailings behaviour and response

*Corresponding author. E-mail address: cristiana@fe.up.pt

¹CONSTRUCT-GEO, University of Porto, Faculty of Engineering, Porto, Portugal.

²Escuela Superior Politécnica del Litoral, Facultad de Ingeniería en Ciencias de la Tierra, Guayaquil, Ecuador.

Submitted on February 4, 2022; Final Acceptance on March 31, 2022; Discussion open until August 31, 2022.

<https://doi.org/10.28927/SR.2022.001122>



This is an Open Access article distributed under the terms of the Creative Commons Attribution License, which permits unrestricted use, distribution, and reproduction in any medium, provided the original work is properly cited.



Figure 1. Google Earth images of the dam: (a) image on 22/7/2018; and (b) image after the collapse (22/12/2019).

mechanics and to objectively determine the probable and/or concurrent causes that led to the failure of this dam. Technical investigations on the causes of Dam I failure were commissioned by both the Authorities (the Federal Public Prosecutor's Office) and the owner of the mining complex (Vale SA). Three main reports on the technical causes of the failure of Feijão Dam I were presented based on the results of those investigations:

- the Expert Panel Technical Report (EPR) by Robertson et al. (2019);
- an independent investigation conducted by CIAEA, whose report is not public;
- the Computational Analysis Report by CIMNE (2021).

Given the need to geotechnically characterise the tailings within the dam for a credible computational model of the failure, an extensive sampling and laboratory testing campaign took place. The Geotechnical Laboratory (LabGEO) of the Civil Engineering Department at the Faculty of Engineering of the University of Porto (Portugal) was invited to conduct the advanced testing program.

This paper describes the experimental program, including the sampling of a large set of undisturbed and reconstituted samples in the post-mortem Tailings Storage Facility (TSF), and the procedures of the laboratory tests. The results obtained from the basic/conventional to the more advanced techniques, using the appropriate methodologies provided the parameters for the construction of constitutive models for numerical simulations. The laboratory procedures included the reconstitution of representative specimens in diverse state conditions and the execution of a wide variety of both conventional and advanced laboratory tests in these specimens. The materials were collected in three different locations near the failure zone. The number of different soils was carefully selected, considering the previous discretisation of limited clusters inside the deposited masses based on in situ tests –performed prior to the failure. The tests result embraced evaluations of the physical, hydraulic and mechanical properties, allowing the definition of fundamental

parameters for the inputs of appropriate constitutive models based in Critical State Soil Mechanics (CSSM) and capable of reproducing a wide range of soil behaviour, from ductile to very brittle, especially the undrained softening underlying the flow liquefaction phenomenon.

2. Site description and material selection

2.1 Considerations about the objectives

With a view to adopting physical, hydraulic and geomechanical parameters representative of the materials involved in the behaviour of this complex soil system, it was necessary to reassess the available results. The models that were adopted for the numerical analysis required the execution of tests of various complexities, from the most elementary (but no less important) to the more advanced, capable of defining the model parameters that would cover the essentials of the mechanical behaviour in conventional soils, but also in liquefiable soils. However, the geotechnical information obtained from previous studies presented significant gaps that were directly relevant to the numerical model under preparation. In particular, there were reasonable doubts about how representative of the dam materials involved in the failure were those selected for testing by the EPR. There were very few laboratory data with reliable measurements of undrained strength in conditions (initial state, consolidation history) similar to those prevailing in the field and there were no systematic data on possible strain rate effects on strength, which was unfortunate considering that viscous creep had been postulated as a possible triggering factor by the EPR (CIMNE, 2021). Therefore, it was considered necessary to obtain new samples from the remaining dam material and to extensively test them in the laboratory.

The nature of the tailings deposited in this TSF had to be dealt with great care. The representativeness of the samples to be retrieved from this huge volume of deposited tailings was carried out in light of strict analyses of historical registered data of the 50 years rising this TSF. More importantly, a



Figure 2. Examples of localised layer variability: (a) layering visible in the field; (b) micro layering, visible on an undisturbed sample from Site 1 (12/19/2019) at LabGEO.

representative number of recently performed in situ tests data; that is, static cone penetration tests with measurement of pore pressures (CPTu) and shear wave velocities (V_s) by seismic flat dilatometer devices (SDMT). The CPTu and V_s profiles were analysed before the decision to program the campaigns to obtain new samples in the remains of the dam revealed an expected high variability/heterogeneity in depth as well as in plan. It was clear that the materials involved in the modelling process should be associated to the deposition phases along the years (when distinct mining fronts and injection/spigotting explain the variability). The interlayering was clear in the intact samples directly obtained in the remaining intact blocks, as observed in the trenches created for such purpose. A very thin layer interstratification and anisotropy at lab scale were also observed (see Figure 2).

Testing these intact/undisturbed samples is important to identify how the results fit into the general framework of each type of material selected to constitute the numerical modelling. It is very difficult to pass from the specificities of these undisturbed stratified (“individual” material distribution and facies, with specific behaviour) to an extrapolation for a unified model of each of the constituents. Therefore, a meticulous identification of burses of more homogeneous masses was carried out and the integral masses (mainly referred to convergent colours with distinctive values specific gravity) were assembled in bags and taken to the laboratory.

This representativeness was naturally highly limited by the condition of the depleted basin and the almost complete disappearance of the dam’s lifting dykes built upstream. However, as will be explained in what follows, areas were sought that contained undisturbed material and different typologies that emerged from the analysis of the public elements available from reports by previous expert panels.



Figure 3. Location of the three sampling sites on B1 dam, after failure.

2.2 Sampling campaigns

The campaigns to collect representative samples of these tailings were carried out in three phases. The first campaign (S1) was carried out on 19th December 2019, the second (S2) on 26th December 2019, and the third (S3-L1 and S3-L4) on the following 12th March 2020. Figure 3 identifies the location and date of the three campaigns in the post-mortem condition of the dam.

After a precise visual identification of the exposed area of the remains of the dam, the first campaign was led to the integral masses (still standing or moved down but preserved) deep in the tailings, to the bottom of the basin of the destroyed dam and heading towards the right margin of the dam. The two other campaigns were conducted in view of the need for additional types of soils and samples for the programmed laboratory tests. These site investigation works were coordinated by the first author, in collaboration with

Professor António Mendonça from the Federal University of Minas Gerais (UFMG) and the local technical support of VALE.

Two materials were identified as prevailing in Site 1 with quite distinct visual properties, namely a red fine tailing material and a dark (black) granular one. These materials clearly differed on some faces from the large masses that had failed –probably due to the relief of the internal part of the drainage basin– along the exposed slide surfaces in a progressive process. As these were shallow areas closer to the basin margins, they did not collapse, but rather slid along these surfaces at the limit of frictional resistance. So, in the very first campaign, it was realised that it would be possible to find “undisturbed” tailings, that is, not collapsed and with the original fabric and inter-particle structure, allowing the execution of several tests in the laboratory if they were directly sampled with thin-walled blocks and tubes, as illustrated in Figure 2a).

The second visit to the dam took place on December 26th, 2019, but it was not possible to access areas within the

volume of the rupture due to the heavy rainfalls at the end of that year, and it was necessary to move to more secure areas behind the crest. On Site 2, located inside the tailing’s reservoir, a brown very fine material was collected for its abundance. Small clusters of red/brownish material were also gathered. A large number of intact/undisturbed samples was also retrieved from this location.

Later on, a third campaign (Site 3) was carried out, and two locations were accessible (these were named S3-L1 and S3-L4). The Local 1 was situated in the upper part of the previous Site 1, in slipped masses difficult to access and where black horizons were dominant, while Local 4 was close to the abutment where the soils from the EPR campaign were collected (see Figure 4). Bags with remoulded but integral samples were collected from each site avoiding segregation and respecting the grain size distribution of the sampled volume of homogenised soil. Intact/undisturbed tailings were also block sampled in these locations.

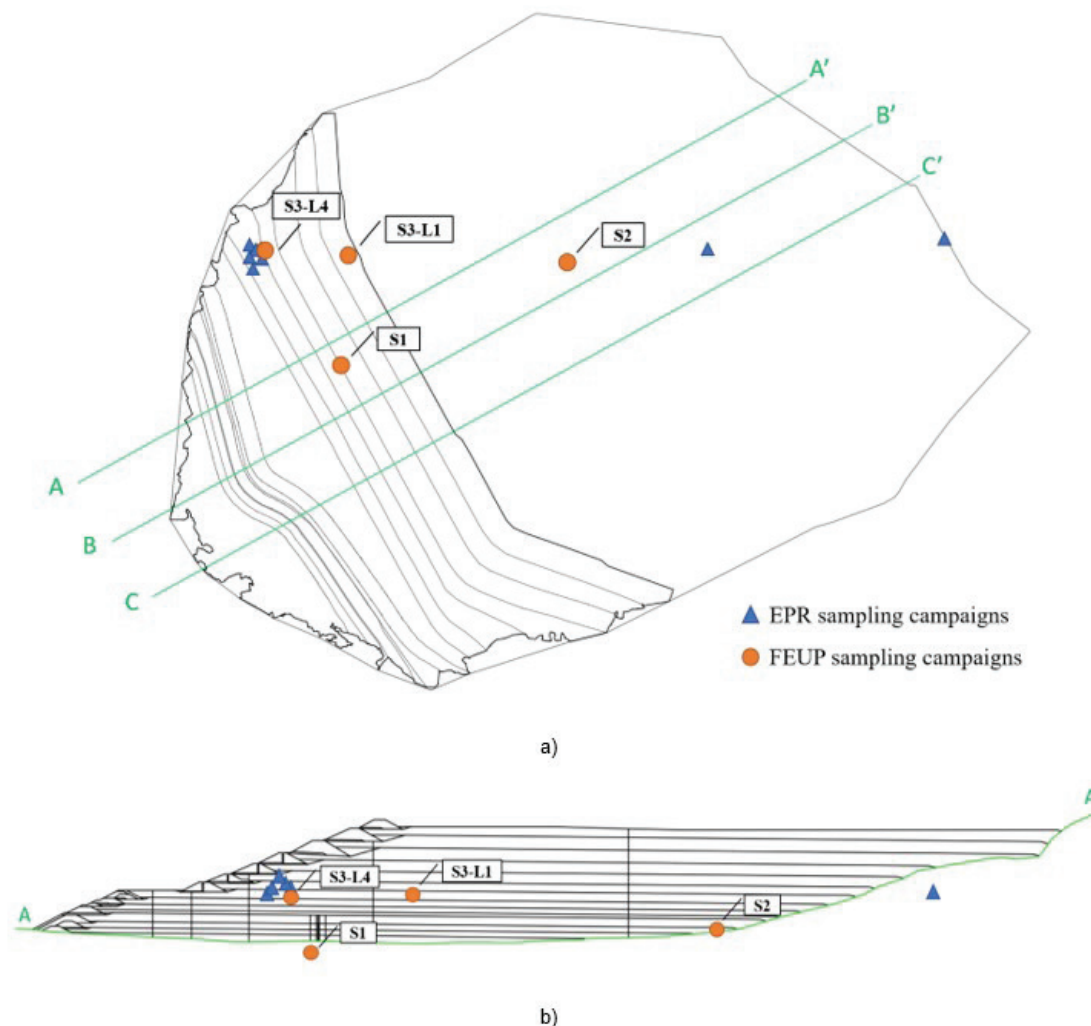


Figure 4. Location of the experimental sites from the different sampling campaigns – Projected position: (a) plan view of the dam; (b) alongside the dam section.

EPR and FEUP sampling locations are projected in Figure 4 on the plan view of the dam and alongside the dam section reference axis A-A'. Most samples from the EPR were clustered at a single location close to the remains of the left abutment of the dam (taken from levels corresponding to intermediate dam filling stages), while other two sites were several hundred meters behind the last crest of the dam, with the intention of recovering slimes. The initial failure surface was very far away from these sampling locations.

FEUP experimental sites are deeper and correspond to older tailings than those obtained in the EPR campaign, except for Site 2, located 200 m behind the final crest of the dam, which was chosen with the intention of recovering slimes. Notwithstanding, FEUP sampling sites are likely closer to the location of the initial failure surface.

2.3 Material selection

Geotechnical characterization of the tailings that constituted the dam was deemed essential to obtain a credible computational model of the failure, but from a practical and effective point of view, a discretisation of limited clusters/blocks inside the deposited masses was pursued. This is well described in the referred CIMNE panel report. In order to simplify the numerical analyses, two modelling decisions were investigated: how many materials can fairly represent the complex distribution of tailings through the dam (heterogeneously distributed and strongly interlayered); and which of the collected materials are compatible with the dominant soil behaviour types present along the dam (coarse to fine granular tailings, silty sands, mostly silts and even slimes).

This subject was initially addressed by analysing the profuse data from several CPTu testing campaigns during the period from 2005 and 2018. The soil behaviour type index $I_{c_{RW}} = 2.60$ proposed by Robertson & Wride (1998) is normally used to separate fine from coarse material. This threshold value has been observed to separate correctly mostly granular and mostly cohesive soils in natural deposits; however, it is unclear if this value is also the best for tailings.

Aided by advanced numerical simulations, CIMNE established a different threshold for $I_{c_{RW}}$ based on the drained and undrained response to CPTu tests, to a higher value of 2.85, optimising the fine and coarse behaviour type horizons. Soils that respond in a drained manner to CPTu penetration would be very permeable. Therefore, permeability was the key property to differentiate fine from coarse soils, and, in this case, was also correlated with important critical state properties. The undrained response to a CPTu was quantified by the normalised excess pore pressure index B_q .

The coarse ($I_{c_{RW}} < 2.85$) and fine ($I_{c_{RW}} \geq 2.85$) fractions of tailings were not homogeneously distributed in the dam body. CPTu results showed that stage changes (different deposition phases) were often coincident with significant changes in mechanical response. To simplify the spatial

distribution of tailings within the dam, blocks were created in the diverse analysed sections by CIMNE. These blocks correspond to a specific section, raising and alignment of the dam and have some allocated data from the corresponding CPTu tests. For practical reasons, only a limited number of material types can be used in the numerical simulation. Thus, CIMNE decided to use three different types of tailings to assign material properties to the different blocks in the model.

Three materials were idealised, covering all material distribution: Fine tailings (when the CPTu indicated a proportion of Fines Content, FC, equal or above 50%); Coarse tailings (when the CPTu indicated a proportion of FC equal or below 10%) and Mixture tailings (for CPTu FC between 10 and 50%). The objectiveness in the sampling campaigns was crucial to retrieve best “material models” in soil behaviour types.

FEUP investigated all remoulded/integral and intact/undisturbed samples obtained in the different sampling campaigns. From the physical properties (mainly particle size distribution, PSD and specific gravity, G_s) and the coloration of the materials found, it was selected a set of three ideal materials to be representative of different tailing materials within the dam identified in the CPTu analyses. The typological classes of soils were named as Type 1 for red fine tailing material collected on Site 1; Type 2 for the brown very fine material collected on Site 2; and Type 3 for the black granular material collected on Site 1.

The undisturbed samples were not selected to define the numerical modelling, as it is very difficult to overcome the specificities of these undisturbed stratified materials to an extrapolation for a unified model of each of the constituents. They will however be addressed in future works. The red/brownish material collected from Site 2 was not considered representative of the tailings reservoir, as it showed a combination of physical characteristics of the soils under evaluation. The samples retrieved from Site 3-Local 4 were also not considered in the numerical modelling as they were too close to the embankment berm and further to the location of the initial failure surface. Nonetheless, after analysing the integral samples collected from Site 3-Local 1, the black coarser tailing was considered an ideal material to be representative of different tailing materials within the dam, given its brittleness and proximity to the initial failure surface location. This material, named Type 4, was not included in the dam's modelling, as it was still being tested and its mechanical characterisation will be presented in an independent paper.

The ideal reconstituted materials tested in this program show similarities in grain size distribution, in comparison with those tested by EPR. However, these materials are more distinctive than those of the EPR, with respect to the more fundamental physical properties (such as the specific gravity, G_s and the shape of the particle size distribution, expressed by the coefficient of uniformity, C_u), for which they almost cover the full range present on the tailing samples.

This division into three typological groups would be later confirmed by the results obtained in laboratory tests for the determination of hydraulic conductivity (permeability), volumetric compressibility in confined conditions (either in isotropic loading or in oedometric loading –unidirectional) and shear strength resistance, in diversified conditions. This extensive and varied testing program had to be developed in a work of such complexity, since different drainage conditions (total drained – or inhibited – not drained) and loading paths must be considered.

3. Geotechnical characterisation of the tailing materials

3.1 Experimental methodology

At an early stage of this process, after visual inspection of the collected soil samples, it became clear that, in order to achieve a broad and comprehensive geotechnical characterisation of the tailing soils of the case study dam, it was necessary to consider different soil types to be tested and analysed in parallel. As such, the typological classes of soils considered representative of the tailings stored in the dam were defined, based on the characteristics of the samples collected during the sampling campaigns previously described, having been selected and identified the following three types of tailings:

- Type 1 – Fine reddish, low-ferrous tailings;
- Type 2 – Fine brownish, moderately ferrous tailings;
- Type 3 – Coarse-grained black iron-rich tailings.

The final selection of these three types of tailings materials was supported by two physical criteria, namely the particle size distribution (PSD) and the specific gravity of the solid particles (G_s). Fine and coarse designation associated with significant distinct permeability values as expressed before. These two criteria were adopted, since it is recognised that soil grading controls the behaviour of the soil, while the different values of the G_s can be associated with the iron content of each tailing.

The experimental program was designed to include laboratory tests that objectively determine the necessary parameters for the calibration of the constitutive models required to perform specialised computational analyses. Therefore, an extensive series of tests was carried out for a general geotechnical characterisation, namely physical, hydraulic and geomechanical parameters, in terms of compressibility and shear strength. The experimental program comprised grain size distribution, specific gravity of solid particles, hydraulic conductivity (permeability in different isotropic stress levels), volumetric compressibility in confined conditions (in isotropic and unidirectional oedometric loading) and strength characterisation in diverse triaxial testing conditions. This experimental plan was discussed with Professors Antonio Gens and Marcos Arroyo, the main authors of the CIMNE report.

Special attention was given to the ultimate strength at constant volume, which is fundamentally mobilised under ‘stable’ behaviour (i.e., critical state condition). For this purpose, tests involving different stress-paths and drainage conditions, necessarily associated with the complex geotechnical structure of the Dam I, were considered. The failure resulting in a flow slide was the result of flow liquefaction within the tailings in the dam. Since only contractive materials have the possibility of undergoing liquefaction, particular emphasis was given on undrained behaviour of very loose samples. The EPR also concluded that the sudden strength loss and resulting failure of the marginally stable dam was due to a critical combination of ongoing internal strains due to creep, and a strength reduction due to loss of suction in the unsaturated zone caused by the cumulative rainfall. For this purpose, a series of triaxial tests were explicitly designed to investigate strain rate effects on undrained strength of tailings.

3.2 Physical characterisation

The particle size distribution analyses and specific gravity were performed according to ISO 17892-4 (ISO, 2016) and ISO 17892-3 (ISO, 2015) standards, respectively, like the corresponding ASTM standards. Figure 5 illustrates the results of the particle size distribution curves of the three types of tailings identified, together with a shaded area corresponding to the reported grading curves of the collected tailings soil samples, as published in the EPR (Robertson et al., 2019).

Soil type 1 corresponds to fine reddish, low-ferrous tailings, with a specific gravity of 3.94. Soil type 2 refers to a fine brownish, moderately ferrous tailings, with specific gravity is equal to 4.55. Soil type 3 is a coarse-grained

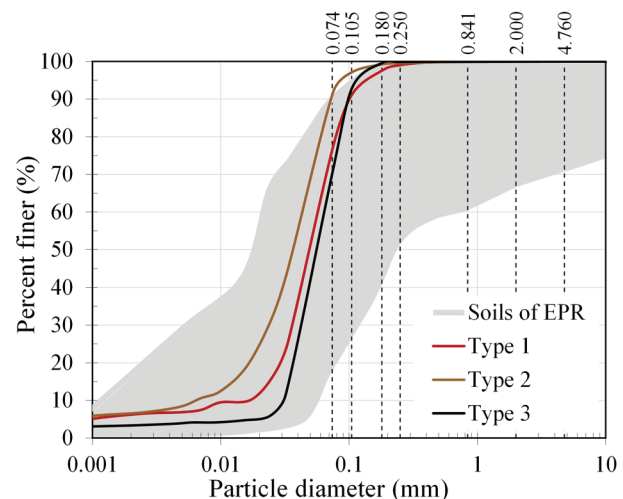


Figure 5. Grading curves of the three types of tailings. Comparison with other soils from Brumadinho dam, according to the Expert Panel Report (EPR) (Robertson et al., 2019).

black iron-rich tailing, with the highest specific gravity of 5.00. The distinct particle densities are related to the initial stages of the tailing depositions, when the process of extracting iron ore from the rocks coming from the mine was less efficient. The percentage of iron is much higher in the dark tailings, produced in the first rising phases of the dam, than in the red, corresponding to more recent operations.

3.3 Compressibility and consolidation characterisation

3.3.1 Oedometric compressibility

Several oedometric consolidation tests were performed to assess the compressibility of the three types of tailings identified in the previous section. The testing process followed the international standard ISO 17892-5 (ISO, 2017). These tests were carried out on remoulded samples using the moist tamping technique, ensuring a loose soil state condition. In-situ void ratios were derived from the analysis of several CPTu tests carried out at different locations and undisturbed block samples tested in the laboratory in this study. Comparisons, prior to the dam failure, between initial void ratios of samples collected during the deposition stages presented systematically dilatant behaviour when tested in the laboratory. These contradict the high values of state parameters derived from CPT and CPTU tests, pointing to contractive behaviour. Knowing that critical state locus is reached independently of the initial void ratio and that it is more clearly reached in triaxial tests from the loosest possible state conditions (Viana da Fonseca et al., 2021), the preparation of the specimens was done with the utmost care to obtain higher values than those referred above determined after the failure for this study. After preparing the samples, these were placed in the oedometer cells and submerged in distilled water for a minimum period of 12 hours, to ensure nearly full saturation of the soil. Subsequently, the samples were subjected to a series of loading and unloading stages to establish the compressibility parameters of the three types of tailings, as illustrated in Figure 6.

Table 1 summarises the compressibility parameters obtained on the oedometer tests for the three types of tailings. It can be observed that the three types of tailings exhibit different compressibility parameters: compressibility index (C_c), recompressibility index (C_r , obtained from the unload-reload cycles of moderate amplitude), expansion index from the final unload at near zero stress (C_s) and other ratios,

namely C_c/C_r . These differences are demonstrative of distinct geomechanical behaviour according to the type of tailing previously defined. Based on these diverse compressibility characteristics, the selection of the three types of tailings to be characterised in further detail was validated, which will be carried out using advanced techniques, as described in the following sections.

In view of these oedometer test results, it was observed that the three types of tailings exhibited a slope change on the compressibility curve for effective vertical stresses (σ'_v) above 3200 kPa. This finding evidences the evolutive nature of these soils, caused mainly by particle breakage (or crushing) or by changes in the shape of particles at higher stresses. On the other hand, no transitional behaviour was observed in these materials, since tests performed at different initial void ratios converged to the same 1D compressibility line (results not shown here, further details in Annex 1 of the CIMNE report).

3.3.2 Isotropic compressibility

A series of isotropic consolidation tests were carried out in triaxial cells as complement to the oedometer consolidation tests, in order to characterise the soil stiffness parameters established in the critical state theory. These tests were performed on remoulded loose specimens using the moist tamping technique. The test procedure included the application

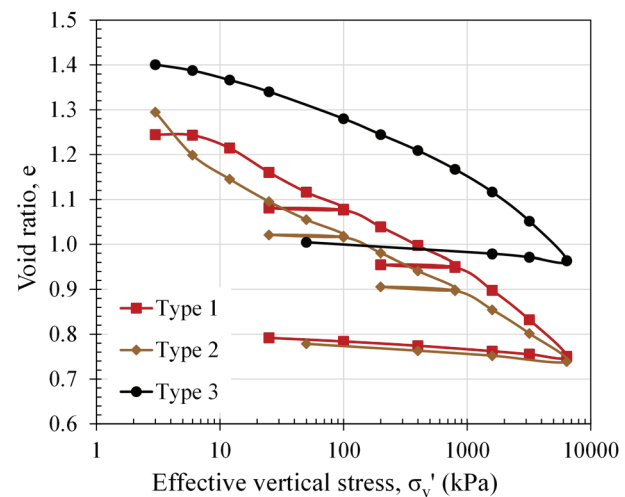


Figure 6. Oedometric compressibility curves for the three different tailings.

Table 1. Oedometric compressibility parameters for the three tailings soil types.

ID	Soil type	e_0 (-)	C_c (-)	C_r (-)	C_c/C_r (-)	C_s (-)
ED_T1	Type 1	1.24	0.2196	0.0097	22.64	0.0181
ED_T2	Type 2	1.30	0.1589	0.0143	11.11	0.0175
ED_T3	Type 3	1.40	0.1925	0.0267	7.21	0.0254

ID: Identification.

of several consolidation stages, with measurement of the volumetric change over time. Since the triaxial cells used for these tests were equipped with bender elements (BE), seismic shear wave velocities, V_s , were measured to estimate the variation of the small-strain stiffness at each consolidation stage, according to the methodology proposed by Viana da Fonseca et al. (2009) and Ferreira et al. (2021). In addition, seismic compressional wave velocities, V_p , were measured to assess the saturation conditions, complementing the verification by Skempton's B parameter, as recommended by Viana da Fonseca et al. (2021). Figure 7 shows the isotropic compressibility curves in the $e - \log p'$ plane, for the three different tailings.

Table 2 includes the isotropic compressibility parameters obtained from the isotropic consolidation tests with seismic wave measurement, where it is confirmed that the three types of tailings present distinct behaviour, as previously verified in the oedometer tests.

3.4 Small-strain stiffness

Small-strain stiffness was measured by means of bender elements during triaxial testing of the different types of tailings. These piezoelectric transducers, which send and receive seismic waves, allow the measurement of P and S-wave velocities at any stress conditions during the triaxial test. The required equipment consists of a function generator (TTi TG1010), an oscilloscope (Tektronix TDS 220) and a

Table 2. Isotropic compressibility parameters for the three tailings soil types.

Material	N (-)	λ_c (-)	κ (-)
Type 1	1.1944	0.049	0.006
Type 2	1.0873	0.046	0.003
Type 3	1.3129	0.028	0.003

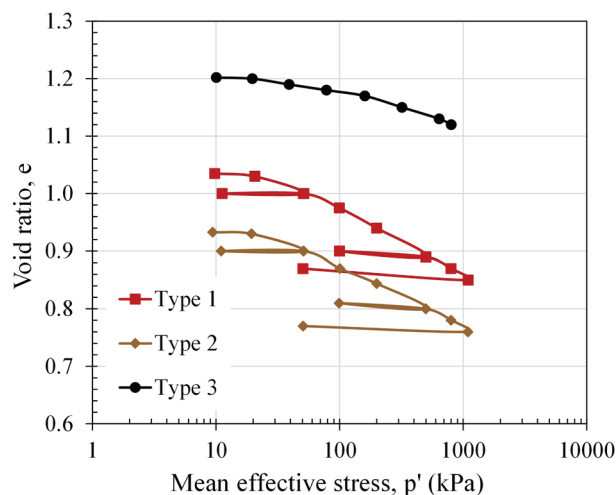


Figure 7. Isotropic compressibility curves for the three types of tailings.

computer for signal acquisition. In these tests, a series of single sinusoidal pulses at different input frequencies was used to excite the transmitter BE, to minimise the uncertainty and subjectivity associated with signal interpretation (Viana da Fonseca et al., 2009). For S-wave measurement, input frequencies ranged from 1 to 10 kHz were used, from which the results in Figure 8 were obtained for the three different tailings.

These results indicate a higher stress-dependency for Type 1, evidenced by the higher stress exponent, which is typically observed in soils with a weaker fabric or inherent structure. Globally, it can be observed that the denser soils exhibit a lower stress-dependency. Further analyses of this behaviour are currently being performed as complementary studies.

P-waves were also measured, using frequencies between 25 to 150 kHz, mainly to assess the saturation conditions of the tested specimens. As established in the wave propagation theory, if the value of the compression wave velocity (V_p) is greater than 1482 m/s, the soil is saturated (Santamarina et al., 2001).

3.5 Hydraulic conductivity/permeability

The hydraulic conductivity or permeability of the three types of tailings was measured by direct constant head permeability tests measured in triaxial cells. The test procedure included soil saturation, by increasing the backpressure up to 300 kPa, while maintaining the same effective confinement of 10 kPa, followed by the flow of deaired water by applying a constant head of about 5 kPa between the ends of the specimen (e.g., 302.5 kPa at the bottom and 297.5 kPa at the top). The determination of the coefficient of hydraulic conductivity (k) of the different soils was carried out at several loading stages and void ratios. Figure 9 shows the

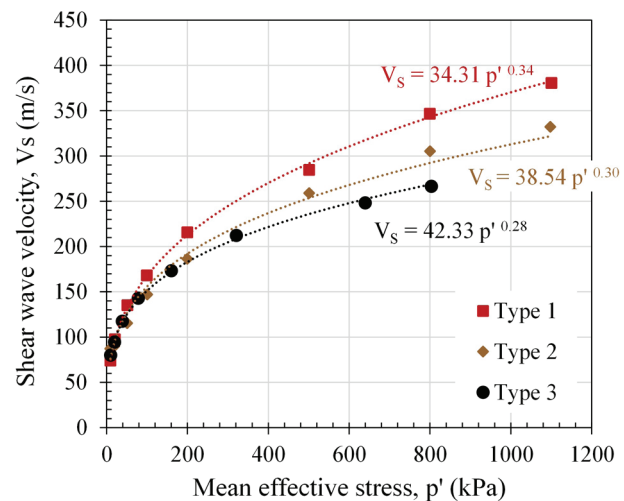


Figure 8. Evolution of shear wave velocities as a function of mean effective stress for the three types of tailings.

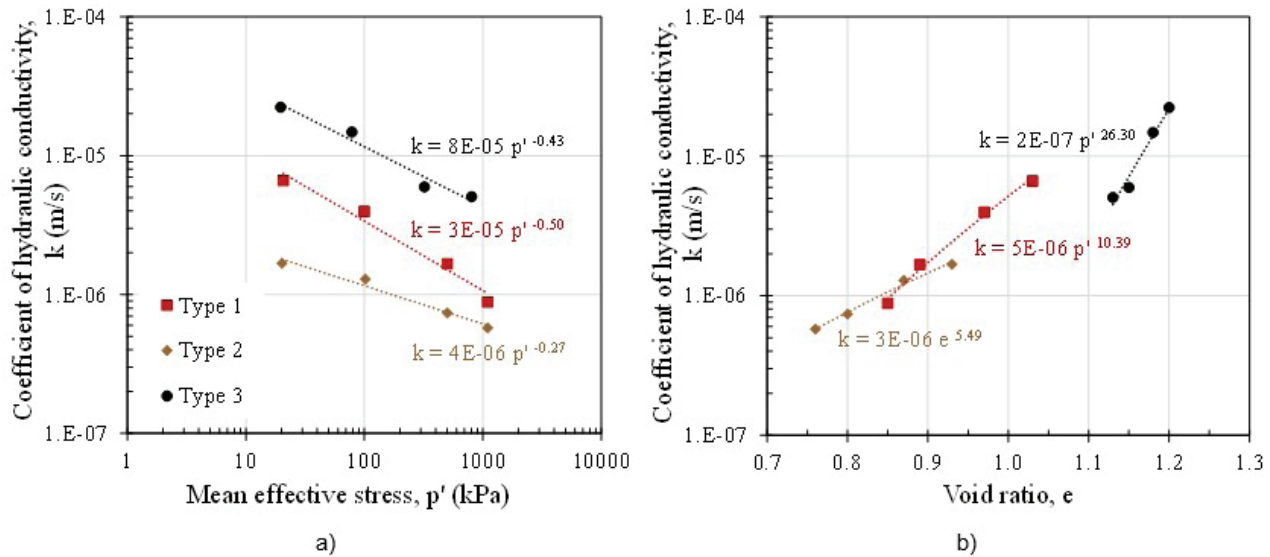


Figure 9. Variation of the coefficient of hydraulic conductivity for the three types as a function of: (a) effective stress conditions; (b) void ratio.

coefficient of hydraulic conductivity curves for the three tailings as a function of the effective stresses and void ratio conditions. The void ratios presented in this figure correspond to the estimated values at each loading consolidation stage, in which permeability was measured.

From Figure 9, it can be observed that the three types of tailings have different permeability characteristics, which is a clear indication of distinct soil behaviour. Since the order of magnitude of permeability is correlated with the particle size distribution of the materials, there is an evident correspondence between these parameters and the grading properties of each type of tailings. Based on the differences in permeability coefficients, the selection of the types of tailings to be characterised is validated.

4. Critical state characterisation

4.1 Specific equipment and procedures

Critical State Soil Mechanics (CSSM) has been increasingly applied to describe the behaviour of these granular mine tailings materials, with clear advantages for its modelling, namely for the stability analyses. The critical state line (CSL) of any soil is independent of its initial stress state and its void ratio, thus representing an ‘ultimate and stable state’ and can be estimated from laboratory triaxial tests. The results allow obtaining the shear-confinement-volume state, represented by three-dimensional invariants in the e - p' - q plane (void ratio, mean and deviatoric effective stresses). The definition of critical state lines (CSL) for each type of tailings was carried out by performing a set of triaxial tests in drained and undrained conditions. Table 3 summarises the adopted testing program for the CSL characterisation, for the three types of tailings.

The critical state parameters of the iron tailing soils were obtained by following the recommended testing procedures proposed by Viana da Fonseca et al. (2021). Hence, triaxial apparatuses were configured to assess the soil behaviour at large deformations by including lubricated end platens and an embedded connection piston into the top cap. The lubricated end platens allowed uniform radial strains and holding the cylindrical shape of the specimen at large axial strain levels (Molina-Gómez & Viana da Fonseca, 2021); while the embedded connection piston allows significantly reduced tilting of the top cap during all phases of triaxial testing (Reid et al., 2021).

All specimens were prepared using the moist tamping technique simultaneously with the under-compaction method (Ladd, 1978). This preparation procedure was selected due to their reliability, reproducibility and capability to achieve a full range of densities (Jefferies & Been, 2016). Although moist tamping with under-compaction method does not represent well the in-situ deposition of tailings, for critical state characterisation this is not an issue, since the critical state parameters are independent of the initial soil fabric (Smith et al., 2019; Molina-Gómez & Viana da Fonseca, 2021; Reid et al., 2021). The preparation comprised the compaction of six layers at a specific water content, which varied from 5% to 10% according to the soil type and a percent of undercompaction (U_n) of 2%. Such procedure ensured the testing of uniform loose samples of 70 mm diameter and 140 mm height –suitable to well-define the critical state locus (CSL) of the studied soils. All specimens were tested in fully saturated conditions. The saturation procedure covered the following phases (Viana da Fonseca et al., 2021): (i) flushing of with 1.5 litres of CO_2 from the bottom drainage line, forcing the air to circulate upwards; (ii) the flushing of 800 ml of de-aired water under a positive effective confining pressure

Table 3. Summary of CSL testing program for the three tailings soil types.

Type	Soil		Preparation State	Test Type	Consolidation
	Condition				p' (kPa)
Type 1	Original	Loose	CID		50, 200, 400
		Dense	CID		100, 200
	Evolved	Loose	CID		200, 500, 800
			CIU		400, 800 (x2)
		Dense	CID		100, 200, 400
Type 2	Original	Loose	CID		100, 200, 400
	Evolved	Loose	CID		50, 100, 400, 800
			CIU		400
		Dense	CID		200
Type 3	Original	Loose	CID		20, 200, 800
	Evolved	Loose	CID		30, 100, 200, 400, 800
			CIU		600, 800, 1200
		Dense	CID		100 (x3), 200

Legend: CID – isotropic consolidated drained tests; CIU – isotropic consolidated undrained tests.

(e.g., cell pressure 20 kPa, bottom back-pressure 10 kPa and the top at atmospheric pressure); and (iii) the application of backpressure increments at a constant effective stress of 10 kPa until reach 300 kPa. The full saturation condition was validated by measuring Skempton's B-value. The specimens were only considered fully saturated for B-values higher than 0.97. Overall, B-values of about 0.98 were achieved. After saturation, the samples were isotropically consolidated at different mean effective stresses. For CSL definition, soil specimens were sheared under drained and undrained conditions at 0.025 mm/min. Such rate is compatible to ensure the drainage and pore pressure build-up of cohesionless soils.

To ensure the accuracy of the results, data have been corrected for membrane restraint using the method indicated in the standard procedure ISO 17892-9 (ISO, 2018). On the other hand, the estimation of the final void ratio of soil specimens was carried out by measuring the water content after testing. To obtain reliable measurements of the final water content and then the void ratio after triaxial testing, the end-of-test soil freezing (EOTSF) technique was adopted (Soares & Viana da Fonseca, 2016). A database containing the results of this critical state characterisation has been made available in the form of Supplementary data to this paper.

4.2 CSL results

The results of all drained and undrained loose triaxial tests were analysed and those considered to have reached the critical state were used to define the critical state parameters of the different types of tailings. A slight deviation from linearity was observed at low mean effective stresses (mostly in the coarser materials below 100 kPa); those results were not considered for the definition of the CSL. In turn, for finer materials, a close approximation to linearity was noted, for the full range of stresses representative of the field conditions, used in this study. Figure 10 presents the stress

paths on the $q - p'$ and $e - \log p'$ invariant plane derived from triaxial test results.

From Figure 10a, c and e, it can be observed that all endpoints define a unique critical state line (CSL) in the $q - p'$ plane, which is clearly represented by a straight line passing through the origin. The CSL projections define a strength parameter M_c equal to 1.42, 1.40 and 1.36 for the type 1, 2 and 3, respectively; and the friction angle of shearing resistance at the critical state (ϕ'_{cs}) varies from 34° to 35°. Figure 10b, d and f shows the best-fit CSL in the $e - \log p'$ plane. In this study, the straight-linear approach ($e_{cs} = \Gamma - \lambda_e \ln p'$) was considered the best-fit to describe the behaviour of the different types of tailings. Although Type 3 data exhibits a non-linear critical state locus in the $e - \log p'$ plane, the stresses and relative density states of the curve part of CSL were considered irrelevant in practical engineering applications. The critical state parameters M_c , λ_e and Γ deducted for the different tailings are very well aligned with data for other tailings in reference databases (e.g., Smith et al., 2019).

4.3 Stress-dilatancy behaviour

Dense samples were avoided to define the CSL, as they may not reach the ultimate state, mainly due to the non-uniform sample densities and strains that develop if shear localisation occurs during testing. However, in plasticity-based constitutive models, the dilatancy parameters must be defined. Soil dilatation only considers the plastic volumetric strains because the elastic volumetric strains are very small and, thus, negligible. Therefore stress-dilatancy of dense samples in drained shear is well established as a fundamental aspect of soil behaviour (Been & Jefferies, 2011).

For this purpose, a set of dense samples were tested in drained conditions for each type of tailings. The equipment and procedures used were the same as previously described, except for the preparation method, as

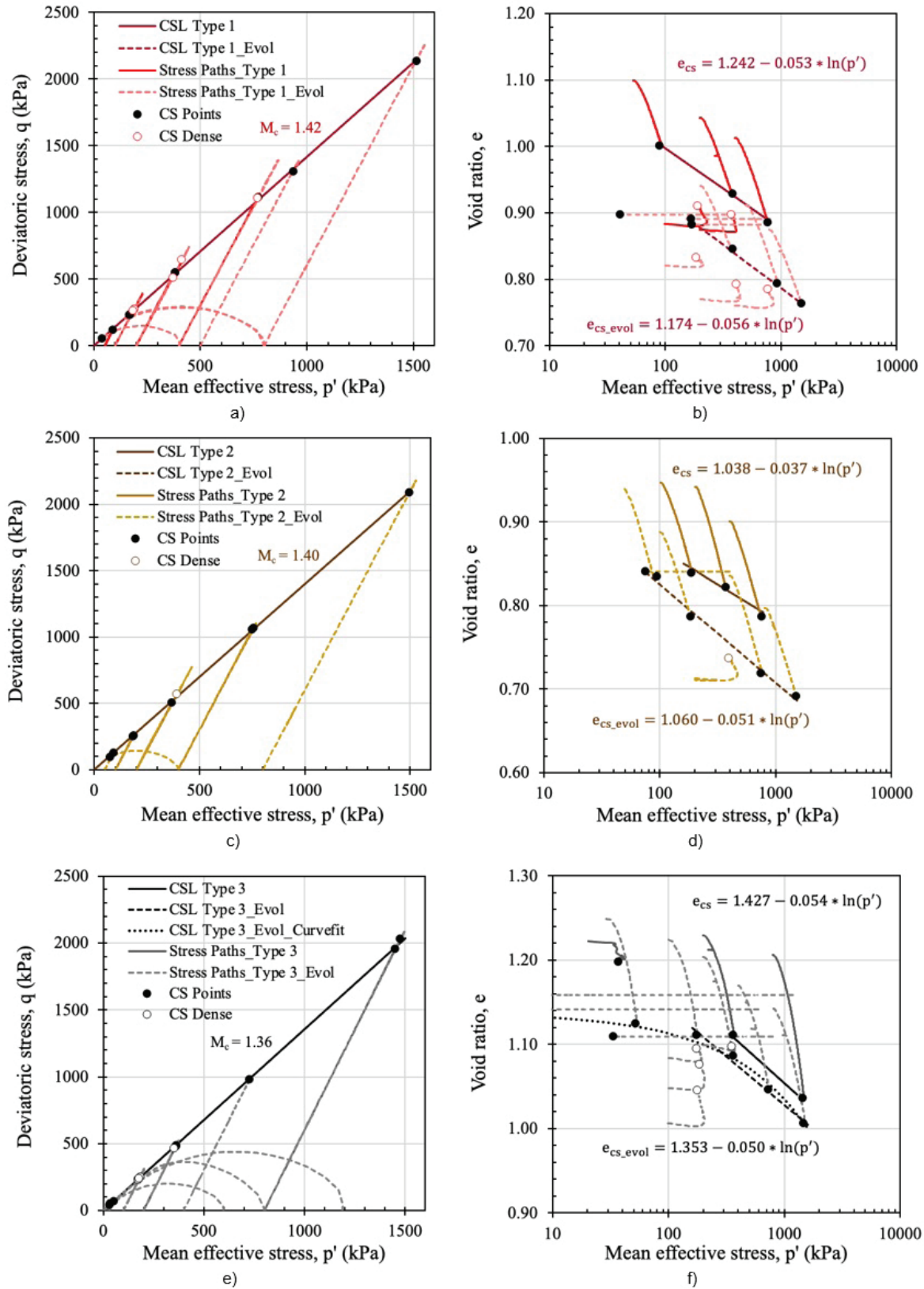


Figure 10. Critical state characteristics: (a) results in p' - q plane of soil Type 1; (b) results in e - $\log p'$ plane of soil Type 1; (c) results in p' - q plane of soil Type 2; (d) results in e - $\log p'$ plane of soil Type 2; (e) results in p' - q plane of soil Type 3; (f) results in e - $\log p'$ plane of soil Type 3.

the samples were statically compacted in a loading frame. The stress-state paths derived from the dense triaxial tests are also represented in Figure 11. Table 4 presents the peak values of deviatoric and mean effective stresses with its corresponding void ratio.

5. Evidences of soil evolution

5.1 Mechanical behaviour evolution

During this experimental program, it became apparent that the behaviour of the three types of tailings evolved, in terms of the CSL positioning in the $e - \log p'$ plane; that is, in terms of compressibility in shear loading. This evolutive behaviour was first observed after high pressure tests (at mean effective stresses above 800 kPa) and, also, after tests on dense samples (statically compacted at very low

void ratios) and can be attributed to two main factors that affect soil particles, namely the evolution of soil grading and of particle morphology (shape and surface roughness). This evolutive behaviour has been previously reported by Bedin et al. (2012) in gold ore tailings.

During consolidation or shear phases, the material may evolve due to particle breakage or crushing. These processes act as a grinder, increasing the fines content and inducing changes in the shape of the particles. The increment of fines content causes additional compressibility and shifts down the CSL position in the $e - \log p'$ plane, while changes of particle shape adjust the critical state parameters M_c , λ_e and Γ . Such effects generate uncertainties in the CSL position.

The evolution in the behaviour of the three types of tailings was only identified in the $e - \log p'$ plane, thus, only affecting λ_e and Γ , not M_c (see Table 5). Therefore, two CSL were defined for each type of tailings, one corresponding to

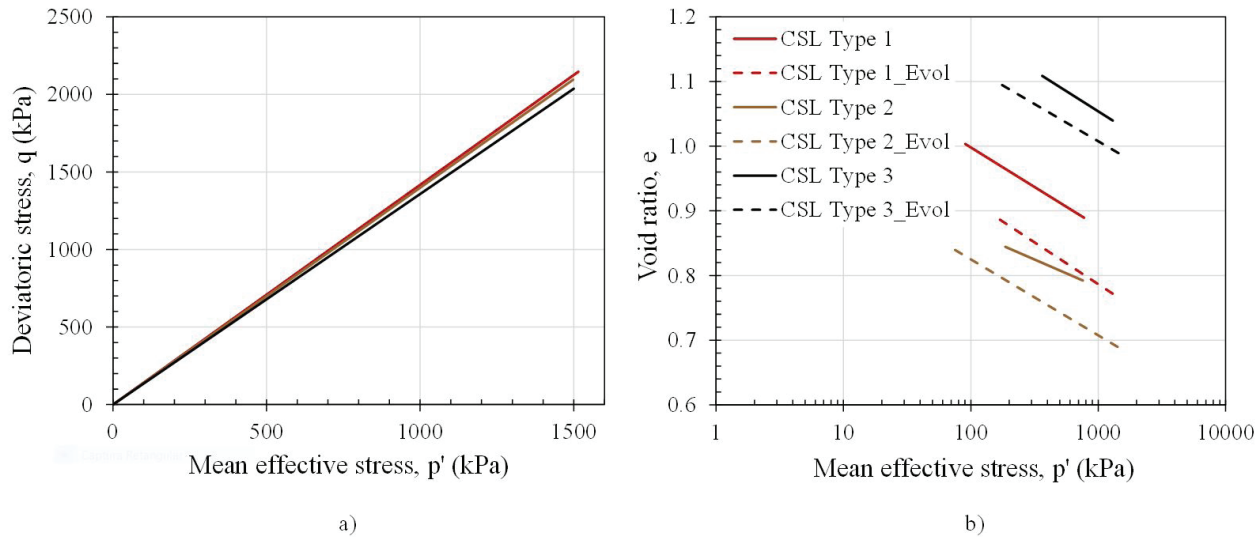


Figure 11. CSL of the three types of tailings in natural and evolved conditions in the: (a) $q - p'$ plot; and (b) $e - \ln p'$ plane.

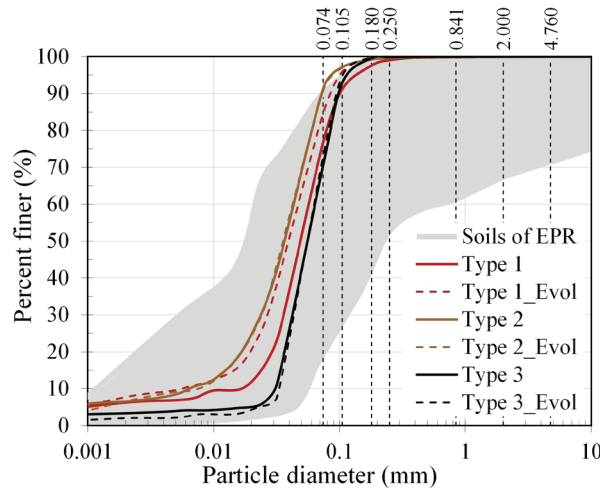
Table 4. Peak values during shearing for the dense tests.

Soil			Peak Values		
Type	Condition	Test ID	p'_{pk} kPa	q_{pk} kPa	e_{pk}
Type 1	Original	Tx_T1_4	229	389	0.89
		Tx_T1_5	414	634	0.87
		Tx_T1_12	217	349	0.82
	Evolved	Tx_T1_13	448	740	0.77
		Tx_T1_14	868	1392	0.77
Type 2	Evolved	Tx_T2_9	465	782	0.72
Type 3	Evolved	Tx_T3_12	194	278	1.08
		Tx_T3_13	204	305	1.06
		Tx_T3_14	205	317	1.01
		Tx_T3_15	375	522	1.09

Table 5. Critical state parameters for the three tailings soil types.

Material	Condition	ϕ'_{cs} (°)	M_c (-)	λ_e (-)	Γ (-)
Type 1	Original	35.0	1.42	0.053	1.24
	Evolved			0.056	1.17
Type 2	Original	34.5	1.40	0.037	1.04
	Evolved			0.051	1.06
Type 3	Original	33.6	1.36	0.054	1.43
	Evolved			0.050	1.35

Note that λ_e represents notation in natural logarithm.

**Figure 12.** Grading curves of the three types of tailings in natural and evolved conditions. Comparison with other soils from Brumadinho dam, according to the Expert Panel Report (EPR) (Robertson et al., 2019).

the natural (original) state and another to the evolved state, as shown in Figure 11.

5.2 Grading evolution

Given the observed changes in soil behaviour, in terms of the critical state parameters, from tests in natural (remoulded) and evolved (reused soil after testing), a series of particle size distribution analyses was performed to assess the effect of crushing (or particle breakage) and the consequent generation of fines, as a result of CSL tests. Figure 12 illustrates the grading evolution of the three types of tailings.

From these results, the evolution of the behaviour in the Type 1 tailing can be attributed to the breakage of particles, which increased the fines content of the sample and consequently the compressibility of this material. However, no significant crushing was observed in Type 2 and Type 3 tailings. Changes in the morphology of the particles can also trigger the evolution of the behaviour of the material (Cho et al., 2006; Yang & Luo, 2015).

5.3 Morphological evolution

The assessment of the changes in particle morphology can be made by the careful observation of microscopic images of the soil in natural (intact) and evolved (after testing) conditions and by the identification of morphology parameters, such as sphericity, convexity, roughness and aspect ratio. For this purpose, scanning electron microscopy (SEM) photographs of the three types of tailings, in natural and evolved conditions, were taken and compared to observe changes in the morphology of the particles. As an example, SEM photos of natural and evolved samples of Types 1 and 3 are shown in Figure 13.

Due to the subjective nature of the visual description, the particle shape of a given soil should be described in quantitative terms such as morphology parameters, and a robust laser scanning technique must be used to make objective and accurate measurements of particle shape. This topic will be addressed in future works.

6. Characterisation in diverse stress-path conditions

6.1 Specific equipment and procedures

Flow liquefaction is a process associated with a pore pressure increase, by which shear strength is reduced as effective stress in the soil approaches zero and is intrinsically related to undrained brittle behaviour of the soil. Only contractive materials have the possibility of undergoing liquefaction. Since the failure of dam B1 involved the phenomenon of flow liquefaction, a proper consideration of the undrained behaviour of the tailing should rely on tests that adopt an initial stress state representative of the in-situ conditions (K_0) and specific stress loading paths occurring in the geotechnical structures. For this purpose, a set of anisotropically consolidated undrained tests were carried out on loose (and even dense samples) to portray the liquefaction, strain softening and strain hardening behaviour of the three tailings. Table 6 summarises the adopted testing program for the undrained behaviour characterisation for the three types of tailings. The correct characterisation of the undrained peak strength is of utmost importance in the

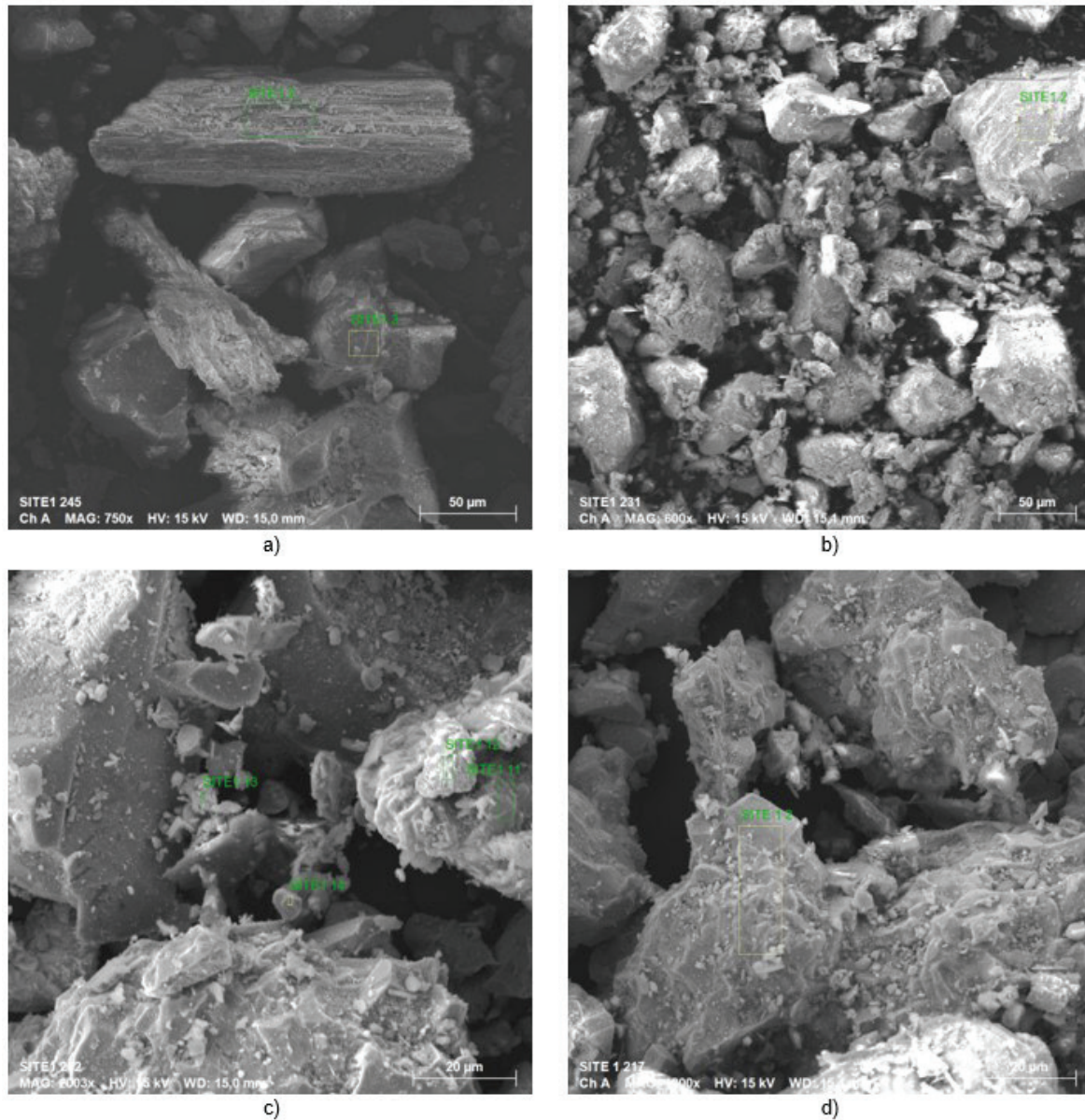


Figure 13. SEM images: Type 1 (a) natural; (b) evolved; Type 3 (c) natural; (d) evolved.

context of stability computations, as it signals the onset of instability (the inability of a soil specimen to sustain a given load or stress).

A fully automated Bishop-Wesley type triaxial apparatus, able to test soil specimens with 50 mm diameter, was used to carry out tests at different stress-path conditions. This triaxial apparatus can independently apply radial and axial stresses under strain or stress control, allowing the soil characterisation under any stress-path combination, representative of the complex behaviour of tailings dams. Besides, it was equipped with piezoelectric transducers for measuring seismic wave velocities (namely P-wave and S-wave) by bender element testing.

The specimens were prepared under very loose conditions (to replicate the deposition process in the tailing dam over the years of operation) using the same techniques previously described. A full saturation condition with B -values higher than 0.98 was achieved applying the same procedures as in the tests performed to reach ultimate critical state. The importance of full saturation is even more pronounced in undrained tests since the development of pore-water pressure strongly depends on the stiffness of the pore fluid. The samples were anisotropically consolidated at different mean effective stresses with a coefficient of lateral earth pressure at rest (K_0) of approximately 0.5. Different undrained shear rates, including strain and stress control, were adopted to assess the effects of loading conditions on the behaviour

Table 6. Summary of the undrained testing program for the three tailings soil types.

Soil		Test ID	Test Type	Preparation State	Consolidation Phase		Shear Phase	
Type	Condition				K_0	p' (kPa)	Type	Rate
Type 1	Original	SP_T1_1	CK ₀ U	Loose	0.5	100	Stress Control (q)	1 kPa/min
		SP_T1_2	CK ₀ U	Loose	0.5	100	Stress Control (q)	1 kPa/min
		SP_T1_3	CK ₀ U	Loose	0.4	200	Stress Control (q)	1 kPa/min
	Evolved	SP_T1_4	CK ₀ U	Dense	0.5	500	Strain Control	0.02 mm/min
		SP_T1_5	CK ₀ U	Loose	0.5	500	Strain Control	0.002 mm/min
		SP_T1_6	CK ₀ U	Loose	0.5	500	Strain Control	0.2 mm/min
		SP_T1_7	CK ₀ U	Loose	0.5	500	Strain Control	0.02 mm/min
Type 2	Original	SP_T2_1	CK ₀ U	Loose	0.5	100	Stress Control (q)	1 kPa/min
		SP_T2_2	CK ₀ U	Loose	0.5	300	Stress Control (q)	1 kPa/min
		SP_T2_3	CK ₀ U	Loose	0.5	400	Strain Control	0.02 mm/min
	Evolved	SP_T2_4	CK ₀ U	Loose	0.5	400	Strain Control	0.002 mm/min
		SP_T2_5	CK ₀ U	Loose	0.5	400	Strain Control	0.2 mm/min
		SP_T2_6	CK ₀ U	Dense	0.5	400	Strain Control	0.02 mm/min
Type 3	Original	SP_T3_1	CK ₀ U	Loose	0.5	50	Stress Control (q)	1 kPa/min
		SP_T3_2	CK ₀ U	Loose	0.5	100	Stress Control (q)	1 kPa/min
		SP_T3_3	CK ₀ U	Loose	0.4	200	Stress Control (q)	1 kPa/min
		SP_T3_4	CK ₀ U	Loose	0.5	100	Stress Control (q)	0.1 kPa/min
	Evolved	SP_T3_5	CK ₀ U	Loose	0.5	100	Strain Control	0.2 mm/min
		SP_T3_6	CK ₀ U	Loose	0.5	100	Strain Control	0.02 mm/min
		SP_T3_7	CK ₀ U	Loose	0.5	100	Strain Control	0.002 mm/min
		SP_T3_8	CK ₀ U	Dense	0.5	100	Strain Control	0.02 mm/min

Legend: CK₀U – anisotropic consolidated undrained tests.

of the studied soils, as referred in Table 6. The estimation of the final void ratio of soil specimens was carried out by measuring the water content after testing, however EOTSF was not used in the tests conducted in the Bishop-Wesley triaxial apparatus because of the handling of these heavy cells and to avoid damage to the BE. For these tests, the specimens were carefully removed from the cell, avoiding possible loss of soil particles and water (Verdugo & Ishihara, 1996), which –if used correctly– may be equally accurate to the EOTSF (Viana da Fonseca et al., 2021). A database containing the results of this advanced experimental program is also available in the form of Supplementary data to this paper.

6.2 Undrained anisotropic behaviour

The stress and state paths of the test performed to assess the undrained behaviour are presented in Figure 14.

In this testing program, all loose samples exhibit positive pore water pressure, revealing the tendency to contractive response over a wide range of confining pressures, as for the dense samples, a stable behaviour was observed. Some of the loose samples presented full liquefaction, with the

annulment of the mean effective stress and deviator stress, while others suffered severe strain softening but with not full liquefaction (i.e., zero effective stress), as a stable critical state is reached. In practice, both instability mechanisms would lead to catastrophic results. The undrained tests featured on Figure 14 highlighted the undrained brittleness in the tailings.

The peak strength points for those samples who experienced instability mechanisms allowed the definition of the instability line (IL) in the $q - p'$ plane. The stress ratio

$$(\eta_{pk} = \frac{q_{pk}}{p'_{pk}})$$

at which peak is reached is about 0.93, 0.94 and 0.89 for the tailing type 1, 2 and 3, respectively. The uniqueness of the instability line in the stress invariant plane is assumed for each soil, and while these criteria have proven useful for limit equilibrium calculations, it is difficult to implement as calibration constraints in the context of numerical modelling (Mánica et al., 2021). From an implementation standpoint, the

normalised undrained strength ratio $S_p = \frac{s_{u,pk}}{p'_0}$ is preferred.

It offers a good template description of undrained peak strength in materials exhibiting static liquefaction and is the

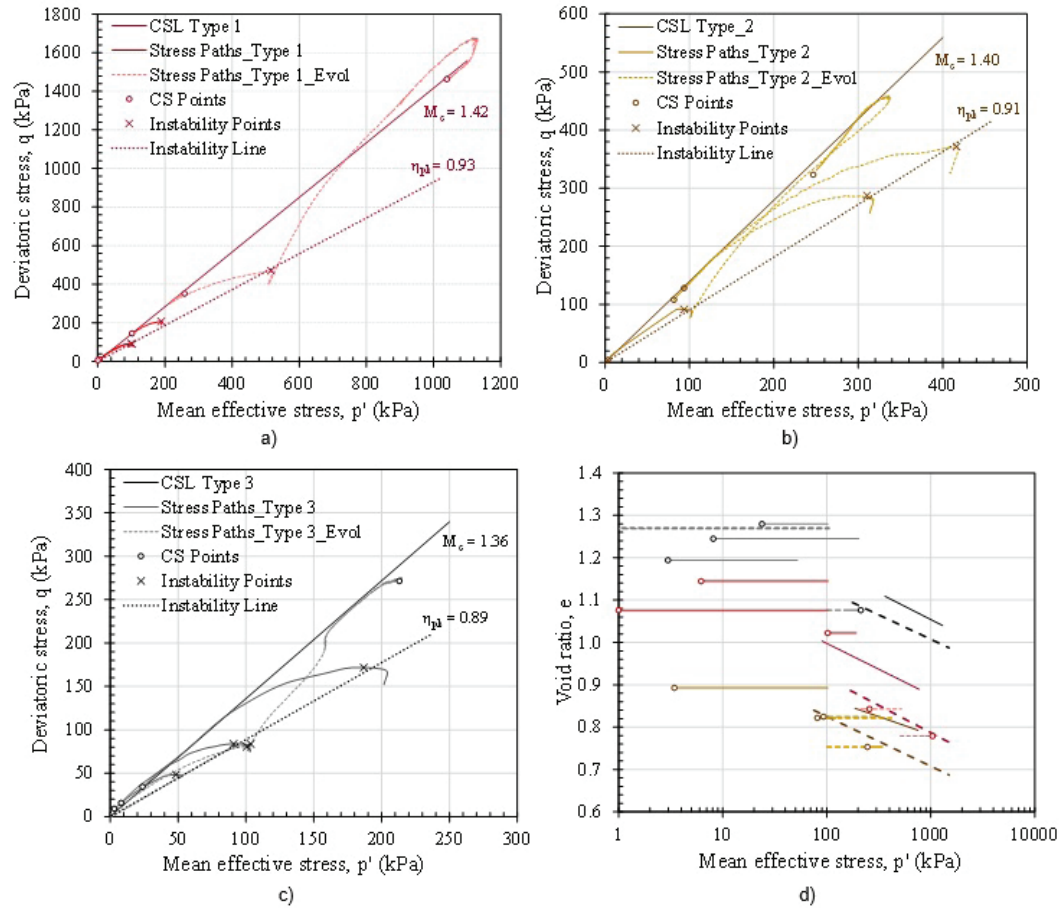


Figure 14. Undrained paths on the $q - p'$ and $e - \log p'$ plane for the different type of tailings.

reason between the peak undrained strength ($s_{u, pk} = \frac{q_{pk}}{2}$) and the mean effective stress after soil consolidation (p'_o).

Figure 15 shows the relationships between the undrained peak strength and the consolidation mean effective stress derived from the undrained triaxial compression tests that exhibit instability mechanisms. The undrained isotropic consolidated tests presented in the CSL section were also added for comparison. The interesting aspect is that the normalised undrained strength ratio did not depend on the type and condition of the soil but on the consolidation path, presenting much larger values of S_p for anisotropic consolidation than for isotropic. The underlying reason is that soil fabric is strain-path dependent (Fourie & Tshabalala, 2005). S_p is dependent on the fabric associated with anisotropy and particle orientation.

The figure clearly shows that the undrained peak strength ratio towards mean effective stress $[(q/p')_p]$ when starting from isotropic consolidation stresses ($K = \sigma'_{ho}/\sigma'_{vi} = 1$) is considerably lower, about half, that at anisotropic consolidation stresses ($K_0 = \sigma'_{ho}/\sigma'_{vo}$, in this case assumed equal to 0.5). Thus, the at rest consolidation condition, assumed representative, should be considered for the modelling of TSF since the maximum undrained strength, which indicates the onset of soil instability,

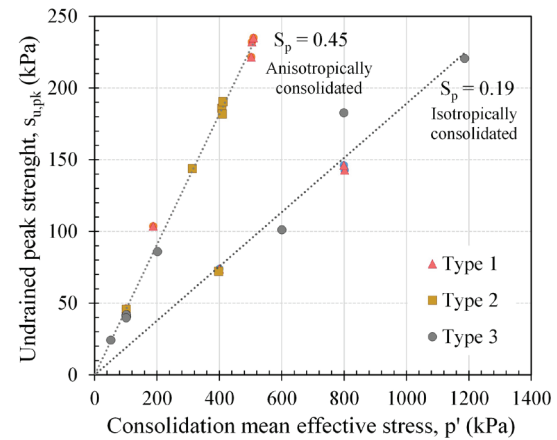


Figure 15. Relation between peak undrained strength and pre-shear consolidation stresses.

depends on the in-situ coefficient of earth pressure at rest (among other factors like stress rotation - see Reid et al., 2022). This also demonstrates the distinct effect of induced stress-anisotropic consolidation conditions on soil behaviour, which has design implications both in limit equilibrium calculations, especially when conducted in effective stresses analyses

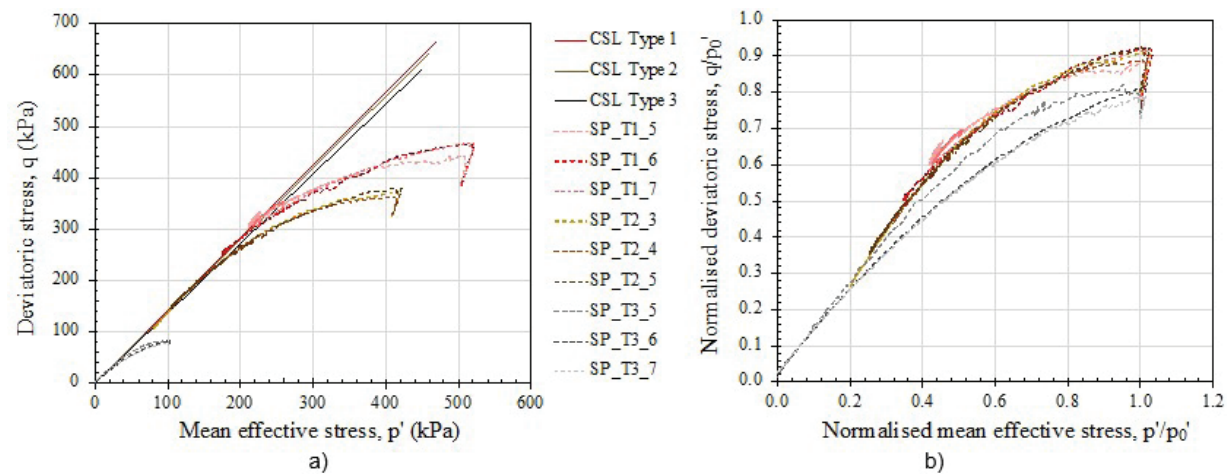


Figure 16. Assessment of stress-strain dependency on the different tailing types.

(Fourie and Tshabalala, 2005), and in the assessment of soil state. In modelling the behaviour of these fragile soils, the resulting undrained peak strength will depend on the specific path by which the failure criterion is attained (Mánica et al., 2021). Studies are progressing for clarification of these factors.

6.3 Assessment of creep or stress-strain dependency

To evaluate creep behaviour, strain rate effects on the tailings were systematically measured in the different reconstituted materials using strain-rate controlled triaxial tests. For this effect, three triaxial specimens of each material under the same consolidation state (density and confining pressure) were sheared, in which the undrained strain rate was systematically varied in a magnitude order of 10%. This set of tests is identified in Table 6 as SP_T1_5, SP_T1_6 and SP_T1_7 for Type 1; SP_T2_3, SP_T2_4 and SP_T2_5 for Type 2; and SP_T3_5, SP_T3_6 and SP_T3_7 for Type 3.

The tests results are presented in Figure 16. The observed effect is equivalent to a change in undrained strength of 2% per order of magnitude change in strain rate. This experimental result suggests that the magnitude of measured strain-rate effects on the tailings was always small and did not anticipate a large role for viscous effects (or “creep”) in the failure.

The experimental result shown in Figure 16 suggests that the magnitude of measured strain-rate effects on the tailings was always small and did not anticipate a large role for viscous effects (or “creep”) in failure.

7. Conclusions

This paper described the experimental forensic characterisation of Brumadinho B1 tailings dam, a case history, which suddenly failed on January 25th of 2019 in Minas Gerais (Brazil). This detailed characterisation comprised an advanced experimental programme using reconstituted samples of three representative soils from Brumadinho B1 tailings dam.

All tests presented herein were carried out in the Geotechnical Laboratory of the Civil Engineering department at the Faculty of Engineering of the University of Porto (Portugal). The results provided the physical, hydraulic, and mechanical parameters for conducting numerical simulations of the soil behaviour using constitutive models based on Critical State Soil Mechanics with Instability Locus.

The outcomes of the programme are summarised as follows.

- Representative typological classes of soils considered representative of the tailings stored in the dam were defined for this research. This selection included a quantitative procedure based on the analysis and comparison of particle size distribution and specific gravity of solid particles results, leading to three clusters with diverse iron and fines contents;
- An evolution of the mechanical behaviour of the studied tailings was observed in the three studied tailings. The evolution of the soil behaviour caused additional compressibility –represented by a shift down of CSL in the $e - \log p'$ plane. However, it did not affect the friction angle of shearing resistance at the critical state. Such an evolution was attributed to changes in the morphology of soil particles and grain size distribution after triaxial testing, as evidenced in Figure 12 and 13;
- From the undrained tests, an instability line was inferred for each soil. However, a comparison between experimental results of isotropic and anisotropic tests revealed higher values of undrained shear strength for the soil specimens consolidated for K_0 of about 0.5. This indicates that there is a significant effect of soil anisotropy on the undrained behaviour of iron tailings from the Brumadinho B1 dam;
- Tests conducted using a systematic combination of shear rates under strain and stress control revealed very similar shear-strain characteristics for all studied

soils. Therefore, negligible viscous effects or “creep” have been observed in the mechanical behaviour of these geomaterials.

Acknowledgements

Acknowledgements are especially due to Prof. Marcos Arroyo and Prof. Antonio Gens, from CIMNE, who were directly involved in the definition of the lab tests to define the necessary constitutive parameters for the models used in the numerical analyses. This was done under a contract between CIMNE and VALE, SA, under a Term of Cooperation of the Federal Public Prosecutor’s Office, (MPF). FEUP, as partner of CIMNE, acknowledges VALE’s collaboration in the field and MPF support, namely in the sampling campaigns. For these, we owe a special and personal acknowledgement to Dr. Sebastião Oliveira (MPF) and Ing. Leonardo Mesquita (PF) for their commitment in organising, executing and illustrating the field work, which enabled the challenging work of collecting the representative samples and their transport to LabGEO in safe conditions, as attested by VALE, SA, officers. A friendly recognition to Prof. Antonio Mendonça of the Federal University of Minas Gerais (BH), for a precious and continuous dedication to sampling and conditioning works, especially in the 2nd and 3rd campaigns. The experimental work in FEUP and the interpretation of the results was financially supported by the referred contract between CIMNE and VALE, and, as agreed with MPF, was also part of the research activities of CONSTRUCT– Institute of Research and Development (R&D) in Structures and Construction, funded by national funds through the FCT/MCTES (PIDDAC), with the Base Funding –UIDB/04708/2020.

Declaration of interest

Not applicable due to absence of conflicting interests.

Authors’ contributions

António Viana da Fonseca: Conceptualisation, Methodology, Validation, Investigation, Resources, Data Curation, Writing - Original Draft & Review, Supervision, Project administration and Funding acquisition. Diana Cordeiro: Conceptualisation, Methodology, Formal analysis, Investigation, Data Curation, Writing - Review & Editing, Visualisation. Fausto Molina-Gómez: Conceptualisation, Formal analysis, Investigation, Visualisation, Writing – review & editing. Davide Besenon: Formal analysis, Investigation, Data Curation, Writing – review & editing. António Fonseca: Methodology, Investigation, Data Curation, Writing, Visualisation. Cristiana Ferreira: Formal analysis, Visualisation, Writing – review & editing.

List of symbols

e	void ratio
e_0	initial void ratio
e_{cs}	critical state void ratio
e_{pk}	void ratio at the peak value of maximum dilation
k	coefficient of hydraulic conductivity
p'_0	mean effective stress of consolidation
p_{pk}	mean effective stress at the peak value of maximum dilation
q	deviatoric stress
q_{pk}	peak deviatoric stress
$s_{u, pk}$	peak undrained shear strength
ASTM	American Society for Testing and Materials
B	Skempton’s pore pressure coefficient
BE	Bender Elements
Bq	pore-pressure index
Cc	compressibility index
CIAEA	Extraordinary Independent Consulting Committee for Investigation
CIMNE	International Centre for Numerical Methods in Engineering
CID	Isotropic consolidated drained tests
CIU	Isotropic consolidated undrained tests
CK_0U	Anisotropic consolidated undrained tests
CO_2	Carbon Dioxide
CPTu	Piezcone Penetration Test
Cr	Recompressibility index
Cs	Expansion index
CSL	Critical State Locus
CSSM	Critical State Soil Mechanics
C_u	coefficient of uniformity
EOTSF	End-of-test soil freezing
EPR	Expert Panel Technical Report
FC	Fines Content
FEUP	Faculty of Engineering of the University of Porto
G_s	Specific gravity of solid particles
I_c	Soil behaviour type index
ID	Identification
IL	Instability Locus
ISO	International Organisation for Standardisation
K_0	Coefficient of earth pressure at rest
LabGEO	Geotechnical Laboratory of the Civil Engineering Department at FEUP
LiDAR	Laser imaging, Detection, and Ranging
M_c	Slope of critical state locus in q - p' plane in compression
MG	Minas Gerais
MPF	Federal Public Prosecutor’s Office
N	Intercept of normal compression line in e - $\log p'$ plane
p'	Mean effective stress
PSD	Particle Size Distribution
SBT	Soil Behaviour Type
SDMT	Seismic Flat Dilatometer Test
SEM	Scanning Electron Microscopy

S_p	Normalised undrained strength ratio
TSF	Tailings Storage Facility
UFMG	Federal University of Minas Gerais
U_n	Percent of undercompaction
UPC	Universitat Politècnica de Catalunya
V_p	P-wave velocity
V_s	S-wave velocity
ϕ'_{cs}	Friction angle at the critical state
ϕ'_{pk}	Peak friction angle
κ	Slope of unloading–reloading line in e -log p' plane
λ_e	Slope of normal compression line / slope of critical state line in e -log p' plane
η_{pk}	Stress ratio at peak undrained strength
σ'_v	Vertical effective stress
ψ	State parameter
Γ	Intercept of critical state line in e -log p' plane

References

- Bedin, J., Schnaid, F., Viana da Fonseca, A., & de Costa Filho, L.M. (2012). Gold tailings liquefaction under critical state soil mechanics. *Geotechnique*, 62(3), 263–267. <http://dx.doi.org/10.1680/geot.10.P.037>.
- Been, K., & Jefferies, M. (2011). Stress-dilatancy in very loose sand. *Canadian Geotechnical Journal*, 41(5), 972–989. <http://dx.doi.org/10.1139/T04-038>.
- Cho, G.-C., Dodds, J., & Santamarina, J.C. (2006). Particle shape effects on packing density, stiffness, and strength: natural and crushed sands. *Journal of Geotechnical and Geoenvironmental Engineering*, 132(5), 591–602. [http://dx.doi.org/10.1061/\(ASCE\)1090-0241\(2006\)132:5\(591\)](http://dx.doi.org/10.1061/(ASCE)1090-0241(2006)132:5(591)).
- CIMNE (2021). *Computational analyses of Dam I failure at the Corrego de Feijao mine in Brumadinho – Final Report*. Retrieved in February 4, 2022, from <http://www.mpf.mp.br/mg/sala-de-imprensa/docs/2021/relatorio-final-cinme-upc-1>
- Ferreira, C., Díaz-Durán, F., Viana da Fonseca, A., & Cascante, G. (2021). New approach to concurrent VS and VP measurements using bender elements. *Geotechnical Testing Journal*, 44(6), 1801. <http://dx.doi.org/10.1520/GTJ20200207>.
- Fourie, A.B., & Tshabalala, L., (2005). Initiation of static liquefaction and the role of K0 consolidation. *Canadian Geotechnical Journal*, 42(3), 892–906. <https://doi.org/10.1139/t05-026>.
- ISO 17892-3. (2015). *Geotechnical investigation and testing — Laboratory testing of soil — Part 3: Determination of particle density*. International Organisation for Standardisation.
- ISO 17892-4. (2016). *Geotechnical investigation and testing — Laboratory testing of soil — Part 4: Determination of particle size distribution*. International Organisation for Standardisation.
- ISO 17892-5. (2017). *Geotechnical investigation and testing — Laboratory testing of soil — Part 5: Incremental loading oedometer test*. International Organisation for Standardisation.
- ISO 17892-9. (2018). *Geotechnical investigation and testing — Laboratory testing of soil — Part 9: Consolidated triaxial compression tests on water saturated soils*. International Organisation for Standardisation.
- Jefferies, M., & Been, K. (2016). *Soil liquefaction: a critical state approach* (2nd ed.). CRC Press.
- Ladd, R. (1978). Preparing test specimens using undercompaction. *Geotechnical Testing Journal*, 1(1), 23. <http://dx.doi.org/10.1520/GTJ10364J>.
- Mánica, M.A., Arroyo, M., Gens, A., & Monforte, L. (2021). Application of a critical state model to the Merriespruit tailings dam failure. *Proceedings of the Institution of Civil Engineers – Geotechnical Engineering*. [ahead of print]. <https://dx.doi.org/10.1680/JGEEN.21.00001>.
- Molina-Gómez, F., & Viana da Fonseca, A. (2021). Key geomechanical properties of the historically liquefiable TP-Lisbon sand. *Soil and Foundation*, 61(3), 836–856. <http://dx.doi.org/10.1016/J.SANDF.2021.03.004>.
- Reid, D., Dickinson, S., Mital, U., Fanni, R., & Fourie, A. (2022). On some uncertainties related to static liquefaction triggering assessments. *Proceedings of the Institution of Civil Engineers – Geotechnical Engineering*. [ahead of print]. <https://doi.org/10.1680/jgeen.21.00054>.
- Reid, D., Fourie, A., Ayala, J.L., Dickinson, S., Ochoa-Cornejo, F., Fanni, R., Garfias, J., Viana da Fonseca, A., Ghafghazi, M., Ovalle, C., Riemer, M., Rismanchian, A., Olivera, R., & Suazo, G. (2021). Results of a critical state line testing round robin programme. *Geotechnique*, 71(7), 616–630. <http://dx.doi.org/10.1680/JGEOT.19.P.373>.
- Robertson, P.K., & Wride, C.E. (1998). Evaluating cyclic liquefaction potential using the cone penetration test. *Canadian Geotechnical Journal*, 35(3), 442–459. <http://dx.doi.org/10.1139/t98-017>.
- Robertson, P.K., de Melo, L., Williams, D.J., & Wilson, G.W. (2019). *Report of the expert panel on the technical causes of the failure of Feijão Dam I*. Retrieved in February 4, 2022, from <http://www.b1technicalinvestigation.com/>
- Santamarina, J.C., Klein, K.A., & Fam, M.A. (2001). *Soils and waves*. J. Wiley & Sons.
- Smith, K., Fanni, R., Chapman, P., & Reid, D. (2019). Critical state testing of tailings: comparison between various tailings and implications for design. In *Proceedings of Tailings and Mine Waste* (pp. 1183–1195). Vancouver.
- Soares, M., & Viana da Fonseca, A. (2016). Factors affecting steady state locus in triaxial tests. *Geotechnical Testing Journal*, 39, 1056–1078. <http://dx.doi.org/10.1520/GTJ20150228>.
- Verdugo, R., & Ishihara, K. (1996). The steady state of sandy soils. *Soil and Foundation*, 36(2), 81–91. http://dx.doi.org/10.3208/sandf.36.2_81.
- Viana da Fonseca, A., Cordeiro, D., & Molina-Gómez, F. (2021). Recommended procedures to assess critical state locus from triaxial tests in cohesionless remoulded

- samples. *Geotechnics*, 1, 95-127. <http://dx.doi.org/10.3390/GEOTECHNICS1010006>.
- Viana da Fonseca, A., Ferreira, C., & Fahey, M. (2009). A framework interpreting bender element tests, combining time-domain and frequency-domain methods. *Geotechnical Testing Journal*, 32(2), 91-107. <http://dx.doi.org/10.1520/GTJ100974>.
- Yang, J., & Luo, X.D. (2015). Exploring the relationship between critical state and particle shape for granular materials. *Journal of the Mechanics and Physics of Solids*, 84, 196-213. <https://doi.org/10.1016/J.JMPS.2015.08.001>.

Supplementary data

All data reported in this paper is fully available as supplemental material at the following locations: <https://s.up.pt/jvo1> and <https://s.up.pt/m13m>

Automated true triaxial apparatus development for soil mechanics investigation

Dionatas Hoffmann Andreghetto^{1#} , Lucas Festugato² ,

Gustavo Dias Miguel² , Andressa da Silva² 

Article

Keywords

True triaxial apparatus
Soil stabilization
Cemented fine sand
Triaxial tests

Abstract

Soil mechanical fully understanding requires considering a three dimensional approach, including soil response under the second principal stress and its potential anisotropy. In order to achieve such soil mechanical understanding, a true triaxial apparatus might be used. Therefore, in the present research an automated true triaxial apparatus was developed comprising its cubical cell, data acquisition and stress control systems. The manufactured apparatus was validated by means a laboratory test campaign where true triaxial test responses were compared to standard drained triaxial tests. True triaxial and standard drained triaxial tests were carried out on both naturally and artificially cemented soils. Results were gathered and compared. A soil mechanical compatibility was observed when test results of the newest true triaxial equipment were compared to test results obtained from a well validated standard triaxial apparatus. Thereby, the present paper reports an affordable successful true triaxial apparatus development demonstrating its efficiency for regular soil mechanical tests. Finally, a full stress rosette was established for a uniform fine sand where some small anisotropy was detected.

1. Introduction

The true triaxial apparatus (TTA) was developed to study the influence of the second normal stress on soil and rock samples and can be divided in three main types according to the boundaries state conditions. Among the possibilities, the soil sample-pressure interface might be rigid or flexible, as well as a mix between rigid and flexible boundaries may also be used. Hambly (1969) reported a rigid boundary true triaxial development, which consisted of a cubic chamber composed by six metal plate faces. Metal plate faces were driven by mechanical transducers and were responsible to apply displacements to the soil samples located in the cubic chamber core. The rigid plate faced TTA type are in general characterized to be a strain-controlled apparatus, where rigid plate faces incrementally apply strains on the soil or rock samples, thence, the three principal stresses might be in fact described as response variables. Strain-controlled TTA is indicated to investigate samples post peak behavior, which might be seen in most of the geotechnical apparatuses, such as standard triaxial (ST), direct simple shear and hollow cylinder devices. Nonetheless, some concerns have risen regarding strain-controlled TTA apparatus, namely, the equipment inability to apply uniform stresses on each sample

face, which may lead to stress concentration in some sample points. Strain-controlled TTA apparatuses can be found in several works such as Airey & Wood (1988), Ibsen & Praastrup (2002), Matsuoka et al. (2002) and Ismail et al. (2005). Alternatively, a flexible boundary TTA type can also be implemented, being them stress-controlled apparatus and, thus, having the main advantage of uniform stress application. In this type of TTA the principal stresses are applied by a flexible intermediating medium such as rubber membranes also known as cushions, which are responsible to create the sample-pressure interface. The flexible boundary TTA type is also found in numerous works such as Ko & Scott (1967), Sture & Desai (1979), Sivakugan et al. (1988), Reddy et al. (1992), Sadek (2006) and Choi et al. (2008). Finally, the last possibility concerns the combination of both rigid and flexible designs, which results in a mixed or hybrid TTA type. Therefore, the mixed or hybrid TTA type may have some rigid faces as well as some flexible faces. In general, this TTA type is composed by rigid faces and flexible faces comprising the cubical faces. Thereby, a mix of strain and stress-controlled interfaces might be expected, thus, combining both main advantages and disadvantages of each TTA types. In this scenario, works with rigid-rigid-flexible boundaries have been found such as Alshibli & Williams (2005),

[#]Corresponding author. E-mail address: dionatas@ufmt.br

¹Universidade Federal de Mato Grosso, Barra do Garças, MS, Brazil.

²Universidade Federal do Rio Grande do Sul, Porto Alegre, RS, Brazil.

Submitted on November 15, 2021; Final Acceptance on March 24, 2022; Discussion open until August 31, 2022

<https://doi.org/10.28927/SR.2022.077321>



This is an Open Access article distributed under the terms of the Creative Commons Attribution License, which permits unrestricted use, distribution, and reproduction in any medium, provided the original work is properly cited.

AnhDan et al. (2005), Penumadu & Prashant (2005), Yin et al. (2009) and Hoyos et al. (2010). In addition, a rigid-flexible TTA boundary configuration can also be seen in works like Shibata & Karube (1965), Sutherland & Mesdary (1969), Lade & Duncan (1973), Lade (1978), Michelis (1988), Silvestri et al. (1988) and Kirkgard & Lade (2011). On the other hand, Sture & Desai (1979), Jamiolkowski et al. (1985), Arthur (1988), Sadek (2006) and Yin et al. (2009) have compared the aforementioned TTA types, describing the advantages and disadvantages of each one.

Therewith, the current paper aims to present a laboratory manufactured TTA. The manufactured TTA described hereafter was developed in the Laboratory of Geotechnical and Geoenvironmental Engineering at the Federal University of Rio Grande do Sul and comprises a mixed or hybrid TTA stress controlled. In this case, the manufactured TTA was set with three flexible faces and three rigid or fixed faces. Nonetheless, on the contrary of some previous works, these rigid faces do not move against the soil sample, serving only as a reaction frame against the flexible face. Silvani (2017) and Silvani et al. (2022) have already reported a similar TTA design, which has been adopted in order to avoid some sample translation movement. Summarizing, the manufactured TTA developed herein might be applied to test ordinary soil samples including natural soils, stabilized soils and weak or lightly cemented rocks that possess a peak strength lower than 1 MPa.

2. The manufactured true triaxial components

The new manufactured True Triaxial Apparatus (TTA) is composed by the main hardware, namely, the data acquisition

device plus the actuation control, a cubical cell, rubber cushions and the monitoring and controlling software. Each TTA component will be described in the sequence. In a first view, Figure 1 depicts a succinct description of the whole TTA components. A user-computer interface (algorithm) was developed based on the LabVIEW® 2013 Software where the user is able to control the TTA. The specimens pressurizing system was made by two Actuator controller Arduinos (AcA), which are responsible for commanding three sets of stepper motors coupled to three manual precision pressure valves. Sample pressure state and displacement response are acquired by three Pressure Transducers (PT) and nine Linear Variable Differential Transducers (LVDT), respectively. In this case, each face or axis is composed by one PT and three LVDTs.

2.1 Cubic cell

The cubic cell was designed to test soils and weak rocks cubic samples, 100 mm edges, at a maximum applied pressure of 1 MPa. It uses the same configuration of the work seen in Reddy et al. (1992) and Sadek (2006), however, instead of stainless steel, it was manufactured in aluminum and age treated. Each of its six faces openings are coupled with flexible or rigid caps. For the flexibles faces, a silicon rubber cushion is placed in direct contact with the sample and it is touched by a set of three LVDTs, which are fixed by a 3D plastic printed support that is bolted to the “top hat” cap. The sealing is made through the straining of the cushion between the “top hat” and the cubic cell. In the opposing end of the cap, three holes were made to install the pressure transducer, the air supply and the wiring of the LVDTs. On each opposing face of the flexible faces, a rigid cap was placed as a reaction to the pressure applied in the cushions/sample.

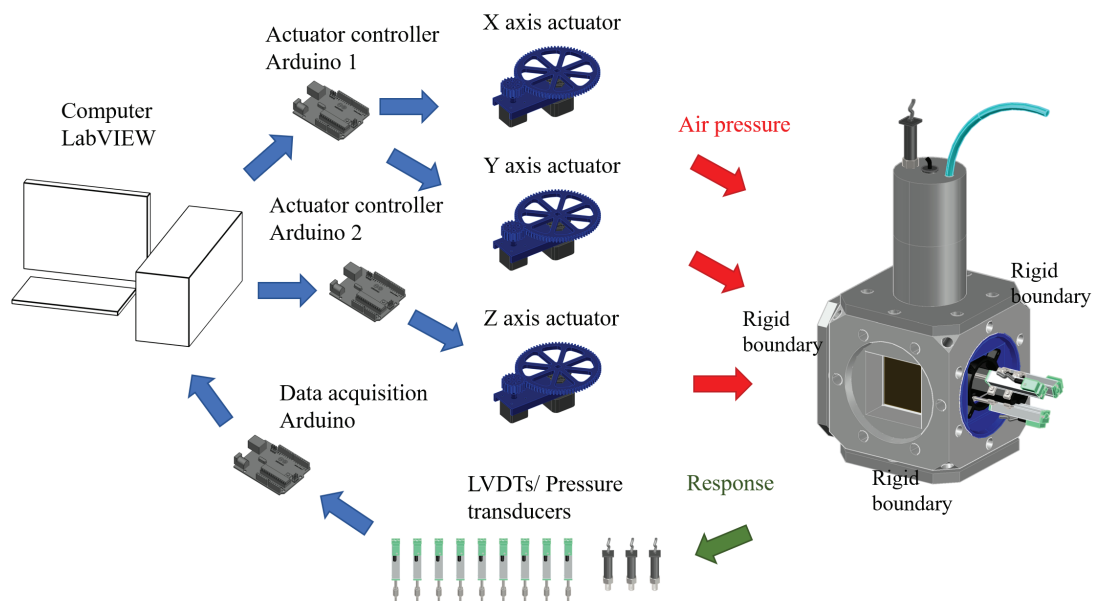


Figure 1. TTA schematic.

In two opposing corners of the cell cube drainage holes were drilled to enable water percolation and to release any generated pore pressure during the test and, in future developments, to allow the control of back pressure. On the other six corners of the cube, installation holes were drilled, that at the time of this work are not in use. An isometric view of the cell can be seen in Figure 2. In Figure 3, all the elements of the “top hat” cap are presented in a sliced view, where LVDTs wiring is omitted. In Figure 4, it is exhibited the LVDTs fixed in the support, the “top hat” and the assembled set. In Figure 5 an isometric view of the rigid cap is represented.

2.2 Silicon rubber cushions

The silicon rubber cushions were manufactured by the authors with Redelease's RX32 high resistance silicon rubber, utilizing 3% of the catalyzer provided by the manufacturer. The process consisted of weighting 300 g of the pre-polymer and 9 g of the catalyzer and mixing both components until homogeneity was achieved. The mixture was vacuumed for 15 min, while the mold was cleaned of any vestiges of previous cushion and an unmolding agent was sprayed over all surfaces. The mixture was poured in the mold the cap was bolted and the cushion was cured for 24 h. Afterwards, the cushion was removed from the mold and cured for six days until the full mechanical properties were achieved. In the fifth day, with a 3D printed template, small magnets were fixed with silicon glue aiming to facilitate the correct positioning of LVDTs fixating points as seen in Figure 6. The mold, cap and a finished cushion are presented in Figure 7. The mold and the cap were machined in aluminum and age treated.

2.3 Data acquisition and transducers

The bridge between the analog signal from the pressure transducers and LVDTs was provided by a digital converter. Three Adafruit ADS 1115 analog to digital converters were used. For greater noise control, each transducer had its own power supply, coupling LM7805 voltage regulators and 100 μ F capacitors. The digital signal was captured by an Arduino Nano microcontroller and sent to the computer via monitoring software. The communication between the Arduino and LabVIEW was made by serial port via USB. The LVDTs were purchased from Lemaq Automação. They are compatible with the Gefran PY-2-C-050, having 50 mm of course, potential difference output up to 5 V and infinite resolution. Coupled with the ADS 1115, the sensibility achieved in the LVDTs was 0,00152 mm, limited by the 15 bits resolution of the digital converter in single comparison. The PT purchased were Ashcroft k1 050 0-150 psi. When connected to the digital converter, they achieved the resolution of 0.5 kPa. All electronic components were purchased, but the circuit was manufactured, designed and Arduino coded by the authors. Figure 8 schematically presents the data acquisition system.

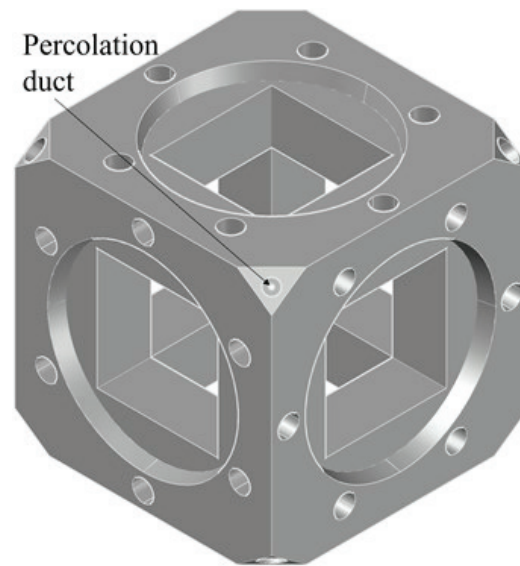


Figure 2. Cubic cell.

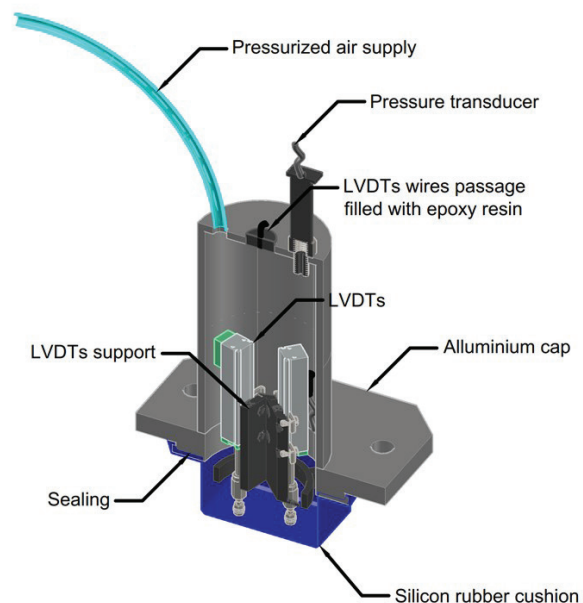


Figure 3. Sliced view of “top hat” cap.

2.4 Actuators

To control the compressed air pressure, three Norgren 11-018-110 precision pressure regulator valves were purchased. Those valves were coupled with NEMA 17 stepper motors with a pair of 3D printed gears and a base, enabling the automatic pressure control when the stepper motors were activated. The gears were fixed with epoxy resin in the handler of the valve and the stepper motor axis. All the described items are indicated in Figure 9.

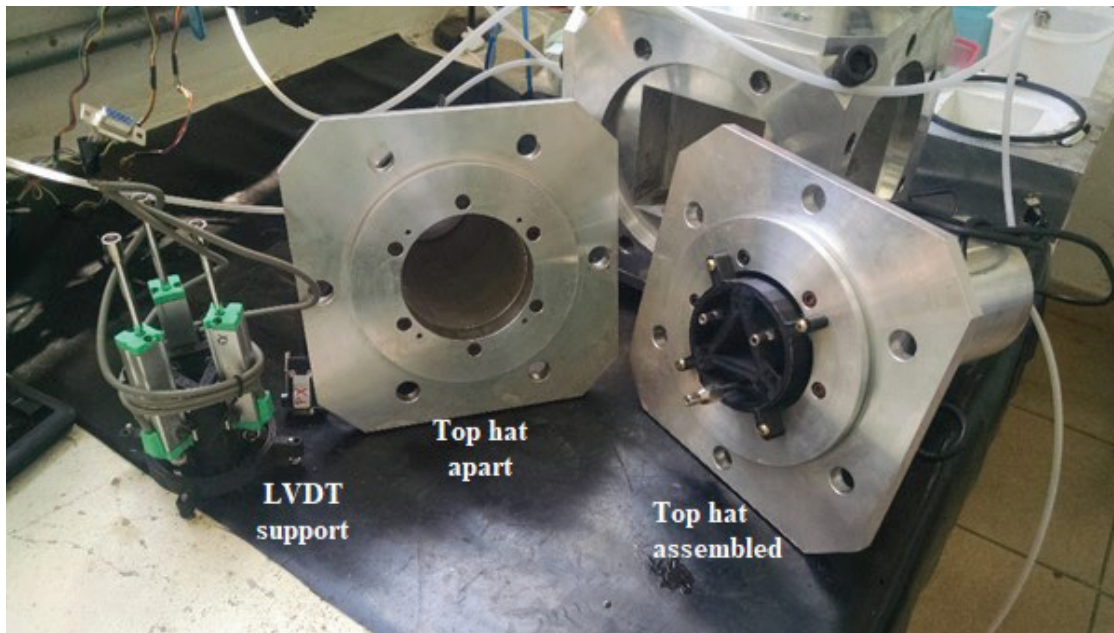


Figure 4. LVDT support (left) and top hat apart (center) and assembled (right).

The gears ratio has both the function of increasing the torque and to decrease the revolution by step of the motors. Aiming to control them, two Arduino Uno microcontroller sets and L298 motor shield were purchased. To power the shield, an external computer power supply with 300 W and 12 V was used. Since each motor shield can be used to control up to two stepper motors, its required at least two Arduinos. The communication between the Arduinos and LabVIEW was achieved by a serial port via USB. All the 3D printing, design, assembly and coding were made by the authors and the electronics components were purchased. The total cost of device consisting of machining of the aluminum parts, electro-mechanic, hydraulic and transducers was around 6500 USD at purchased time.

2.5 Monitoring and controlling software

To perform the monitoring and controlling of the apparatus, a software was developed in LabVIEW. Since LabVIEW does not support natively the communication between itself and Arduino, the code was first needed to be written, since only some libraries with basic Arduinos functions as analog read or digital write are available. The final code was achieved using the serial communication protocol, so the computer could communicate with each Arduino using different serial ports. The proceeding modules were developed as consolidation and shearing.

3. Apparatus validation

To assess the performance of the apparatus, a series of tests was made. Two types of soils, with and without

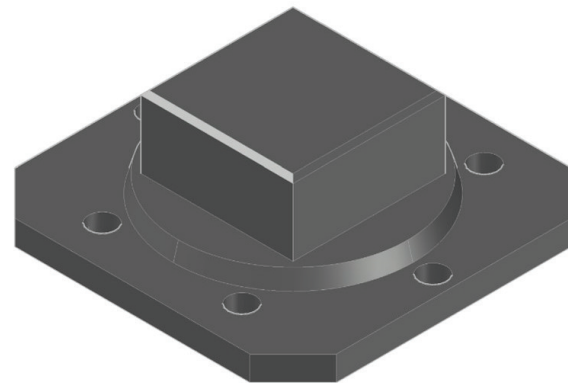


Figure 5. Rigid cap.

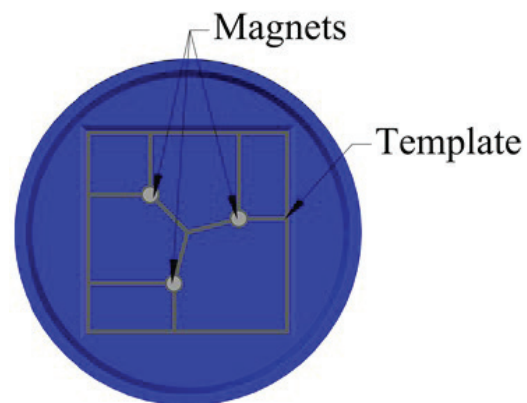


Figure 6. Magnets fixing template.

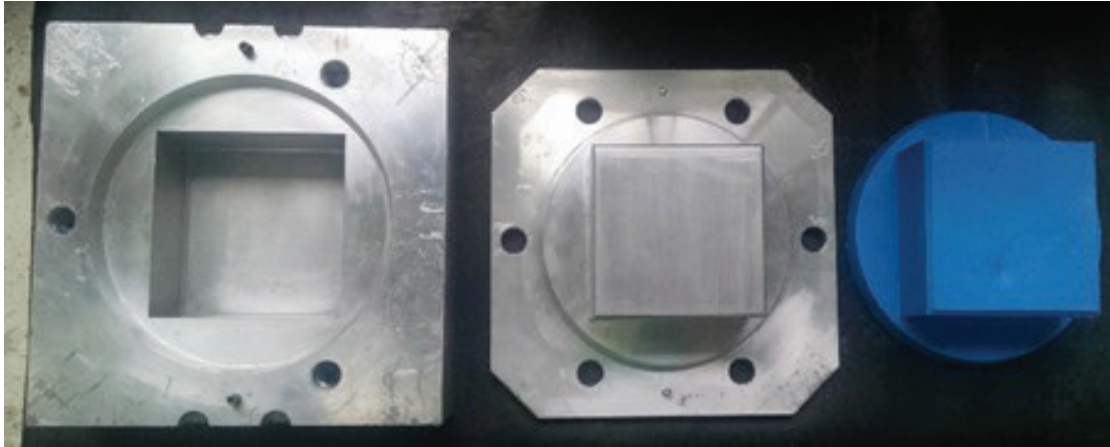


Figure 7. Mould (left), cap (center) and cushion (right).

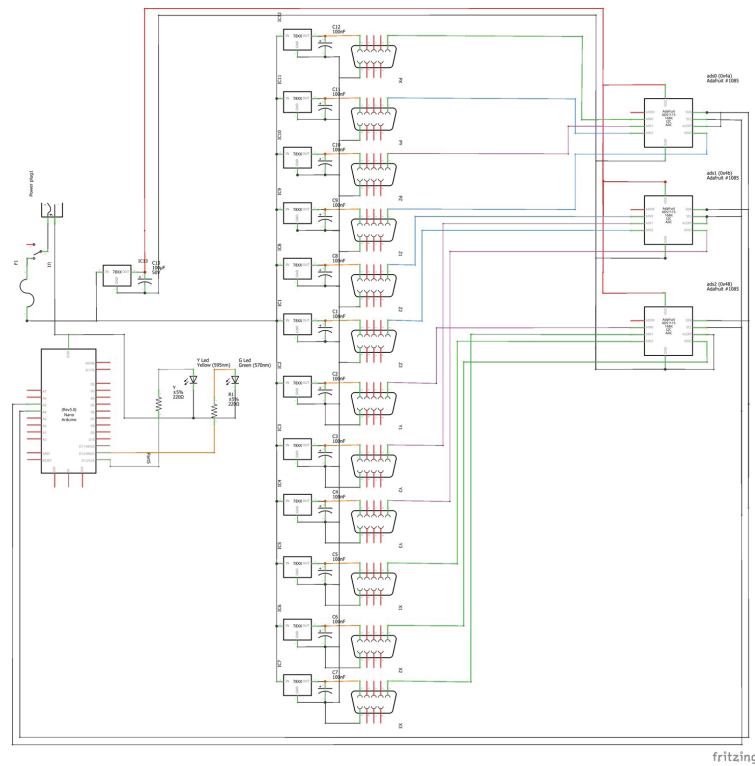


Figure 8. Data acquisition schematic.

cement addition, were tested in the developed TTA and in a conventional ST aiming to compare and validate the new apparatus.

3.1 Uniform fine sand

The first investigated soil was Osorio sand, extracted from a city near Porto Alegre, in southern Brazil. It was classified as a non-plastic uniform fine sand (SP), with specific gravity

of the solids of 2.65. The mineralogical analyses shown that the sand composition was predominantly quartz. The mean diameter (D_{50}) was 0.250 mm and the uniformity (C_u) and curvature (C_c) were 2.11 and 1.15, respectively. The minimum and maximum void ratios were 0.60 and 0.90. The soil characterization was presented by Marques et al. (2021).

To set the sample inside the cubic cell, two additional caps were 3D printed and all rigid caps were bolted in place, remaining only the top face opened, as seen in Figure 10.

All the inside faces of the cube were lubricated with vaseline to avoid shearing transfer. The soil was then mixed with distilled water, aiming the moisture content of 10% and a relative density of 50%. These parameters were defined to compare the results with the ones of Consoli et al. (2009). The mixture was then placed in the center of the cell and compacted in three layers until the 100 mm height was achieved. After that, the two printed caps were removed, all the cushions were lubricated in all external surface that touched the sample or the cubic cell, and all the “top hats” were bolted in place.

With the moulded sample in place, the software-controlled step proceeded. To inundate the sample, 30 kPa of confining pressure was applied and at least two time the void volume was percolated with ascendant flow of distilled water. Afterwards the sample was confined to consolidation pressures of 50, 75 and 100 kPa. The shearing, considering Lode angle 0° , was performed increasing the pressure in the vertical axis and reducing the pressure in both horizontal axes, maintaining the same mean stress, at an increase rate of 2 kPa/

min in the vertical axis and at a decrease rate of 1 kPa/min in the horizontal axis until the failure of the sample was observed. The obtained results are presented in the Figure 11.

The obtained friction angle of 38.4° was compared with the 37° achieved in Consoli et al. (2009). The difference can be the result of the different type of test, strain-controlled vs stress controlled, distinct geometry of sample, cubical of 100 mm of edge opposing to cylindrical 100 mm of diameter and 200 mm of height as seen in Ferreti (2012), Lan et al. (2018), Tripura & Das (2017) or the natural material variability.

3.2 Cemented uniform fine sand

To further validate the apparatus, tests with cemented sand were performed in the TTA and the ST. The Osorio sand, same as utilized in the previous experiment, was mixed with high initial strength Portland cement (Type III), with specific gravity of 3.15. The samples were moulded with moisture content of 8.5%, cement content of 3.3% by of dry sand, and a target dry density of 15.0 kN/m^3 . Cylindrical specimens with 100 mm diameter and 200 mm height were moulded for ST tests and cubical specimens with 100 mm edges were prepared for TTA tests. The process of mixture and moulding was made in 1h or less, lower than the cement setting time of 3.25 h. The moulded samples were placed in polypropylene bags to maintain the moisture content and proceeded to a humid room with temperature within $23 \pm 2^\circ \text{C}$ and relative humidity above 95%. The samples were maintained in the humid room for six days and, in the seventh day, tested. The sample acceptance was a 1% of deviance in dry density and dimensions and 0.5% in moisture content.

The tests were performed following the procedure described in the previous test, except that for the ST tests the samples were back pressured with 300 kPa and Skempton B parameter higher than 0.99. During shearing, both apparatuses performed an increase of the vertical pressure, with a rate of 2 kPa/min, and the mean stress were maintained by reducing either the confining pressure or the horizontal pressures, with

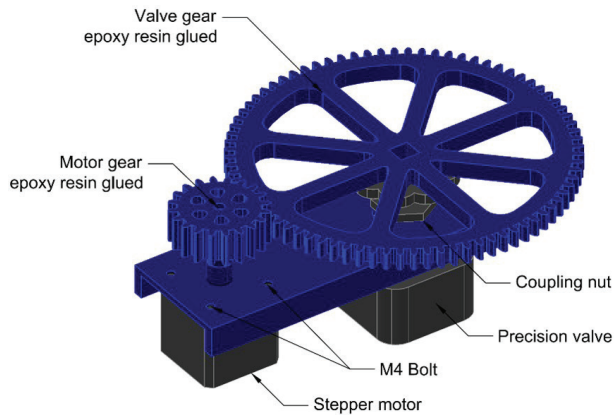


Figure 9. Pressure control actuators.

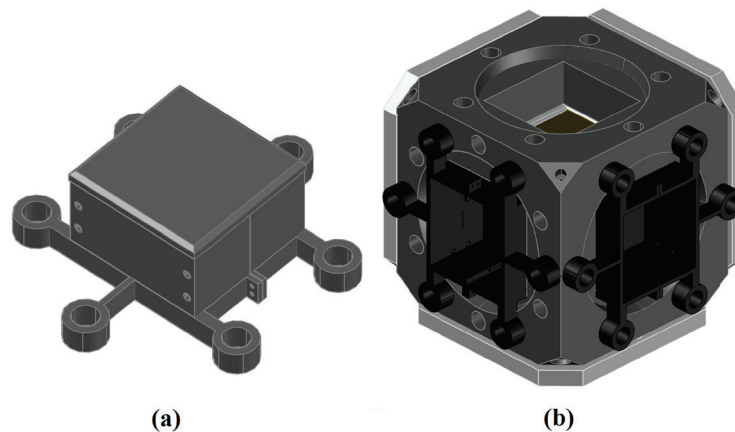


Figure 10. (a) 3D printed cap; (b) sample positioning.

a rate of 1 kPa/min. For the ST, three samples were tested under the confining pressures of 50, 100 and 200 kPa. For the TTA, nine tests were performed, three under 50 kPa, two under 75 kPa, two under 100 kPa, one under 125 kPa and one under 150 kPa of confining pressure. The tests were finished when the strain was observed without a significative stress.

The ST tests resulted in a friction angle of 33.6° and a c' of 3.3 kPa, while the TTA tests resulted in a friction angle of 34.3° and a c' of 8.4 kPa (Figure 12). These differences can be derived from either the geometry of the samples and/or natural material variability. Similar results were observed in the works of Reddy & Saxena (1993).

3.3 Cemented clayey sand

To further validate the TTA, a battery of tests involving Botucatu residual soil, a clayed sand described also in the work of Consoli et al. (2018). The same mold and acceptance criteria from the previous tests were utilized. The moisture content targeted this time was 10% and a dry density of

14.6 kN/m³ and 1.07% by mass of dry soil of type III Portland cement. The same curing procedure was performed, with two days of curing in climate-controlled room and in the third day the test were performed.

A total of four samples were tested, two in TTA and two in ST, with 100 and 150 kPa consolidation pressures. For the TTA, the ending of the tests was characterized by the rupture of the cushion, while for the ST the high strain without an increase of the stress were noted. The results of those tests can be seen in Figure 13. A fair agreement of the results from the different apparatuses can be observed. The small difference in the results could be attributed to distinct local strain measurements systems: Hall effect transducers for ST tests and LVDTs for TTA tests.

3.4 Uniform sand under TTA

The last tests set was performed utilizing the same Osorio sand and the same procedures described in item 3.1. To fully assess the apparatus capacity, a full rosette was developed, utilizing the angles of 0, 30, 60, 90, 120, 150 and 180° between σ_z and the loading path in the octahedral plane, all under the same mean stress of 100 kPa (Figure 14.). In Figure 15, it is exhibited the performance of the samples in the previous tests, with the stress strain behaviour.

The results demonstrated a certain level of anisotropy in the material, potentially caused by the specimens' preparation method, and an internal consistency of the results. When comparing the results of Lode angles 0 and 120° , the first shows a higher stress then the second. The same can be seen for 30 and 150° and also for 60 and 180° . Those results correspond to the same type of tests, axial compression, simple shear and axial extension, but with a different alignment with the compaction axis. Overall, the tests shown a low noise level and consistency.

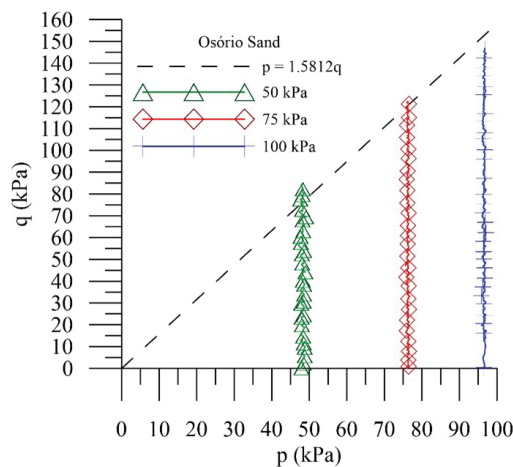


Figure 11. Shear response of Osorio Sand.

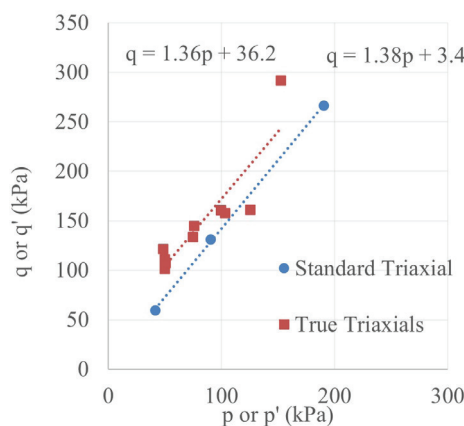


Figure 12. Cemented Osorio sand response.

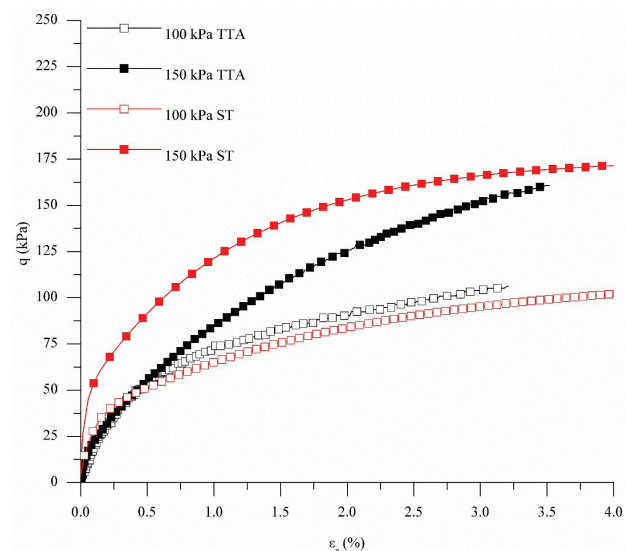


Figure 13. TTA vs ST of cemented Botucatu clayey sand.

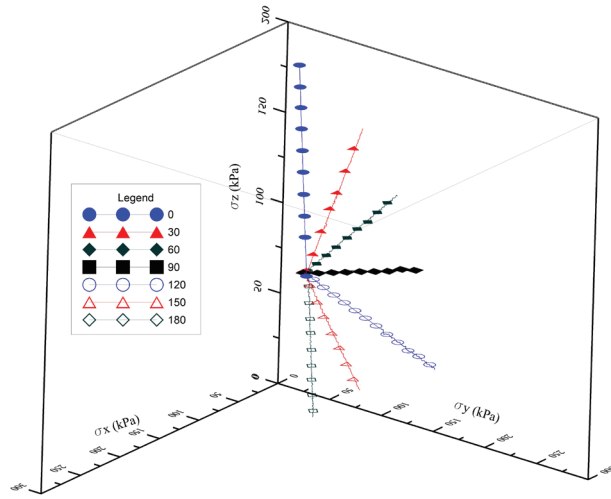


Figure 14. Uniform sand stress rosette.

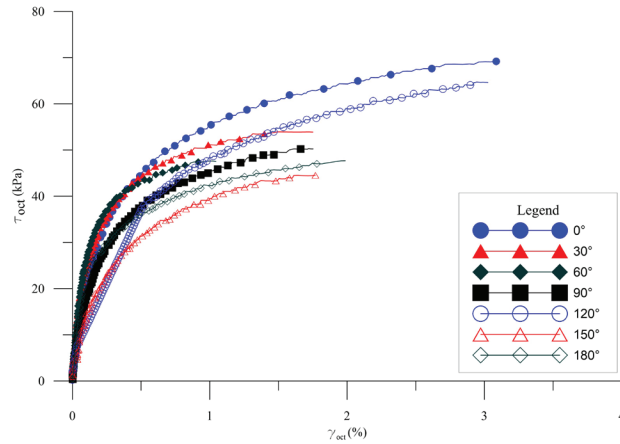


Figure 15. Stress strain behavior of uniform sand under TTA.

4. Conclusion

This paper reported a successful and affordable development of an automated true triaxial apparatus. The TTA main components were based on open source tools, which enabled the production of an accessible and effective equipment. The manufactured true triaxial test results exhibited well agreement when compared to other test results from other testing equipment, such as a well validated standard triaxial apparatus. Anisotropy in Osorio sand was observed.

Acknowledgements

The authors wish to explicit their appreciation to FAPERGS/CNPq 12/2014 – PRONEX (grant # 16/2551-0000469-2), MCT-CNPq (INCT, Universal & Produtividade em Pesquisa) and MEC-CAPES (PROEX) for the support to the research group.

Declaration of interest

The authors declare that no conflict of interest to disclose by this paper.

Authors' contributions

Dionatas Hoffmann Andreghetto: Conceptualization, Investigation, Hardware, Software, Data curation, Visualization, Writing – original draft. Lucas Festugato: Conceptualization, Data curation, Methodology, Supervision, Validation, Writing – review & editing, Funding acquisition, Resources. Gustavo Dias Miguel: Formal Analysis, Investigation, Methodology, Writing – review & editing. Andressa da Silva: Writing – review & editing.

List of symbols

p	Mean Stress
q	Deviatoric stress ($\sigma_1 - \sigma_3$)
AcA	Actuator controller Arduinos
C_s	Coefficient of curvature
C_u	Coefficient of uniformity
D_{50}	Mean diameter
$LVDT$	Linear Differential Transducer
PT	Pressure Transducers
ST	Standard Triaxial
TTA	True Triaxial Apparatus
ε_a	Axial strain
γ_{oct}	Distortional strain in octahedral plane
σ_x	Horizontal stress x
σ_y	Horizontal stress y
σ_z	Vertical stress z
τ_{oct}	Shear stress in octahedral plane






References

- Airey, D.W., & Wood, D.M. (1988). The cambridge true triaxial apparatus. In R. Donaghe, R. Chaney, and M. Silver, (Eds.), *Advanced triaxial testing of soil and rock, ASTM STP 977* (pp. 796). ASTM International.
- Alshibli, K.A., & Williams, H.S. (2005). A true triaxial apparatus for soil testing with mixed boundary conditions. *Geotechnical Testing Journal*, 28(6), 534-543.
- AnhDan, L. Q., Koseki, J., Hayano, K., & Sato, T. (2005). True triaxial apparatuses with two rigid boundaries, site characterization and modeling (GSP138). In *Geo-Frontiers Congress*. Austin, Texas, GeoInstitute of ASCE.
- Arthur, J.R.F. (1988). State-of-the-art paper: cubical devices: versatility and constraints, advanced triaxial testing of soil and rock. In R.T. Donaghe, R.C. Chaney, and M.L. Silver (Eds.), *ASTM STP 977* (pp. 743). ASTM International.

- Choi, C., Arduino, P., & Harney, M.D. (2008). Development of a true triaxial apparatus for sands and gravels. *Geotechnical Testing Journal*, 31(1), 32-44.
- Consoli, N.C., Festugato, F., & Heineck, K.S. (2009). Strain-hardening behaviour of fibre-reinforced sand in view of filament geometry. *Geosynthetics International*, 16(2), 109-115.
- Consoli, N.C., Winter, D., Leon, H.B., & Scheuermann Filho, H.C. (2018). Durability, strength, and stiffness of green stabilized sand. *Journal of Geotechnical and Geoenvironmental Engineering*, 144(9), 04018057.
- Ferreti, E. (2012). Shape-effect in the effective laws of plain and rubberized concrete. *CMC Tech Science Press*, 30(3), 237-248.
- Hambly, E.C. (1969). A new true triaxial apparatus. *Geotechnique*, 19(2), 107-124. <http://dx.doi.org/10.1680/geot.1969.19.2.307>.
- Hoyos, L.R., Perez-Ruiz, D.D., & Puppala, A.J. (Feb 20-24, 2010). A refined true triaxial cell for modeling unsaturated soil response under suction controlled stress paths. In *GeoFlorida 2010: Advances in Analysis, Modeling and Design*, Orlando, Florida, Reston, VA: ASCE, pp. 381-389.
- Ibsen, L.B., & Praastrup, U. (2002). The danish rigid boundary true triaxial apparatus for soil testing. *Geotechnical Testing Journal*, 25(3), 1-12.
- Ismail, M.A., Sharma, S.S., & Fahey, M. (2005). A small true triaxial apparatus with wave velocity measurement. *Geotechnical Testing Journal*, 28(2), 1-10.
- Jamiolkowski, M., Ladd, C.C., Germaine, J.T., & Lancellotla, R. (Aug 12-16, 1985). New developments in field and laboratory testing of soils. In *Proceedings of the 11th International Conference on Soil Mechanics and Foundation Engineering* (Vol. 1, pp. 57-153). San Francisco. Rotterdam, The Netherlands: A. A. Balkema.
- Kirkgard, M.M., & Lade, P.V. (2011). Anisotropic three dimensional behavior of a normally consolidated clay. *Canadian Geotechnical Journal*, 30(5), 848-858.
- Ko, H.Y., & Scott, R.F. (1967). A new soil testing apparatus. *Geotechnique*, 17(1), 40-57.
- Lade, P.V. (1978). Cubical triaxial apparatus for soil testing. *Geotechnical Testing Journal*, 1(2), 93-101.
- Lade, P.V., & Duncan, J.M. (1973). Cubical triaxial tests on cohesionless soil. *Journal of the Soil Mechanics and Foundations Division*, 99(10), 793-812.
- Lan, G., Wang, Y. & Chao, S. (2018). Influences of specimen geometry and loading rate on compressive strength of unstabilized compacted earth block. *Advances in Materials Science and Engineering*, 2018, 5034256. <https://dx.doi.org/10.1155/2018/5034256>.
- Marques, S.F.V., Festugato, L., & Consoli, N.C. (2021). Stiffness and strength of an artificially cemented sand cured under stress. *Granular Matter*, 23, 35. <http://dx.doi.org/10.1007/s10035-021-01099-1>.
- Matsuoka, H., Sun, D., Kogane, A., Fukuzawa, N., & Ichihara, W. (2002). Stress-strain behaviour of unsaturated soil in true triaxial tests. *Canadian Geotechnical Journal*, 39(3), 608-619.
- Michelis, P. (1988). A true triaxial cell for soil and rock. In R.T. Donaghe, R.C. Chaney and M.L. Silver (Eds.), *Advanced Triaxial Testing of Soil and Rock, ASTM STP 977*. American Society for Testing and Materials, pp. 806-818.
- Penumadu, D., & Prashant, A. (Jan 24-26, 2005). Automated flexible boundary true triaxial system for cohesive soils, site characterization and modeling (GSP138). In *Geo-Frontiers Congress 2005*, Austin, TX, Reston, VA: Geo-Institute of ASCE.
- Reddy, K. R. & Saxena, S. K. (1993). Effects of cementation on stress-strain and strength characteristics of sands. *Soils and Foundations*, 33(4), 121-135.
- Reddy, K.R., Saxena, S.K., & Budiman, J.S. (1992). Development of a triaxial testing apparatus. *Geotechnical Testing Journal*, 15(2), 89-105.
- Sadek, T. (2006). *The multiaxial behaviour and elastic stiffness of hostun sand* [Doctorship tesis, University of Bristol]. University of Bristol Repository.
- Shibata, T., & Karube, D. (Sept 8-15, 1965). Influence of the Variation of the Intermediate Principal Stress on the Mechanical Properties of Normally Consolidated Clays. In *Proceedings of the 6th International Conference on Soil Mechanics and Foundation Engineering* (Vol. 1, pp. 359-363). Montreal, Canada. Toronto: University of Toronto Press.
- Silvani, C. (2017). *Artificially cemented soil tested in a cubical cell: isotropy at small strains and at failure* [Doctoral Thesis, Federal University of Rio Grande do Sul]. Lume digital repository <https://lume.ufrgs.br/handle/10183/157899> (in Portuguese).
- Silvani, C., Ibraim, E., Scheuermann Filho, H.C., Festugato, L., Diambra, A., & Consoli, N.C. (2022). Sand-fly ash-lime blends: mechanical behaviour under multiaxial stress condition. *Journal of Materials in Civil Engineering*, [ahead of print].
- Silvestri, V., Yong, R.N., & Mohamed, A.M.O. (1988). A true triaxial testing cell, advanced triaxial testing of soil and rock. In ASTM International. *ASTM STP 977* (pp. 819-833). ASTM International.
- Sivakugan, N., Chameau, J. L., Holtz, R. D., & Altschaeffl, A. G. (1988). Servo-controlled cuboidal shear device. *Geotechnical Testing Journal*, 11(2), 119-124.
- Sture, S., & Desai, C.S. (1979). Fluid cushion truly triaxial or multi-axial testing device. *Geotechnical Testing Journal*, 2(1), 20-33.
- Sutherland, H.B., & Mesdary, M.S. (Aug 25-29, 1969). The influence of the intermediate principal stress on the strength of sand. In *Proceedings of the 7th International Conference on Soil Mechanics and Foundation Engineering* (Vol. 1, pp. 391-399). Mexico City, Sociedad Mexicana de Mecanica.

- Tripura, D. D. & Das, S. (2017). Shape and size effects on the compressive strength of cement stabilised rammed earth. *AEI 2017: Resilience of the Integrated Building*, 1210-1217. <https://doi.org/10.1061/9780784480502.028>.
- Yin, J.H., Cheng, C.M., Kumruzzaman, M., & Zhou, W.H. (2009). New mixed boundary, true triaxial loading device for testing three-dimensional stress-strain strength behavior of geomaterials. *Canadian Geotechnical Journal*, 47(1), 1-15.

Behavioural analysis of iron ore tailings through critical state soil mechanics

João Paulo de Sousa Silva^{1#} , Pedro Pazzoto Cacciari² , Vidal Felix Navarro Torres³ ,
Luís Fernando Martins Ribeiro¹ , André Pacheco de Assis¹ 

Article

Keywords

Critical state
Iron ore
Laboratory tests
Numerical model calibration
NorSand
Tailings

Abstract

Understanding the geotechnical properties of iron ore tailings is currently one of the major challenges in the mining industry. With transitions from drained to undrained conditions occurring in seconds, recent dam problems have been a challenge to solve with classical soil mechanics, which provides few means to explain how such phenomena develop. There is also an increasing propensity in technical and scientific circles to seek constitutive models that are based on critical state soil mechanics and that allow for the analysis of tailings behaviour. However, there is still a lack of knowledge and information about the critical state properties of iron ore tailings. The present research experimentally and numerically investigated the effectiveness of modelling the behaviour of iron ore tailings. The aim of these experiments was to assess the critical state parameters of tailings from a significant iron ore operation site in *Quadrilátero Ferrífero* (Minas Gerais state, Brazil). The results indicated that the selected numerical model (NorSand) was adequate to evaluate the behaviour of the studied mine tailings. The numerical results showed consistent adherence to the experimental results of both drained and undrained tests, with deformations below 5% and samples in which the state parameter had a small magnitude.

1. Introduction

The first industrial iron ore extraction in Brazil occurred in *Quadrilátero Ferrífero* (QF). Today, the region remains among the most significant iron ore producers globally. The area known as QF is located in the central region of the state of Minas Gerais in Brazil. It comprises a series of hills covering approximately 7,000 km². The QF deposit was formed in the lower Proterozoic between 1.9 and 2.7 billion years ago (Dorr, 1969). With approximately 200 million tons of iron ore production per year, the QF is responsible for approximately 40% of all Brazilian iron ore production.

After many years of mineral industry operations in the QF, the region most conducive to tailings disposal has become unavailable. Many constraints hamper the utilization of conventional tailings storage facilities (TSFs) in the remaining areas. There is a need to reconcile tailings disposal and mining activities to produce lower environmental and social impacts, highlighting the importance of understanding the geotechnical behaviour of tailings (Davies, 2002). Some of these tailings have demonstrated brittle behaviour (Soga

& Mitchell, 2005; Schnaid et al., 2013), which increases the criticality of structures that are close to areas occupied by humans.

Thus, national legislation has been revised, indicating an urgent need to safely dismantle dozens of upstream tailings dams in the QF region. TSFs are among the most challenging structures to operate in the mining industry. Some of these structures are likely to be subject to piping, collapse, and flow failure and should be monitored carefully (Li et al., 2018; Olivier et al., 2018). The density and fineness of the tailings particles, which are typically uniform with little or no plasticity, usually define the behaviour of the tailings at a TSF.

Relevant research indicates that critical state theory is an attractive tool for describing the mechanical behaviour of non-cohesive soils (Dafalias & Popov, 1975; Casagrande, 1976; Jefferies, 1993; Dafalias & Manzari, 1997; Dafalias, 1986; Dafalias & Manzari, 2004; Boulanger & Ziotopoulou, 2015). The importance of this tool is highlighted by the fact that in situ soils may present a wide spectrum of states. However, obtaining undisturbed samples from noncohesive soils is complex, costly, and potentially unreliable.

[#]Corresponding author. E-mail address: eng.jpssilva@gmail.com

¹Universidade de Brasília, Brasília, DF, Brasil.

²Laboratório Geotécnico Vale, Santa Luzia, MG, Brasil.

³Instituto Tecnológico VALE, Santa Luzia, MG, Brasil.

Submitted on May 24, 2021; Final Acceptance on December 3, 2021; Discussion open until August 31, 2022.

<https://doi.org/10.28927/SR.2022.071921>



This is an Open Access article distributed under the terms of the Creative Commons Attribution License, which permits unrestricted use, distribution, and reproduction in any medium, provided the original work is properly cited.

Jefferies et al. (2015) argue that the major restriction of using the most comprehensive numerical analyses in engineering practice is the time and effort undertaken to create models. In their view, this limitation restricts the practice of engineering to commercial geotechnical modelling platforms, such as FLAC, PLAXIS, or SIGMA/W.

In the present study, the NorSand (Jefferies, 1993) model was selected because it is relatively simple and based on a small number of parameters. This model is a generalized critical state model based on the state parameter (ψ).

$$\psi = e - e_c \quad (1)$$

The state parameter is a fundamental characterizing parameter for soils (Been & Jefferies, 1985) that represents the difference between the current (e) and void ratio (e_c) at the critical state. The NorSand model includes associated plasticity and allows dilation, similar to that observed in natural soil, by introducing limited hardening. This limited hardening causes yielding in unloading conditions, replicating observed soil behaviour with second-order detail.

2. Materials and methods

The activities involved in mining and processing iron ore on site are shown in the flow chart in Figure 1. Ore processing ranges from simple crushing and screening methods to more sophisticated processes to upgrade the ore quality. These are physical processes that remove impurities by

segregating particles that have an anomalous particle density or gravity. After the screening stage, the fine material, with gradation below the sinter feed (particles diameters from 0.15 to 6.3 mm), moves on to the desliming stage through a sequence of hydrocyclone batteries to remove the finer material. After this stage, the slimes are stored in the TSF. The remaining material moves on to the reverse cationic flotation process, which isolates the fine-grained ore (pellet feed), and the flotation tailings are also stored in the TSF.

The procedure for collecting and preparing the samples investigated in this study was conducted in two phases: (1) The tailings samples were collected at the exit of iron ore beneficiation plants (IBPs, Plant 1 and Plant 2). In this case, to reduce the influence of fluctuations in the plant's operation, the samples were composed of subsamples collected over three weeks every other day. (2) Preparation of tailings blends from Plant 1 in a mixer by adding 60% flotation tailings from Plant 2.

The tailings produced at the IBPs considered here were mainly composed of silica and iron, as shown in Table 1. FT-P1 and FT-P2 were disposed of in the same TSF without deposition of slimes. Figure 2 shows an optical microscopy image of the flotation iron ore tailings. The aim of this research was to investigate the mechanical behaviour of tailings at the TSF. Thus, composite samples BL-2&1 had the same composition proportions. In this paper, the BL-2&1 composite material was considered representative of the tailings in a TSF.

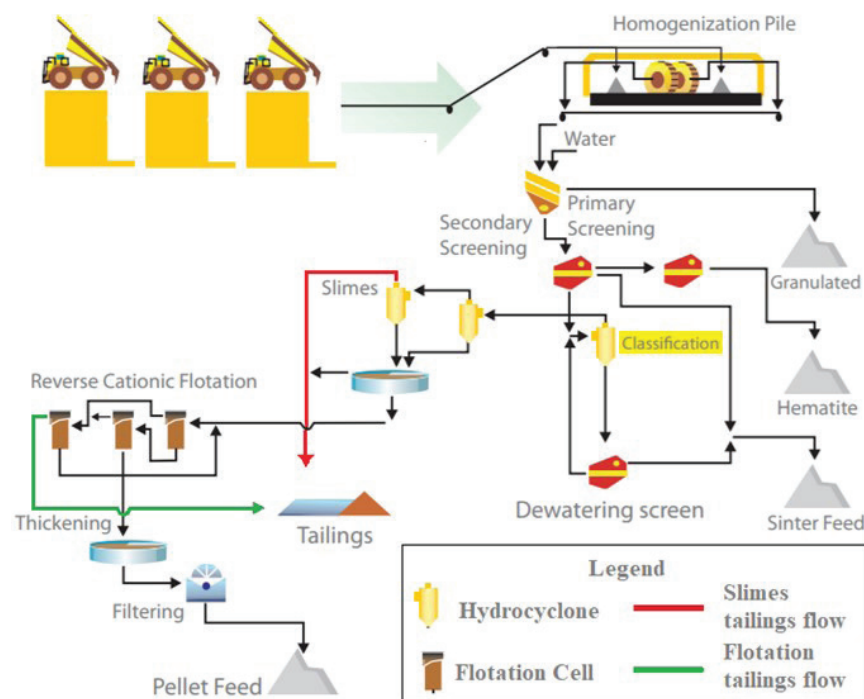


Figure 1. Simplified flow chart showing typical iron ore processing (Silva et al., 2021).

The preliminary stage of this study involved tailings characterization. The laboratory tests included tests to determine the general chemistry, calcination loss, specific gravity, grain size distribution, Atterberg limits, and standard Proctor parameters. Instead of using the conventional relative density test (maximum and minimum void ratio), the Brazilian mining industry has been applying the Proctor test as a standard to control the density of tailings at TSFs. There is empirical evidence showing that the void ratio (e) determined in the field can be out of the range corresponding to standard laboratory relative density testing (Lunne et al., 2019).

According to ASTM guidelines, these tailings are typically fine grains of industrial silt sands with minimal or

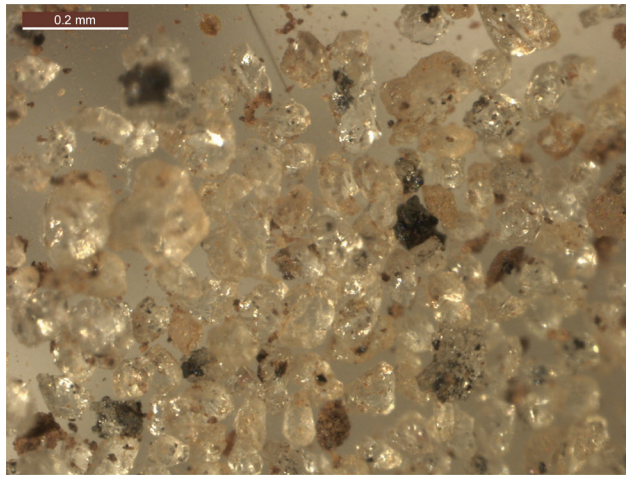


Figure 2. Optical microscopy of flotation iron ore tailings.

Table 1. Chemical composition of the tailings studied and calcination losses.

Chemical composition (%)	Tailings	
	FT-P1	FT-P2
Fe	25.44	13.48
SiO ₂	61.23	80.22
P	0.027	0.016
Al ₂ O ₃	0.79	0.028
Mn	0.021	0.001
TiO ₂	0.058	0.001
CaO	0.017	0.007
MgO	0.91	0.16
Calcination losses	0.91	0.16

no plasticity. The e_{max} and e_{min} of the flotation tailings are approximately 1.1 and 0.6, respectively. Table 2 summarizes the basic geotechnical properties of the flotation and composite tailings samples. The specific gravity ranges from 3.2 to 3.8, which is consistent with typical metal tailings but much higher than that of natural soils. This table also shows the typical characteristics of nine flotation tailings from QF (Silva et al., 2013); the data are from nine IBPs that predominantly process haematite ore. Notably, this work intends to evaluate the ability of NorSand to predict the behaviour of granular iron ore tailings. It is not the intention of this study to represent a specific deposit.

Figure 3 shows the grain-size distributions of BL-2&1, which are the flotation tailings used to create the blend and slime tailings from Plant 1 for comparison. Figure 3 also shows data on iron ore tailings from Silva et al. (2013). Currently, IBPs process itabirite, which has a lower Fe content and generates finer tailings than iron does. According to the Unified Soil Classification System, these tailings are silty or silty sand. NorSand is a mathematical framework that is validated across a wide range of soil types. All these iron ore tailings have grain sizes within NorSand's limits verified by Jefferies et al. (2015); as shown on Figure 3.

Triaxial tests were conducted to investigate the dilatancy and critical state behaviour of BL-2&1. A triaxial testing system was used to conduct consolidated undrained (CU) and consolidated drained (CD) triaxial compression tests on the tailings according to ASTM standards D4767-11 and D7181-11, respectively. The testing programme involves dense specimens (four CD tests) and loose specimens (four CD and four CU tests). The triaxial test specimens were 3.91 cm in diameter and 8 cm in height. The dense specimens were remoulded to reach approximately 105% of the maximum dry density identified via Proctor test. In contrast, the loose specimens were compacted to approximately 75% of the Proctor test density.

A relevant aspect of reconstitution is that it can achieve a uniform density throughout the specimen. Therefore, moist tamping and compaction techniques were adopted to obtain six equal volume layers. For the loose specimens, it was only necessary to place the tamper and apply a light load before the layer reached the specified thickness. On the other hand, for the dense specimens, it was necessary to also use a Harvard miniature compaction apparatus (Figure 4). This compaction tamper consists of a metallic cylinder with a spring inside, which is compressed during the compaction process.

Table 2. Basic geotechnical parameters of iron ore tailings from the Brazilian QF.

Tailings	G_s	Void ratio		Standard Proctor		Atterberg limits			Classification
		e_{min}	e_{max}	ρ_d (kN/m ³)	w (%)	LL	PL	PI	USCS
FT-P1	3.8	0.59	1.13	19	14		NP		ML
FT-P2	3.2	0.6	1.1	18	14		NP		ML
BL-2&1	3.6	0.85	1.31	22	12		NP		ML
Typical	3-4.2			17-19	11-15		NP		ML

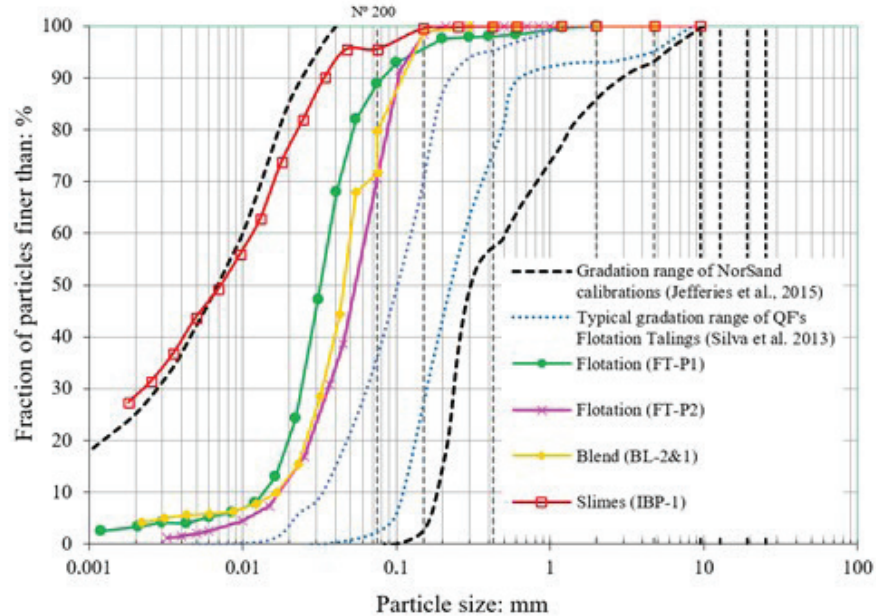


Figure 3. Grain size distributions of iron ore tailings from the Brazilian QF.



Figure 4. Dense specimen preparation method.

The saturation of the specimens was achieved by flushing de-aired water through the specimens. This process did not result in full saturation. Thus, the water pressure was increased gradually, and the degree of saturation was checked by the 'B-test' (Skempton's B value > 95%). According to Verdugo & Ishihara's (1996) proposal, an additional consolidation step was applied at the end of the test (after shear) to generate apparent cohesion and make it feasible to handle the specimens without material loss. This made it possible to determine void ratio (e) from the final moisture content and volume measured. This corresponds to ASTM method B, with the adjustments proposed by Verdugo & Ishihara. Freezing was not performed at the end of the test.

Bender element (BE) tests have gained popularity in recent years and are rapidly extending from research to practice. The BE values of the shear modulus (G) are usually chosen as a starting point for calibration. In practice, the value introduced by the NorSand calibration of CU triaxial tests has been proportional to but lower than the value measured by geophysical methods.

In such an analysis, it is helpful to divide the soil behaviour into distortional and volumetric strains. Moreover, for soils, it is convenient to represent elasticity in terms of the shear modulus (G) and bulk modulus (K). Equations 2 and 3 show the relation between these parameters:

$$G = E / [2(1 + \nu)] \quad (2)$$

$$K = E / [3(1 - 2\nu)] \quad (3)$$

where E is Young's modulus and ν is Poisson's ratio. NorSand assumes a constant Poisson's ratio, so there is a direct link between K and G . Bellotti et al. (1996) performed extensive testing to investigate the elasticity of Ticino sand and measured Poisson's ratios between 0.1 and 0.3.

The shear modulus (G_{max}) and its variation with both e and confining stress were measured in a triaxial cell by performing isotropic consolidation tests with BEs. After determining the critical state and the dilatancy parameters of the BL-2&1 tailings, the model was calibrated using the free software NorTxI (Jefferies & Been, 2016). The aim of the calibration was to establish parameters that best represent the selected flotation tailings. Subsequently, more advanced numerical simulations were performed on the commercial numerical modelling platform FLAC3D. The NorSand model was implemented as a user-defined model on this platform. FLAC3D version 6.0 was customized to incorporate the NorSand model and was developed in a partnership between ITV (Instituto Tecnológico Vale) and Itasca. After that, Itasca incorporated this development into Version 7 of its software. The development documentation is attached to this paper, including the source code implemented in C++ and the DLL files.

3. Mechanical properties of the tailings

3.1 Triaxial tests

Table 3 shows the physical properties of the BL-2&1 tailings specimens. There was some difference between the moulding

conditions specified and obtained, so the values were slightly lower than those reported in section 2. Figures 5 and 6 show compressive triaxial test results under both dense and loose conditions. These figures also show the axial strain against the deviatoric stress and the mean effective stress. Figure 5 shows the derived critical state line (CSL) obtained from the post-peak portion of the undrained tests of the loose specimens. Some specimens appear to reach a steady state at approximately 6% strain but then dilate at higher strains. The quasi-steady state in this test must not be understood as a critical state but instead as a transient condition under which the specimens transition from contractive to dilative behaviour.

3.2 Critical state and dilatancy (model calibration)

Figure 6 shows the state diagram of eight drained and four undrained triaxial compression tests. These data have been used to estimate the CSL shown in Figure 7. One critical state theory axiom is that the soil state moves to the critical state with increasing shear strain. In the Figure 7, it is possible to observe this phenomenon in the results for both dense and loose samples. However, in the four dense CD tests, the deformation required to reach the CSL is outside the practicable limits of the triaxial assembly. A conventional semilog idealisation of the CSL can be fitted to the data using the properties $\Gamma = 1.28$ and $\lambda_{10} = 0.19$. Occasionally, this semilog trend is not a particularly good representation of the CSL, and an improved CSL is given by power-law idealisation with $C_a = 1.13$, $C_b = 0.23$, and $C_c = 0.27$. Over the stress range of the data (approximately 60–2000 kPa), both models are equally suitable within a precision of approximately $e = \pm 0.02$. The semi-log CSL has the advantage of the least number of parameters; on the other hand, many workers applying critical state models prefer the power-law CSL, so this is the reason for presenting both.

Table 3. Triaxial tests on the BL-2&1 tailings: physical properties of the specimens.

Specimen			Initial			Post-consolidation	
Test	Condition	Test type	γ (kN/m ³)	γ_d (kN/m ³)	w (%)	Mean effective stress (kPa)	Void ratio (e)
1	dense	CD	24.5	22.6	8.74	50	0.67
2	dense	CD	24.4	22.5	8.68	100	0.64
3	dense	CD	24.6	22.6	8.82	150	0.62
4	dense	CD	24.5	22.6	8.65	300	0.55
5	loose	CD	17.6	16.7	5.38	100	0.92
6	loose	CD	17.6	16.7	5.56	300	0.85
7	loose	CD	17.7	16.7	5.61	400	0.8
8	loose	CD	17.6	16.6	5.34	600	0.78
9	loose	CU	17.7	16.7	5.9	100	0.94
10	loose	CU	17.6	16.7	5.44	200	0.87
11	loose	CU	17.6	16.7	5.44	400	0.86
12	loose	CU	17.7	16.7	5.61	600	0.84

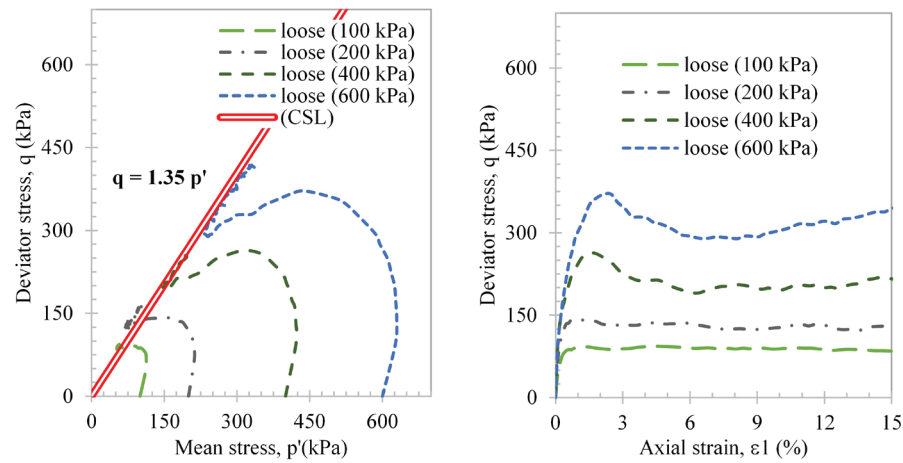


Figure 5. CU triaxial test – loose specimens.

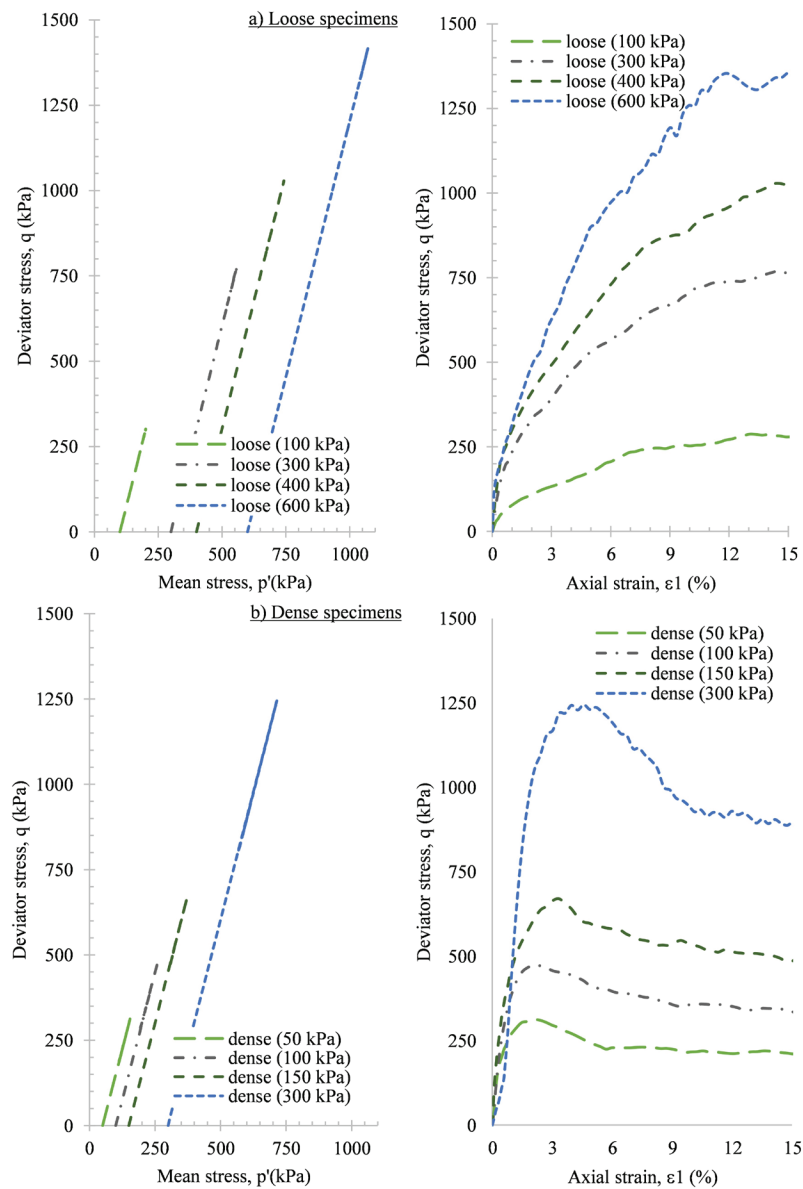


Figure 6. CD triaxial test stress path: (a) loose specimens; (b) dense specimens.

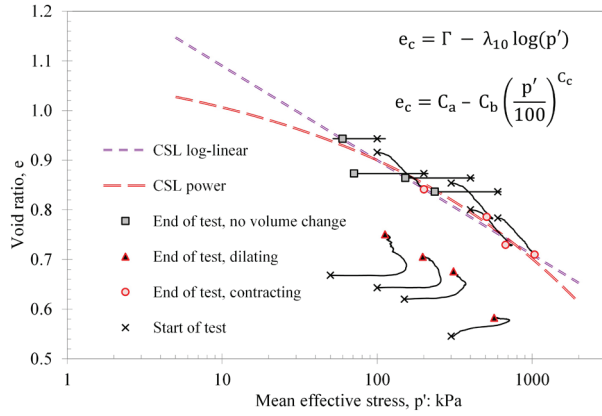


Figure 7. State diagram of triaxial test results with the corresponding log-linear and power-law CSL.

Figure 8 shows the maximum stress ratio η_{max} measured against the peak dilation of BL-2&1. Equation 4 shows the flow rule from Nova & Wood (1982), which was fitted to determine the critical stress ratio ($M_{tc} = 1.35$) and the parameter N_{tc} (0.20) of work dissipation by plastic volumetric strain (Nova & Wood, 1982; Jefferies & Been, 2016).

$$\eta_{max} = M_{tc} - (1 - N_{tc}) D_{min} \quad (4)$$

The stress ratio (η) and the equivalent dilatancy (D) were obtained by triaxial compression. The M_{tc} value determined in the CD tests is similar to that inferred from Figure 8.

Equation 5 is the state–dilatancy law proposed by Been & Jefferies (1985):

$$D_{min} = \chi_{tc} \psi \quad (5)$$

The state–dilatancy parameter χ_{tc} is obtained by plotting the maximum dilation versus ψ at maximum dilation. The determination of this law for BL-2&1 is shown in Figure 9. The trend line with $\chi_{tc} = 3.9$ is forced to intercept zero (a theoretical requirement):

3.3 Elasticity and plasticity

The five parameters (Γ , λ , M , N , and χ) defined thus far reflect the intrinsic behaviour of soil and its relationship between the current state and the critical state. Typically, parameters are defined from triaxial compression tests, and the subscript TC is used. These are not parameters of the NorSand model but a set of fundamental characteristics shared by many critical state soil mechanics models. Other parameters will be necessary for adequate representation of the deformational behaviour of any soil. Henceforth, the elastic and plastic properties were identified with numerical calibration.

The calibration of the plasticity and elastic parameters was performed according to the methodology proposed by

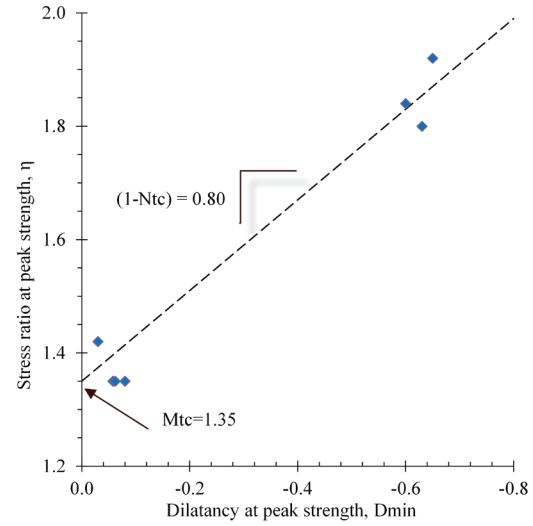


Figure 8. Stress–dilatancy of BL-2&1 at peak strength (η_{max} versus D_{min}).

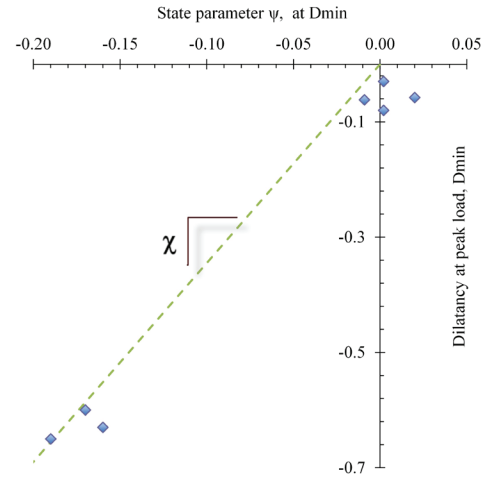


Figure 9. State–dilatancy of BL-2&1 at peak load (D_{min}). Note: theory requires trend to pass through the origin.

Jefferies & Been (2016). The dimensionless modulus H is a plastic hardening parameter in NorSand. The software NorTx1 (Excel VBA) allows for determining the parameter H by optimizing a set of drained triaxial test data. In this process of iterative forward modelling (IFM), an initial value of H is guessed, and the theoretical stress–strain behaviour is computed using NorSand (Jefferies & Been, 2016). Other soil properties are kept fixed. A trend is generally found in the form of

$$H = H_0 - H_y \psi \quad (6)$$

Some variability arises among tests because fabric effects are not included in the constitutive model. The H relation in Equation 6 provides a good fit across the suite

of BL-2&1 tests with the properties $H_0 = 85$ and $H_y = 850$, as shown in Figure 10.

Elasticity is essential to consider understanding how the undrained strength and stiffness of this material develop. Although elastic behaviour used to be challenging to measure, the advent of geophysical methods has made elastic measurements routine in practice in the laboratory and in situ.

The elastic shear modulus was determined with BE testing, and the results fit a power law. For dense samples, the proportionality constant and the exponent are 70 and 0.53, respectively; For loose samples, the best fit was obtained with

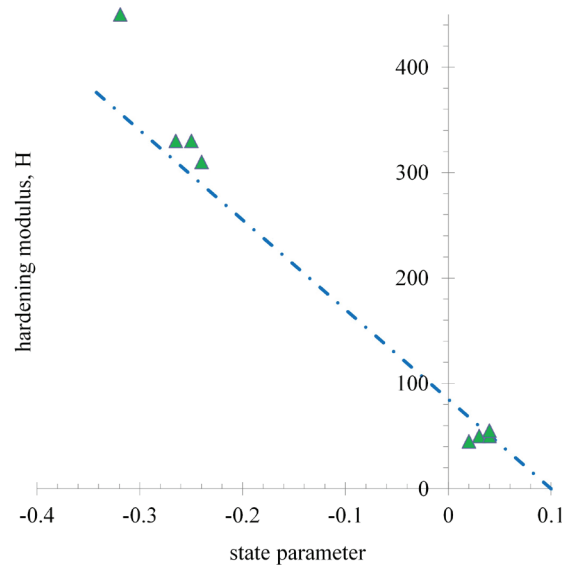


Figure 10. Fit across the BL-2&1 tailings (properties $H_0 = 85$ and $H_y = 850$).

39 and 0.6. The fit of the elastic model to the measured data using these soil properties is shown in Figure 11. Poisson's ratio was not measured, and a value of 0.2 was assumed for modelling.

3.4 NorSand performance validation

The properties of BL-2&1 derived from the drained and undrained triaxial tests are summarized in Table 4. The drained triaxial tests for loose and dense BL-2&1 tailings are presented in Figures 12a and 12b, respectively. In Figure 12a, it is possible to see that both the stress/strain graphs and the volumetric strain/axial strain graphs indicate the models'

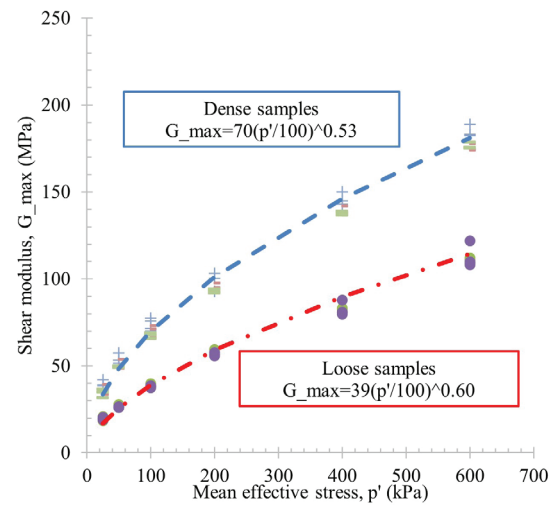


Figure 11. Variation of G_{max} with p' .

Table 4. NorSand soil properties of the BL-2&1 tailings and the typical range for sands.

	BL-2&1	Typical range (*)	Comment
CSL			
Γ	1.28	0.9–1.4	'Altitude' of CSL defined at 1 kPa
λ_{10}	0.19	0.03–0.15	Slope of CSL defined on base 10
CSL_a	1.13	-	Parameter for curved CSL analogous to Γ
CSL_b	0.23	-	Parameter for curved CSL analogous to λ
CSL_c	0.27	-	Parameter for curved CSL analogous to an exponent of the stress level
Plasticity			
M_{tc}	1.35	1.2–1.5	Critical friction ratio, with triaxial compression as a reference condition
N_{tc}	0.20	0.2–0.5	Volumetric coupling parameter
χ_{tc}	3.45	2.5–4.5	Relates minimum dilatancy to corresponding ψ , with triaxial as a reference condition
H	n/a	50–500	Plastic hardening modulus for loading
H_0	85	-	Often equal to $f(\psi)$
H_ψ	850	-	$H = H_0 - H_\psi \cdot \psi$
Elasticity			
G	39 and 70	-	Shear modulus
G_{exp}	0.6 and 0.53	-	Soil property
ν	0.2 (adopted)	0.1–0.3	Poisson's ratio

(*) NorSand typical range for sands (Jefferies et al., 2015).

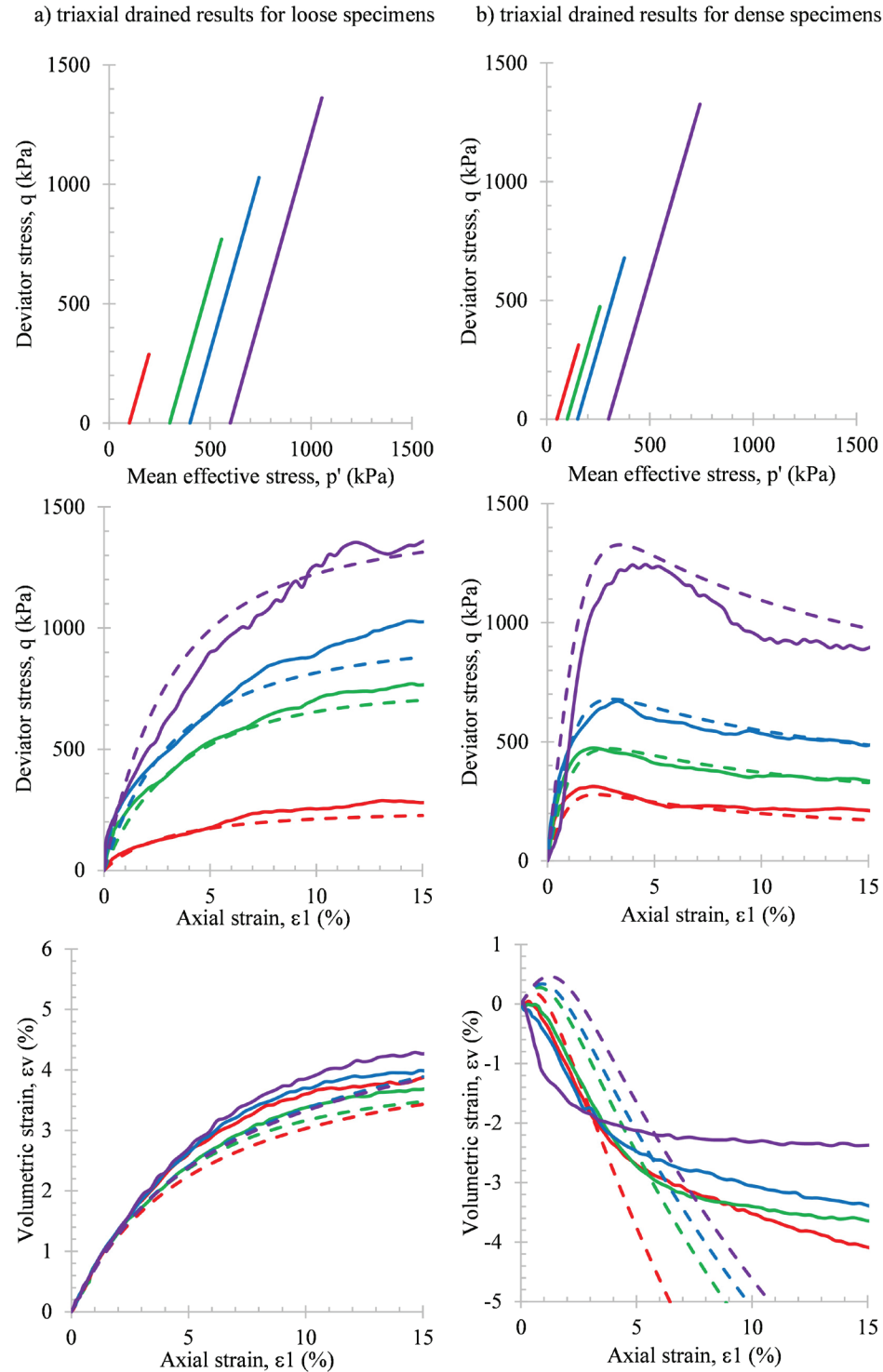


Figure 12. Drained triaxial test on samples and flotation tailings: calibrations of NorSand for the BL-2&1 sample: (a) loose specimens; (b) dense specimens. Continuous and dashed lines represent experimental and numerical results, respectively.

adherence to the experimental data. On the other hand, for dense specimens (Figure 12b), there is good adherence between only the experimental and numerical stress/strain curves. However, the relationship between axial and volumetric deformations shows adherence only until the peak deviator

stress. After reaching this value, the experimental volumetric deformation is reduced considerably and diverges from the model results. This divergence may be associated with the formation of shear bands and limitations of the boundary conditions defined in the modelling (Oda & Kazama, 1998).

Figure 13 shows two tailings specimens after drained shear. The well-defined rupture plane in Figure 13b is experimental evidence of the shear band hypothesis. The Tx12 software (VBA code) implements the NorSand model as a single Cauchy stress tensor, so shear bands are not allowed in this implementation. To assess the hypothesis of localization, complementary analyses were performed with the NorSand UDM for FLAC3D software.

Figure 14 shows the simulated triaxial tests for loose and dense conditions (i.e., ψ of 0.2 and -0.27, respectively). Cylindrical specimens were modelled with a 3.7 cm diameter and 8-cm height and sheared up to 20% deformation at a constant speed. The effective confining stress was fixed at 100 kPa. The horizontal displacement at the top and bottom was restricted to simulate the nonlubricated test conditions.

Despite the inaccuracy of the boundary conditions, the simplicity of the mesh, and the lack of proper calibration,

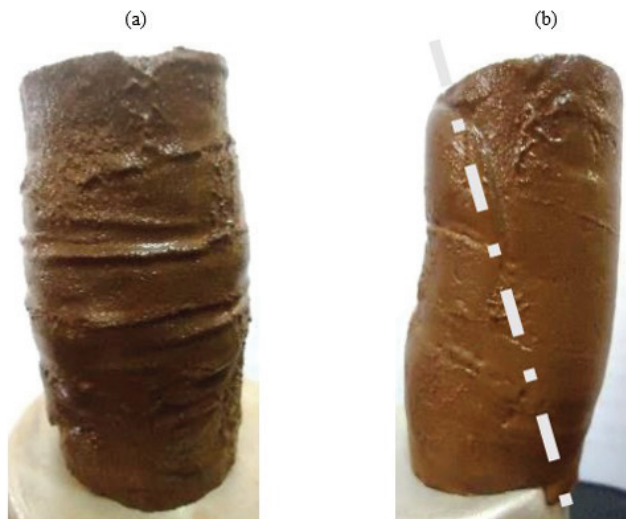


Figure 13. Photographs of two specimens ((a) loose and (b) dense) sheared in a drained triaxial test.

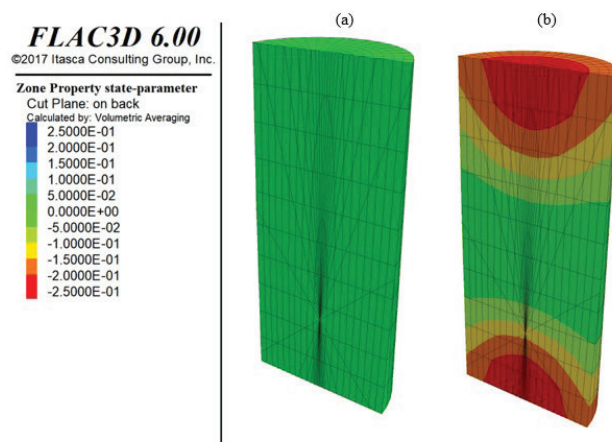


Figure 14. 3D numerical simulation of drained triaxial tests with compaction of approximately (a) 78% and (b) 105% of the standard Proctor dry density.

insightful observations can be made. First, the loose specimen was in a critical state condition in the shearing phase, and second, the dense specimen also converged to a steady state, but only the middle portion reached the critical state condition. Third, there is a notable anisotropy of the specimen results in this last case. These findings are consistent with the experimental observations and support the hypothesis that shear bands tend to form in dense samples.

Finally, Figure 15 shows the experimental results against the numerical predictions of the undrained tests for the loose samples. Again, the adherence of the numerical results to the experimental data is acceptable. However, the experimental results of the two specimens indicated that the strength increased at larger deformations (with a threshold of approximately 10% axial deformation). The increase in apparent strength during the tests is not predicted by the NorSand model. This may be associated with a boundary condition at large deformation in the tests. In other words, the specimens' loss of symmetry in the test influences the results. Figure 16 shows a post-rupture photograph of a specimen consolidated at 600 kPa. An increase in the specimen's central section is evident, corroborating the hypothesis of loss of symmetry at a large deformation.

4. Conclusion

This study critically evaluated the predictive capacity of NorSand, a critical state model, to represent the behaviour of iron ore tailings from the QF in Minas Gerais. Additional characterization of the tailings soils was presented to provide a broader description of the materials. The selected model

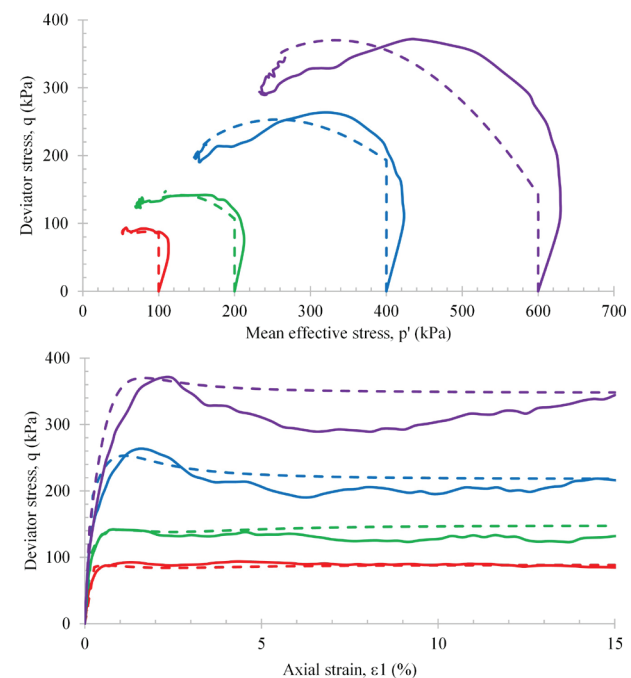


Figure 15. Comparison between experimental (continuous lines) and numerical (dashed lines) results: undrained triaxial test of a loose sample of BL-2&1 tailings.



Figure 16. Photograph of the undrained triaxial test result of a loose specimen (~78%) of flotation tailings (BL-2&1).

was adequate to evaluate the behaviour of these mine tailings. There was a consistent adherence of the simulation results to the experimental results of drained and undrained tests for deformations below 5% and specimens in which the state parameter had a small magnitude.

The predictions of the volumetric deformation model did not adhere to the experimental observations for dense drained tests, particularly after reaching the peak strength. This divergence may be associated with the appearing of shear bands. A multielement simulation showed that the formation of shear bands occurs in only dense specimens, which is coherent with the suggested hypothesis. Additional studies are needed to elucidate this issue.

Acknowledgements

The authors would like to acknowledge the University of Brasília (UnB) and the professors of the Graduate Program in Geotechnics at UnB for the knowledge provided. The present research was intended to test the validity of the NorSand model and verify its applicability to granular iron ore tailings. To achieve this goal, NorSand was implemented as a new user-defined constitutive model (UDM) in FLAC3D (Itasca, 2016). The model implemented was NorSand in its static (NorSand-M, monotonic) and dynamic (NorSand-PSR, with principal stress rotation) forms. As a sponsor of our research, Vale Institute of Technology (ITV) hired Itasca, the platform's developer, to implement a new numerical model as a UDM in FLAC3D. To contribute effectively and broadly to the practice of engineering, ITV abdicated the development rights and intellectual property. The authors would like to thank ITV for this effort.

Declaration of interest

The authors have no conflicts of interest to declare. All co-authors have observed and affirmed the contents of the paper, and there is no financial interest to report.

Authors' contributions

João Paulo de Sousa Silva: conceptualization, data curation, methodology, visualization, writing – original draft. Pedro Pazzoto Cacciari: formal analysis, validation. Vidal Felix Navarro Torres: validation. Luís Fernando Martins Ribeiro: supervision, formal analysis, methodology. André Pacheco de Assis: supervision, validation, writing – review & editing.

List of symbols

BL-2&1	blended tailings from iron ore operation plants 2 and 1
C_a	parameter for curved CSL analogous to Γ
C_b	parameter for curved CSL analogous to λ
C_c	parameter for curved CSL analogous to an exponent of the stress level
CD	consolidated drained triaxial compression tests
CSL	critical state line or critical state locus
CU	consolidated undrained triaxial compression tests
D	dilatancy
DLL	Dynamic-link library is Microsoft's implementation of the shared library concept in the Microsoft Windows and OS/2 operating systems.
E	Young's modulus
FT	flotation tailings from iron ore operation
FT-P1	flotation tailings from iron ore operation plant 1
FT-P2	flotation tailings from iron ore operation plant 2
G	shear modulus
G_0	initial shear modulus
G_{max}	shear modulus (the 'max' subscript is currently used geotechnical practice to denote elasticity)
G_s	specific gravity
H	dimensionless modulus is a plastic hardening parameter in NorSand.
H_0	plastic hardening parameter
H_y	plastic hardening parameter
IBPs	iron ore beneficiation plants
IFM	iterative forward modelling
K	bulk modulus
LL	liquid limit
M	critical friction ratio
M_{tc}	critical friction ratio (with triaxial as a reference condition)
ML	low-plasticity silt
NorTxI	free software in VBA
NP	non-plastic
N_{tc}	volumetric coupling parameter
P1	mineral processing plant 1

P2	mineral processing plant 2
PI	plasticity index
PL	plastic limit
TSFs	tailings storage facilities
UDM	User Defined constitutive Models for Itasca software
USCS	Unified Soil Classification System
VBA	Visual Basic for Applications
e	void ratio of the soil
e_{max}	minimum void ratio of the soil
e_{min}	minimum void ratio of the soil
e_c	void ratio at the critical state
p'	mean effective stress
w	water content
Γ'	'Altitude' of CSL defined at 1 kPa
γ	dry density
γ_d	dry density
η	stress ratio, volumetric coupling parameter
η_{max}	stress ratio, volumetric coupling parameter
λ	slope of CSL
λ_{10}	slope of CSL defined on base 10
ν	Poisson's ratio
χ	state-dilatancy parameter
χ_{tc}	state-dilatancy parameter (relates minimum dilatancy to corresponding ψ , with triaxial as a reference condition)
ψ	state parameter

References

- Been, K., & Jefferies, M. (1985). State parameter for sands: *Geotechnique* V35, N2, June 1985, P99–112. *International Journal of Rock Mechanics and Mining Sciences & Geomechanics Abstracts*, 22(6), 198. [http://dx.doi.org/10.1016/0148-9062\(85\)90263-3](http://dx.doi.org/10.1016/0148-9062(85)90263-3).
- Bellotti, R., Jamiolkowski, M., Lo Presti, D.C.F., & O'Neill, D.A. (1996). Anisotropy of small strain stiffness in Ticino sand. *Geotechnique*, 46(1), 115–131. <http://dx.doi.org/10.1680/geot.1996.46.1.115>.
- Boulanger, R.W., & Ziotopoulou, K. (2015). *PM4Sand (version 3): A sand plasticity model for earthquake engineering applications, Report No. UCD/CGM-15/01*. Center for Geotechnical Modeling, Department of Civil and Environmental Engineering, University of California.
- Casagrande, A. (1976). *Liquefaction and cyclic deformation of sands—a critical review: Harvard Soil Mechanics Series No. 88*. Harvard University.
- Dafalias, Y. (1986). Bounding surface plasticity. I: mathematical foundation and hypoplasticity. *Journal of Engineering Mechanics*, 112(9), 966–987. [http://dx.doi.org/10.1061/\(ASCE\)0733-9399\(1986\)112:9\(966\)](http://dx.doi.org/10.1061/(ASCE)0733-9399(1986)112:9(966)).
- Dafalias, Y., & Manzari, M. (1997). A critical state two-surface plasticity model for sands. *Geotechnique*, 47(2), 255–272. <http://dx.doi.org/10.1680/geot.1997.47.2.255>.
- Dafalias, Y., & Manzari, M. (2004). Simple plasticity sand model accounting for fabric change effects. *Journal of Engineering Mechanics*, 130(6), 622–634. [http://dx.doi.org/10.1061/\(ASCE\)0733-9399\(2004\)130:6\(622\)](http://dx.doi.org/10.1061/(ASCE)0733-9399(2004)130:6(622)).
- Dafalias, Y., & Popov, E. (1975). A model of nonlinearly hardening materials for complex loading. *Acta Mechanica*, 21, 173–192. <http://dx.doi.org/10.1007/BF01181053>.
- Davies, M. (2002). Tailings impoundment failures: are geotechnical engineers listening? *Geotechnical News – Vancouver*, 20(3), 31–36.
- Dorr, J.V.N. (1969). *Physiographic, stratigraphic and structural development of the Quadrilátero Ferrífero, Minas Gerais, Brazil (No. 641-A, pp. A1–A110)*. US Government Printing Office. <https://doi.org/10.3133/pp641A>.
- Jefferies, M. (1993). Nor-Sand: a simple critical state model for sand. *Geotechnique*, 43(1), 91–103. <http://dx.doi.org/10.1680/geot.1993.43.1.91>.
- Jefferies, M., & Been, K. (2016). Soil liquefaction: a critical state approach, 2nd edition. *Environmental Earth Sciences*, 75(12), 1014. <https://doi.org/10.1007/s12665-016-5600-y>.
- Jefferies, M., Shuttle, D., & Been, K. (2015). Principal stress rotation as cause of cyclic mobility. *Geotechnical Research*, 2(2), 66–96. <http://dx.doi.org/10.1680/gr.15.00002>.
- Li, W., Coop, M.R., Senetakis, K., & Schnaid, F. (2018). The mechanics of a silt-sized gold tailing. *Engineering Geology*, 241, 97–108. <http://dx.doi.org/10.1016/j.enggeo.2018.05.014>.
- Lunne, T., Knudsen, S., Blaker, Ø., Vestgård, T., Powell, J., Wallace, C.F., Krogh, L., Thomsen, N.V., Yetginer, G., & Ghanekar, R.K. (2019). Methods used to determine maximum and minimum dry unit weights of sand: is there a need for a new standard? *Canadian Geotechnical Journal*, 56(4), 536–553. <http://dx.doi.org/10.1139/cgj-2017-0738>.
- Nova, R., & Wood, D.M. (1982). A constitutive model for soil under monotonic and cyclic loading. In G.N. Pande & C. Zienkiewicz (Eds.), *Soil mechanics-transient and cyclic loads* (pp. 343–373). Wiley.
- Oda, M., & Kazama, H. (1998). Microstructure of shear bands and its relation to the mechanisms of dilatancy and failure of dense granular soils. *Geotechnique*, 48(4), 465–481. <http://dx.doi.org/10.1680/geot.1998.48.4.465>.
- Olivier, G., De Wit, T., Brenguier, F., Bezuidenhout, L., & Kunjwa, T. (2018). Ambient noise Love wave tomography at a gold mine tailings storage facility. *Geotechnique Letters*, 8(3), 178–182. <http://dx.doi.org/10.1680/jgele.18.00016>.
- Schnaid, F., Bedin, J., Fonseca, A.J.P.V., & Costa Filho, L.M. (2013). Stiffness and strength governing the static liquefaction of tailings. *Journal of Geotechnical and Geoenvironmental Engineering*, 139(12), 2136–2144. [http://dx.doi.org/10.1061/\(ASCE\)GT.1943-5606.0000924](http://dx.doi.org/10.1061/(ASCE)GT.1943-5606.0000924).
- Silva, J.P.S., Cacciari, P.P., Ribeiro, L.F., & Jefferies, M. (2021). Influence of compaction on small-strain shear modulus of iron ore tailings. In X. Geng (Eds.), *Proceedings of the Institution of Civil Engineers-Geotechnical Engineering* (pp. 1–30). London: Institution of Civil Engineers.
- Silva, J., Mendes, M., Milonas, J., Pirete, W., & Souza, W. (2013). Geotechnical parameters of iron ore tailings from the Quadrilátero Ferrífero after different treatments and

- ore processing. In R. Jewell, A.B. Fourie, J. Caldwell & J. Pimenta (Eds.), *Proceedings of the 16th International Seminar on Paste and Thickened Tailings* (pp. 261–271), Belo Horizonte, June 2013. Austrália: ACG. https://doi.org/10.36487/ACG_rep/1363_20_Silva.
- Soga, K., & Mitchell, J. (2005). *Fundamentals of soil behavior* (3rd ed.). Wiley.
- Verdugo, R., & Ishihara, K. (1996). The steady state of sandy soils. *Soil and Foundation*, 36(2), 81-91. http://dx.doi.org/10.3208/sandf.36.2_81.

Contaminant transport model in transient and unsaturated conditions applied to laboratory column test with tailings

Eliu James Carbaja¹ , Mariana dos Santos Diniz¹ ,

Roberto Lorenzo Rodriguez-Pacheco² , André Luís Brasil Cavalcante^{1#} 

Article

Keywords

Unsaturated porous medium
Unsaturated flow
Contaminant transport
Tailing

Abstract

Mining is an important economic activity in the modern world. However, despite the generated benefits, mining produces tremendous volumes of tailings, an environmental liability with numerous adverse effects. Researches about contaminant transport in tailings dam are important to assess the degree of contamination and to propose preventive or remedial measures. In geotechnical practice, the flow of solutes is generally characterized by numerical solution of the Richards equation to describe water movement followed by advection-dispersion equation to describe contaminant movement. This study aimed to model and simulate contaminant transport in a laboratory column test, using a new analytical formulation and mathematical codes, through tailings in transient unsaturated conditions. The analytical solution for the Richards equation was used to simulate the variation in the volumetric water content and to determine the transient contaminant plume using the advection-dispersion equation subsequently. The models were used to calibrate experimental data from hydraulic characterization and contamination tests. Finally, the normalized contaminant plume (c_w/c_0) was simulated as a function of time and space. Comparisons with experimental data showed that the analytical formulations adequately expressed the process of contaminant infiltration through the unsaturated porous medium. The formulations offered effectively and are configured as a new approach to solve various contamination problems in transient unsaturated conditions, providing insights into many complex processes that occur in the lab tests and requires far less computational effort compared with current programs to modeling the solute transport using numerical solutions, as the versatile commercial Software HYDRUS.

1. Introduction

A wide range of everyday human activities, such as tailings dams, release different types of contaminants to the soil surface. These contaminants pollute the subsurface through uncontrolled spills, leaks, dumps and disposal (Rutsch et al., 2008; Seferou et al., 2013; Adnan et al., 2018; Akbariyeh et al., 2018). Contaminant transport may lead to severe problems with the quality of the groundwater and the porous medium. A deeper understanding of hydrodynamic and hydrogeochemical processes of the unsaturated zone is essential to assess the vulnerability of an aquifer to contamination. In this sense, many studies related to water flow and solute movement in the subsurface have been made to a wide range of conditions involving different scales, types of soils, contaminants and

models of resolution (Bertolo, 2001; Rutsch et al., 2008; Mustafa et al., 2016; Sopilniak et al., 2017; Joshi & Gupta, 2018; Akbariyeh et al., 2018; Godoy et al., 2019).

In geotechnical practice, the flow of solutes is generally characterized by numerical solution of the Richards equation to describe water movement followed by advection-dispersion equation to describe contaminant movement (Richards, 1931). When applied, especially, in the field scale, this numerical solution is highly complex, computationally expensive. It inhibits insights that can be obtained from analytical solutions. One of the most versatile commercial software is HYDRUS.

HYDRUS is a Microsoft Windows based modeling environment for simulating water flow, heat, and solute transport in two- and three-dimensional variably saturated and unsaturated media. The program numerically solves the

[#]Corresponding author. E-mail address: abrasil@unb.br

¹Universidade de Brasília, Departamento de Engenharia Civil e Ambiental, Brasília, DF, Brasil.

²Instituto Geológico y Minero de España, Grupo de Investigación Recursos Minerales, Madrid, España.

Submitted on October 20, 2021; Final Acceptance on February 21, 2022; Discussion open until August 31, 2022.

<https://doi.org/10.28927/SR.2022.076021>



This is an Open Access article distributed under the terms of the Creative Commons Attribution License, which permits unrestricted use, distribution, and reproduction in any medium, provided the original work is properly cited.

Richards equation for saturated-unsaturated water flow and advection-dispersion equations for heat and solute transport (Šimůnek et al., 2016).

This study aims to model and simulate the contaminant transport in a laboratory column test, using a new analytical formulation and mathematical codes, through tailings in transient unsaturated conditions, providing insights into many complex processes that occur in the lab tests and requires far less computational effort compared with current programs to modeling the solute transport using numerical solutions, as the Software HYDRUS.

This paper innovates by developing a computational code that allows coupling the analytical solution of the Richards Equation proposed by Cavalcante & Zornberg (2017) to solve the infiltration problem taking into account the phenomena of transport of contaminants to unsaturated porous media, solved from the analytical solution proposed by Brenner (1962), described in terms of volumetric water content.

2. Contaminant transport modeling in an unsaturated porous medium

The study of contaminant transport in unsaturated porous media requires understanding the physical and biophysicochemical phenomena associated with water and solute flow in the soil.

In nature, a porous medium may exist in saturated or unsaturated conditions, where the underground water table delimits each zone. Below the water level, the soil is normally saturated. In this zone, the voids in the soil are entirely filled with water, and the pressure is positive. Above the water level, the soil may be unsaturated. In this zone, the pore pressure is negative and determined by the difference between the air and water pressure in the voids. The negative pressure is known as total suction, which consists of the sum of the matric and osmotic suctions.

The unsaturated zone plays a crucial role in contamination processes. This zone is essentially a natural filter, which reduces or attenuates the contamination of microbiological, physical and chemical constituents to nonhazardous levels by acting as a channel through which various liquid or vapor compounds circulate, attenuate and transform as they move from the surface to the unsaturated zone. Furthermore, contaminants can remain in this zone for decades, affecting the plants and animals and contaminating aquifers long after a spill.

When contaminants begin their trajectory on the surface of the terrain and are dragged by the waters that infiltrate the unsaturated zone, they are subjected to a series of transport mechanisms, which define how a specific compound will move in the porous medium. The movement of these compounds depends not only on the flow of the fluid in which these substances are dissolved but also on the soil-contaminant

interactions related to the chemical and biological processes to which these substances are subjected.

The analysis of contaminant transport from saturated to unsaturated porous media is relatively simple. For this purpose, reformulating the transport equations in terms of the volumetric water content of the porous medium suffices because varying the required parameters in an unsaturated porous medium reduces the conductive cross-section through which a contaminant can flow (Fityus et al., 1999).

2.1 Flow in unsaturated porous media

Water flow in unsaturated porous media is governed by the Richards equation, which is a mass conservation equation that combines the Darcy-Buckingham law and the continuity equation.

The continuity equation is based on the principle of mass conservation, i.e., on the fact that the difference between the masses of fluid entering and leaving an infinitesimal control volume equals the rate of change in mass storage in that volume. Considering that water, at the tension levels of this study, is incompressible, the following formulation is derived:

$$\frac{\partial \theta_w}{\partial t} = -\frac{\partial v_z}{\partial z} \quad (1)$$

where $\theta_w = \theta_w(z, t)$ is the volumetric water content [$L^3.L^{-3}$], and $v_z = v_z(z, t)$ is the fluid velocity [$L.T^{-1}$] in the z -direction. The fluid velocity can be defined using the Darcy-Buckingham law (Buckingham, 1907; Narasimhan, 2004), which is the unsaturated version of Darcy's law, as follows:

$$v_z = -k_z(\psi) \frac{\partial \phi}{\partial z} \quad (2)$$

where $k_z(\psi)$ is the hydraulic conductivity expressed in terms of suction [$L.T^{-1}$] in the z -direction; $\psi = \psi(z, t)$ is the total suction of water [$M.L^{-1}.T^2$]; and $\phi = \phi(z, t)$ is the hydraulic head of the fluid [L], which is defined as follows:

$$\phi = -z + \frac{\psi}{\rho_w g} \quad (3)$$

where z is the elevation head [L]; ρ_w is the density of water [$M.L^{-3}$]; and g is the gravitational acceleration [$L.T^{-2}$]. By combining Equations 2 and 3, the following expression is derived:

$$v_z = -k_z(\psi) \left(\frac{1}{\rho_w g} \frac{\partial \psi}{\partial z} - 1 \right) \quad (4)$$

Now, by combining Equations 1 and 4, the Richards equation for one-dimensional, unsaturated, transient flow in the z -direction is obtained as follows:

$$\frac{\partial \theta_w}{\partial t} = \frac{\partial}{\partial z} \left[k_z(\psi) \left(\frac{1}{\rho_w g} \frac{\partial \psi}{\partial z} - 1 \right) \right] \quad (5)$$

Cavalcante & Zornberg (2017) rewrote the Richards equation as a modified version of the Fokker-Planck equation to enable an analytical solution to the transient flow problem in unsaturated conditions. The modified version proposed by Cavalcante & Zornberg (2017) is as follows:

$$\frac{\partial \theta_w}{\partial t} = \frac{\partial}{\partial z} \left(D_z(\theta_w) \frac{\partial \theta_w}{\partial z} \right) - a_s(\theta_w) \frac{\partial \theta_w}{\partial z} \quad (6)$$

where D_z is the unsaturated diffusivity of water in the z -direction [$L^2.T^{-1}$], which is expressed as follows:

$$D_z(\theta_w) = \frac{k_z(\theta_w)}{\rho_w g} \frac{\partial \psi}{\partial \theta_w} \quad (7)$$

and a_s is the unsaturated advective flow [$L.T^{-1}$], as given by the following equation:

$$a_s(\theta_w) = \frac{\partial k_z(\theta_w)}{\partial \theta_w} \quad (8)$$

Using this representation of the Richards equation and the specific hydraulic functions (constitutive models), Cavalcante & Zornberg (2017) analytically solved the unsaturated flow problem for transient flow conditions. The adopted hydraulic functions involve a logarithmic relationship between the suction and the volumetric water content (soil water retention curve) $[\psi(\theta_w)]$ and a linear relationship between the unsaturated hydraulic conductivity and the volumetric water content $[k_z(\theta_w)]$. Therefore, Cavalcante & Zornberg (2017) proposed the following equation to determine $\psi(\theta_w)$:

$$\psi(\theta_w) = \frac{1}{\delta} \ln \left(\frac{\theta_w - \theta_r}{\theta_s - \theta_r} \right) \quad (9)$$

where θ_s is the saturated volumetric water content [$L^3.L^{-3}$]; θ_r is the residual volumetric water content [$L^3.L^{-3}$]; and δ is a fitting parameter [$M^{-1}.L^1.T^2$]. In contrast, Cavalcante & Zornberg (2017) proposed the following equation to determine $k_z(\theta_w)$:

$$k_z(\theta_w) = k_s \left(\frac{\theta_w - \theta_r}{\theta_s - \theta_r} \right) \quad (10)$$

where k_s is the saturated hydraulic conductivity [$L.T^{-1}$].

Cavalcante & Zornberg (2017) presented analytical solutions for the Richards equation, with various initial and boundary conditions, using the characteristic curve and the unsaturated hydraulic conductivity function defined by Equation 9 and Equation 10. The constitutive model by Cavalcante & Zornberg (2017) is the most convenient when compared with other constitutive models because only one fitting parameter is needed; also, this model makes it possible to linearize the Richards equation and, therefore, to solve the problem analytically.

This study used a solution for a soil column of finite length, with a constant infiltration rate imposed on the upper

boundary. Specifically, in this case, the initial condition is described by the uniform initial water content as follows:

$$\theta_w(z, 0) = \theta_i \quad (11)$$

where θ_i is the initial volumetric water content [$L^3.L^{-3}$].

A Neumann boundary condition is adopted, which involves a constant infiltration rate imposed on the upper boundary of the domain as follows:

$$\left(\bar{D}_z \frac{\partial \theta_w}{\partial z} - k_z \right) \bigg|_{z=0} = v_0 \quad (12)$$

where v_0 is the infiltration rate [$L.T^{-1}$]. The maximum infiltration rate that can be physically imposed corresponds approximately to the saturated hydraulic conductivity of the porous medium (k_s). Specifically, the maximum infiltration rate that can be imposed is as follows:

$$v_{0,\max} = \frac{\theta_s k_s}{(\theta_s - \theta_r)} \quad (13)$$

For a soil column of finite length L , the lower boundary condition adopted in this study is described as follows:

$$\frac{\partial \theta_w}{\partial z}(L, t) = 0 \quad (14)$$

This lower boundary condition implies that the water content and, therefore, the suction reach constant values at a given depth. Thus, at a given depth, the hydraulic gradient in the z -direction is equal to one.

The analytical solution that corresponds to this initial condition and the boundary conditions is as follows (Cavalcante & Zornberg, 2017):

$$\theta_w(z, t) = \theta_i + \left(\frac{v_0}{k_s} (\theta_s - \theta_r) - \theta_i \right) D(z, t) \quad (15)$$

where:

$$D(z, t) = 1 - \sum_{m=1}^{\infty} \frac{\frac{2\bar{a}_s L}{\bar{D}_z} \beta_m \left[\beta_m \cos\left(\frac{\beta_m z}{L}\right) + \frac{\bar{a}_s L}{2\bar{D}_z} \sin\left(\frac{\beta_m z}{L}\right) \right] \exp\left(\frac{\bar{a}_s z}{2\bar{D}_z} - \frac{\bar{a}_s^2 t}{4\bar{D}_z} - \frac{\beta_m^2 \bar{D}_z t}{L^2}\right)}{\left[\beta_m^2 + \frac{\bar{a}_s L}{\bar{D}_z} + \left(\frac{\bar{a}_s L}{2\bar{D}_z}\right)^2 \right] \left[\beta_m^2 + \left(\frac{\bar{a}_s L}{2\bar{D}_z}\right)^2 \right]} \quad (16)$$

and β_m are the eigenvalues that correspond to the positive roots of the following equation:

$$\beta_m \cot(\beta_m) - \frac{\beta_m^2 \bar{D}_z}{\bar{a}_s L} + \frac{\bar{a}_s L}{4\bar{D}_z} = 0 \quad (17)$$

The results can be calculated accurately by considering only the first four terms of the series described by Equation 17. In this case, Equation 17 can be approximated as follows:

$$\begin{aligned}
 D(z, t) = & \frac{1}{2} \operatorname{erfc}(Z_{-1}) + \sqrt{\frac{\bar{a}_s^2 t}{\pi \bar{D}_z}} \exp\left(-\frac{(z - \bar{a}_s t)^2}{4 \bar{D}_z t}\right) - \\
 & - \frac{1}{2} \left(-1 + \frac{\bar{a}_s z}{\bar{D}_z} + \frac{\bar{a}_s^2 t}{\bar{D}_z}\right) \exp\left(\frac{\bar{a}_s z}{\bar{D}_z}\right) \operatorname{erfc}(Z_{+1}) + \\
 & + \sqrt{4 \frac{\bar{a}_s^2 t}{\pi \bar{D}_z}} \left[1 + \frac{\bar{a}_s}{4 \bar{D}_z} (2L - z + \bar{a}_s t)\right] \\
 & \exp\left(\frac{\bar{a}_s L}{\bar{D}_z} - \frac{1}{4 \bar{D}_z t} (2L - z + \bar{a}_s t)^2\right) - \\
 & - \frac{\bar{a}_s}{\bar{D}_z} \left[2L - z + \frac{3 \bar{a}_s t}{2} + \frac{\bar{a}_s}{4 \bar{D}_z} (2L - z + \bar{a}_s t)^2\right] \\
 & \exp\left(-\frac{\bar{a}_s L}{\bar{D}_z}\right) \operatorname{erfc}\left(\frac{2L - z + \bar{a}_s t}{2 \sqrt{\bar{D}_z t}}\right) \\
 Z_{\pm 1} = & \frac{z \pm \bar{a}_s t}{2 \sqrt{\bar{D}_z t}}
 \end{aligned} \quad (18)$$

where $\operatorname{erfc}(Z)$ is the complementary error function, which is defined as follows:

$$\operatorname{erfc}(Z) = 1 - \frac{2}{\pi} \int_0^Z \exp(-t^2) dt \quad (19)$$

2.2 Contaminant transport

The movement of a solute through a saturated porous medium primarily results from two simultaneous mechanisms: advection and hydrodynamic dispersion. The hydrodynamic dispersion corresponds to the combined action of the mechanical dispersion and molecular diffusion mechanisms. Besides that, there are interactions between the porous medium and the solute, defined as sorption, limiting the contaminant transport. All these mechanisms are described as functions of the volumetric water content to analyze the effect of this variation on the contaminant plume.

Solutes are transported in a porous medium by the flow of the percolating fluid without changing their concentration in the solution, which is a process known as advection. The mass flow by advection is as follows:

$$J_a = \theta_w v_p c_w \quad (20)$$

where $J_a = J_a(z, t)$ is the mass flow by advection of the contaminant per unit area and per unit time [$\text{M.L}^{-2}.\text{T}^{-1}$]; $c_w = c_w(z, t)$ is the contaminant concentration [M.L^{-3}]; $\theta_w = \theta_w(z, t)$ is the volumetric water content [$\text{L}^3.\text{L}^{-3}$] obtained by Cavalcante & Zornberg (2017); and $v_p = v_p(\theta_w)$ is the percolation rate [L.T^{-1}]. The percolation rate is the effective flow velocity that corresponds only to the pores through which the solute actually percolates and is defined as follows (Hillel, 2003; Bear & Cheng, 2010):

$$v_p = \frac{k_z i}{\theta_w} \quad (21)$$

where i is the hydraulic gradient [L.L^{-1}].

As contaminant molecules are transported, they tend to deviate from the main trajectory, some at a higher velocity than others, thus causing dilution of the solution. The components resulting from the dilution are the result of mechanical dispersion; i.e., they are a consequence of velocity heterogeneity inside the system and molecular diffusion due to different concentration gradients (Freeze & Cherry, 1979). Therefore, the sum of those terms can be expressed by the hydrodynamic dispersion coefficient as follows:

$$D_h = D_m + D^* \quad (22)$$

where $D_h = D_h(z, t)$ is the hydrodynamic dispersion coefficient [$\text{L}^2.\text{T}^{-1}$]; $D_m = D_m(z, t)$ is the mechanical dispersion coefficient [$\text{L}^2.\text{T}^{-1}$]; and $D^* = D^*(z, t)$ is the molecular diffusion coefficient [$\text{L}^2.\text{T}^{-1}$].

Mechanical dispersion is predominantly a function of both the heterogeneities in hydraulic conductivity and porosity (intrinsic properties of the porous media) and of the fluid flow. The mechanical dispersion coefficient, D_m , is given by:

$$D_m = \alpha_d v_p \quad (23)$$

where α_d is the longitudinal dispersivity coefficient [L].

The mass flow by mechanical dispersion in unsaturated porous media is described by Fick's first law as follows:

$$J_m = -\theta_w D_m \frac{\partial c_w}{\partial z} \quad (24)$$

where $J_m = J_m(z, t)$ is the mass flow by mechanical dispersion of the contaminant per unit area per unit time [$\text{M.L}^{-2}.\text{T}^{-1}$].

The molecular diffusion mechanism in porous media will differ from that in free water because of the effects of porosity and tortuosity. It is caused by the random movement of contaminant molecules in the liquid phase of the porous medium. The rate of movement is determined by the concentration gradient in the medium. The dissolved solute moves from an area of higher concentration to an area of lower concentration. This phenomenon occurs independently of the flow velocity, and the molecular diffusion coefficient, D^* , is defined as follows:

$$D^* = \tau D_0 \quad (25)$$

where D_0 is the molecular diffusion coefficient in the aqueous solution [$\text{L}^2.\text{T}^{-1}$] and $\tau = \tau(z, t)$ is the tortuosity factor [L.L^{-1}], which is defined as follows (Viotti et al., 2005):

$$\tau = \frac{(\theta_s - \theta_w)^{10/3}}{\theta_s^2} \quad (26)$$

The mass flow by molecular diffusion in unsaturated porous media is described by Fick's first law as follows:

$$J^* = -\theta_w D^* \frac{\partial c_w}{\partial z} \quad (28)$$

where $J^* = J^*(z, t)$ is the mass flow by molecular diffusion of the contaminant per unit area and per unit time [$M \cdot L^{-2} \cdot T^{-1}$].

During contaminant transport through unsaturated porous media, interactions occur between the contaminants and the soil particles that delay or accelerate the contamination process. Bear & Cheng (2010) state that most processes involve contaminant mass transfer from the liquid phase to the solid phase (sorption). In some cases, the reverse (desorption) process occurs. Sorption is geochemically quantified using the retardation factor, R (Fetter, 1999).

According to Van Genuchten & Dalton (1986) and Bear & Cheng (2010), the retardation phenomenon in an unsaturated porous medium can be formulated using a linear sorption isotherm, assuming that the percolation rate, v_p , is constant in space and time whenever solute concentration levels are low. In this case, the retardation factor in an unsaturated porous medium is calculated as follows:

$$R = 1 + \frac{\rho_d K_d}{\theta_w} \quad (29)$$

where $R = R(z, t)$ is the retardation factor [dimensionless], ρ_d is the dry density of the soil [$M \cdot L^{-3}$], and K_d is the equilibrium distribution coefficient [$L^3 \cdot M^{-1}$].

The equilibrium distribution coefficient measures the amount of chemical substance adsorbed onto soil per amount of water, and it is obtained using the batch equilibrium adsorption test. The linear sorption isotherm is appropriate for cases in which the sorption potential proportionally increases with the concentration and is defined as follows:

$$c_s = K_d c_w \quad (30)$$

where $c_s = c_s(z, t)$ is the adsorbed contaminant concentration [$M \cdot M^{-1}$].

It is important to highlight that most of the contaminants of concern coming from tailings would be metals speciated as cations and cations complexes (e.g., the nickel and cobalt), and their interaction with the porous media is complicated and, under different geochemical conditions, unable to be expressed with reversible and linear sorption represented by an equilibrium distribution coefficient. However, sometimes, this most straightforward form of adsorption linear isotherm is very appropriate at low contaminant concentrations and, for this reason, is used in many studies (Srinivasan & Mercer, 1988; Barone et al. 1992; Mallants et al., 2011).

Column and batch techniques are either commonly used in the laboratory to determine equilibrium distribution coefficients. It should be noted that aspects of transport kinetics, adsorption kinetics, and porous media surface area are not replicated well in batch tests because the results are determined in the equilibrium sorption behavior of a specific compound-sediment combination. Batch tests,

despite their limitations, are used in geotechnical practice due to relatively fast and straightforward. However, column experiments always remain limited in their transferability to real-world conditions because of experimental restrictions (such as those imposed by limitations of scale), which means that processes that might co-occur in nature cannot be fully reproduced in a laboratory. Moreover, chemical processes cannot be separated completely from physical processes in column tests (Porro et al., 2000; Banzhaf & Hebig, 2016).

It is important to highlight that when the sorption isotherms are not linear, it is possible to manipulate mathematically and linearize them. Despite the inherent bias of this methodology, as expressed by Foo & Hameed (2010), linearization remains a confident option in the literature, applied in over 95% of the liquid-phase adsorption systems. Therefore, the next challenge in the adsorption field is the identification and clarification of both isotherm models in various adsorption systems.

Models of contaminant transport in physical equilibrium (the advection-dispersion equation – ADE) are based on the classic description of uniform solute flow and transport. The matrix of the porous medium consists of solid particles or impermeable aggregates separated by pores or fractures, wherein solute flow and transport occur (Šimůnek & Van Genuchten, 2008). This formulation is based on the mass conservation equation (or continuity equation) for only one direction. The z -axis of a representative elementary volume in the ADE is as follows:

$$\frac{\partial c_w}{\partial t} = -\frac{v_p}{R} \frac{\partial c_w}{\partial z} + \frac{D_h}{R} \frac{\partial^2 c_w}{\partial z^2} \quad (31)$$

where z is the spatial coordinate [L], and t is the time [T].

Brenner (1962) analytically solved the ADE for the following boundary conditions:

Initial condition

$$c_w(z, 0) = 0 \quad (32)$$

Upper boundary condition

$$\left(v_p c_w - D_h \frac{\partial c_w}{\partial z} \right) \Big|_{z=0} = \begin{cases} v_p c_0 & 0 < t < t_0 \\ 0 & t > t_0 \end{cases} \quad (33)$$

where c_0 is the initial concentration of the applied solute and is constant in the upper boundary [$M \cdot L^{-3}$], and t_0 is the time of application of the displacing solution.

Lower boundary condition

$$\frac{\partial c_w}{\partial z}(L, t) = 0 \quad (34)$$

where L is the study sample length [L].

Under these hypotheses, the analytical solution by Brenner (1962) is as follows:

$$c_w(z, t) = \begin{cases} A(z, t) & 0 < t < t_0 \\ A(z, t) - A(z, t - t_0) & t > t_0 \end{cases} \quad (35)$$

where:

$$A(z, t) = \frac{1}{2} \operatorname{erfc} \left(\frac{Rz - v_p t}{2\sqrt{D_h R t}} \right) + \sqrt{\frac{v_p^2 t}{\pi D_h R}} \exp \left[-\frac{(Rz - v_p t)^2}{4D_h R t} \right] - \frac{1}{2} \left(1 + \frac{v_p z}{D_h} + \frac{v_p^2 t}{D_h R} \right) \exp \left(\frac{v_p z}{D_h} \right) \operatorname{erfc} \left(\frac{Rz + v_p t}{2\sqrt{D_h R t}} \right) + 2\sqrt{\frac{v_p^2 t}{\pi D_h R}} \left[1 + \frac{v_p}{4D_h} \left(2L - z + \frac{v_p t}{R} \right) \right] \exp \left[\frac{v_p L}{D_h} - \frac{R}{4D_h t} \left(2L - z + \frac{v_p t}{R} \right)^2 \right] - \frac{v_p}{D_h} \left[2L - z + \frac{3v_p t}{2R} + \frac{v_p}{4D_h} \left(2L - z + \frac{v_p t}{R} \right)^2 \right] \exp \left(\frac{v_p L}{D_h} \right) \operatorname{erfc} \left[\frac{R(2L - z) + v_p t}{2\sqrt{D_h R t}} \right] \quad (36)$$

Another way of presenting the analytical solution by Brenner (1962) is in its dimensionless form as follows:

$$C(Z, T) = \begin{cases} B(Z, T) & 0 < T < T_0 \\ B(Z, T) - B(Z, T - T_0) & T > T_0 \end{cases} \quad (37)$$

where:

$$B(Z, T) = \frac{1}{2} \operatorname{erfc} \left(\frac{RZ - T}{2\sqrt{\frac{RT}{P}}} \right) + \sqrt{\frac{PT}{\pi R}} \exp \left[-\frac{P(RZ - T)^2}{4RT} \right] - \frac{1}{2} \left[1 + P \left(Z + \frac{T}{R} \right) \right] \cdot \exp(PZ) \operatorname{erfc} \left(\frac{RZ + T}{2\sqrt{\frac{RT}{P}}} \right) + 2\sqrt{\frac{PT}{\pi R}} \left[1 + \frac{P}{4} \left(2 - Z + \frac{T}{R} \right) \right] \exp \left[P - \frac{PR}{4T} \left(2 - Z + \frac{T}{R} \right)^2 \right] - P \left[2 - Z + \frac{3T}{2R} + \frac{P}{4} \left(2 - Z + \frac{T}{R} \right)^2 \right] \exp(P) \operatorname{erfc} \left[\frac{R(2 - Z) + T}{2\sqrt{\frac{RT}{P}}} \right] \quad (38)$$

where $C = C(Z, T)$ is the normalized concentration ($C = c_w/c_0$); T is the normalized time ($T = v_p t / L$); Z is the normalized spatial coordinate ($Z = z / L$); and P is the Peclet number ($P = v_p L / D_h$).

After applying the consolidation theory induced by micro-collapses, it is necessary for its validation by comparing values obtained in the field. Thus, the consistency of the method was through the Guelph Permeameter. The depth and place of the test were the same that the undisturbed samples. In the end, some comparisons of the alternative and classical theories were executed.

3. Materials and methods

3.1 Materials

Data from laboratory tests conducted by Rodríguez-Pacheco (2002) were used in this study, e.g., the soil water

retention curve, the sorption isotherm, and the breakthrough curve of deformed samples of nickel tailings. The samples were collected from the Cuban nickel industry located in the northeast of the province of Holguín in Cuba, where ore is extracted from lateritic nickel ore deposits in the municipalities of Mayari and Moa. Ore is extracted from those deposits using the open-pit mining method (Rodríguez-Pacheco, 2002). Nickel and cobalt concentrates are extracted using the metallurgical process of ammoniacal carbonate leaching (ACL) and of sulfuric acid leaching (SAL). In this paper, the transport of contaminants through the tailings generated by the SAL process was studied. These beneficiation processes generate large volumes of tailings, which are mixed, diluted in water, and transported in pipes as a viscous liquid (pulp) to tailings dams (Rodríguez-Pacheco, 2002; Sosa, 2016).

The experiments and details on the composition of SAL Tailing are described in Rodríguez-Pacheco (2002). In synthesis, the predominant mineral is hematite (about 70%), followed by aluminum (about 10%) and quartz (3%). The SAL residue has little organic matter content, on average 0.6%. The SAL Tailing has a high specific weight (Table 1) with very fine granulometry.

Rodríguez-Pacheco (2002) used two suction control methods to collect experimental data for the soil water retention curve to cover the most extensive possible range of suction values. Thus, the psychrometric method was chosen for suction values ranging from 100 to 10 000 kPa, in small, cylindrical samples (15 mm in diameter and 12 mm in height) compacted with controlled moisture and an initial dry density to complement the suction-controlled oedometer test (axis translation technique) for suction values ranging from 10 to 900 kPa, which were difficult to measure accurately using the psychrometric method.

The soil water retention curve of the experimental data is shown in Figure 1 for drying and wetting trajectories determined using the psychrometric and suction-controlled oedometric techniques for remolded samples with an initial void ratio of 1.75. For the tests performed by Rodríguez-Pacheco (2002), Figure 1 shows that the two suction measurement techniques overlap well. However, more tests are needed to reach such a conclusion. This finding indicates that, in this study, the osmotic suction corresponds to a small portion of the total suction because the psychrometric technique measures the total suction. The oedometric technique with axis translation measures only the matric suction.

Figure 1 also shows the phenomenon of hysteresis, defined by the different drying and wetting paths. In general,

Table 1. Characteristics and physical properties of the column used in the contaminant transport tests (Rodríguez-Pacheco, 2002).

Column characteristics					Physical indices					Velocity
L (cm)	D (cm)	V (cm ³)	M (g)	V_p (cm ³)	ρ_d (g/cm ³)	ρ (g/cm ³)	ρ_s (g/cm ³)	n	θ	v_p (cm/h)
5	1.6	10.55	15.52	6.06	1.56	2.15	3.88	0.61	0.61	1.2

where, with respect to column characteristics, L is the column length [L], D is the diameter [L], V is the total volume [L³], M is the mass of tailing [M], and V_p is the pore volume [L³].

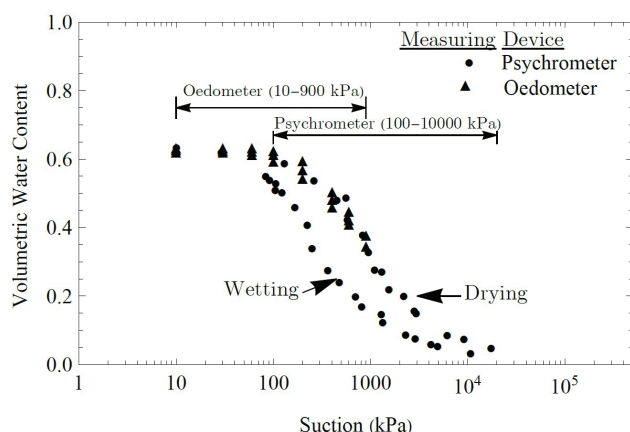


Figure 1. Soil water retention curve for the drying and wetting trajectories of SAL tailings (Rodríguez-Pacheco, 2002).

more water is retained by the system during drying than is adsorbed by the system at the same magnitude of suction during wetting. The possible causes of the phenomenon are the contact angle between a fluid and a solid, entrapment of air, and different spatial connectivity of pores during drying and wetting (Gennes et al., 2004).

Rodríguez-Pacheco (2002) performed a laboratory batch test to construct the Ni^{2+} solute sorption isotherm. This test was performed at a controlled temperature of $22 \pm 2^\circ\text{C}$, with an initial pH of 6.9. The metal was dissolved in 0.01 mM KNO_3 with an electrolyte support of pH = 5.5. This solution is the same as that used by Rodríguez-Pacheco (2002) in column tests. Rodríguez-Pacheco (2002) used a Ni salt, $(\text{NO}_3)_2\text{6H}_2\text{O}$, to prepare the solution of the metal. In Figure 2, the experimental Ni^{2+} sorption isotherm data reveal a linear behavior.

In results showed by Rodríguez-Pacheco (2002), nickel sorption had different behaviors when tested in SAL and ACL tailings. In ACL, sorption showed a non-linear isotherm. In SAL, a linear isotherm is well adjusted (Figure 2). It is important to note that the equilibrium distribution coefficient depends on the solute concentration. Also, according to Godoy et al. (2019), the sorption phenomenon is strongly correlated to the cation exchange capacity and significantly correlated to mesoporosity and microporosity of the porous medium.

Rodríguez-Pacheco (2002) conducted laboratory column tests with a stainless-steel column. He placed a polyvinyl chloride (PVC) membrane, which is inert and resistant to high pressures, to construct the breakthrough curve of Ni^{2+} . The tailings samples were packed in the columns in compressed layers and subjected to vibrations until reaching a uniform density of 1.55 g/cm^3 . The columns were saturated with an electrolyte solution of 0.1 mM KNO_3 for 24 hours to fully saturate the pores, which would avoid any cavities, which would favor preferential flow. The same electrolyte solution was passed through the column until steady-state conditions were reached, which was achieved when the flow rate, pH, and electrical conductivity of the solution entering and leaving

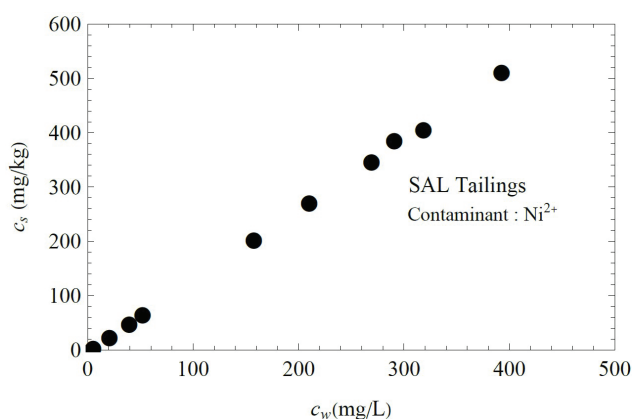


Figure 2. Ni^{2+} sorption isotherm from SAL tailings (Rodríguez-Pacheco, 2002).

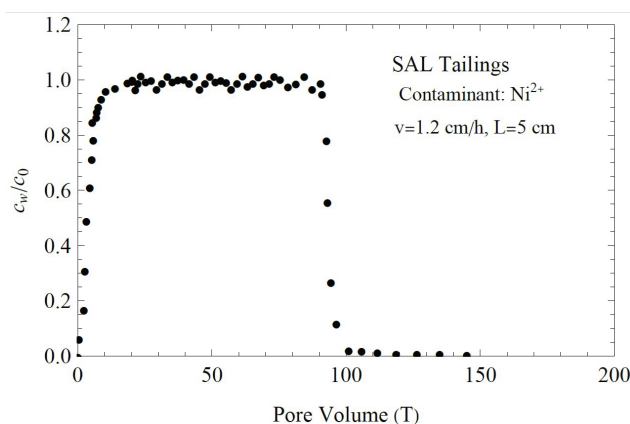


Figure 3. The breakthrough curve of Ni^{2+} from SAL tailings (Rodríguez-Pacheco, 2002).

the column were equal. The tailings columns were loaded with solutes in a steady-state and a constant downward flow. Effluents were collected at varying time intervals. Table 1 outlines the different parameters of the column used in the contaminant transport tests.

The column test was performed by continuously injecting 91 pore volumes of solution for the sorption process and 127 pore volumes of solute-free solution for the desorption process. Table 2 outlines the main conditions and characteristics of the column test of Ni^{2+} with sorption and desorption processes in SAL tailings used by Rodríguez-Pacheco (2002).

Figure 3 presents the experimental data of the breakthrough curve of Ni^{2+} constructed from the column test with SAL tailings. This figure shows that 14 pore volumes must be passed to reach a normalized concentration equal to or close to 1 ($c_w/c_0 \approx 1$).

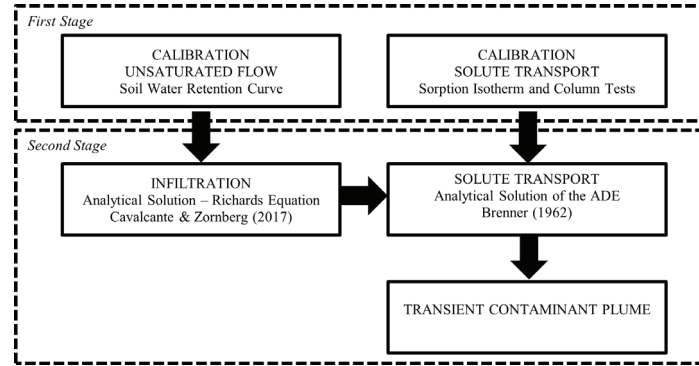
3.2 Method

Figure 4 presents a flowchart of the method used to implement the model for contaminant transport in unsaturated porous media.

Table 2. Characteristics and concentrations in the column test (Rodríguez-Pacheco, 2002).

Contaminant	V_{ps}	V_{pd}	$v(\text{cm/h})$	$C_0 (\text{mg/L})$	$C_w (\text{mg/L})$
Ni^{2+}	91	127	1.2	534	5.72

where V_{ps} is the pore volume of the solution injected in sorption and V_{pd} is the pore volume of the contaminant-free solution injected in desorption.

**Figure 4.** Flowchart of the method of analysis.

The first stage included calibration of the solute flow and the experimental transport data through analytical formulations. Then, the strategy proposed by Bear & Cheng (2010) was used to fit the experimental data. The authors recommend using the least-squares minimization method, which consists of minimizing the error, E , expressed as the squared sum of the difference between a sample of actual values and a sample of estimated values, and is described by the following equation:

$$E = \sum_{i=1}^n \left[(c/c_0)_m - (c/c_0)_c \right]^2 \quad (39)$$

where $(c/c_0)_m$ is the difference between the experimental normalized concentration and $(c/c_0)_c$ is the theoretically calculated normalized concentration.

The second stage included contaminant transport simulations for unsaturated conditions. Modeling was performed using analytical formulations and mathematical codes to simultaneously analyze the solute flow and the effect of varying the volumetric water content on the contaminant plume using the data obtained from the calibration process. To simulate the contaminant infiltration process and, therefore, the variation in the volumetric water content in unsaturated conditions, the analytical solution by Cavalcante & Zornberg (2017) was used. This solution presents a distribution of the volumetric water content within the porous medium that varies in space and time. In turn, the analytical solution of the ADE for contaminant transport by Brenner (1962), rewritten in terms of the volumetric water content, was used to simulate the advance of the contaminant plume.

3.3 Model calibration

The calibrations of the experimental data for the hydraulic characterization tests and the contamination of SAL tailings are presented in this section.

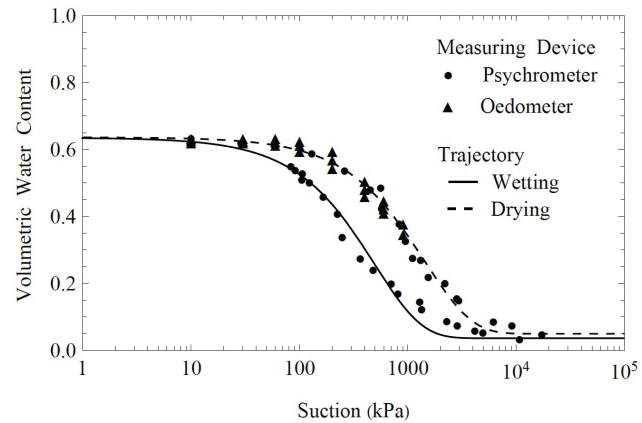
**Figure 5.** Constitutive Model of Cavalcante & Zornberg (2017) applied for drying and wetting trajectories of the SAL tailings.

Figure 5 shows the experimental soil water retention curve for drying and wetting trajectories with an initial void ratio of 1.75. These experimental data were fitted using the constitutive model by Cavalcante & Zornberg (2017). The fitted parameters and their error values are presented in Table 3. The analysis of the error values shows that the constitutive model by Cavalcante & Zornberg (2017) fitted the experimental data of the soil water retention curve very well for wetting and drying trajectories.

Figure 6 shows the Ni^{2+} solute sorption isotherm as a linear curve in the experimental data. Therefore, these data were fitted using a linear regression isotherm. The value of the equilibrium distribution coefficient, $K_d = 1.31 \text{ L/kg}$, was calculated from this fitting adjustment.

In Figure 7, the experimental elution (sorption – desorption) curve of Ni^{2+} is shown. These experimental data were model using the analytical solution for the ADE by Brenner (1962). The parameters R and P , calibrated using the ADE, and the error value is presented in Table 4. Therefore,

Table 3. Parameters of the soil water retention curve fitted using the Constitutive Model of Cavalcante & Zornberg (2017).

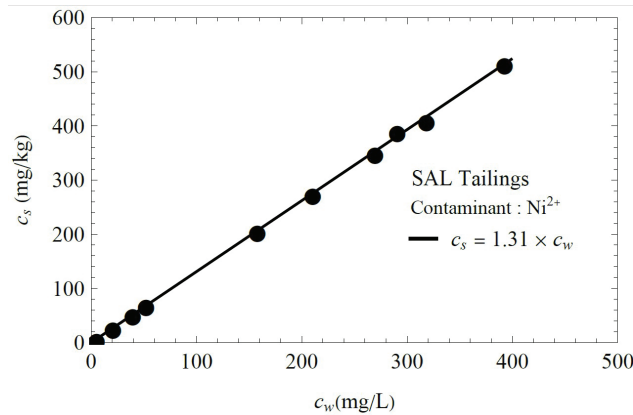
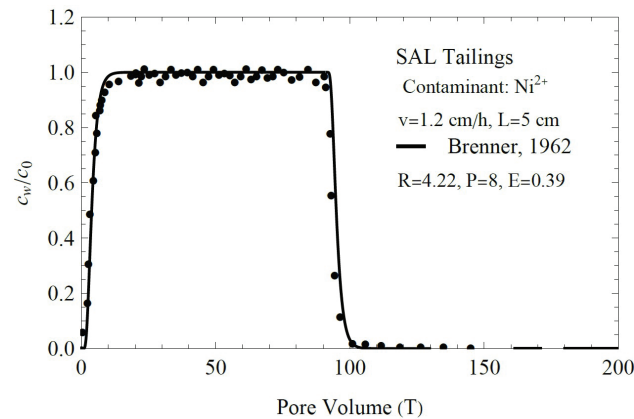
Trajectory	e	θ_s	θ_r	δ	E
Drying	1.75	0.636	0.049	0.00069	0.0162
Wetting	1.75	0.635	0.036	0.00201	0.0199

where e is the void ratio, θ_s is the saturated volumetric water content, θ_r is the residual volumetric water content, δ is the fitting parameter, and E is the adjust error.

Table 4. Calibrated parameters of the ADE model – Brenner (1962).

Solute	R	P	D_h (m ² /s)	α_d (m)	E
Ni ²⁺	4.22	8	2.08×10^{-8}	0.00625	0.39

where R is the retardation factor, P is the Peclet number, D_h is hydrodynamic dispersion coefficient, α_d is longitudinal dispersivity coefficient and E is the adjust error.

**Figure 6.** Ni²⁺ sorption isotherm fitted using the linear model for the SAL tailings.**Figure 7.** Breakthrough curve of Ni²⁺ modeled by Brenner (1962).

the analytical model by Brenner (1962) reliably represents the experimental elution curve of Ni²⁺.

The retardation factor of the studied contaminant is greater than 4 (Table 4). Therefore, the tailings have a good capacity to sorb the studied solute. The value of the Peclet number ($P=8$) shows that advection and mechanical dispersion are the predominant mechanisms in the column test and that molecular diffusion processes are negligible. The value of the error ($E=0.39$) shows that the model by Brenner (1962) reliably fits the experimental data of the breakthrough curve.

4. Results and discussion

The results and analyses of the modeling of the contaminant transport in SAL tailings in unsaturated conditions are presented in this section. In the simulations, a continuous source of contamination is placed in the upper limit of the SAL tailings of the column under analysis. Also, the initial volumetric water content of the SAL tailings is considered to be already equal to the residual volumetric water content (θ_r), with an initial concentration equal to zero; i.e., before the unsaturated flow phenomenon occurs, the tailings profile already contains moisture, and the initial concentration of nickel is zero. This model also assumes that the tailings column is a finite medium.

The parameters used for the one-dimensional modeling of contaminant transport in unsaturated conditions, which describe both the hydraulic and contaminant transport parameters, were calculated as follows:

- The saturated volumetric water content ($\theta_s = 0.635$), residual volumetric water content ($\theta_r = 0.036$) and fitting hydraulic ($\delta = 0.00201$) parameters were calculated by calibrating the experimental data of the soil water retention curve of the SAL tailings using the constitutive model by Cavalcante & Zornberg (2017).
- The hydraulic gradient ($i = 1.1$) and real average saturated hydraulic conductivity ($k_s = 5.26 \times 10^{-6}$ m/s) of the tailings were obtained from the doctoral thesis of Rodríguez-Pacheco (2002).
- The column length ($L = 0.5$ m) and the dry density of the tailings ($\rho_d = 1560$ kg/m³) were calculated from the column test.
- In the column length, $z = 0$ indicates the top of the sample, where the contaminant transport starts.
- The Ni²⁺ equilibrium distribution coefficient ($K_d = 1.31 \times 10^{-3}$ m³/kg) was calculated by calibrating the experimental data from the batch test using a linear model.
- The values of the molecular diffusion coefficient of Ni²⁺ in an aqueous solution ($D_0 = 6.79 \times 10^{-10}$ m²/s) are outlined in Fetter (1999).
- The dispersivity coefficient ($\alpha_d = 0.00625$ m) of Ni²⁺ was calculated by calibrating the experimental data from the column test using the analytical solution of the ADE model by Brenner (1962).

Figure 8 shows the time history of volumetric water content (θ_v) for different locations. The curves of the volumetric water content start at the value of the *residual volumetric water content* ($\theta_r = 0.036$) in unsaturated conditions and end at the value of the saturated volumetric water content ($\theta_s = 0.635$) when all voids are filled with the contaminant. This figure shows a transition zone characterized by the marked increase in the volumetric water content with infiltration time.

The volumetric water content is the ratio of the volume of water to the unit volume of soil. This parameter has an important role for contaminant transport over space and time. As can be observed in Figure 8, the volumetric water content is higher near the top of the specimen, and lower at greater depths. It can also be seen that in the first few minutes, the increasing of the volumetric water content is more pronounced.

Figure 9 illustrates the time history of matric suction at different locations. The data in this figure show that, as expected, the matric suction is maximal when the volumetric water content is minimal (Figure 8) and equal to the residual volumetric water content (θ_r) in unsaturated conditions. Minimal matric suction is also observed when the volumetric water content (Figure 8) is maximal and equal to the saturated volumetric water content (θ_s) in saturated conditions. This figure also shows a transition zone characterized by a marked decrease in matric suction as the volumetric water content increases (Figure 8).

Matric suction is the free energy change in a unit volume of water when isothermally transferred from the soil water state to the free water state (Zhang & Lu, 2019). In Figure 9, one can observe that the matric suction is lower near the top of the specimen, and higher at greater depths. It is correct because the top of the specimen became saturated firstly (Figure 8). It can also be seen that in the first few minutes, the decreasing of the matric suction is more pronounced.

Figure 10 shows the time history of unsaturated hydraulic conductivity at different locations. The data in this figure show that, as expected, the hydraulic conductivity is minimal when the volumetric water content (Figure 8) is minimal and equal to θ_r in unsaturated conditions. The data also show that the hydraulic conductivity is maximal when the volumetric water content (Figure 8) is maximal and equal to θ_s in saturated conditions. This figure also shows a transition zone characterized by a marked increase in hydraulic conductivity as the volumetric water content increases (Figure 8).

Unsaturated hydraulic conductivity refers to a measure of water-retaining ability of the soil when the pores are not saturated with water. As can be observed in Figure 10, the unsaturated hydraulic conductivity is higher near the top of the specimen, and lower at greater depths. It is correct because the top of the specimen became saturated firstly (Figure 9). It can also be seen that in the first few minutes, the increasing of the unsaturated hydraulic conductivity is more pronounced. Combining Figures 9 and 10, one can

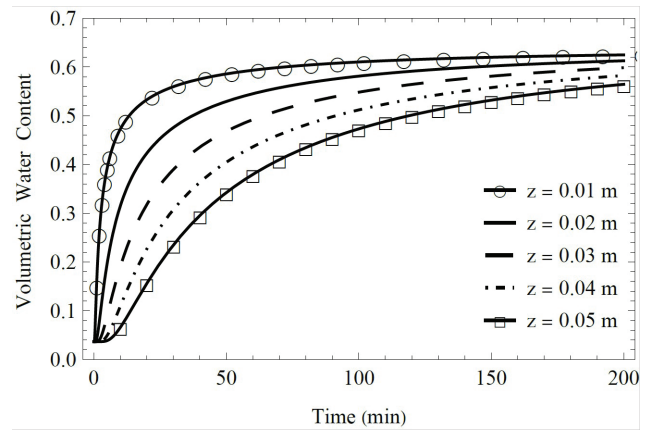


Figure 8. Predicted time history of volumetric water content at different locations.

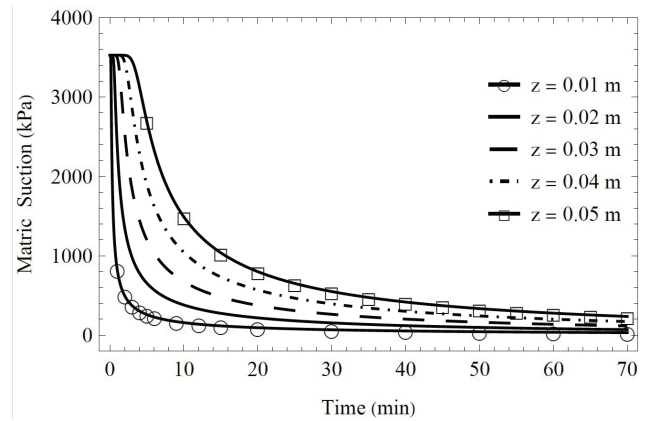


Figure 9. Predicted time history of matric suction at different locations.

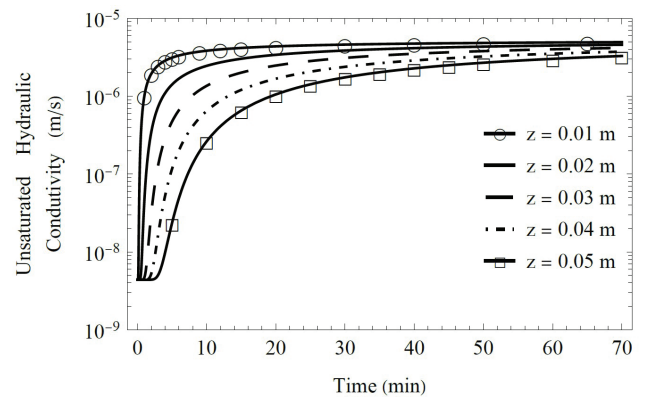


Figure 10. Predicted time history of unsaturated hydraulic conductivity at different locations.

confirm that the matric suction influences the behavior of unsaturated soils in terms of permeability.

Figures 11a, 11b, and 11c illustrate the time history, at different locations, of the degree of saturation, the contaminant percolation rate, and the tortuosity factor, respectively. The data in these figures show that, as expected, the degree of

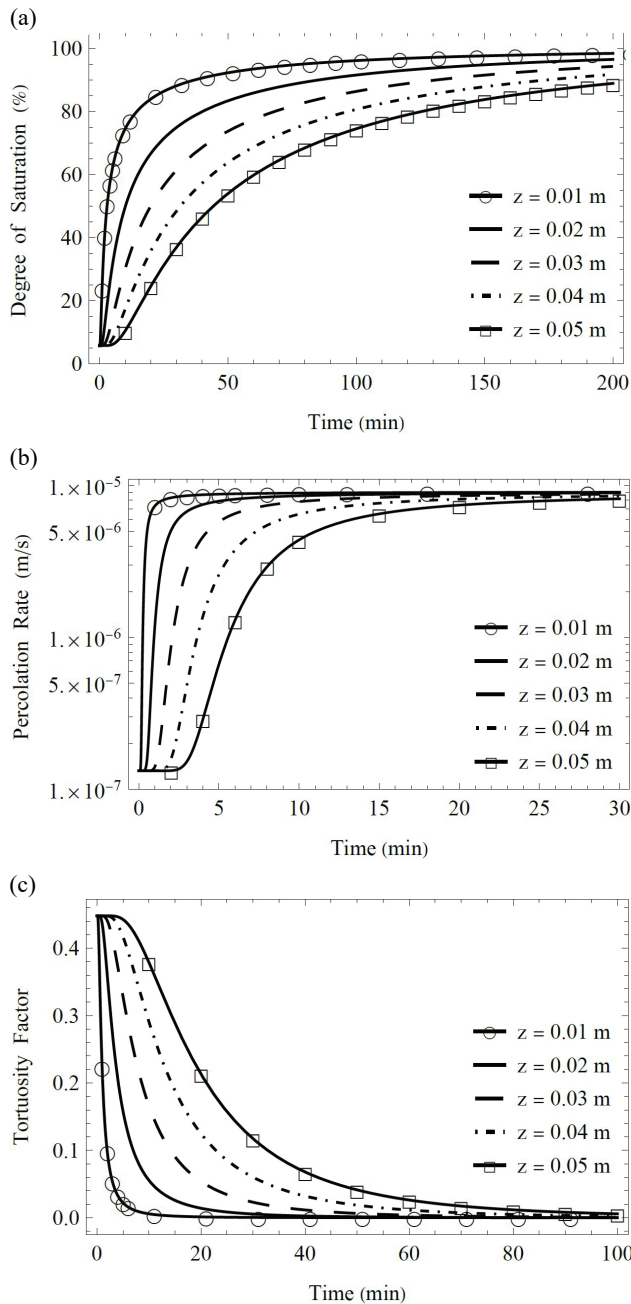


Figure 11. Predicted time history, at different locations, of: (a) Degree of saturation, (b) Contaminant percolation rate, and (c) Tortuosity factor.

saturation, the percolation rate, and the tortuosity factor are practically zero when the volumetric water content (Figure 8) is minimal and equal to θ_r in unsaturated conditions. Conversely, when the volumetric water content (Figure 8) is maximal and equal to θ_s in saturated conditions, the degree of saturation, percolation rate, and tortuosity factor are maximal. The curves have similar shapes because these physical quantities are directly proportional to the volumetric water content (Figure 8).

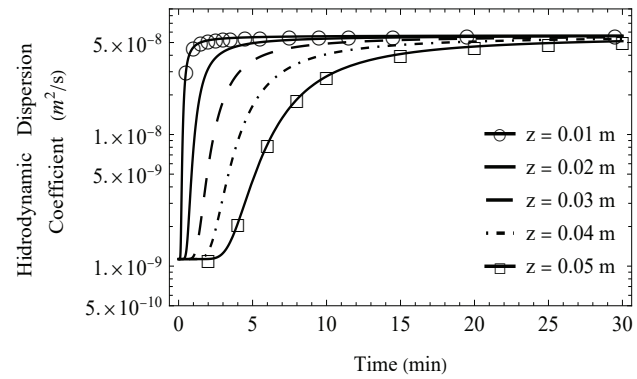


Figure 12. Predicted time history of hydrodynamic dispersion coefficient of Ni^{2+} at different locations.

As can be observed in Figure 11, the degree of saturation, the percolation rate and the tortuosity factor are higher near the top of the specimen, and lower at greater depths. It is correct because the top of the specimen became saturated firstly (Figure 9). It can also be seen that in the first few minutes, the increasing of the unsaturated hydraulic conductivity is more pronounced. At near the top of the specimen, the degree of saturation is reached after 180 min. The tortuosity is an intrinsic property of a porous material usually defined as the ratio of actual flow path length to the straight distance between the ends of the flow path (Bear, 1988). Therefore, the tortuosity factor is expected to change during the transport of the contaminant.

Figure 12 shows the time history of the hydrodynamic dispersion coefficient of Ni^{2+} at different locations. This figure shows that the hydrodynamic dispersion coefficient is minimal when the volumetric water content (Figure 8) is minimal and equal to θ_r in unsaturated conditions. In these conditions, the hydrodynamic dispersion coefficient equals the molecular diffusion coefficient because the percolation rate is zero; therefore, contaminants are only transported at a microscopic scale. Conversely, the hydrodynamic dispersion coefficient is maximal when the volumetric water content (Figure 8) is equal to θ_s in saturated conditions. In these conditions, the hydrodynamic dispersion coefficient equals the mechanical dispersion coefficient; therefore, contaminants are predominantly transported at a macroscopic scale. This figure also shows a transition zone characterized by a marked increase in the hydrodynamic dispersion coefficient as the volumetric water content increases (Figure 8).

The hydrodynamic dispersion coefficient is one of the most important parameters in the prediction of contaminant concentrations in soil using advection–dispersion models. It is a measure for describing the mixing processes of solutes in porous media. As can be observed in Figure 12, the hydrodynamic dispersion coefficient is higher near the top of the specimen, and lower at greater depths. It can also be seen that in the first few minutes, the increasing of the hydrodynamic dispersion coefficient is more pronounced.

Figure 13 illustrates the time history of the retardation factor of Ni^{2+} at different locations. A comparison of Figures 13 and 8 shows that the retardation factor is maximal when the volumetric water content is minimal and equal to the residual volumetric water content θ_r in unsaturated conditions. Therefore, contaminants are transported only at a microscopic scale by the mechanism of molecular diffusion because the percolation rate is virtually zero. Also, the retardation factor is minimal when the volumetric water content (Figure 8) is maximal and equal to the saturated volumetric water content θ_s ; thus, the percolation rate is also maximal in saturated conditions. Therefore, contaminants are predominantly transported at a macroscopic scale due to advection and mechanical dispersion mechanisms. Figure 13 also shows a transition zone characterized by the marked increase in the retardation factor when the volumetric water content increases (Figure 8).

The retardation factor is a measure of the ability of the ground to restrain the migration of the contaminant. It shows how many times the migration of the substance is subjected to adsorption slower than the actual speed of water flow in the pore spaces (Mikołajków, 2003). In Figure 9, one can

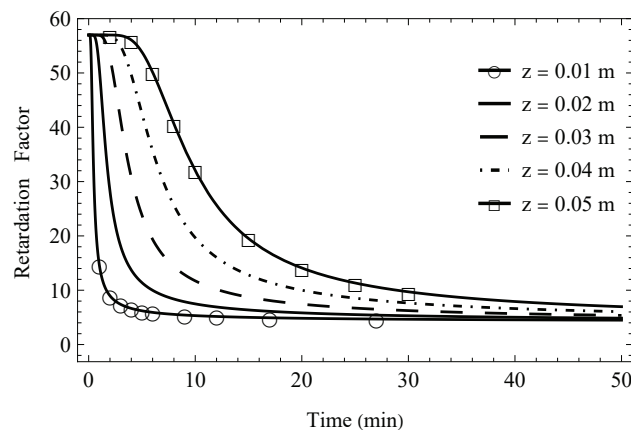


Figure 13. Predicted time history of retardation factor of Ni^{2+} at different locations.

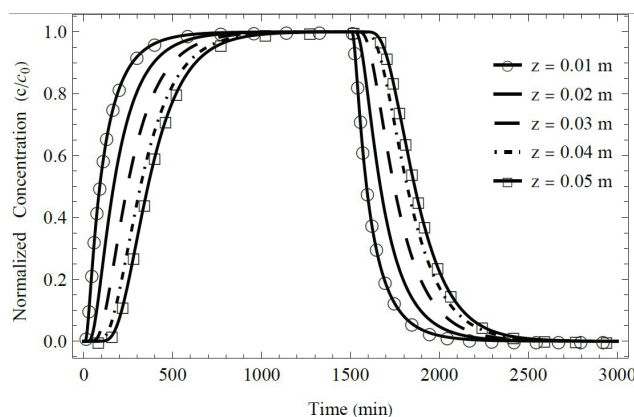


Figure 14. Predicted time history of normalized concentration of Ni^{2+} at different locations.

observe that the retardation factor is lower near the top of the specimen, and higher at greater depths. It is correct because the top of the specimen became saturated firstly (Figure 8) and the unsaturated hydraulic conductivity is greater (Figure 10). It can also be seen that in the first few minutes, the decreasing of the retardation factor is more pronounced.

Figure 14 shows a time history of the normalized concentration of Ni^{2+} at different locations. An analysis of Figure 14 shows that, as expected, as the depth increases, the elution curve shifts to the right, thereby increasing the time for the normalized concentration to approach one in the ascending section of the curve (sorption process) as well as the descending section of the curve (desorption process). Figure 14 also shows that as the infiltration time increases, the normalized concentration increases proportionally until it reaches its maximum in the sorption process. As the infiltration time increases, the normalized concentration decreases until reaching its minimum in the desorption process.

As can be observed in Figure 14, the normalized concentration of Ni^{2+} is higher near the top of the specimen, and lower at greater depths, during the sorption process. It can also be seen that it becomes lower near the top of the specimen, and higher at greater depths, during the desorption process. For this experiment, after 1500 min, the desorption process begins.

5. Conclusions

Based on the experimental soil water retention curve of SAL tailings, the osmotic suction of these tailings is negligible. This is important because the model by Cavalcante & Zornberg (2017) adopted in this study disregards osmotic suction effects and considers the gradient of osmotic suction as approximately zero, since it is related to the concentration of salts in the soil and its variations over space, in general, are not significant. Although for the data of this research, the results obtained by the two types of equipment resulted in a small contribution of osmotic suction, it is important to emphasize that for contaminated soils, this is not always observed.

The constitutive models proposed by Cavalcante & Zornberg (2017) have only a single fitting parameter in contrast to other constitutive models, such as the model by Van Genuchten (1980), which makes it easier to understand and mathematically handle the model because, in addition to being a single parameter, this parameter has a physical meaning. Except for the hydraulic fitting parameter (δ), all other parameters (θ_r , θ_s , and k_s) of the constitutive model can be directly calculated from geotechnical tests. These constitutive models reliably fit the experimental data of the soil water retention curve of the SAL tailings for the wetting and drying trajectories.

The analytical solution of the Richards equation by Cavalcante & Zornberg (2017) for unsaturated and transient flow conditions represents the variation in the volumetric

water content in one-dimensional space and time. Controlling the volumetric water content was crucial in modeling the contaminant infiltration process and, therefore, the advance of the contaminant plume in space and time in unsaturated conditions in SAL tailings. Furthermore, this relation allows us to use the various analytical solutions for contaminant transport in saturated conditions for unsaturated conditions by replacing the porosity with the volumetric water content.

The unsaturated hydraulic conductivity function was derived using constitutive models proposed by Cavalcante & Zornberg (2017), based on the fitting parameter δ , obtained from the soil water retention curve and the saturated hydraulic conductivity. These parameters contributed to a reliable representation of the hydraulic conductivity of the SAL tailings and, therefore, to the determination of the percolation rate, which is used to determine the contaminant mass flow by advection and hydrodynamic dispersion.

The calibration of the experimental data of the breakthrough curve of Ni^{2+} showed that the retardation factor is greater than 4. Hence, the SAL tailings have a good capacity of sorption for the studied solute, which is environmentally beneficial due to the ability of the SAL tailings to retain and decrease the advance of this metal through its porous matrix.

The analytical solution by Cavalcante & Zornberg (2017) adequately represented the contaminant infiltration process and, therefore, the variation in the volumetric water content in unsaturated conditions in space and time, and the analytical solution by Brenner (1962) adequately represented the contaminant plume in space and time through the SAL tailings, with the initial and boundary conditions established in our problem. Controlling the volumetric water content was crucial for analyzing its effect on the contaminant transport mechanisms and contaminant plume.

Based on analytical solutions, the present model has simplifications with specific initial and boundary conditions and a linear sorption isotherm (mathematically expressed in terms of the equilibrium distribution coefficient). Despite its limitations, it adequately represented the contamination transport of nickel in SAL tailing in Cuba.

The model advantages are that it allows validating numerical approaches, providing insights of many complex processes that occur in the field and in the lab and field and requires far less computational effort compared with current programs to modeling the solute transport using numerical solutions, as the versatile commercial Software HYDRUS 2D/3D (Šimůnek et al., 2016).

As expected, in the process of simulating contaminant transport for SAL tailings in unsaturated conditions, the volumetric water content is minimal and equal to the residual volumetric water content, which implies that the hydraulic conductivity and, consequently, the percolation rate are virtually zero. Furthermore, the retardation factor is maximal. Therefore, in these conditions, contaminants are transported only at a microscopic scale by the mechanism of molecular diffusion because the percolation rate is zero.

As the infiltration progresses, the volumetric water content increases until reaching its maximum value, which is equal to the saturated volumetric water content; therefore, the hydraulic conductivity and the percolation rate also increase until reaching their maximum values, and the retardation factor decreases until reaching its minimum value. This occurs when the tailings are in *saturated conditions*. Therefore, contaminants are predominantly transported at a macroscopic scale by the mechanisms of advection and mechanical dispersion.

Acknowledgements

This study was financed in part by the Coordination for the Improvement of Higher Education Personnel – Brasil (CAPES) – Finance Code 001. The authors also acknowledge the support of the National Council for Scientific and Technological Development (CNPq Grant 304721/2017-4, 435962/2018-3, 140923/2020-9 and 305484/2020-6), the Foundation for Research Support of the Federal District (FAPDF) (Projects 0193.002014/2017-68 and 0193.001563/2017), and the University of Brasília.

Declaration of interest

The authors have no conflicts of interest to declare. All co-authors have observed and affirmed the paper's contents, and there is no financial interest to report.

Authors' contributions

Eliu James Carbajal: conceptualization, data curation, methodology, software, writing – original draft. Mariana dos Santos Diniz: conceptualization, data curation, methodology, software, writing. Roberto Lorenzo Rodriguez-Pacheco: investigation, writing. André Luís Brasil Cavalcante: formal analysis, funding acquisition, supervision, methodology, project administration, resources, validation, writing – review & editing, software.

List of symbols

ACL	Ammoniacal Carbonate Leaching
ADE	Advection-Dispersion Equation
SAL	Sulfuric Acid Leaching
Ni^{2+}	Nickel (II)
$(c/c_0)_c$	Theoretically calculated normalized concentration.
$(c/c_0)_m$	Experimental normalized concentration
a_s	Unsaturated advective flow
C	Normalized concentration
c_0	Initial concentration of the applied solute
c_s	Adsorbed contaminant concentration
c_w	Contaminant concentration
D^*	Molecular diffusion coefficient


D_0	Molecular diffusion coefficient in the aqueous solution
D_h	Hydrodynamic dispersion coefficient
D_m	Mechanical dispersion coefficient
Dz	Unsaturated diffusivity of water in the z-direction
e	Void Ratio
E	Adjust Error
g	Gravitational acceleration
i	Hydraulic gradient
J^*	Mass flow by molecular diffusion of the contaminant per unit area and per unit time
J_a	Mass flow by advection of the contaminant per unit area and per unit time
J_m	Mass flow by mechanical dispersion of the contaminant per unit area per unit time
K_d	Equilibrium distribution coefficient
k_s	Saturated hydraulic conductivity
k_z	Hydraulic conductivity expressed in terms of suction in the z-direction
L	Sample length
P	Peclet number
R	Retardation factor
T	Normalized time
t	Time
t_0	Time of application of the displacing solution
v_0	Infiltration rate
$v_{0,max}$	Maximum infiltration rate
v_p	Percolation rate
v_z	Fluid velocity in the z-direction
Z	Normalized spatial coordinate
z	Spatial coordinate
α_d	Longitudinal dispersivity coefficient
β_m	eigenvalues
δ	Fitting parameter, Cavalcante & Zornberg (2017) coefficient
ϕ	Hydraulic head
θ_i	Initial volumetric water content.
θ_r	Residual volumetric water content
θ_s	Saturated volumetric water content
θ_w	Volumetric water content
ρ_d	Dry density of the soil
ρ_w	Density of water
τ	Tortuosity factor
ψ	Total suction of water

References


- Adnan, S., Iqbal, J., Maltamo, M., & Valbuena, R. (2018). GIS-based DRASTIC model for groundwater vulnerability and pollution risk assessment in the Peshawar District, Pakistan. *Arabian Journal of Geosciences*, 11(16), 458. <http://dx.doi.org/10.1007/s12517-018-3795-9>.
- Akbariyeh, S., Bartelt-Hunt, S., Snow, D., Li, X., Tang, Z., & Li, Y. (2018). Three-dimensional modeling of nitrate-N transport in vadose zone: roles of soil heterogeneity and groundwater flux. *Journal of Contaminant Hydrology*, 211, 15-25. <http://dx.doi.org/10.1016/j.jconhyd.2018.02.005>.
- Banzhaf, S., & Hebig, K.H. (2016). Use of column experiments to investigate the fate of organic micropollutants: a review. *Hydrology and Earth System Sciences*, 20(9), 3719-3737. <http://dx.doi.org/10.5194/hess-20-3719-2016>.
- Barone, F.S., Rowe, R.K., & Quigley, R.M. (1992). A laboratory estimation of diffusion and adsorption coefficients for several volatile organics in a natural clayey soil. *Journal of Contaminant Hydrology*, 10(3), 225-250. [http://dx.doi.org/10.1016/0169-7722\(92\)90062-J](http://dx.doi.org/10.1016/0169-7722(92)90062-J).
- Bear, J. (1988). *Dynamics of fluids in porous media* (761 p.). Courier Corporation.
- Bear, J., & Cheng, A. (2010). *Modeling ground water flow and contaminant transport*. New York: Springer. <https://link.springer.com/book/10.1007%2F978-1-4020-6682-5>.
- Bertolo, R.A. (2001). *Hidrodinâmica and hidrogeoquímica da Zona não saturada do Aquífero Adamantina em Urânia-SP*. [Thesis Doctoral, University of São Paulo]. University of São Paulo (in Portuguese).
- Brenner, H. (1962). The diffusion model of longitudinal mixing in beds of finite length. Numerical values. *Chemical Engineering Science*, 17, 229-243. [http://dx.doi.org/10.1016/0009-2509\(62\)85002-7](http://dx.doi.org/10.1016/0009-2509(62)85002-7).
- Buckingham, E. (1907). *Studies on the movement of soil moisture* (USDA Bureau of Soils, Bull. no. 38). Washington, DC: Government Printing Office.
- Cavalcante, A.L.B., & Zornberg, J.G. (2017). Efficient approach to solving transient unsaturated flow problems. I: analytical solutions. *International Journal of Geomechanics*, 17(7), 04017013. [http://dx.doi.org/10.1061/\(ASCE\)GM.1943-5622.0000875](http://dx.doi.org/10.1061/(ASCE)GM.1943-5622.0000875).
- Fetter, C.W. (1999). *Contaminant hydrogeology* (500 p.). New Jersey: Prentice Hall.
- Fityus, S.G., Smith, D.W., & Booker, J.R. (1999). Contaminant transport through an unsaturated soil liner beneath a landfill. *Canadian Geotechnical Journal*, 36(2), 330-354. <http://dx.doi.org/10.1139/t98-112>.
- Foo, K.Y., & Hameed, B.H. (2010). Insights into the modeling of adsorption isotherm systems. *Chemical Engineering Journal*, 156(1), 2-10. <http://dx.doi.org/10.1016/j.cej.2009.09.013>.
- Freeze, R. A. & Cherry, J.A. (1979). *Groundwater* (604 p.). Prentice Hall.
- Gennes, P.-G., Brochard-Wyart, F., & Quéré, D. (2004). *Capillarity and wetting phenomena: drops, bubbles, pearls, waves* (308 p.). New York, USA: Springer Verlag.
- Godoy, V.A., Zuquette, L.V., & Gómez-Hernández, J.J. (2019). Spatial variability of hydraulic conductivity and solute transport parameters and their spatial correlations to soil properties. *Geoderma*, 339, 59-69. <http://dx.doi.org/10.1016/j.geoderma.2018.12.015>.
- Hillel, D. (2003). *Introduction to environmental soil physics* (498 p.). Academic press.

- Joshi, P., & Gupta, P.K. (2018). Assessing groundwater resource vulnerability by coupling GIS-Based DRASTIC and solute transport model in Ajmer District, Rajasthan. *Journal of the Geological Society of India*, 92(1), 101-106. <http://dx.doi.org/10.1007/s12594-018-0958y>.
- Mallants, D., Van Genuchten, M.T., Jacques, D., & Seetharam, S. (2011). Leaching of Contaminants to Groundwater. In F.A. Swartjes (Ed.), *Dealing with contaminated sites: from theory to practical application* (pp. 787–850). Dordrecht, Netherlands: Springer Verlag. https://doi.org/10.1007/978-90-481-9757-6_18.
- Mikołajków, J. (2003). Laboratory methods of estimating the retardation factor of migrating mineral nitrogen compounds in shallow groundwater. *Geological Quarterly*, 47, 91-96.
- Mustafa, S., Bahar, A., Aziz, Z.A., & Suratman, S. (2016). Modelling contaminant transport for pumping wells in riverbank filtration systems. *Journal of Environmental Management*, 165, 159-166. <http://dx.doi.org/10.1016/j.jenvman.2015.09.026>.
- Narasimhan, T.N. (2004). Darcy's law and unsaturated flow. *Vadose Zone Journal*, 3(4), 1059. <http://dx.doi.org/10.2113/3.4.1059>.
- Porro, I., Newman, M.E., & Dunnivant, F.M. (2000). Comparison of batch and column methods for determining strontium distribution coefficients for unsaturated transport in basalt. *Environmental Science & Technology*, 34(9), 1679-1686. <http://dx.doi.org/10.1021/es9901361>.
- Richards, L.A. (1931). Capillary conduction of liquids through porous mediums. *Physics*, 1(5), 318-333. <http://dx.doi.org/10.1063/1.1745010>.
- Rodríguez-Pacheco, R.L. (2002). *Estudio experimental de flujo y transporte de cromo, níquel y manganeso en residuos de la zona minera de Moa (Cuba): influencia del comportamiento hidromecánico* [Thesis Doctoral, Universidad Politécnica de Cataluña]. Universidad Politécnica de Cataluña (in Spanish). <https://www.tdx.cat/handle/10803/6223>
- Rutsch, M., Rieckermann, J., Cullmann, J., Ellis, J.B., Vollertsen, J., & Krebs, P. (2008). Towards a better understanding of sewer exfiltration. *Water Research*, 42(10-11), 2385-2394. <http://dx.doi.org/10.1016/j.watres.2008.01.019>.
- Seferou, P., Soupios, P., Kourgialas, N.N., Dokou, Z., Karatzas, G.P., Candasayar, E., Papadopoulos, N., Dimitriou, V., Sarris, A., & Sauter, M. (2013). Olive-oil mill wastewater transport under unsaturated and saturated laboratory conditions using the geoelectrical resistivity tomography method and the FEFLOW model. *Hydrogeology Journal*, 21(6), 1219-1234. <http://dx.doi.org/10.1007/s10040-013-0996-x>.
- Šimůnek, J., & Van Genuchten, M.T. (2008). Modeling nonequilibrium flow and transport processes using HYDRUS. *Vadose Zone Journal*, 7(2), 782-797. <http://dx.doi.org/10.2136/vzj2007.0074>.
- Šimůnek, J., Van Genuchten, M.T., & Šejna, M. (2016). Recent developments and applications of the HYDRUS computer software packages. *Vadose Zone Journal*, 15(7), 1-25. <http://dx.doi.org/10.2136/vzj2016.04.0033>.
- Sopilniak, A., Elkayam, R., Rossin, A.V., & Lev, O. (2017). Emerging organic pollutants in the vadose zone of a soil aquifer treatment system: pore water extraction using positive displacement. *Chemosphere*, 190, 383-392. <http://dx.doi.org/10.1016/j.chemosphere.2017.10.010>.
- Sosa, E.R. (2016). *Caracterização e aproveitamento dos rejeitos oriundos de processos hidrometalúrgicos do níquel e cobalto com um enfoque geoambiental*. [Thesis Doctoral em Geotecnia. Publicação: G.TD-123/16]. Department of Civil and Environmental Engineering, University of Brasília. (in Portuguese). <https://repositorio.unb.br/handle/10482/22164>.
- Srinivasan, P., & Mercer, J.W. (1988). Simulation of biodegradation and sorption processes in ground water. *Ground Water*, 26(4), 475-487. <http://dx.doi.org/10.1111/j.1745-6584.1988.tb00414.x>.
- Van Genuchten, M.T. (1980). A closed-form equation for predicting the hydraulic conductivity of unsaturated soils. *Soil Science Society of America Journal*, 44, 892-898. <http://dx.doi.org/10.2136/sssaj1980.03615995004400050002x>.
- Van Genuchten, M.T., & Dalton, F.N. (1986). Models for simulating salt movement in aggregated field soils. *Geoderma*, 38(1), 165-183. [http://dx.doi.org/10.1016/0016-7061\(86\)90013-3](http://dx.doi.org/10.1016/0016-7061(86)90013-3).
- Viotti, P., Papini, M.P., Stracqualursi, N., & Gamba, C. (2005). Contaminant transport in an unsaturated soil: laboratory tests and numerical simulation model as procedure for parameters evaluation. *Ecological Modelling*, 182(2), 131-148. <http://dx.doi.org/10.1016/j.ecolmodel.2004.07.014>.
- Zhang, C., & Lu, N. (2019). Unitary definition of matric suction. *Journal of Geotechnical and Geoenvironmental Engineering*, 145(2), 02818004. [http://dx.doi.org/10.1061/\(ASCE\)GT.1943-5606.0002004](http://dx.doi.org/10.1061/(ASCE)GT.1943-5606.0002004).

Execution energy of continuous flight auger piles as an assessment tool to evaluate the mechanical response of the soil mass

Darym Júnior Ferrari de Campos¹ , Luan Carlos de Sena Monteiro Ozelim¹ ,

André Luís Brasil Cavalcante^{1#} , Carlos Medeiros Silva¹ ,

José Camapum de Carvalho¹ 

Article

Keywords

Continuous flight auger piles
Execution energy
Spatializations

Abstract

Allying technology, theory and engineering practice is one of the main challenges of modern foundation engineering. Current foundation and retaining walls designs may lead to oversizing or undersizing due to the spatial variability of the stratigraphic profile. As the design procedure of piled foundations involves defining the setting depth of the tip, sometimes the piles may not behave as expected, as the soil mass may change significantly even in a small region. In this paper, a study was conducted on the geoeconomic behavior of the soil mass and of the piles of a construction site located in Brasília, DF, Brazil. Previous studies showed that the energy needed to drill a continuous flight auger pile (CFAP) can be related to the strength of the drilled strata. Therefore, a methodological framework was built to further discuss how the geomechanical behavior of CFAPs foundations could be assessed by analyzing the energy needed to drill such piles. Statistical methods, in special the Bootstrap method, were used to assess the possible influences of construction procedures on pile behavior. It was studied how the execution energies of piles vary with initial depth and relative position in the terrain, as well as the influences that they suffer because of the order of execution within a same foundation group and due to the proximity to surrounding retaining walls. The proposed methodology can be used to improve the energy control procedure and performance evaluation of CFAPs, allowing a complementary reliability assessment for the foundation and retaining walls designs and implementations.

1. Introduction

Piles are deep foundation elements which are also useful in retaining wall structures. For their implementation, there are several execution techniques, among which the continuous flight auger piles (CFAPs) are very popular. Currently, due to the tight schedules of engineering works, which may come together with a non-rare planning deficiency, the complete control of the construction site is not observed, making it hard to propose adaptations to current standards and even to enable a proper real-time monitoring of the foundation implementation.

When it comes geotechnical designs, safety analyses are usually based on deterministic methods, treating the calculated parameters as absolute truths. Thus, it is common to neglect some of the peculiarities of each construction site, which are known to be prone to geological-geotechnical and even geomorphological variability in the soil-foundation system. Thus, understanding the drilling environment contributes

significantly to engineering practice. In this sense, there have been some previous works by Silva (2011) and Ozelim et al. (2018, 2019), where it was investigated and verified that strength parameters can be estimated from the drilling data of geomaterials.

The problem that was sought to be solved with this paper is to further investigate how the drilling energy of CFAPs can be used to assess the geomechanical behavior of foundations constituted by this type of pile. Therefore, the goal is to enhance execution control methods that provide greater safety, executive quality, economy and reliability for the implementation of CFAPs' designs. Based on two survey campaigns, one with two mixed survey type (MS) and another with four Standard Penetration Tests (SPT), and CFAPs execution data from a construction site located in Brasília (porous red clay soil), capital of Brazil, a methodological framework is proposed, based on statistical analyses, to establish relations between the mechanical response of the soil mass and the execution energy of the piles drilled in

[#]Corresponding author. E-mail address: abrasil@unb.br

¹Universidade de Brasília, Department of Civil and Environmental Engineering, Brasília, DF, Brazil.

Submitted on January 17, 2022; Final Acceptance on April 21, 2022; Discussion open until August 31, 2022.

<https://doi.org/10.28927/SR.2022.000622>



This is an Open Access article distributed under the terms of the Creative Commons Attribution License, which permits unrestricted use, distribution, and reproduction in any medium, provided the original work is properly cited.

it. In short, the foundation piles had 0.5 m of diameter and the retaining wall consisted of juxtaposed piles of 0.4 m of diameter. The lengths of the piles ranged from 8-14 m and 10-14 m, respectively.

For this purpose, the SCCAP methodology (Silva, 2011) will be used as basis for this framework to calculate the execution energies of the CFAPs. Also, statistical analyses will be performed on the spatialization of the SPT results and on the execution energy of the piles at different locations in the construction site and its boundaries (retaining walls). In special, it will be studied how the execution energy of the piles is influenced by the pile position inside the site and by the order of execution of the foundation blocks.

2. Continuous flight auger piles

Using CFAPs as a foundation solution dates back to the 50s in the United States, being later spread throughout Europe and Japan in the 1980s, and was first performed in Brazil in 1987. Due to the increasing evolution of the technology and types of equipment, the monitoring control tools tend to become more reliable and the diversity of diameters and depths options tends to grow (Antunes & Tarozzo, 1996).

The execution process consists, basically, of the following steps cited by Caputo et al. (1997): positioning of the equipment according to the location of the pile predicted in the design, drilling and concreting simultaneous to the auger extraction of the ground and, finally, placing the steel reinforcement inside the recently concreted shaft. In technological terms, there is an electronic monitoring during all these phases, generating a large amount of excavation data. For example, it is possible to gather data regarding depth, tower inclination, penetration and extraction velocities of the auger, torque, work on drilling the pile, execution time, pressure of concrete injection, volume of pumped concrete and overconsumption of concrete.

According to Antunes & Tarozzo (1996) and Rajapakse (2016), the CFAPs are greatly adequate as a foundation solution in constructions executed in large urban centers, becoming attractive due to reliability, productivity and low frequency of vibrations and noises. In Brazil, it is the preferred technique of the builders when it comes to deep foundations, especially for foundations lying below the water level combined with retaining wall structures of juxtaposed piles, as is the case hereby analyzed.

3. Execution energies

Determining the properties and behavior of soils are very complex issues since one must deal with the geotechnical uncertainties coming from the natural variability of their constituent materials as well as with the errors of measurement during the tests performed. About 65% of the Brazilian territory consists of tropical soils, which are most

highly weathered due to the influence of high temperatures, rainfall distribution, fauna and flora (Toledo et al., 2000).

During the installation of a pile in a certain type of soil, it is possible to obtain several useful drilling information by means of monitoring sensors. Thus, it would be interesting to associate this data with a scalar metric, such as the energy consumed to drill each pile shaft, which could be correlated to the pile bearing capacity. This would allow one to have real-time feedback on the suitability of the initial pile design and to understand the behavior and mechanical response of the soil mass.

In order to quantify the energy required to install a pile, Silva & Camapum de Carvalho (2010) evaluated formulations based on the principle of conservation of energy. They further proposed a methodology of execution control based on statistical elements, which was later incorporated into a monitoring software of excavated piles, especially CFAPs. This methodology, called SCCAP, represents an automated real-time control routine that records the energy or work performed by the forces applied to the helicoid during the execution of each pile. According to Silva et al. (2012), the forces acting on the machine are presented in Figure 1 and the energy required to install a pile can be calculated as in Equation 1.

$$W_R = \int_0^{Zb} mhc.g.dZ + \int_0^{Zb} F_{di}.dZ + \int_0^{m2\pi} F_i.r.d\theta \quad (1)$$

in which: W_R = work done or execution energy [M][L]²[T]⁻²; Zb = pile total length [L]; mhc = mass of drilling system [M];

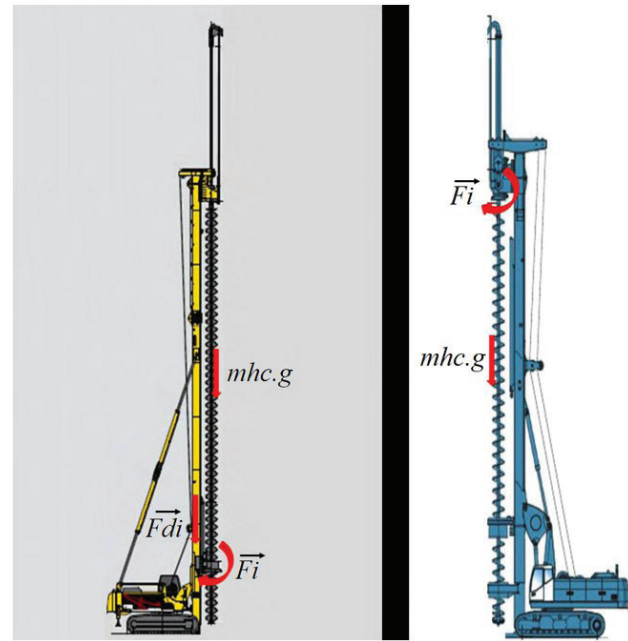


Figure 1. Drilling system and forces: (a) bottom drive CFA; (b) standard CFA (Silva, 2011).

g = gravity acceleration $[L][T]^{-2}$; F_{di} = downward force applied to the drill $[M][L][T]^{-2}$; F_i = force applied for drill revolution $[M][L][T]^{-2}$; m = number of drill revolutions; r = helical drill radius $[L]$.

From the value of the execution energy and from the geometry of the drilled shaft, it is possible to calculate the specific energy in a given region of the site, which simply indicates the amount of energy spent per unit volume of drilled material. Visualizing the spatial distribution of specific energy allows one to compare different piles performances in the intervention site, as not necessarily the piles in a given design have the same diameter and depth.

For the execution energy analysis, the stress state is fundamentally important because the evolution of the construction from the beginning of the constructive procedures until the end of the consolidation period can affect the stresses transmitted to the drilling machine during the installation of the piles. The understanding of these changes in stress state enable a comparison between energetic measurements throughout the execution process. Following this reasoning, there are in the literature a series of studies that discusses the evolution of the stress state during construction, highlighting the change of horizontal stress during the various stages of construction. It is worth mentioning two studies, from a numerical and an experimental point of view.

According to Costa (2005), the use of advanced numerical methods represents a useful tool for estimating the behavior of geotechnical interventions. On the other hand, the study published by Richards et al. (2007) indicates the need for experimental evaluations as well. For both, even though in slightly different contexts, the stress states were analyzed during excavations of clay soils, discussing the behavior of a retaining wall structure along all of its constructive stages.

At all stages, a general decrease of the total horizontal stresses on both sides of the walls was observed, either due to the removal of the soil weight or due to the movement of the walls towards the cut. This is a consequence of the stress redistribution in the vicinity of these walls, making it clear that the farther from the wall, the lower the stress disturbances are observed. It is undeniable that soil matrices have different chemical and mechanical characteristics, but when it comes to physical behavior, the phenomena involved in the mobilization of stresses in the massif are similar.

In order to assess how the drilling energy is affected by the stress changes in the construction site, probabilistic tools will be considered, as the variability of the properties involved does not allow a deterministic approach on this matter. Some tools will be used to compare energy measurements throughout the terrain, as well as to check if particular groups of data can be considered equal from a statistical point of view. In the next section, the methods used will be discussed.

4. Probabilistic tools in foundation analysis

When comparing two values, instead of considering only point estimates, confidence intervals (CI) can be taken into

account. This comes from the fact that when point estimates are considered, it is not possible to get a clear idea of the dispersion of the data and how the sample estimates differ from the population ones. CIs, on the other hand, enable one to have a better notion of the real population parameters.

Literature reveals a great variety of methodologies to determine the confidence intervals of a given measure. In special, the so-called z and t approaches are widely known as alternatives to evaluate the CI of means of a population (Moore et al., 2013). Both approaches rely on considering normality at some stage of the theoretical development of the method. In general, determining the distribution of the statistics which characterizes the hypothesis test behind the confidence interval evaluation is highly complex, being in most cases analytically unviable. This way, more general methods have been built.

Even though the determination of the confidence interval is deeply related to hypothesis testing, a specific test will also be considered in the present paper. The test whose null hypothesis is the equality of distribution between two samples is needed to check if different drilling energy samples are statistically equal or not.

With respect to building confidence intervals, the Bootstrap method shall be applied. This latter method also performs well when the equality of distribution test is considered. Thus such method is also applied in that case.

In order to familiarize the reader with respect to the Bootstrap method, one may refer to the works of Efron (1979, 1982) and Efron & Tibshirani (1993).

5. Materials and methods

In order to better exemplify the use of the methodological framework hereby presented, a construction site, with a porous clay soil, was selected, for which the entire executive procedure of the CFAPs of the retaining wall and foundation structures were controlled by the same machine-operator setup. In short, the foundation piles had 0.5 m of diameter and the retaining wall consisted of juxtaposed piles of 0.4 m of diameter. The lengths of the piles ranged from 8-14 m and 10-14 m, respectively. In addition, besides the CFAPs data, this specific site has been characterized by field tests. The characteristic subsoil of the region is composed of a porous red clay with low resistance in the first meters. As one goes deeper, the presence of more resistant silty materials is identified. More detailed information will be described in the next topic.

Subsequently, all data from the original geotechnical designs and drilling sensors were collected, as well as reports about the excavation of the site and the execution of each pile. The dataset was collected during the whole construction period.

To enhance data visualization, RockWorks® software was used to spatialize field survey data, generating 3D models and cross-sections of the stratigraphy and bearing capacity

of the natural and excavated terrain. Such spatializations are achieved primarily by performing interpolations. In the present paper, the *Inverse-Distance Anisotropic* weighted distance method was used with the aid of the *Smooth Grid* data filter. With this method, to estimate the value of the spatialized property at a reference point, the weighted mean of the property values at the nearest points is considered, where the weights are the inverse of the distance between each surrounding point and the reference one.

In the case of data from the execution reports of the piles, an automated code was implemented in Mathematica® software, allowing the calculation of the execution energy, both accumulated in a meter-by-meter of depth manner and, finally, its normalized value by the volume of excavated material (specific energy). It is important to note that for the two-dimensional spatialization of the data, the idea of separating the data in similar groups was used. This process, known as *clustering*, applies a series of algorithms that group data according to common characteristics. Such a procedure is necessary to indicate which are the typical values of the execution energy around which the other values are grouped. To perform this procedure, the *ClusteringComponents* function of the Mathematica® software was used. All the calculated energy values have also been incorporated into RockWorks® in order to create three-dimensional energy profiles.

Finally, the general analyzes of the geotechnical behavior of the soil and the piles of the construction studied were carried out. At first, the stratigraphy of the site and its strength were assessed by means of regular soil survey techniques. Since such surveys were carried out at different moments throughout the years, it was relevant to carry out a brief climatic overview to characterize the conditions at which data was collected. Secondly, it was spatially analyzed how the energy and the specific energy are distributed along the whole construction site. Also, the Bootstrap statistical method was used to investigate the influence on the execution

energy of both the horizontal and vertical distances of the foundation piles with respect to the retaining walls and the order of pile execution per foundation block.

6. Analysis and results

6.1 A brief characterization of the site and the piles studied

In order to carry out the analysis, a local residential ongoing construction site was chosen. The site is characterized by large flat/gently undulating surfaces. According to the planialtimetric analysis, the mean inclination of the terrain is about 5.5% with an average altitude of 1034.5 m above sea level. The geotechnical design prescribed the execution of 320 juxtaposed CFAPs for the retaining wall structure with 0.4 m of diameter and varying the length between 10 and 14 m. For the foundation, 316 piles were drilled after soil excavation, all of them with 0.5 m of diameter and with lengths varying between 8 and 14 m. The next analyses topics will complement and bring more site information and features needed for the present paper.

Previously to the piles execution, two survey campaigns were carried out for the investigation of the subsoil. The location of the two investigations is illustrated in. Figure 2. It should be noted that both campaigns were executed in different years, but coincidentally operated at the same time of year. Both campaigns were carried out in the rainy season in March of 2014 and of 2016, respectively.

The first campaign was a MS type and consisted of two sampling sites, encompassing both percussion and rotary sampling methodologies. This MS was executed two years before the construction and its results are illustrated in Figure 3.

After executing the retaining wall and performing the excavation to reach the quota to drill the foundation piles,

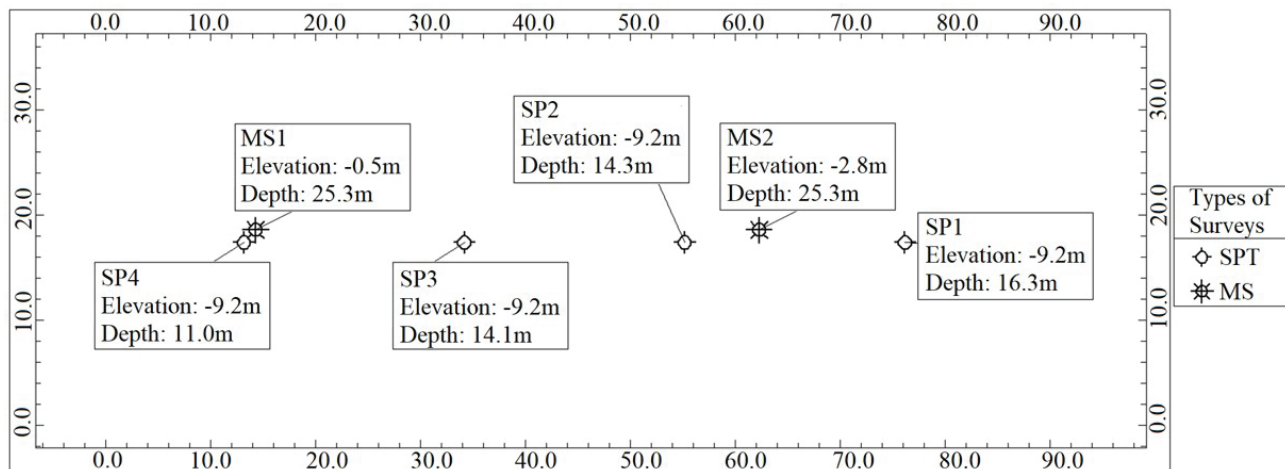


Figure 2. Location of the two survey campaigns (MS and SPT).

the second survey campaign began, but this time only with percussion sampling techniques. Thus, Figure 4 presents the results of four SPTs.

Making a parallel between these two survey campaigns and the superficial morphology of the soil, a certain parallelism is verified between the weathered mantles when considering the impenetrable quota (NSPT = 50 blows/30 cm) of the MS and the geomorphology of the soil (Figure 3). The same parallelism is not observed with respect to the SPT borehole results shown in Figure 4. A priori, this would point to the unsatisfactory quality of this second survey campaign, however, if one considers the SP4 result and the first peak corresponding to 50 blows/30 cm in the SP1, the same parallelism trend is verified. The most important, however, seems to be the verification of the expected deepening for this impenetrable limit established when drilling SP2 and SP3, indicating a possible stress relief in the central region of the site, which is compatible with one of the motivating purposes of this paper, i.e., the influence of the boundary

conditions on the pile bearing capacity evaluated through the energy control in the pile execution phase.

6.2 Stratigraphic profile and NSPT spatializations

In previous works, the stratigraphy and number of SPT blows (NSPT) of both the undisturbed and excavated sites were spatialized (Ferrari de Campos et al., 2019). Two three-dimensional models were created, as shown in Figure 5, for the complete construction site. To better illustrate a representative cross section of the terrain, two transverse sections were strategically located in between the locations of the survey campaigns (Figure 6).

6.3 Execution energy

6.3.1 Cumulative; meter-by-meter and total energy

The accumulated energy was calculated to analyze the total energy of execution, investigating if this metric can be used to assess the mechanical behavior of the stratigraphic

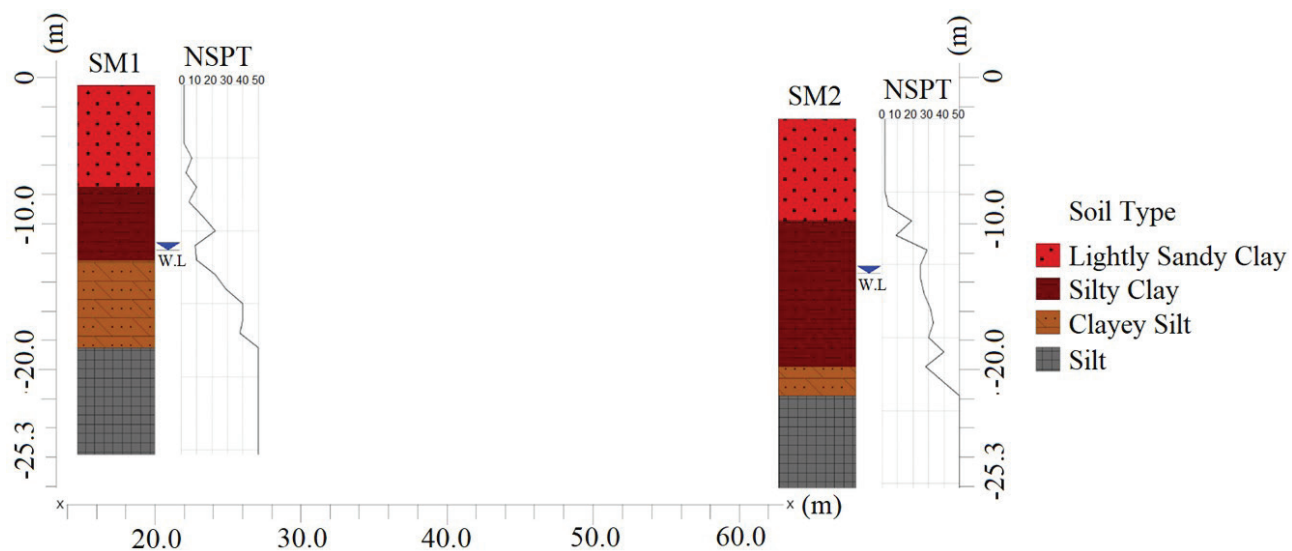


Figure 3. Section with the results of the first survey campaign.

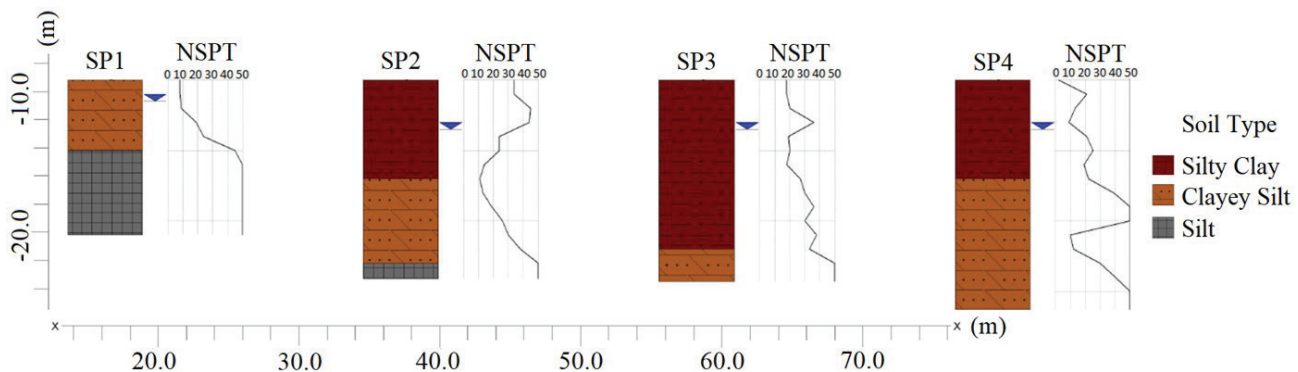


Figure 4. Section with the results of the second survey campaign.

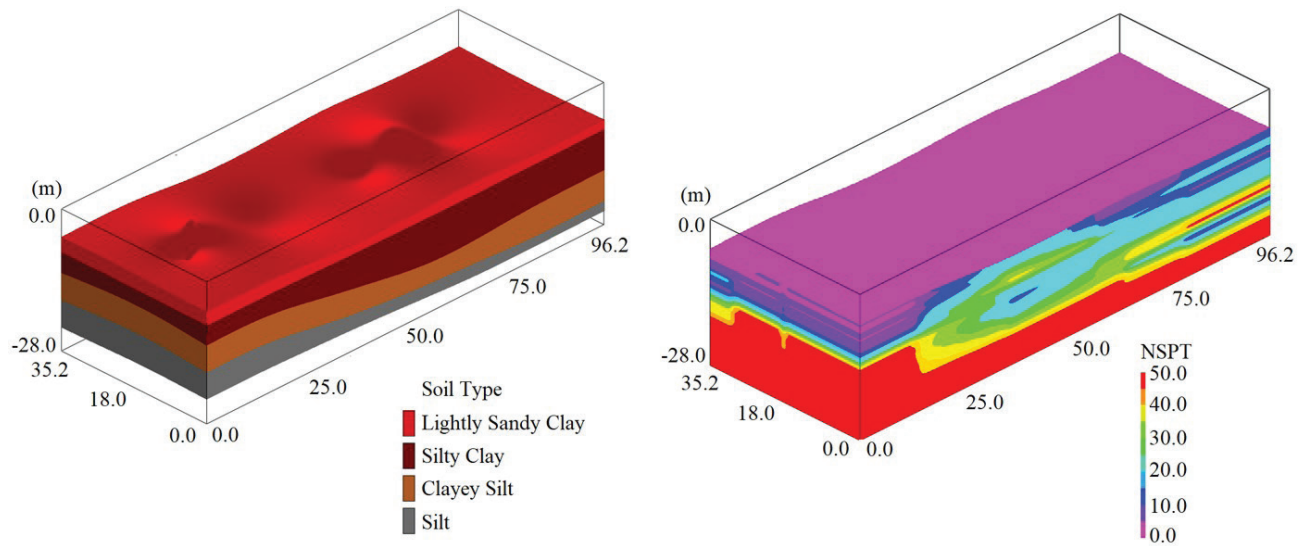


Figure 5. 3D models for stratigraphy and NSPT of the two survey campaigns.

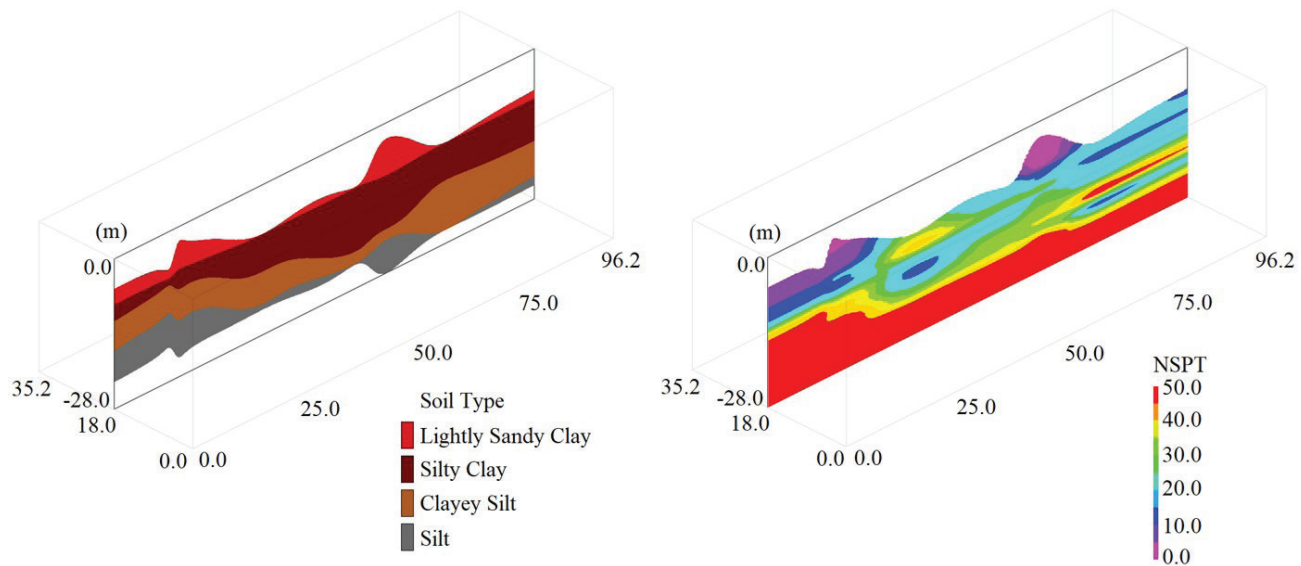


Figure 6. 3D cuts for stratigraphy and NSPT of the two survey campaigns.

profile in terms of resistance. Since the piles cover almost all the site area, it was possible to obtain a highly dense interpolation domain. Also, the energy needed to excavate each meter of soil (meter by meter) was calculated in order to verify the changes among soil layers. Thus, the graphs plotted in Figure 7 and Figure 8 show two examples of energy report results generated by the code developed. Figure 7 refers to a retaining wall pile, while Figure 8 refers to a foundation pile.

Figure 9 shows the histograms of the sampled total energies of execution for the piles of the retaining wall (left) and foundation structures (right).

When visualizing the histograms above, multimodal graphs are illustrated, where several peaks are observed, representing some typical total energy values. The physical

interpretation of these peaks can account for several factors such as the length of the pile, the drilling of layers of different types of soils and the effect of stresses in the soil mass. The presence of three typical values of total energy is highlighted in the second histogram, which refers to foundation piles, and shall be discussed later.

6.3.2 Spatializations

A spatialized map was created from the interpolated total energy values in every area of the site. Figure 10 shows the behavior of the total energies of the foundation piles. It was observed that for the retaining wall piles, it was not

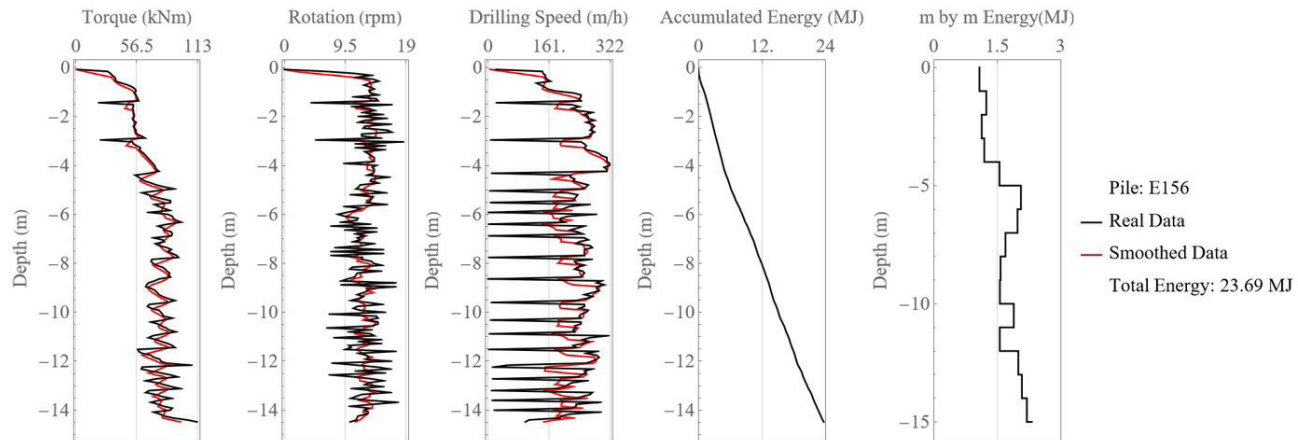


Figure 7. Calculated execution energy: E156 retaining wall pile (0.4 m of diameter).

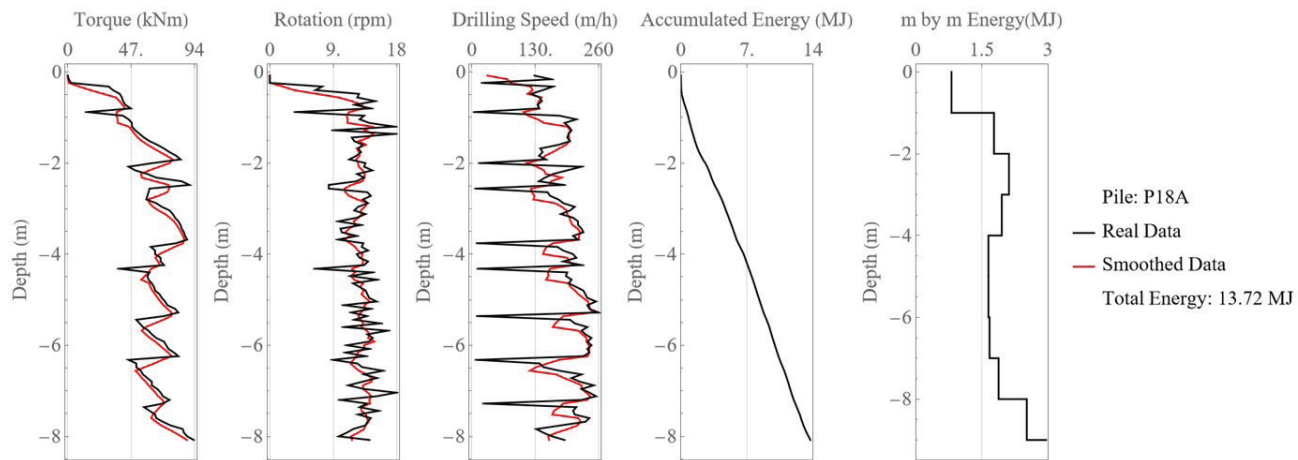


Figure 8. Calculated execution energy: P18A foundation pile (0.5 m of diameter).

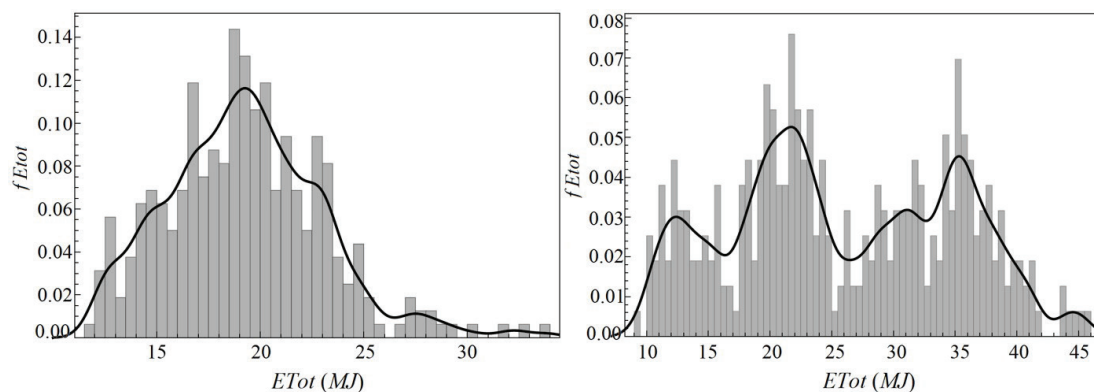


Figure 9. Total energy frequency curve of the retaining wall (left) and foundation piles (right).

possible to perform a spatial interpolation of the surface in a significant and coherent manner, since it was a perimetric data.

Individually, each pile has a certain volume (m^3). Also, during the drilling process, each slice excavated also has a given volume, which is related to the slice height and to the diameter of the pile. With such information, the total energy per

excavated volume of soil was normalized and the spatialized results are presented in Figure 11. This normalization neutralizes the effect of the length and diameter of the pile, allowing a more accurate statistical analysis of the data collected.

In the case of the meter by meter energy, the results were spatialized similarly to the NSPT and stratigraphy

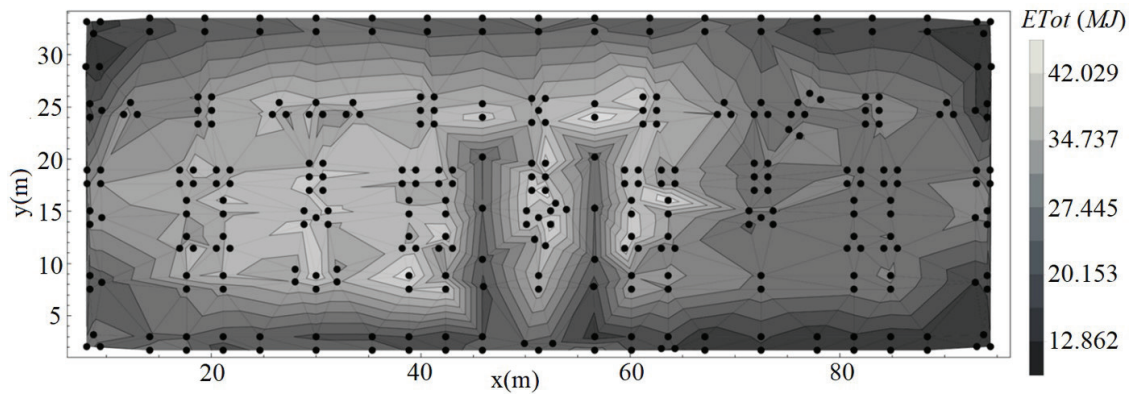


Figure 10. Total energy frequency curve of the foundation piles.

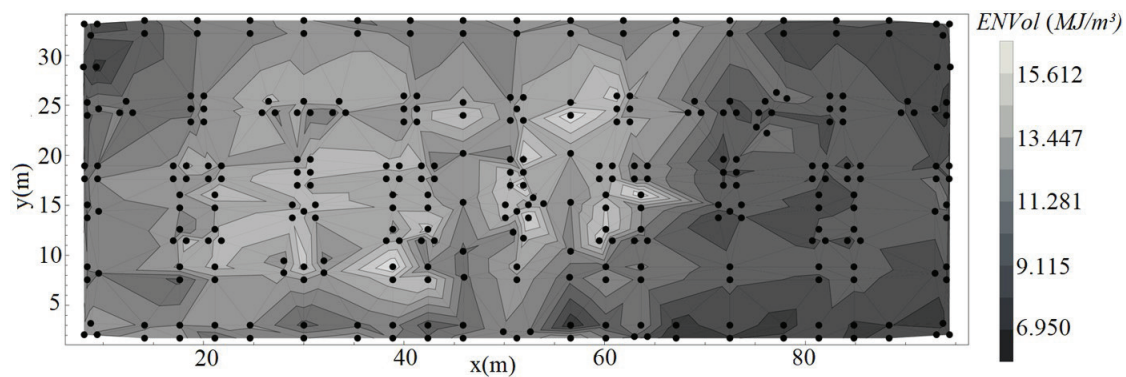


Figure 11. Spatialization of the energy density of execution of the foundation piles.

profiles. Two different sections, as indicated in Table 1, were chosen to illustrate the energy spatialization and are shown in Figure 12.

7. Discussions

7.1 Survey campaigns and their spatializations

Although the spatial distribution of the stratigraphic profile of the site is not frequently considered in everyday designs, this information may be of great interest, especially to obtain a better understanding of the soil mass in points other than the ones actually sampled during the preliminary surveys.

NSPT surveys may be subject to criticism because of the possibility of observing some dispersion between the results of different campaigns. Even though they have been done in very near places, the results from the two survey campaigns studied in the present paper showed significant variations. Ferrari de Campos et al. (2019) carried out an exhaustive analysis of the procedures needed to make the results of both the campaigns compatible. Such differences are due, on the one hand, to the variation in tactile-visual typification of the samples collected by the two survey teams

responsible for the studies and, on the other hand, to the variations in the number of blows recorded by each survey campaigns as a consequence of the stress relief imposed by the excavation of the terrain.

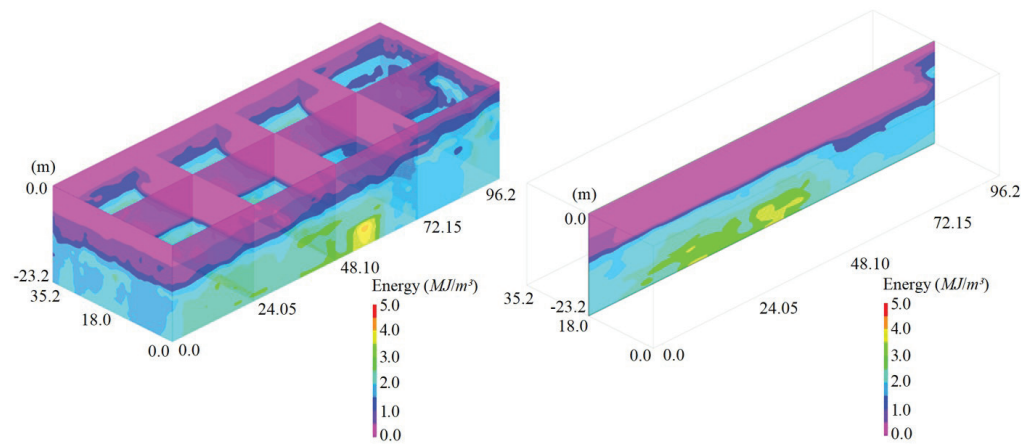
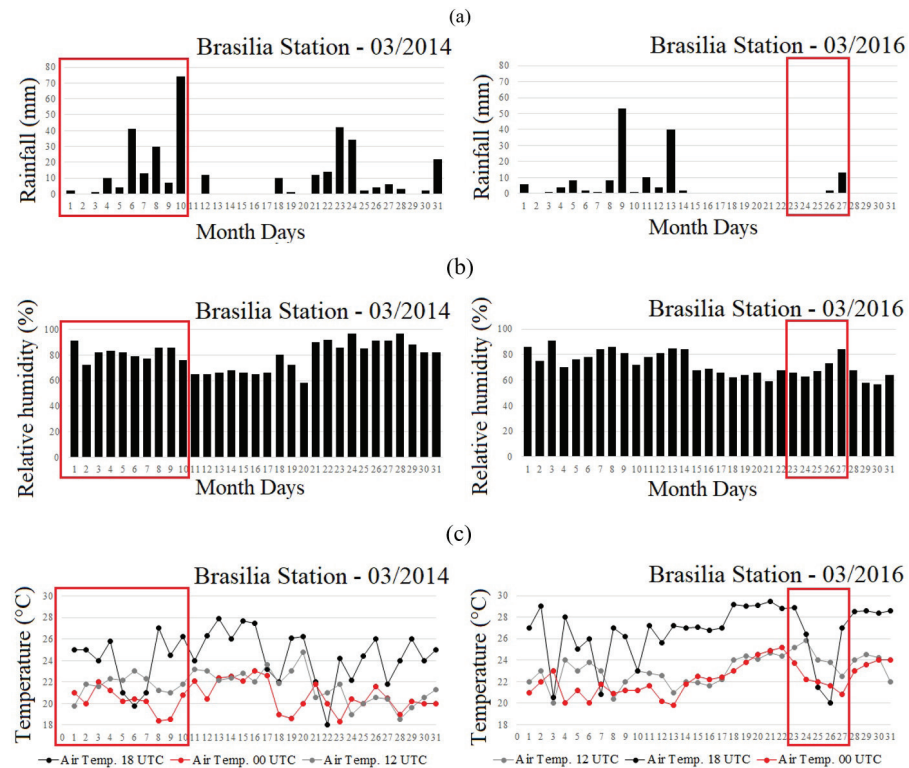
Also, besides the factors discussed by Ferrari de Campos et al. (2019), any climatic variability during the periods between the execution of the two surveys can also impact the survey's results. Analyzing the rainfall distribution, relative humidity and air temperature, according to data from the National Institute of Meteorology (INMET, 2021) in Brasília, a comparison is made between the dates of the survey campaigns studied, as seen in Figure 13.

Although both campaigns were executed in March, a higher concentration of rainfall, higher relative humidity and lower temperature were observed in the first survey campaign, which would lead to a worse behavior of the soil, as the analysis of Figure 3 and Figure 4 suggest. Another influencing factor is that the executive process of the surveys was different, as there was water circulation during the first campaign.

It is worth mentioning that Ferrari de Campos et al. (2021) carried out a discussion about the bearing capacity of continuous flight auger piles in terms of their execution energy and of rainfall data. In that study, those authors showed

Table 1. Coordinates of the cutting steps for the retaining wall and foundation structure.

3D Energy cuts – Retaining wall and foundation structure	Coordinates (m)					
	Xi	Yi	Zi	Xf	Yf	Zf
3D Representation 1	0.0	0.0	0.0	0.0	35.20	-23.2
	0.0	0.0	0.0	96.20	0.0	-23.2
	96.20	0.0	0.0	96.20	35.20	-23.2
	0.0	35.20	0.0	96.20	35.20	-23.2
	24.05	0.0	0.0	24.05	35.20	-23.2
	48.10	0.0	0.0	48.10	35.20	-23.2
	72.15	0.0	0.0	72.15	35.20	-23.2
	0.0	18.0	0.0	96.20	18.0	-23.2
3D Representation 2	0.0	18.0	0.0	96.20	18.0	-23.2

**Figure 12.** 3D Representation 1 and 2: Execution energy density (MJ/m^3) of all piles.**Figure 13.** (a) Daily Rain; (b) Relative air humidity; (c) Air temperature.

that pluviometry events impact the energy needed to execute this type of pile and, therefore, also impact its mechanical behavior up to three meters of its depth. Wetting/drying cycles and resulting stresses imposed on the soil mass while performing excavations also alter the mechanical response of piles when loaded.

This need for compatibilization between survey teams and campaigns, as well as time of execution may not be ideal. Therefore, in the next subsection, it will be discussed how the execution energy can be used as a powerful and simple tool to evaluate the support capabilities of the terrain.

7.2 Execution energy

7.2.1 Evolution of the stress state

As discussed by Ferrari de Campos et al. (2019), most of the procedure carried out to make the survey results compatible was related to correcting the stress state in the site before and after the excavation of the site. It is important to highlight that the actual stress state the foundations will be subjected to during their lifecycle is the one after excavation.

While analyzing the execution energy, the stress state is also fundamental since the construction steps, especially excavations, affect the stresses transmitted to the drill during

the execution of the piles. In particular, the horizontal stresses impact the energy needed to drill a given pile because, in general terms, an increase in the horizontal stresses tends to increase the frictional force that counterposes the rotation of the helical drill, thus increasing the work of this dissipative force and consequently the execution energy as a whole.

7.2.2 Spatial assessment of site resistance

Observing the plots in Figure 10 and Figure 11, using the execution energy to evaluate the behavior of the piles can be considered an interesting tool, allowing the designers to have a visual understanding of the energetic expenditure (and, therefore, bearing capacity) of the terrain as a whole.

To make the visualization even clearer, it is possible to cluster similar energetic expenditures instead of directly interpolating the drilling energy of each pile. These clustered results for total energy and volumetric energy density can be seen in Figure 14 and Figure 15, respectively. This construct was performed by applying the *ClusteringComponents* function to the *ListDensityPlot* function of the Mathematica® software for the data in question.

Figure 14 shows four characteristic regions. In special, low and medium energy expenditures are observed at the extremities of the site, possibly due to the loosening effect

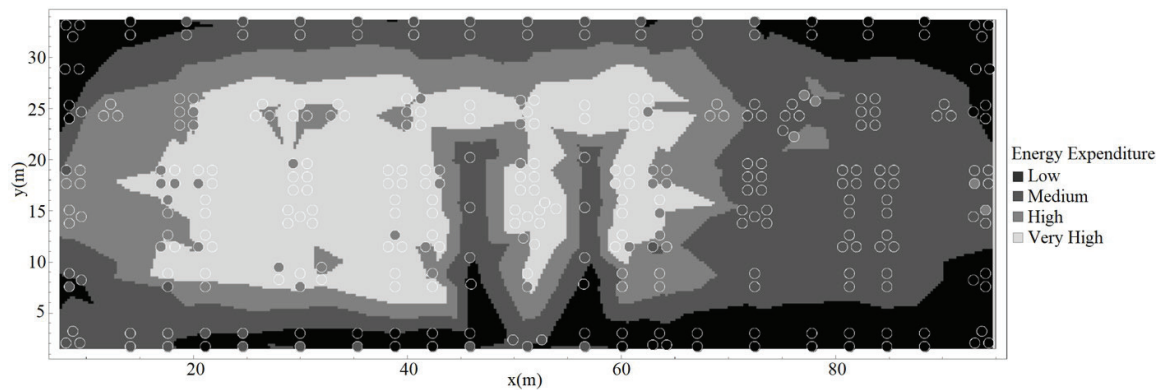


Figure 14. Spatialization of total energy expenditure demanded for the foundation structure.

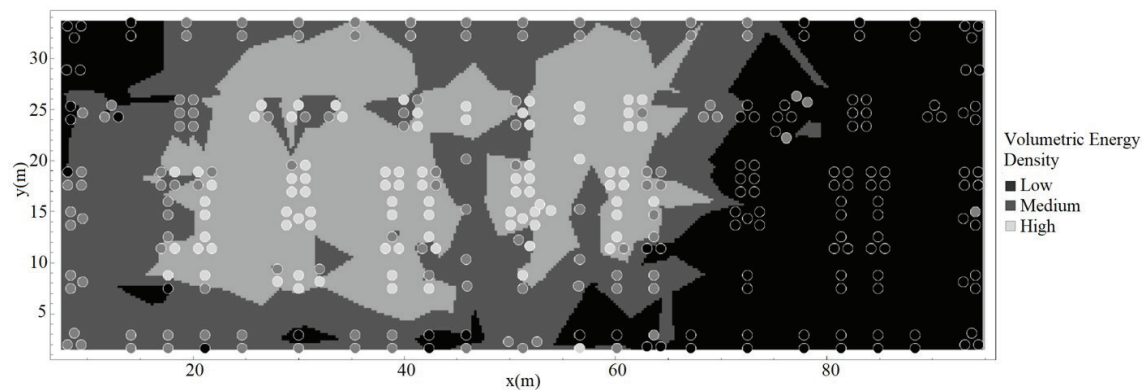


Figure 15. Spatial volumetric energy density for foundation piles.

of horizontal stresses caused by the unloading of soil by the excavation and by the retaining wall construction. On the other hand, high and very high energy expenditures are seen in the central-west part of the site, being directly correlated to the existence of the more competent soil layers when compared to the stratigraphy of the surveys located in this region.

Looking closely at Figure 15, a certain similarity to Figure 14 is perceived. This fact is expected because the influence of the stress state in the soil and the resistant soil layers remains the same, only changing the impact of the length of the pile, which has been neutralized in Figure 15. Another difference is observed that, in terms of energy expenditure, there were three characteristic regions. The characteristic values observed above are in accordance with the peaks observed in the histogram presented in Figure 9.

7.2.3 Assessments of site's bearing capacity by using execution energies and bootstrap statistical simulations

In order to validate the usage of execution energies as metrics for estimating the potential bearing capacity of piles drilled in a given type of soil, it is imperative to first understand which external and internal factors impact these energetic measurements. In the following topics, several factors that would impact the values of the execution energy densities (specific energy) were considered. Both the measured values and the Bootstrap resampling method were combined to present a robust statistical framework for the analysis.

Bootstrap is a non-parametric estimation method introduced by Efron (1979, 1982), which allows one to estimate the confidence interval of a given statistic of interest. In short, the Bootstrap method is a statistical inference method based solely on the available data (sample). One of the greatest advantages of the method is that the latter does not rely on any consideration of the random variables involved (Ozelim & Cavalcante, 2018).

The core of the Bootstrap method is that it assumes that the sample collected is representative of the population from which the former has been drawn and that the observations are independent and identically distributed. Thus, the Bootstrap method is capable of estimating the sampling distribution of a given statistic (for example, the mean and variance of the population) (Ozelim & Cavalcante, 2018).

Such methods were used to understand the possible impact of different factors on the execution energy measurements. In special, it was considered the influence of morphological factors such as the pile positioning with respect to the retaining wall, the execution order of the pile inside a foundation block, the influence of the retaining walls at the edges of the excavated terrain and the impact that the retaining walls have on the execution of piles which go below the wall's setting depth.

In general, by selecting subgroups of the measured energy values, a resampling random Bootstrap algorithm was

used to calculate the mean values, coefficients of variation and confidence interval for some parameters of interest. For this, 10.000 replicates or resamplings were performed in all statistical procedures.

It is interesting to notice that the calculation of confidence intervals with the Bootstrap method may outcome asymmetric intervals, i.e., not centered around the mean value of the parameter of interest. In addition, this method always maintains the physical meaning of the variables involved (strictly positive, for example) since the values of the statistics are always calculated from the sampled data. It should be emphasized that the confidence interval that will be shown in the analyzes have a 95% confidence level, considering the trend correction and BCa acceleration. Also, the hypothesis test of the equality of distribution of two different samples will be evaluated.

7.2.3.1 Influence of pile positioning

One of the main precautions that must be taken during the execution of a foundation refers to the control of the positioning of the piles in relation to the geomorphology of the site. In addition, in order to understand how the execution energies can be used as metrics to assess the competency of a given terrain, one must investigate if the piles arrangement can influence other piles in terms of execution energy. According to Figure 16, all foundation piles were divided into three groups.

The idea is to test whether or not the execution energy of foundation piles is affected by their positions with respect to the retaining wall. The following hypothesis test was considered:

- H0: The energy samples from any two groups being compared belong to the same distribution;
- H1: Reject H0.

Table 2 shows the p values for the hypothesis tests and in the sequence, in Figure 17, the histogram of specific energy values and the 95% confidence interval of the respective

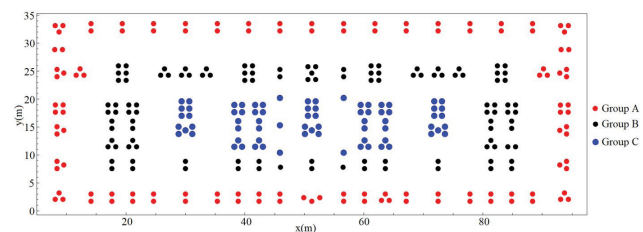


Figure 16. Division of the groups related to the foundation piles.

Table 2. Hypothesis test results (p value): piles positioning.

Piles Positioning	Group A	Group B	Group C
Group A	1	0	0
Group B	0	1	0.0007
Group C	0	0.0006	1

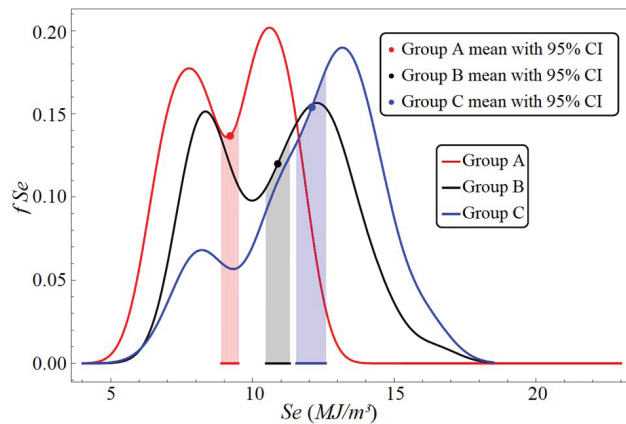


Figure 17. Histogram with 95% confidence interval for groups A, B and C.

mean of each group were presented. In such table, bold cells indicate that the null hypothesis is accepted and the other cells indicate that the alternative hypothesis is accepted, which represents the rejection of the null hypothesis with a 5% tolerance.

It is evident that the groups A, B and C do not come from the same distribution, and cannot be considered statistically equal. This conclusion makes complete sense, since it shows that physically each group represents regions with different characteristics. This way, it can be seen that the positioning of the piles with respect to the retaining wall is an important factor.

7.2.3.2 Influence of execution order per foundation block

According to the current Brazilian standard ABNT NBR 6122 (ABNT, 2019), 5D-distance and 12 h lag are requirements to execute neighboring piles, precisely to prevent the sectioning of shafts. In order to investigate if the executive order of piles impacts their execution energies, a statistical analysis for each of the three groups previously defined will be performed. The order of execution of each pile with respect to its foundation block is illustrated in Figure 18.

Groups A, B and C are still considered for this type of analysis because a statistical difference between the specific energy values between them was previously observed. Thus, for each group, the same hypothesis test previously enunciated was carried out. On the other hand, instead of comparing all the piles inside a given group, the piles which were executed in the same sequence were compared (first piles to be executed for each foundation block with other piles in the sequence and so on). The p values are presented from Table 3 to Table 5.

Each group will be analyzed separately. Group A fits the null hypothesis for most of the cases, indicating that all the specific energies of first piles executed in each foundation block have the same distribution like the ones executed secondly and thirdly. This indicates that executive order is

Table 3. Hypothesis tests results (p value): execution sequence of Group A.

Execution sequence	1st	2nd	3rd	4th
1st	1	0.1321	0.4913	0.001
2nd	0.1298	1	0.6165	0.0312
3rd	0.4868	0.6183	1	0.0162
4th	0.0009	0.0292	0.0139	1

not important. By observing in Table 3, the sub-group of the fourth piles in the sequence was neglected in the analyses. The reason for the exclusion is that the sample considered is too small, consisting of only two blocks which had four piles. Small samples as these invalidate any statistical analysis.

Group B results were similar to group A, making it clear that the specific energies are not influenced by executive order of the piles in each foundation block. For the cells that are not in bold, the hypothesis test failure can be attributed to two factors: number of piles in the sample (there are only four blocks with four and six piles) and variations in the foundation's executive procedure. Note that for the sub-group of fifthly executed piles, the expected behavior occurred.

As in the cases of groups A and B, for group C the expected behavior was verified. It is noted, however, that for the third and sixth piles executed, the null hypothesis was rejected. These rejections can be attributed to the same factors discussed for group B (sample size and executive procedures).

7.2.3.3 Edge Influence in the Group A

The first analysis showed that the position of the piles with respect to the retaining walls is an important factor. For the closest group to the wall, Group A, it is also important to understand if the edges of the wall impact the specific energy values differently when compared to the other regions. This way, it was decided to divide Group A into eight regions for this analysis, as observed in Figure 19.

The intention of this analysis was to investigate the existence of characteristic regions in terms of execution energy between each sub-region, mostly considering the position with regard to the retaining wall. Analogously, the p values results for the equality of distribution hypothesis test for the eight regions are shown in Table 6 and the complete histogram with all 95% confidence intervals for the mean specific energy values is illustrated in Figure 20.

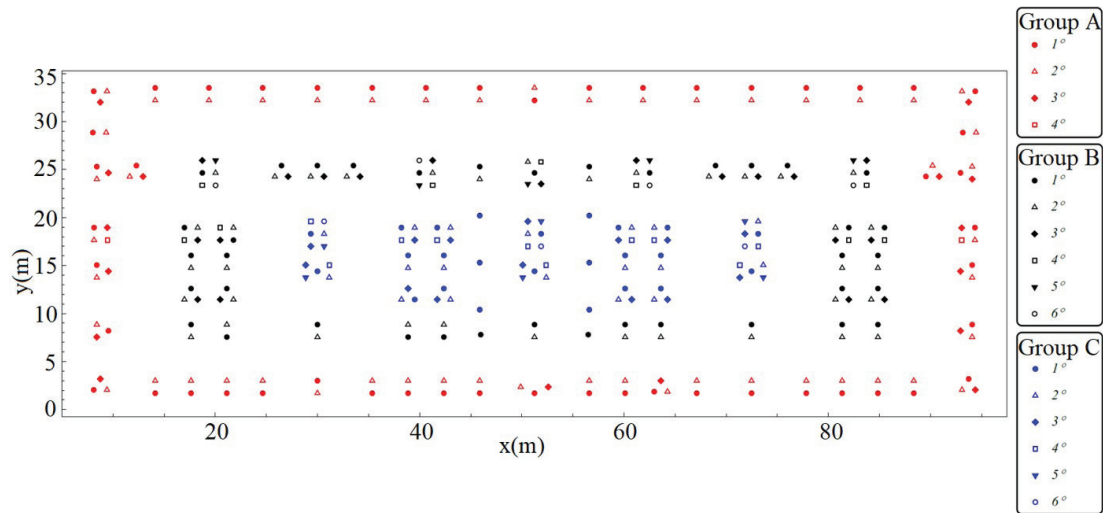
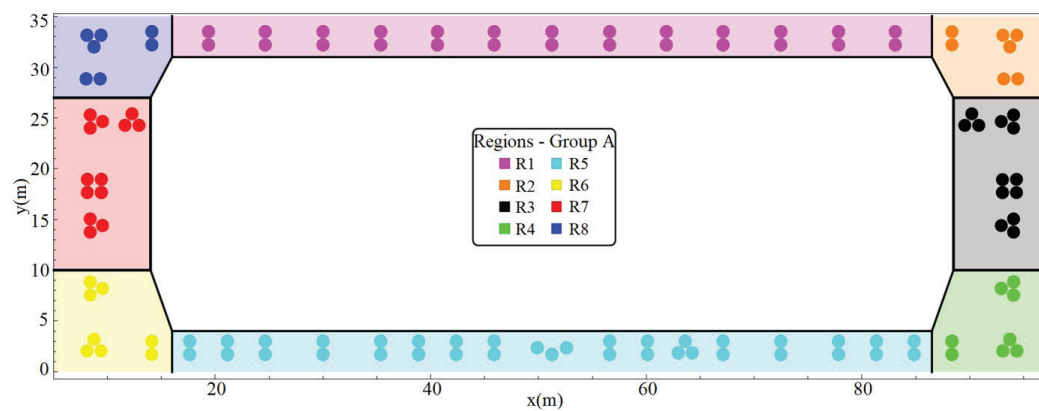
Table 6 reveals that several of the sub-regions can be considered statistically equivalent. Observing each relation, it is possible to compare the position of each sub-region and the spatialization of the volumetric energy density for the foundation piles, located in Figure 15. Certain regions tend to present similar characteristics in terms of execution energy, depending on the positioning in relation to their stratigraphy and the effect of the stress state.

Table 4. Hypothesis tests results (p value): execution sequence of Group B.

Execution sequence	1st	2nd	3rd	4th	5th	6th
1st	1	0.6883	0.3584	0.0012	0.106	0.0075
2nd	0.6924	1	0.7753	0.6322	0.7657	0.3294
3rd	0.3484	0.7788	1	0.8073	0.8925	0.4125
4th	0.0145	0.6378	0.8006	1	0.9519	0.3872
5th	0.0988	0.763	0.9853	0.9498	1	0.5152
6th	0.007	0.32	0.4135	0.3959	0.514	1

Table 5. Hypothesis tests results (p value): execution sequence of Group C.

Execution sequence	1st	2nd	3rd	4th	5th	6th
1st	1	0.5411	0.0005	0.6005	0.3691	0.0405
2nd	0.5329	1	0.0518	0.8831	0.5821	0.1914
3rd	0.0002	0.0544	1	0.0275	0.0348	0.018
4th	0.5857	0.8831	0.0304	1	0.6041	0.1487
5th	0.3647	0.5705	0.0365	0.5993	1	0.3867
6th	0.0445	0.194	0.0203	0.1511	0.4002	1

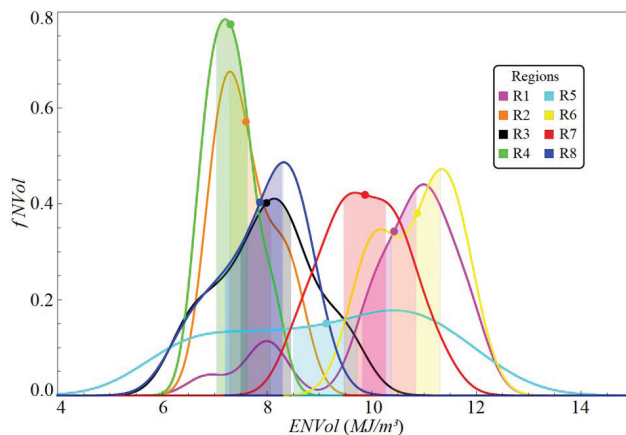
**Figure 18.** Execution order per foundation block.**Figure 19.** Regions belonging to group A.

The main focus of this section analysis is to understand whether the piles in the corners suffer significantly more

influence from the piles executed along the sides of the polygon delimited by the retaining wall. It is noted that for

Table 6. Hypothesis tests results (p value): execution sequence of Group C.

Group A zones	R1	R2	R3	R4	R5	R6	R7	R8
R1	1	0	0	0	0.0045	0.369	0.1619	0
R2	0	1	0.3051	0.237	0.0371	0.0001	0	0.4387
R3	0	0.2927	1	0.0648	0.0418	0	0	0.7514
R4	0	0.2358	0.0599	1	0.0092	0	0	0.0874
R5	0.0041	0.0363	0.0432	0.0096	1	0.0142	0.1703	0.0907
R6	0.3693	0	0	0.0001	0.0144	1	0.0097	0.0005
R7	0.1656	0	0.0002	0	0.1755	0.0094	1	0.0006
R8	0	0.4442	0.7536	0.0929	0.0888	0.0004	0.0003	1

**Figure 20.** Histogram with 95% confidence interval for the regions of group A.

region 1, regions 6 and 7 can be considered statistically equivalent. In this case, this similarity is more related to the predominant soil layer than the position in relation to the wall.

On the other hand, for region 2, there is correspondence with regions 3, 4 and 8. The correspondence with the piles of region 3 is mainly due to the predominant soil layer being the same. Another point is that for regions 4 and 8, the correspondence by influence of the stresses (corners) is clear. It is important to note that region 6 (lower left corner) is not related to the other edge regions (2, 4 and 8) because it does not suffer from the same effects. For region 6, the garage ramp pushed the retaining wall further away from the foundations, changing the effect of stresses on the piles of that region.

Region 3 has the same type of correspondence described in relation to regions 2, 4 and 8. The same holds for region 4 in relation to the regions 2, 3 and 8.

Region 5 has correspondence in relation to the regions 7 and 8. This relationship stems mainly from the predominant soil type in the excavated profile.

Region 6 is only related to region 1. This relation comes from the similarity of stresses for both groups (horizontal neighborhood effect) and the most common type of soil in the profile.

Region 7 shows similarity to the regions 1 and 5. This correspondence stems mainly from the similarity of the stress

state between these regions (neighborhood from the sides of the polygon defined by the retaining wall).

Finally, for region 8, similarities with regions 2, 3, 4 and 5 were found.

7.2.3.4 Influence area of retaining wall structure on foundations

During the executive procedure of a retaining wall structure or, depending on the case, only after its execution, excavation is carried out to implement the foundations. This process of excavation provokes a stress relief in the soil mass, implying in redistributions of stresses until the re-establishment of the equilibrium.

The construction under consideration had its foundation executed 30 days after the implementation of the retaining wall. According to Figure 21, there is a section in profile in which both structures' piles coexist. The probable influence of the wall on the energy spent in the execution of the foundations will be analyzed. For this, a representative area of interest was selected within the site. The specific energy spent to drill the overlapping area (from -9.2 m to -15 m) between foundation and retaining wall piles will be analyzed.

This area was selected because the foundation and retaining walls are close to each other and the total number of piles is sufficient to carry out statistical analyses. Figure 22 shows the histogram of specific energies and the confidence intervals for their mean values for the foundation piles, named R3-A, and the retaining wall piles, R3-B.

The results showed that, in comparative terms, the energies used to excavate the same material in the overlapping region (from -9.2 m to -15 m) in both structures are not equivalent. Physically, this result demonstrates that these distinct characteristics may be related to the effect of the total horizontal stress state, which is severely impacted by the process of unloading the soil. Also, the movement of the walls after being submitted to the horizontal load is another important factor which can be considered, indicating that there is a great influence on the behavior of foundation piles while compared to nearby piles in the retaining wall. In addition, this result also indicates that tests performed before and after the excavation, such as SPT, are strongly influenced by stress relief.

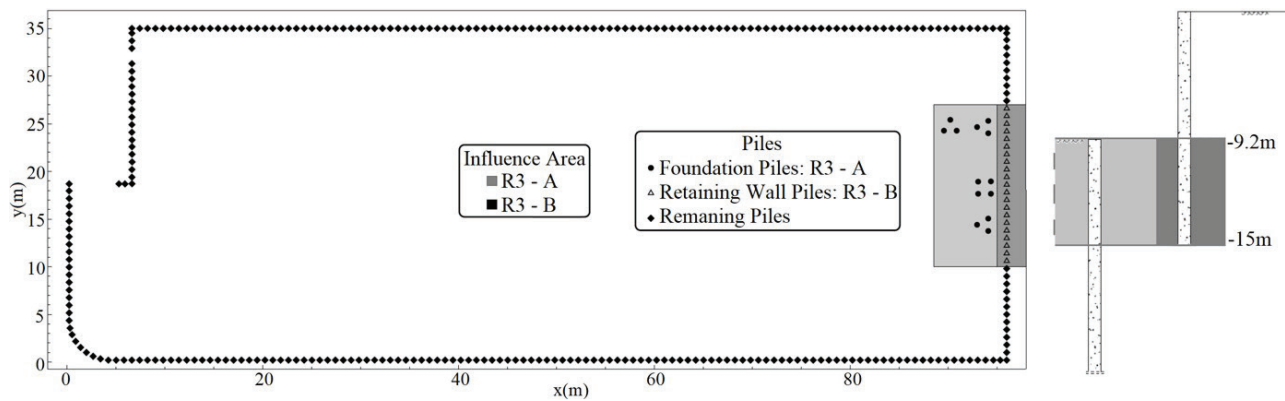


Figure 21. Stretch corresponding to the influence area.

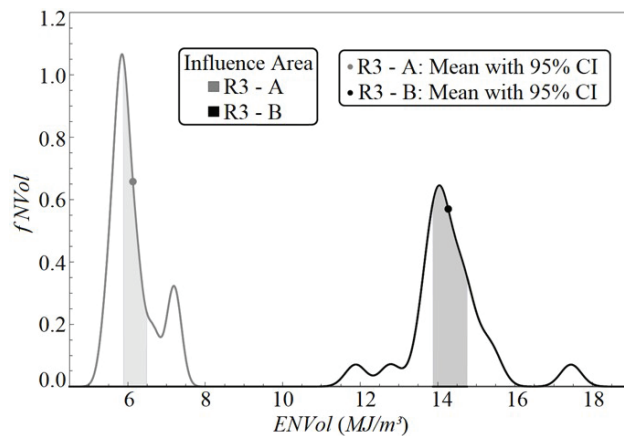


Figure 22. Histogram with 95% confidence interval of piles belonging to influence area.

8. Conclusion

Prior knowledge of local geology and geomorphology is important to perform any type of modeling, be it three-dimensional or two-dimensional. By combining this knowledge with the professional experience, the uncertainties arising from natural soil variability can be considerably mitigated.

Allying the results of the measured execution energies with the Bootstrap resampling method, it was possible to study how the positioning of the piles in the site, as well as the proximity to the retaining wall piles, impact these energetic metrics. The analysis carried out also revealed that the executive order per foundation block does not impact the execution energy when the piles are in the same region.

Regarding the pile execution, it is possible to say that the energy demanded is influenced by the type and competence of the soil being drilled. In the regions where the foundation piles are close to the retaining wall, a general decrease in the execution energy has been observed, which has been attributed to the changes in the horizontal stresses due to stress redistribution. Moving away from the wall, the reductions

are less significant, and energy values are mostly impacted by the competence of the stratigraphic profile being drilled.

In accordance to the previous work by Ozelim & Ferrari de Campos (2016), where a new mathematical model was built to correlate the cumulative execution energy to the cumulative blows of SPT, the spatializations presented in the present paper confirm that there is a good correlation between the accumulated execution energy density and the accumulated NSPT values. Following this reasoning, as the NSPT is used to verify the bearing capacity of the piles, the use of the execution energy represents a promising tool for the actual verification of the performance of the foundation piles.

Not only the bearing capacity itself, but stress-strength constitutive parameters such as Young's Moduli (Ozelim et al., 2018) and Unconfined Compressive Strength (Ozelim et al., 2019) have shown to be related to the execution energy of CFAPs. This reinforces the importance of the present paper, as understanding how the execution energy behaves in real applications is crucial to use this metric as a proxy for the mechanical behavior of the pile during its lifetime. This physical/engineering understanding of the execution energy can be combined to the previous mathematical and statistical correlations and build a powerful estimator of CFAPs response to real-world scenarios.

Geotechnical Engineering, especially the branch dedicated to foundations, has evolved in a substantial way in recent years. This evolution is due in large part to the advent of technologies that allow to simulate and test more precise models of soil's behavior. However, the advances which are currently used in foundation engineering practice are more related to enhanced executive procedures than to a broader understanding of the phenomena involved during the foundations execution. In this sense, the present paper sought not only to list but also to discuss a number of fundamental issues which may show up during the energetic control of the execution of CFAPs.

In summary, foundation designers must analyze the construction site in an integrated way, trying to understand how the stratigraphy, the stress history and the quality of

execution procedures can be integrated in order to ensure reliable solutions.

Acknowledgements

A. L. B. Cavalcante thanks the Coordination for the Improvement of Higher Level Personnel (CAPES), the Brazilian Research Council (CNPq - grant number 305484/2020-6) and University of Brasília for supporting this paper.

Declaration of interest

The authors have no conflicts of interest to declare. All coauthors have observed and affirmed the contents of the paper and there is no financial interest to report.

Authors' contributions

Darym Júnior Ferrari de Campos: conceptualization, data curation, visualization, software, writing – original draft. Luan Carlos de Sena Monteiro Ozelim: methodology, supervision, validation, software, writing – review & editing. André Luís Brasil Cavalcante: formal analysis, investigation, writing – review & editing. Carlos Medeiros Silva: data curation, conceptualization. José Camapum de Carvalho: supervision, conceptualization, formal analysis.

List of symbols

2D	Two-dimensional
3D	Three-dimensional
p	p value
t	Time
Φ	Diameter

References

- ABNT NBR 6122. (2019). *Design and execution of foundations*. ABNT - Associação Brasileira de Normas Técnicas, Rio de Janeiro, RJ (in Portuguese).
- Antunes, W.R., & Tarozzo, H. (1996). *Fundações: teoria e prática* (2nd ed.). PINI Ltda (in Portuguese).
- Caputo, A.N., Tarozzo, H., Alonso, U.R., & Antunes, W.R. (1997). *Estacas hélice continua: projeto, execução e controle*. ABMS – Associação Brasileira de Mecânica dos Solos e Engenharia Geotécnica, São Paulo (in Portuguese).
- Costa, P.M. (2005). *Escavações escoradas em solos argilosos moles: análise do comportamento considerando os efeitos da consolidação* [MSc Thesis, University of Porto]. University of Porto's repository (in Portuguese). <https://hdl.handle.net/10216/12092>
- Efron, B. (1979). Bootstrap method: another look at the Jackknife. *The Analysis of Statistics*, 7(1), 1-26.
- Efron, B. (1982). *The jackknife, the bootstrap and other resampling plans* (CBMS-NSF Monographs, 38). Society for Industrial and Applied Mathematics.
- Efron, B., & Tibshirani, R.J. (1993). *An introduction to the bootstrap*. Chapman & Hall.
- Ferrari de Campos, D.J., Ozelim, L.C.S.M., Camapum de Carvalho, J., & Cavalcante, A.L.B. (2019). Efeitos do período de execução e alívio de tensões na interpretação de sondagens. In *Anais do 9º Seminário de Engenharia de Fundações Especiais e Geotecnia* (Vol. 1, pp. 1-10). São Paulo: ABMS/ABEF.
- Ferrari de Campos, D.J., Camapum de Carvalho, J., Gitirana, G.F.N., Cavalcante, A.L.B., & Ozelim, L.C.S.M. (2021). Analysis of the bearing capacity of continuous flight auger piles in terms of their excavation energy and of rainfall data. *Matec Web of Conferences*, 337, 1-5. <https://doi.org/10.1051/mateconf/202133703010>.
- Instituto Nacional de Meteorologia – INMET. (2021). Retrieved in March 1, 2021, from <http://www.inmet.gov.br/portal/index.php?r=tempo/graficos>
- Moore, D.S., Notz, W.I., & Flinger, M.A. (2013). *The basic practice of statistics* (6th ed.). New York.
- Ozelim, L.C.S.M., & Cavalcante, A.L.B. (2018). Representative elementary volume determination for permeability and porosity using numerical three-dimensional experiments in microtomography data. *International Journal of Geomechanics*, 18(2), 04017154. [http://dx.doi.org/10.1061/\(ASCE\)GM.1943-5622.0001060](http://dx.doi.org/10.1061/(ASCE)GM.1943-5622.0001060).
- Ozelim, L.C.S.M., & Ferrari de Campos, D.J. (2016). On the analysis of execution energies for continuous flight auger piles to reduce costs and to enhance productivity and reliability of foundations. In *Proceedings of the 4th International Conference on New Developments in Soil Mechanics and Geotechnical Engineering* (Vol. 1, pp. 609-615). Nicosia: Near East University.
- Ozelim, L.C.S.M., Ferrari de Campos, D.J., Camapum de Carvalho, J., & Cavalcante, A.L.B. (2018). Indirect in-situ tests during the execution of deep foundations: relating the excavation energies to the Young's moduli of the surrounding soils. In *Proceedings of the GeoMEast International Congress and Exhibition on Sustainable Civil Infrastructures* (pp. 191-205). USA: Springer.
- Ozelim, L.C.S.M., Ferrari de Campos, D.J., Camapum de Carvalho, J., & Cavalcante, A.L.B. (2019). On the relation between the excavation energies of continuous flight auger piles and the unconfined compressive strength of the surrounding soils. In *Proceedings of the XVI Pan-American Conference on Soil Mechanics and Geotechnical Engineering* (pp. 1117-1124). Amsterdam: IOS Press.
- Rajapakse, R. (2016). *Pile design and construction rules of thumb* (2nd ed.). Elsevier.
- Richards, D.J., Powrie, W., Roscoe, H., & Clark, J. (2007). Pore water pressure and horizontal stress changes measured during construction of a contiguous bored pile multi-propped retaining wall in Lower Cretaceous clays. *Geotechnique*, 57(2), 197-205. <http://dx.doi.org/10.1680/geot.2007.57.2.197>.

- Silva, C., & Camapum de Carvalho, J. (2010). Monitoring and quality control of continuous flight auger piles during the execution of the building. In *Anais do XV Congresso Brasileiro de Mecânica dos Solos e Engenharia Geotécnica* (pp. 1-12). Gramado: ABMS.
- Silva, C.M. (2011). *Energy and reliability in continuous flight auger type foundation works* [PhD thesis, University of Brasilia]. University of Brasilia's repository (in Portuguese). <https://repositorio.unb.br/handle/10482/10456>
- Silva, C.M., Cavalcante, A.L.B., & Camapum de Carvalho, J. (2012). On modelling continuous flight auger pilings by means of energy. *International Journal of Science and Engineering Investigations*, 1(9), 11-16. Retrieved in March 1, 2021, from <http://www.ijsei.com/papers/ijsei-10912-03.pdf>
- Toledo, M.C., Fairchild, T.R., & Taioli, F. (2000). Intemperismo e formação do solo. In W. Teixeira, M. C. M. Toledo, T. R. Fairchild & F. Taioli (Orgs.), *Decifrando a terra* (pp. 139-165). Oficina de Textos (in Portuguese).

TECHNICAL NOTES

Soils and Rocks
v. 45, n. 2

Undrained shear strength correlation analysis based on vane tests in the Jacarepaguá Lowlands, Brazil

Magnos Baroni^{1#} , Marcio de Souza Soares de Almeida² 

Technical Note

Keywords

Organic soil
Piezocone test
Plasticity index
Undrained shear strength
Vane test
Soft soil

Abstract

The test sites analyzed here consist of clay deposits located in the Jacarepaguá Lowlands in Rio de Janeiro, characterized by high plasticity, high compressibility and low undrained shear strength. The deposits are made up of lightly overconsolidated aged clays, montmorillonite being the predominant clay mineral. Soft clay deposits are usually superficial, with thicknesses generally varying between 6 m and 17 m and geologically recent and originated from marine regressions and transgressions, that occurred between 6000 and 3500 years ago. The objective of this study is to analyze a large database of undrained shear strength measurements obtained by 461 vane tests performed at 15 different sites. In general, most of the data correspond to very soft clays, with undrained shear strength values lower than 25 kPa. The undrained shear strength measurements are correlated with plasticity index and with maximum excess pore pressure, measured with piezocone tests. The method for estimating the undrained shear strength $s_{u(DT)}$ of soil from the excess pore pressure generated during piezocone dissipation tests proposed by Mantaras et al. (2015) was validated against the vane test database.

1. Introduction

The Jacarepaguá Lowlands, shown in Figure 1, is a coastal region formed mainly by thick deposits of soft and very soft organic clays with high plasticity, high compressibility, and low undrained shear strength (e.g. Baroni & Almeida, 2017; Riccio et al., 2013; Almeida et al., 2008; Futai et al., 2008; Almeida et al., 2007). It is limited to the South by the Atlantic Ocean, to the West and North by the Pedra Branca Massif, and to the East by the Tijuca Massif. It extends around 22 km along the East-West axis and 4 to 6 km along the North-South axis, with a total area of 120 km². Due to the scarcity of land with better subsoil conditions, several infrastructure projects were carried out in this region in the last decade, such in 2007 the Pan-American Games, in 2014 the FIFA World Cup and in 2016 the Olympic and Paralympic Games.

The undrained shear strength s_u of soft soil is a fundamental parameter controlling the stability of structures built on these soils. However, s_u is dependent on various factors affecting soil behavior such as the mode of failure, stress paths, strain rate, anisotropy, temperature, stress history, clay structure, among other factors (Bjerrum, 1973; Ladd et al., 1977; Wroth, 1984). The undrained shear strength of soft clays is

often obtained using in situ vane tests, especially in very soft clay deposits, due to the difficulty of extracting undisturbed samples. Correlations of the s_u with the stress history (e.g., overconsolidation ratio, preconsolidation stress) have been presented by various authors (e.g., Mesri, 1975; Ladd et al., 1977; Ng et al., 2017). However, such correlations require good quality undisturbed samples, which are not easily obtained in very soft soil deposits, and for this reason are not addressed in the present technical note. The objective of this study is to analyze the results of 461 good quality in situ vane shear tests performed at 15 different sites located in the Jacarepaguá Lowlands. The undrained shear strength measurements are then correlated with soil parameters including Atterberg limits and piezocone measurements. Compressibility studies in this region have recently been reported (Baroni & Almeida, 2017).

2. Jacarepaguá Lowlands general characteristics

The subsoil of Jacarepaguá Lowlands is composed of deposits of very soft clay with high organic matter content, formed in the Quaternary period (Suguio & Martin, 1981). The deposits are geologically recent and originated from marine regressions

[#]Corresponding author. E-mail address: magnos.baroni@ufsm.br

¹Universidade Federal de Santa Maria, Departamento de Transporte, Santa Maria, RS, Brasil.

²COPPE-UFRJ – Instituto Alberto Luiz Coimbra de Pós-Graduação e Pesquisa de Engenharia, Rio de Janeiro, RJ, Brasil.

Submitted on June 22, 2021; Final Acceptance on January 26, 2022; Discussion open until August 31, 2022.

<https://doi.org/10.28927/SR.2022.072721>



This is an Open Access article distributed under the terms of the Creative Commons Attribution License, which permits unrestricted use, distribution, and reproduction in any medium, provided the original work is properly cited.



Figure 1. Location of the Jacarepaguá Lowlands and studied sites.

and transgressions, that occurred between 6000 and 3500 years before present (Costa Maia et al., 1984). Soft clay deposits are usually superficial, with thicknesses generally varying between 6 m and 17 m, although deposits of 22 m (Riccio et al., 2013) and 28 m (Almeida et al., 2008) have been reported. Superficial fill sand layers, deposited for the temporary traffic of vehicles, are commonly found at some sites.

In general, the local clay deposits present a superficial layer varying from 1.0 m to 4.0 m in thickness, which may reach organic matter content values up to 60% (Baroni & Almeida, 2017). These deposits have high water content (w) reaching 950% for the top crust organic layers, then decreasing to around 100% for deeper layers. These deposits are classified as organic soils and not as peat soils (Landva & Pheeney, 1980).

The soil bulk unit weight (γ) was generally very low, with average values on the order of 13 kN/m³, while the specific gravity of soil particles (G_s) varied between 2.44 and 2.66. In general, the grain size distribution showed more than 50% of fines and X-ray diffraction analysis indicated that montmorillonite was the predominant clay mineral, which is compatible with the high activity value presented in Table 1. The presence of quartz, kaolinite and muscovite were also detected by the X-ray diffraction measurements.

A summary of typical soil properties is also presented in Table 1, with the soil being classified as a black, high plasticity, very soft, high-organic, sandy silty clay with extremely low undrained shear strength (BS, 2018a, b). The presence of humic acids associated with a low pH value was also detected (see Table 1). The low values of the specific gravity of soil particles (G_s) and of the bulk unit weight (γ) result from high values of organic matter content (OM), and are compatible with the literature (Coutinho & Lacerda, 1987; Mitchell & Soga, 2005).

All clay deposits in this region have high water content, plasticity and compressibility, with compression ratios

Table 1. Typical properties of the soil tested.

Properties	Range/Value
pH	3.36
Activity, $A = I_p/\% < 0.002\text{mm}$	6-6.4
Electrical conductivity, EC (mS/cm)	6.59
Salinity (%)	0.35
Sulphate (mg/L)	4551
Chloride (mg/L)	505

($CR = CC/(1+e_o)$) typically around 0.45 (Almeida & Marques, 2013). In the superficial layers, where high organic clay soils and roots are found, the overconsolidation ratio (OCR) values may reach high values on the order of 8 (Baroni & Almeida, 2017). The OCR decreases with increasing depth, reaching typical values between 1 and 2 (Baroni & Almeida, 2017) as a result of aging and water level fluctuations (Parry & Wroth, 1981). The values of the coefficient of consolidation (c_v) are generally very low, on the order of 3×10^{-8} m²/s (Almeida & Marques, 2013).

The typical values of water content (w) and liquid limit (w_L) below the crust layer are $w = 175\%$ and $w_L = 150\%$, respectively. Clays with natural moisture close to or above the liquidity limit are found along the entire Brazilian coast (Coutinho & Lacerda, 1987; Almeida & Marques, 2003; Oliveira et al., 2010; Coutinho & Bello, 2014; Jannuzzi et al., 2015; Baroni & Almeida, 2017).

In general, the soil parameters are more scattered in the top organic clay layers. The plasticity index ($I_p = w_L - w_p$) is greater than 80% in the deeper layers of clay, reaching 500% in the shallower clay layers, indicating that the deposits have a high plasticity. Below a depth of 3 m the average I_p value is 110% (Baroni & Almeida, 2017). Equation 1 shows the local relationship (Baroni, 2016) between the plasticity index and the liquid limit, the 0.7 angular coefficient obtained is similar to the well-known 0.73 Casagrande's coefficient.

$$I_p = 0.7w_L - 6.12 \quad (1)$$

Table 2 presents the range of geotechnical parameters for the 15 sites studied. It shows that the average value of the liquidity index ($I_L = (w - w_p)/I_p$) is typically greater than unity, suggesting that clays may be sensitive (Mitchell & Soga, 2005). Some data are limited, such as clay sensitivity and liquidity index, and therefore are not correlated with vane undrained shear strength.

3. Undrained shear strength data bank

Most vane tests presented here were performed using vane borer equipment, having been used with excellent results

in the last two decades in Brazil (Baroni & Almeida, 2012; Coutinho & Bello, 2014), and considered in the literature to be quite reliable for measuring low undrained shear strength values (e.g. Selänpää et al., 2017).

Figure 2 presents water content and undrained shear strength profiles for the studied deposits. Higher values of water content are observed (Figure 2a) for the top 3 m deep superficial layer as these present higher organic matter content values. Figure 2b shows data from the 461 vane test results used herein. The water level variation at the surface and associated soil dryness, in addition to the presence of roots in this region, result in higher values of s_u (Figure 2b). Below depths of 3 m the expected trend of decreasing

Table 2. Physical properties and undrained shear strength - average values from 15 sites.

	Site 1	Site 2	Site 3	Site 4	Site 5	Site 6	Site 7	Site 8	Site 9	Site 10	Site 11	Site 12	Site 13	Site 14	Site 15
w (%)	294	247	277	244	174	130	115	149	108	94	104	-	250	-	-
w_p (%)	76	64	67	80	71	42	44	56	-	-	21	-	84	-	-
w_L (%)	223	289	204	206	200	123	132	150	-	-	43	-	243	-	-
I_p (%)	148	224	139	124	135	80	88	94	-	-	13	-	159	-	-
I_L (%)	1.58	0.85	1.51	1.29	1.13	1.08	0.82	0.81	-	-	2.63	-	1.52	-	-
γ (kN/m ³)	11.5	12.3	12.5	12.4	14.2	13.7	14.1	14.0	13.4	13.6	13.3	-	12.1	-	-
OM (%) ^a	16.8	18.7	-	-	12.4	-	-	-	-	-	-	-	-	-	-
s_u (kPa)	11.8	13.8	10.1	17.5	12.8	5.4	40.5	4.0	9.8	8.4	43.4	13.6	17.4	10.6	24.5
[N° of points]	[41]	[43]	[26]	[103]	[42]	[10]	[50]	[14]	[15]	[12]	[25]	[13]	[33]	[13]	[21]
$s_{t(average)}$ ^b	10.1	6.4	10.5	-	9.3	4.2	-	7.5	5.3	11.1	3.4	4.5	5.6	10.3	-

^a Organic Matter; ^b Clay Sensitivity - s_t

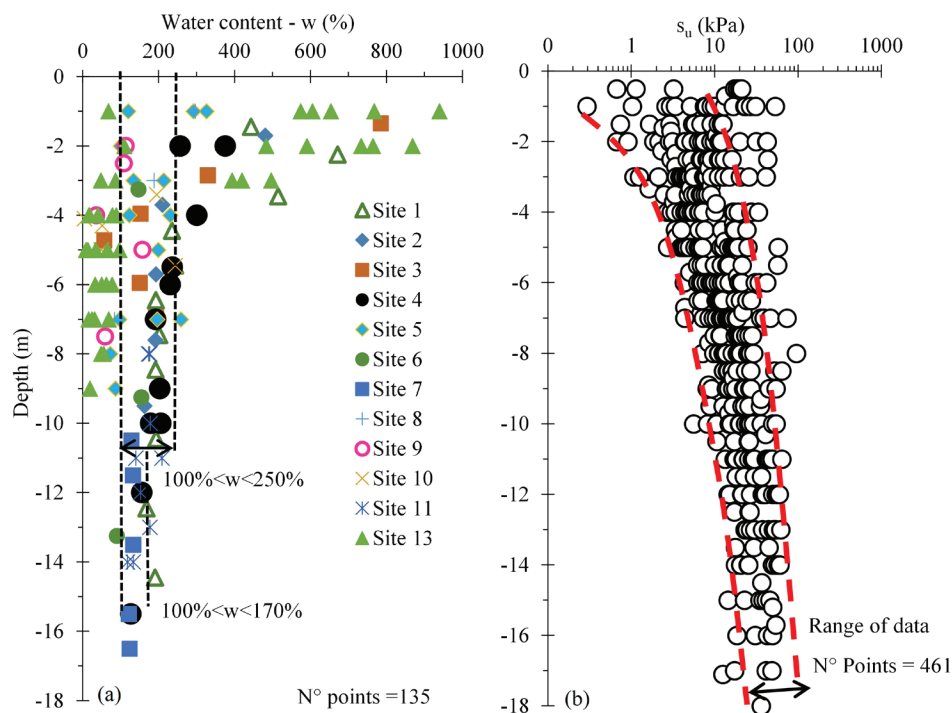


Figure 2. (a) Soil moisture content, 12 sites and (b) undrained shear strength.

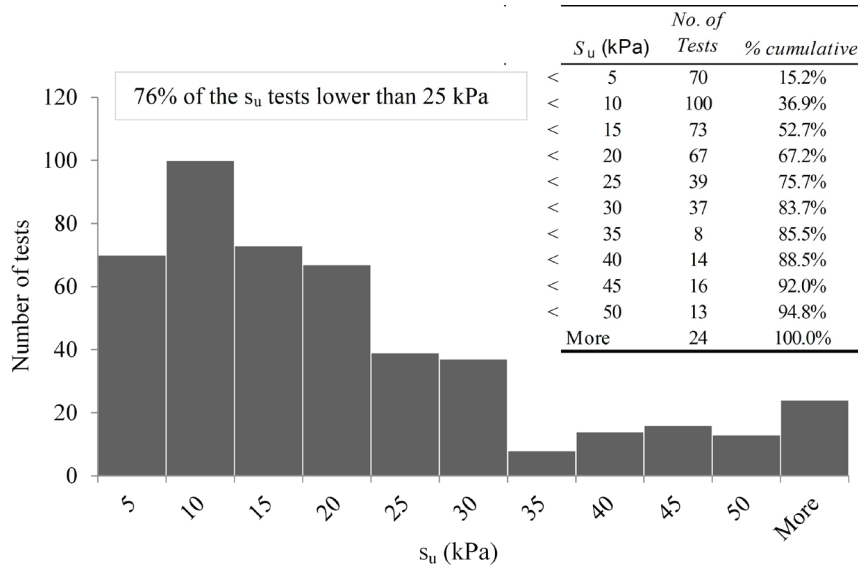


Figure 3. Histogram of undrained shear strength values measured.

water content (w) with increasing effective stresses and the consequent increase in undrained shear strength (Atkinson, 1981) is observed.

The histogram shown in Figure 3 indicates that 70 out of the 461 measurements of s_u presented values of s_u lower than 5 kPa. Approximately 76% of the tests resulted in values of s_u lower than 25 kPa, which classifies the deposits studied here as very soft clay (Terzaghi & Peck, 1967). This range of strength variation is consistent with values found in other Brazilian deposits (e.g. Lacerda & Almeida, 1995; Almeida & Marques, 2003; Schnaid, 2009; Coutinho & Bello, 2014; Jannuzzi et al., 2015).

4. Undrained shear strength versus plasticity index

The relationship between the undrained strength normalized by the vertical in situ effective stress s_u/σ'_{vo} and the plasticity index I_p of the studied clays is presented in Figure 4, with the curves of young and aged clays proposed by Bjerrum (1973) and Chandler (1988) for OCR = 1 “young” clay and $m_{fv} = 0.95$, in order to predict OCR from field vane test data. It is extended here for a wider range of plasticity index values. Although some scatter is observed for the available data, the points are distributed in a regular pattern in Figure 4, generally falling between the two proposed curves for young and aged clays, which is consistent with the geology of the clay deposit. The points outside the range of variation, indicate the presence of sand lenses or shells fragments in the soil. The linear relationship between s_u/σ'_{vo} and I_p proposed by Skempton (1957) for stiffer, less plastic clays does not fit well with the present database for very soft high plasticity clays.

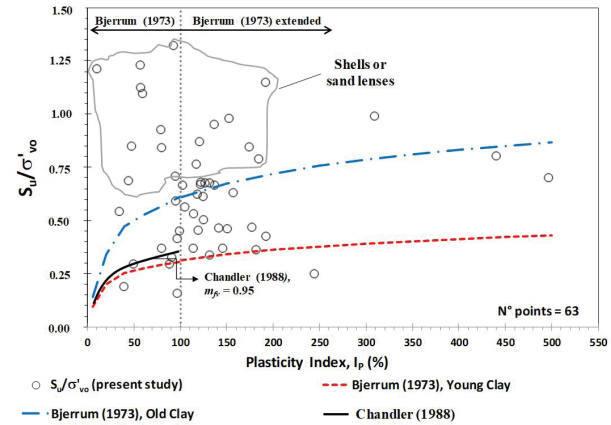


Figure 4. Correlation between s_u/σ'_{vo} and soil plasticity index (I_p).

5. Undrained strength versus excess pore pressure

A method for estimating the undrained shear strength $s_{u(DT)}$ of soil from the excess pore pressure generated during piezocone dissipation tests was proposed by Mantaras et al. (2015). Using the principles of cavity expansion and critical state soil theory, the authors obtained consistent estimates of s_u according to Equation 2.

$$s_{u(DT)} = Du_{max} / 4.2 \log(I_r) \quad (2)$$

The values of $s_{u(DT)}$ obtained from Equation 2 are compared here with values of $s_{u(VT)}$ obtained by means of the vane equipment (reference test), and the $s_{u(CPTU)}$ obtained with the

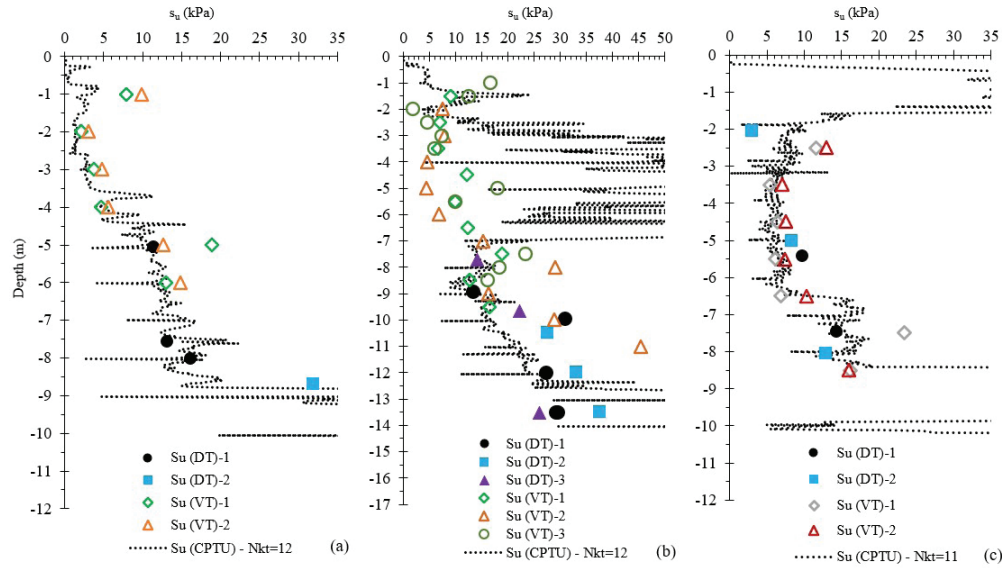


Figure 5. Comparison of s_u obtained through different methodologies: (a) site 10, (b) site 13 and (c) site 14.

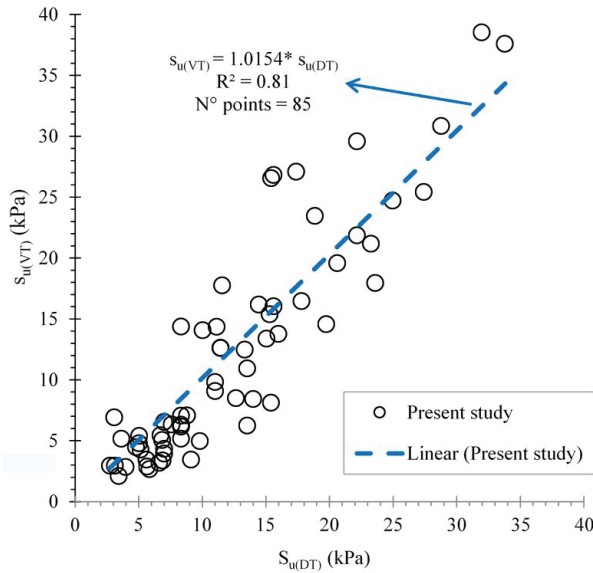


Figure 6. s_u measured with vane tests versus $s_{u(DT)}$ estimated with the CPTU dissipation test.

piezocone test using calibrated N_{kt} parameters (Lunne et al., 1997). Figure 5 shows the profiles obtained for three of the studied sites. The results of the correlation proposed by Mantaras et al. (2015) are in good agreement with the measured values from the vane tests and piezocone tests (CPTU). In the region under study, the cone factor N_{kt} varies randomly with the depth, and it is not uncommon to use different N_{kt} values for the estimation of the s_u profile in the same location. The tests performed indicate that the lower limit and upper limit values of N_{kt} are 6 and 18, respectively, with $N_{kt} = 12$ a typical average value.

Figure 6 correlates 85 results of $s_{u(VT)}$ and $s_{u(DT)}$ for tests at nearby boreholes carried out at similar depths. As shown in Figure 6, the $s_{u(DT)}$ values are around 1.5% lower than the $s_{u(VT)}$ values, indicating that Equation 2 can be applied for estimation of s_u for the Jacarepaguá Lowlands.

6. Conclusions

Results of 461 vane tests performed at 15 different sites located in the Jacarepaguá Lowlands in Rio de Janeiro were analyzed here. In general, most of the data correspond to very soft clays, with undrained shear strength values lower than 25 kPa. The soil profiles show, as expected, a decrease in water content and a corresponding increase in undrained shear strength with depth.

As expected, the undrained shear strength, normalized with effective stresses, increased with the plasticity index in a nonlinear trend, within the range of young and aged clays proposed by Bjerrum (1973) and Chandler (1988).

A correlation proposed in the literature to obtain the undrained shear strength from the maximum excess pore pressure measured with piezocone tests was validated against the vane test database.

Acknowledgements

The authors are indebted to COPPE-UFRJ technical staff for performing the tests and providing most data bank information developed here, and also to all researchers and individuals that have furnished information for the data base. Financial support for the present study was given by Brazilian funding agencies CNPq, FAPERJ and MCT/INCT-Reageo.

Declaration of interest

The authors have no conflicts of interest to declare. All co-authors have observed and affirmed the contents of the paper and there is no financial interest to report.

Authors' contributions

Magnos Baroni: conceptualization, methodology, investigation, data curation, writing – original draft, validation, writing – review & editing. Marcio Almeida: conceptualization, data curation, methodology, supervision, validation, writing – review & editing.

List of symbols

A	Activity
CC	compression index
$CPTU$	piezocone test
EC	electrical conductivity
G_s	specific gravity of soil particles
G	soil shear modulus
I_L	liquidity index
I_r	soil rigidity index
I_p	plasticity index
OM	organic matter
OCR	overconsolidation ratio
c_v	coefficient of consolidation
e_o	initial void ratio
s_u	undrained shear strength
$s_{u(DT)}$	undrained shear strength of soil from the excess pore pressure generated during piezocone dissipation
s_t	clay sensitivity
w_L	liquid limit
w	natural water content w_p plastic limits
Δu_{max}	maximum normalized excess pore pressure
γ	soil bulk unit weight
σ'_{v0}	vertical in situ effective stress

References

- Almeida, M.S.S., & Marques, M.E.S. (2003). The behaviour of Sarapuí soft clay. In T.S. Tan, K.K. Phoon, D.W. Hight & S. Leroueil *Characterization and engineering properties of natural soils* (pp. 477-504). CRC Press.
- Almeida, M.S.S., & Marques, M.E.S. (2013). *Design and performance of embankments on very soft soils*. CRC Press. <https://doi.org/10.1201/b15788>.
- Almeida, M.S.S., Ehrlich, M., Spotti, A.P., & Marques, M.E.S. (2007). Embankment supported on piles with biaxial geogrids. *Proceedings of the Institution of Civil Engineers - Geotechnical Engineering*, 160(4), 185-192. <http://dx.doi.org/10.1680/geng.2007.160.4.185>.
- Almeida, M.S.S., Futai, M.M., Lacerda, W.A., & Marques, M.E.S. (2008). Laboratory behaviour of Rio de Janeiro soft clays - Part 1: index and compression properties. *Soils and Rocks*, 31(2), 69-75.
- Atkinson, J.H. (1981). *Foundations and slopes: an introduction to applications of critical state soil mechanics*. John Wiley & Sons.
- Baroni, M. (2016). *Geotechnical behavior of extremely soft clay of Baixada Jacarepagua, RJ*. [Doctoral thesis, Federal University of Rio de Janeiro]. Federal University of Rio de Janeiro's repository (in Portuguese). <http://www.coc.ufrj.br/pt/teses-de-doutorado/391-2016/8231-magnos-baroni>.
- Baroni, M., & Almeida, M.S.S. (2012). In situ and laboratory parameters of extremely soft organic clay deposits. In *Proc. 4th International Conference on Site Characterization - Geotechnical and Geophysical Site Characterization 4* (pp. 1611-1619), Porto de Galinhas, September 2012. CRC Press.
- Baroni, M., & Almeida, M.S.S. (2017). Compressibility and stress history of very soft organic clays. *Proceedings of the Institution of Civil Engineers - Geotechnical Engineering*, 170(2), 148-160. <http://dx.doi.org/10.1680/jgeen.16.00146>.
- Bjerrum, L. (1973). Problems of soil mechanics and construction of soft clays and structurally unstable soils. In *Proc. 8th International Conference on Soil Mechanics and Foundation Engineering* (Vol. 2, pp. 111-159), Moscow, August 1973. USSR National Society for Soil Mechanics and Foundation Engineering.
- BS EN ISO 14688-1. (2018a). *Geotechnical investigation and testing — Identification and classification of soil - Part 1: Identification and description*. British Standards Institution, London.
- BS EN ISO 14688-2. (2018b). *Geotechnical investigation and testing. Identification and classification of soil Principles for a classification*. British Standards Institution, London.
- Chandler, R.J. (1988). The in-situ measurement of the undrained shear strength of clays using the field vane. In *Vane shear strength testing in soils field and laboratory studies* (pp. 13-44). ASTM International. <https://doi.org/10.1520/STP10319S>.
- Costa Maia, M.C.A., Martin, L., Flexor, J.M., & Azevedo, A.E.G. (1984). Evolução holocênica da planície costeira de Jacarepaguá (RJ). In *Proc. XXXIII Congresso Brasileiro de Geologia* (pp. 105-118), Rio de Janeiro, RJ. SBGEO (in Portuguese).
- Coutinho, R.Q., & Bello, M.I.M.C.V. (2014). Geotechnical characterization of Suape soft clays, Brazil. *Soils and Rocks*, 37(3), 257-276.
- Coutinho, R.Q., & Lacerda, W.A. (1987). Characterization and consolidation of Juturnaiba organic clays. In *International Symposium on Geotechnical Engineering of Soft Soils* (Vol. 1, pp. 17-24), Mexico.

- Futai, M.M., Almeida, M.S.S., & Lacerda, W.A. (2008). Laboratory behaviour of Rio de Janeiro soft clays. *Soils and Rocks*, 31(2), 77-84.
- Jannuzzi, G.M.F., Danziger, F.A.B., & Martins, I.S.M. (2015). Geological-geotechnical characterization of Sarapuí II clay. *Engineering Geology*, 190, 77-86. <http://dx.doi.org/10.1016/j.enggeo.2015.03.001>.
- Lacerda, W.A., & Almeida, M.S.S. (1995). Engineering properties of regional soils: residual soils and soft clays. State-of-the art lecture. In *Proc. X Pan-American Conference on Soil Mechanics and Foundation Engineering* (Vol. 4, pp. 133-176), Guadalajara, November 1995. Sociedad Mexicana de Mecánica de Suelos.
- Ladd, C.C., Foott, R., Ishihara, K., Schlosser, F., & Poulos, H.G. (1977). Stress deformation and strength characteristics. State-of-the-Art Report. In *Proc. 9th International Conference on Soil Mechanics and Foundation Engineering* (Vol. 2, pp. 421-494), Tokyo. Japanese Society of Soil Mechanics and Foundation Engineering.
- Landva, A.O., & Pheeney, P.E. (1980). Peat fabric and structure. *Canadian Geotechnical Journal*, 17(3), 416-435. <http://dx.doi.org/10.1139/t80-048>.
- Lunne, T., Robertson, P.K., & Powell, J.J.M. (1997). *Cone Penetration Testing in geotechnical practice*. E & FN Spon.
- Mantaras, F.M., Odebrecht, E., & Schnaid, F. (2015). Using piezocone dissipation test to estimate the undrained shear strength in cohesive soil. *Canadian Geotechnical Journal*, 52(3), 318-325. <http://dx.doi.org/10.1139/cgj-2014-0176>.
- Mesri, G. (1975). Discussion of "New design procedure for stability of soft clays". *Journal of Geotechnical and Geoenvironmental Engineering*, 101(4), 409-412. <http://dx.doi.org/10.1061/AJGEB6.0005026>.
- Mitchell, J.K., & Soga, K. (2005). *Fundamentals of soil behavior*. John Wiley & Sons.
- Ng, I.T., Yuen, K.V., & Dong, L. (2017). Estimation of undrained shear strength in moderately OC clays based on field vane test data. *Acta Geotechnica*, 12(1), 145-156. <http://dx.doi.org/10.1007/s11440-016-0433-0>.
- Oliveira, H.M., Ehrlich, M., & Almeida, M.S.S. (2010). Embankments over soft clay deposits: contribution of basal reinforcement and surface sand layer to stability. *Journal of Geotechnical and Geoenvironmental Engineering*, 136(1), 260-264. [http://dx.doi.org/10.1061/\(asce\)gt.1943-5606.0000200](http://dx.doi.org/10.1061/(asce)gt.1943-5606.0000200).
- Parry, R.H.G., & Wroth, C.P. (1981). Shear stress-strain properties of soft clay. In E.W. Brand & R.P. Brenner (Eds.), *Soft clay engineering*. (Developments in Geotechnical Engineering Book Series, Vol. 20, pp. 311-364). Elsevier.
- Riccio, M., Baroni, M., & Almeida, M.S.S. (2013). Ground improvement in soft soils in Rio de Janeiro: the case of the Athletes' Park. *Proceedings of the Institution of Civil Engineers. Civil Engineering*, 166(6), 36-43. <http://dx.doi.org/10.1680/cien.13.00008>.
- Schnaid, F. (2009). *In situ testing in geomechanics*. Taylor and Francis.
- Selänpää, J., Di Buò, B., Lämsivaara, T., & D'Ignazio, M. (2017). Problems related to field vane testing in soft soil conditions and improved reliability of measurements using an innovative field vane device. In V. Thakur, J. L'Heureux & A. Locat (Eds.), *Landslides in sensitive clays* (Vol. 46, pp. 121-131). Springer. https://doi.org/10.1007/978-3-319-56487-6_10.
- Skempton, A.W. (1957). Discussion of "Further data on the c/p ratio in normally consolidated clays". *Proceedings - Institution of Civil Engineers*, 7(2), 305-307.
- Suguio, K., & Martin, L. (1981). Progress in research on Quaternary sea level changes and coastal evolution in Brazil. In *International Symposium Holocene Sea-Level Fluctuations, Magnitude and Causes, IGCP Project 61 meeting* (pp. 166-181), Columbia.
- Terzaghi, K., & Peck, R.B. (1967). *Soil mechanics in engineering practice* (2nd ed.). Wiley.
- Wroth, C.P. (1984). The interpretation of in-situ soil tests. *Geotechnique*, 34(4), 449-489. <http://dx.doi.org/10.1680/geot.1984.34.4.449>.

Influence of addition of butadiene copolymer and modified styrene on the mechanical behavior of a sand

Thiago Manes Barreto¹ , Lucas Mendes Repsold² ,

Nathália Araújo Boaventura de Souza e Silva^{3#} , Michéle Dal Toé Casagrande³  **Technical Note**

Keywords

Polymeric sands
Butadiene-styrene polymer
Embankments-soft soils
Slope stabilization method

Abstract

Butadiene-styrene copolymer (SBR) is an elastomer composed of 75% butadiene and 25% styrene and is widely used in the automotive industry in tire production. This elastomer can be produced from two polymerization processes: emulsion or solution polymerization. This paper presents the mechanical behavior of a polymer reinforced sand compared to pure sand. Direct shear tests were performed on pure sand specimens and with the addition of modified styrene butadiene-styrene copolymer (XSBR). The polymeric sand specimens had 10% moisture content, 50% relative density, with water-polymer mass ratios of 1:1, 1:2, and 1:4, with no curing time, or with curing times 48, 72, 96, 576, and 720 h. Improvements were verified in the strength parameters of sand specimens with polymer addition, while comparing with pure sand parameters, showing that the improvement of soils with polymers is satisfactory for application in geotechnical works, such as: embankments in soft soils, soils for shallow foundations and for slope stability.

1. Introduction

Due to the importance of soil to the construction process and the significant variability of properties it can present, soils are subjected to careful analysis, aiming at the characterization and estimation of soil mechanical strength parameters. In geotechnical engineering, there are situations where the soil is not able to withstand increases in stress when compared to its natural state of equilibrium. One of the most common solutions is the partial/total removal of poorly resilient soil layers, followed by their replacement with a soil that meets the minimum geotechnical design requirements. However, this solution may become unfeasible in cases involving large volumes of soil, or even in the absence of nearby borrow/dump areas. As an alternative, soil improvement/stabilization processes have been developed to alter the geotechnical properties of the soil, in situ, for use in geotechnical works. These processes can be performed using several methodologies, varying with project resources and specifications.

As presented in Vendruscolo (1996), soil stabilization is an old technique, developed for paving, which was widely used in other areas, such as: foundations, slope stabilization, retaining works, and dams. On the other hand, Vargas (1977) defines soil stabilization as a process that provides greater

stable resistance to loads, wear or erosion. Stabilization can be reached through compaction, grain size correction, and addition of substances that provide cohesion (from cementation or agglutination of grains). Furthermore, the soil's own plasticity can provide some degree of cohesion.

According to Almeida et al. (2016), among the stabilization methods (mechanical, physical and chemical), the chemical stabilization process is the one that presents the largest number of reactions between soil, stabilizing additive and water, to obtain a new material, with better properties than pure soil. As expected, the stabilization characteristics are closely related to the behavior and quality of the soil, as the largest and most heterogeneous component of the mixture. Louzada et al. (2019) suggest that regardless of the soil improvement technique, whether physical or chemical, the improvement of mechanical parameters is attractive according to technical, economic and environmental points.

Studies are being developed to provide more sustainable, less costly and technically efficient solutions to enable the use of new materials in soil stabilization/strengthening processes. These include the use of municipal solid waste (MSW) (Vizcarra et al., 2013), Polyethylene Terephthalate (PET) fibers (Casagrande et al., 2007; Louzada et al., 2019), natural fibers (Sotomayor & Casagrande, 2018) and polymers, aiming to improve the mechanical strength properties of the

[#]Corresponding author. E-mail address: boaventura.nathalia@gmail.com

¹Pontifícia Universidade Católica do Rio de Janeiro, Departamento de Engenharia, Rio de Janeiro, RJ, Brasil.

²Universidade de Porto, Porto, Portugal.

³Universidade de Brasília, Departamento de Engenharia Civil e Ambiental, Brasília, DF, Brasil.

Submitted on August 23, 2021; Final Acceptance on February 4, 2022; Discussion open until August 31, 2022.

<https://doi.org/10.28927/SR.2022.074521>



This is an Open Access article distributed under the terms of the Creative Commons Attribution License, which permits unrestricted use, distribution, and reproduction in any medium, provided the original work is properly cited.

soil, as a result, increasing the strength, durability of the soil, as well as reducing compressibility.

The application of polymers and enzymes as materials to improve soil characteristics is not a current technique. Studies by Lambe (1952) and Murray (1952) have already demonstrated the use of these polymeric materials to aggregate particles. However, in recent years, research and use of these products has intensified (Hollaway, 2009).

Khatami & O'Kelley (2013) worked with a biopolymer at different dosages in a sandy soil, they proved that increasing the addition of the polymer increased the mechanical parameters studied. Malko et al. (2016) studied the application of enzymes for soil stabilization in paving and the investigation proved that the use of this material, in the different types of soil horizons studied, led to a mechanical improvement of the soil. Okonta (2019) aiming to improve the strength parameters of a sandy soil in South Africa applied an acrylic polymer at different curing times and temperatures, the study proved that the addition of the polymer solution is effective in generating cementation between grains.

There are some studies conducted in subtropical and tropical climate regions to evaluate the application of polymers in soil improvement found in Qatar (Iyengar et al., 2013), Iran (Naeini et al., 2012) and Australia (Georgees et al., 2015).

Garcia et al. (2015) verified high increments in the cementation, tensile and shear strengths of a sandy soil added with polymer when compared to pure sand and another sand with artificial cementation.

Kolay et al. (2016) evaluated the use of acrylic-based polymer in a clay soil and a silty soil. They used polymer content ranging from 2-5% according to the dry weight of the soil with three curing times (7, 14, and 28 days).

They evaluated Atterberg limits, compaction, unconfined compression and ISC (California Support Index). The clay soil with polymer obtained the greatest gain in unconfined strength and improvement in ISC while no significant gains were observed for the silty soil. Few changes in the characterization tests were observed for both soil types.

Given this background, this study consists of evaluating the mechanical behavior and permeability of a pure sandy soil compared to an abundance of different mixtures of sandy soil and liquid polymer: modified butadiene-styrene sand polymer (XSBR). The use of this mixture as an alternative to reinforced soil mixes can be presented as a new solution for geotechnical works such as embankments, shallow foundation soils.

2. Materials and methods

2.1 Materials

In this experimental program, direct shear tests were performed based on the procedures described in ASTM D 3080 (ASTM, 2011). These tests were used to evaluate the effect of adding the XSBR polymer on the strength parameters of the sandy soil. The grain size distribution curve of the soil used in this study is shown in Figure 1. The sandy soil used in this research has a specific gravity (G_s) of 2.65, coefficient of uniformity (C_u) of 3.27, coefficient of curvature of 0.87, average diameter of 0.58 mm and minimum and maximum void ratios of 0.71 and 0.96, respectively. According to the ASTM D 2487 classification, this soil is a medium sand

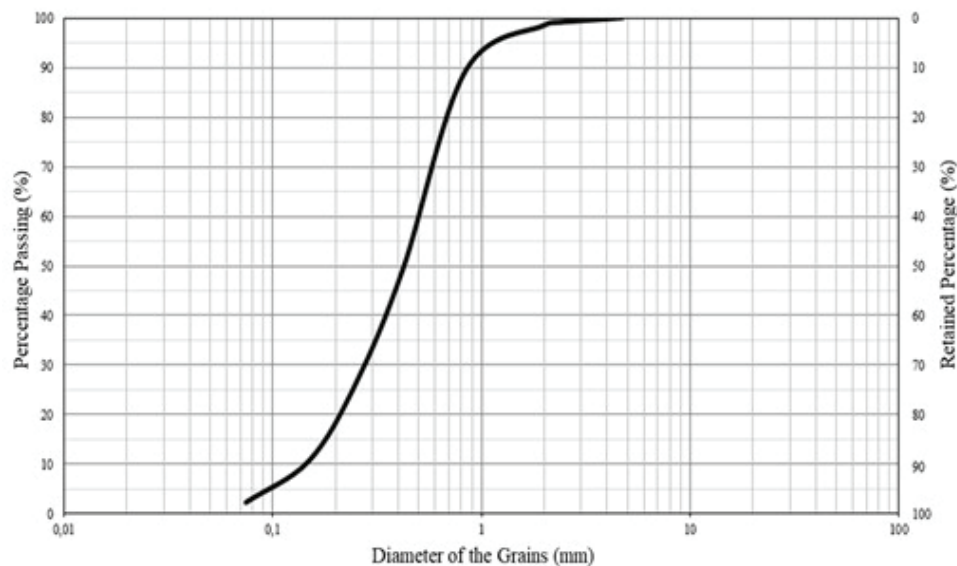


Figure 1. Grain-size distribution.

while the USCS (ASTM, 2000) classifies this material as SP, which corresponds to a poorly graded sand.

In the chemical analysis (Table 1), the soil shows a considerable amount of silica (SiO₂) and alumina (Al₂O₃), as well as small amounts of some oxides, such as potassium (K₂O), titanium (TiO₂) and iron (Fe₂O₃). The soil has a pH value of 4.4, proving that the composite matrix is acidic.

According to Ahmed et al. (2013), techniques based on chemical stabilization with the SBR polymer are widely used in the transportation industry, among the main applications are the control of dust generated from the passage of cars on unpaved roads, erosion control, control of fixation and leaching of waste and recycled materials

The XSBR polymer used in this study consists of two monomers, butadiene and styrene, and was obtained commercially as a liquid solution. The use of XSBR polymer, from the environmental point of view, is the replacement of more environmentally aggressive materials such as cement and lime. Both materials, in their procurement and production are highly polluting and, unquestionably, have aggression to the soil and groundwater. SBR is an example of a non-toxic liquid additive, water-soluble, derived from styrene and butadiene monomers. The physicochemical properties of the copolymer are presented in Table 2.

2.2 Specimen preparation

Specimens of sand and polymer-sand mixtures had 10% moisture content, 50% relative density, with different water-polymer mass ratios, with no curing time, or with curing times ranging from 24 to 792 h, as shown in Table 3.

The Water/Polymer Ratio determined in this study (1:1, 1:2 and 1:4) was from higher polymer dosages to lower ones. The value of 1:4 is the recommended value and usually used for this type of polymer. Also, for this reason, longer curing times were observed.

To ensure the relative density of 50%, the mass of mixture required to fill the known volume of the mold was calculated, and after that, manual compaction of the specimen inside the mold was performed. The specimens of the sandy soil and the soil-polymer mixture were molded in square metal molds with dimensions of 100 mm × 100 mm × 20 mm. Figure 2 presents a typical specimen. For each mixture, three specimens were tested for shear strength. All specimens were made using the same methodology, under the same conditions of temperature and relative water content (20 °C and 70%, respectively). To compare the results, the specimens were also made without the addition of the copolymer, i.e. pure sandy specimens. The use of 10% moisture and 50% density, was used for comparison between the sand without addition and in the other dosages, because they are common values in the proportions used.

The curing method used for the composites was air curing (external). After brief observations and tests, such as curing with application at high temperatures and curing

Table 1. Chemical composition of the sand soil.

Mixture	Percentage of compounds (%)					
	SiO ₂	Al ₂ O ₃	K ₂ O	TiO ₂	Fe ₂ O ₃	Others
Sandy matrix	66.02	30.01	3.20	0.50	0.21	0.06

Table 2. Physicochemical properties of XSBR copolymer.

Appearance	Liquid
Odor	Characteristic
pH	8.5-9.5
Melting Point	Not applicable
Boiling Point	100 °C
Evaporation Rate	Similar to water
Density	~ 1.0
Solubility in water	Miscible

Table 3. Mixture ratio and curing time.

Soil	Polymer	Water/Polymer Ratio	Curing Time (h)
Sand	Styrene-butadiene Polymer (XSBR)	1:1	72
		1:2	72
		1:4	72
			96
			120
			576
			720

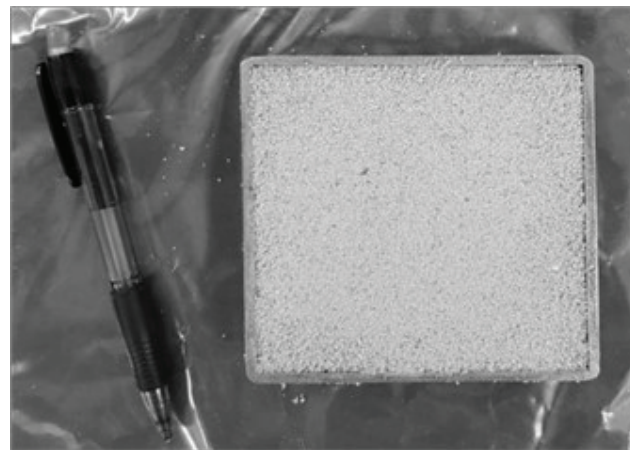


Figure 2. Soil specimen – square shape.

with water, it was found that the simplest form and with possible application in real works would be the air curing method. The polymer used, for being similar to glue in its composition, has the effect called “glue effect”, in which the catalyst for the activation of the glue is basically oxygen.

The influence of the addition of the XSBR copolymer on the shear strength parameters of the sand was evaluated using the direct shear test.

2.3 Direct shear test

Direct shear tests were performed with the sand soil and the sand-XSBR mixtures, attempting to determine the shear strength of these mixtures. The direct shear test was performed in a split metal box, where the upper half slides relative to the lower half. Prismatic square section soil specimens were used in this process. At first, the specimen was compressed by a normal force and then the application at a constant rate of a shear force. This shear force imposes a horizontal displacement on the specimen until failure of the specimen (in this test, the failure plane is horizontal). The tests were performed on similar specimens for each soil and mixture. The normal stress values applied were those of 50, 100, and 150 kPa.

2.4 Permeability test

The permeability test used in this research was the variable head permeability test. It was performed to analyze the permeability of the soil specimen with polymer. The permeability test was performed according to the Standard Test Method for Leaching Solid Material in a Column Apparatus (ASTM, 1995). It was decided to adapt the existing permeameter in the Geotechnical and Environmental Laboratory at PUC-Rio (Pontifical Catholic University of Rio de Janeiro), where it was possible to apply the same type of pressure and percolate water through the specimen. For each stress increment the pore pressure value in the specimen was measured. Increments were applied until specimen saturation was reached, when Skempton's parameter B approaches 1 ($B = \Delta u / \Delta \sigma_c$).

2.5 SEM analysis

The methods and procedures adopted for specimen preparation for SEM analysis were the same as those used for specimen preparation for direct shear testing, as were the environmental conditions, such as temperature and water content. The standard specimen used in the analysis is cylindrical, 20 mm high and 5 mm in diameter, as shown in Figure 3.

The analyses were performed on specimens with 1:4 water/polymer ratio and for two different curing times, 576 and 720 h.

3. Results and analysis

The results of the direct shear tests of both mixtures (pure sand and sand -XSBR) can be expressed in terms of shear strength behavior and horizontal displacement. As the mixtures were subjected to many curing times, it is important

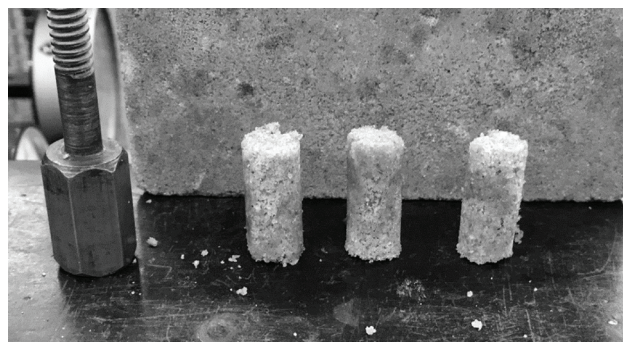


Figure 3. Standard specimens for SEM analysis.

to evaluate the influence of the water-polymer ratio on the specimens for each of these curing times.

Figure 4 shows the shear test results for the pure sand specimen and all the results at 72 h of curing, but with water-to-polymer ratio of 1:1, 1:2 and 1:4, respectively. Figure 5 shows the stress *versus* displacement plot and the Mohr-Coulomb failure envelope of the results presented in Figure 4.

Figure 6 shows the shear test results for the pure sand specimen and all results with 1:4 water/polymer ratio, but at 72, 96, 120, 576, 720 h of curing, respectively.

In Figure 7, show the stress x displacement plot and the Mohr-Coulomb failure results envelope from Figure 6. In Table 4 all the results of the strength values (angle of friction and cohesion) have been compiled.

The results of mixtures with high water-polymer ratio, such as 1:4, revealed a substantial increase in shear strength when compared to the pure sand specimen and lower water-polymer ratios (1:1 and 1:2).

Analyzing the data presented, it can be seen that increasing the curing time is critical to improving the strength. As for the dosages with (1:4), there are higher values in the cohesive interception when compared to (1:2 or 1:1). The variation of the friction angle is not significant, which shows that the action of the polymer takes place at the grain bonding.

Because it is a new use of this type of stabilization in soils (with polymer), often when applying the studies already consolidated for saturated soils the interpretation of the results becomes more complex. In the observed, throughout the research, one should consider ideal values of water-polymer ratio, in addition to the type of soil to be used, and the influence of curing and time. When these factors are evaluated, it is observed that there is not an exactly proportional growth between the values of the angle of friction and cohesion over time.

Sand-XSBR (1:4) had a change in the friction angle, however, the values are close to each other, with an average of 39°. Despite the stabilization applied the base substrate is a sand, and the angle of friction is a fundamental part of the strength in sands.

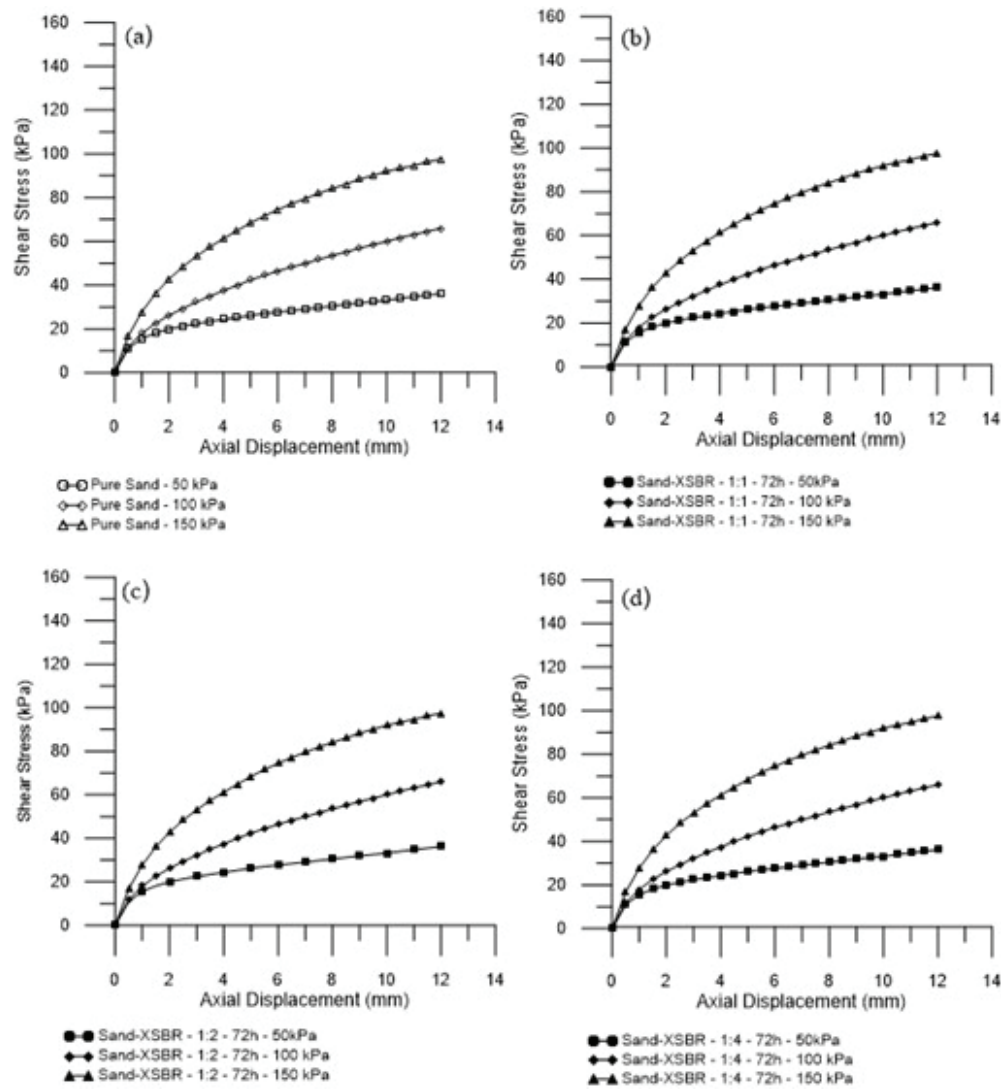


Figure 4. Shear stress versus horizontal displacement: (a) pure sand; (b) sand-XSBR – 1:1 – 72 h; (c) sand-XSBR – 1:2 – 72 h; (d) sand-XSBR – 1:4 – 72 h.

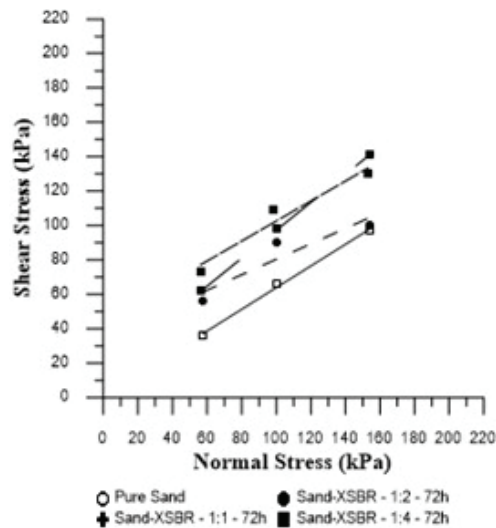


Figure 5. Mohr-Coulomb failure envelope with 72 h of curing.

Table 4. Final strength parameters.

Specimen	Mixtures		Strength parameters	
	Water/ Polymer Ratio	Curing time (h)	ϕ' (°)	c' (kPa)
Pure sand	-	-	33	0
Sand-XSBR	1:1	72	25	36
Sand-XSBR	1:2	72	39	16
Sand-XSBR	1:4	72	30	47
Sand-XSBR	1:4	96	40	44
Sand-XSBR	1:4	120	37	43
Sand-XSBR	1:4	576	41	51
Sand-XSBR	1:4	720	38	84

Evaluating only the cohesive intercept at 72 h, 96 h, and 120 h there is a variation, although considered insignificant, such changes are attributed to the polymer settling/curing

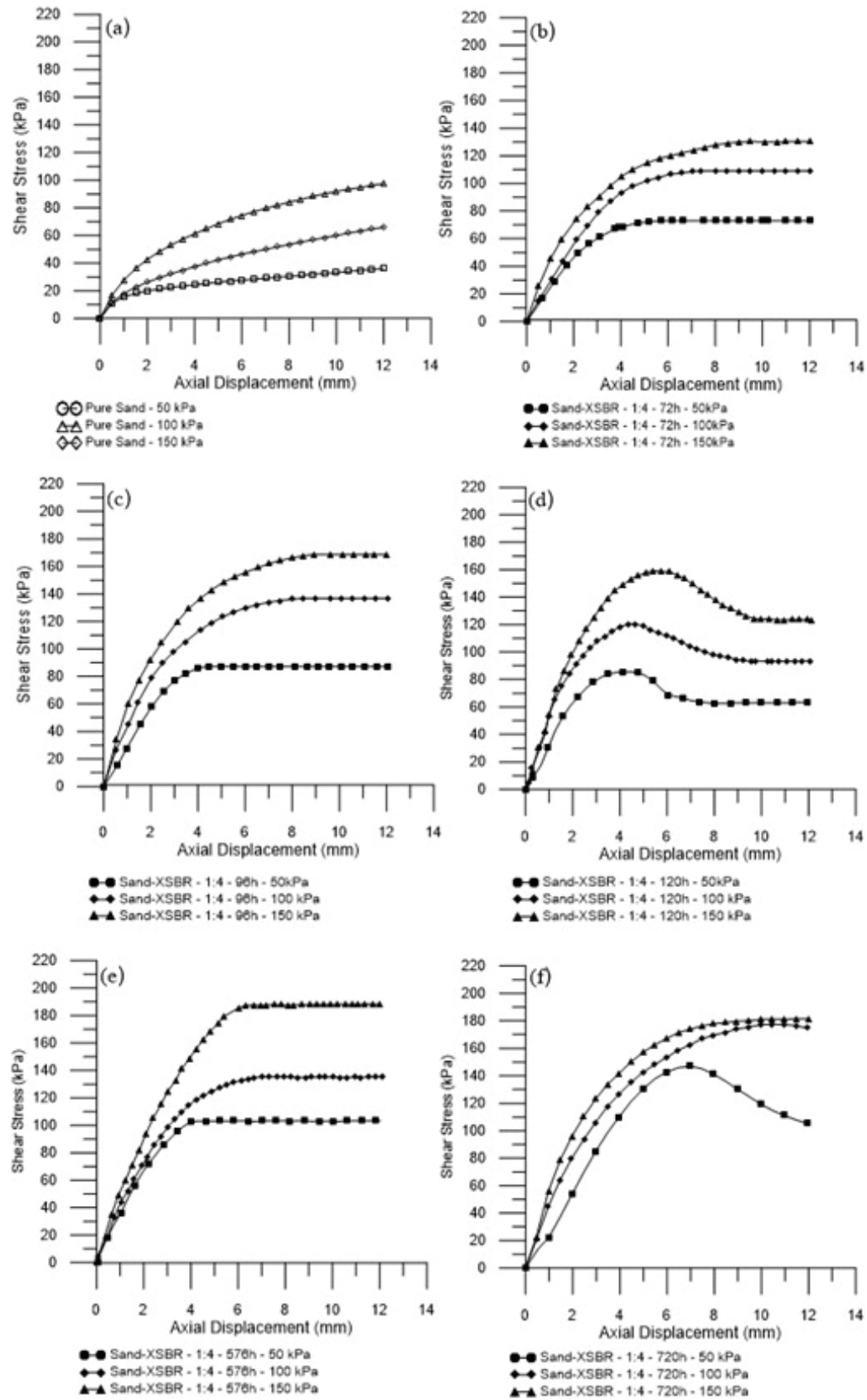


Figure 6. Shear stress *versus* horizontal displacement: (a) pure sand; (b) sand-XSBR – 1:4 – 72 h (c) sand-XSBR – 1:4 – 96 h; (d) sand-XSBR – 1:4 – 120 h; (e) sand-XSBR – 1:4 – 576 h; (f) sand-XSBR – 1:4 – 720 h.

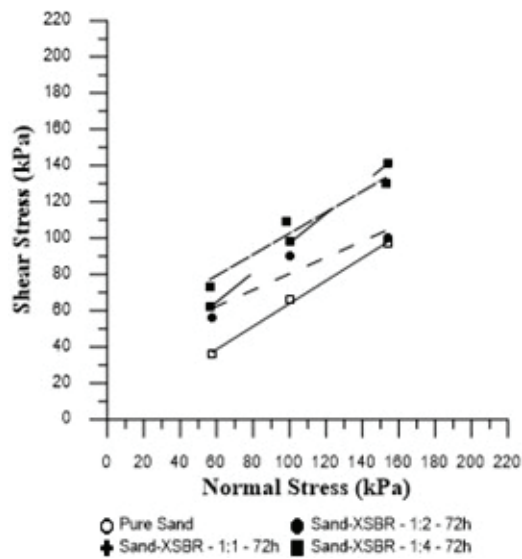


Figure 7. Mohr-Coulomb failure envelope – sand-XSBR – 1:4.

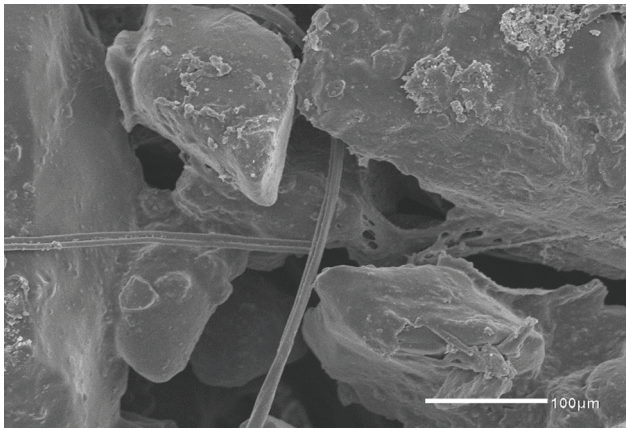


Figure 8. SEM analysis – Soil/water/polymer – 576 h (100 μm)

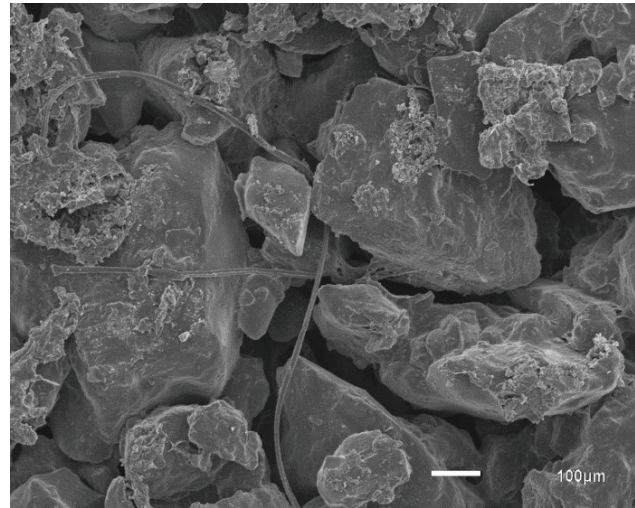


Figure 9. SEM analysis – Soil/water/polymer – 576 h (100 μm)

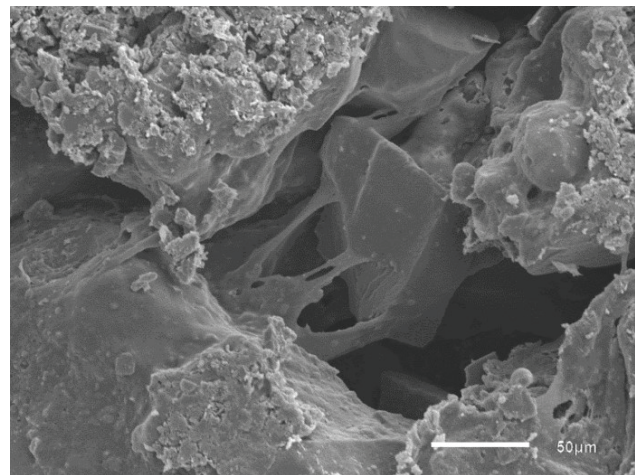


Figure 10. SEM analysis – Soil/water/polymer – 720 h (50 μm).

time, the specimens used, and the mathematical model itself. Observing the time of 576 h, there is a considerable and more stable increase. When completing the study, at 720 h you really see the considerable gain in the cohesive intercept and the stabilization of the friction angle value.

The permeability test was performed on all specimens at 576 h. The values found were extremely close, with minimal variations between specimens (not significant in the order of magnitude of the test). This value was used for having the proportion considered ideal and with the longest curing time, so the value of sand-XSBR was 1.16×10^{-3} .

Finally, the SEM analysis images (Figures 8 to 11) show an elastic structure that connects the soil grains. The polymer vice creates “bridges” to the soil matrix. In the Figures it is possible to observe that the sand grains become more tightly bound together. Between the grains it is possible to

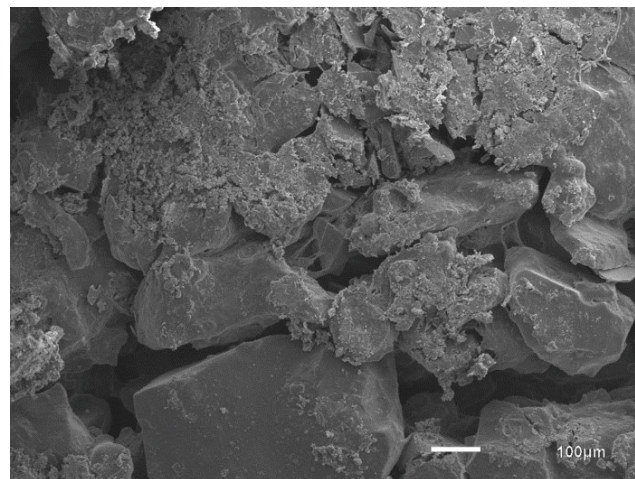


Figure 11. SEM analysis – Soil/water/polymer – 720 h (100 μm).

see something that binds these grains together, like a glue, which is possibly the polymer. With increasing curing time, this bonding is more intense.

4. Conclusions

This paper presented a study of the influence of the addition of Modified Butadiene-Styrene Copolymer on the mechanical behavior of a sand. Direct shear tests were performed on soil specimens of pure sand and sand/polymer mixtures with 10% moisture content, 50% relative density and different water-polymer mass ratios, without curing time or with curing times ranging from 24 to 792 h.

The results show an improvement in the strength parameters of the sand/polymer specimens. It is possible to verify especially an increase in the cohesion parameter, absent in the pure sand. This improvement is related to the water/polymer ratio and the curing time.

The mixtures with 1:4 (water/polymer) content showed significant increases in cohesion. The highest cohesion value of the mixture was found in a 1:4 (water/polymer) specimen.

It is concluded that the addition of polymer modifies the behavior of the stress *versus* displacement pattern of the material.

For any mixture studied, the values of the friction angle did not vary more than 8° from the initial value of the pure sand studied (33°). For short curing times, the mixtures showed no significant changes in behavior, while for long curing times, the mixtures showed the best behaviors.

The addition of modified butadiene-styrene copolymer in sands is an advantage for allowing the reduction of the amount of water needed to improve the mechanical characteristics of the soil. In addition, the modified butadiene-styrene copolymer when added to the soil, forming a composite in which there is the presence of cohesive interception that is not common in sandy soils. Thus, the sand with Modified Butadiene-Styrene Copolymer has the friction action coming from the sand (angle of friction) and by the action of the copolymer there is cohesion of the soil grains (cohesive interception).

Finally, the permeability of the pure sand showed no significant variations when compared to the permeability of the soil/polymer mixture. In both the pure and polymer blended condition, the soil exhibits permeability characteristic of fine sands.

Acknowledgements

The authors would like to thank CAPES - *Coordenação de Aperfeiçoamento de Pessoal de Ensino Superior* - Brazil and CNPq - *Conselho Nacional de Desenvolvimento Científico e Tecnológico* for the financial support to this research.

Declaration of interest

The authors have no conflicts of interest to declare. All co-authors have observed and affirmed the contents of the paper and there is no financial to report.

Authors' contributions

Thiago Manes Barreto: Conceptualization, Data curation, Visualization, Writing – original draft. Lucas Mendes Repsold: Conceptualization, Data curation, Methodology, Validation, Writing – original draft. Nathália Araújo Boaventura de Souza e Silva: Formal Analysis, Investigation, Methodology, Project administration, Writing – review & editing. Michéle Dal Toé Casagrande: Supervision, Validation, Writing – review & editing.

List of symbols

k	Permeability coefficient
c'	Effective cohesion
R^2	Coefficient of determination
φ'	Effective friction angle

References

- Ahmed, F.B., Atemimi, Y.K., & Ismail, M.A.M. (2013). Evaluation the effects of styrene butadiene rubber addition as a new soil stabilizer on geotechnical properties. *The Electronic Journal of Geotechnical Engineering*, 18, 735-748.
- Almeida, G.B.O., Casagrande, M.D.T., & Cavalcante, E.H. (2016). Avaliação da resistência à compressão simples de misturas de solo e escória de cobre aditivadas com cimento Portland aplicadas à pavimentação. In *Proceedings of the XVIII Congresso Brasileiro Mecânica dos Solos e Engenharia Geotécnica* (pp. 1-7). Sete Lagoas: ABMS.
- ASTM D2487. (2000). *Standard Practice for Classification of Soils for Engineering Purposes (Unified Soil Classification System)*. ASTM International, West Conshohocken, PA. <https://doi.org/10.1520/D2487-00>.
- ASTM D3080. (2011). *Standard Test Method for Direct Shear Test of Soil Under Consolidated Drained Conditions*. ASTM International, West Conshohocken, PA.
- ASTM D4874. (1995). *Standard Test Method for Leaching Solid Material in a Column Apparatus*. ASTM International, West Conshohocken, PA.
- Casagrande, M.D.T., Coop, M.R., & Consoli, N.C. (2007). Closure to “Behavior of a fiber-reinforced bentonite at large shear displacements”. *Journal of Geotechnical and Geoenvironmental Engineering*, 133(12), 1635-1636. [http://dx.doi.org/10.1061/\(ASCE\)1090-0241\(2007\)133:12\(1635\)](http://dx.doi.org/10.1061/(ASCE)1090-0241(2007)133:12(1635)).
- Garcia, N.F., Valdes, J.R., & Cortes, D.D. (2015). Strength characteristics of polymer bonded sands. *Geotechnique*

- Letters*, 5(3), 212-216. <http://dx.doi.org/10.1680/jgele.15.00089>.
- Georgees, R.N., Hassan, R.A., Evans, R.P., & Jegatheesan, P. (2015). Effect of the use of a polymeric stabilizing additive on unconfined compressive strength of soils. *Transportation Research Record: Journal of the Transportation Research Board*, 2473(1), 200-208. <http://dx.doi.org/10.3141/2473-23>.
- Hollaway, L. (2009). Polymer composites in construction: a brief history. *Engineering and Computational Mechanics*, 162(3), 107-118. <https://doi.org/10.1680/eacm.2009.162.3.107>.
- Iyengar, S.R., Massad, E., Rodriguez, A.K., Bazzi, H.S., Little, D., & Hanley, H.J.M. (2013). Pavement subgrade stabilization using polymers: characterization and performance. *Journal of Materials in Civil Engineering*, 25(4), 472-483. [http://dx.doi.org/10.1061/\(ASCE\)MT.1943-5533.0000612](http://dx.doi.org/10.1061/(ASCE)MT.1943-5533.0000612).
- Khatami, H.R., & O'Kelley, B.C. (2013). Improving mechanical properties of sand using biopolymers. *Journal of Geotechnical and Geoenvironmental Engineering*, 139(8), 1402-1406. [http://dx.doi.org/10.1061/\(ASCE\)GT.1943-5606.0000861](http://dx.doi.org/10.1061/(ASCE)GT.1943-5606.0000861).
- Kolay, P.K., Dhakal, B., Kumar, S., & Vijay, K.P. (2016). Effect of liquid acrylic polymer on geotechnical properties of fine-grained soils. *International Journal of Geosynthetics and Ground Engineering*, 2(4), 1-9. <http://dx.doi.org/10.1007/s40891-016-0071-5>.
- Lambe, T.W. (1952). Summary of the conference on soil stabilization. In *Proceedings of the Conference on Soil Stabilization*. Massachusetts: MIT.
- Louzada, N.S.L., Malko, J.A.C., & Casagrande, M.D.T. (2019). Behavior of clayey soil reinforced with polyethylene terephthalate. *Journal of Materials in Civil Engineering*, 31(10), 04019218. [http://dx.doi.org/10.1061/\(ASCE\)MT.1943-5533.0002863](http://dx.doi.org/10.1061/(ASCE)MT.1943-5533.0002863).
- Malko, J.A.C., Brazetti, R., Casagrande, M.D.T., & Silva, B.A. (2016). Applicability of soil-enzyme for paving. *Japanese Geotechnical Society Special Publication*, 2(61), 2082-2085. <https://doi.org/10.3208/jgssp.OTH-10>.
- Murray, G.E. (1952). Soil stabilization by chemical means. In *Proceedings of the Conference on Soil Stabilization* (pp. 107-117). Massachusetts: MIT.
- Naeini, S.A., Naderinia, B., & Izadi, E. (2012). Unconfined compressive strength of clayey soils stabilized with waterborne polymer. *KSCE Journal of Civil Engineering*, 16(6), 943-949. <http://dx.doi.org/10.1007/s12205-012-1388-9>.
- Okonta, F. (2019). Pavement geotechnical properties of polymer modified weathered semi-arid shale subgrade. *International Journal of Pavement Research and Technology*, 12(1), 54-63. <http://dx.doi.org/10.1007/s42947-019-0007-2>.
- Sotomayor, J.M., & Casagrande, M.D.T. (2018). The performance of a sand reinforced with coconut fibers through plate load tests on a true scale physical model. *Soil and Rocks*, 41(3), 361-368. <http://dx.doi.org/10.28927/SR.413361>.
- Vargas, M. (1977). *Introdução à mecânica dos solos*. McGraw Hill (in Portuguese).
- Vendruscolo, M.A. (1996). *Análise numérica e experimental do comportamento de fundações superficiais assentes em solo melhorado* [Master's Dissertation, Federal University of Rio Grande do Sul]. Federal University of Rio Grande do Sul's repository. <http://hdl.handle.net/10183/1453>.
- Vizcarra, G.O.C., Casagrande, M.D.T., & Motta, L.M.G. (2013). Applicability of municipal solid waste incineration ash on base layers of pavements. *Journal of Materials in Civil Engineering*, 26(6), 06014005. [http://dx.doi.org/10.1061/\(ASCE\)MT.1943-5533.0000903](http://dx.doi.org/10.1061/(ASCE)MT.1943-5533.0000903).

CASE STUDY

Soils and Rocks
v. 45, n. 2

Effect of engineering geological properties on dam type selection of the Qadis Khordak Dam, Afghanistan

Sayed Mohammad Alipoori¹ , Gholam Reza Lashkaripour^{1#} ,

Mohammad Ghafoori¹ , Naser Hafezi Moghadas¹ 

Case Study

Keywords

Engineering geology
Dam type selection
Lugeon
RQD
Permeability
Joint study

Abstract

This paper deals with engineering geological properties of Qadis Khordak dam site in Northwest Afghanistan. This study is based on on-site and laboratory tests, surface discontinuity surveying, drilled borehole and permeability test of dam foundation. The engineering geological properties at the dam site were studied in order to evaluate geotechnical characteristics of rock masses at dam foundation, geotechnical properties of alluvium at dam axis, reservoir and borrow materials. The structural geological studies also carried out due to stability and safety of dam on their abutments reservoir and seismicity. Existence of a fault, high permeable zone at dam foundation and the thickness of alluvium at dam axis, are the most engineering geological issues that cause change on dam type selection. In the feasibility phase, the dam type was chosen as the concrete face rock-fill dam, because of state of engineering geological properties of dam site. However, in the design phase dam type has been changed as a rock-fill with a clay core.

1. Introduction

Dams have been part of human efforts as a mechanism to harness the environment for over 6000 years. Since then, dam-engineering and technology have advanced to allow the safe operation of Gargantuan earth and rock structures such as the Tarbela dam in Pakistan (approximately 13.69 km³) and enormous concrete and steel structures, such as the Three Gorges dam in China – approximately 39.3 km³ (Stewart, 2016). Afghanistan is a country which is located on an arid to semi-arid climate with a wide distribution of precipitation as low as 75 mm per year in Farah province to 1100 mm per year in Parwan province (Favre & Kamal, 2004). In order for Afghanistan to overcome both the quick growth in population and the spatially and temporally irregular precipitation and irrigation losses, infrastructure development is fundamental (Brown & Lall, 2006; Bosshard, 2012; Tortajada & Biswas, 2014).

Qadis Khordak reservoir dam site is located at the Southeast Qadis district, Badqis province in the north western part of the country (Figure 1). Qadis Khordak dam is a 32 m in height and the capacity of reservoir is approximately 5,000,000 m³. Geographical coordinates of dam site are 63° 34' 49.4 E, 34° 42' 39.8N. The selection of the type of dam requires collaboration among experts representing several disciplines-including planners, hydrologists, geo

engineer, geotechnical, hydraulic, and structural engineers to ensure economical and appropriate designs for the physical elements, such as topography, geology and foundation conditions, borrow materials, hydrology, and seismicity. Engineering geology studies are an important parts of dam site investigation. In recent years, the analysis of the dam location characteristics was the main consideration for many investigators (Lashkaripour & Ghafoori, 2002; Romanov et al., 2003; Ghobadi et al., 2005; Kocbay & Kilic, 2006; Unal et al., 2007; Ghafoori et al., 2011; Uromeihy & Farrokhi, 2012). The importance of geological factors on the suitability of a dam site has been thoroughly discussed (Oliveira, 1979; Anderson & McNicol, 1989) and in some cases generally accepted criteria for chosen the type of dam have been challenged (Bell, 1993).

The safety of a dam can be estimated when the features of its foundation are measured accurately, and the design of the dam is proportional to the features of the foundation. This is why identifying engineering geological features controlling the stability of the foundation is necessary for safe and economical design. Many dams have failed during or after construction because of the weak foundation of the rock mass. This is the reason of the proficiency of designers and construction personnel without knowledge of geology studies and geological engineering could not guarantee the safety of the dam. The choice of the dam location in any

[#]Corresponding author. E-mail address: lashkaripour@um.ac.ir

¹Ferdowsi University of Mashhad, Faculty of Science, Department of Geology, Mashhad, Iran

Submitted on May 6, 2021; Final Acceptance on March 23, 2022; Discussion open until August 31, 2022.

<https://doi.org/10.28927/SR.2022.070621>



This is an Open Access article distributed under the terms of the Creative Commons Attribution License, which permits unrestricted use, distribution, and reproduction in any medium, provided the original work is properly cited.

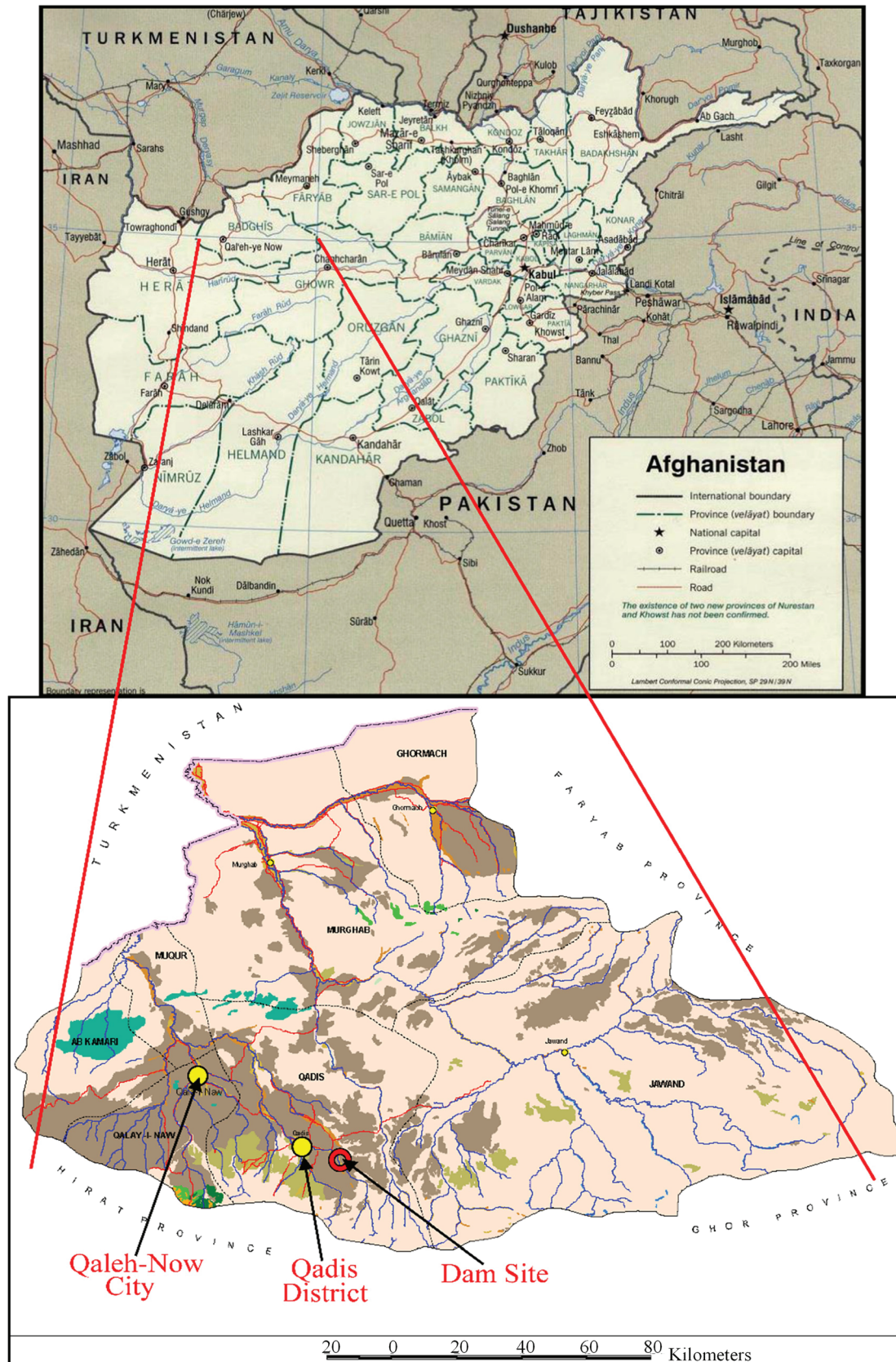


Figure 1. Geographical location of Qadis Khordak dam site.

area mainly depends on the situation of the dam area and the dam reservoir (El-Naqa, 1994). Suitable information on the geological condition, geotechnical parameters and hydrogeological conditions of dam area is vital to design and guarantee the safety of dam body. The importance of geotechnical studies becomes even more important as the dimensions of such structures are increased in height, depth and volume of reservoir (Haftani et al., 2014).

Apparently, there are not always proper conditions of the ground and rocks of the dam in a given site, so it is the engineer's responsibility to state the weakness of the ground, reservoir, and accessory structures of the dam. The most important responsibility is to study the geology, the geological engineering, and geotechnical condition of the area where the dam is to be constructed (Heidari, 2000).

2. Geological conditions of dam site

2.1 Regional geology

Afghanistan is composed of a complex collage of mostly Gondwanan derived terranes which were accreted onto the southern margin of Eurasia prior to, and during, the India-Eurasia collision (Celâl Sengör, 1984; Boulin, 1991). The study areas are comprised of intrusive igneous rock such as andesite, basaltic andesite, rhyolite, trachyte and conglomerate that are likely from the Eocene-Oligocene. The average study area height summit between 1600 and 1850 m above the sea level. Creeks of the all drain inlets to the Qadis Khordak river. The study area is a rugged mass with dendritic drainage pattern. The vegetation cover seen only in the river bed.

2.2 Specific geological conditions of dam site

At the proposed Qadis Khordak dam site, the river flows through a meandering course making a convex shape towards the left bank. rock units upper Eocene-Oligocene in terms of lithological and petrographic are highly variable, so that the lava Andesite, Basaltic Andesite, Trachyte with a combination of Ignimbrite and Tuffs and pyroclastic included with age of the primitive Eocene-Oligocene is formed. These rocks have been altered in different parts of the reservoir at different levels. Andesitic rocks, Basalt and Trachyte due to high resistance compared with pyroclastic rocks make up the crest prominent areas.

In the northern part of the study area, in abutments, bed and reservoir, light green-gray colored rocks of volcanic Breccia (pyroclastic rocks of Lithic Tuffs, Tuff, and Crystalline Tuff) with age of Oligocene has been seen. The field of these rocks are included mostly of tuff and crystalline tuff which can be seen mostly in the dam axis and reservoir. The results of drilling of the boreholes are indicative of high thickness of these rocks more than 60 m in abutments and reservoir.

The youngest sediments of the dam axis, including the recent sediments. Bed rock of reservoir in deeper depth and

near the bed river are covered with alluvial deposit mostly coarse grains and flood sediment pertain to current bed or old terraces. Terrace normally can be seen in the borders of the river bed with different thickness. In the present, nearly all of the alluvial terraces have been used as agriculture fields. Figure 2 shows the geological map of dam site.

2.2.1 Left abutment

The left abutment hill makes a steep hill slope, at about 55°-75° from the river bed level and consists of light brown Andesite. The height of the abutment is more than 30 m from the river bed and gets increased. The left abutment covered by a thin layer of residual soil. There are joints and normal separation at this abutment (Figure 3).

2.2.2 Right abutment

Right abutments consist of dark grey Basaltic Andesite. The natural slope of the right abutment is approximately 40°-50° and has about 26 m height. The joints in the right abutment strike approximately N-S and dips at 30°-80° towards upstream and downstream. The right abutment also intersected by another set of horizontal joints (Figure 3).

2.2.3 River bed

The river bed is about 46 m wide with the bed level at 1610 m above sea level and occupied by the present day riverine deposit in the form of clay, silt, sand, cobble, gravel and boulder located both upstream and downstream of the dam axis. The alluvial sediment almost has 20-25 m thickness in the dam axis.

2.2.4 Reservoir

The reservoir of Qadis Khordak dam will extend upstream to the full reservoir level of 1640 m above sea level and will come under its submergence. The reservoir spread is bounded by high mountains trending EES- WNW on either side of Qadis Khordak river. Geologically, these high mountains comprise the intrusive igneous rock formations belonging to Eocene-Oligocene age represented by varieties of porphyry andesite, basaltic andesite, trachyte andesite and volcanic tuff. The reservoir rim formed of hard and compact intrusive igneous rocks is expected to be tight. The chance of reservoir leakage through the right bank is more than the left bank and need to be considered during design and construction phases.

2.2.5 Structural geology

Tectonics studies of the dam axis including the description of the main faults and joints to serve as the main structures and tectonic rock mass, are affected site. Structurally, the

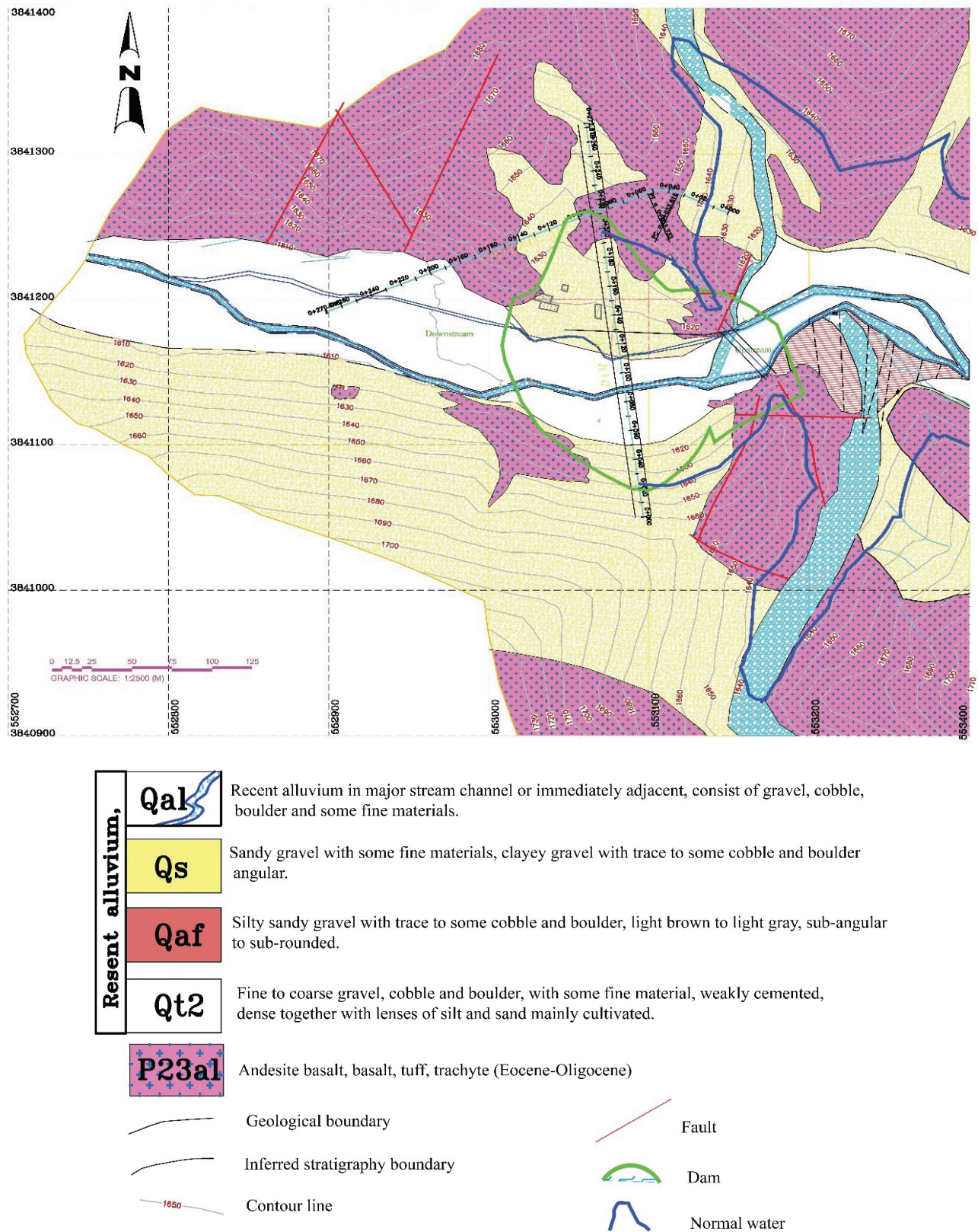
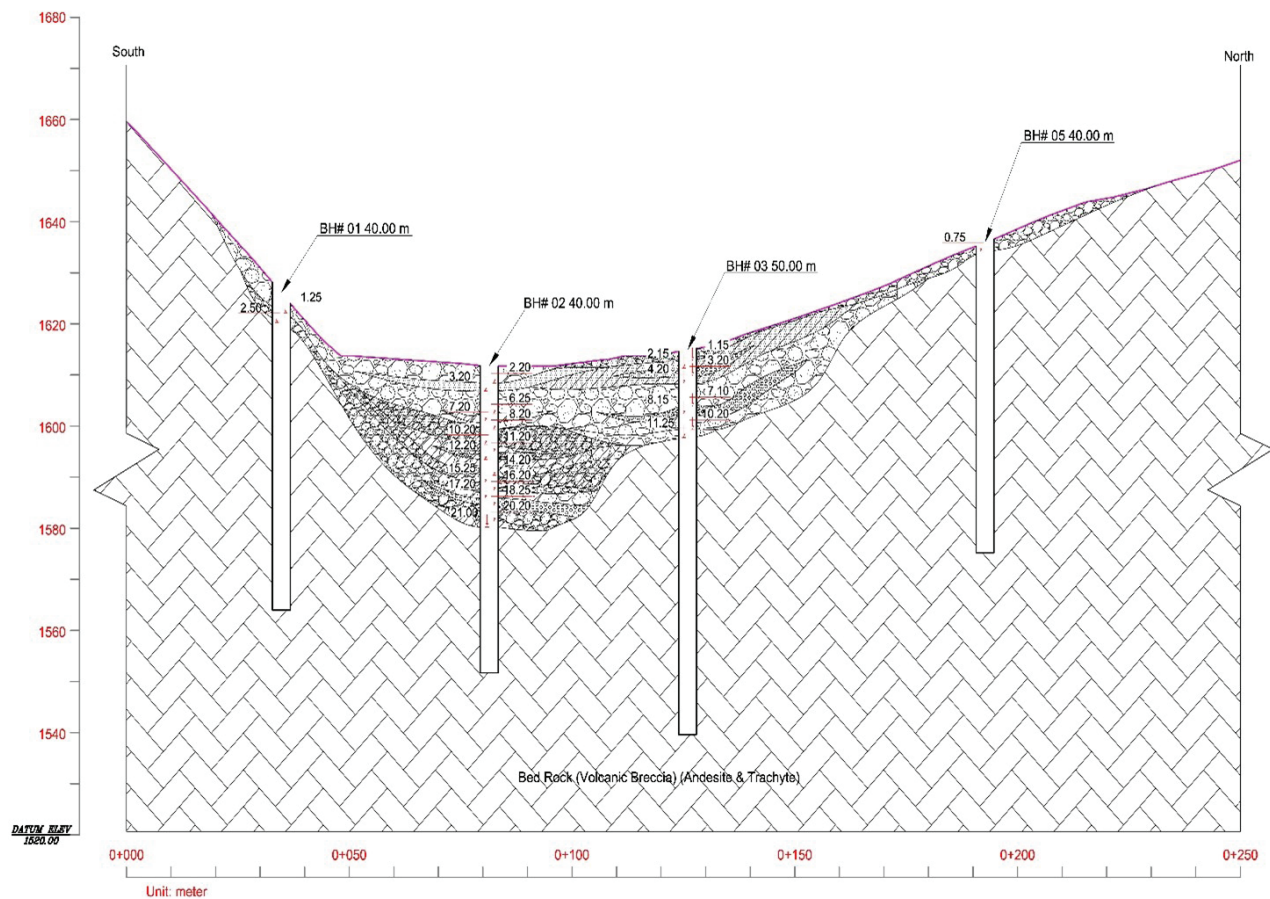


Figure 2. Geological map of the dam site.



Legend	
Material description (USCS Classification)	
Gravelly Silt with Sand	
Silt with Sand	
Gravelly Silt	
Silty Gravel with Sand	
Silty Gravel	
Clay Gravel with Sand	
Silty Sand with Gravel	
Poorly Graded Gravel	
Silty, Clayey Gravel with Sand	
Sandy Silty Clay	
Poorly Graded Gravel with Silt	
Well Graded Gravel with Silt and Sand	
Silty, Clayey sand with Gravel	

Figure 3. Geological cross section of dam axis.

intrusive rock has been gently fractured. The pillow lava unconformity is the main unconformity in the site project. The main and nearest fault in the dam area is the thrust fault. There is not any evidence of new structural activity such as

quaternary fault and fold. The main trend of joints is WN-SE, EN-SW and E-W. Joints have not spread in the intrusive igneous rock because of inherent properties of intrusive igneous rock, but in the sedimentary rock these two joint

sets clearly appear at the downstream of the study area. The local drainages, valleys and river appear to be controlled by these joints and fractures.

3. Engineering geological properties of the dam site

In the feasibility study, detailed design and construction phases of the dam, the regional and local engineering geology are very important (Lashkaripour & Ghafoori, 2002). Engineering geological and rock mechanics studies mainly include discontinuity surveying according to ISRM (Brown, 1981), core drilling according to ASTM D2113 (ASTM, 2008a), *in-situ* and laboratory tests according to ASTM Standards (ASTM, 1999, 2001, 2003).

During drilling, discontinuities (such as dip/dip direction, roughness, infilling, and spacing) in the rocks were investigated according to ISRM (Brown, 1981). The discontinuities systems properties rock is highly affected by the mechanical behavior of rock. Discontinuities can cause changes in value in some rock masses properties, increasing on amount of permeability and plasticity and decreasing on the value of strength (Bell, 2007; Goodman, 1989).

3.1. Joint study

To know the status of discontinuities permeated in the mechanical items of rock masses requires the information collected from the field. After this phase, data analysis was carried out using software Dips. In Figures 4 to 6, the polar graphs, rosette charts and discontinuities in dam system are provided, respectively.

Based on data from the study of the right and left abutment, discontinuity systems include the direction and amount of joint dip, presented in Table 1.

Based on the field studies it was observed that the reservoir area and the proposed axis is affected by the three major joints with two main fault systems. As it is indicated in Table 1, joint systems are mostly low and relatively high steep slopes (more than 30°). With regard to the general trend of the main faults in the region, it can be concluded that the joint system is created by the dominant tectonic forces.

Summing up the results of field investigations and geotechnical borehole data shows that joints dips are close to vertical but what is at ground level can be seen, the dominant slope of joint looks sharp. Generally, in the study area, we have low to moderate joint surface with weathering, a moderate joint surface without weathering, and flat and rough joint surface. The samples obtained from exploratory drilling indicates that the lower depths to the surface of the joint is almost no weathering. The space between the joints more by iron oxide, clay and rock material have been filled. Other parameters are spacing and persistence discontinuities. Based on field data, the continuity in the joints are mostly

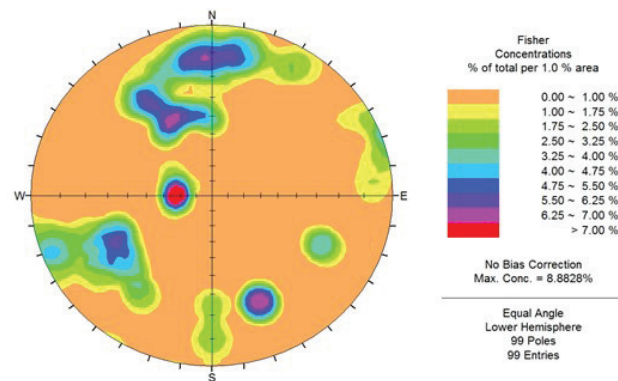


Figure 4. Polar discontinuities in Qadis Khordak dam site.

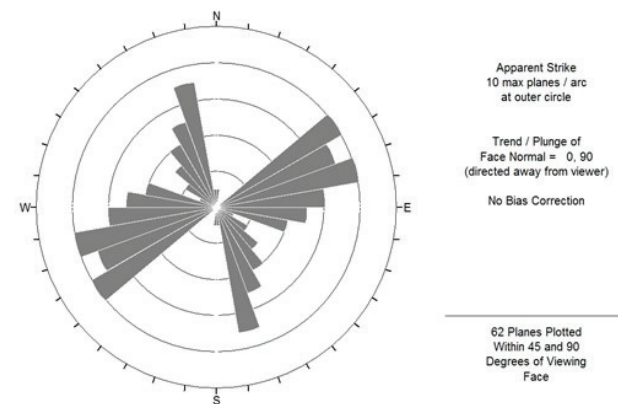


Figure 5. Rosette chart for discontinuities in the Qadis Khordak dam site.

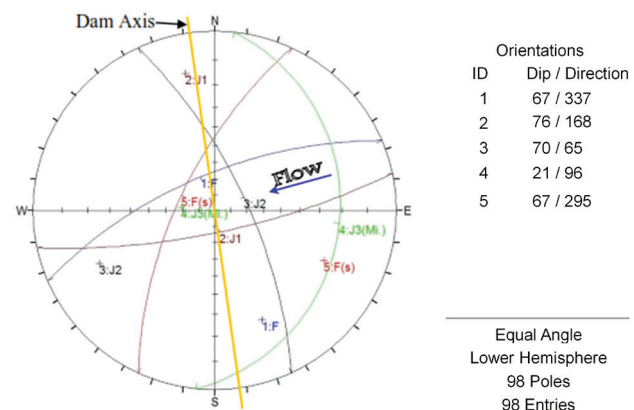


Figure 6. The main planes of discontinuities in the Qadis Khordak dam site.

Table 1. Discontinuity types in Qadis Khordak dam site.

Discontinuity type	Dip	Dip direction
Fault	67°	337°
Fault	67°	295°
Joint	76°	168°
Joint	70°	65°
Joint	21°	96°

in the range of 3-10 m and space are in the range of 0.6-2 m. Discontinuities mainly undulating surfaces and comes with a slickenside effects of the dominant features of the discontinuities. The opening of a joint dominant between 1 to 5 mm (towards closed joints), and the level of opening at the surface locally are more than 10 mm.

3.2. Strength of rock units

One of the most important aspects that should be considered during the design and construction of a dam is rock mass quality. The first stage of design of a dam is estimation of ground strength, permeability, and other factors with the required level of accuracy; these should be determined through a diversity of tests (Lashkaripour & Ghafoori, 2002). According to ISRM (Bieniawski & Bernede, 1979), several uniaxial compressive strength tests have been conducted on over 130 m of rock core samples to determine the strength of rock units that underlie the foundation of the dam. The results of compression tests on different rock units in dry and saturation conditions are shown in Table 2.

The compressive strength of the bedrock based on uniaxial compressive strength test performed on the core samples obtained within 20.3-154.6 MPa which classifies the strength of the bedrock as moderately hard rock to very hard rock medium strong to strong (Bieniawski & Bernede, 1979).

Table 2. Summary of laboratory testing results.

Parameters	Rock unit		
	Min	Max	Average
Uniaxial compressive strength (MPa)	20.3	154.6	59.5
Modulus of elasticity (GPa)	2.15	19.44	7.12
Internal friction angle, ϕ (°)	54	66.5	60.8
Cohesion (MPa)	0.13	3.54	1.1

3.3. Rock quality designation (RQD)

In geotechnical terms, degree of fracturing in drill cores is one of the simplest and easiest methods to describe the quality of the rock mass. Based on the results of geotechnical data, the average rock quality designation (RQD) is in the midrange, and varies from 54 to 94 according to the Deere classification (Deere & Deere, 1989). The rock mass quality (RQD) in many boreholes in both abutments are good and excellent (Deere & Deere, 1989). The jointing between the rock mass is in the range of low to medium and permeability of the rock mass is due to high hydraulic opening joints.

3.4. Permeability

During the core drilling, in-situ permeability tests were performed in the Qadis Khordak dam foundation directly in the vertical boreholes. The main reasons for carrying out of this test was to measure the permeability of each section of rock masses of the dam foundation and its banks (Vaskou et al., 2019). As shown in Table 3, permeability in boreholes is measured in the lugeon scale. Table 3 shows the results of lugeon and RQD values for dam site. The results reveal that permeability is in the range of impervious to very high permeability. High permeability is one of the main geological engineering problems of Qadis Khordak dam. The results of the permeability tests from boreholes which are located along the dam axis indicate very high permeability ($LU > 100$) to 20 m depth, with increasing depth from 20 to 40 m permeability of the rock mass decreases ($30 < LU < 60$). The results of lugeon tests in many sections including the left and right abutments show the permeability is in the range of medium, high to very high.

Table 3. Results of the rock quality designation and lugeon test for the boreholes in the dam site.

Boreholes	Location	Geotechnical parameters					
		Lugeon value, LU			RQD (%)		
		Average	Min	Max	Average	Min	Max
BH N5	Right abutment	94	28	>100	65	23	91
BH N2	River bed	30	5	69	91	70	100
BH N3	River bed	43	5	>100	90	65	100
BH N4	River bed	40	40	40	94	88	100
BH 1	Dam reservoir	41	9	>100	77	50	100
BH 2	Dam reservoir	19	2	65	80	39	100
BH 3	Dam reservoir	54	30	79	54	0	88
BH 4	Dam reservoir	34	1	93	78	0	100
BH 5	Dam reservoir	6	2	11	80	21	95
BH 6	Dam reservoir	>100	>100	>100	82	28	100
BH 7	Dam reservoir	98	76	>100	58	28	89
BH 8	Dam reservoir	1	1	1	89	69	100
BH 9	Dam reservoir	96	76	>100	77	44	100
BH N1	left abutment	27	6	96	92	80	100

4. Slope stability

In terms of morphology as well as the reservoir were, especially the left side of the reservoir walls, are generally steep slopes. According to various studies under the present conditions, the reservoir wall is stable and no major potential for instability domains overlooking the reservoir. However, at the present there are signs of local instability in left seaside heights can be seen which are outside of the reservoir. In this region, the instability in the surface material and small volume are product of alternation and weathering of bed rock. Slide in this area are mostly circular slides.

As mentioned before the slide regions are outside of the reservoir level. Therefore, it can be expected that with filling the reservoir nothing happens.

In parts of reservoir walls, especially the left seaside, which alluvial sediments located in the steep slope of the hillside, the probability of surface slide in the perimeter of the lake, can be expected. Certainly, with filling the lake and washing the loose alluvial sediments, it can be expected that there will be stable condition. Therefore, in the future, the wall of reservoir will be stable and there is no potential for major instability except local slides in surface weather zones and rock fall of the small and separate rock blocks.

5. Discussions

During the feasibility study and detailed design phases, selection of the site and the type of dam should be carefully considered. Generally, initial designs and estimates for several types of dams and appurtenant structures are required before one can be proved the most suitable and economical. It is, therefore, important to understand that the project is likely to be unduly expensive unless decisions regarding the site selection and the type of dam are based upon adequate study.

The availability of suitable rock and fine borrow materials for embankment dam is a factor favorable to the selection of an embankment dam. Every local resource that reduces the cost of the project without sacrificing the efficiency and quality of the final structure should be used. In Qadis Khordak site there are fine and coarse borrow materials in large quantity and accessible for construction of rock-fill dam with a clay core.

In this site some local faults were observed, therefore in active seismic location which rock-fill dam shows better resistance based on the flexibility to the movement and seismicity. In addition, there are three joints sets and local faults in left and right abutment of dam axis, which have made faulted and jointed blocks in the dam axis. The faulting and different joint systems also significantly affect the permeability of rock units in the dam foundation.

The thickness of alluvial sediments of river bed in dam site and reservoir is about 20-25 m. In similar situation, the rock-fill dam was recommended, because constructing

concrete dam or other gravity structures may cause settlement in foundation of dam.

6. Conclusions

In the feasibility stage, the dam type was chosen as the concrete face rock-fill dam, depending on state engineering geological properties of dam site. In design stage, dam type has been changed as a rock-fill dam with a clay core. The thickness of alluvial sediments of river bed in dam site, three joints sets and local faults in left and right abutment of dam axis and necessary of using cutoff wall in alluvial foundation, availability of large quantity of borrow materials for rock-fill dam are the main engineering geological properties concern for changing dam type from concrete face rock-fill to a rock-fill dam with a clay core.

With regard to geological conditions in order to prevent water seepage under the dam foundation and seeking and maintaining dam safety, cutoff wall in alluvial foundation and grout curtain consisted of three parts, including the right abutment, the bed and left abutment is essential too.

Due to the characteristics of the foundation rock, excavation operations will be combined by blasting. Therefore, many fractures in rock surfaces will be created. For this reason, and in order to prevent water leakage and flushing of clay core, modifying treatment of trench is necessary. Consolidation grouting consists of filling opened joints, open layered surfaces, faults zones and cavities in the rock mass.

Acknowledgements

The authors wish to express their appreciation to the many engineers, geologists and technical staff of Omran Holding Group who contributed to the work reported in the paper.

Declaration of interest

The authors declare that they have no known competing financial interests or personal relationships that could have appeared to influence the work reported in this paper.

Authors' contributions

Sayed Mohammad Alipoori: Data curation, Writing-Original draft preparation. Gholam Reza Lashkaripour: Conceptualization, Methodology, Validation. Mohammad Ghafoori: Reviewing and Editing. Naser Hafezi Moghadas: Reviewing and Editing.

List of symbols

<i>ASTM</i>	American Society for Testing and Materials
<i>BH</i>	Borehole
<i>E</i>	East
<i>ISRM</i>	International Society for Rock Mechanics
<i>LU</i>	Lugeon

<i>Max</i>	Maximum
<i>Min</i>	Minimum
<i>N</i>	North
<i>RQD</i>	Rock Quality Designation
<i>S</i>	South
<i>W</i>	West
ϕ	Internal friction angle

References

- Anderson, J.G.C., & McNicol, R. (1989). The engineering geology of the Kielder Dam. *Quarterly Journal of Engineering Geology and Hydrogeology*, 22(2), 111-130. <http://dx.doi.org/10.1144/GSL.QJEG.1989.022.02.03>.
- ASTM C88-99. (1999). *Test method for soundness of aggregates by use of sodium sulfate or magnesium sulfate*. ASTM International, West Conshohocken, PA. <https://doi.org/10.1520/C0088-99A>.
- ASTM C127-01. (2001). *Test method for specific gravity and absorption of coarse aggregate*. ASTM International, West Conshohocken, PA. <https://doi.org/10.1520/C0127-01>.
- ASTM C131-03. (2003). *Test method for resistance to degradation of small-size coarse aggregate by abrasion and impact in the Los Angeles machine*. ASTM International, West Conshohocken, PA. <https://doi.org/10.1520/C0131-03>.
- ASTM D2113-08. (2008a). *Practice for rock core drilling and sampling of rock for site investigation*. ASTM International, West Conshohocken, PA. <https://doi.org/10.1520/D2213-08>.
- Bell, F.G. (1993). *Engineering geology*. Blackwell Scientific Publications.
- Bell, F.G. (2007). *Engineering geology* (2nd ed.). Butterworth-Heinemann.
- Bieniawski, Z.T., & Bernede, M.J. (1979). *ISRM Suggested methods for determining the uniaxial compressive strength and deformability of rock materials*. Pergamon Press.
- Bosshard, P. (2012). *Infrastructure for Whom? A Critique of the Infrastructure Strategies of the Group of 20 and the World Bank*. International Rivers.
- Boulin, J. (1991). Structures in Southwest Asia and evolution of the eastern Tethys. *Tectonophysics*, 196(3-4), 211-268. [http://dx.doi.org/10.1016/0040-1951\(91\)90325-M](http://dx.doi.org/10.1016/0040-1951(91)90325-M).
- Brown, C., & Lall, U. (2006). Water and economic development: the role of variability and a framework for resilience. *Natural Resources Forum*, 30(4), 306-317. <http://dx.doi.org/10.1111/j.1477-8947.2006.00118.x>.
- Brown, E.T. (1981). *ISRM suggested methods for Rock characterization testing and monitoring*. Pergamon Press.
- Celâl Sengör, A.M. (1984). The Cimmeride orogenic system and the tectonics of Eurasia. In A.M. Celâl Sengör, *The Cimmeride Orogenic System and the Tectonics of Eurasia* (vol. 195). Geological Society of America. <https://doi.org/10.1130/SPE195-p1>.
- Deere, D.U., & Deere, D.W. (1989). *Rock quality designation (RQD) after twenty years* (Final report, No. GI-89-1). U.S. Army Engineer Waterways Experiment Station.
- El-Naqa, A. (1994). Rock mass characterization of Wadi Mujib dam site, Central Jordan. *Engineering Geology*, 38(1-2), 81-93. [http://dx.doi.org/10.1016/0013-7952\(94\)90026-4](http://dx.doi.org/10.1016/0013-7952(94)90026-4).
- Favre, R., & Kamal, G.M. (2004). *Watershed atlas of Afghanistan: working document for planners* (2 Vols.). Kabul: Afghanistan Information Management Services.
- Ghafoori, M., Lashkaripour, G.R., & Azali, S.T. (2011). Investigation of the geological and geotechnical characteristics of Daroongar Dam Northeast Iran. *Geotechnical and Geological Engineering*, 29(6), 961-975. <http://dx.doi.org/10.1007/s10706-011-9429-6>.
- Ghobadi, M.H., Khanlari, G.R., & Djalali, H. (2005). Seepage problems in the right abutment of the Shahid Abbaspour Dam, Southern Iran. *Engineering Geology*, 82(2), 119-126. <http://dx.doi.org/10.1016/j.enggeo.2005.09.002>.
- Goodman, R.E. (1989). *Introduction to rock mechanics* (Vol. 2). Wiley.
- Haftani, M., Gheshmipour, A.A., Mehinrad, A., & Binazadeh, K. (2014). Geotechnical characteristics of Bakhtiary dam site, SW Iran: the highest double-curvature dam in the world. *Bulletin of Engineering Geology and the Environment*, 73(2), 479-492. <http://dx.doi.org/10.1007/s10064-013-0498-z>.
- Heidari, F. (2000). *Evaluation of engineering geology and geotechnical issues Karun 2, Axis A3* [Unpublished master's dissertation]. University of Isfahan (in Persian).
- Kocbay, A., & Kilic, R. (2006). Engineering geological assessment of the Obruk dam site (Corum, Turkey). *Engineering Geology*, 87(3-4), 141-148. <http://dx.doi.org/10.1016/j.enggeo.2006.04.005>.
- Lashkaripour, G.R., & Ghafoori, M. (2002). The engineering geology of the Tabarak Abad Dam. *Engineering Geology*, 66(3-4), 233-239. [http://dx.doi.org/10.1016/S0013-7952\(02\)00044-3](http://dx.doi.org/10.1016/S0013-7952(02)00044-3).
- Oliveira, R. (1979). Engineering geological problems related to the study, design and construction of dam foundations. *Bulletin of the International Association of Engineering Geology*, 20(1), 4-7. <http://dx.doi.org/10.1007/BF02591232>.
- Romanov, D., Gabrovšek, F., & Dreybrodt, W. (2003). Dam sites in soluble rocks: a model of increasing leakage by dissolutional widening of fractures beneath a dam. *Engineering Geology*, 70(1-2), 17-35. [http://dx.doi.org/10.1016/S0013-7952\(03\)00073-5](http://dx.doi.org/10.1016/S0013-7952(03)00073-5).
- Stewart, A.K. (2016). Dams in Afghanistan. In J. Shroder & S. J. Ahmadzai, *Transboundary water resources in Afghanistan* (pp. 213-268). Elsevier. <https://doi.org/10.1016/B978-0-12-801886-6.00009-4>.
- Tortajada, C., & Biswas, A.K. (2014). Infrastructure and development, an editorial. *International Journal of Water Resources Development*, 30(1), 3-7. <http://doi.org/10.1080/07900627.2014.891927>.

- Unal, B., Eren, M., & Yalcin, M.G. (2007). Investigation of leakage at Ataturk dam and hydroelectric power plant by means of hydrometric measurements. *Engineering Geology*, 93(1-2), 45-63. <http://doi.org/10.1016/j.enggeo.2007.02.006>.
- Uromeihy, A., & Farrokhi, R. (2012). Evaluating groutability at the Kamal-Saleh Dam based on Lugeon tests. *Bulletin of Engineering Geology and the Environment*, 71(2), 215-219. <http://doi.org/10.1007/s10064-011-0382-7>.
- Vaskou, P., Quadros, E.F., Kanji, M.A., Johnson, T., & Ekmekci, M. (2019). ISRM suggested method for the lugeon test. *Rock Mechanics and Rock Engineering*, 52(10), 4155-4174. <http://doi.org/10.1007/s00603-019-01954-x>.



- > **Prospecção Geotécnica**
Site Investigation
- > **Consultoria Geotécnica**
Geotechnical Consultancy
- > **Obras Geotécnicas**
Ground Treatment-Construction Services
- > **Controlo e Observação**
Field Instrumentation Services and Monitoring Services
- > **Laboratório de Mecânica de Solos**
Soil and Rock Mechanics Laboratory

Certificada ISO 9001 por



Geocontrolo



Parque Oriente, Bloco 4, EN10
2699-501 Bobadela LRS
Tel. 21 995 80 00
Fax. 21 995 80 01
e.mail: mail@geocontrole.pt
www.geocontrole.pt


Geocontrolo
Geotecnia e Estruturas de Fundação SA

BELGO GABION. THE BEST CHOICE TO INCREASE YOUR CONSTRUCTION QUALITY.



Belgo Geotech provides steel solutions, for geotechnical applications, to the market. Our products include **gabions**, **rockfall mesh**, **Dramix®** steel fibers, **galvanized pannels** and **meshes for rock support** and **reinforcement systems**, **PC Strand for cable bolts** and **thread bars**. We also offer qualified technical support to meet all of your project's needs. **Our geotechnics feature the strength of steel.**



Learn more at: belgogeotech.com.br

BELGO
GeoTech

Belgo Bekaert Arames

ArcelorMittal

BEKAERT
better together

BUILDING THE WORLD, BETTER



ENGINEERING AND ARCHITECTURAL CONSULTANCY

- > GEOLOGY, GEOTECHNICS, SUPERVISION OF GEOTECHNICAL WORKS
- > EMBANKMENT DAMS, UNDERGROUND WORKS, RETAINING STRUCTURES
- > SPECIAL FOUNDATIONS, SOIL IMPROVEMENT, GEOMATERIALS

DF+, YOUR TRUST FIRST

**GEOLOGICAL, GEOTECHNICAL
ENGINEERING AND WATER
RESOURCES SOLUTIONS FOR THE
MINING SECTOR AND OTHERS.**



DF+ IS A COMPANY WITH A FOCUS ON THE MINERAL SECTOR AND MORE THAN 15 YEARS OF EXPERIENCE. WE OPERATE IN ALL PHASES OF A PROJECT, FROM FEASIBILITY STUDIES AND PROJECT DEVELOPMENT TO TECHNICAL MONITORING OF CONSTRUCTION AND MINE CLOSURE.

**JOIN OUR SOCIAL NETWORKS TO
KNOW MORE ABOUT OUR SERVICES.**



AVE BARÃO HOMEM DE MELO, 4554 - 5th floor
ESTORIL, BELO HORIZONTE/MG

+55 31 2519-1001

comercial@dfmais.eng.br



**DF+ GEOTECHNICAL ENGINEERING
AND WATER RESOURCES**

PIONEERING AND INNOVATION

SINCE 1921

 **TEIXEIRA DUARTE**
ENGENHARIA E CONSTRUÇÕES, S.A.

PORT FACILITY CONSTRUCTION
NACALA - MOZAMBIQUE



Building a better world.
teixiraduarteconstruction.com



Safety is our nature

SISTEMAS DE ALERTA E MONITORAMENTO

Sistemas de Alerta e Alarme

Ideal para identificação de agentes
deflagradores e monitoramento de
eventos

Rua Visconde de Pirajá, 82 | Ipanema
22410-003 | Rio de Janeiro | RJ | Brasil.
Tel.: + 55 21 3624.1449
www.geobruigg.com



Parceria:



The Best Solution!

Tecnilab Portugal, S.A. will provide you with answers to your Geotechnical engineering needs.

Tecnilab Portugal, S.A. is a professional Geotechnical engineering company and has a lot of experience as a professional group that mainly engages in measurement engineering in dam, subway(Metro), harbor, power plant, soft ground and structure construction.

WE ARE THE DISTRIBUTOR OF PORTUGAL OF ACE INSTRUMENT CO., LTD. IN KOREA.

ACE INSTRUMENT CO., LTD. is a company that obtains worldwide reputation for supplying high precision, high reliability products in all Geotechnical instruments, data logger and in-situ test equipments. Independently developed automatic monitoring system can be used anywhere in the world, including buildings, bridges, ground and any constructions.

Data Acquisition System & Web Monitoring Program



Sales company



Tecnilab Portugal, S.A.

A: Rua Gregorio Lopes, Lote 1512B 1449-041 Lisboa Portugal

T: +351 217 220 870 F: +351 217 264 550

www.tecnilab.pt

Manufacturer



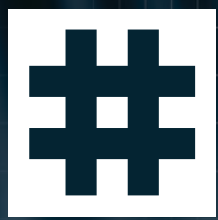
ACE INSTRUMENT CO., LTD.

The first value in Geotechnical & Structural Instrumentation

A: 9, Dangjung-ro 27 beon-gil, Gunpo-si, Gyeonggi-do, Korea

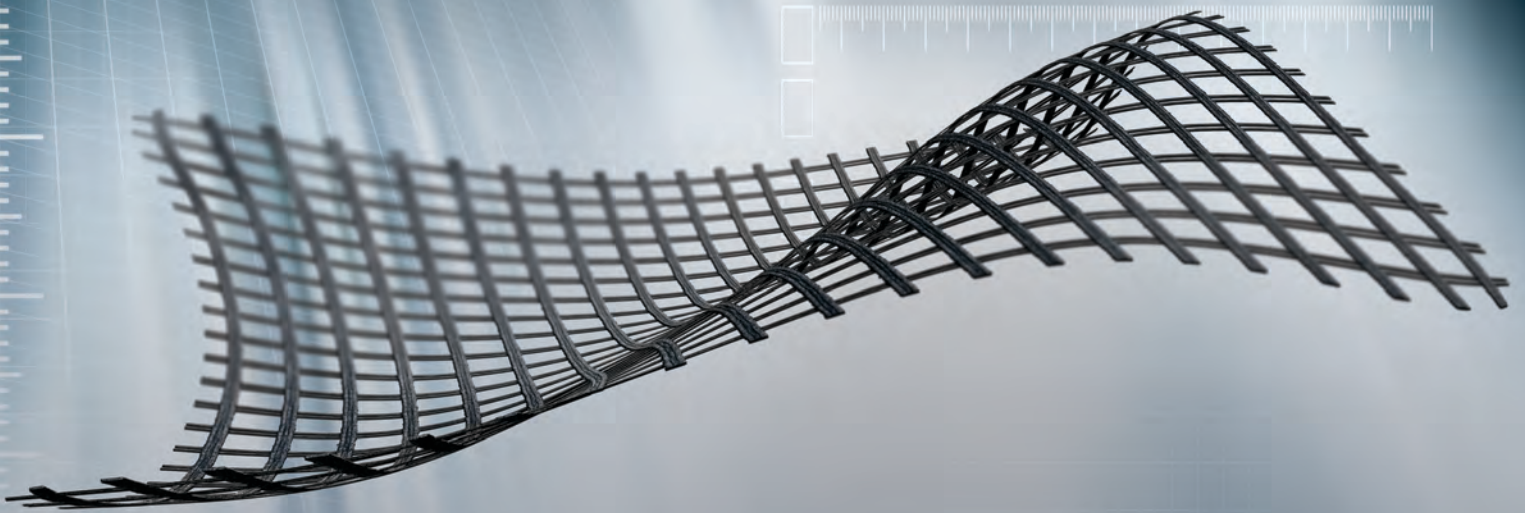
T: +82 31 459 8753-7 F: +82 31 459 8758 E: acens@naver.com

www.aceinstrument.com



HUESKER

Ideen. Ingenieure. Innovationen.



LEADER IN GEOSYNTHETICS

Experience HUESKER's geosynthetic building materials, systems and services now.



www.HUESKER.com

Find HUESKER in Social Media:



ENGINEERING AND ENVIRONMENTAL CONSULTANTS



COBA



GEOLOGY AND GEOTECHNICS

Hydrogeology • Engineering Geology • Rock Mechanics • Soil Mechanics • Foundations and Retaining Structures • Underground Works • Embankments and Slope Stability
Environmental Geotechnics • Geotechnical Mapping



- Water Resources Planning and Management
- Hydraulic Undertakings
- Electrical Power Generation and Transmission
- Water Supply Systems and Pluvial and Wastewater Systems
- Agriculture and Rural Development
- Road, Railway and Airway Infrastructures
- Environment
- Geotechnical Structures
- Cartography and Cadastre
- Safety Control and Work Rehabilitation
- Project Management and Construction Supervision



PORTUGAL

CENTER AND SOUTH REGION
Av. 5 de Outubro, 323
1649-011 LISBOA
Tel.: (351) 210125000, (351) 217925000
Fax: (351) 217970348
E-mail: coba@coba.pt
www.coba.pt

Av. Marquês de Tomar, 9, 6º.
1050-152 LISBOA
Tel.: (351) 217925000
Fax: (351) 213537492

NORTH REGION

Rua Mouzinho de Albuquerque, 744, 1º.
4450-203 MATOSINHOS
Tel.: (351) 229380421
Fax: (351) 229373648
E-mail: engico@engico.pt

ANGOLA

Praceta Farinha Leitão, edifício nº 27, 27-A - 2º Dto
Bairro do Maculusso, LUANDA
Tel./Fax: (244) 222338 513
Cell: (244) 923317541
E-mail: coba-angola@netcabo.co.ao

MOZAMBIQUE

Pestana Rovuma Hotel. Centro de Escritórios.
Rua da Sé nº114. Piso 3, MAPUTO
Tel./Fax: (258) 21 328 813
Cell: (258) 82 409 9605
E-mail: coba.mz@tdm.co.mz

ALGERIA

09, Rue des Frères Hocine
El Biar - 16606, ARGEL
Tel.: (213) 21 922802
Fax: (213) 21 922802
E-mail: coba.alger@gmail.com

BRAZIL

Rio de Janeiro
COBA Ltd. - Rua Bela 1128
São Cristóvão
20930-380 Rio de Janeiro RJ
Tel.: (55 21) 351 50 101
Fax: (55 21) 258 01 026

Fortaleza

Av. Senador Virgílio Távora 1701, Sala 403
Aldeota - Fortaleza CEP 60170 - 251
Tel.: (55 85) 3261 17 38
Fax: (55 85) 3261 50 83
E-mail: coba@esc-te.com.br

UNITED ARAB EMIRATES

Corniche Road - Corniche Tower - 5th Floor - 5B
P. O. Box 38360 ABU DHABI
Tel.: (971) 2 627 0088
Fax: (971) 2 627 0087

MACCAFERRI

Learn more about **GAWAC® 3.0 software**

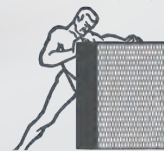
Developed to support engineers, designers and students in a fast and reliable way to perform the analyzes of gabion retaining wall.

The great advantage of **GAWAC® 3.0** is the inclusion of the stability analysis in serviceability conditions, through the GSC (Gabion Serviceability Coefficient). This type of analysis allows the user to evaluate the cross sections of the gabion walls in the most suitable conditions through the best performance and optimization of the gabion materials. The software allows the user to choose the type of gabion with the coating and mesh technologically appropriate to the work environment, in addition to allowing the use of international standards, various calculation analyzes with a detailed printable report.



NEW SOFTWARE FEATURES

- **New user-friendly** interface;
- Consider the **influence of the mesh**;
- **Service Limit State (SLS) and Ultimate Limit State (ULS)** are considered in the stability analysis;
- Consider the **long-term performance of the gabion** based on the type of mesh and coating;
- **Serviceability conditions** performed by layer;
- Optimized design with the use of **Strong Face Gabion**.



**GABION
STRONG
FACE**



Visit our website to **learn more**
about Strong Face Gabion and
download **GAWAC® 3.0**.



/maccaferri



/maccaferrimatrix



@Maccaferri_BR



/MaccaferriWorld



/maccaferriworld



The Ground is our Challenge

MAIN ACTIVITY AREAS

Consultancy, Supervision and Training

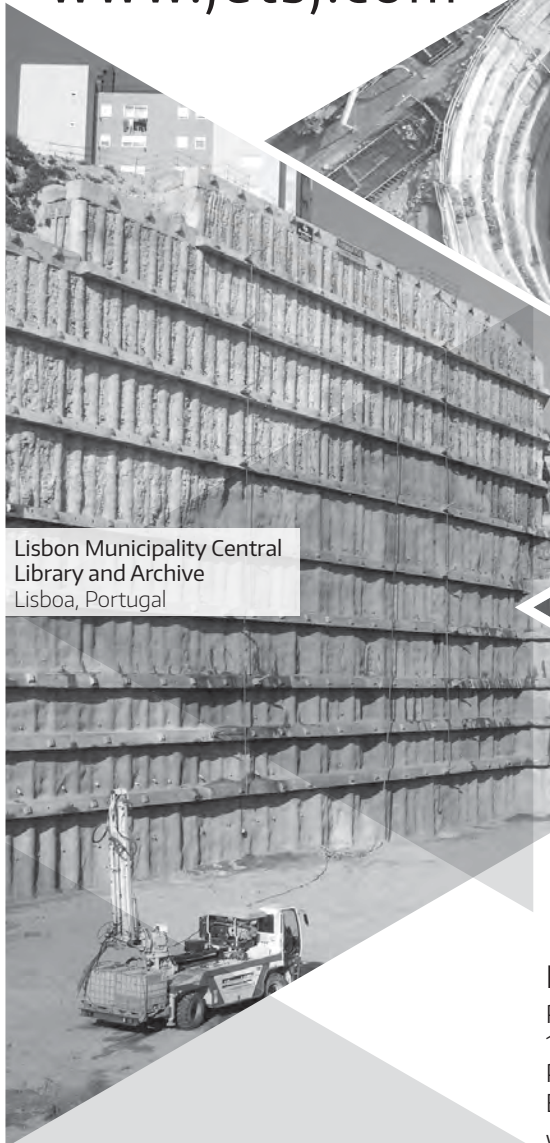
- Earth Retaining Structures
- Special Foundations
- Ground Improvement
- Foundations Strengthening and Underpinning
- Façades Retention
- Tunnels and Underground Structures
- Slope Stability
- Geological and Geotechnical Investigation
- Demolition

www.jetsj.com



Tool Plazas P2 and P3
Santa Catarina, Brazil

Mining Shaft
Kamsar, Guiné



Lisbon Municipality Central
Library and Archive
Lisboa, Portugal



Solar Santana Building
Lisboa, Portugal

Main Office

Rua Julieta Ferrão, 12 - Office 1501

1600-131 LISBOA, Portugal

Phone.: [+351] 210 505 150 / 51

Email: info@jetsj.com

www.linkedin.com/company/jetsj-geotecnia-lda/

Guide for Authors

Soils and Rocks is an international scientific journal published by the Brazilian Association for Soil Mechanics and Geotechnical Engineering (ABMS) and by the Portuguese Geotechnical Society (SPG). The aim of the journal is to publish original papers on all branches of Geotechnical Engineering. Each manuscript is subjected to a single-blind peer-review process. The journal's policy of screening for plagiarism includes the use of a plagiarism checker on all submitted manuscripts.

Soils and Rocks embraces the international Open Science program and is striving to meet all the recommendations. However, at this moment, the journal is not yet accepting preprints and open data, and has not adopted open peer reviews.

Soils and Rocks provides a manuscript template available at the journal's website.

1. Category of papers

Submissions are classified into one of the following categories:

Article – an extensive and conclusive dissertation about a geotechnical topic, presenting original findings.

Technical Note – presents a study of smaller scope or results of ongoing studies, comprising partial results and/or particular aspects of the investigation.

Case Study – report innovative ways to solve problems associated with design and construction of geotechnical projects. It also presents studies of the performance of existing structures.

Review Article – a summary of the State-of-the-Art or State-of-the-Practice on a particular subject or issue and represents an overview of recent developments.

Discussion – specific discussions about published papers.

Authors are responsible for selecting the correct category when submitting their manuscript. However, the manuscript category may be altered based on the recommendation of the Editorial Board. Authors are also requested to state the category of paper in their Cover Letter.

When submitting a manuscript for review, the authors should indicate the category of the manuscript, and is also understood that they:

- a) assume full responsibility for the contents and accuracy of the information in the paper;
- b) assure that the paper has not been previously published, and is not being submitted to any other journal for publication.

2. Paper length

Full-length manuscripts (Article, Case Study) should be between 4,000 and 8,000 words. Review articles should have up to 10,000 words. Technical Notes have a word count limit of 3,500 words. Discussions have a word count limit of 1,000 words. These word count limits exclude the title page, notation list (e.g., symbols, abbreviations), captions of tables and figures, acknowledgments and references. Each single column and double column figure or table is considered as equivalent to 150 and 300 words, respectively.

3. Scientific style

The manuscripts should be written in UK or US English, in the third person and all spelling should be checked in accordance with

a major English Dictionary. The manuscript should be able to be readily understood by a Civil Engineer and avoid colloquialisms. Unless essential to the comprehension of the manuscript, direct reference to the names of persons, organizations, products or services is not allowed. Flattery or derogatory remarks about any person or organization should not be included.

The author(s) of Discussion Papers should refer to himself (herself/themselves) as the reader(s) and to the author(s) of the paper as the author(s).

The International System (SI) units must be used. The symbols are recommended to be in accordance with Lexicon in 14 Languages, ISSMFE (2013) and the ISRM List of Symbols. Use italics for single letters that denote mathematical constants, variables, and unknown quantities, either in tables or in the text.

4. Submission requirements and contents

A submission implies that the following conditions are met:

- the authors assume full responsibility for the contents and accuracy of the information presented in the paper;
- the manuscript contents have not been published previously, except as a lecture or academic thesis;
- the manuscript is not under consideration for publication elsewhere;
- the manuscript is approved by all authors;
- the manuscript is approved by the necessary authorities, when applicable, such as ethics committees and institutions that may hold intellectual property on contents presented in the manuscript;
- the authors have obtained authorization from the copyright holder for any reproduced material;
- the authors are aware that the manuscript will be subjected to plagiarism check.

The author(s) must upload two digital files of the manuscript to the Soils and Rocks submission system. The size limit for each submission file is 20 MB. The manuscript should be submitted in docx format (Word 2007 or higher) or doc format (for older Word versions). An additional PDF format file of the manuscript is also required upon submission. Currently, the journal is not accepting manuscripts prepared using LaTeX.

The following documents are required as minimum for submission:

- cover letter;
- manuscript with figures and tables embedded in the text (doc or docx format);

manuscript with figures and tables embedded in the text for revision (PDF format);

- permission for re-use of previously published material when applicable, unless the author/owner has made explicit that the image is freely available.

4.1 Cover letter

The cover letter should include: manuscript title, submission type, authorship information, statement of key findings and work novelty, and related previous publications if applicable.

4.2 Title page

The title page is the first page of the manuscript and must include:

- A concise and informative title of the paper. Avoid abbreviations, acronyms or formulae. Discussion Papers should contain the title of the paper under discussion. Only the first letter of the first word should be capitalized.
- Full name(s) of the author(s). The first name(s) should not be abbreviated. The authors are allowed to abbreviate middle name(s).
- The corresponding author should be identified by a pound sign # beside his/her and in a footnote.
- The affiliation(s) of the author(s), should follow the format: Institution, (Department), City, (State), Country.
- Affiliation address and e-mail must appear below each author's name.
- The 16-digit ORCID of the author(s) – mandatory
- Main text word count (excluding abstract and references) and the number of figures and tables

4.3 Permissions

Figures, tables or text passages previously published elsewhere may be reproduced under permission from the copyright owner(s) for both the print and online format. The authors are required to provide evidence that such permission has been granted at the moment of paper submission.

4.4 Declaration of interest

Authors are required to disclose conflicting interests that could inappropriately bias their work. For that end, a section entitled “Declaration of interest” should be included following any acknowledgments and prior to the “Authors’ contributions” section. In case of the absence of conflicting interests, the authors should still include a declaration of interest.

4.5 Authors’ contributions

Authors are required to include an author statement outlining their individual contributions to the paper according to the CASRAI CRediT roles (as per <https://casrai.org/credit>). The minimum requirements of contribution to the work for recognition of authorship are: a) Participate actively in the discussion of results; b) Review and approval of the final version of the manuscript. A section entitled “Authors’ contributions” should be included after the declaration of interest section, and should be formatted with author's name and CRediT role(s), according to the example:

Samuel Zheng: conceptualization, methodology, validation. **Olivia Prakash:** data curation, writing - original draft preparation. **Fatima Wang:** investigation, validation. **Kwame Bankole:** supervision. **Sun Qi:** writing - reviewing and editing.

Do not include credit items that do not follow the Taxonomy established by CASRAI CRediT roles.

The authors’ contributions section should be omitted in manuscripts that have a single author.

5. Plagiarism checking

Submitted papers are expected to contain at least 50 % new content and the remaining 50 % should not be verbatim to previously published work.

All manuscripts are screened for similarities. Currently, the Editorial Board uses the plagiarism checker Plagius (www.plagius.com) to compare submitted papers to already published works. Manuscripts will be rejected if more than 20 % of content matches previously published work, including self-plagiarism. The decision to reject will be under the Editors’ discretion if the percentage is between 10 % and 20 %.

IMPORTANT OBSERVATION: Mendeley software plug-in (suggested in this guide) for MS-Word can be used to include the references in the manuscript. This plug-in uses a field code that sometimes includes automatically both title and abstract of the reference. Unfortunately, the similarity software adopted by the Journal (Plagius) recognizes the title and abstract as an actual written text by the field code of the reference and consequently increases considerably the percentage of similarity. Please do make sure to remove the abstract (if existing) inside Mendeley section where the adopted reference is included. This issue has mistakenly caused biased results in the past. The Editorial Board of the journal is now aware of this tendentious feature.

6. Formatting instructions

The text must be presented in a single column, using ISO A4 page size, left, right, top, and bottom margins of 25 mm, Times New Roman 12 font, and line spacing of 1.5. All lines and pages should be numbered.

The text should avoid unnecessary italic and bold words and letters, as well as too many acronyms. Authors should avoid to capitalize words and whenever possible to use tables with distinct font size and style of the regular text.

Figures, tables and equations should be numbered in the sequence that they are mentioned in the text.

Abstract

Please provide an abstract between 150 and 250 words in length. Abbreviations or acronyms should be avoided. The abstract should state briefly the purpose of the work, the main results and major conclusions or key findings.

Keywords

A minimum of three and a maximum of six keywords must be included after the abstract. The keywords must represent the

content of the paper. Keywords offer an opportunity to include synonyms for terms that are frequently referred to in the literature using more than one term. Adequate keywords maximize the visibility of your published paper.

Examples:

Poor keywords – piles; dams; numerical modeling; laboratory testing

Better keywords – friction piles; concrete-faced rockfill dams; material point method; bender element test

List of symbols

A list of symbols and definitions used in the text must be included before the References section. Any mathematical constant, variable or unknown quantity should appear in italics.

6.1 Citations

References to other published sources must be made in the text by the last name(s) of the author(s), followed by the year of publication. Examples:

- Narrative citation: [...] while Silva & Pereira (1987) observed that resistance depended on soil density
- Parenthetical citation: It was observed that resistance depended on soil density (Silva & Pereira, 1987).

In the case of three or more authors, the reduced format must be used, e.g.: Silva et al. (1982) or (Silva et al., 1982). Do not italicize “et al.”

Two or more citations belonging to the same author(s) and published in the same year are to be distinguished with small letters, e.g.: (Silva, 1975a, b, c.).

Standards must be cited in the text by the initials of the entity and the year of publication, e.g.: ABNT (1996), ASTM (2003).

6.2 References

A customized style for the Mendeley software is available and may be downloaded from this link.

Full references must be listed alphabetically at the end of the text by the first author’s last name. Several references belonging to the same author must be cited chronologically.

Some formatting examples are presented here:

Journal Article

Bishop, A.W., & Blight, G.E. (1963). Some aspects of effective stress in saturated and partly saturated soils. *Géotechnique*, 13(2), 177-197. <https://doi.org/10.1680/geot.1963.13.3.177>

Castellanza, R., & Nova, R. (2004). Oedometric tests on artificially weathered carbonatic soft rocks. *Journal of Geotechnical and Geoenvironmental Engineering*, 130(7), 728-739. [https://doi.org/10.1061/\(ASCE\)1090-0241\(2004\)130:7\(728\)](https://doi.org/10.1061/(ASCE)1090-0241(2004)130:7(728))

Fletcher, G. (1965). Standard penetration test: its uses and abuses. *Journal of the Soil Mechanics Foundation Division*, 91, 67-75.

Indraratna, B., Kumara, C., Zhu S-P., Sloan, S. (2015). Mathematical modeling and experimental verification of fluid flow through deformable rough rock joints. *International Journal of Geomechanics*, 15(4): 04014065-1-04014065-11. [https://doi.org/10.1061/\(ASCE\)GM.1943-5622.0000413](https://doi.org/10.1061/(ASCE)GM.1943-5622.0000413)

Garnier, J., Gaudin, C., Springman, S.M., Culligan, P.J., Goodings, D., Konig, D., ... & Thorel, L. (2007). Catalogue of scaling laws and similitude questions in geotechnical centrifuge modelling. *International Journal of Physical Modelling in Geotechnics*, 7(3), 01-23. <https://doi.org/10.1680/ijpmg.2007.070301>

Bicalho, K.V., Gramelich, J.C., & Santos, C.L.C. (2014). Comparação entre os valores de limite de liquidez obtidos pelo método de Casagrande e cone para solos argilosos brasileiros. *Comunicações Geológicas*, 101(3), 1097-1099 (in Portuguese).

Book

Lambe, T.W., & Whitman, R.V. (1979). *Soil Mechanics, SI version*. John Wiley & Sons.

Das, B.M. (2012). *Fundamentos de Engenharia Geotécnica*. Cengage Learning (in Portuguese).

Head, K.H. (2006). *Manual of Soil Laboratory Testing - Volume 1: Soil Classification and Compaction Tests*. Whittles Publishing.

Bhering, S.B., Santos, H.G., Manzatto, C.V., Bognola, I., Fasolo, P.J., Carvalho, A.P., ... & Curcio, G.R. (2007). *Mapa de solos do estado do Paraná*. Embrapa (in Portuguese).

Book Section

Yerro, A., & Rohe, A. (2019). Fundamentals of the Material Point Method. In *The Material Point Method for Geotechnical Engineering* (pp. 23-55). CRC Press. <https://doi.org/10.1201/9780429028090>

Sharma, H.D., Dukes, M.T., & Olsen, D.M. (1990). Field measurements of dynamic moduli and Poisson’s ratios of refuse and underlying soils at a landfill site. In *Geotechnics of Waste Fills - Theory and Practice* (pp. 57-70). ASTM International. <https://doi.org/10.1520/STP1070-EB>

Cavalcante, A.L.B., Borges, L.P.F., & Camapum de Carvalho, J. (2015). Tomografias computadorizadas e análises numéricas aplicadas à caracterização da estrutura porosa de solos não saturados. In *Solos Não Saturados no Contexto Geotécnico* (pp. 531-553). ABMS (in Portuguese).

Proceedings

Jamiolkowski, M.; Ladd, C.C.; Germaine, J.T., & Lancellotta, R. (1985). New developments in field and laboratory testing of soils. *Proc. 11th International Conference on Soil Mechanics and Foundation Engineering*, San Francisco, August 1985. Vol. 1, Balkema, 57-153.

Massey, J.B., Irfan, T.Y. & Cipullo, A. (1989). The characterization of granitic saprolitic soils. *Proc. 12th International Conference on Soil Mechanics and Foundation Engineering*, Rio de Janeiro. Vol. 6, Publications Committee of XII ICSMFE, 533-542.

Indraratna, B., Oliveira D.A.F., & Jayanathan, M. (2008b). Revised shear strength model for infilled rock joints considering overconsolidation effect. *Proc. 1st Southern Hemisphere International Rock Mechanics Symposium*, Perth. ACG, 16-19.

Barreto, T.M., Repsold, L.L., & Casagrande, M.D.T. (2018). Melhoramento de solos arenosos com polímeros. *Proc. 19º Congresso Brasileiro de Mecânica dos Solos e Engenharia Geotécnica*, Salvador. Vol. 2, ABMS, CBMR, ISRM & SPG, 1-11 (in Portuguese).

Thesis

Lee, K.L. (1965). *Triaxial compressive strength of saturated sands under seismic loading conditions* [Unpublished doctoral dissertation]. University of California at Berkeley.

Chow, F.C. (1997). *Investigations into the behaviour of displacement pile for offshore foundations* [Doctoral thesis, Imperial College London]. Imperial College London's repository. <https://spiral.imperial.ac.uk/handle/10044/1/7894>

Araki, M.S. (1997). *Aspectos relativos às propriedades dos solos porosos colapsáveis do Distrito Federal* [Unpublished master's dissertation]. University of Brasília (in Portuguese).

Sotomayor, J.M.G. (2018). *Evaluation of drained and non-drained mechanical behavior of iron and gold mine tailings reinforced with polypropylene fibers* [Doctoral thesis, Pontifical Catholic University of Rio de Janeiro]. Pontifical Catholic University of Rio de Janeiro's repository (in Portuguese). <https://doi.org/10.17771/PUCRio.acad.36102>*

* official title in English should be used when available in the document.

Report

ASTM D7928-17. (2017). Standard Test Method for Particle-Size Distribution (Gradation) of Fine-Grained Soils Using the Sedimentation (Hydrometer) Analysis. *ASTM International*, West Conshohocken, PA. <https://doi.org/10.1520/D7928-17>

ABNT NBR 10005. (2004). Procedure for obtention leaching extract of solid wastes. *ABNT - Associação Brasileira de Normas Técnicas*, Rio de Janeiro, RJ (in Portuguese).

DNIT. (2010). Pavimentação - Base de solo-cimento - Especificação de serviço DNIT 143. *DNIT -Departamento Nacional de Infraestrutura de Transportes*, Rio de Janeiro, RJ (in Portuguese).

USACE (1970). Engineering and Design: Stability of Earth and Rock-Fill Dams, Engineering Manual 1110-2-1902. Corps of Engineers, Washington, D.C.

Web Page

Soils and Rocks. (2020). *Guide for Authors*. Soils and Rocks. Retrieved in September 16, 2020, from <http://www.soilsandrocks.com/>

6.3 Artworks and illustrations

Each figure should be submitted as a high-resolution image, according to the following mandatory requirements:

- Figures must be created as a TIFF file format using LZW compression with minimum resolution of 500 dpi.
- Size the figures according to their final intended size. Single-column figures should have a width of up to 82 mm. Double-column figures should have a maximum width of 170 mm.
- Use Times New Roman for figure lettering. Use lettering sized 8-10 pt. for the final figure size.
- Lines should have 0.5 pt. minimum width in drawings.
- Titles or captions should not be included inside the figure itself.

Figures must be embedded in the text near the position where they are first cited. Cite figures in the manuscript in consecutive numerical order. Denote figure parts by lowercase letters (a, b, c, etc.). Please include a reference citation at the end of the figure caption for previously published material. Authorization from the copyright holder must be provided upon submission for any reproduced material.

Figure captions must be placed below the figure and start with the term "Figure" followed by the figure number and a period. Example:

Figure 1. Shear strength envelope.

Do not abbreviate "Figure" when making cross-references to figures.

All figures are published in color for the electronic version of the journal; however, the print version uses grayscale. Please format figures so that they are adequate even when printed in grayscale.

Accessibility: Please make sure that all figures have descriptive captions (text-to-speech software or a text-to-Braille hardware could be used by blind users). Prefer using patterns (e.g., different symbols for dispersion plot) rather than (or in addition to) colors for conveying information (then the visual elements can be distinguished by colorblind users). Any figure lettering should have a contrast ratio of at least 4.5:1

Improving the color accessibility for the printed version and for colorblind readers: Authors are encouraged to use color figures because they will be published in their original form in the online version. However, authors must consider the need to make their color figures accessible for reviewers and readers that are colorblind. As a general rule of thumb, authors should avoid using red and green simultaneously. Red should be replaced by magenta, vermillion, or orange. Green should be replaced by an off-green color, such as blue-green. Authors should prioritize the use of black, gray, and varying tones of blue and yellow.

These rules of thumb serve as general orientations, but authors must consider that there are multiple types of color blindness, affecting the perception of different colors. Ideally, authors should make use of the following resources: 1) for more information on how to prepare color figures, visit <https://jfly.uni-koeln.de/>; 2) a freeware software available at <http://www.vischeck.com/> is offered by Vischeck, to show how your figures would be perceived by the colorblind.

6.4 Tables

Tables should be presented as a MS Word table with data inserted consistently in separate cells. Place tables in the text near the position where they are first cited. Tables should be numbered consecutively using Arabic numerals and have a caption consisting of the table number and a brief title. Tables should always be cited in the text. Any previously published material should be identified by giving the original source as a reference at the end of the table caption. Additional comments can be placed as footnotes, indicated by superscript lower-case letters.

When applicable, the units should come right below the corresponding column heading. Horizontal lines should be used at the top and bottom of the table and to separate the headings row. Vertical lines should not be used.

Table captions must be placed above the table and start with the term “Table” followed by the table number and a period. Example:

Table 1. Soil properties.

Do not abbreviate “Table” when making cross-references to tables. Sample:

Table 1. Soil properties

Parameter	Symbol	Value
Specific gravity of the sand particles	G_s	2.64
Maximum dry density (Mg/m ³)	$\rho_{d(max)}$	1.554
Minimum dry density (Mg/m ³)	$\rho_{d(min)}$	1.186
Average grain-size (mm)	d_{50}	0.17
Coefficient of uniformity	C_u	1.97

6.5 Mathematical equations

Equations must be submitted as editable text, created using MathType or the built-in equation editor in MS Word. All variables must be presented in italics.

Equations must appear isolated in a single line of the text. Numbers identifying equations must be flushed with the right margin. International System (SI) units must be used. The definitions of the symbols used in the equations must appear in the List of Symbols.

Do not abbreviate “Equation” when making cross-references to an equation.